Luminescent Self-assembled Supramolecular Polymers and Microspheres Based on Benzene-1,3,5-tricarboxamide (BTA) Derivatives

Savyasachi A. J., M.Sc, M.Phil.

April 2017

University of Dublin
Trinity College

Based on research carried out under the direction of
Prof. Thorfinnur Gunnlaugsson

A thesis submitted to the School of Chemistry, University of Dublin, Trinity College for the degree of Doctor of Philosophy

Declaration

This thesis is submitted for the degree of Doctor of Philosophy to the University of Dublin, Trinity College and has not been submitted before for any degree to this or any other university. Other than where acknowledged, all work described herein is original and has been carried out by the author. I agree that the Library may lend or copy this thesis upon request. This permission covers only single copies made for study purposes, subject to normal conditions of acknowledgment.

_____

Savyasachi A. J.

Abstract

This thesis, entitled ‘‘Luminescent Self-assembled Supramolecular Polymers and Microspheres Based on Benzene-1,3,5-tricarboxamide (BTA) Derivatives’’ describes the syntheses and characterisation of a new range of tripodal molecules containing terpyridine binding motif and their various supramolecular self-assembly formation. The thesis is divided into five chapters.

Chapter 1, the introduction, provides an overview of functional supramolecular materials and the various potential mechanisms for their formation, through diverse supramolecular interactions. The relevant literature and recent advances in the self-assembly of tripodal systems in the formation of supramolecular polymers will be reviewed, with a particular focus on soft materials and systems exhibiting gelation. Recent examples of supramolecular gels from low-molecular weight gelators (LMWGs), as well as higher-ordered aggregates, and their various applications are also discussed. Additionally, this chapter provides an overview of the lanthanide metal ions; detailing the advantages of their interesting photophysical properties *etc*. The remainder of the chapter covers a short review of the most relevant examples of supramolecular materials contributed by the Gunnlaugsson group in recent times.

Chapter 2 describes the design and synthesis of a family of tripodal ligands based on the benzene-1,3,5-tricarboxamide (BTA) core bearing chiral centres, incorporated using a range of amino acids and the terpyridine functionality at the periphery. The europium Eu(III)- directed self-assembly of a pair of enantiomers in solution at two different ligand concentrations are studied through spectroscopic titrations using techniques such as UV-visible absorption, fluorescence and phosphorescence spectroscopy. The titration data was then analysed using non-linear regression fitting (using SPECFIT®) to determine the speciation and relative stability (global stability constants, logβ) for the formation of various self-assembled supramolecular structures at different concentration. The formation of 1:1, 2:1 and 3:1 (M:L) species formed at lower concentration ($C_L = 5 \times 10^{-6}$ M) and 1:1 and 3:2 (M:L) species formed at higher concentration ($C_L = 1 \times 10^{-6}$ M) was observed.

Chapter 3 then focusses on the self-assembly properties of the synthesised BTA molecules described in Chapter 2 for the formation of gels and higher-ordered aggregates (such as microspheres). The analysis of the gels using scanning electron microscopy (SEM), transmission electron microscopy (TEM) and rheology measurements are presented. The

properties of the microspheres using various microscopic techniques such as SEM, TEM, Helium Ion Beam microscope (HIB), and focussed-ion beam (FIB) microscopy are discussed. Furthermore, the mechanism of the formation of the microspheres and formation of interesting morphologies formed upon addition of Ln(III) (Ln = Eu(III) and Tb(III)) salts to the solution of microspheres are presented. The chapter concludes with the investigation of the mechanical strength using atomic force microscopy (AFM) and thermal stability of the microsphere formations, in addition to the self-sorting behaviour of these tripodal compounds.

Chapter 4 describes the investigations of the microspheres using laser-scanning confocal microscopy (LSCM). The static imaging of the fluorescent microspheres and the real-time imaging of the formation of microspheres in solution are described. Ln(III) containing luminescent microspheres formed upon addition of Ln(III) salts (Ln = Eu and Tb) to the pre-formed organic microspheres are discussed. These luminescent microparticles are also investigated for their CPL emission.

Finally, Chapter 5 gives the experimental details and procedures for the work carried out in the preceding chapters. Following this, literature references and supplementary data and spectra are provided in the appendices.

Acknowledgements

First and foremost, I would like to sincerely thank my supervisor Prof. Thorri Gunnlaugsson for his patient guidance, constant support and enthusiasm over the past four and half years and for welcoming me to Trinity College. I am truly grateful for all your advice and motivation given to mentor me during tough times.

I sincerely thank to Prof. John Boland, CRANN, Trinity College, for co-supervising me and helping me in performing microscopic experiments. Many of the results presented in this thesis, could not have been achieved without your guidance during my PhD.

I thank Prof. Clive Williams, School of Biochemistry, Trinity College, Dublin for helping me in joining Trinity College.

I must also thank our collaborator Dr. Robert Pal, Department of Chemistry, Durham, University, UK, for all the help to carry out the optical microscopic investigations of the samples particularly discussed in Chapter 4. Many of the results within this thesis could not have been achieved without their input and knowledge.

All the members of staff in the School of Chemistry, especially Dr. John O'Brien, Dr. Manuel Reuther, Dr. Martin Feeney, and Dr. Gary Hessman for their assistance with characterisation.

To all the past, present, and visiting members of the TG group, thanks for all the nice memories. It's been great time working in this place with you guys.

Massive thanks to all the postdocs in the group for being willing to help in dealing many issues. A big thank you for Dr. Oxana Kotova for setting me on the path to chemistry of tripodals. Many useful discussions, ideas and valuable suggestions with you helped me assemble this thesis. Thanks Oxana, for that and for helping in experiments and many microscopy sessions which helped to gain so much of results and tricky images shown throughout this thesis. Dr. Emma Veale, Thank you for valuable suggestions for experiments, synthetic procedures and corrections. Dr. Sandra Bright, thank you for all your help with confocal microscopy imaging and experiments. A big thank you for Shaun Mills for all the AFM measurements on the samples. Dr. Ciaran O'Reilly, for the discussions which made my experimental procedures simpler. Dr. Shanmugaraju, thanks for the suggestions and tips for making things easier with the experiments and also for keeping me updated with things happening back home. Dr. Dawn Barry, thanks for all the discussions and suggestions on the microparticles. Dr. Chris Hawes, thanks for useful recommendations and tips on experiments, which saved lot of time. Dr. Gearoid O'Maille, thanks for all the

helping in organising things. Dr. Esther Surrender, you have been a good friend from the beginning, thanks for all the memories. Dr Fergus Poynton, thanks for all the help and talks on synthesis and purification techniques. My thanks too to previous postdocs; Dr. Steve Comby, for the valuable conversation on the measurements and others. I also thank Dr. Johnathan Kitchen, Dr. Komala Pandurangan, Dr. Jenn Jones, Dr. Miguel Martinez-Calvo, for sharing their expertise and experience.

To those I watched pass through the lab before me Dr David Caffrey, Dr Joseph Byrne, thanks for the memories. To all the PhD crew; Sam Bradberry and Dr Helen Burke, my fourth year buddies, thanks for all the helpful conversations and good times and memories in the lab, during course work and outside as well. Eoin McCarney, Bjørn la Cour Poulsen, Anna Aletti you guys have been a good friends from the start, thanks for all the beautiful times we had in our corner in the office. It was a pleasure sharing bench with you guys, thanks for the memories. Amy Lynes, Dermot Gillen, Sandra Estalayo, Elena Calatrava, you guys make it a pleasure to work in place like this and thank you for willing to read anything. Guys who recently started; Bruno D'Agostino, Hannah Dalton, Isabel Hegarty, Jason Delente, Emanule Cappello, enjoy the rest of your time in the group. All you people have made my PhD a memorable experience.

Massive thanks to friends in Dublin over the past few years, flatmates and others. You guys have always given me things outside the lab to look forward, which kept me active and keep going. Thanks for all the nice memories.

Finally, I thank my family; parents, grandparents, aunt(s), uncle(s), brother, cousins, you all have given me an unconditional support for everything I ever needed. I could not have come this far without you people behind me. Thank you for your everlasting love and continuous inspiration. I will always be truly grateful.

Abbreviations

1D	one dimensional
2D	two dimensional
3D	three dimensional
AFM	Atomic Force Microscope
Ar	antenna
Ar	Antenna ground state
AuNPs	gold nanoparticles
BCP	block copolymer
bpy	2,2'-bipyridine
br	Broad
BTA	1,3,5-benzenetricarboxamide
BTAC	BTA connected to ethyl cinnamate
CB[8]	Cucurbit[8]uril
CD	Circular Dichroism
CDSA	crystallization driven self-assembly
CGC	Critical gelation concentration
cm	Centimetre
CPL	Circularly polarised light
CTAT	cetyltrimethylammonium tosylate
d	Doublet
DLS	Dynamic Light Scattering
DMPC	dimyristoylphosphatidylcholine
DNA	Deoxyribonucleic acid
ε	Molar absorption coefficient
E	Energy
EDCI	N-ethyl-N′-(3-dimethylaminopropyl)carbodiimide
EDX	Energy-dispersive X-ray
EPL	Elliptically polarised light
equiv.	Equivalents
ET	energy transfer
FIB	Focused ion beam
FOV	Field of view
FITC-dextran	fluorescein isothiocyanate–labeled dextran
G′	storage modulus (solid like behaviour of gel)
G″	loss modulus (liquid like behaviour of gel)
GdL	glucono-δ-lactone
g_{lum}	Dissymmetry factor values
H	hydrophobic
HA	hydroxyapatite
HBC	hexa-peri-hexabenzocaronine
HL	Helical light
HOBt	1-hydroxybenzotriazole

hν	Energy (photon)
$h\nu_{ex}$	Excitation energy
ICP	infinite coordination polymer
ISC	intersystem crossing
ISEs	induced secondary electrons
K	Kelvin
kJ	Kilojoules
$kJmol^{-1}$	kilo joules per mole
λ	wavelength
LED	light-emitting diode
LMWG	low molecular weight gelators
Ln	Lanthanide
LSCM	Laser Scanning Confocal Microscopy
M	Molar
m	Multiplet
m.p.	Melting point
m/z	Mass to charge ratio
M:L	Metal to ligand ratio
MALDI	Matrix-assisted laser desorption/ionisation
MCH	methylcyclohexane
mg	Milligrams
MHz	Megahertz
min	Minutes
mL	Millilitre
MLCT	Metal to ligand charge transfer
mM	Millimolar
mm	Millimetre
MM2	Molecular mechanics
mmol	Millimole
MOFs	metal organic frameworks
mol	Mole
MRI	Magnetic resonance imaging
ms	millisecond
mV	Millivolts
µL	Microlitre
µm	Micrometre
µM	Micromolar
µs	Microseconds
NIR	Near Infrared
NMR	Nuclear magnetic resonance
nN	nanonewton
Np	naphthol
NP	Nanoparticle

ns	Nanosecond
NT	nanotubes
o	Ortho
OF	oligofluorene
OLEDs	Organic light emitting diodes
OM	optical microscope or microscopy (as relevant)
OPV	oligo(phenylene vinylene)
P	polar
p	Para
P	Luminescent probe
PA	peptide amphiphile
PEG	Polyethylene glycol
Pery	perylene bisimide
PET	Photo-induced electron transfer
PFS	poly(ferrocenyldimethylsilane)
pH	$-\log[H^+]$
pK_a	$-\log K_a$ (where Ka is the acidity constant)
ppm	Parts per million
Ppy	polypyrrole
ps	Picosecond
q	Quartet
q	Number of metal-bound water molecules
Q	Quencher
q value	hydration state
qu	Quintet
R	Gas constant (8.31×10^{-3} kJ/Kmol)
RNA	Ribonucleic acid
ROI	Region of Interest
RT	Room temperature
S	Electron spin
s	Second or singlet (as relevant)
S_0	Singlet ground state
S_1	First singlet excited state
S_2	Rigidity factor
SDS	sodium dodecyl sulfate
SEM	Scanning Electron Microscopy or microscope (as relevant)
SMLM	Single molecule localisation microscopy
SOPVs	S-oligo(p-phenylene vinylene)s
SPR	Surface Plasmon Resonance
STED	stimulated emission depletion microscopy
t	Time or triplet (as relevant)
T	Temperature
T_1	First triplet excited state

TBA	tetrabutylammonium
TEM	Transmission electron microscopy or microscope (as relevant)
TERS	Tip Enhanced Raman Scattering
TGA	Thermogravimetric analysis
T_{gel}	thermal stability of the gel
TLC	thin layer chromatography
tpy	2,2',6',2''-terpyridine
TRLM	time resolved or time-gated luminescence microscopy
U	Unit of enzyme
Upy	2-ureido-4-pyrimidone moiety
UV	Ultraviolet
UV-vis	Ultraviolet-visible
v/v	Volume to volume ratio
w/v	weight/volume
x	Number of metal-bound N-H oscillators
XRF	X-ray Fluorescence
XRPD	X-ray powder diffraction
δ	Delta
ΔE	Energy difference
ε	Molar absorption coefficient
λ_{em}	Emission wavelength
λ_{ex}	Excitation wavelength
λ_{max}	Maximum absorbance or intensity at corresponding wavelength
τ	Variable time
τ_{D2O}	Lifetime in deuterated water
τ_{H2O}	Lifetime in non-deuterated water
τ_{obs}	Observed lifetime
τ_{rad}	Radiative lifetime
ΔH	enthalpy
μL	microliter
μm	micrometre
μN	micronewton
μs	microsecond

Table of Contents

Abstract……...i
Acknowledgements……...……...iii
Abbreviations……v
Table of Contents……...……...ix

Chapter 1. Introduction

1 Introduction……2
1.1 Functional Supramolecular polymeric materials……4
1.2 Hydrogen bonded supramolecular polymers and gels……..…...14
1.2.1 Self-assembly of benzene-1,3,5-tricarboxamide scaffolds……..15
1.2.2 Self-assembly of 1,3,5-cyclohexyltrisamide-based scaffolds…….....25
1.3 Supramolecular gels from low molecular weight gelators (LMWG) and its applications…….....29
1.4 Self-assembly of molecules to higher ordered aggregates……...38
1.5 Lanthanide metal ions……..44
1.5.1 Properties of lanthanides…….....45
1.5.2 Photophysical properties of the lanthanides……45
1.5.3 Lanthanide luminescent quenching……..48
1.6 Advances in the Gunnlaugsson group……..48
1.7 Work described in this thesis……53

Chapter 2. Europium directed self-assembly studies of tripodal ligands

2 Introduction……..56
2.1 Design and synthesis of chiral tripodal ligands **89 (*R,R,R*)** and **89(*S,S,S)***……..…57
2.2 Complexation and spectroscopic analysis of ligands **89R** and **89*S*** with Eu(III**)**….61
2.3 Mass spectrometric analysis of the ligands **89**R and **89S** and their Eu(III) complexes……63
2.4 Determination of bound water molecules (q values) for **Eu.89R** and **Eu.89S** …...64
2.5 UV-vis absorption and luminescence emission investigation of **89R** and **89S** in solution ……..……..64
2.5.1 UV-**vis absorption titration** of **89 (R** and **S)** with $Eu(CF_3SO_3)_3$ in MeOH at $c_L = 5 \times 10^{-6}$ M ……....……...67
2.5.2 Fluorescence titration of **89 (R** and **S)** with $Eu(CF_3SO_3)_3$ in MeOH at $c_L = 5 \times 10^{-6}$ M……...……68
2.5.3 Eu(III) centred luminescence titration of **89 (R** and **S)** with $Eu(CF_3SO_3)_3$ in MeOH at $c_L = 5 \times 10^{-6}$ M……..…...……....68
2.5.4 Non-linear regression analysis of the UV-vis, fluorescence and Eu(III) centred emission titration data ……...……..71
2.5.5 Titration of **89R** with $Eu(CF_3SO_3)_3$ in CD_3OD at $c_L = 5 \times 10^{-6}$ M ……74
2.5.6 The Lifetime of Eu(III) centred emission during the titration of ligands **89** (**R** and **S**)……..……..…78
2.6 Monitoring self-assembly processes of chiral tripodal ligands with Eu(III) by UV-vis absorbance and luminescence spectroscopy at $c_L = 1 \times 10^{-5}$ M...……..79

2.6.1 UV-vis absorption titration of **89R** with $Eu(CF_3SO_3)_3$ in MeOH at $c_L = 1 \times 10^{-5}$ M. 79
2.6.2 Fluorescence titration of **89R** with $Eu(CF_3SO_3)_3$ in MeOH at $c_L = 1 \times 10^{-5}$ M.....80
2.6.3 Eu(III) centred luminescence titration of **89R** with $Eu(CF_3SO_3)_3$ in MeOH at $c_L = 1 \times 10^{-5}$ M……...……...81
2.6.4 Non-linear regression analysis of the changes in the UV-vis absorption, fluorescence and Eu(III) centred emission titration data $c_L = 1 \times 10^{-5}$ M…81
2.7 Conclusions……..……84

Chapter 3. Gelation and Microspheres formation from tripodal ligands in solution

3 Introduction……..87
3.1 Design and self-assembly studies of the tripodal molecules……..……..88
3.2 Gelation properties of the tripodal molecules…….....89
3.2.1 Thermogravimetric analysis of **88** gel……...…...91
3.2.2 Reversible stimuli responsive properties of **88** gel.……...……..92
3.2.3 Thermal stability and enthalpy of gelation **88** gel……93
3.2.4 Morphology studies of **88** gels by electron microscopy ……..94
3.2.5 Rheological studies of **88** gel...…….95
3.3 Microspheres formation from chiral derivatives of terpyridine tripodal molecules **89** – **91** (R and S)……..99
3.3.1 Investigation of microsphere formation in different organic solvents/H2O media using SEM …….…...…….....**.....**102
3.4 Dynamic light scattering measurement of microspheres in solution…….…..104
3.5 Investigation of the aggregation process in the formation of microspheres using fluorescence ……...106
3.6 Transfer of **89S** microspheres by static interaction in SEM……...108
3.7 Understanding the mechanism of formation of microspheres. ……..110
3.7.1 Determination of "Critical urea concentration" for the prevention of microspheres formation…….....……...111
3.7.2 Time dependent degradation of microspheres using urea...…….……..112
3.8 Interaction of microspheres with lanthanides ……114
3.8.1 Interactions with Lanthanides ……114
3.8.2 Effect of different counter ions on formation of microspheres chains and network……...116
3.8.3 Spectrophotometric studies of lanthanide based microsphere chains…....118
3.8.4 Energy dispersive X-ray (EDX) analysis of microsphere chains …..……121
3.9 Focused Ion Beam (FIB) microscopy of microspheres …….……...….123
3.10 Atomic Force Microscopy (AFM) with Raman spectroscopy analysis of **89S** microspheres……...126
3.11 Mechanical properties of solid microspheres evaluated using AFM …….....130
3.11.1 Microspheres size distribution measurements using AFM ……....130
3.11.2 Lateral force displacement studies of microspheres using AFM……....131

3.11.3 Mechanical strength measurements of microspheres using AFM ……134
3.12 Thermal stability of solid microspheres……..……..136
3.13 Formation of single layered crosslinked networks of microspheres ……137
3.14 Etching of solid microspheres in $Eu(CF_3SO_3)_3$ aqueous solution ……....140
3.15 Self-sorting of non-chiral and chiral tripodal molecules: embedding the microspheres in gel matrix …….……..142
3.16 Conclusions……147

Chapter 4: Optical microscopy studies of microspheres
4 Introduction……154
4.1 Optical microscopy of microspheres…….……154
4.2 Laser Scanning Confocal Microscopy (LSCM) of microspheres (in fluorescence mode)……..……....155
4.3 LSCM Imaging of **89S** microspheres in solution……...……157
4.3.1 Real-time investigation of the formation of **89S** microspheres in solution using LSCM……...158
4.4 Stability of **89S** microspheres in H_2O……160
4.5 Interaction of solid microspheres with Urea in solution……....162
4.5.1 Disassembly of microspheres using solution of Urea (curea = 1 and 10% w/v)…….....162
4.5.2 Effect of Urease on urea bound disassembled microspheres…….....164
4.6 Effect of 355 nm UV irradiation on **89S** microspheres……..165
4.7 Lanthanide based Luminescent microspheres ……..166
4.7.1 Determination of minimum amount of Ln(III) ions required for the formation of luminescent microspheres …….……...167
4.8. Investigation of Lanthanide based luminescent microspheres using LSCM…….....171
4.8.1 Eu(III) and Tb(III) based luminescent **89S** microspheres……..171
4.8.2 Mixed Eu(III)-Tb(III) based luminescent **89S** microspheres…….....173
4.8.3 Time gated imaging and spectral measurements of Ln(III)-**89S** microspheres……..……174
4.8.4 Mixture of Eu(III)-**89S** microspheres and Tb(III)-89S microspheres……178
4.9 Circularly polarised luminescence (CPL) of Ln(III)-microspheres.....…….....181
4.9.1 CPL measurements of Ln(III)-**89** (R and S) microspheres …….....182
4.9.2 Time gated helically luminescence light (HLL) measurement of Ln(III)-**89S** (R and S) microspheres…….....……184
4.10 Conclusion……..188

General Conclusion……..193

Chapter 5: Experimental details
5.1 General Experimental details……..……..…….197
5.1.1 Ultraviolet-visible spectroscopy…….....198
5.1.2 Fluorescence measurements……...198
5.1.3 Eu(III) centred emission measurements……198
5.1.4 Life time measurements of Eu(III) complexes……...199

5.2 Experimental details for Chapter 2……199
5.3 Experimental Details for Chapter 3……...212
5.4 Experimental Details for Chapter 4……...222

References……..229
Appendix 2……243
Appendix 3……275
Appendix 4……291

Chapter 1

Introduction

1 Introduction

Supramolecular Chemistry has been described as 'chemistry beyond the molecule', involving the design and construction of complex supermolecules using smaller building blocks held together through various non-covalent interactions.[1] Generally these interactions are weaker than covalent bonds, and include van der Waals forces, dipole–dipole interactions, hydrogen bonding, π–π interactions, metal–ligand interactions and many more.[1-2] In the field of supramolecular chemistry, self-assembly describes the process where relatively simpler/smaller subunits with complementary functionalities interact spontaneously with one another to organise themselves into more complex (supramolecular) structures. Nature provides us many inspiring examples of such systems, for example, proteins, enzymes, metallo-proteins, *etc*. One of the most common examples is the DNA double helix structure; in which two entwined strands are held together through by π–π stacking and H-bonding by its complimentary units.[1] This is a perfect combination between organic, covalent, macromolecular and supramolecular chemistry, demonstrating that reversibility is necessary for the self-assembly process which allows supramolecular systems to adapt to local changes.

Supramolecular chemistry provides the framework for the design of molecules with interactive properties.[3] The large variety of potential supramolecular interactions available having different specificities offers endless possibilities for the construction of diverse non-covalent supramolecular structures with tuneable properties and functionalities.[4] Such systems have found applications in sensors,[5-6] luminescent materials,[7-9] gels and materials chemistry,[10-15] light emitting devices,[16-17] biological and cell imaging probes,[18-25] and so on. Since supramolecular chemistry has expanded and found application in many other areas of study, this multidisciplinary field bridges the chemical, physical and biological sciences among others.[26]

Recognition of this relatively new field of chemistry was achieved when the 1987 Nobel Prize in Chemistry was awarded to Lehn, Pedersen, and Cram for the design and development of cryptands,[27] crown ethers[28] and cavitands[29] respectively. Because of such an achievement and endless potential, supramolecular chemistry has gained immense interest among chemists who wish to understand the intermolecular interactions involved in building supramolecular structures. Over the past few decades, this field has expanded towards construction of larger and more complex architectures like macromolecules and multimetallic helicates,[30-36] rotaxanes,[37-41] metal organic frameworks (MOFs) and

clusters.[42-45] Such studies have guided the design and construction of complex synthetic molecular machines, the discovery of which lead to the recent Nobel Prize in Chemistry (2016) being awarded to Jean-Pierre Sauvage, Sir J. Fraser Stoddart, and Ben L. Feringa for their pioneering work.[46]

The concept of building such complex structures started a few decades ago when Sauvage reported the synthesis of interlocked molecules using template synthesis.[47-50] Some years later Stoddart used non-covalent interactions between electron rich and electron poor aromatic rings to develop catenanes and rotaxanes which act as molecular shuttles.[51-52] The concept of this molecular machinery increased when the research groups of Sauvage and Stoddart separately demonstrated controlled translational motion in catenanes and rotaxanes as a response to electrochemical potential, chemical or pH changes.[53-54]

In parallel to these discoveries, Feringa introduced the concept of rotary molecular motors using overcrowded alkenes, which has also been important to the progress in molecular machines.[55] Subjecting these overcrowded alkenes to cycles of light irradiation and thermal relaxation led to unidirectional 360^{o} rotation of a rotor component around a stator. Over the years, many molecular motors have been designed.[56-58] Utilising these developments, Feringa was able to demonstrate the moving action of a molecular chassii like structure in which four attached rotating molecular motors act as wheels to propel the ‘‘nano car’’ on a surface.[59]

Such achievement is truly inspirational for the chemist working in the area of supramolecular chemistry. Gunnlaugsson and Leigh have also made important contributions to the development of interlocked systems and rotaxanes,[60-64] highlighting the significance of supramolecular interactions in the development of building complex molecular structures. Over the years, Gunnlaugsson and co-workers alongside Bünzli, Steed, Faulkner, Meijer and many more, have given significant contribution to the field of self-assembly facilitating and understanding of the principles behind intermolecular interactions and guiding the development of new materials.

The objective described in this thesis is to develop tripodal molecules based on the benzene-1,3,5-tricarboxamide (BTA) framework possessing chiral centres connected to 2,2′,6′,2″-terpyridine (tpy) units through a spacer. Using these systems, a self-assembly process is observed both in the free ligand and upon addition of metal ions, with the aim of strengthening our understanding the properties of these systems, principally with regard to their ability to form new soft materials. In order to give an introduction to the research detailed it this thesis, this chapter will briefly cover related topics and examples, beginning

with general examples of functional materials made from supramolecular interactions before discussing the BTA core based and other tripodal molecules. Particular attention will then be drawn towards the development of soft materials and some of the interesting examples of spherical morphologies formed from supramolecular interactions. The remainder of this chapter will focus on the use of lanthanide metal ions within this area of research and the contribution of Gunnlaugsson group to the field of supramolecular chemistry, and finally a note on the structure of this thesis, and the objectives and aims of the work will be introduced at the end of this chapter.

1.1 Functional Supramolecular polymeric materials

Supramolecular polymers are polymeric arrays of monomeric units held together by reversible and directional noncovalent interactions such as hydrogen bonds, π-π interactions and metal-ligand binding *etc*. The resulting materials therefore maintain their polymeric properties in solution. The directionality and strength of the interactions are precisely tuned so that the resulting array of molecules behaves as a polymer.[65]

The first example of linear supramolecular polymers was reported by Fouquey *et al*. in 1990 using the concept of molecular recognition.[66] Over time many researchers have developed strategies and designed molecules to self-assemble into 2D structures and other nanoscale motifs.[67] Supramolecular polymers are broadly classified into two categories based on the mechanism of formation. One includes those formed through isodesmic supramolecular polymerization where the monomers undergo stepwise reversible association, which is identical throughout the polymerization process. Hence, characterized

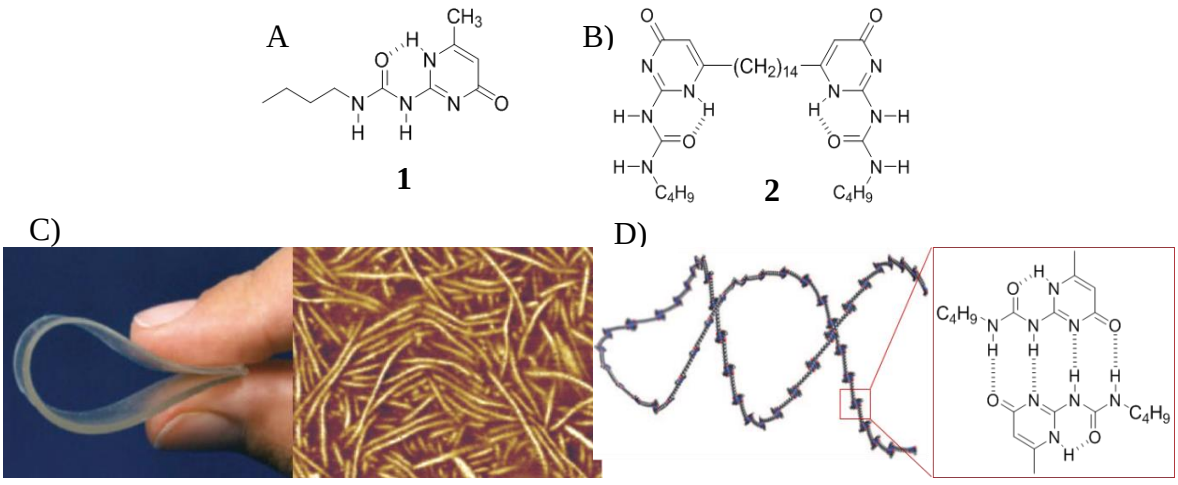

Figure 1.1: A) Ureido-pyrimidinone (Upy) unit; B) Linear molecule with 2 Upy moieties at at both ends; C) supramolecular polymeric material made from 2 and its AFM images showing nanofibres and D) Schematic representation of the supramolecular polymer formed through quadruple H-bonding between self-complimentary Upy moieties. Reproduced from ref.[69-70]

by having the same association constant in every step of monomer addition. This is usually characterized by high polydispersity and absence of the critical concentration and critical temperature. Another is those formed by cooperative supramolecular polymerization, the polymer chain growth occurs in at least two stages. The first stage consists of isoseismic polymerization until the nucleus is formed, with association constant K_n (nucleation stage). After the formation of the nucleus, elongation stage occurs with the further addition of monomers to nucleus with an association constant K_e, higher than K_n. This is usually characterized with: *1*) existence of critical concentration and critical temperature, representing the monomers in equilibrium with supramolecular polymer, and *2*) Having time lag in the formation of supramolecular polymer, however, this time lag can be reduced by seeding, which includes the addition of preformed nucleus.[65]

Proper design of the molecular building blocks to tune the directionality and strength of the interaction between the molecules plays a crucial role in achieving functional supramolecular polymeric materials. Depending on the molecular structure and the functional groups present, molecules self-assemble to form different shapes, sizes and structures. Early examples of supramolecular polymers show self-assembly of monomers using secondary interactions.[68] Meijer *et al*. applied this concept using two 2-ureido-4-pyrimidone moiety (Upy), **1** as an end group in a linear molecule with long alkyl chains (**2**) that forms a supramolecular polymer by the reversible linking of self-complementary quadruple hydrogen bonded end groups (Figure 1.1, A, B and D). These supramolecular polymers behave like conventional polymers and exhibit high mechanical properties as shown in Figure 1.1C.[69-70]

Stupp *et al.* showed the self-assembly of a biological molecule, a large peptide amphiphile (PA) **3** aggregates to form a bioactive filament resembling collagen and hydroxyapatite (HA).[71] The three key structural features introduced in **3** were: *1*) a long hydrophobic alkyl chain; *2*) an amino acid segment (having the tendency to form β sheets) and *3*) a polar unit bearing the phosphorylated serine residues for interacting with calcium ions to direct the mineralisation of HA and cell adhesion ligand RGD. This cone-shaped molecule aggregates because of the hydrophobic effect, wherein the alkyl chains are buried inside the fibre and the β sheets are outside arranged in a twisted helical fashion along with the polar head group (Figure 1.2). Mineralisation of this filament was achieved by diffusing $CaCl_2$ and Na_2HPO_4 on their surface. Preferential alignment of the crystallographic C axis of the HA with the PA fibre axis was observed, which helps the nucleation of HA on the PA

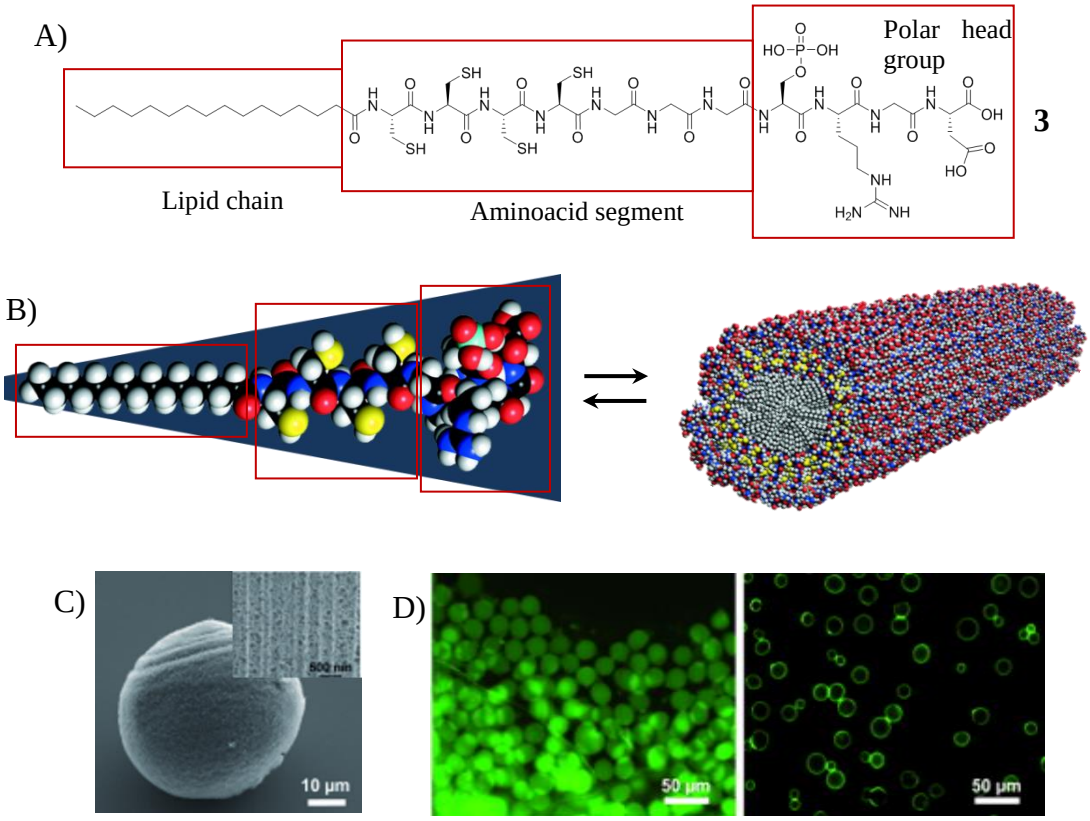

Figure 1.2: A) Chemical structure of the peptide amphiphile (**3**) and B) molecular model of **3** showing the conical shape of molecule and a schematic representation of its self-assembly into cylindrical micelles. C) SEM image of a microcapsule made from PA-biopolymer combination and D) fluorescence microscopy image of microcapsules with encapsulated fluorescent tagged proteins and containing fluorescent labelled PA in its shell. Images reproduced from ref.[71, 77]

filament surface. Furthermore, stacking of the cell binding RGD ligands in the PA assemblies helps to bind to receptors on the cell surface, which allows the PA filaments to exhibit a high density of biological signals spatially to receptors over long distance. The advantage of this kind of material over covalent chains is that (because of the strong interactions between supramolecular assemblies and receptors) these can be self-assembled by the cell itself, in order to fit the local geometry by easily breaking and reforming non-covalent bonds *in situ*.[72] Similar supramolecular filaments, formed by the assemblies of molecules containing peptide segments conjugated to lipid chains, were found to be very bioactive *in vivo*, for example in regeneration of bone and cartilage, growth of blood vessels and more.[73-74]

Similar peptide amphiphiles, when in contact with oppositely charged biopolymers in dilute solutions, self-assemble to form supramolecular polymeric filaments which act as membranes at the interface of the solutions. The microstructure of the resulting material consists of highly ordered nanofibre bundles.[75] Optimisation of this process to the

micrometre scale using materials with similar properties has paved the way for demonstrating the synthesis of cell like microcapsule structures. These microcapsules were employed for encapsulating and releasing fluorescent tagged proteins (Figure 1.2, C and D).[76]

Addition of functional groups to these materials results in the formation of supramolecular copolymers with hybrid functional properties. This approach was illustrated by Schenning *et al.* in the design of a light emitting supramolecular copolymer which optimises energy transfer in materials to perform as OLEDs.[77-78] The material was designed using three π conjugated oligomers, oligofluorene (OF, blue, **4**), oligo(phenylene vinylene) (OPV, green, **5**) and perylene bisimide (Pery, red-emitting, **6**) chromophores functionalised with two self-complimentary quadruple hydrogen bonding Upy moieties as end groups. These self-assemble to form supramolecular polymers both in solution and in bulk (Figure 1.3, A and B). Upon excitation of the oligofluorene part of the polymer chain with light, energy transfers to the other chromophores resulting in emission from all three components. Appropriate mixing of these components resulted in the combination of emission from the three chromophores yielded the white light emitting material.

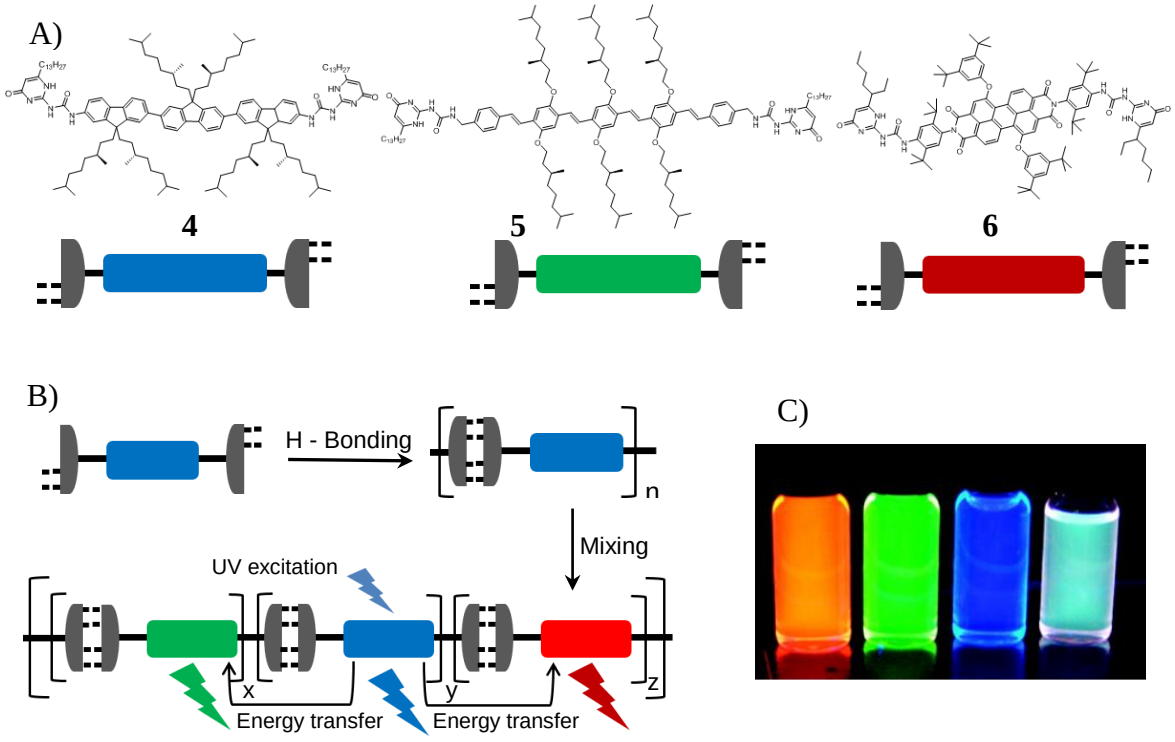

Figure 1.3: A) Chemical structure of chromophores with di-functionalised Upy moieties as end group (**4, 5, 6**) and its schematic representation; B) Schematic representation of H-bonded supramolecular polymers illustrating white light emission and C) Solutions of pure supramolecular polymers **4, 5, 6** and mixture in $CHCl_3$ showing the emission under UV irradiation (λ_{ex} = 365 nm). Images reproduced from ref.[77]

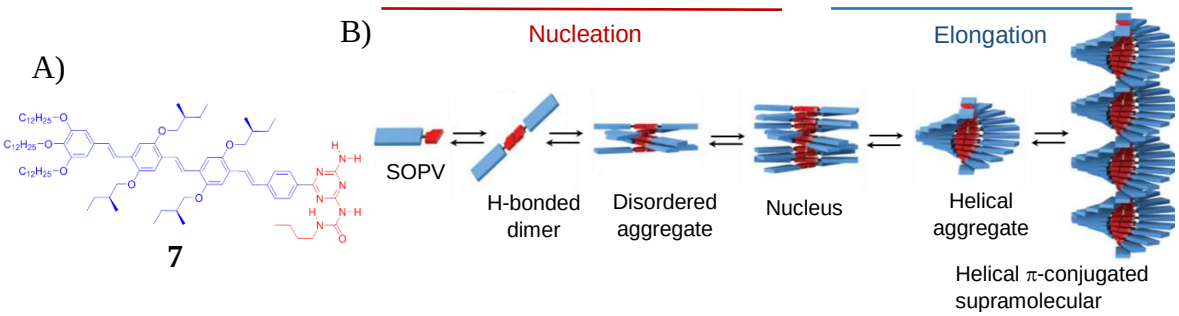

Figure 1.4: Molecular structure of SOPV (**7**) and its schematic representation of the hierarchical aggregation pathways, initiated by quadruple hydrogen-bonded dimer to form elongated supramolecular polymer. Images reproduced from ref.[79]

Furthermore, Meijer and co-workers modified the OPVs using appropriate chiral groups at the periphery and introducing alkyl chains and ureidotriazine moiety on both ends to obtain S-oligo(*p*-phenylene vinylene)s (SOPVs) **7**, which dimerise through H-bonding between the ureidotriazine end groups to form π-conjugated dimers. In apolar solvents these dimers undergo a self-assembly process by hierarchical organisation and subsequently forming reversible helical columnar supramolecular structures (Figure 1.4).[79-81] In construction of polymer chains from the dimerised product, π - π stacking plays a key role in the self-assembly of the dimers and the chiral groups in the periphery take control of the supramolecular chirality resulting in helical structures.[82] An interesting feature of these polymeric materials is the ability to control their length and properties by varying parameters such as solvent polarity and temperature. Formation of these helical architectures was analysed by UV-vis absorption, fluorescence and circular dichroism spectroscopy and microscopic techniques.

Manners *et al.* applied this hierarchically-organised self-assembly process to cylindrical triblock co-micelles for the construction of superstructures, where the self-assembly process was controlled by solvent composition.[83] A block copolymer (BCP) was formed using a crystallisable poly(ferrocenyldimethylsilane) (PFS) chain possessing either polar (P) **8** or hydrophobic (H) **9** blocks, in which PFS part acts as the core-forming block and P/H blocks remains in the co-micelles periphery. Copolymers **8** and **9** self-assemble to form cylindrical micelles in complementary polar solvents by stacking of the P/H segments. Addition of complementary polar copolymers to the cylindrical micelles results in the formation of triblock co-micelles (P-H-P or H-P-H), by means of living crystallization driven self-assembly (CDSA) approach in hexane/i-PrOH mixture (1:3 v/v) (Figure 1.5A).

By appropriately modifying the length of the P/H segment in copolymers, the resulting P-H-P triblock co-micelles undergo a hierarchical self-assembly process by side-

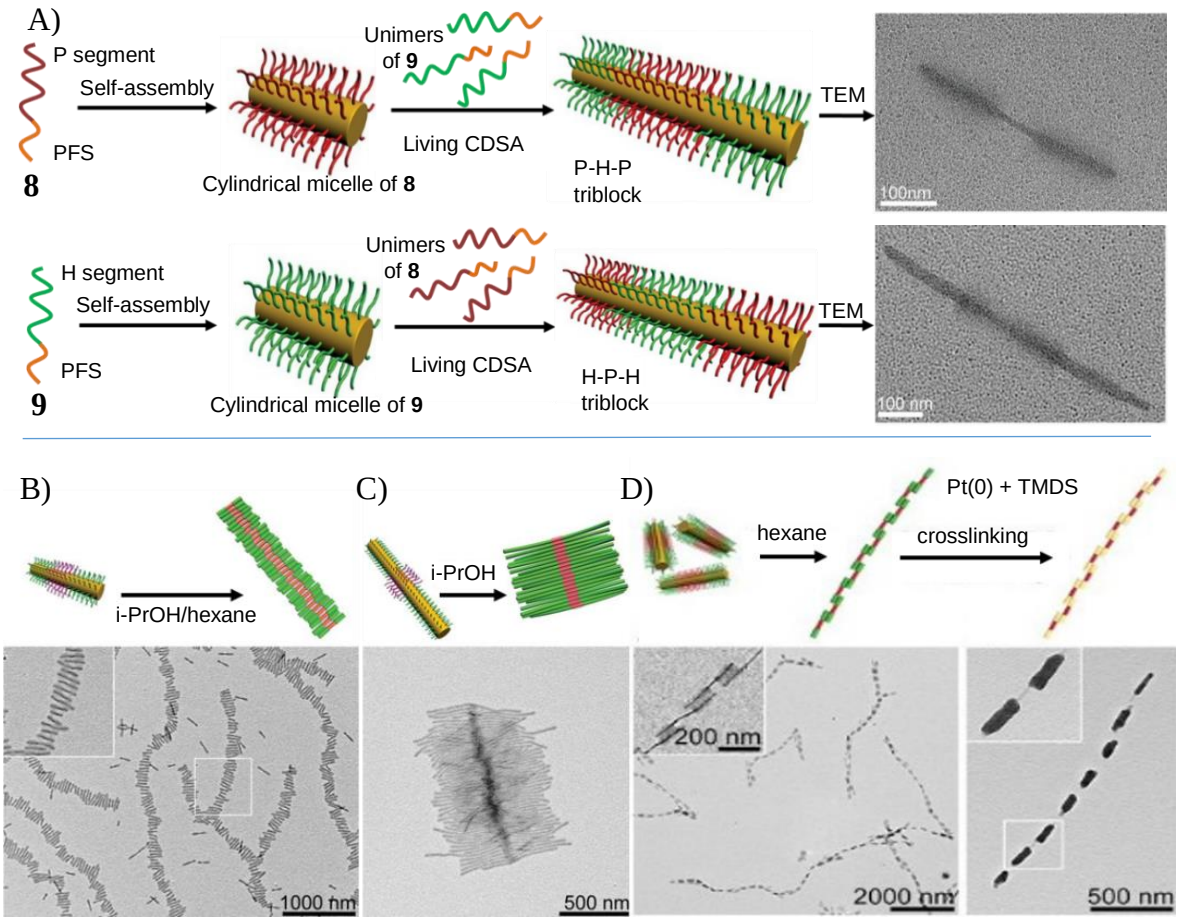

Figure 1.5: A) Schematic representation of P-H-P and H-P-H triblock comicelle and its corresponding TEM images; B) to D) TEM images of self-assembled P-H-P triblock comicelle in various solvent medium forming different superstructures. Images reproduced from ref.[83]

by-side stacking to form well-defined "train track–like" superstructures in polar media, as observed by TEM shown in Figure 1.5B. Significantly tighter packing was observed on increasing the length of the P-segment in P-H-P triblock co-micelles. By varying the length of the P-segment, an array of well-defined cylindrical superstructures of length 1 – 10 μm was obtained in a polar solvent medium. This is presumably because of the smaller diameter of the terminal P-segment in the co-micelle reducing the steric repulsion between co-micelles, thus helping the central H-segment to pack more tightly (Figure 1.5C, dark part). In nonpolar media, the P-H-P triblock co-micelle with a bigger terminal P-segment, undergoes end-to-end aggregation resulting in the formation of linear chain-like superstructures, which were further crosslinked by addition of Pt nanoparticles *via* coordination through pyridyl groups in P-segments (Figure 1.5D).[84-85] Similarly, in other nonpolar media, P-H-P aggregates by inter-micellar association, forming multidimensional superstructures.

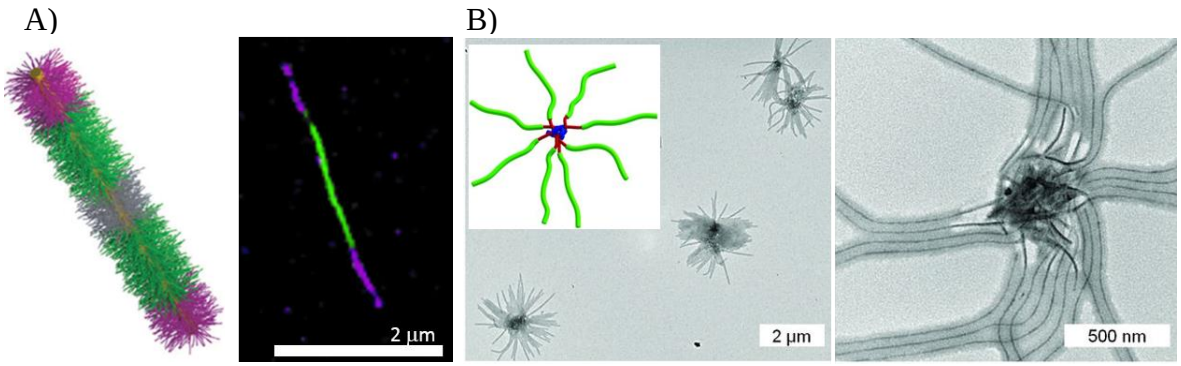

Figure 1.6: A) Schematic representation of triblock comicelle prepared from fluorescent dye tagged block copolymer and its SMLM image (640 nm laser) and B) inset: schematic representation of spherical supermicelle from non-centrosymmetrical triblock comicelle and its TEM images. Images reproduced from ref.[86-88]

Contrary to P-H-P, the H-P-H triblock co-micelle undergoes hierarchical self-assembly in polar medium to form a range of multi-dimensional superlattices on varying the H-segment lengths. Similar triblock co-micelles prepared using different fluorescent dye tagged copolymers displayed colour coded blocks in high resolution on imaging under stimulated emission depletion microscopy (STED) and single molecule localisation microscopy (SMLM) (Figure 1.6A).[86] Similarly, spherical supermicelles (size 1-5 µm) were also observed from non-centrosymmetric amphiphilic triblock co-micelles (Figure 1.6B).[87-88] Recently, interaction of DNA with triblock co-micelles having positively charged terminal groups was reported, indicating the potential application of hierarchical self-assembly materials in biomedical applications.[89] This 'living CDSA' approach was applied to different copolymers to obtain cylindrical and spherical structures[90-91] and also in the preparation of BCP nanoparticles[92-93] and planar molecules.[94-95] From these observations, it is understood that the hierarchical self-assembly process is readily controlled by altering the co-micelle architecture and the polarity of the medium.

Aida and co-workers applied this approach of co-assembly for the constructions of organic heterojunctions using two planar molecules, gemini-shaped hexa-*peri*-hexabenzocoronene (HBC) derivatives **10** and **11,** having the potential to form nanotubular structures independently.[96] Compound **10** undergoes tubular self-assembly on diffusing CH_3OH vapour into its THF solution. The nanotubes formed were stabilised by metal coordination on treating the tubular structures of **10** with Cu^{2+} ions. This makes the surface charged, aiding homogeneous dispersion due to electrostatic repulsion resulting in seed nanotubes ($NT_{1\text{-}Cu}$, Figure 1.7B). On sequential addition of **11** to a homogeneous solution of seeded nanotubes of **10** ($NT_{1\text{-}Cu}$) at 50 ^oC followed by cooling, **11** undergoes stepwise co-

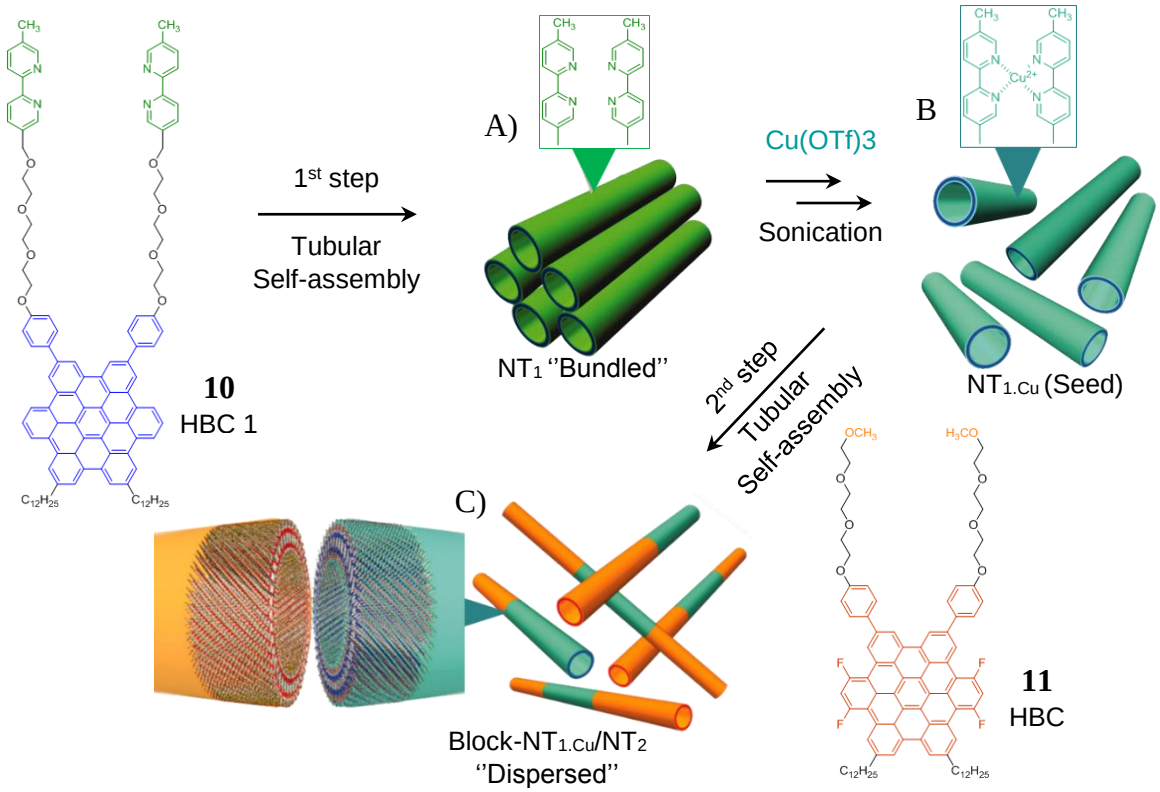

Figure 1.7: Schematic illustration of: A) nanotubes (NT_1), and B) $NT_{1.Cu}$ nanotubes form **10**; (C) block $NT_{1.Cu}/NT_2$ (dispersed) formed by co-assembly of **11** on seeded $NT_{1.Cu}$ and D) cross section of block $NT_{1.Cu}/NT_2$ at the hetero junction. Images reproduced from ref.[96]

assembly at the ends of $NT_{1\text{-}Cu}$ to form two component blocked nanotube segments (Figure 1.7C). This hybrid structure was found to function as a p-n junction with communication at the interface of the heterojunctions between two electronically dissimilar nanotubes by charge transport and excitation energy transfer. This phenomenon is not observed in two homotropically assembled nanotubes.[96]

Another elegant application of hierarchical self-assembly is shown by Scherman, Abell and co-workers in the instantaneous formation of microcapsules though a gold-nanoparticle - copolymer composite, held together by cucurbit[8]uril (CB[8], **12**).[97] Here, **12** (CB[8]) acts as host encapsulating two guest moieties, methyl viologen (MV^{2+}, an electron deficient moiety), functionalised on gold nanoparticles (**13**) (AuNPs) and a naphthol (Np) moiety functionalised on a copolymer (**14**). Upon mixing these three components using a simple T junction geometry in the presence of oil as carrier phase, droplets were formed on thorough mixing. Collecting and drying these droplets on glass slides resulted in the formation of microcapsules with high monodispersity and narrow size distribution (Figure 1.8D). The microcapsules collapsed after dehydration and upon rehydration, they revealed their hollow nature. Furthermore, on using a Rhodamine-B tagged copolymer, **15** in place of

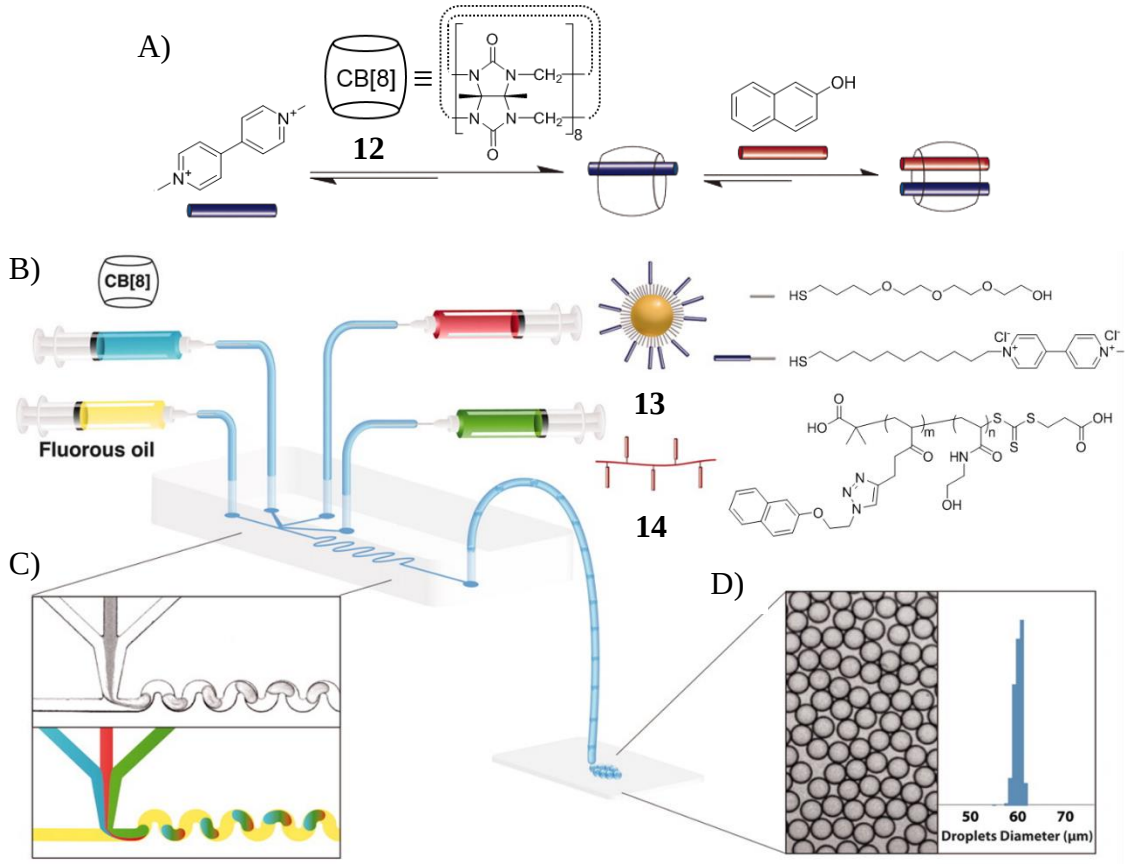

Figure 1.8: Schematic representation of A) Three component formation of CB(8) ternary complex in H_2O; B) microdroplet formation using T junction device; C) Expanded view of T junction with wiggled channel for rapid mixing of reagents and D) monodispersity of microdroplets with narrow size distribution. Images reproduced from ref.[97]

14 and fluorescein isothiocyanate–labeled dextran (FITC-dextran) in the medium, the microcapsules formed showed rhodamine fluorescence (red) on the exterior and FITC green fluorescence in the encapsulated medium (Figure 1.9). The encapsulated cargo was released with control in the presence of $Na_2S_2O_4$. Moreover, the encapsulated materials can be analysed by SERS. In this case, barrel-shaped CB[8] (**12**) plays a key role by forming a 1:1:1

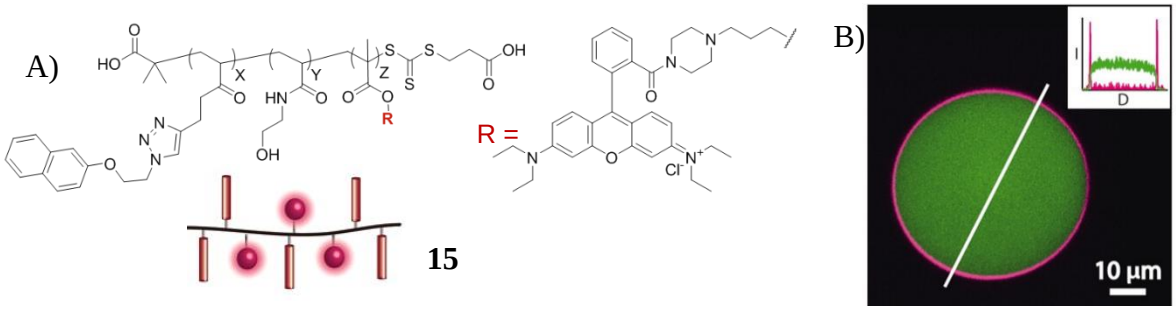

Figure 1.9: A) Chemical structure and schematic representation of rhodamine-B containing copolymer and B) LSCM image of capsules containing aqueous solutions of CB[8] (**12**), **13**, **15**, and FITC-dextran. Inset: display the corresponding fluorescence intensity profiles. Images reproduced from ref.[97]

ternary host-guest complex, in which it holds **13** and **15** moieties in its cavity, acting as molecular "handcuff". This complex three component host-guest interaction is helpful in fusing materials with high selectivity binding affinity in aqueous medium.[98-99] Using this approach, new stimuli responsive materials with high mechanical strength displaying fast healing and cargo release were reported.[100-106]

Recently Scherman, Abell *et al.* extended the strategies of hierarchical self-assembly to prepare similar spherical supramolecular microcapsules using amphiphilic block copolymer **16.**[107] The block copolymer **16,** tagged with electron donating azobenzene moiety, forms spherical micelles at the interface of microdroplet and solvent. This is later crosslinked with another copolymer **17** using the same CB[8] (**12**) to form a microcapsule *via* the 1:1:1 heteroternary complex. The obtained microcapsules displayed the ability to encapsulate dual cargo (hydrophobic and hydrophilic components) in the compartments (Figure 1.10), in which the hydrophilic cargo FITC dextran is loaded in the core (green) and hydrophobic Nile red trapped in the micelle (red). The encapsulated dual cargo was released in a controlled manner under UV irradiation, whereupon the azobenzene changes conformation resulting in dissociation of the 1:1:1 heteroternary complex and the selective

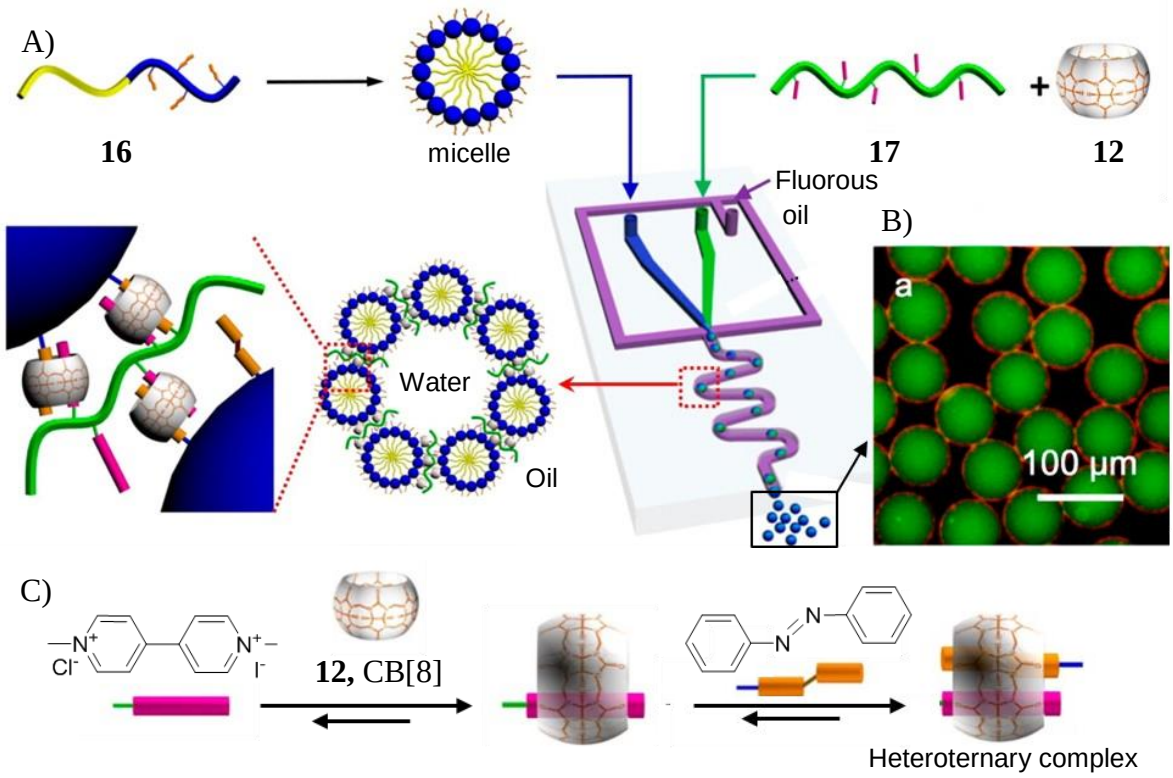

Figure 1.10: A) Schematic representation of the hierarchical assembly of microcapsules from an amphiphilic copolymer; B) fluorescent microscopy image of microcapsules containing FITC-dextran cargo and Nile red (red) and C) stepwise formation of three component heteroternary host-guest complex. Images reproduced from ref.[107]

release of FITC dextran, while Nile red is held in the micelle (Figure 1.10A). This kind of approach is highly applicable to photoswitchable materials,[108-111] controlled encapsulation and release of guests,[112-114] the formation of hybrid supramolecular colloidal hydrogels,[115-116] interfacial self-assembly,[117] controlled self-sorting,[118] supramolecular alignment of Au nanorods,[119] and many more. Very recently, the Scherman group has extended this strategy even further, towards developing a hyper-branched polymer using a BTA based tripodal molecule functionalised with the azobenzene moiety as a guest molecule.[120]

Similar functional materials and nanosized self-assembled architectures formed through other supramolecular interactions like H-bonding and other noncovalent interactions will be discussed in following sections.

1.2 Hydrogen bonded supramolecular polymers and gels

Hydrogen bonded supramolecular polymers are an important class of materials. In such materials, H-bonds play the key role in the formation of an array of structures.[1] An early and simple example of such a system exhibiting helical structures is reported by Lehn and co-workers, where they observed the polyassociation of supramolecular liquid crystalline species, **18** (TP_2) and **19** (TU_2) bearing complementary components to form helical structures (Figure 1.11). The chirality in this system is controlled using different types of tartaric acid (D-, L- or the meso form) connected to pyridine (P) or uracil (U) derivatives.[121]

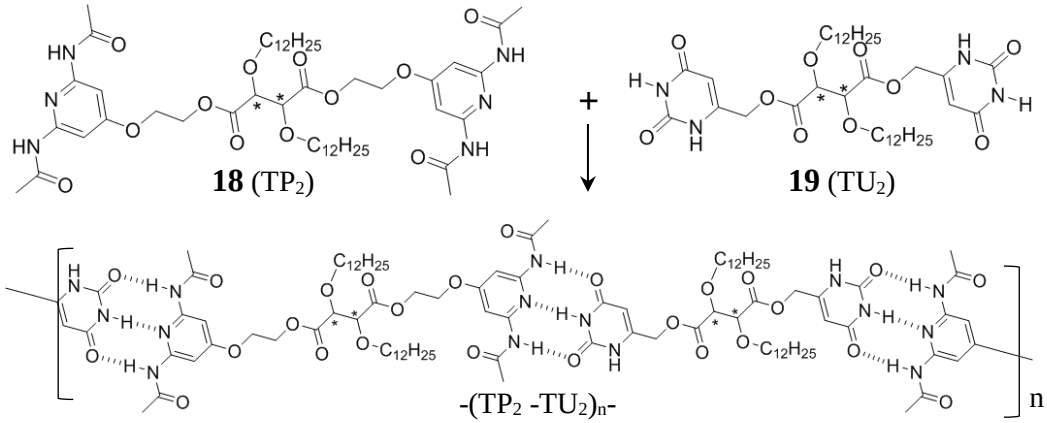

Figure 1.11: Molecular structures of **18** (TP_2) and **19** (TU_2) and its polyassociation to form liquid crystalline materials. Structures reproduced from ref.[121]

Gels can be considered as comprising a solid matrix that immobilizes the liquid component by surface tension effects. Gels are an important class of soft materials which have found its application used in many areas, from food, cosmetics, pharmaceuticals, petroleum and many more.[12] Gels are broadly classified depending on their composition. For example, gels formed in water and organic solvent are termed as hydrogels and organogels,

respectively.[122] When the liquid component is replace by gas, then it is termed as aerogel. Incorporating metal ions through coordination interactions with the LMWG results in metallogels.[10] Supramolecular gels are formed by self-assembly of LMWGs through non-covalent interactions such as H-bonding, solvophobic effects, metal ligand interactions, ion pair coupling, *etc*. During the gelation process, the molecules are dissolved in a certain solvent and then induced to self-assemble, rendering them less soluble. This causes further assembly forming one dimensional fibres. These fibres grow in three dimensions forming a cross-linked and entangled fibrous network. This network encapsulates the solvent in its matrix thus forming a gel.

1.2.1 Self-assembly of benzene-1,3,5-tricarboxamide scaffolds

In the past few decades the benzene-1,3,5-tricarboxamide (BTA) motif has attracted considerable interest as a building block for one dimensional supramolecular polymers because of the tendency of three amide groups to form intermolecular H-bonding interactions.[123] These interactions have enabled BTA-based systems to form nanostructured architectures with various applications. The BTA molecule consists of a benzene core substituted with three amide groups at the 1, 3 and 5 positions. The amide groups on the benzene ring can be attached either *via* the carbonyl group, giving C=O centred BTAs or attached *via* nitrogen giving N centred BTAs (Figure 1.12). When all the substituent R groups are same, the molecule becomes C_3-symmetric.[123] In this chapter, we focus on C=O centred, symmetric molecules.

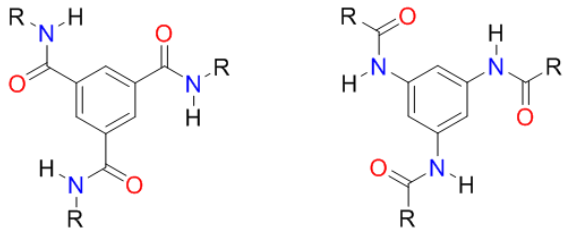

Figure 1.12: General structure for C=O and N centred BTA molecules.

The nature of the side chains (R) plays an important role in the behaviour of the BTA molecules. BTA derivatives bearing polar water soluble groups (**20**) can form hydrogels,[124-126] nonpolar substituents on the BTA (**21-22**) can act as organogelators,[127] and groups with coordinating moieties (**21-22**) yield metallogels (Figure 1.13A).[128-129] Substituents with bulky groups (**23**) often self-assemble in a distorted manner and the resulting columnar self-assembled structure has voids making a porous organic material (Figure 1.13B).[130-131] Many BTA molecules with long alkyl chains (**24-25**) are known for their liquid crystalline

properties (Figure 1.13C).[132-134] Recently, BTA with an azobenzene moiety (**26**) was used in making microcapsules, using cucurbit[8]uril as host in presence of ditopic methyl viologen monomer, by making ternary host-guest interactions (Figure 1.13D).[120] BTAs appended with water-soluble MRI active Gd(III) complexes at the periphery (**27**) are explored as MRI contrast agents (Figure 1.13E).[135-136] Furthermore, they are well known for self-assembling in unidirectional supramolecular polymers and other nanostructured materials which will be

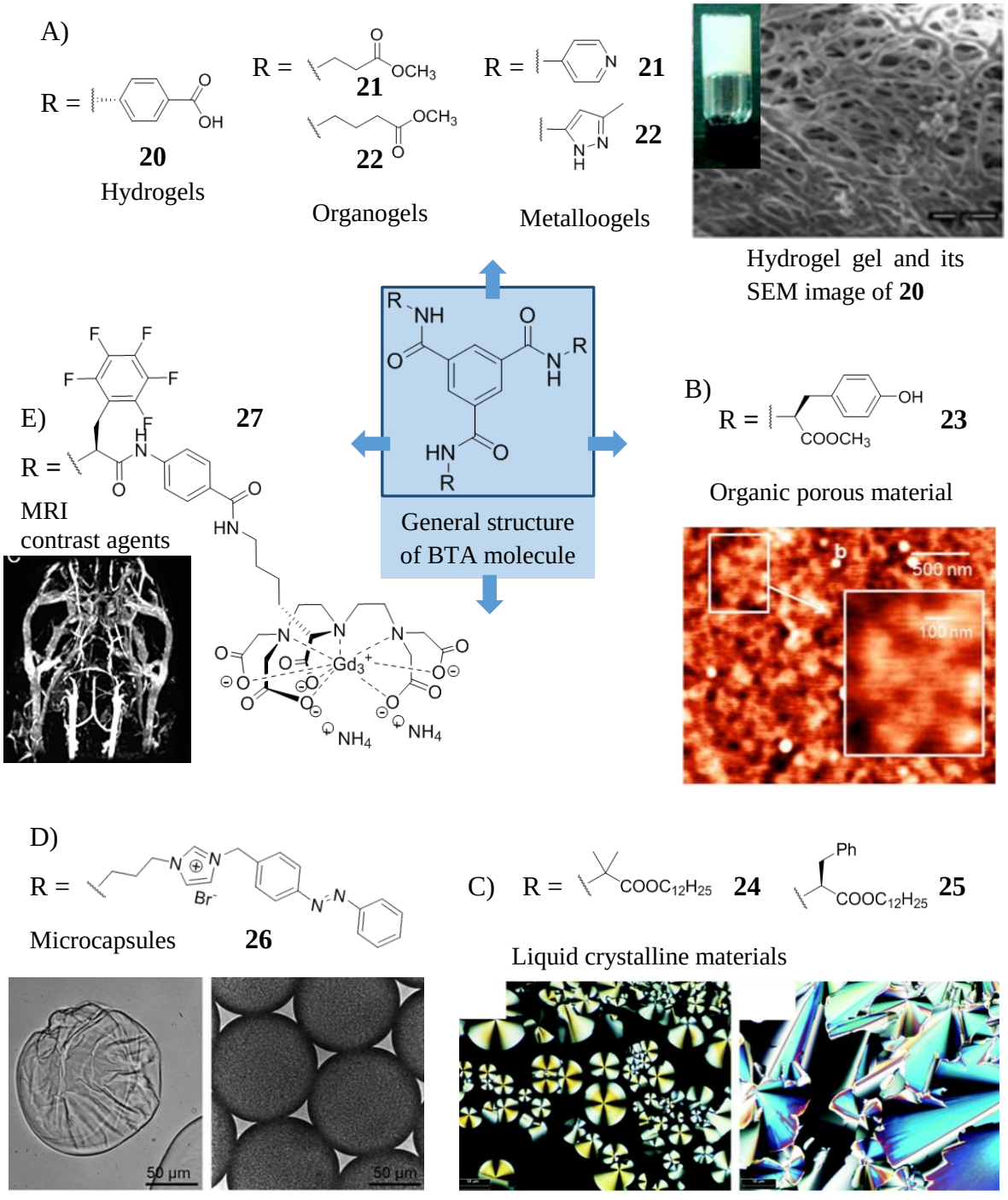

Figure 1.13: Generalised view of BTA molecules with different substituents found application in different fields of research. Images reproduced from ref.[123, 126,127, 129, 131 133,120,134]

discussed in the coming sections. Gunnlaugsson *et al*. reported the bowl shaped structures from N-CH_3 substituted BTA molecules.[137]

Due to their facile synthesis and the facility to append a variety of different substituents to the side chain of the BTA scaffold, a wide range of BTA homologues are available.[123] Arising from this, BTA scaffolds have emerged as useful systems to study and understand the structural variation and the role of solvent on the self-assembly mechanisms of supramolecular polymers. Over the years, such studies have proven to be very helpful in designing the molecules that self-assemble into well-defined nanostructures with high stability and great applicability.[65]

One of the simplest example of such BTA molecules self-assembling as one dimensional supramolecular polymers was reported by Banerjee *et al*. There, the C=O centred BTA molecules were equipped with enantiomeric pairs of chiral amino acids, **28** (R/S) and **29,** self-assembling through triple H-bonding and forming intertwining triple helical cylindrical nanofibres.[138-139]

Single crystal X-ray analysis confirms that the molecule **28R** has crystallographic 3-fold symmetry within a hexagonal unit cell, facilitating columnar packing parallel to the crystallographic c-axis (Figure 1.14B). These exhibit the handedness of the triple helical nanofibres on one hand, but they can also be tuned by reversing the chiral nature of the molecular building blocks. This triple helical structure is formed through intermolecular hydrogen bonds with an overall right-handed twist and other non-covalent interactions including π – π stacking interactions between the central aromatic moieties (Figure 1.14B).

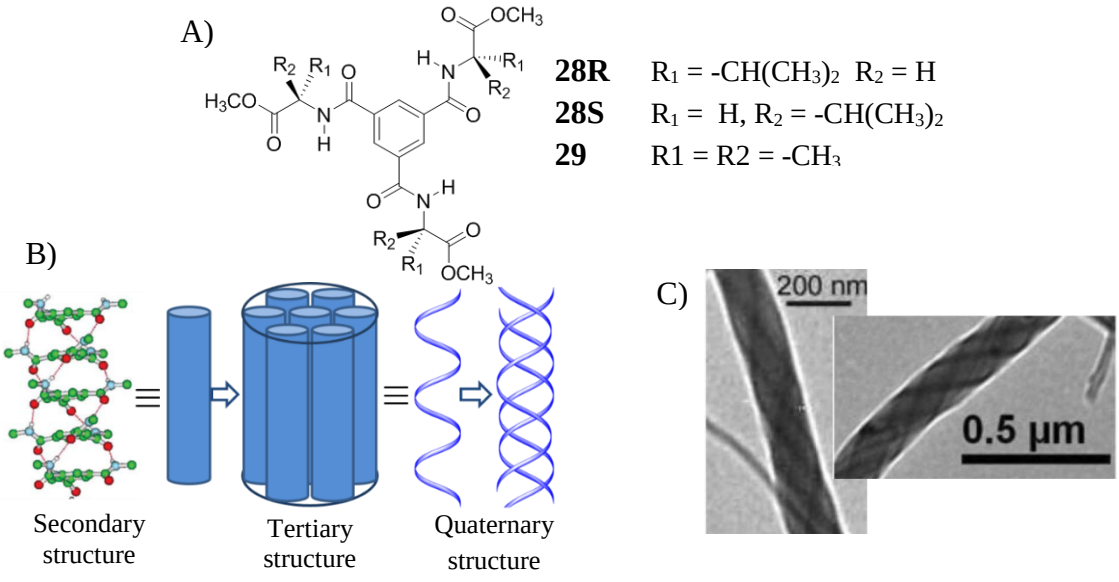

Figure 1.14: A) and B) Molecular structure of **28 R/S** and **29** and its schematic representation of self-assembly forming fibres. C) TEM images of **28R** and **29S**. Reproduced form ref.[137]

This type of self-assembly can be analysed using TEM. The formation of the opposite chiral construction from these enantiomeric pairs of discotic molecules revealed that, control over chirality was possible using different substituents, as observed in TEM images (Figure 1.14C).

Meijer and co-workers used simple BTA molecules with achiral and chiral aliphatic side chains to study self-assembly using different spectroscopic techniques in solution, using methylcyclohexane (MCH) as solvent. Circular Dichroism (CD) spectroscopy studies of BTA systems with simple alkyl chains containing a chiral centre (**30**) showed a strong Cotton effect centred around 220 nm in dilute solution, confirming the helical nature of the BTA aggregate.[140] No Cotton effect was observed for **31** and **32** under similar conditions. Further studies revealed that the chiral groups in the side chains direct the self-assembly towards one helical conformation over the other.[141-142]

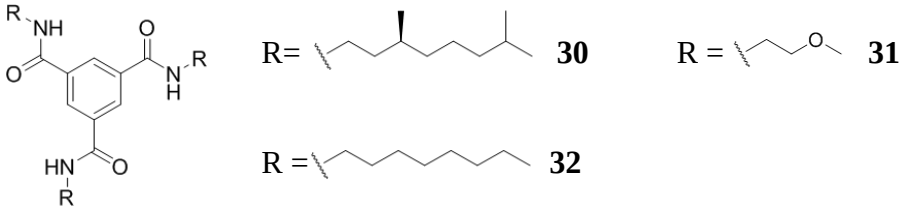

Figure 1.15: Chemical structures of BTA with different side chains. Reproduced from ref.[142]

Further CD experiments carried out on mixed systems of **30** and **32** in heptane displays the 'sergeants-and-soldiers' principle. A composition (by concentration) of 4% **30**, directs the whole assembly in the same handedness as columns exclusively consisting of **30** by amplification of the chirality of whole supramolecular chain formed by **32**.[143] Many other BTA molecules with chiral aliphatic side chains showed similar behaviour.[140] In these systems, it was also observed that addition of competitive solvents such as acetonitrile to the solutions of BTA helical aggregates results in the dissolution of supramolecular polymers formed by reversible intermolecular H-bonding interactions.

Since the side chains have a significant effect on the self-assembly of BTAs, it can be tuned by modifying the BTA periphery. It can be predicted that the introduction of $\pi - \pi$ or H-bonding groups might increase intermolecular interactions. Amino acids are readily available as enantiomers and easily modifiable fragments; incorporation of such groups on to BTA is expected to amplify the chiral properties in the BTA supramolecular polymers.[138, 144]

Palmans and co-workers used an enantiomeric pair of C_3-symmetric and unsymmetric BTAs with phenylalanine and long alkyl chains, **33** (R/S, mono derivative) and

34 (R/S, tris derivative) to examine the effect of bulky groups on self-assembly (Figure 1.16A).[145] Compound **33** (R and S both) in methylcyclohexane (MCH) displayed negative and positive CD effects in the range of 205 – 275 nm ($\Delta\varepsilon$ = 30 L mol^{-1}cm^{-1} at 220nm) for **33R** and **33S** respectively (Figure 1.16B), indicating the helical organisation of BTA chromophore. However, under similar conditions, **34** (R/S) showed mirror image CD spectra as expected for an enantiomeric pair of molecules, with an interestingly bisignate Cotton effect in the region of 200 – 270 nm (Figure 1.16B), which is different to the mono derivative **33** (R/S). In addition, the value of $\Delta\varepsilon$ = 76 L mol^{-1}cm^{-1} at 220 nm observed was significantly higher than **33**.

These systems were further analysed by variable temperature UV-vis absorption and CD measurements in order to understand the mechanism of the supramolecular aggregation. Upon cooling the MCH solution of **33S** (from 90 – 20 ^{o}C), both the CD and UV-vis absorption spectra at 225 nm showed sigmoidal dependence with temperature, indicating isodesmic type self-assembly. But in the case of **34S,** variable temperate UV-vis absorption spectra in MCH showed minor changes, which were too small to assess the degree of aggregation. The temperature dependent CD measurements showed linear variation of the CD signal intensity upon cooling (90 – 20 ^{o}C), suggesting ill-defined aggregation with no evidence of cooperative aggregation. Interestingly, **34** (R/S) cannot be fully dissolved or aggregated in the measured temperature range, making it difficult to determine the mechanism of self-assembly. While the previously observed BTA with a less bulky chiral centre and shorter alkyl chain (**30**) showed strong cooperative aggregation,[143, 146] the presence of one bulky chiral centre, (for *e.g.* phenyl group in **33**) is sufficient to change the

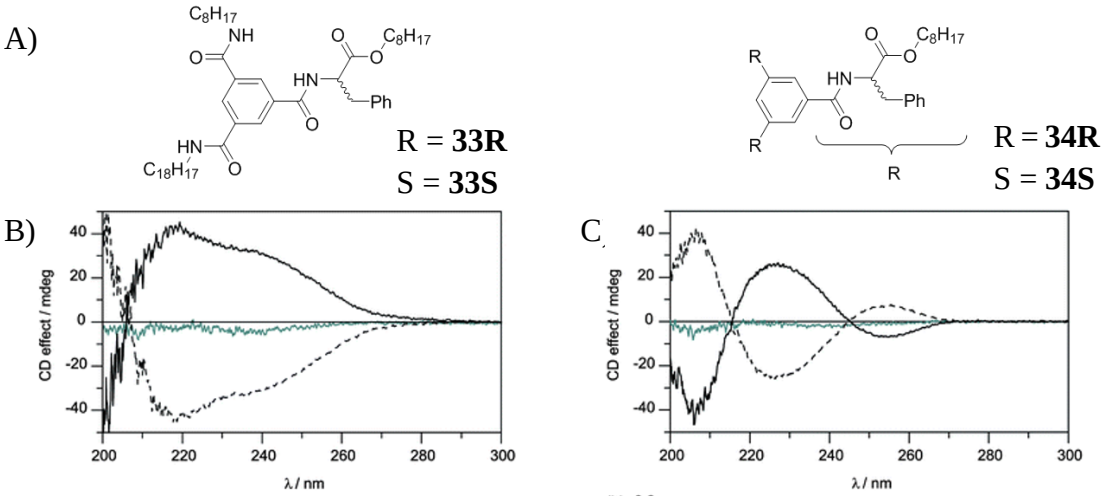

Figure 1.16: A) chemical structures of unsymmetrical and symmetrical BTA with chiral side chains; B) CD spectra of **33R** (dashed black line) and **33S** (solid black line). C) CD spectra of **34R** (dashed black line) and **34S** (solid black line). Images reproduced from ref[144]

self-assembly mechanism to isodesmic behaviour, as observed in **33**. This suggests that the introduction of one bulky chiral group has a huge influence on the type of self-assembly process observed.

As discussed above, BTA derivatives self-assemble by co-operative three fold helical hydrogen bonding.[123, 147] Many versatile derivatives of BTA have been synthesised by incorporating different functional groups such as alkyl,[148] aryl,[126] pyridyl,[131] bipyridyl[149] dipeptide and oligo peptide,[150-151] oligo(p-phenylenevinylene),[152] *etc* for the formation of supramolecular polymers. Recently, Haldar *et al.* used BTA derivatives with simple side chains containing β-alanine **35** and γ-aminobutyric acid **36** to investigate the effect of side chain-side chain interactions in the assembly process.[125] Compound **36** was found to form a thermoreversible opaque gel in aromatic hydrocarbon solvents like toluene, *o*-xylene, *m*-xylene, *p*-xylene. But, under similar conditions, **35** did not show any aggregation and failed to form a gel. The SEM images of the xerogels of **36** of organic solvents showed unbranched fibres with an entangled network (Figure 1.17B). To examine the morphological difference between non-gelator **35** and gelator **36**, solutions of both molecules in 1,2-dichlorobenzene were drop-cast and analysed using SEM, where **35** showed the unbranched polydispersed rigid crystalline morphology whereas gelator **36** showed the long fibrous entangled network similar to its xerogel, which can grow into a 3D network entrapping the solvent resulting in the gelation.

A)

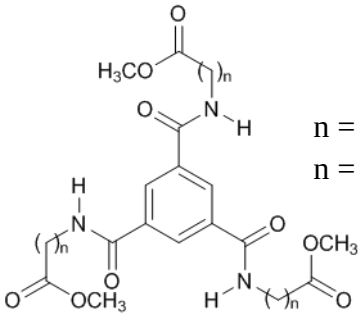

B)

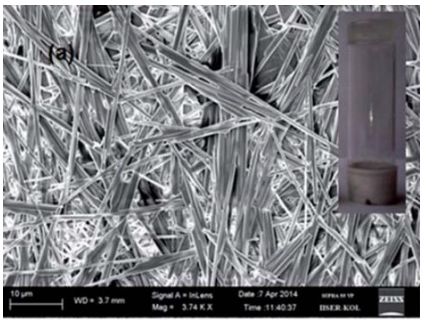

C)

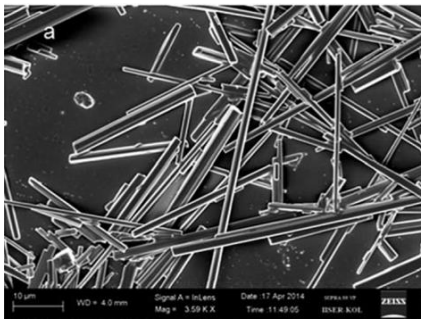

Figure 1.17: Molecular structures of BTA with alkyl side chains **35** and **36**; SEM of B) xerogel of **36** from toluene and C) dropcast solution of **35** 1,2-dichlorobenzene showing crystalline morphology. Images reproduced from ref.[124]

X-ray crystallographic analysis showed both **35** and **36** form individual columnar structures *via* threefold H-bonding. Detailed analysis shows that the secondary structure of **36** further self-assembled through multiple additional hydrophobic interactions by side chain-side chain intermolecular/intercolumnar interactions (between the γ-amino butyric acid β-methylenes and between the ester methyl groups) which gives additional support for the formation of supramolecular networks. Ligand **35** formed self-assembled bundle-like structures, indicating the effect of side chain interactions on the formation of quaternary structures.

The previously discussed BTAs self-assembled in cooperative fashion to form supramolecular polymers in organic solvents. For several other systems, H-bond driven self-assembly in water have been reported,[71, 153-154] but only a few examples of BTA derivatives forming supramolecular polymers in water have been reported.[126, 155]

Meijer, Palmans and co-workers reported the water soluble BTA molecules (**37** – **39**) bearing amphiphilic side chains. The alkyl chains shielded the H-bonding central BTA core and hydrophilic ethylene glycol motifs helped in water solubility (Figure 1.18A).[156] The chiral centre in **38** helped to give information on the helical arrangement of the supramolecular polymers. The cryo-TEM analysis carried out on aqueous solutions of **37** and **38** showed the formation of long thin fibres of micrometre length and approx. 5 nm diameter (Figure 1.18B). In comparison, **37** showed a slightly larger diameter and a subtle

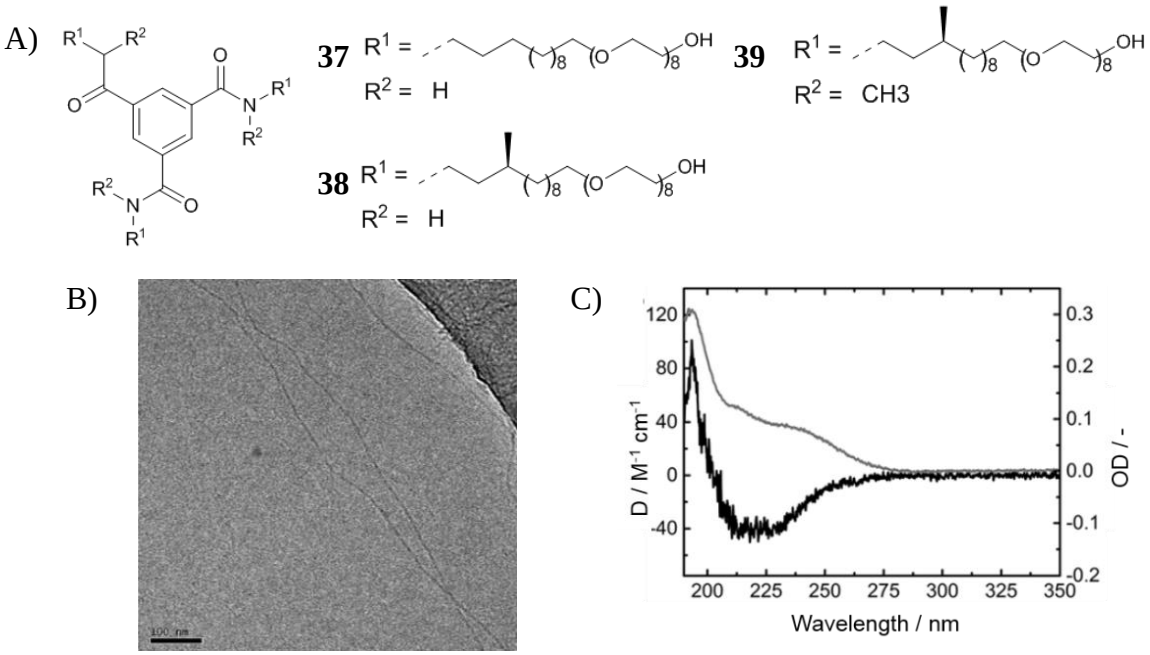

Figure 1.18: Chemical structures of BTA with amphiphilic side chains. B) TEM of **37** showing fibrillar aggregates and C) UV-vis absorption (grey) and CD (black) of **38.** Images reproduced from ref.[155]

and periodic variation in diameter and contrast, which was not observed in **38**. Such structures are often seen for helical fibres (Figure 1.18B). From CD experiments, **38** in H_2O showed a Cotton effect at 220 nm ($\Delta\varepsilon$ = 40 $M^{-1}cm^{-1}$), similar to its helical columnar aggregates in organic solvents (Figure 1.18C).

These results suggest that minimal difference in the hydrophobic chains has a significant effect on the columnar packing of monomers. The UV absorption of **37** observed over time showed a red shift of the absorption maximum at 192 nm, suggesting the formation of initially helical stacks that eventually convert to structures, as seen in TEM. Such changes are not observed for **38**, which suggests the stereogenic methyl group in the side chain drives the molecule towards columnar packing. However, **39** did not show any of the changes in its UV absorption spectrum that were observed for **37** and **38** in H_2O, signifying the inability of **39** to form intermolecular H-bonds,[157] due to the lack of an NH group necessary for H-bonding. This indicates the importance of H-bonding for the formation and stabilisation of aggregates. Very recently Meijer and Palmans *et al*. reported similar BTAs with amphiphilic side chain demonstrating the importance of balance between the hydrophobicity and hydrophilicity required to form ordered and stable supramolecular polymers in water.[158]

Using the principle of hydrophobic shielding of the H-bonding BTA core, more water soluble compounds with peripheral hydrophilic gadolinium chelates (**27** and **40)** were reported by Palmans and Meijer.[136, 159] The peripheral paramagnetic Gd(III) ion chelates were introduced with aim of increasing the ionic character of the molecule, forming supramolecular polymers which could result in a new class of MRI contrast agents. The balance between attractive forces (π - π stacking, dipole interactions, and solvophobic effects) and repulsive forces in **40**, enable the formation of stable and non-interacting columnar assemblies of several length scales (25 – 75 nm, depending on the concentration) with controlled shape, size and stability (Figure 1.19). This approach paves the way for solving great challenges faced in the formation of functional supramolecular polymers in water.

Recently, Wang, Liu and co-workers reported a non-chiral BTA connected to ethyl cinnamate (BTAC) **41** possessing increased π surface area, that self-assembled to form a gel (c = 15 mg/mL) in 60 % DMF/H_2O mixture.[160] Despite its achiral nature, the molecule was found to simultaneously form left (*M*) and right (*P*) handed twists in unequal number. When the *M* twists are more in number than *P* twists, CD spectra showed a negative Cotton effect; being reverse when the *P* twist were in more number, suggesting uneven symmetry breaking

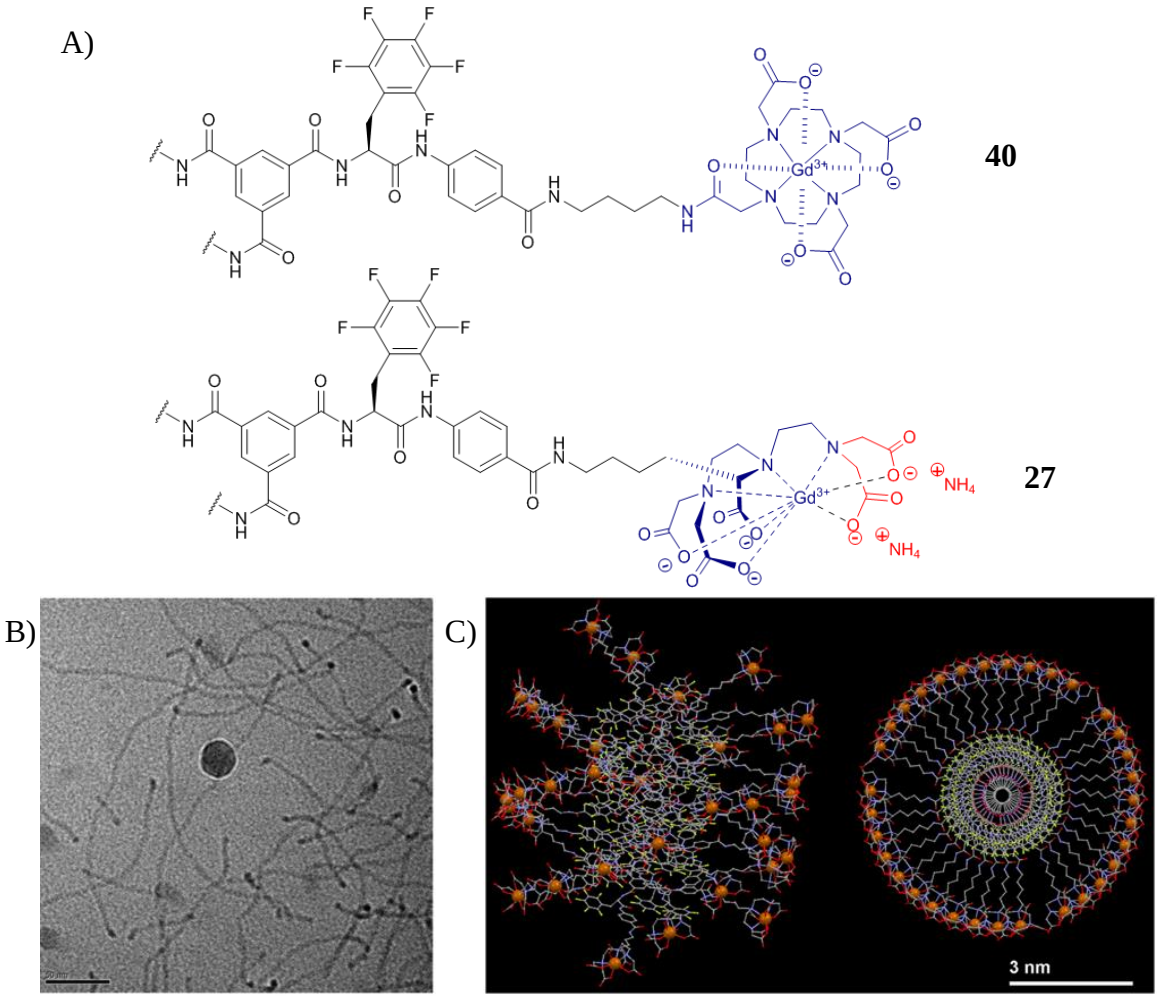

Figure 1.19: A) Chemical structures of BTAs with peripheral hydrophilic metal complexes. B) TEM micrographs of self-assembled monomers of **40** in citrate buffer (100 mM, pH 6) and C) schematic representation of stack of **27** (left: side view and right: top view). Images reproduced from ref.[135]

and resulting in bulk macroscopic chirality of the gels. The SEM images also showed an unequal number of *P* and *M* twists in the same sample.

At an early stage of gelation some of the BTAC molecules (**41**) preorganise themselves, facilitating the formation of one-dimensional helical aggregates with predominantly either *P* or *M*, conformation. Further aggregation then follows the original chiral conformation due to steric hindrance caused by crowded molecular packing. Thus formed helical nanostructures undergo hierarchical self-assembly, forming larger twisted ribbons with unequal numbers of *P* and *M* conformation (Figure 1.20A).

Control over the handedness of the twists and macroscopic chirality of **41** gel could be gained by addition of a chiral dopant, 1-cyclohexyl ethylamine, **42** (R/S). Gels formed from a mixture of **41**/**42R** (1:3 molar ratio), showed only *M* twists in the SEM image and a strong CD signal with an exciton-type Cotton effect at 409 nm and a crossover at 330nm

(Figure 1.20B). Contrary to the above, the **41**/**42S** gel showed only *P* twists and a mirror image of the CD response. Interestingly, even after removal of the chiral additive **42** (R/S) by vacuum drying, the macroscopic chirality of the system was retained. This was possibly because of a small amount of **42** (R/S) reacting with **41** through an amide-ester exchange reaction, forming **43**, which later directs the helical self-assembly formation in the absence of **42**. Similar results were obtained when other chiral amines were used in place of **42**. However, macroscopic chirality was not observed when additives possessing two chiral centres were used. Thus, addition of external chiral entities, enables control over the chirality of the system. Such principles help to develop systems with highly ordered arrangement of assemblies at the molecular level. Similar to this, supramolecular chirality was observed to form other non-chiral systems through the assembly of achiral monomers at air water/interface.[161-162]

In addition to this, many other BTA derivatives with increased π surface area can be formed by introducing different moieties like bipyridine,[163-164] [164]naphthalene diimide,[165]

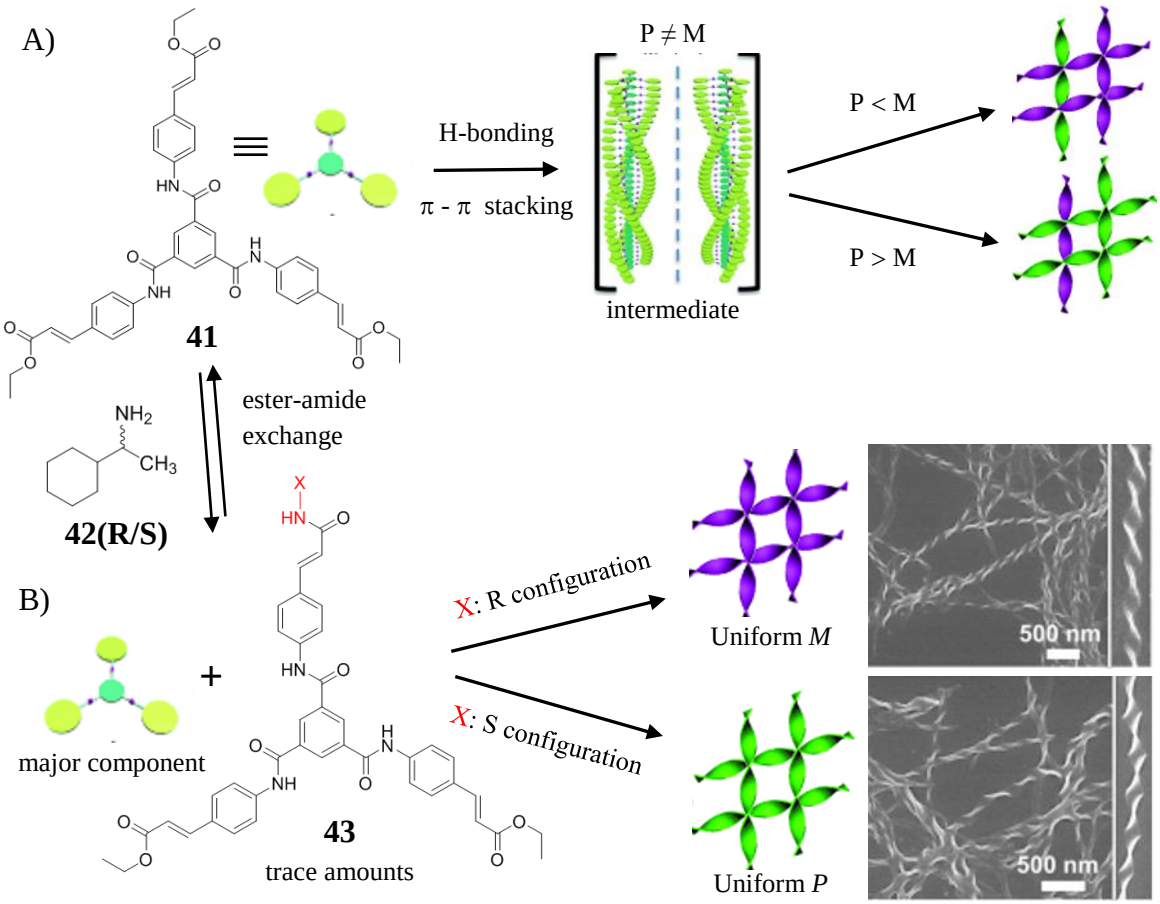

Figure 1.20: A) chemical structure of **41** and schematic representation of gel formation with both *P* and *M* twists. B) gel formation of **41** in presence of **42 (R/S)** by controlling chirality. Images reproduced from ref.[159]

etc. Self-assembled structures of such BTAs exhibit interesting properties such as functional supramolecular polymers,[166] columnar liquid crystalline mesophases,[167] remnant polarisation in bulk phases,[168] *etc*. Similar to BTAs, other systems exhibiting self-assembly result in the formation of nanostructures and functional materials will be discussed in the following sections.

1.2.2 Self-assembly of 1,3,5-cyclohexyltrisamide-based scaffolds

Another class of C_3-symmetric ligand well known to form one dimensional columnar structures are the 1,3,5-cyclohexyltrisamide-based scaffolds. Feringa, Van Esch and co-workers, formed efficient hydrogelators using 1,3,5-cyclohexyltrisamide-based scaffolds conjugated to amino acids, which are further connected to various side chains.[169] These molecules were designed according to modular architecture (Figure 1.21A), which helps obtain hydrogels the properties of which can be controlled at the molecular level. In 1,3,5-cyclohexane-trisamide, three H-bonding amide groups align perpendicular to the mean plane of the molecule and parallel to each other. This supports the self-complementary uniaxial intermolecular interactions, which helps unidirectional self-assembly, subsequently leading to gelation.[170-172] Among the molecules prepared according to the modular architecture shown in Figure 1.21A, molecules **44**-**46** with hydrophobic substituents (R) and hydrophilic side chains (X), formed a gel in aqueous solution. Compounds **47**-**48,** lacking hydrophobic substituents, failed to gel under similar conditions, thus highlighting the importance of hydrophobic groups in the gelation process in aqueous media.

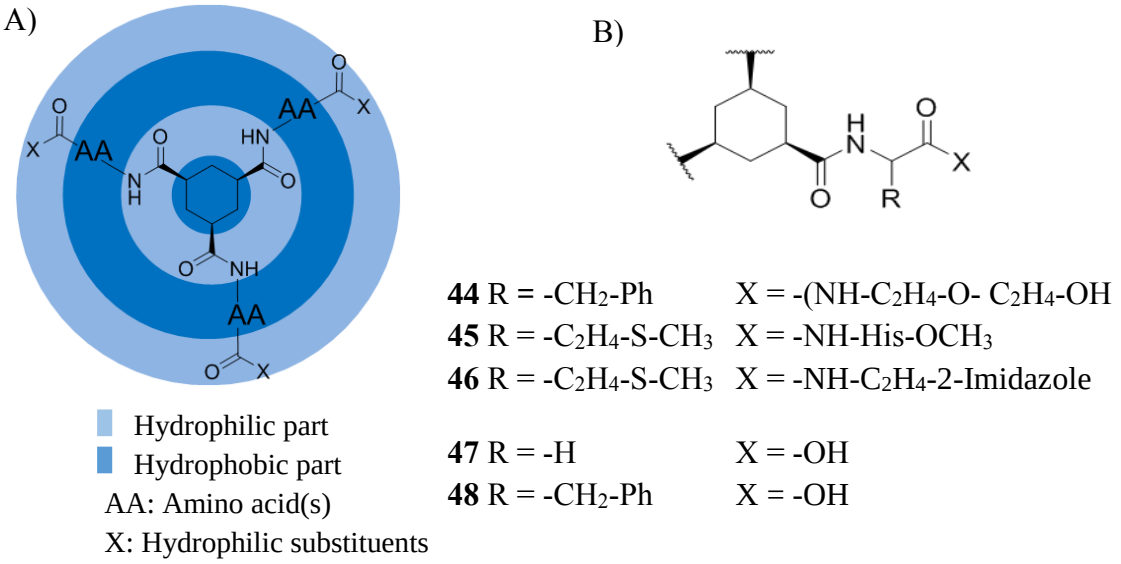

Figure 1.21: A) Schematic representation of modular architectures of gelators and B) molecular structures of **44**-**48**. Reproduced from ref.[168]

Later Van Esch *et al.* showed compound **49** exhibits orthogonal self-assembly behaviour in water, where in the presence of surfactant, **49** undergoes concurrent self-assembly process, where formation of a fibrillar network with encapsulated micelles was observed, showing the two independent supramolecular structures coexisting in the same system.[173] In another observation, compounds **50** and **51** and other modified gelators showed gelation in the presence of spherical micelle-forming surfactants, such as alkyl trimethylammonium bromide (C_nTAB, n = 12, 14, 16), cetyltrimethylammonium tosylate (CTAT) or sodium dodecyl sulfate (SDS) and even in presence of zwitterionic lipids such as dipalmitoylphosphatidylcholine (DPPC), dimyristoylphosphatidylcholine (DMPC), and dioleoylphosphocholine (DOPC) that form bilayer vesicles showing interpenetrating networks (Figure 1.22, D and E).[174-177] Hence, orthogonal self-assembly of hydrogelators and surfactants was proven to be a valid strategy towards self-assembled interpenetrating networks and nanoarchitectures, and various organisations of micelles or vesicles coexisting with fibrous networks.[178-180] This indicated dependence of the gelation ability of the molecules on the strength of the intermolecular interactions, which vary according to the structural parameters of the molecules.[181-183]

As discussed above and in sections 1.2.1, both 1,3,5-substituted cyclohexyl scaffolds and BTAs [145, 170, 181, 184] form hydrogen bonded self-assembled columns. The ability of both of these C_3-symmetric molecules to form one dimensional structures is examined using

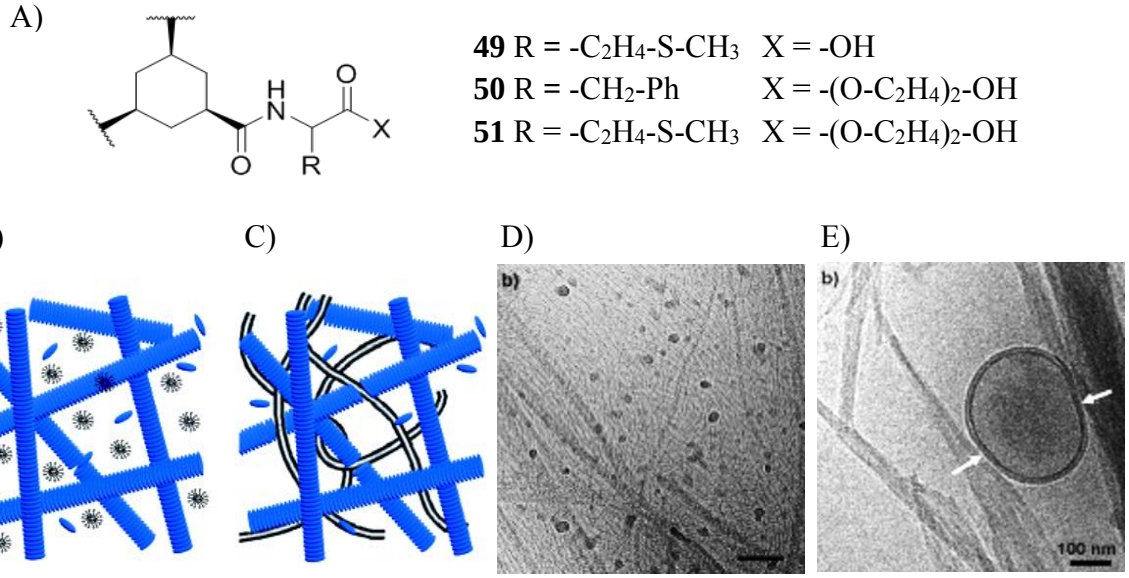

Figure 1.22: A) Molecular structures of **49** – **51**. B) and C) schematic representation of the orthogonal self-assembly strategy using C_3-symmetric molecules and surfactants forming a more complex and compartmentalised structure. TEM images of fibrous network of D) **50** (2mM) in presence of CTAT (100 mM, as cylindrical micelles) and E) Unilamellar DODAB vesicles and fibres of **51**. Images reproduced from ref[173]

simple alkyl-derived low molecular weight gelators (LMWG) and thickeners based on the cyclohexane and BTA core. Hence, in order to have a better understanding of the self-assembly properties of these two scaffolds, molecules **52** and **53**, and **54** and **55**, respectively, with the same substituents were analysed and compared (Figure 1.23 A and B).[144]

The benzene core based molecules **52** and **53** were found to show poor aggregation without showing any signs of gelation, indicating the poor influence of H-bonding units, which might be due to sterically demanding R groups. However, cyclohexyl-cored compounds **54** and **55** exhibited aggregation properties, forming gels. From the crystal structure of the cyclohexane cored compound **56**, the orientation of the amide groups was found to be perpendicular to the plane of the core and parallel to each other, this enabling stronger one dimensional H-bonding and increased gelation ability.[169, 172] However, in the benzene core compounds, the H-bonding units preferred to be in plane of the core because of delocalisation, as observed in the crystal structure of **57** (Figure 1.23 C).[183-184] The type and number of H-bonding units and substituents (R groups) also have significant influence on aggregation of molecules.[132, 144, 147, 158] From these results, the cyclohexyl scaffolds were

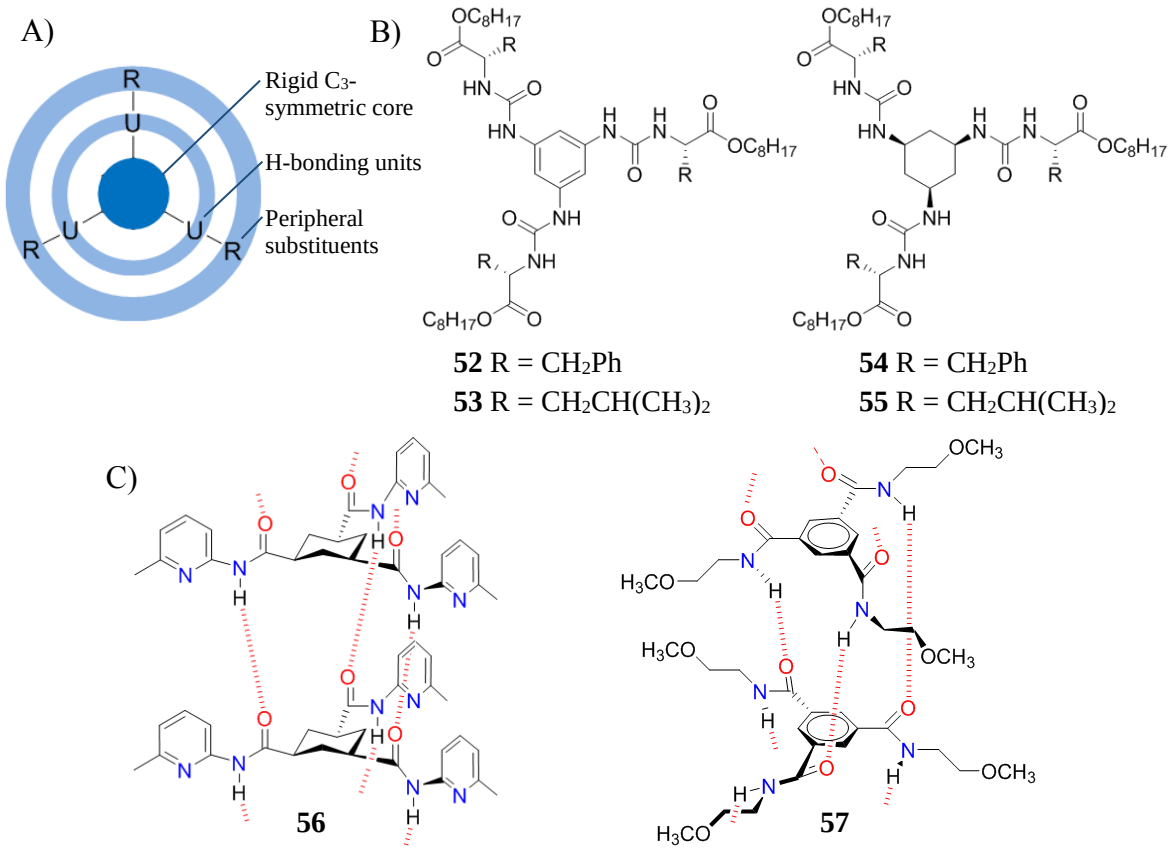

Figure 1.23: A) Schematic design of the *C*$_3$-symmetric compound; B) molecular structure of the tris urea based compounds **52 – 55** and C) representation of translational H-bonded stack of cyclohexane tricarboxamides (**56**) and triple helical H-bonded benzene tricarboxamide derivative (**57**) (from crystal structure). Structures reproduced from ref.[143, 171, 183]

found to be better at forming one dimensional structures and in the formation of gels compared with BTA scaffolds.

It is well known that the properties of the bulk material depend on the self-assembly rate of the building blocks/monomers. Smith, Suzuki and other groups reported the *in situ* formation of a supramolecular gelator using two component systems, which later self-assemble through non-covalent interactions to form a gel.[185-188] The examples of such two-component gel systems are discussed in further sections. Ulijn and co-workers reported the effect of the rate of enzyme-catalysed in-situ gelator formation on the morphology of gels. Wherein, upon simply increasing the enzyme concentration, the control over the formation of nanometre to micrometre fibres was achieved which consequently resulted in a gel with higher thermal stability.[189]

Van Esch and co-workers showed that catalytically controlling the *in situ* formation of the cyclohexane core based gelator (which ultimately self-assembles to form gels) allowed for indirect control of the morphology and properties of the gel.[190-191] On mixing clear aqueous solutions of **58** and **59** at pH 5.0 (in 0.1 M phosphate buffer), the acidic condition catalysed the *in situ* formation of compound **60**, which underwent immediate self-assembly to form an opaque/turbid gel in the same medium (Figure 1.24). Furthermore, similar results were obtained on mixing **58** with **59** at pH 7.0 in the presence of aniline (due to an aniline catalysed reaction) which results in compound **60**, which subsequently formed a gel. The gels obtained were pH responsive with thermal stability up to 120 ^{o}C. However, in the absence of a catalyst at pH 7.0 only turbid solutions were observed, with no gel formation. The final turbidity was lowest for acid catalysed sample and highest for the uncatalysed sample, indicating clear influence of catalysis on the formation of the gelator (Figure 1.25A).

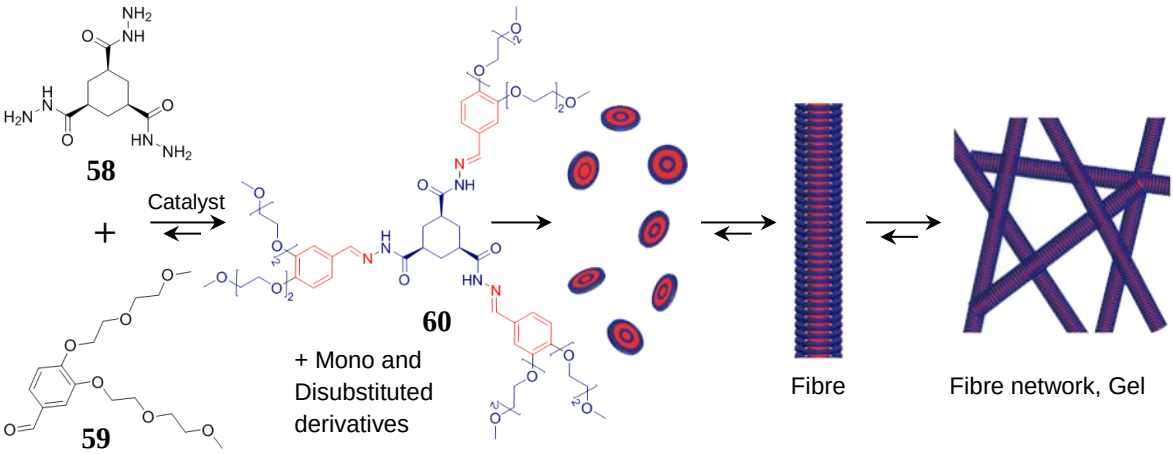

Figure 1.24: A) Catalytic formation of tris hydrazine hydrogelator (**59,** Blue: hydrophilic, red: hydrophobic functional groups), which eventually self-assembles to fibres, which leads to gelation. Images reproduced from ref.[189]

SEM analysis of these samples revealed that the morphology of both catalysed samples showed a highly branched entangled fibrous network, but only thick and less branched fibres were seen in the uncatalysed sample (Figure 1.25B). Moreover, the catalysed samples had greater mechanical stability as determined by rheology, where the storage modulus (G') increased by an order of magnitude to 50 kPa and 55 kPa for the acid and aniline catalysed sample respectively. This clearly indicates the influence of the catalyst on the *in situ* formation of the gelator, which subsequently influences the gelation process.

Self-assembly of smaller building blocks leading to soft materials like gels and their applications will be discussed in further sections.

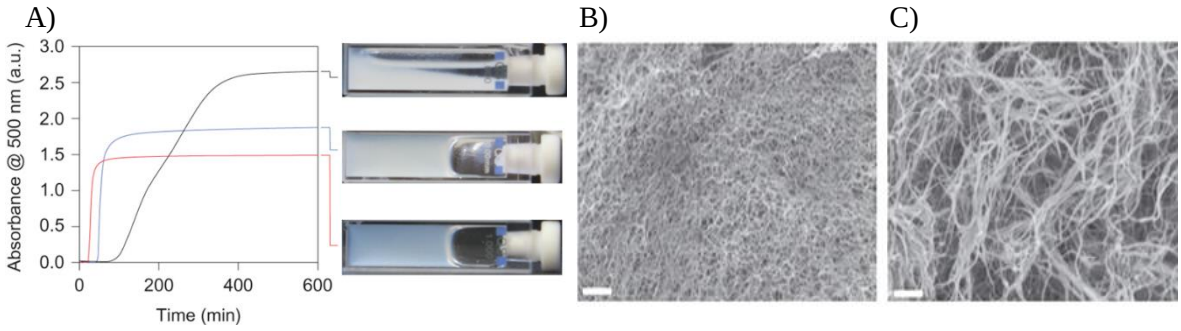

Figure 1.25: A) Turbidity measurements of **60** gel showing absorbance at 500 nm as a measure of structure formation (red: pH 5.0; blue: 10 mM aniline at pH 7.0; black: pH 7.0 ([**57**] = 8 mM; 0.1 M phosphate buffer)). Thus showing the acid catalysed **60** gel is more transparent. SEM images of B) aniline catalysed **60** gel showing dense branched fibres and C) uncatalysed gel showing thick, less branched fibres. Images reproduced from ref.[189]

1.3 Supramolecular gels from low molecular weight gelators (LMWG) and its applications

In the previous sections, BTA derivatives which form gels were discussed. Gels are usually composed of very high volume of liquid immobilised by a crosslinked network of fibres. This network can be formed by chemically cross-linking polymer chains *via* covalent bonds in polymers such as in hydrogels.[192-193] In high molecular weight biopolymer molecules such as collagen and pectin, the network can be formed by entangled molecular chains.[194-195] In the case of supramolecular gels, low molecular weight gelators (LMWG) self-assemble to form gels.[12-13, 196-198] An advantage of supramolecular gels over others types is their inherent reversibility, which is important in applications such as delivery systems[199-200] Gels in which weak forces hold fibres, recover faster to their original state after breaking, exhibiting thixotropic behaviour. Such materials are often suitable for printing, injection and other processing methods.[201] In this section, recent examples of supramolecular gels as smart materials will be discussed highlighting modern applications.

In supramolecular gels, self-assembly can be induced by a heat-cool cycle, changes in pH, or charge, addition of metal salts and by mixing of more than one material that give rise to gels, *etc*. Since highly directional non-covalent interactions are essential, the design of the molecule is important and the balance of solubility has to be taken into account. In addition to this, a number of strategies have to be included, emphasising known gelator.[11, 202-203]

The discovery of gels was serendipitous and were usually observed during recrystallisation process. From the early 1990s research groups began strategically designing low molecular weight systems for gelation.[204-207] From the past decade metal complexes were are also being investigated as supramolecular metallogelators, due to their better control over the self-assembly process.[205, 208-209] Gunnlaugsson *et al* also contributed towards the development of low molecular weight supramolecular gels and metal based supramolecular gels,[210] which will be discussed in more detail in the later sections of this chapter.

Generally, single-component systems self-assemble to form gels. Using more than one component, however gives further opportunity for tuning the properties of the gels.[11] Hirst and Smith highlighted this aspect in their review with the examples of two component systems exhibiting control over the self-assembly process.[211] In true two component systems, the individual components form gels only upon addition of second component. In this case, usually the self-assembly is controlled by manipulating the single molecular recognition events. In some cases, the second component significantly modifies the behaviour of the known gels by allowing the self-assembly of simpler building blocks to form complex functional materials at the macroscopic level.

Smith *et al*. have studied further multicomponent systems, using dendritic L-lysine-based peptide with carboxylic acids groups (**61**) and different aliphatic and aromatic diamines (**62** – **66**) self-assembling *via* H-bonding in toluene (Figure 1.26A).[212] They showed that increasing the length of the aliphatic diamine chain (**62 – 63**, C8 – C12) lead to a dramatic increase in the thermal stability of gels (4 – 105 ^{o}C). The role of **62 – 63** in tuning the transcription of chirality from the molecular level to the macroscopic level was highlighted.[212] Furthermore, varying the molar ratio of **61** to **62 - 63** resulted in significant differences in the thermal stability and morphology of the assembles species.[213] For the **61:62** system (1:4.5 molar ratio) the morphology changed from nanofibres to platelets (Figure 1.27A). Whereas, for **61:63** (1:5 molar ratio) system, (**63** with a shorter chain length), interesting morphologies like nanoscale ‘rosettes’ were observed (Figure 1.27B).

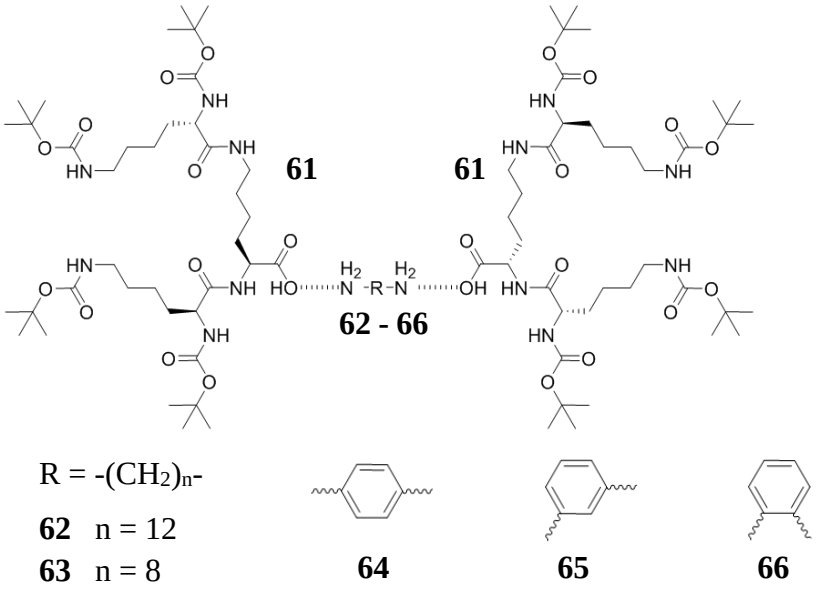

Figure 1.26: Structure of dendron **61** and diamines **62** – **66.** Images reproduced from ref.[213, 214]

The effect of aromatic diamines **64 – 66** indicates the importance of molecular geometry in intermolecular interactions for the formation of gels.[214] Mixing **61** with **64**, **65** or **66** in toluene, results in different behaviour; **61:64** formed gels, **61:65** formed irreproducible partial gels, while **61:66** did not form a gel. In the **61:64** gel, 1:1 molar ratio was found in gel network by NMR and this ratio remained the same even when three equivalents of **64** was added to the system, with the excess remaining in solution. Interestingly, mixing **61** with **64**, **65** and **66** in (1:1:1:1) together in toluene resulted in gel formation. From NMR studies of the solution component, the majority of **64** was involved in gelation with significantly less of **65** and **66**, highlighting the importance of molecular geometry in gelation (Figure 1.26). Many other examples of similar multi-component systems showing control over gelation and gel morphology through component selection exists,[215-216] opening up the opportunity for further development of smart soft materials.

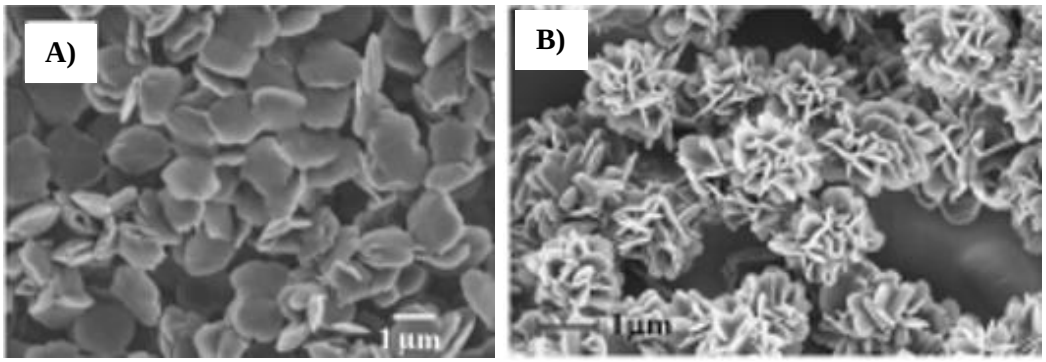

Figure 1.27: SEM images of gels obtained from A) **61:62** (1:4.5 molar ratio); B) **61:63** (1:5 molar ratio). Images reproduced from ref.[213]

Recently Adams and co-workers reported a two component gel systems with self-sorted networks using two pH responsive gelators, which form two independent fibrous networks upon slow decrease of pH.[217-219] As the pH decreases, the gelator with the highest pKa assembles first and buffers the system. Later the second gelator assembles when the pH corresponds to its pKa. This kind of approach most often results in a self-sorted network in which each fibre are made exclusively of one gelator. Later, Adams *et al.*, used two gelators **67** and **68**, where **67** is both pH and light sensitive, for the development of a spatially resolved multicomponent system.[220]

The trans isomer of stilbene-based gelator **67** (c = 5 mg/ml) formed a hydrogel by controlled decrease of pH from 10 to 4. The pH was changed uniformly throughout the sample by hydrolysing glucono-δ-lactone (GdL) to gluconic acid.[221] Gelator **67** has a pKa of 5.8 and forms a gel when the pH is below this (Figure 1.28B). However, the cis-isomer of **67**, did not form gels under similar conditions, resulting only in precipitate, proving this isomer to be an inefficient gelator. When **67** gel was irradiated with 365 nm light-emitting diode (LED) using a mask, selective spatial conversion of the gel to liquid was achieved, similar to other light-triggered gelators. Morphology of the gel before irradiation consisted

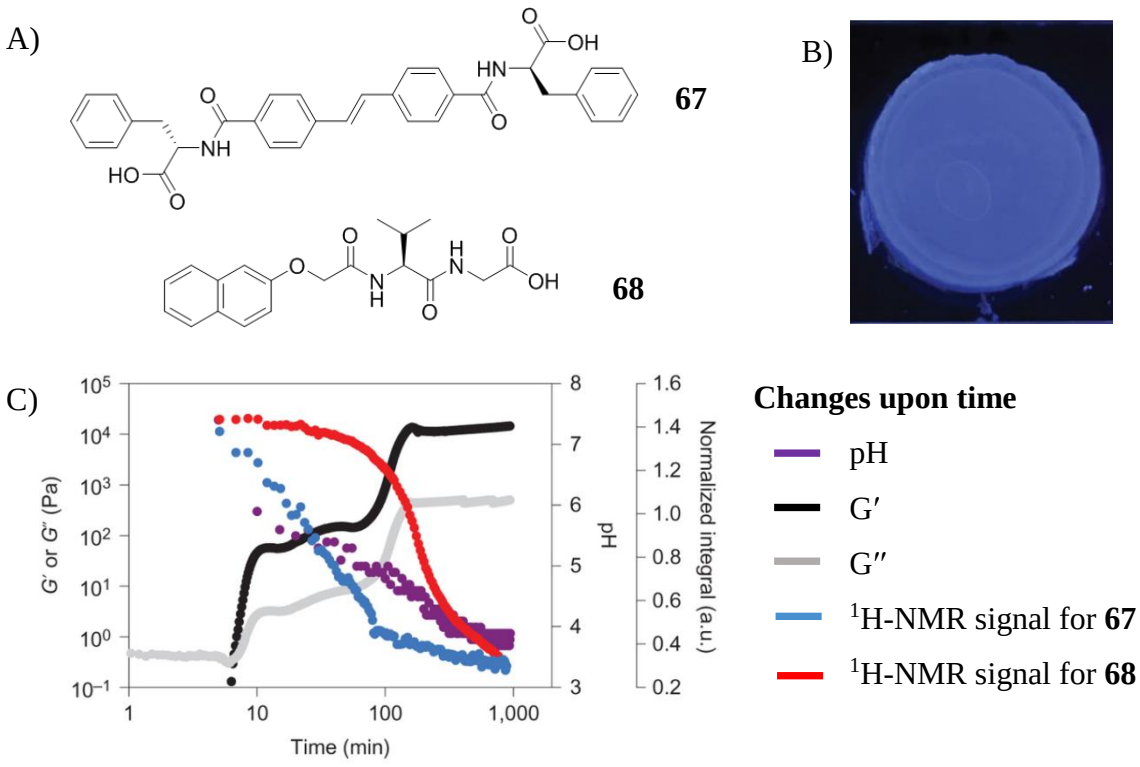

Figure 1.28: A) Chemical structures of **67** and **68**; B) **67**/**68** mixed gel under 365 nm UV light and C) multi scale diagram showing the evolution of pH (Purple), G′ (black), G″ (grey), and H-NMR integrals with time for a mixture of **67** (blue) and **68** (red). Images reproduced from ref.[220]

of the fibres formed by self-assembly of **67**. After irradiation, the sample's morphology was similar to those observed from *cis*-**67**.

On mixing **67** with second gelator **68**, a solution with pH 10 was prepared (c = 5 mg/ml each). The gel formed from **68** alone is not affected by 365 nm LED irradiation. Gels were formed from a mixed solution of **67** and **68**, using GdL which allows slow pH change, facilitating monitoring of the gelation process. From ^{1}H-NMR spectroscopy, the gelation process was followed, as the molecules self-assemble into fibres. The plot of integral size for **67** and **68** is shown in Figure 1.28C.

Evolution of the ^{1}H-NMR spectra as the pH decreases clearly indicates a sequential assembly process, with **67** disappearing before **68** due to its apparent higher pKa (Figure 1.28C, blue and red). Rheological measurements performed in parallel, showed an increase of both storage modulus (G′) and loss modulus (G″) after 8 minutes and a second increase after 20 minutes, indicating the gelation of **67**, which is common for this kind of gelator when using GdL (Figure 1.28C, black and grey).[222] As the pH drops to 5, **68** also starts to disappear in ^{1}H-NMR. A significant increase in G′ and G″ was observed, corresponding to gelation of **68** alone. This confirms that the self-assembly of **67** and **68** is a sequential process along the multi length scale. The final **67/68** gels formed from self-sorting mixture were translucent and homogeneous with no phase separation (Figure 1.28B). The identification of the self-sorted network was complicated by the similar morphology displayed by both components.

On irradiating the **67/68** gel with a 365 nm LED, it retained structural integrity, but a decrease in gel strength was observed. When the irradiation was continued, rheological data showed a gradual decreased in G′ and G″ which stabilised after 2 hrs, with the values being lower than irradiated the **67/68** gel. However this data was in close agreement with that of the **68** gel alone. Furthermore, under irradiation of **67/68** gel, fibres formed from only **67** were selectively removed as it was isomerised and the 68 network remained undisturbed. Using this methodology further, spatial patterning of the **67/68** gel was achieved by selective irradiation using a star shaped mask. (Figure 1.29A). From SEM, the areas not irradiated were not affected and still composed of fibres of the **67/68** gel. The exposed part, however showed a dense network with some aggregates, similar to cis-**67**, indicating the disruption of only **67** fibres in the irradiated region (Figure 1.29, B and C).This kind of methodology

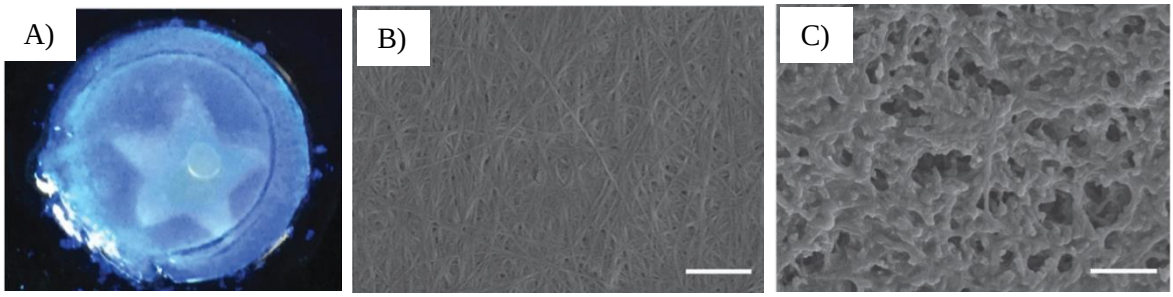

Figure 1.29: A) The **68/67** mixed gel irradiated with 365 nm UV light using a star shaped mask. An SEM image of **67/68** mixed gel, B) sample taken from the edge (non-irradiated region) and C) sample taken from the centre (irradiated region). Images reproduced from ref.[220]

opens up the opportunity for development of spatially-resolved gels and of spatially controlling the properties of these gels.

From the examples discussed above the need for controlling the properties of gels is highlighted. This can be achieved by understanding how to control intermolecular interactions. But still it is difficult to predict the effect of primary supramolecular interactions on the bulk material properties.

Steed and co-workers employed the metal-ligand interactions and anion binding in order to gain control over the assembly process and monitor the strength of the resulting bulk material. In some cases, the anion was used to tune the strength of the gel, wherein the anion reduces gel strength by interacting with α-tape H-bond between bis-urea gelators (Figure 1.30A).[223-224] Addition of metal salts (eg. Cu(II) and Ag(I)) to pyridyl urea gelators, **69** and **70**, results in gel formation, wherein, metal-pyridine interactions reduce the urea-pyridyl

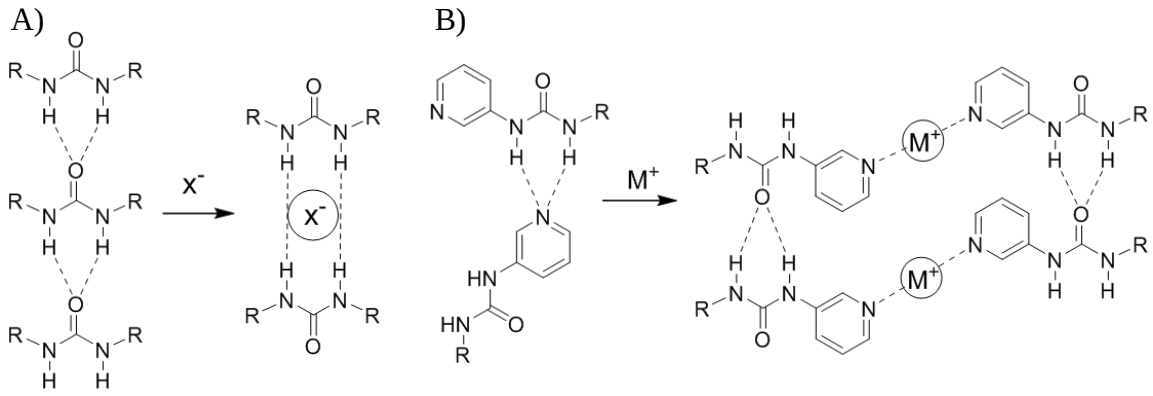

Figure 1.30: Schematic representation of A) interaction of anion (X^-) in α-tape H-bonding between urea motif of bis(urea) LMWG reducing the gel strength. B) Metal ion (M^+) interacting with pyridyl nitrogens forcing the urea motifs to form α-tape H-bonding and metal coordination cross-linking the fibres to increases the gel strength. Images reproduced from ref.[223, 225, 228]

interactions, forcing the urea groups to form H-bonds leading to fibre formation (Figure 1.30B).[225-227]. Such manipulations allows control over the bulk material properties.

Steed, Resnati and co-workers used halogen bonding as a new tool for intermolecular interaction in the development of two-component supramolecular gels in polar media.[228] Bis(pyridyl urea) derivatives **69** and **70** form gel in presence of halogen bond donor **71** through halogen bonding. Halogen bond donor **72** also forms a gel when treated with **73**, $(C_4H_9)_4N^+ I^-$ (**74**) or **69** (Figure 1.31).

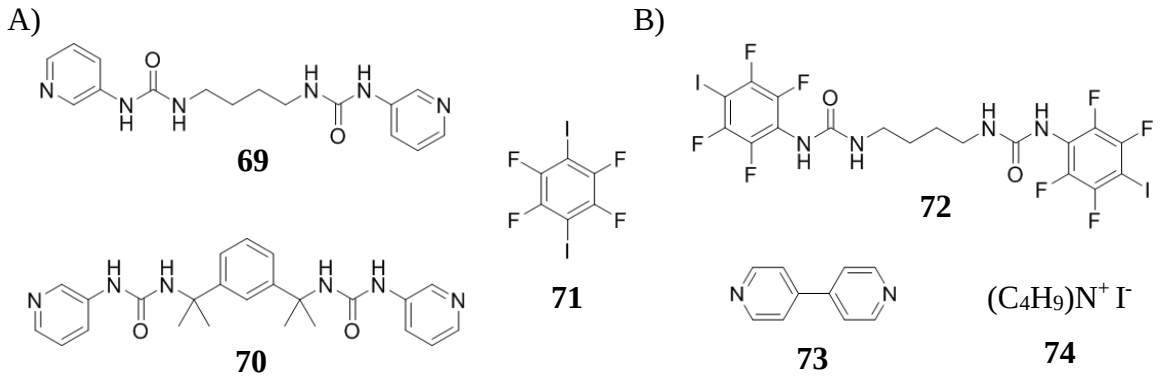

Figure 1.31: Chemical structures of A) Halogen bonding acceptors (**69** and **70**), B) halogen bonding donor (**72**) based on bis(urea) LMWG forming halogen bonded two component co-gels and co-crystals. Structures reproduced from ref.[228]

A Mixture of **69/71** formed an opaque gel (1% w/v, 1:1 molar ratio) in CH_3OH or in aqueous mixture CH_3OH, CH_3CN, DMSO (4:1 v/v) upon fast cooling of a hot solution (60 ^oC) in dry ice bath. However, slow cooling of the same mixture to room temperature, resulted in co-crystallisation of **69:71** (1:1). From SEM analysis, two dimensional hexagonal platelet morphology was observed for **69** crystal alone, which changed to one dimensional needle-like structures upon forming **69:71** co-crystal (Figure 1.32, A and B). Single crystal X-ray crystallography of **69:71** co-crystal showed the urea moieties forming double, anti-parallel α-tape H-bonding (Figure 1.32B). The additive **71** forms Halogen bonds with **69**, acting as a bridge in connecting the two urea tapes, supporting the formation of two dimensional sheet structures. The X-ray powder diffraction (XRPD) pattern of the xerogel of the fast cooled **69/71** gel matched the single crystal structure of **69:71** co-crystal, thus suggesting the gel structure is similar to the crystals, which supports the involvement of halogen bonding in gelation.

Although **70** was not able to form a strong α-tape H-bonding network because of its sterically hindered nature, it forms a fairly strong **70/71** mixed gel (1 % w/v, 1:1 molar ratio) in CH_3OH/H_2O (4:1 v/v) on fast cooling. Similar to the previous case, **70:71** (1:1) co-crystal

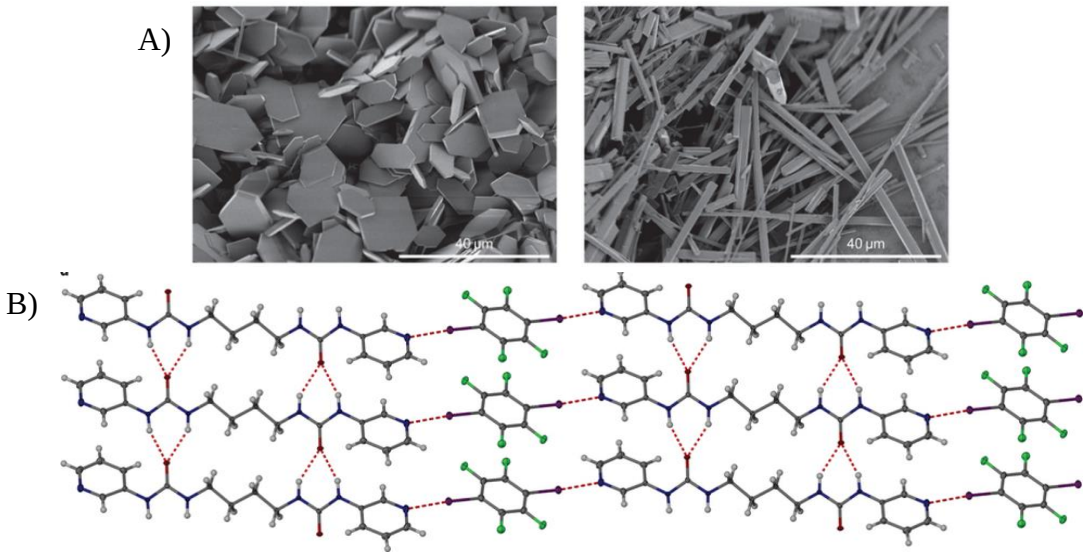

Figure 1.32: A) SEM images of **69** crystal and **69:71** (1:1) co-crystal, B). X-ray crystal structure of **69:71** co-crystal showing α-tape H-bonding between urea moieties and halogen bonding between **69** and **71**. Structures reproduced from ref.[228]

was obtained upon slow cooling of the solution, but in this case, **71** shows two different environments (Figure 1.33A). One molecule of **71** forms halogen bonding bridges between a pair of **70**, but the second **71** is not involved in halogen bonding, forming only weak H···F and I···I interactions. Arising from this, one of the pyridyl nitrogens H-bonds with solvent H_2O and the urea moieties do not form an α-tape H-bonding network, explaining the weak nature of the **70/71** gel.

In the case of halogen bonding donor bis(urea) derivative **72**, gels of **72/73** and **72/74** were formed (Figure 1.33, B and C). The **72/73** co-gel obtained was less crystalline showing smaller fibres, and was considerably more stable when formed without fast cooling (Figure 1.33D). Similarly, mixtures of halogen bond acceptor **69** and halogen bond donor **72** formed a **69/72** (1% total concentration) mixed gel through complementary halogen bonding interactions, in DMSO/H_2O (3:1), upon warming and cooling. This further explains the involvement of halogen bonding in gelation.

From these examples, halogen bonding proved to be a new and versatile approach for inducing the fibre formation and hence has resulted in the development of two component gels in polar media. The advantage of halogen bonding over H-bonding is that, *1*) halogen bonds tend to be more directional, *2*) the interaction strength can be tuned depending on the polarisability of donor halogen atom, *3*) The hydrophobic nature of halogen bonds allows them to be used in aqueous conditions, *4*) it can be integrated into the gelator structure or can be introduced by addition of second component. Such benefits increase the toolkit for controlling supramolecular gel formation and manipulating bulk material properties.[229]

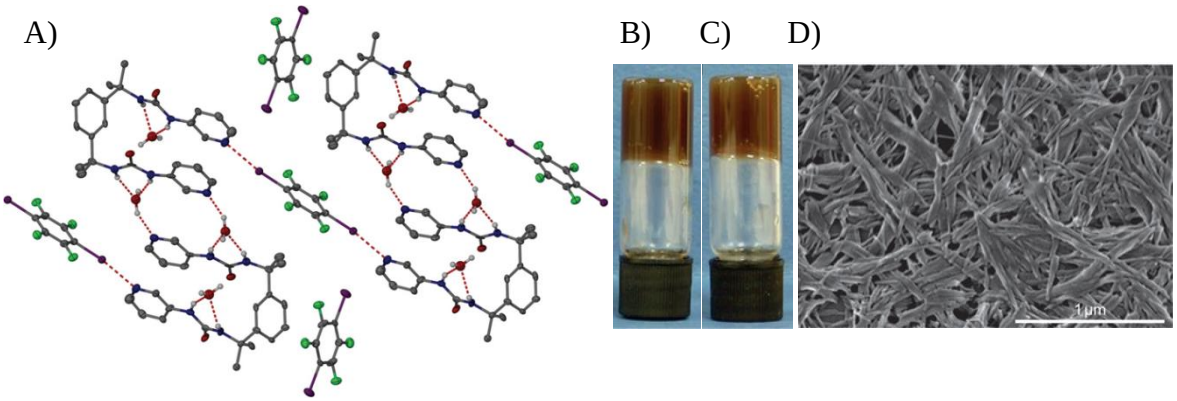

Figure 1.33: A) Crystal structure of **70:71** co-crystal; B) and C) Pictures of **72/73** and **72/74** gel (1% each) in DMSO/H_2O (3:1) and D) SEM image of **72/73** gel. Structures reproduced from ref.[228]

Development of gels as functional smart materials has included growing organic, inorganic and protein crystals.[230] Improved physical characteristics, and facile recovery of crystals grown in the gel, make supramolecular gels a better medium for crystal growth.[231] Steed *et al.* used a supramolecular gel based on bis(urea) gelators for the growth of molecular crystals of organic and pharmaceutical compounds.[232] Compound **75** was chosen because it forms gels in various organic and aqueous media and a Cu(II) based metallogel from **70** has also been explored. Dissolving bis(urea) gelator **75** and anticonvulsant carbamazepine **76** (1% w/v each) in toluene by heating and cooling resulted in gel formation, followed by crystals of **76** formed after around 8-12 hrs (Figure 1.34). The presence of **76** crystal had no effect on the mechanical properties of **75** gel on storage and loss moduli. An increase in yield stress was observed, however which is due to the physical support of the gel by solid **76** crystals, contrary to the effect of anion binding by bis(urea) gels. Addition of excess tetrabutylammonium (TBA) acetate, resulted in the dissolution of gels and **76** crystals were recovered without any degradation. This example highlights the use of supramolecular gels as a new medium to grow crystals, as it allows access to a wide range of solvent systems and its reversibility helps in facile release of crystals grown in the gel media.

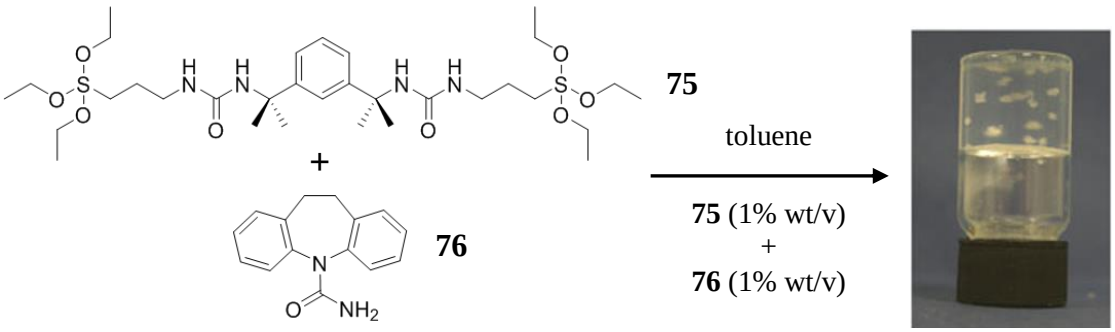

Figure 1.34: A) Chemical structure of bis(urea) gelator **75** and carbamazepine **76** and the picture of **75** gel with crystals of **76**. Structures reproduced from ref.[232]

Very recently, Steed *et. al.* developed bis(urea) gelator **77** with a functional group configuration specifically similar to highly polymorphic drug ROY (**78**).[233] On cooling the hot solution of **77** (1% wt/v) and **78** (100 mg/ml) in toluene, a gel was formed with red crystals of **78**. The surface of the fibre consisted of an ordered arrangement of o-nitroaniline-derived functional groups of **77**, which chemically mimic o-nitroaniline substituent in **78**, allowing epitaxial crystal growth. This results in the formation of a metastable red form of **78** in a specific manner, instead of its usual thermodynamic yellow polymorph (Figure 1.35).

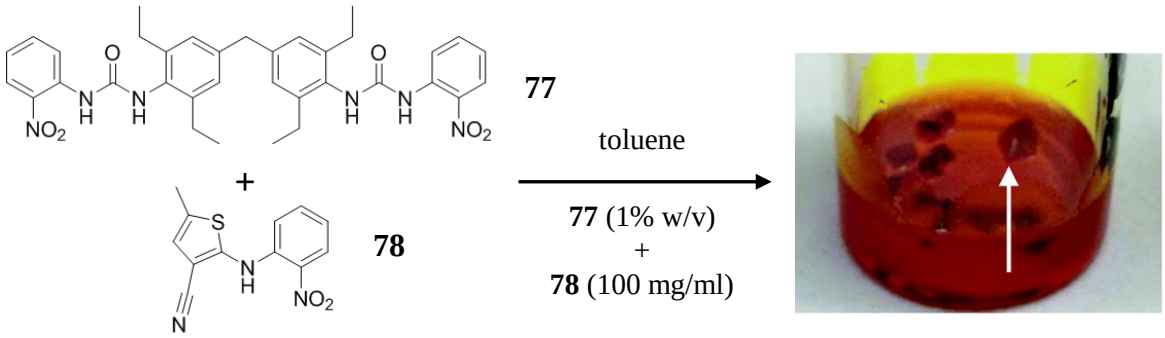

Figure 1.35: A) Chemical structure of bis(urea) gelator **77** and ROY **78** and the picture of **77** gel with crystals of **78** of R form. Images reproduced from ref.[233]

Similarly in another case, using calixarene diammonium salt and bis-crown ether, a two component supramolecular co-gel was reported, in which the hydrophobic cavities on the gel surface act as anchor sites allowing the hydrophobic drug molecule to nucleate resulting in the growth of crystals.[234] This new approach employs gelators with a design that enables crystal growth in its fibres, paving the way for application of supramolecular gels in crystallising polymorphic pharmaceutical agents in a controlled manner, thus inducing nucleation in compounds that have proven difficult to crystallise.

In this section, various supramolecular interactions and their manipulation leading to the formation of fibres, gels, crystals and aggregates in various conditions and controlling its properties were discussed. Similar intermolecular interaction leading to formation of higher aggregates of different morphology will be discussed in the following sections.

1.4 Self-assembly of molecules to higher ordered aggregates

The self-assembly of smaller building units to form higher ordered aggregates of larger size has become a burgeoning field of study. Micro and nanometre sized particles play important roles in many application like bio-sensing,[235] catalysis,[236] optics[237] and more.

Vesicles are spherical lipid bilayers consisting of enclosed fluid. Such hollow structures have attracted considerable interest due to their potential in guest inclusion and stabilisation of reactive intermediates.[238-239] Vesicles are used as spherical transporters in

practical applications such as delivery systems.[240-241] A number of strategies were designed for construction of such structures. Azumaya's group reported an adamantane-based molecules comprising multiple branches forming networked structures with cavities and one dimensional channels.[242] One example is an adamantane-based cage like molecule, **79** which spontaneously self-assembles to form hollow spherical aggregates in CH_3OH/THF (1:2 v/v) (Figure 1.36B).[243] The aggregates were of narrow size distribution, with a diameter of 230 nm, and were robust and stable even after drying. In more polar CH_3OH/THF (1:1 v/v) solvent mixture, bigger aggregates were observed. But, in CH_3OH/THF (1:4 v/v), spherical aggregates were not present, highlighting the importance of balance between the polar/nonpolar ratios of the solvent media. TEM analysis confirms the hollow nature of the particles as clear contrast is seen between the thicker peripheries (darker, as it doesn't permit the transmission of electrons) and lighter centre (Figure 1.36C).

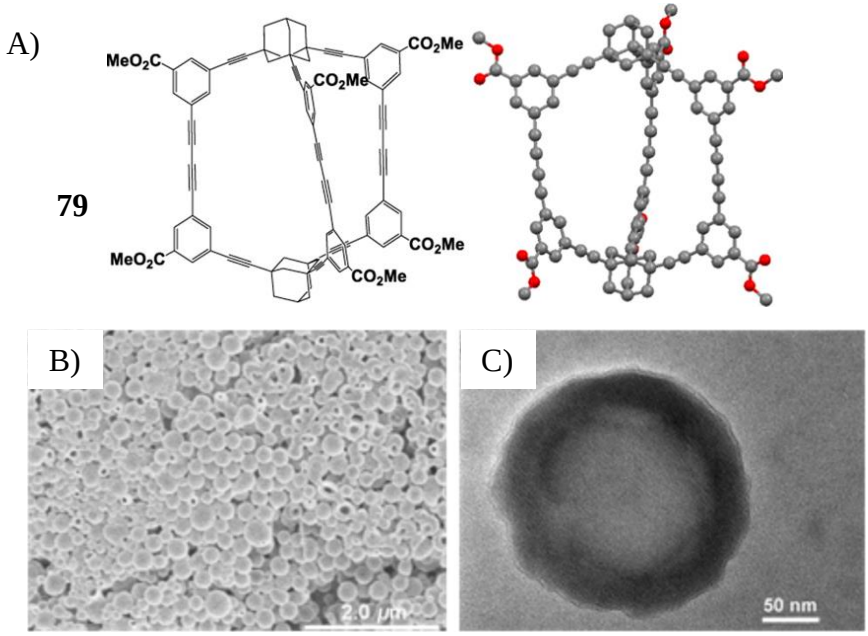

Figure 1.36: A) Molecular structure of adamantane-based cage type molecule **79** and its crystal structure; B) SEM and C) TEM iamges of hollow spherical assemblies of **79** formed in CH_3OH/THF (1:2 v/v). Image reproduced from ref.[243]

Similar spherical nano/microstructures are also reported from amphiphilic molecules. Liu *et al.* showed two triangular amphiphilic derivatives, **80** and **81** containing an imine bond and alkyl chains in the periphery, acting as building blocks in the formation of soft colloidal materials.[244] The triangular structure provides more acting sites for the interactions and the alkyl chains make the molecule hydrophobic, enhancing its aggregation property. Despite similar structures **80** and **81** showed different assembly behaviour **80**, with additional H-bonding sites, self-assembled to furnish microstructures with solvent-regulated

morphologies and hollow spheres being one of them. Among different organic solvents, **80** formed microspheres with different morphologies in polar solvents like DMSO, CH_3OH, THF, ethyl acetate, *etc.* In DMSO, solid spherical particles were formed with a smooth surface (Figure 1.37B), whereas in CH_3OH, spheres with a rough surface morphology was observed (Figure 1.37C). The assemblies obtained in ethyl acetate and acetone showed regular and uniform flower-like surface morphology (Figure 1.37 D and E). The solid nature of these spheres was confirmed by TEM analysis (inset in respective images). The hollow spheres obtained in THF were further confirmed with Laser Scanning Confocal Microscopy (LSCM) showing the large difference in the relative luminescence of the inner and outer ring (Figure 1.37, F and G). On decreasing the polarity of the solvent, **80** formed organogels in nonpolar solvents like toluene, cyclohexane and petroleum ether. These drastic changes in the assembly of molecule **80** in different solvent media signifies the influence of solvent polarity on the various non-covalent interactions responsible for assembly process and fabrication of the morphology of aggregated systems. In addition to this, the molecule-solvent interactions are greatly influenced by solvent polarity and structural factors.[245]

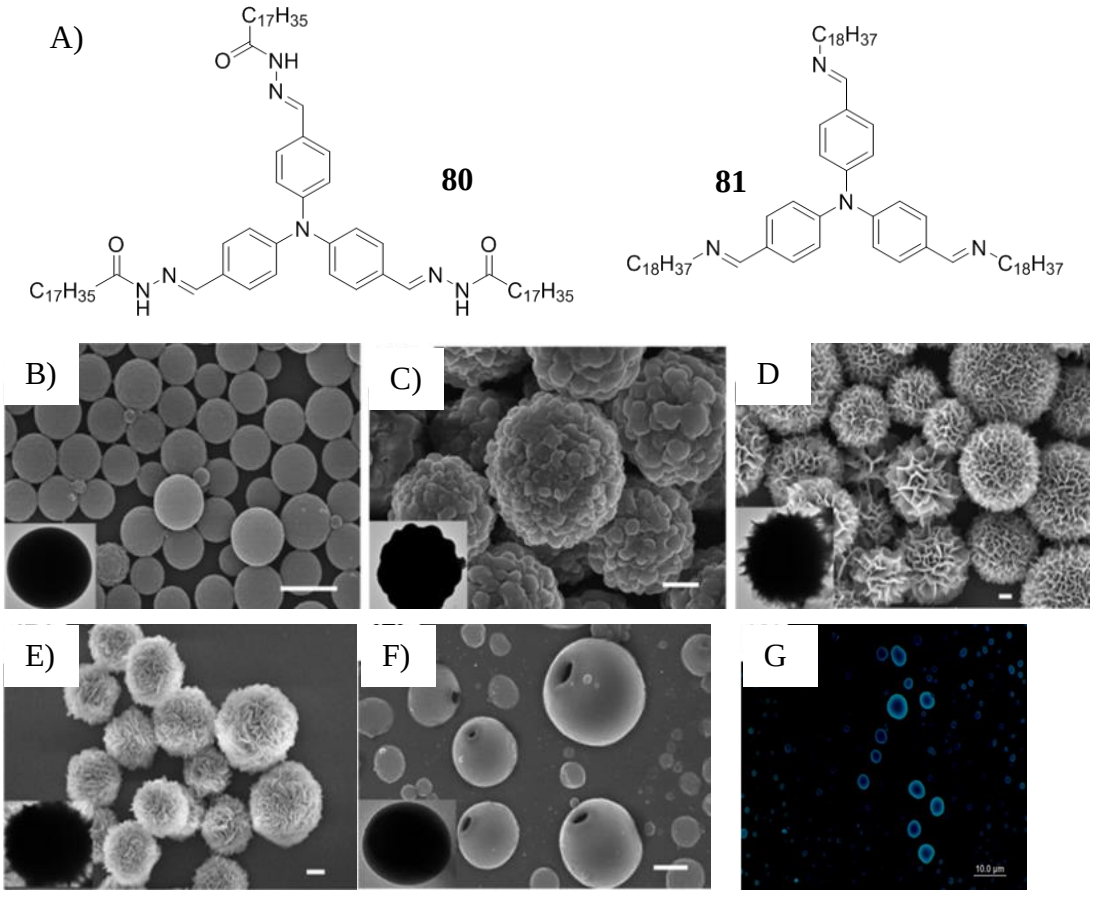

Figure 1.37: A) Molecular structures of **80** and **81**. SEM images of assemblies of **80** formed in B) DMSO; C) CH_3OH; D) ethylacetate; E) acetone; F) THF. Scale bar 2 μm and G) LSCM image of **80** hollow spheres, Scale bar 10 μm. Images reproduced from ref.[244]

However, **81,** lacking the amide group, neither showed any ordered structures in polar solvents nor did it form gels in nonpolar media. This again highlights the role of strong H-bonding, π – π stacking and Van der Waals interactions in the formation of higher ordered aggregates formation.

Higher ordered hollow structures formed from assemblies of mesoscopic amphiphilic systems have also been reported by Mirkin and co-workers.[246] Hollow cylindrical structures were obtained using a rod shaped mesoscopic metal-polymer amphiphile **82**, the structure of which has a hard hydrophilic metal domain (Au) and a soft hydrophobic domain made of conducting polymer polypyrrole (Ppy). It was hypothesised that the two different block phases segregate and align in a particular way that increase the interactions between similar blocks. In **82**, the diameter of the polymer portion (~360 nm) is smaller than the metal domain (400 nm) (Figure 1.38A), which helps these building blocks to self-organise into curved cylindrical architectures, such as bundles, tubes and sheets in aqueous media. The variation of the block length of the Au and Ppy portions in **82**, allows control over the morphology of these assembled superstructures.

Compound **82** with a 1:4 Au/Ppy block length ratio formed hollow tubular structures on suspending in water. Due to the longer polymer length, the average rod head area (a_h) is smaller, allowing less curved packing of **82** (Figure 1.38, B and E). **82** with 3:2 Au/Ppy block length ratio with a shorter polymer chain length, also formed tubular structures and this assembly process continued to complete the closed tubular structure with open ends

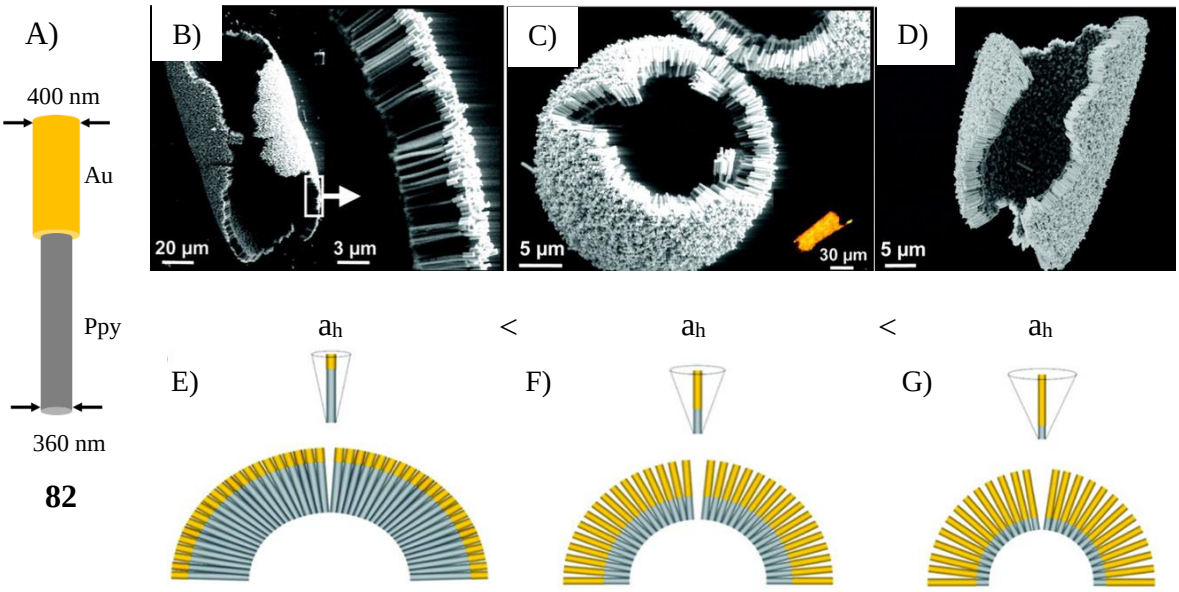

Figure 1.38: A). Schematic representation of Au/Ppy rod **82**. SEM images of assemblies of **82** with B) 1:4 Au/Ppy block length ratio; C) 3:2 Au/Ppy block length ratio; D) 4:1 Au/Ppy block length ratio and E) – G) Representation of packing of **82** forming tubes of different diameters, corresponding to those shown in B - C. Images reproduced from ref.[246]

(Figure 1.38, C and F). In the case of **82** with a 4:1 Au/Ppy block length ratio bearing the shortest polymer chain length, an open tubular structure was observed with higher curvature, due to the larger rod head area (Figure 1.38, D and F). In these highly ordered assemblies, a single layer of **82** rods were observed in all the cases, in which all the metal domains are in the exterior and the polymer chains are facing inside. This example introduced the concept of using polymer chains of different lengths and the role of metals in hybrid materials for constructing two and three dimensional structures with controlled morphology.

Another elegant example of such higher ordered assemblies using metal ions and organic compound is shown by Mirkin *et al.*[247] Using a modified Tröger's base ligand with terminal Aryl-COOH groups **83** and **84**, a coordination polymer was obtained upon reacting with Zn(II) (Figure 1.39A). Upon slow diffusion of ether into a DMF solution of **83** and **84** in the presence of $Zn(CH_3COO)_2$, a fluorescent, amorphous, infinite coordination polymer (ICP) particles were obtained. The average diameter of ICP particles of **83** and **84** were 2.18 ± 1.44 and 2.84 ± 0.62 μm, respectively and the shape remained spherical in other organic solvents, water and even after drying. Energy-dispersive X-ray (EDX) spectroscopy and elemental analysis confirmed 1:1 (M:L) structures.

The formation of these particles was analysed by following the time dependent transformation from precursors to particles using SEM. Upon slow diffusion of ether into a solution of mixed **83** (or **84)** and $Zn(CH_3COO)_2$ in DMF with stirring, the precipitates formed at different times were isolated by centrifugation, repeated washing with CH_3OH, and imaged using SEM. In the beginning (5 min), nanometre sized globular seeds were

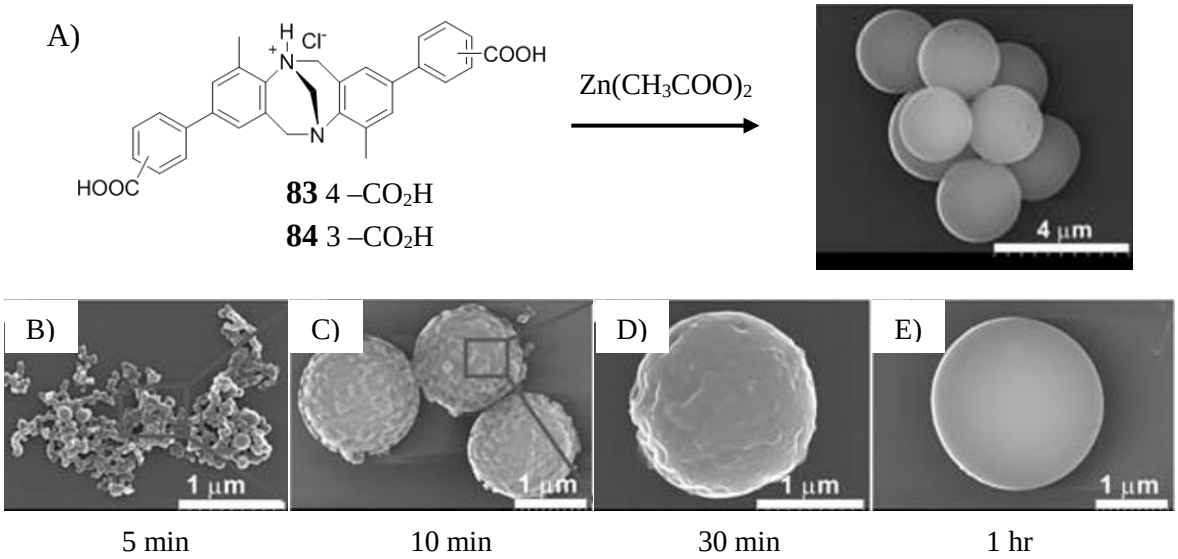

83 4 –CO_2H
84 3 –CO_2H

Figure 1.39: A) Synthesis of ICP particles from **83** and **84** with Zn(II) metal ions and B) SEM images of monitoring of **83** ICP particle formation at different time intervals. Images reproduced from ref.[247]

formed (Figure 1.39B), these agglomerate, forming spherical particle with rough surface in 10 min. (Figure 1.39C). As the reactions proceeds, the particle's surface becomes smoother after 30 min (Figure 1.39D). Finally after 1 hr, smooth-surfaced particles were observed (Figure 1.39E). From these observations, the constructed mechanism for the formation of these particles shows that, upon reacting **83** and **84** with $Zn(CH_3COO)_2$ a linear oligomeric chain is formed which nucleates to form seeds. These further undergo a series of aggregation processes and addition of new layers of seeds, finally forming ICP particles as shown in Figure 1.40. Thus formed **83** and **84** particles were stable up to ~400 ^oC as determined by TGA analysis.

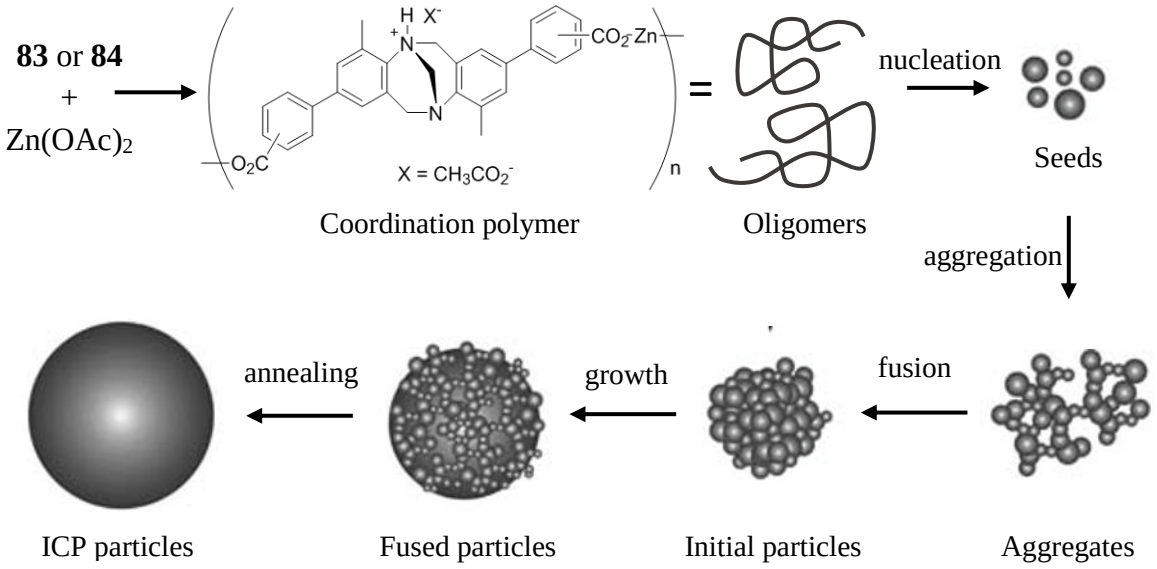

Figure 1.40: A) Proposed mechanism of the ICP particle formation. Images reproduced from ref.[247]

Applying this strategy of using the initiation solvent in the preparation of micro and nanoparticles, several other particles composed of a polymerised metal-ligand network using Zn, Cu and Ni were also reported.[248] Aggregation of such metal- based polymeric chains forming spherical particles, highlights the role of metal ions and opens up new ways of making nanosized materials.

Similarly, luminescent spherical particles with lanthanide (III)–based coordination polymers in the form of simple microspheres or core-shell species for sensing purposes were reported by Oh and co-workers.[249] Using Eu(III) and Tb(III) metal salts in the presence of isophthalic acid (**85**), simple luminescent microspheres were obtained. However, when the reaction was performed in presence of carboxylic acid terminated silica particles, core-shell type luminescent particles were formed (Figure 1.41, B and D inset). The isolated particles were sized ~0.7 μm and ~1.1 mm for the simple and core-shell microparticles, respectively

(Figure 1.41, B and D). The presence of Eu(III) and Tb(III) ions resulted in red and green emission from particles as observed from confocal microscopy (Figure 1.41, C and E). The initial luminescent intensity of the Tb-based microspheres was much stronger than from the Eu-based ones. These luminescent particles were employed for selective sensing of metal ions due to their better dispersity in comparison with other heterogeneous solid sensors.[250] The advantage of such sensors is that the turn off luminescence can easily be recognised by the naked eye and has higher sensitivity than other known sensors, making these superior candidates. Both EuCP and TbCP were selective towards Cu^{2+} detection among various metal ions with TbCP superior to EuCP in this regard.

Development of such luminescent functional materials by lanthanide coordination are very useful for many applications. Therefore, the properties and application of lanthanides will be discussed in the following sections.

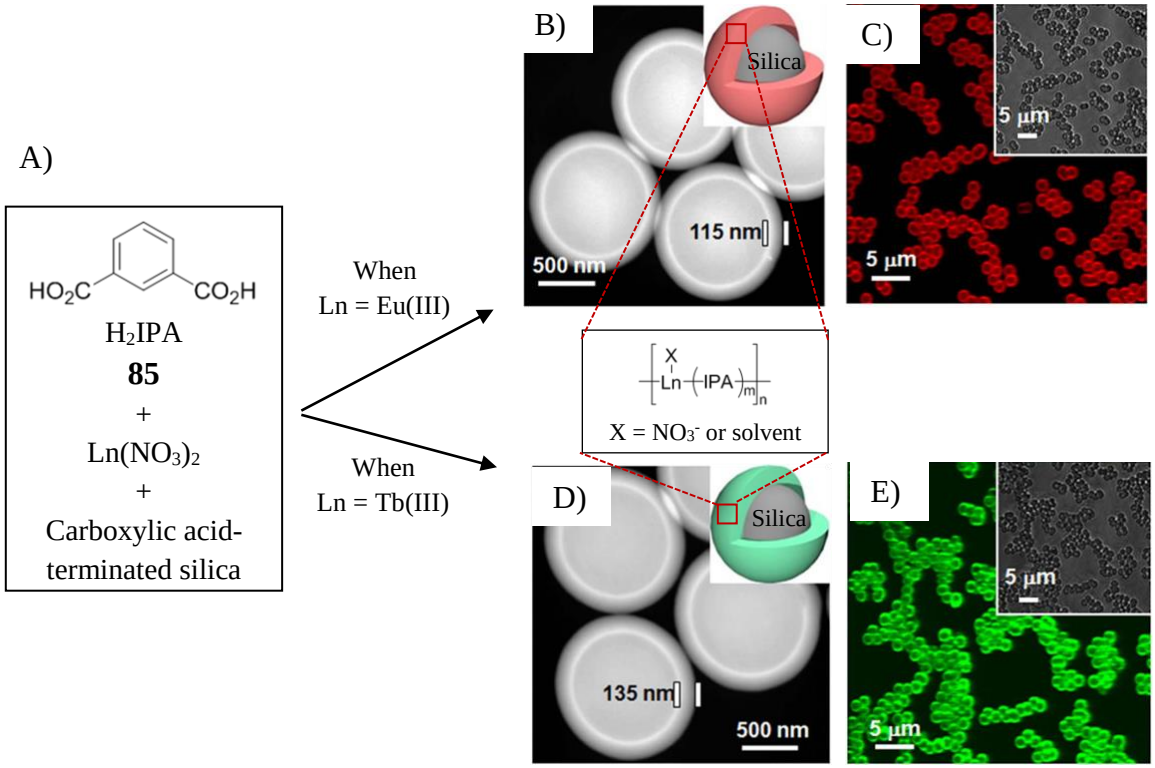

Figure 1.41: A) Synthesis of Ln-based luminescent core-shell microspheres. Images reproduced from ref [249]

1.5 Lanthanide metal ions

Lanthanide coordination chemistry has been significantly used in supramolecular chemistry because of the metal's unique magnetic and photophysical properties.[20, 251] Recently many lanthanide-based functional supramolecular structures have been produced, and with the constant follow of new structures designed for various applications.[30, 252] The properties of

the lanthanide ions were explored with a view to utilising their distinctive features for the development of various hybrid material such as organic light emitting diodes (OLEDs),[253] films,[254] luminescent gels,[255] pH sensors,[256-257] MRI contrast agents,[258-259] and many more.

1.5.1 Properties of lanthanides

The lanthanides (Ln) belong to the first row of the f-block of the periodic table of the elements, comprising fifteen elements, starting from lanthanum (^{57}La) to lutetium (^{71}Lu). Ln are usually found in their most stable trivalent state. Ln(III) ions have shown to adopt [Xe]4f^n (n = 0 – 14) electronic configurations, by gradually filling the 4*f* orbitals, which are shielded by the external filled outer subshells, 5s and 5p. Across the f-block of the periodic table, the gradual decrease in the ionic radii is observed, known as *lanthanide contraction*.[17, 260] Due to the high ionisation potential and charge densities of the lanthanides, the Ln(III) ions form strong coordination bonds of an electrostatic nature with a wide range of ligands. Thus, they can be referred as strong Lewis acids, preferentially binding ligands containing atoms of basic character, such as oxygen, nitrogen, or fluoride (having Lewis basic character). Furthermore, lanthanide metal ions have variable and high coordination numbers, up to 9 in solution. In order to satisfy these high coordination requirements, ligands with several donor atoms are required to form highly stable lanthanide complexes.[261-262] The distinctive photophysical properties of the Ln(III) and the benefits of its utilisation will be discussed in the next section.

1.5.2 Photophysical properties of the lanthanides

The unique photophysical properties of the Ln(III) ions essentially arise from the shielding of their 4*f* valence electrons by the filled 5s^2 and 5p^6 orbitals, which results in only minor disturbance of the electronic configuration by interactions with ligands.[263] The 4*f* electrons have the ability to undergo *f-f* transitions, giving rise to characteristic narrow line-like emission bands in their emission spectra. These bands are specific for each Ln ion, which covers the entire spectrum from ultraviolet-visible (UV-vis) to near-Infrared (NIR).[264-265] Most of the Ln(III) ions are luminescent except La(III) and Lu(III) and the colour of the emitted light depends on the lanthanide ion, for example Eu(III) is red and Tb(III) is green. Among the lanthanides exhibiting luminescence, some show fluorescent character, others phosphorescent character, or both.[17, 260]

During the fluorescence process, photon emission occurs through radiative decay of $S_0 \rightarrow S_1$ spin allowed transition, with no change in the spin ($\Delta S = 0$). This process happens in a short period of time, usually within the time frame of 10^{-12} to 10^{-6} s. Conversely,

phosphorescence involves a change in spin multiplicity ($\Delta S \neq 0$). As the radiative decay process takes place though a spin-forbidden $T_1 \rightarrow S_0$ transition, it is much slower than fluorescence, occurring from 10^{-6} s to 1 s.[251, 260] Additionally, some Ln(III) are more emissive than others in terms of intensities.[17, 265-266] The luminescence lifetimes of Ln(III) are long due to the Laporte forbidden nature of *f-f* transitions, leading to emission occuring in microseconds [Yb(III) and Nd(III)] to millisecond [Eu(III) and Tb(III)] range. This long luminescence lifetime makes Ln(III) ions highly desirable for the development of luminescent probes and sensors for *in vivo* imaging of biological materials, where the measurements are based on delay between excitation of the probe and Ln(III) luminescence.[267-269] Using this time gated technique, the autofluorescence associated with probes/chromophores, which is normally in the nanosecond range, can rejected by incorporating a time delay (Figure 1.42).[270]

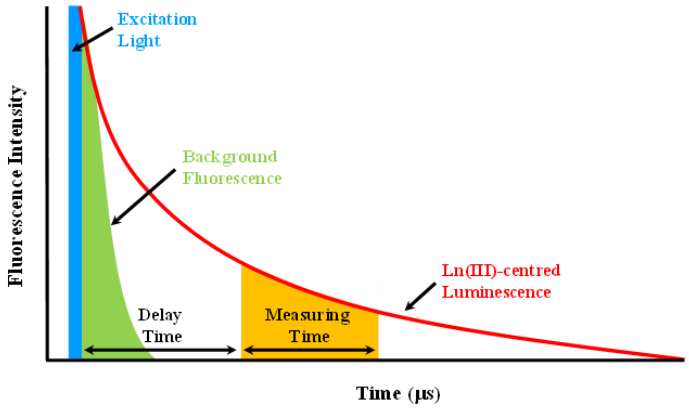

Figure 1.42: Illustration of the time delay between excitation and recording the emission in order to avoid short lived autofluorescence. Image reproduced from ref.[270]

One of the drawbacks associated with the use of Ln(III) as luminescent probes is that, because of its low molar absorption coefficient ($\varepsilon < 1\ M^{-1}cm^{-1}$), direct excitation of the metal ion is very inefficient.[271] The most effective way to solve this problem is through the so-called "antenna effect", where an organic chromophores with high molar absorptivity is used as an "antennae", from which the lanthanides are excited indirectly (Figure 1.43A).[271-272]

As illustrated in the modified Jablonski diagram in Figure 1.43B, upon irradiation of the lanthanide complex, the singlet ground state (S_0) of the antenna (Ar) absorbs a photon of light ($h\upsilon$), corresponding to its required excitation energy, generating a first excited higher vibrational level singlet state (S_1). The molecule then undergoes *internal conversion* to the lower vibrational level of the S_1 state. This excited singlet state can either be deactivated to the ground state to give molecular fluorescence ($S_1 \rightarrow S_0$) or can undergo non-radiative *intersystem crossing (ISC)* from the S_1 to a triplet state (T_1). This triplet state (T_1) can also

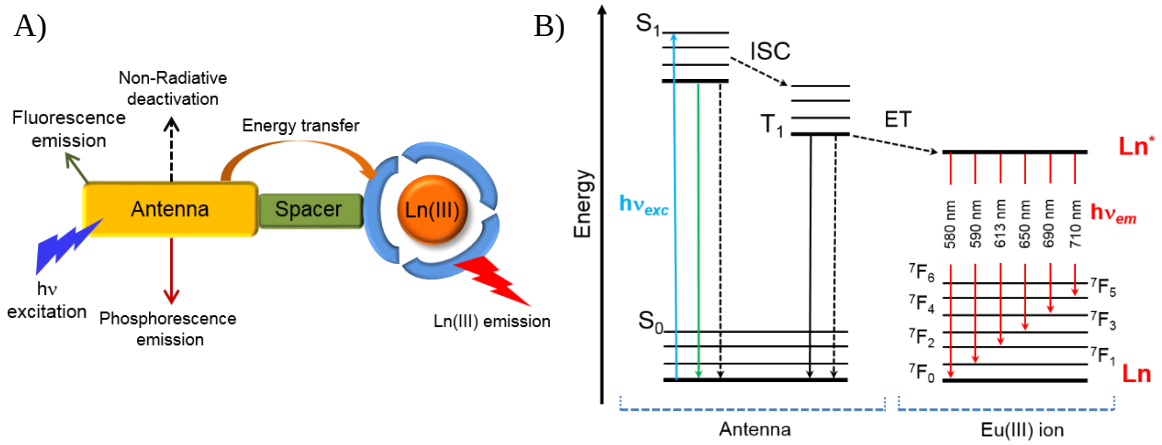

Figure 1.43: A) Schematic representation of the antenna effect, illustrating various ways of possible electronic deactivation for excited state Ln(III) complex. B) Simplified Jablonski diagram representing the sensitisation pathway for Eu(III) ion through 'antenna effect'. Images reproduced from ref.[272]

be deactivated to its ground state (S_0) resulting in molecular phosphorescence. Or the complex may transfer energy non-radiatively to lanthanide ion, resulting in the population of an excited state of the lanthanide. In case of the Eu(III) ion, population of its lowest excited state, $^5D_0$ occurs through intramolecular energy transfer (ET) of the sensitising chromophore. Then this energy can be deactivated by a radiative transition to its ground state electronic levels, ^7F_J (ΔJ = 0 – 5), giving rise to its characteristic sharp, line-like luminescence or alternatively *via* a range of non-radiative deactivations, such as vibrational collision, *etc*.[16, 260, 266]

When the energy level of the antenna triplet excited state is 1700 cm^{-1} higher than the accepting Ln(III) energy level, thermal back energy transfer is minimised. When the energy gap is less than 1500 cm^{-1}, however, it can result in the repopulation of ligand triplet state, increasing the chances of non-radiative quenching modes.[273] Among Ln(III) ions, Eu(III) and Tb(III) are among the most extensively studied, with the excited state energies of 17200 cm^{-1} and 20500 cm^{-1}, respectively.

In addition to the fluorescence ($S_1 \rightarrow S_0$) and phosphorescence ($T_1 \rightarrow S_0$) radiative decays discussed above, other non-radiative decays compete with the population of the Ln(III) excited state. These are deactivation of the singlet excited state (S_1) by collisional and vibrational quenching with the surrounding molecules and also includes quenching of the triplet excited state (T_1) by molecular oxygen.[16, 23] Vibrational quenching has proven to quench the luminescence of the Ln(III) to greatest extent. This phenomenon will be discussed in the following section.

1.5.3 Lanthanide luminescence quenching

As mentioned above, a typical luminescence quenching mode involves energy transfer from Ln(III) excited state to coordinated or diffusing solvent molecules (most often from water molecules).[260] These quenching processes occur both in the inner and outer coordination sphere of the Ln(III) through vibronic coupling with O-H, N-H, and C-H stretching modes. This quenching phenomenon allows us to examine the coordination environment of the Ln(III) by determining the number of water molecules bound to the metal (the hydration state – *q* value) directly within the inner coordination sphere. This relationship was described mathematically by Horrock and co-workers, estimating the number of O-H oscillators directly bound to the metal centre in Eu(III) complexes.[274-275] This method was developed on the hypothesis that, in deuterated solvents, the O-D oscillator contributes less to the deactivation processes of the excited Eu(III) ions to a much lesser extent than O-H oscillators.[20, 276] Further modification of this expression on considering the effect of N-H and C-H vibrations was presented by Parker *et al*.[277] as given in Equation 1.1 for the purpose of calculating q values for Eu(III) derivatives,

$$q^{\mathrm{Eu(III)}} = \mathrm{A}\left[\left(\frac{1}{\tau_{\mathrm{H_2O}}} - \frac{1}{\tau_{\mathrm{D_2O}}}\right) - 0.25 - 0.075x\right] \qquad \text{Equation 1.1}$$

Where, τ_{H2O} and τ_{D2O} = life time of Eu(III) recorded in H_2O and D_2O.

Using Equation 1.1 specifically for Eu(III) in H_2O, the proportionality constant (A) is determined as 1.2 ms and the correction terms, -0.25 and -0.075 corresponds to quenching by second sphere water molecules and N-H oscillators, respectively. *x* is the number of amide N-H oscillators bound directly to the metal *via* the oxygen atom of the carbonyl group.[278] The best way to minimise the vibrational deactivation of Ln(III) luminescence is by using the ligands that form stable complexes with minimal high energy vibration, and avoid deactivating solvent coordination by shielding the Ln(III) from the solvent environment. Ligands with appropriate chromophores and multidentate binding abilities with high coordination environment are best suited to ensure high emission intesity, and in the development of Ln(III) luminescent materials.[23, 279] Gunnlaugsson *et al.* have contributed to the area of lanthanide coordination with the view of development of soft and luminescent materials, which will be discussed in the next section.

1.6 Advances in the Gunnlaugsson group

The Gunnlaugsson group has established expertise for the development of novel luminescent Ln(III) probes. As discussed in Section 1.1, self-assembly of molecules can be used as an

effective pathway for the development of supramolecular architectures and the group has developed many examples of such designs. In an attempt to take this work to the next level, the research group has focussed intensely on multimetallic luminescent Ln(III) self-assemblies for the development of soft materials like gels, as there is a need for such molecular materials in hydrometallurgy, cosmetics, food processing, lubrications, drug delivery, protein crystallisations *etc*.[13, 232] Metal-directed synthesis is recognised as being a key approach to the formation of such assemblies.[280]

Gunnlaugsson *et al*. detailed the first example of a terpyridine based tripodal molecule **86** exhibiting gelation properties in the presence of Eu(III) ions (Figure 1.44A).[281] This was achieved using the C_3-symmetrical benzene-1,3,5-tricarboxamide (BTA) core (known for its formation of triple stranded hydrogen bonding), connected to three 2,2′,6′,2″-terpyridyl (tpy) moieties, which are expected to coordinate the Ln(III) and function as a sensitizing antenna for the population of the $^5D_0$ excited state of Eu(III).

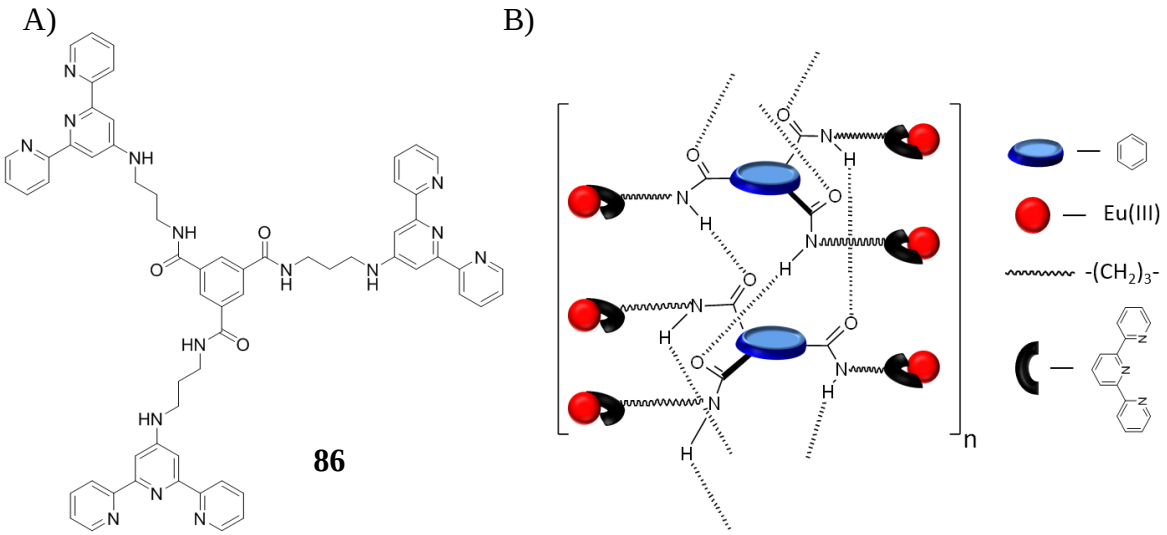

Figure 1.44: A) Molecular structure of the tripodal tpy based ligand **86**. B) Schematic representation of the threefold hydrogen bonding in helices of **86** showing the europium binding sites on the outside of the helix. Images reproduced from ref.[282]

Spectrophotometric studies conducted in solution of ligand **86** with Eu(III) ions indicated the formation of a (**Eu:86**) complex with a 1:1 stoichiometry. Energy transfer from ligand **86** to the $^5D_0$ excited state of Eu(III) ions gave rise to the characteristic Eu(III) emission. Nonlinear regression analysis of the experimental data confirmed the formation of 1:1 and 3:2 (**M:86**) species. These results clearly demonstrate that the equilibrium process **Eu + 86** ↔ **Eu:86** can be shifted to higher stoichiometry and formation of higher order self-assemblies. Both **86** and **$EuCl_3$-86** gels were formed in H_2O/MeOH mixture. The

mechanism of the $EuCl_3$ gel formation is the collective result of the threefold intermolecular hydrogen bonding possibly with additional π– π stacking between the tpy moieties (as depicted in Figure 1.44B) along with binding of the 2D polymers with Eu(III) ions into 3D structures. All the gels formed were luminescent with characteristic Eu(III) emission. In collaboration with Prof. J. Boland, SEM analyses of the dried samples showed fibrous microstructures consisting of long intertwining bundles (Figure1.45A). **$EuCl_3$-86** gave rise to the formation of more ordered gels (Figure 1.45B) showing "rope-type" assembly of strands.

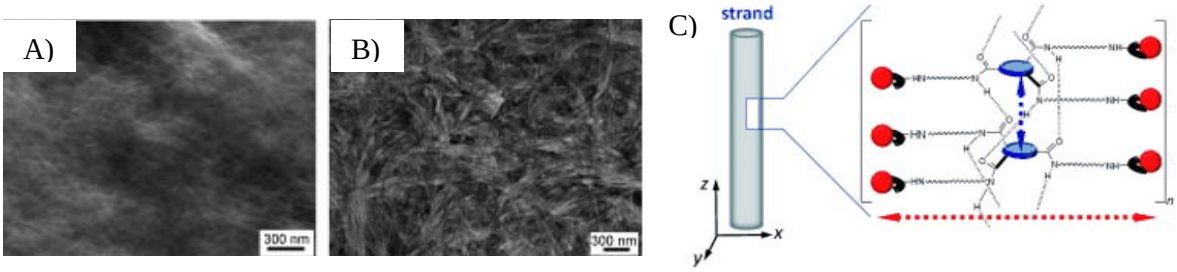

Figure 1.45: SEM images of A) of ligand **86** gel; B) **$EuCl_3$-86** supramolecular gels and C) schematic representation of the self-assembly of **86** and Eu(III) ions within $EuCl_3$-**86** gels. Images reproduced from ref.[282]

Continuing this work, Gunnlaugsson and Boland reported the interesting phenomenon of the growth of crystalline salt wires on the surface of the above described gel matrix upon drying.[282] Employing the supramolecular gel based on compound **86**, which form two-dimensional supramolecular polymers, it was possible to grow nanowires of common halide salts (NaCl, KCl, and KI), from a dropcast supramolecular gel. The same types of wires were also obtained using the **$EuCl_3$-86** gels. SEM images of the dried gels in ambient conditions followed by vacuum drying showed signs of thin wires growing from the surface of the dried gel with a diameter of 130-200 nm (Figure 1.46).

Further investigations revealed evidence for the base growth mechanism where crystal growth appears to draw some of the gel strands up from the substrate (Figure 1.46C), strongly suggesting that nanowire growth results from diffusion and crystallisation of ions at the lower face of a small seed crystal formed within the gel surface. This is similar to the base growth mechanism suggested for porous membrane wire growth.[282] Closer examination of the nanowires using transmission electron microscopy (TEM) diffraction pattern, unveils their cubic, single-crystal morphology. EDX spectroscopy confirmed the expected 1:1 stoichiometry of sodium chloride, while the diffraction pattern indicated a cubic single-crystal structure. This phenomenon was also found to follow with different salts like

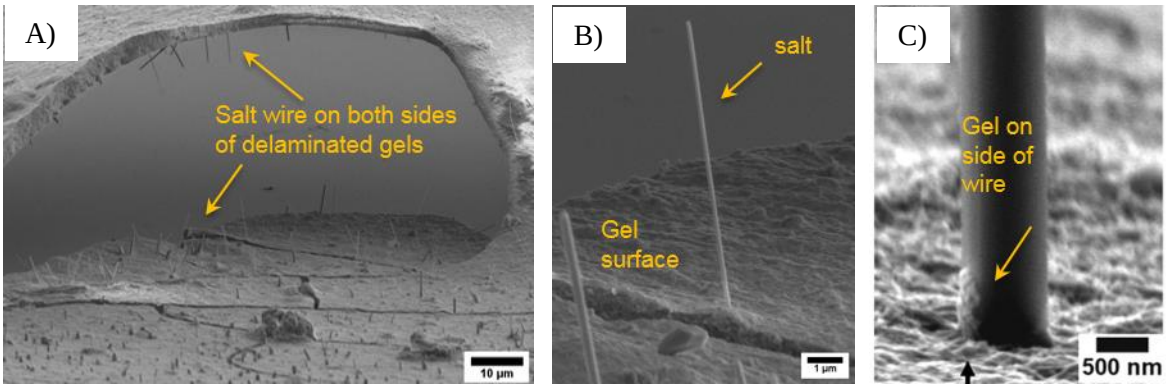

Figure 1.46: A) Growth of nanowires seen on both sides of delaminated gel film; B) NaCl nanowires grown from a Eu(III) gel; C) Gel observed on the side of nanowires. Images reproduced from ref.[283]

potassium iodide and potassium chloride, displaying the compatibility of these gels to a range of common salts. The approach described here shows the applicability of supramolecular gels towards the development of single-crystal nanowires of unprecedented dimensions and provides an opportunity to test the properties of these important nanoscale material systems.

Recently, Gunnlaugsson *et al.* reported Ln(III) (Ln = Eu and Tb)-based luminescent metallogels with self-healing properties prepared from cross-liking gels of 1:3 and 1:2 (**Ln:87)** stiochiometries through their terminal carboxylic groups.[255] In order to obtain gels, initaially, the 1:3 (**Ln:87**) metal complex (**Ln(87)$_3$**) was prepared by microwave irradiaton. Upon addition of excess of Ln(CH_3COOH)$_3$ to **Ln(87)$_3$**, soft gel-like precipitate was observed at various (**Ln(87)$_3$:Ln(CH_3COOH)$_3$**) stiochiometries after further microwave irradiation at 75 ^oC, which, later upon centrifugation, resulted in the formation of robust gels. The most appropriate ratio was found to be 1:0.5 for both Eu(III) and Tb(III) in forming the most stable gel (Figure 1.47A). Both the gels obtained were slightly opaque and were highly luminescent under UV-light irradiation, displaying green and red emission for Tb(III) and Eu(III) respectively (Figure 1.47,B and C). Both gels showed similar morphologies on microstructural analysis. Transfering these gels onto quartz slides (Figure 1.47D) showed the respective Ln(III) sharp line like emission. Simple mechanical mixing of equal volumes of these two Ln(III) gels, yielded yellow-orange luminescent Eu(III)/Tb(III) gel (Figure 1.47D), showing two main emission bands at 545 nm and 616 nm for Tb(III) and Eu(III) emissions respectively (Figure 1.47E).

The formed supramolecular gels showed interesting self-healing behaviour, and materials with such features are of particular interest as they have the tendency to mimic

naturally occuring biopolymers.[283-284] When the gel was cut in two and brought togather,they reassembled through self-healing without use of any external stimuli (Figure1.48). Since both Tb(III) and Eu(III) gels are formed by dynamic processes, second Ln(III) ions added to the **Ln:87$_3$** complex recognise and bind to the terminal carboxylic groups to form a three dimentional coordination network. As this recognition process occurs at the edge of the cut, it helps in potential self-healing of the cut gels. The SEM images showed that, at first glance, the gels showed similar morphology, with fibres of 30-50 nm and interwined bundles similar to cotton like structures. However, closer observation revealed that, the Tb(III) gels have more densely packed fibrous network in comparision with the Eu(III) gels. This explains the difference in the gel volume, although they were prepared from the same concentration and volume. Moreover, the Tb(III)/Eu(III) mixed gel morphology was different from its individual component gels in terms of packing and porosity. Rheological measurements also

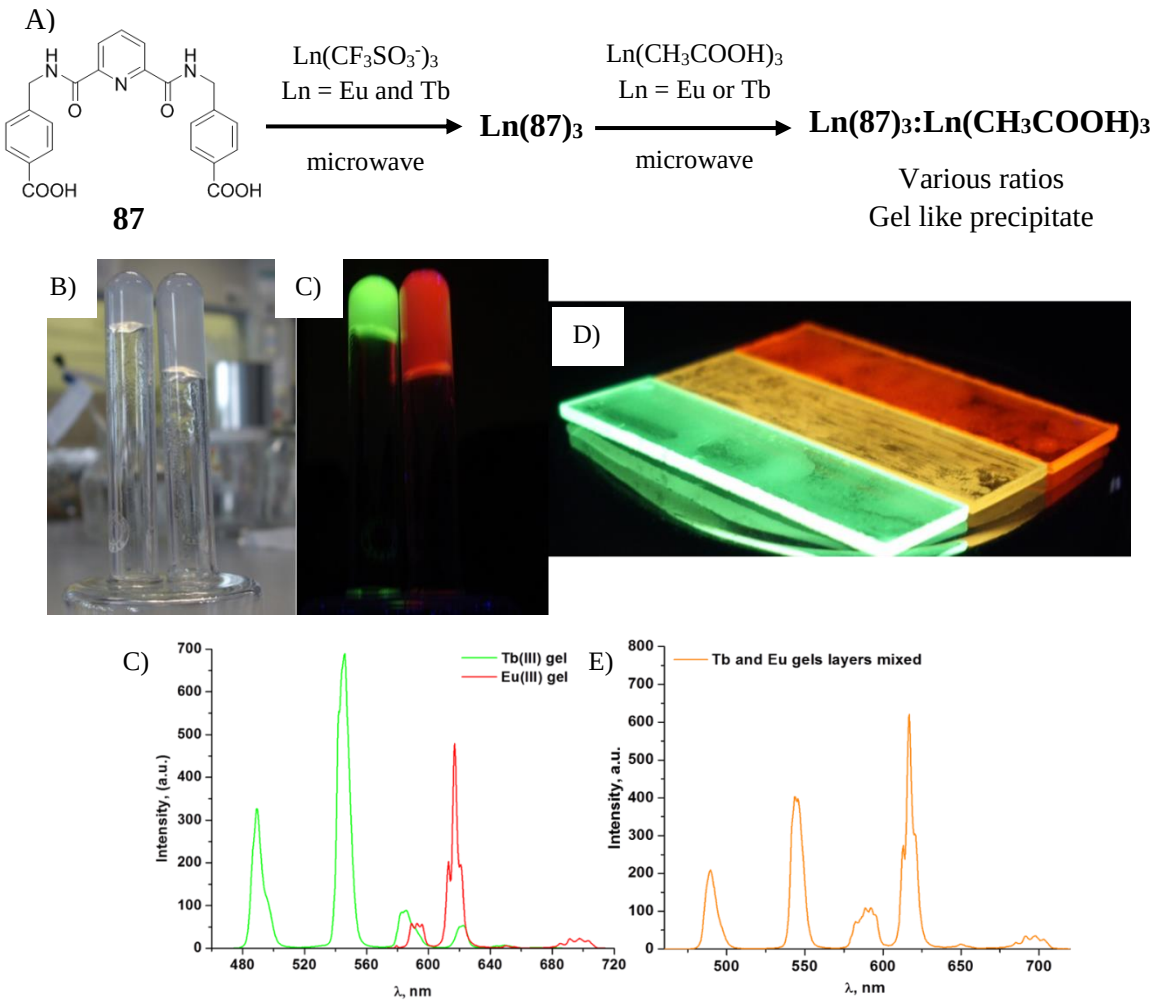

Figure 1.47: A) Synthesis of gel forming complex, **Ln(87)$_3$:Ln(CH$_3$COOH)$_3$**; B) and C) Eu(III) and Tb(III) gels in daylight and under UV; D) Luminescence of Eu(III), Tb(III), and Eu(III)/ Tb(III) gels on quartz plates; luminescence spectra of D) Eu(III) and Tb(III) and E) Eu(III)/Tb(III) mixed gel. Images reproduced from ref.[255]

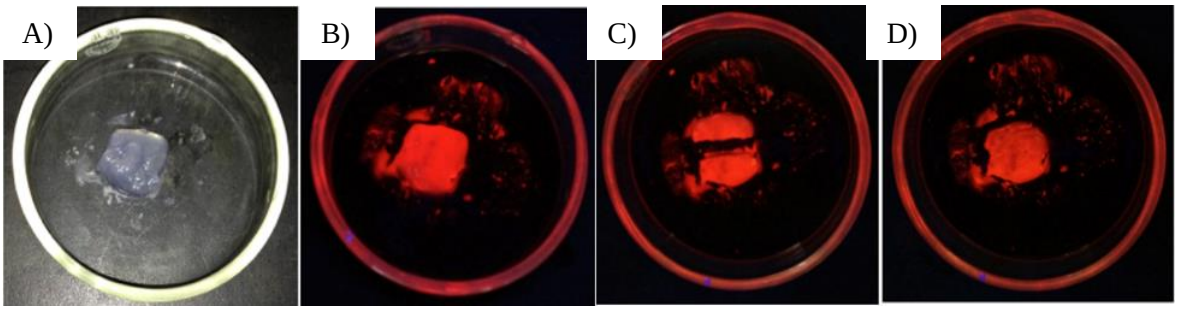

Figure 1.48: Healing experiment of Eu(III) gel. A) in the day light; B) under UV light; C) Gel cut in to halves; D) self-healed gel. Images reproduced from ref.[255]

confirmed the self-healing nature of individual and Tb(III)/Eu(III) mixed gels, where the same value of G′ was observed, which was at the start of the experiment .

In addition to this, many other Ln(III) based self-assembled systems, including luminescent metallogels,[285] monometallic and mutimetallic assemblies,[30, 286] thin films,[287] interlocked systems,[63-64] dual resposive logic mimicing systems,[288] MOFs,[289] luminescent contrast agents for microdamaged bone,[18] and MRI probes[290] were also reported from the Gunnlaugsson group.

1.7 Work discribed in this thesis

The objective of the work described in this thesis was to build upon the earlier work within the Gunnlaugsson group, relating to the self-assembly of the tripodal molecule described above in Section 1.6. New BTA core based tripodal molecules were designed to be utilised in the development of soft material and micro-structured particles.

In Chapter 2, the design and synthesis of the new tripodal molecules incorporating chiral centres using various amino acids and a tpy moieties at the peripheries of the molecules are discussed. The synthesised molecules are investigated for their abilities in the formation of supramolecular self-assembled structures, wherein the metal-directed self-assembly in solution with Eu(III) at different ligand concentrations analysed using photophysical techniques are discussed. Additionally, the analysis of the photophysical titrations data using non-linear regression analysis (SPECFIT®) for the determination of the solution speciation distribution and stability constants (logβ values) of the self-assembled species formed in solution, upon addition of Eu(III), are also discussed.

In Chapter 3, the abilities of these synthesised BTA molecules to self-assemble resulting in the formation of soft materials and microparticles are presented. Gels formed from an achiral BTA molecule are analysed using various microscopic techniques and rheological measurements. The formation of microspheres from chiral BTA derivatives and

their analysis using various microscopic and spectroscopic techniques is then discussed. Furthermore, the mechanism of the formation of these micro-structured morphologies, and their behaviour in the presence of metals are also presented. The use of FIB techniques confirming the solid nature of the microparticles are reported. Using AFM, the lateral force displacement studies and mechanical stiffness measurements performed on the microspheres are discussed. The formation of a monolayered network of the interconnected microspheres is exhibited. Additionally, the self-sorting properties of the achiral and chiral BTA derivatives exhibiting orthogonal self-assembly behaviour when mixed together forming independent 1D fibrous structures and microspheres are discussed.

In Chapter 4, the microspheres are examined using optical microscopy. The luminescent microspheres were probed using LSCM and the formation of microspheres in solution is monitored in real-time. The Ln(III) containing luminescent particles formed upon addition of Ln(III) ions onto microparticles are also described. In addition to this, the circularly polarised luminescence (CPL) of the Ln(III) luminescent microspheres is measured and reported.

Lastly, in Chapter 5, general experimental procedures and relevant characterisation data are provided for all the compounds described in the preceding chapters of this thesis.

Chapter 2

Europium directed self-assembly studies of tripodal ligands

2 Introduction

As previously discussed in Chapter 1, Section1.6, the tripodal ligand **86** self-assembles into one dimensional supramolecular polymers through π – π stacking and threefold hydrogen bonding between the BTA cores of adjacent molecules, leading to gelation.[281-282] It was envisaged that incorporation of chiral moieties into the BTA core of **86**, as shown in Figure 2.1 would direct the disc shaped molecules towards the formation of self-assembled, helical and columnar structures.[141, 156] This project aims to build on previous work reported by the Gunnlaugsson group into the lanthanide directed self-assembly of tpy based tripodal molecules into supramolecular polymers.[281] In the current work the appropriate modifications to such systems were explored and better understanding of the assembly process was elucidated. The main topics that have been addressed in the design and study of these ligands and complexes include:

- Modifications of the BTA ligands by incorporating the achiral amino acid glycine and the chiral enantiomers (R and S) of alanine, phenylalanine and leucine;
- The effect of concentration of the molecule on the formation of supramolecular polymers;
- Sensitisation of Ln(III) centred emission;
- Gel formation experiments and analysis using microscopic and other techniques.

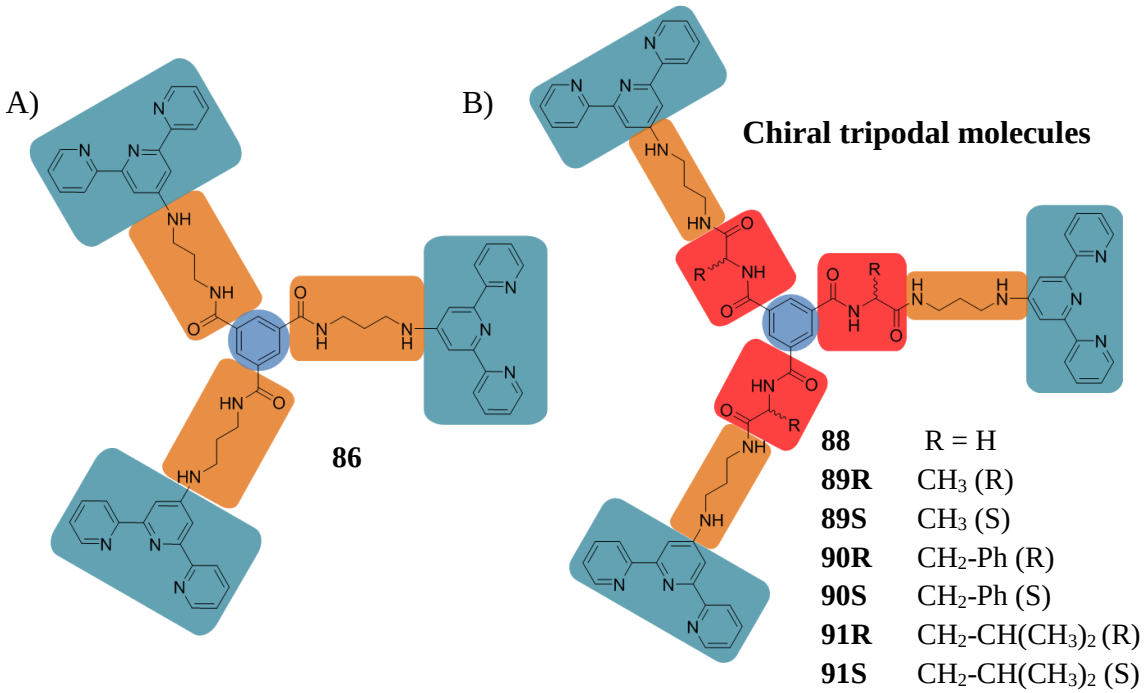

Figure 2.1: Schematic representation of A) BTA tripodal molecule **86** and B) new molecules **88** – **91** with chiral centres using aminoacids (red region).

2.1 Design and synthesis of *R* and *S* tripodal BTA ligands

The objective of this PhD research is to develop tpy based molecules with various chiral centres using appending amino acids, namely alanine, phenylalanine and leucine, and to study the effects of their chirality on the formation of linear supramolecular polymers as well as europium directed three dimensional structures based on these tripodal ligands. Therefore, Glycine was used as non-chiral amino acid and the three chiral amino acids were chosen because of the different sized chiral groups. In a similar manner to previous work,[281] the structure of these novel ligands was based on the C_3-symmetric benzene-1,3,5-tricarboxamide (BTA) central core in order to facilitate the initial formation of one dimensional polymers through $\pi - \pi$ stacking interactions and three fold H-bonding.[145] In order to introduce chirality into the tripodal systems, the syntheses of the molecules started

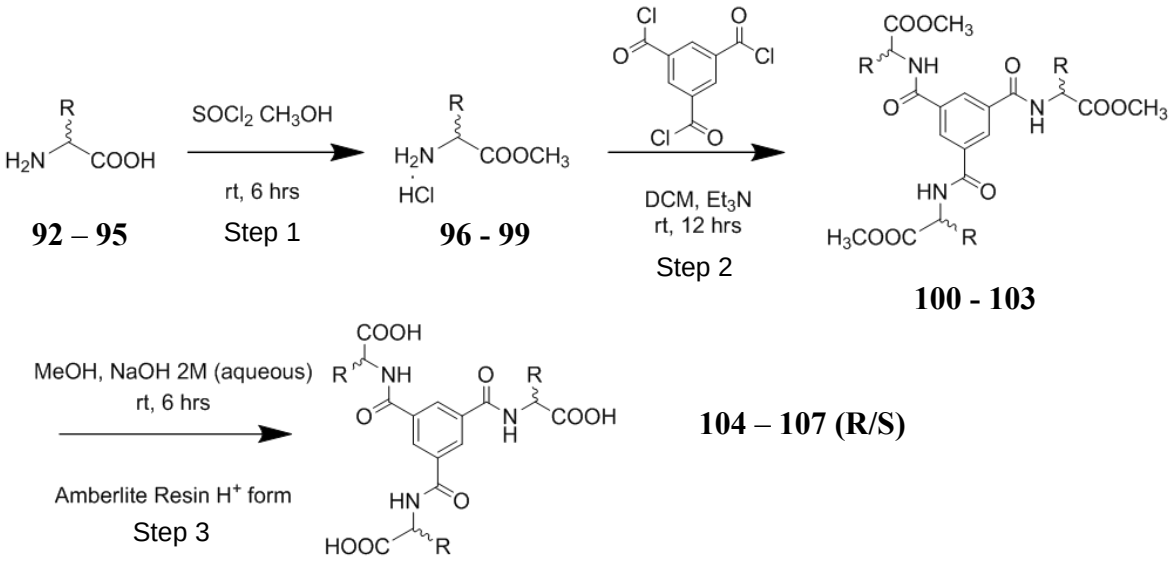

Scheme 2.1: Synthesis of amino acid functionalised tripodal ligands **104 - 107.**

Table 2.1: Synthesised precursors **92** – **107** using the above scheme 2.1.

R (substituent at chiral centre)	Compounds synthesised			
	Starting material	Step 1	Step 2	Step 3
H	**92**	**96**	**100** (67%)	**104** (81%)
CH_3 (*R*)	**93R**	**97R**	**101R** (85%)	**105R** (85%)
CH_3 (*S*)	**93S**	**97S**	**101S** (69%)	**105S** (85%)
CH_2-Ph (*R*)	**94R**	**98R**	**102R** (63%)	**106R** (78%)
CH_2-Ph (*S*)	**94S**	**98S**	**102S** (67%)	**106S** (87%)
CH_2-$CH(CH_3)_2$ (*R*)	**95R**	**99R**	**103R** (62%)	**107R** (81%)
CH_2-$CH(CH_3)_2$ (*S*)	**95S**	**99S**	**103S** (68%)	**107S** (73%)

from the BTA core, where the chiral groups were incorporated using the three different amino acids mentioned above. This functionalised BTA core was then connected to a 2,2',6',2''-terpyridine (tpy) group, through a short C_3 carbon chain, to complete the tripodal structure.

The syntheses of the enantiomeric pairs of *R* and *S* tripodal molecules are shown in Scheme 2.1 - 2.3. Ligands based on this framework with three terpyridyl moieties are capable of fulfilling the high coordination requirements of Ln(III), yielding the coordinatively saturated chelates through the coordination of three tpy groups.[281] As discussed in Chapter 1, Section 1.5, the direct excitation of Eu(III) is known to be very inefficient in order to achieve its high luminescence intensity,[291] and therefore this challenge must be overcome through the use of an appropriate sensitising antenna. Here the tpy moiety **108** was selected as a suitable sensitiser for Eu(III) emission as its derivatives have previously been shown to be effective as light-harvesting units.[281, 292-293]

As shown in Scheme, 2.1, the synthesis of **104** - **107** was achieved in three steps in good yields and the precursors obtained in the scheme 2.1 are listed in Table 2.1 with their

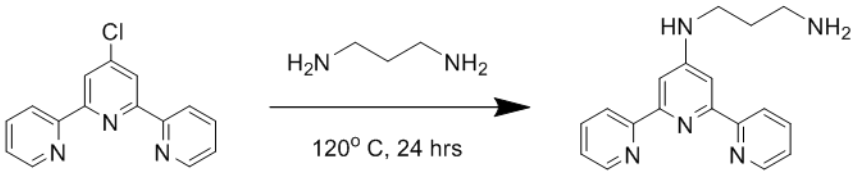

108 (80%)

Scheme 2.2: Synthesis of amino terpyridine **108.**

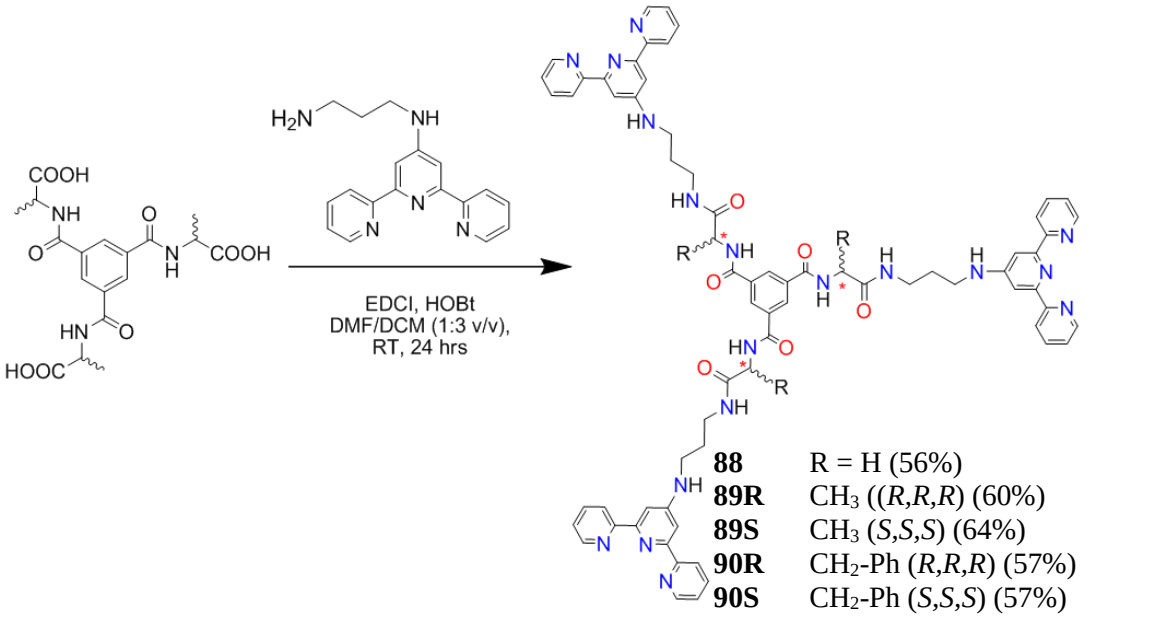

88	R = H (56%)
89R	CH_3 ((*R*,*R*,*R*) (60%)
89S	CH_3 (*S*,*S*,*S*) (64%)
90R	CH_2-Ph (*R*,*R*,*R*) (57%)
90S	CH_2-Ph (*S*,*S*,*S*) (57%)
91R	CH_2-$CH(CH_3)_2$ (*R*,*R*,*R*) (61%)
91S	CH_2-$CH(CH_3)_2$ (*S*,*S*,*S*) (69%)

Scheme 2.3: Synthesis of tripodal molecules **88 – 91.**

corresponding yields. The synthesis of chiral *R* and *S* benzene-1,3,5-tricaboxamide amino acid derivatives, **104, 105 - 107(R)** (*R,R.R*) and **105 - 107(S)** (*S,S,S*) (Scheme 2.1) was accomplished by first reacting (either the *R* or the *S* enantiomer) of the relevant amino acids [**92, 93 - 94(R** and **S)**] with thionyl chloride in CH_3OH at room temperature for 6 hours. Following this, the CH_3OH and thionyl chloride was removed under reduced pressure and the resulting solid was redissolved in dichloromethane (CH_2Cl_2), cooled to 0 ^oC and triethylamine was added to it in order to neutralise the remaining trace amounts of thionyl chloride. To this, a solution of 1,3,5-benzene tricarbonyl chloride dissolved in $CHCl_2$ was added dropwise. The resulting solution was bought to room temperature and stirred for a further 12 hours. After the reaction was complete (monitored by TLC using 90% $CHCl_3/CH_3OH$ as the eluent), the reaction mixture was diluted with CH_2Cl_2 and the organic layer was washed with saturated aqueous $NaHCO_3$ and H_2O, and dried over Na_2SO_4. The organic solvent was removed under reduced pressure to obtain the crude product which was purified by silica gel column chromatography performed manually by gravity (90% $CHCl_3/CH_3OH$) to give the pure compounds **100, 101 - 103 (R** and **S)** in approximately 80 - 85% yields. *In situ* synthesis of methyl ester amino acid salts (**96 – 99**) was found to be efficient in synthesising the compounds **100 – 103** with significantly higher yield, in comparison to the lower yields (30 – 40 %) when commercially available **96 – 99** were used. The successful coupling of the methyl ester of amino acids [**96, 97 - 99 (R** and **S)**] to the benzene tricarbonyl chloride was confirmed by ^1H NMR (400 MHz, $CDCl_3$) analysis, which showed the presence of a singlet at 3.77 – 3.83 ppm (for the methyl ester group), multiplets at 4.21 – 5.06 ppm (for the H at αC of chiral centres) and multiplets at 1.58 – 3.24 ppm (for the H at βC of sides chains) for the amino acid methyl triester, see Appendices A1 - A7 for ^1H and ^{13}C NMR spectra of **100, 101 – 103 (R** and **S)**.

The triesters were hydrolysed using basic conditions by stirring **100, 101 - 103 (R** and **S**) in a mixture of 2M NaOH (aqueous) and MeOH at room temperature for 6 hours (Scheme 2.1) and the reaction mixture was neutralised with Amberlite IR 400 H^+ ion exchange resin, followed by removal of the resin by filtration. The resulting organic layer was removed under reduced pressure to obtain the hydrolysed products **104, 105 - 107(R)** and **105 - 107(S)** in ~72% yield. The formation of the products were confirmed using ^1H NMR (400 MHz, DMSO-d_6), which showed the loss of the methyl ester groups (Figures A2.8.1 – A2.14.2 in the appendix), while the IR spectrum showed the appearance of broad peak around 3291- 3395 cm^{-1} corresponding to an O-H stretch. The formation of the benzene

tricarboxamide triacids **104 - 107 (R** and **S)** was also confirmed by ESI+ MS analysis where the [M+H] peak was observed for each molecule at respective m/z values.

The synthesis of the terpyridine antenna (**108**) with an amino propane carbon chain linker was accomplished by reacting 4′-chloro-2,2′:6′,2″-terpyridine with 1,3-diamino propane at 130 ^{o}C for 24 hours (Scheme 2.2). Upon completion of the reaction, the reaction mixture was quenched with ice cold H_2O resulting in the formation of a white precipitate, which was dried and redissolved in CH_2Cl_2 and washed with H_2O. This organic layer was then dried over Na_2SO_4, filtered and the solvent removed under reduced pressure to yield a white solid giving compound **108** in 80 % yield.

Next, **88 - 91** were prepared by employing a peptide coupling reaction, where the appropriate enantiomer, (**104, 105 - 107(R)** or **105 - 107(S)**), was stirred in a mixture of anhydrous DMF/DCM (1:3 v/v) at 0 ^{o}C with *N*-ethyl-*N*′-(3-dimethylamino-propyl)carbodiimide hydrochloride **(**EDCI·HCl) and 1-hydroxybenzotriazole (HOBt) (Scheme 2.3) for 30 min before amino terpyridine **108** was added. The resulting reaction was left to stir at room temperature under argon for 24 hrs, after which the solvent was removed under reduced pressure, and neutralised by the addition of ice cold water, resulting in the formation of a white precipitate, which was filtered and dried under vacuum, dissolved in $CHCl_3$, washed with a sat. solution of $NaHCO_3$, H_2O and dried over Na_2SO_4. The resulting organic layer was removed under reduced pressure to obtain the crude compound, which was further purified by column chromatography on neutral alumina (performed manually by gravity using 90% $CHCl_3$/EtOH) as eluent giving **88** – **91** in 60% yield. The formation of

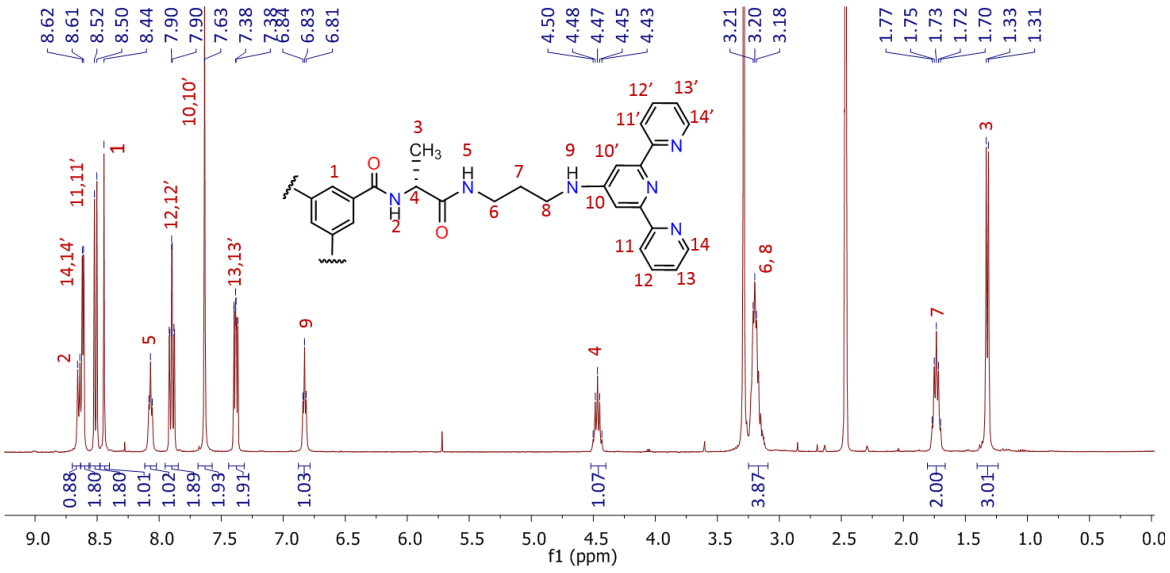

Figure 2.2: ^{1}H NMR (600 MHz, DMSO-d_6) spectrum of ligand **89R**. (see Appendix A2.18.1 for ^{1}H NMR spectrum of ligand **89S**).

the products were confirmed by ^{1}H NMR (600 MHz, DMSO-d_6) analysis, which showed the presence of aromatic peaks in the range of 8.69 - 7.42 corresponding to the tpy groups and a new peak appearing at 8.10 for NH due to formation of new amide bond (see Figure 2.1 for the ^{1}H NMR spectra of **89S**). The formation of an amide bond was also confirmed by IR spectra showing the bands for N-H stretching frequencies between 3258 and 3291 cm^{-1} for compounds **88** – **91**. The formation of the tpy trimers **88 - 91** was also confirmed by HR-MALDI MS analysis, where the signals corresponding to [M+H] species were observed at respective m/z values (See Appendices A2.17 – A2.21 for the MALDI mass spectra of **88** – **91**).

2.2 Complexation and spectroscopic analysis of ligands 89R and 89S with Eu(III)

With the aim of investigating the behaviour of **88 – 91** in solution at lower concentrations, the metal directed self-assembly of these molecules was studied. Of these, the alanine derivative **89** (R and S) was chosen for study because of its smaller sized chiral group. Hence, the complexation and the Eu(III) directed self-assembly of **89** (**R/S**) has been studied in detail and as such, these will be discussed in this chapter. The self-assembly of the other synthesised molecules/ligands will be discussed in the later chapters.

By employing the established procedure used in the Gunnlaugsson group for the syntheses of Ln(III) complexes under thermodynamic control, the ligands **89R** and **89S** were reacted with 1 mole equivalent of $Eu(CF_3SO_3)_3$ in CH_3OH at 70 ^oC under microwave irradiation for 60 minutes. After which, the reaction mixture was concentrated to half of its initial volume and the Eu(III) complexes precipitated upon ether diffusion to yield **Eu.89R** and **Eu.89S** as white solids in near quantitative yields. ^{1}H-NMR spectra of the Ln(III) complexes are generally complex due to the paramagnetic nature of Ln(III) ions, including Eu(III). As a result of this, the proton resonances can broaden and shift, sometimes beyond recognition making the spectrum difficult to interpret. As with their corresponding ligands, **89R** and **89S**, the ^{1}H-NMR spectra of both complexes were found to be identical. The ^{1}H-NMR spectrum of **Eu.89R** was different from its corresponding ligand (**89R)** with many resonances showing dramatic changes, where the significant broadening in the aromatic region of tpy moiety, 8.5 – 7.3 ppm and the presence of the peaks at ~ 13.5 and ~ -1.0 ppm were observed, which is due to paramagnetic nature of the Eu(III) ion, thus confirming the complexation of **89R** with Eu(III). The ^{1}H-NMR spectrum of **Eu.89S** also showed similar behaviour. The ^{1}H-NMR spectra of **Eu.89R** and **Eu.89S** are provided the in Appendix Figures

A2.23.1 and A2.23.2. **Eu.89R** and **Eu.89S** were also characterised by mass spectrometry analysis which are discussed in next section.

The spectroscopic properties of the synthesised 1:1 (M:L) complex and its corresponding ligands were investigated in CH_3OH solution. The photophysical properties of the complexes were evaluated in order to understand the binding modes of tpy moieties to the Eu(III) ion.

The formation of the complexes was further evaluated by recording the absorption, fluorescence emission and excitation spectra and the delayed Eu(III) centred emission of both complexes in CH_3OH solutions at room temperature (Figure 2.3). The absorption spectrum of **Eu.89R** ($c = 5 \times 10^{-6}$ M) showed a hypochromic shift in the band centred at 280 nm and the appearance of a new band at 326 nm, in comparison with **89R**, indicating the complexation of the tpy group to Eu(III) (Figure 2.3, black). Excitation of the compound at 280 nm gave rise to fluorescence with a λ_{max} at 410 nm (Figure 2.3), green. At the same time, the phosphorescence emission spectra of **Eu.89R** were recorded showing the bands corresponding to the $^5D_0 \rightarrow {}^7F_J$ transitions of the Eu(III) ions (Figure 2.3 red), where $J = 0$ (580 nm), 1 (595nm), 2 (618 nm), 3 (650 nm) and 4 (698 nm), which confirmed the occurrence of energy transfer from the antenna to the metal ion. The same results were obtained for **Eu.89S**.

Infrared spectroscopy of the complexes also showed changes with respect to the ligands, including the shift of the carbonyl band by 39 and 37 cm^{-1} from 1584 and 1583 cm^{-1}

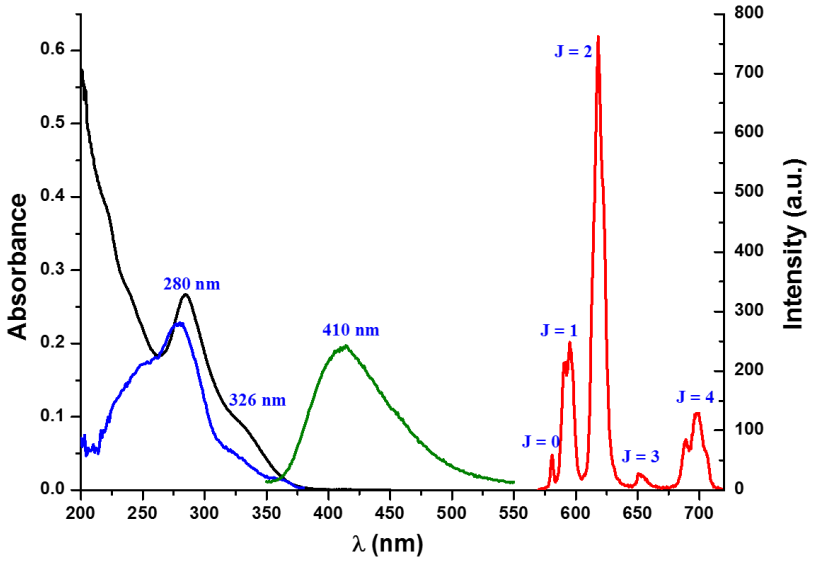

Figure 2.3: Absorption (black), excitation (blue), fluorescence (green) and europium (III) centred emission (red) spectra of **Eu.89R** in MeOH, λ_{ex} = 280 nm ($c = 5 \times 10^{-6}$ M)

to 1623 and 1620 cm^{-1} for **Eu.89R** and **Eu.89S**, respectively, as well as general changes in the fingerprint region, including the presence of a band centred at 1256 and 1250 cm^{-1} associated with the trifluoromethansulphonate ($CF_3SO_3^-$) anions.

2.3 Mass spectrometric analysis of the ligands 89R and 89S and their Eu(III) complexes

Both **89R** and **89S** were analysed using matrix-assisted laser desorption ionisation mass spectrometry (MALDI). The mass spectrum of **89R** showed a peak at m/z = 1285.5948 corresponding to the [M+H] species (Appendix, Figure A.2.17.2). Similarly, ligand **89S** also showed a peak at m/z = 1285.5946, corresponding to the [M+H] species (Appendix, Figure A2.18.3).

The successful complexation of ligands **89R** and **89S** with Eu(III) was confirmed by MALDI+ spectrometry, where the characteristic isotopic distribution patterns of the Eu(III) complexes were matched to the calculated spectra. As shown in Figure 2.4, the experimental isotopic distribution pattern of **Eu.89R** with maximum m/z = 1735.4237 [**Eu.89R**$(CF_3SO_3)_2]^+$, was found to match perfectly with calculated spectrum, indicative of a 1:1 (Eu:L) stoichiometry. This was also found to be the case with **Eu.89S**, which gave *m/z* = 1735.4211 [**Eu.89S**$(CF_3SO_3)_2]^+$ (see Appendix A2.23.2 for **Eu.89S**). Having characterised the complexes **Eu.89R** and **Eu.89S** as formed under thermodynamic control, the next step was to investigate the kinetics of the self-assembly process in solution, the results of which will be discussed in the following sections.

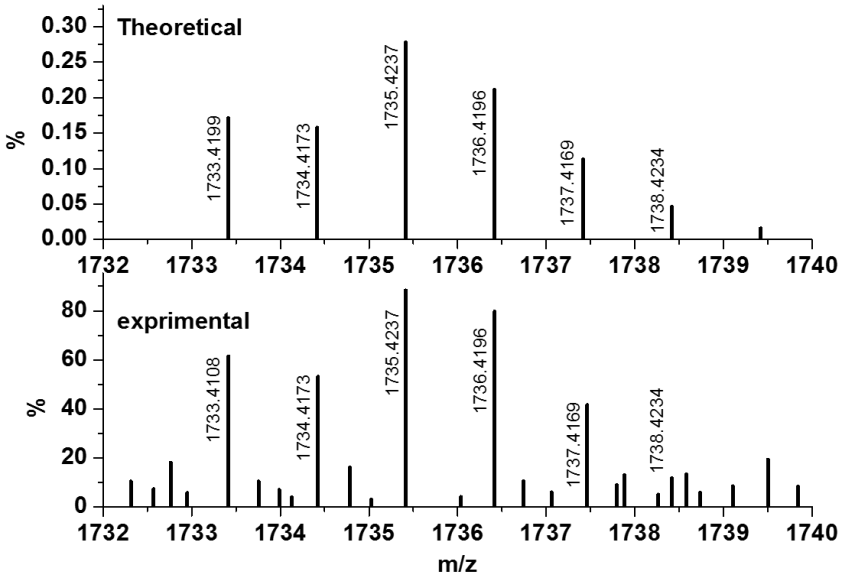

Figure 2.4: The calculated and experimental isotopic distribution patterns (MALDI$^+$) for **Eu.89R** (see Appendix A2.23.2 for **Eu.89S**).

2.4 Determination of bound water molecules (q values) for Eu.89R and Eu.89S

As discussed in Chapter 1, Section 1.5.1, Ln(III) ions are known to possess high coordination numbers, this number is generally nine for Eu(III).[262] If this requirement cannot be met by suitable coordination ligands, the remaining coordination sites are usually occupied by solvent molecules, such as water or CH_3OH. Tripodal ligands appended with the tpy chemical unit have been shown to coordinate *via* the nitrogens of all nine pyridine moieties from the three terpyridine units to form 1:1 [**Ln:L**] stoichiometric bundles,[280-281, 294] coordinatively saturating the Eu(III) ions with no bound solvent molecules.

The excited state lifetimes of **Eu.89R** and **Eu.89S** were examined to determine the respective hydration states (*q*) and therefore, the number of solvent molecules within the first coordination sphere of the Eu(III) centre. The luminescence lifetimes of each complex in both CH_3OH (τ_{CH3OH}) and CD_3OD (τ_{CD3OD}) were determined by fitting the Ln(III) excited state decay profiles of the most intense Ln(III) transition ($^5D_0 \rightarrow {}^7F_2$ band centred at 617 nm). The *q* values, where *q* = number of metal bound H_2O molecules, were determined using an equation reported by Parker *et al.* (Chapter 1, Section 1.5.3).[274, 277]

The decay curves were best fitted to monoexponential decays with $\tau_{CH3OH} = 0.76 \pm 0.01$ ms and $\tau_{CD3OD} = 1.27 \pm 0.02$ ms for **Eu.89R,** while **Eu.89S** yielded $\tau_{CH3OH} = 0.9 \pm 0.02$ ms and $\tau_{CD3OD} = 1.43 \pm 0.02$ ms and resulted in $q = 0$ for both complexes indicating the full saturation of Eu(III) coordination environment in both complexes. These results provide strong evidence for the coordination of three terpyridine moieties to Eu(III) confirming the 1:1 (Eu:L) stoichiometries (see Appendix, Table A2.1 for the summary of all *q* values obtained). The following section will focus on UV-vis absorbance and luminescence spectroscopic studies, in order to have a better understanding of the binding process and to ascertain the stoichiometric ratio between the ligands **89R** and **89S** and Eu(III) in solution.

2.5 UV-vis absorption and luminescence emission investigation of 89R and 89S in solution

Having shown the ability of ligands **89R** and **89S** for binding to Eu(III) ions through the formation of thermal complexes, more detailed investigations of self-assembly were carried out. The formation of the Ln(III)-directed self-assembly was followed by observing the evolution and changes in absorbance, fluorescence and delayed Ln(III)-emission over the cause of self-assembly process in CH_3OH. The absorption spectrum of **89R** (recorded at $c = 5 \times 10^{-6}$ M) shown in Figure 2.5A (black) displays a λ_{max} band centred at 280 nm (terpyridine $\pi \rightarrow \pi^*$ transition). Excitation at this wavelength gives rise to a fluorescence emission with

λ_{max} at 410 nm, Figure 2.5A (blue). Upon diluting this solution, only a decrease in the absorbance and the fluorescence intensities were observed without showing any shift in the λ_{max} values, indicating a lack of aggregation (Figure 2.5 B and C). Similar behaviour was observed upon repeating the experiment three times. Detailed measurements for the determination of ε values for **89R** and **89S** is provided in appendix A2.24.1 – A2.25.2. Where the ε obtained for **89R** and **89S** were ε_{280nm} = 97944 ± 465 M^{-1} cm^{-1} and 110816 ± 729 M^{-1} cm^{-1}, respectively under identical conditions.

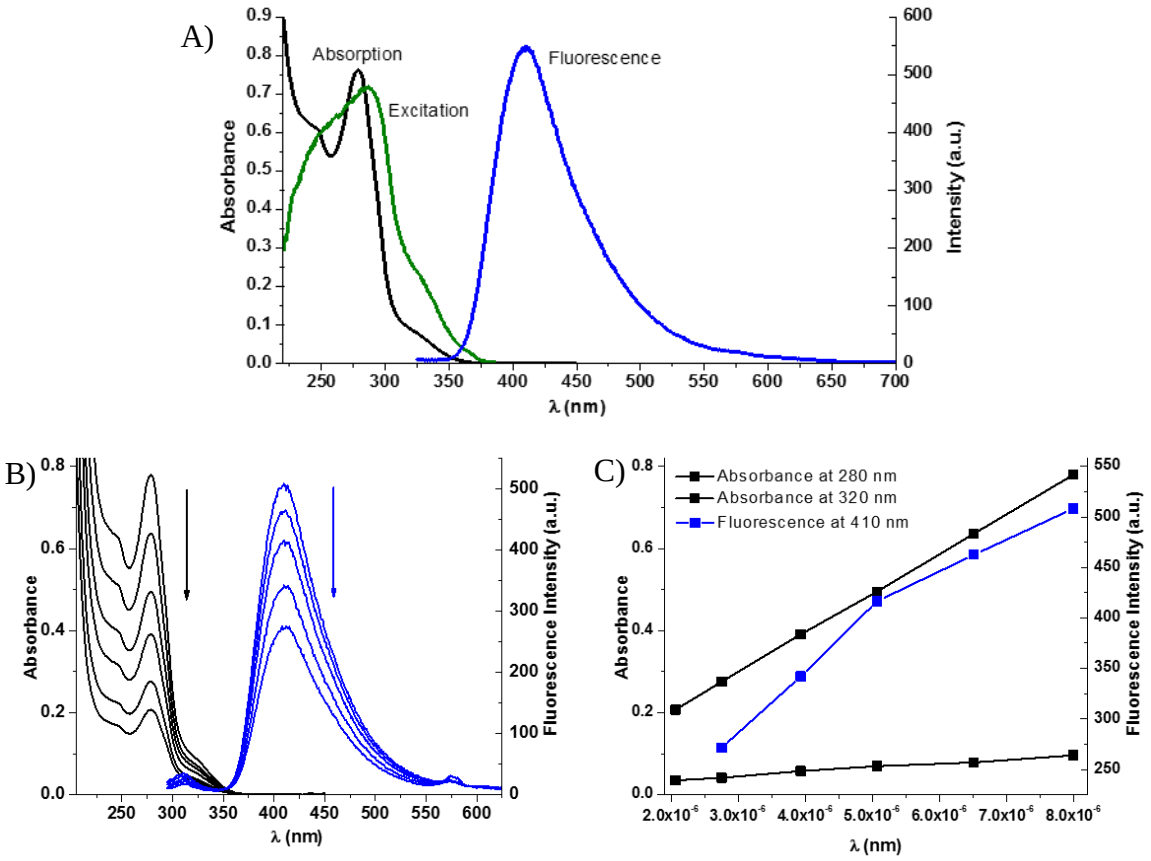

Figure 2.5: A) Absorption (black), emission (blue, λ_{ex} = 280 nm) and the excitation (green, λ_{em} = 410 nm) spectra of **89R** in MeOH (c = 5 × 10^{-6} M). B) Decreases in the absorbance and fluorescence intensity on diluting the solution and C) its corresponding binding isotherm.

The fluorescence intensities of **89R** and **89S** were proportional to concentration over a limited range of optical densities,[277] as such the luminescence behaviour of each ligand *vs* concentration were measured, the results of which are shown in Figure 2.6A. Above concentration of 6.5 × 10^{-6} M the fluorescence intensity decreased, most likely due to the formation of aggregates through the dimerisation of the molecules by intermolecular three-fold hydrogen bonding between BTA moieties. Dimerisation of the molecules was also confirmed by the mass spectrometry analysis, where one of the precursors, **101R,** with a

BTA core showed the peak for its dimerised molecule at m/z = 953.3391 for [M_2.Na] (Figure 2.6B). Similar dimerised molecules were also observed with other precursors (Appendix A2.1.3), with the same decrease of fluorescence intensity at higher concentrations. Therefore, using a concentration of less than 6 $\times 10^{-6}$ M was considered appropriate for spectroscopic studies in which it is assumed that the ligands exist in solution as single molecules. With this observation, in order to understand the effect of concentration on the self-assembly properties of the molecules, metal directed self-assembly studies were carried out at different concentrations.

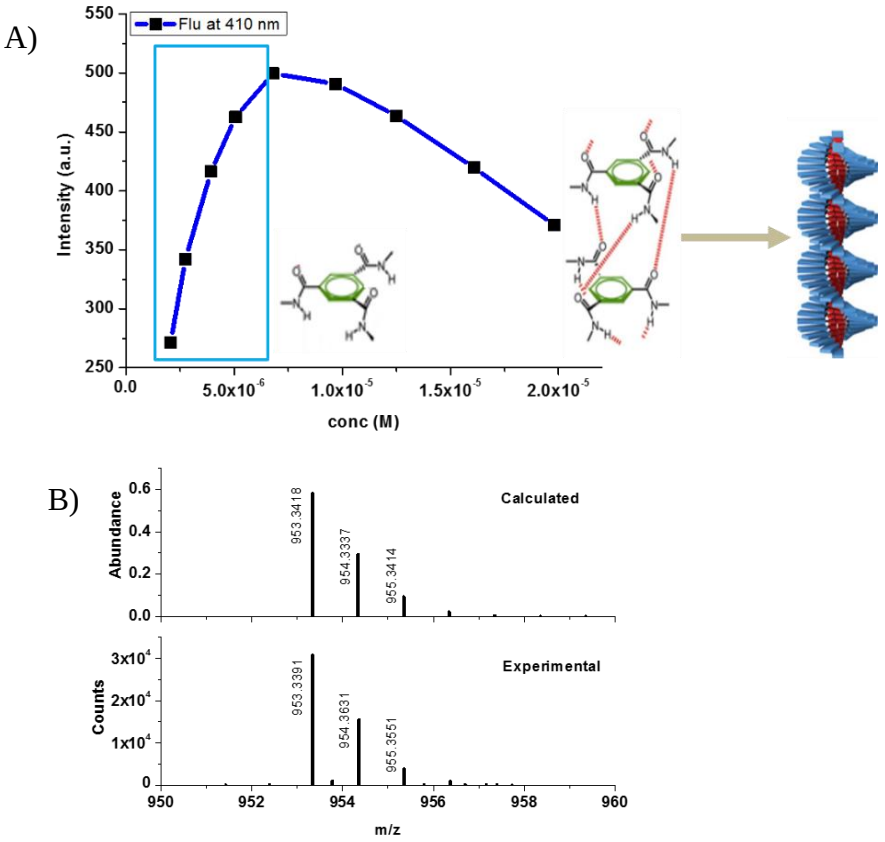

Figure 2.6: A) Fluorescence intensity of **89R** monitored at 410 nm versus concentration. B) Calculated and experimental isotopic distribution patterns of dimerized **101R,** confirming the dimerisation of BTA core.

The interaction of the synthesised tripodal molecules with Eu(III) ions was studied by titrating the compounds with $Eu(CF_3SO_3)_3$ in solutions of MeOH. Of the compounds synthesised, the self-assembly behaviour of the alanine derivatives (**89R** and **89S)** was studied in detail at different concentrations. These results will be discussed in the following sections. It should be stated that all titrations performed showed both of the enantiomers to exhibit similar behaviour. Therefore, only the results from the photophysical titration of **89R** will be discussed here; photophysical data for the titration of **89S** are provided in the

Appendix (A24.1 – A24.3). The results were reproduced several times (4 – 5 times) using fresh stock solutions of the ligands and of the metal salts to ensure the reproducibility of the data.

2.5.1 UV-vis absorption titration of 89Rwith $Eu(CF_3SO_3)_3$ in MeOH at $c_L = 5 \times 10^{-6}$ M

Metal directed self-assembly studies of **89R** and **89S** were carried out by titrating the ligands with $Eu(CF_3SO_3)_3$ in CH_3OH at a concentration of 5×10^{-6} M. Stock solutions (2.7 mL, 5×10^{-6} M) of ligands were prepared and titrated against known volumes of standard solutions of $Eu(CF_3SO_3)_3$ over a range of 0 → 5 equivalents. Both the UV-vis absorbance and luminescence spectra of the solutions were subsequently recorded following each addition. In all measurements, an excess of Eu(III) ions was added to ensure the saturation of all the binding sites of the ligand.

Firstly, the self-assembly process between Eu(III) and the ligand was studied by monitoring the changes in the UV-vis absorption spectrum of **89R** in MeOH. Addition of Eu(III) to **89R** ($c = 5 \times 10^{-6}$ M) resulted in a hypochromic shift of the band centred at 280 nm, associated with the $\pi \rightarrow \pi^*$ transition of tpy moiety. Simultaneously with the appearance of a new band (a shoulder) centred at approximately 326 nm was observed indicating the binding of Eu(III) to tpy moieties (figure 2.7). The presence of an isobestic point at 292 nm indicated the existence of equilibrium between the species present in the reaction mixture. The spectra after these changes under kinetic control matched the spectra recorded above for the metal complex [**Eu.89R**$(CF_3SO_3)_2$] prepared under thermodynamic control (Figure 2.3).

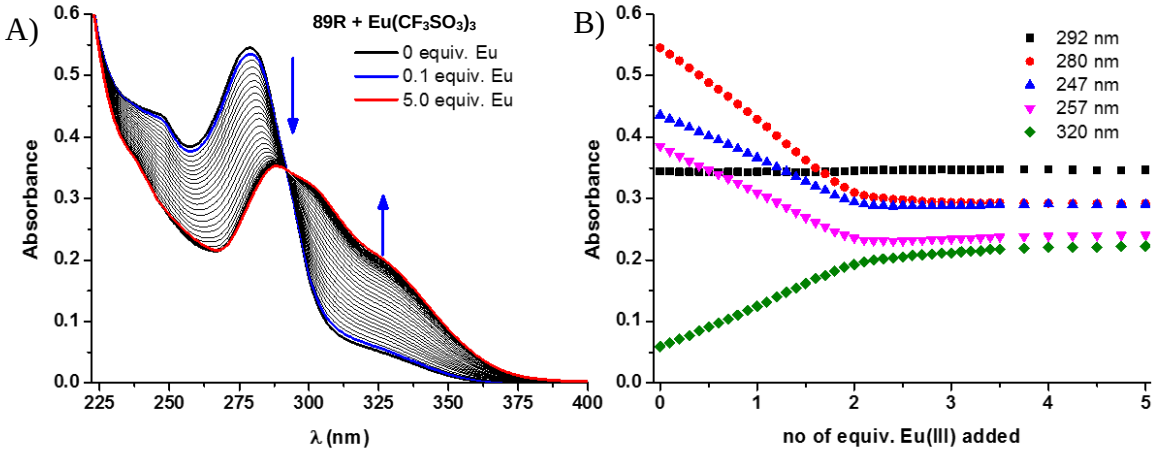

Figure 2.7: A) Changes in the absorption spectrum of **89R** (5×10^{-6} M) upon titrating with $Eu(CF_3SO_3)_3$ (0 → 5 equiv.) in MeOH at 22 °C. B) Binding isotherms for the complexation of **89R** recorded at 247, 257, 280, 292 and 320 nm. The titration shown here represents the reproducible trends observed several times (4 - 5 times).

The experimental binding isotherms at several wavelengths displayed a plateau, in the value of absorbance beyond the addition of 2 equiv. of Eu(III) (Figure 2.7B). These changes indicate the shift of the equilibrium and evolution of different stoichiometric species in solution upon increasing Eu(III) concentration.

2.5.2 Fluorescence titration of 89R with $Eu(CF_3SO_3)_3$ in MeOH at $c_L = 5 \times 10^{-6}$ M

Simultaneously with monitoring the changes in the ligand absorbance, the changes in the fluorescence spectra of **89R** upon Eu(III) addition were also monitored. Excitation into the terpyridine band at 280 nm, gave rise to a fluorescence emission with λ_{max} at 410 nm, which was gradually quenched (by 86%) upon addition of *ca*. 2.0 equiv. of Eu(III) ions, after which the ligand fluorescence was no longer observed (Figure F2.8B). This quenching is a direct consequence of the energy transfer from the excited state of the ligand to the metal centre indicating the complex formation between the Eu(III) ions and tpy moieties. Excitation spectra were also recorded at intervals of 0.5 equiv. of Eu(III) ions, confirming that a decrease in intensity was observed with increasing concentration of Eu(III) ions, supporting the quenching of fluorescence. Fluorescence excitation spectrum of **89R** upon addition of Eu(III) ions is provided in the Appendix, Figure A2.25.2.

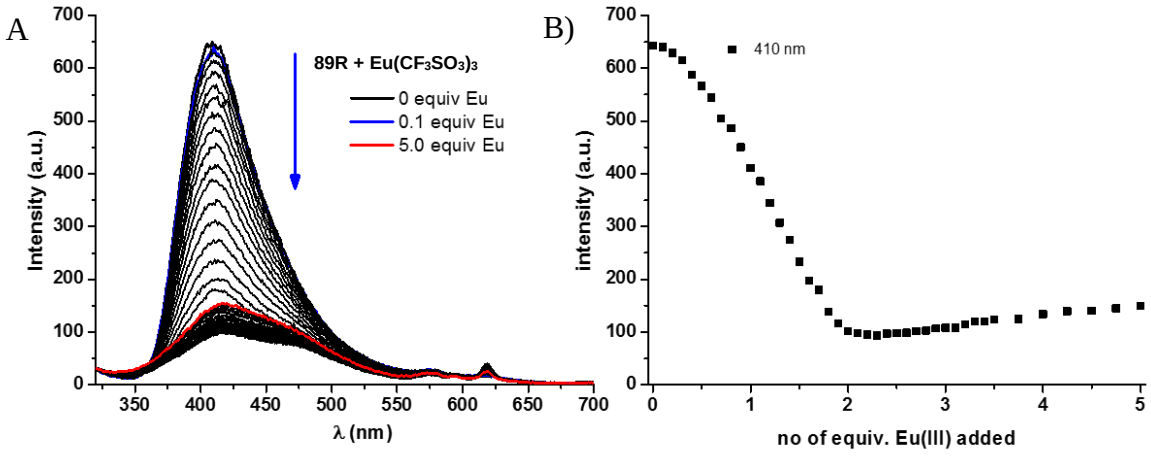

Figure 2.8: A) Fluorescence spectra of **89R** (5×10^{-6} M) upon titrating with $Eu(CF_3SO_3)_3$ ($0 \rightarrow 5$ equiv.) in MeOH at 22 °C. B) Binding isotherm of the complexation of **89R** recorded at 410 nm. The titration shown here represents the reproducible trends observed several times (4 - 5 times), which was in good agreement with UV-vis absorption titrations.

2.5.3 Eu(III) centred luminescence titration of 89R with $Eu(CF_3SO_3)_3$ in MeOH at $c_L = 5 \times 10^{-6}$ M

Phosphorescence emission spectra were also measured upon excitation at 280 nm of the same solution above. The overlaid spectra and the corresponding titration profile are shown below in Figure 2.9. Upon addition of Eu(III) to the solution of **89R,** a gradual enhancement

of the Eu(III) centred emission was observed until the addition of 2 equiv. of metal ion, indicating the energy transfer from the tpy 'antenna' to the Eu(III) ion centre. In particular the $^5D_0 \rightarrow ^7F_{1\text{-}4}$ transitions were observed, with the emission bands centred at 580, 595, 650 (very weak) and 697 nm, respectively and with the most intense band at 618 nm. After the addition of 2 equiv., there was a sharp decrease in the emission intensity, suggesting that the 2:1 (M:L) stoichiometry was the most emissive. As the Eu(III) concentration increased, the plateau at *ca* 3.0 equiv. was observed showing the formation of less emissive species. During the course of Eu(III) addition, the hypersensitive $^5D_0 \rightarrow ^7F_2$ transition, which is sensitive to coordination geometry, was broad during the addition of 0 → 3.0 equivalents, but thereafter resolved as a single peak from 3.0 equiv. onwards. These changes in both the ground state and excited electronic state spectra provide clear information of the formation of self-assemblies in CH_3OH upon addition of Eu(III). A luminescence enhancement at 618 nm can be seen from the binding isotherms (Figure F2.9B). Similar results were shown previously within the Gunnlaugsson group, where the energy transfer from a tpy moiety to Eu(III) ions facilitated Eu(III) centred emission.[281] The excitation spectra of phosphoresce emission recorded on emitting at λ_{em} = 618 nm, shows the band at λ_{max} = 285 nm identical to absorption spectrum which follows the same trend as the Eu(III) emission profile very closely (Figure 2.10). This confirms the transfer of energy from excited state of ligand to the Eu(III) centres.

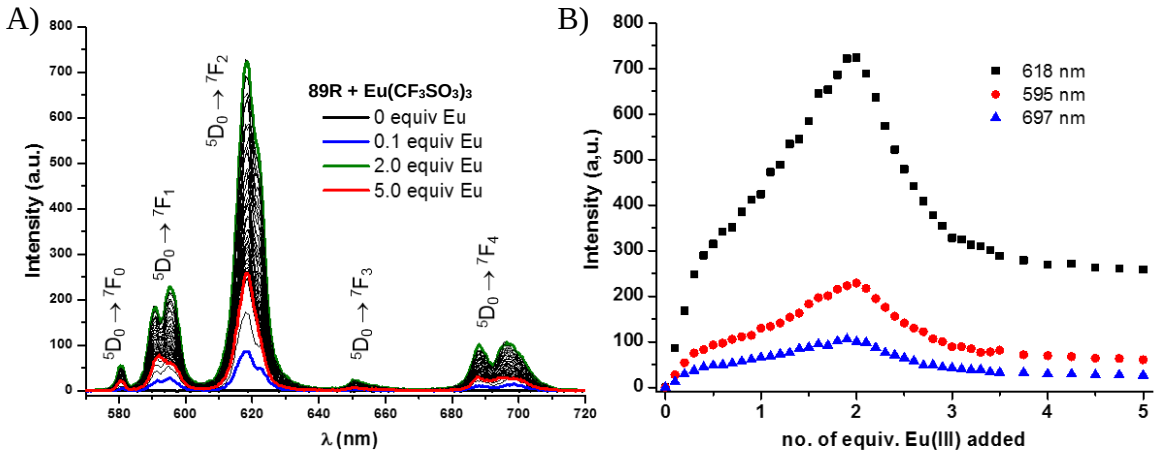

Figure 2.9: A) Phosphorescence spectra from the titration of **89R** (5×10^{-6} M) with $Eu(CF_3SO_3)_3$ (0 → 5 equiv.) in MeOH at room temperature upon excitation at 280 nm. B) Binding isotherms of the complexation of **89R** measured at 618, 595 and 697 nm. The titration shown here represents the reproducible trends observed several times (4 - 5 times), which was in good agreement with UV-vis absorption and fluorescence titrations.

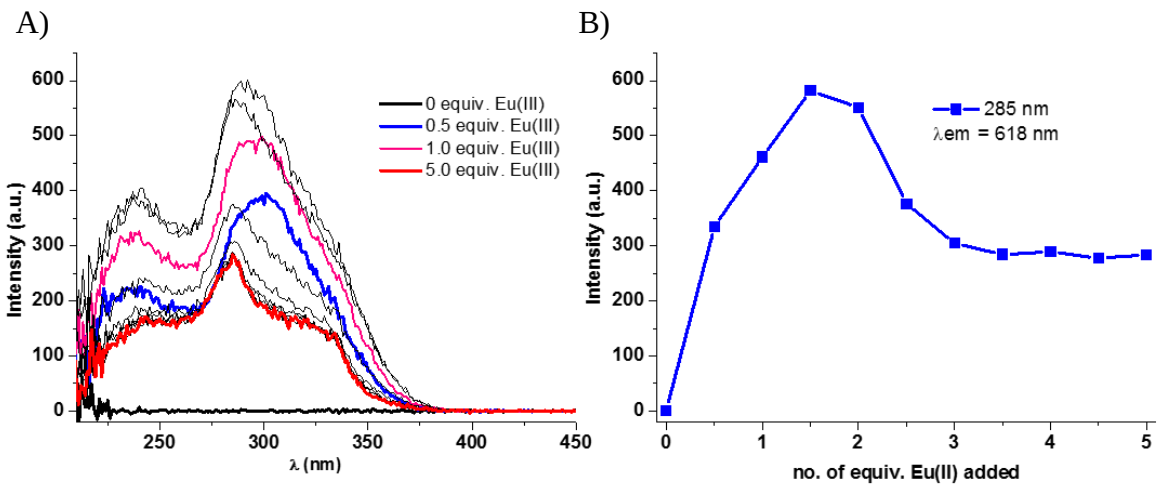

Figure 2.10: A) Phosphorescence excitation spectra from the titration of **89R** (5×10^{-6} M) with $Eu(CF_3SO_3)_3$ ($0 \rightarrow 5$ equiv.) in MeOH at room temperature upon emission at 618 nm. B) Variation of 285 nm band upon addition of Eu(III) ions.

The Eu(III) centred luminescence lifetimes during the course of titration was determined by fitting the Eu(III) excited state decay profiles of the most intense peak (λ = 618 nm) to monoexponential decays. The lifetime values recorded for Eu(III) emission during the course of titration is given in Table 2.2. After investigating the spectroscopic properties of ligands **89R** and **89S**, these results were analysed to understand the binding modes of the above self-assembled systems, the results of which will be discussed in the next section.

Table 2.2: Summary of lifetime values of Eu(III) during the titration of **89R** and **89S** in CH_3OH and CD_3OD at concentration $c_L = 5 \times 10^{-6}$ M.

Ligands	**Equivalent of Eu added**								
	0.5	**1.0**	**1.5**	**2.0**	**2.5**	**3.0**	**3.5**	**4.0**	**4.5**
	Lifetimes of Eu (ms)								
89R in CH_3OH 5×10^{-6} M	0.69 ±0.03	0.67 ±0.04	0.66 ±0.02	0.65 ±0.02	0.57 ±0.04	0.5 ±0.01	0.47 ±0.04	0.45 ±0.01	0.44 ±0.01
89S in CH_3OH 5×10^{-6} M	0.9 ±0.04	0.81 ±0.01	0.77 ±0.01	0.70 ±0.04	0.66 ±0.02	0.62 ±0.03	0.6 ±0.01	0.58 ±0.03	0.57 ±0.00
89R in CD_3OD 5×10^{-6} M	2.0 ±0.03	1.66 ±0.02	1.54 ±0.02	1.45 ±0.02	1.45 ±0.01	1.66 ±0.03	1.74 ±0.01	1.81 ±0.02	1.86 ±0.04

2.5.4 Non-linear regression analysis of the UV-vis, fluorescence and Eu(III) centred emission titration data

In order to gain a more detailed understanding of the self-assembly process and to obtain more detail on the formation of different stoichiometric species in solution, the spectroscopic changes were analysed by fitting the global changes to various M:L complexation equilibria using the non-linear regression analysis programme SPECFIT.[295-296] SPECFIT uses a non-linear least square regression method to minimise the differences between experimental data obtained from spectroscopic measurements and theoretically calculated data from proposed model. The stepwise equilibrium equations used as model for formation of various M:L species in solution can be expressed as follows:

Thus the global stability constant, $\beta_{3:1}$ is the product of step wise equilibrium constants, *K*, given by, $\beta_{3:1} = K_{1:1} \times K_{2:1} \times K_{3:1}$.

$$Eu + L \xrightleftharpoons{K_{1:1}} EuL \qquad K_{1:1} = \frac{[EuL]}{[Eu][L]}$$

$$EuL + Eu \xrightleftharpoons{K_{2:1}} Eu_2L \qquad K_{2:1} = \frac{[Eu_2L]}{[EuL][Eu]}$$

$$Eu_2L + Eu \xrightleftharpoons{K_{3:1}} Eu_3L \qquad K_{3:1} = \frac{[Eu_3L]}{[Eu_2L][Eu]}$$

In general, the equation for the equilibrium

$$mEu + nL \xrightleftharpoons{\beta_{m:n}} Eu_mL_n$$

Can be written as:

$$\beta_{m:n} = \frac{[Eu_mL_n]}{[Eu]^m[L]^n}$$

The stability binding constants are quoted as logarithmic values and as such, shall be quoted as $\log\beta_{m:n}$ in this thesis.

In order to evaluate the number of species formed, the changes in the spectra were analysed using evolving factor analysis, which suggests the presence of four species in the case of UV-vis absorption and fluorescence titrations and three species for the Eu(III) centred emission titrations. This is in line with the successive formation of complexes with 1:1, 2:1 and 3:1 metal to ligand (M:L) stoichiometries. In all cases, the data could be

satisfactorily fitted to Equations 1- 3, and the resulting stability constants are listed in Table 2.3.

The results obtained from the fitting of the UV-vis titrations data of both enantiomers, **89R** and **89S**, showed that the recalculated absorption spectrum (Figure 2.11A) corresponded to the experimental one and indicated the formation of three species, the 1:1, 2:1 and 3:1 M:L complexes. The experimental binding isotherms for this, Figure 2.11B, showed an excellent fit with the calculated titration data. In turn, speciation-distribution diagram (Figure 2.11C) indicated the presence of three major complex species in solution was generated. Upon the addition of Eu(III) to the solution of ligand **89R** (or **89S**), the formation of Eu:L stoichiometric species was found be dominant in solution, reaching a maximum of 71%, upon the addition of 1.0 equivalent of Eu(III) in both cases. Upon the addition of more Eu(III) ions, the formation of a second species with Eu_2:L stoichiometry was observed with the simultaneous consumption of the Eu:L species, indicating the

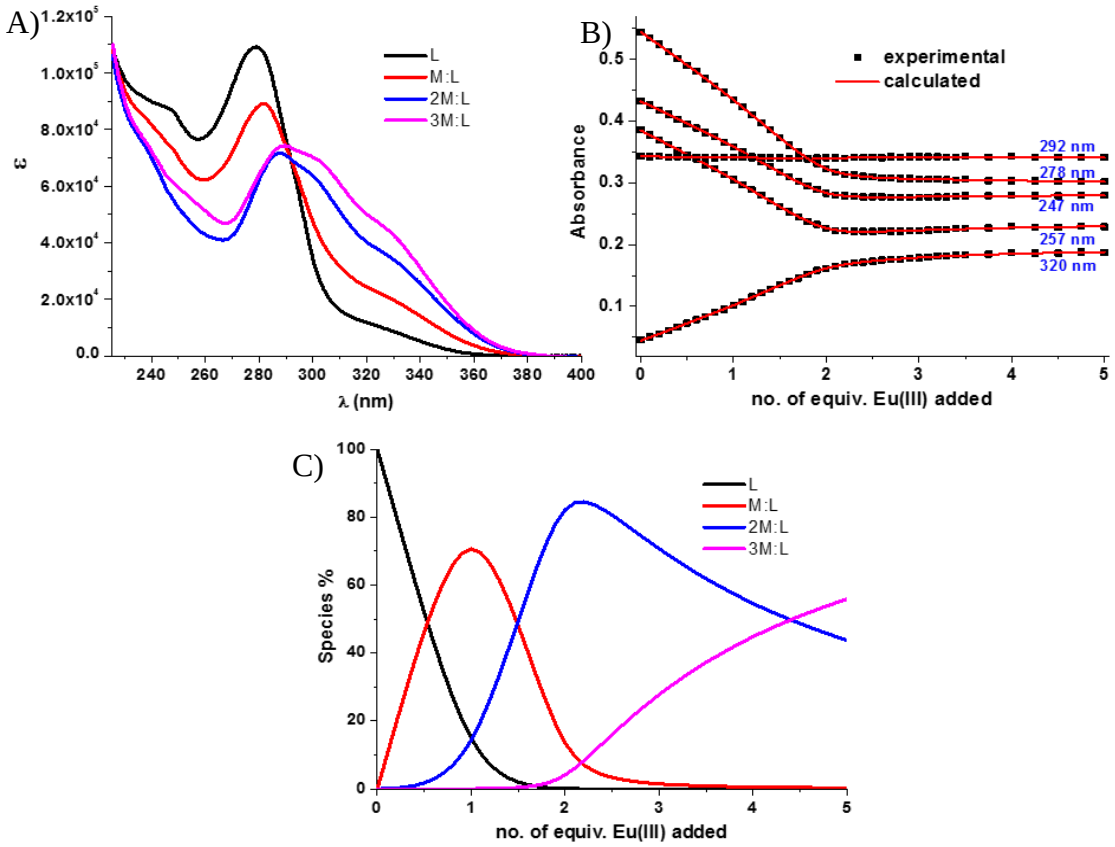

Figure 2.11: A) Recalculated absorption spectra, B) Experimental binding isotherms for the UV-vis titration and their corresponding fit, C) Speciation distribution diagram obtained from the fitting of UV-vis titration of **89R** (5×10^{-6} M) with $Eu(CF_3SO_3)_3$ in MeOH at 22 ºC by means of SPECFIT (see appendix A2.27.1 for fluorescence fit).

equilibrium was being greatly shifted towards the formation of second species on increasing the concentration of Eu(III) reaching a maximum of 84% upon the addition of 2 equivalents of the metal. Further addition of Eu(III) ions beyond 2 equiv. resulted in the formation of a third type of species with the Eu_3:L stoichiometry reaching an observed maximum of 55% upon the addition of 5.0 equivalents of Eu(III) with the simultaneous decrease in the concentration of the Eu_2:L species.

Following the determination of the yield of the species, binding constants were obtained using the nonlinear regression analysis as the cumulative values for the species formed. In each case, the Eu:L species were obtained with the binding constant of *ca.* $\log\beta_{1:1}$ = 8.49 ± 0.16 and 8.51 ± 0.36 for **89R** and **89S**, respectively. The second 2:1 stoichiometric species were formed with binding constants of *ca.* $\log\beta_{2:1}$ = 15.6 ± 0.17 and 16.1 ± 0.4. While the binding constants for the third type of species with 3:1 stoichiometry were found to be $\log\beta_{3:1}$ 20.6 ± 0.19 and 21.6 ± 0.41 for **89R** and **89S,** respectively.

Comparing the results of UV-vis data for the titrations of **89R** and **89S** with Eu(III), it is possible to conclude that the speciation distribution diagram in both cases follows the same trend with the Eu_3:L stoichiometric species being predominant in solution at the end of the titration, with 56% and 78% yields for **89R** and **89S** respectively, in presence of higher quantities of Eu(III) above 2.0 equivalents (see Appendix A2.28.1 for Absorption fitting data of **89S**).

Table 2.3: The summary of the results obtained through fitting of the data from the UV-vis and fluorescence titrations of **89R** and **89S** (c = 5×10^{-6} M) with $Eu(CF_3SO_3)_3$ in CH_3OH.

Ligand	$\log\beta_{1:1}$	$\log\beta_{2:1}$	$\log\beta_{3:1}$	% Yield of 1:1 species at 1.0 equiv.	% Yield of 2:1 species at 2.0 equiv.	% Yield of 3:1 species at 5.0 equiv.
Absorbance						
89R	8.49 ± 0.16	15.6 ± 0.17	20.6 ± 0.19	70.5 %	84.4 %	55.8 %
89S	8.51 ± 0.36	16.1 ± 0.40	21.6 ± 0.41	59.0 %	83.8 %	78.3 %
Fluorescence						
89R	8.7 ± 0.2	15.8 ± 0.2	21.6 ± 0.22	74 %	68 %	87.4 %
89S	8.50*	15.7 ± 0.1	21.9 ± 0.2	69 %	62 %	93 %

* The value has been proposed manually and fixed in order to achieve better fit of the experimental data in accordance with results of factor analysis.

Non-linear regression analysis of the fluorescence data showed that the binding constants for both the ligands (**89S** and **89S)** match each other supporting the results observed in the fitting of absorbance data (see Appendix figure A2.27.1 and A2.28.2 for the fluorescence data of **89R** and **89S** respectively). The speciation distribution diagram also showed that the most predominant species in solution at the end point was the 3:1 (Eu:L) stoichiometry, being formed in 87 % and 93 % yields for **89R** and **89S** ligands respectively, supporting the results observed in the absorbance fit. The minor difference in the relative percentage formation of species **89R** and **89S** is well in the range of experimental errors. (See Table 2.3 for the summary of UV-vis and fluorescence fitting data of titrations of **89R** and **89S**). Comparing these results to the previously reported titrations from our laboratory performed using **86** (c_L = 1 × 10^{-5} M),[281] showed that, **86** formed 1:1 and 3:2 (Eu:L) species with log$\beta_{1:1}$ = 7.2 ± 0.3 and log$\beta_{3:2}$ = 23.3 ± 0.4. The self-assembly studies of **86** at c_L = 5 × 10^{-6} M were not performed. However, the comparison of self-assembly properties between these systems at c_L = 1× 10^{-5} M were performed and will be discussed in the following sections.

2.5.5 Titration of 89R with $Eu(CF_3SO_3)_3$ in CD_3OD at $c_L = 5 \times 10^{-6}$ M

Attempts to fit the data obtained from phosphorescence titration performed in CH_3OH were unsuccessful, and as such the binding constants from the Eu(III) centred emission data could not be obtained. This is most likely due to the quenching effects of the Eu(III) emission observed through the titration. Another possible deactivation pathway is vibrational energy transfer through solvent molecules of CH_3OH (discussed in Chapter 1, Section 1.5).

The excited state energy of Eu(III) is 17,200 cm^{-1}. As the coupling between the excited states of the Eu(III) and the third vibrational overtone of O-H (and also C-H to lesser extent) oscillators of the CH_3OH is possible, the excited state energy of Eu(III) undergoes vibrational deactivation resulting in the quenching of its luminescence.[277] It has been shown that the corresponding O-D oscillators possess lower stretching frequencies. In the case of O-D oscillators they were approximately 200 times less effective towards the quenching of Eu(III) emission than the corresponding O-H oscillators.[297] Therefore, in order to avoid the vibrational quenching by the O-H oscillators, a series of photophysical titrations were conducted between the **89R** (c = 5×10^{-6} M) and $Eu(CF_3SO_3)_3$ in CD_3OD as the solvent (Figure 2 .12).

The UV-vis absorption titrations performed in CD_3OD were found to be analogous to those performed in CH_3OH (Figure 2.12, A and D). Upon excitation of the ligand at 280

nm, the fluorescence emission spectrum was observed with λ_{max} at 410 nm. The broad emission band was significantly quenched (by 86%) upon the addition of Eu(III) ions (Figure 2.12, B). The changes in the fluorescence spectra of **89R** upon interaction with Eu(III) followed the same trend as observed in the absorption spectrum at 410 nm, showing a plateau upon the addition of 2.5 equivalents of Eu(III) (Figure 2.12E).

The same solutions were also excited at 280 nm following each addition, to yield the Eu(III) centred emission spectrum (Figure 2.12C). The four emission bands, $J = 0 – 4$ were observed showing an efficient energy transfer from the tpy moiety to the Eu(III) metal centre. Variations in the intensity at 618 and 697 nm were monitored (Figure 2.12F) and they were well in agreement with the changes observed in UV-vis absorption and fluorescence titration data in CD_3OD. From the experimental binding isotherms of the phosphorescence titrations, a bell shaped curve is observed where a gradual decrease in the emission after the addition of 2.0 equivalents of Eu(III) might suggest the presence of vibrational quenching from the O-D oscillators in CD_3OD.

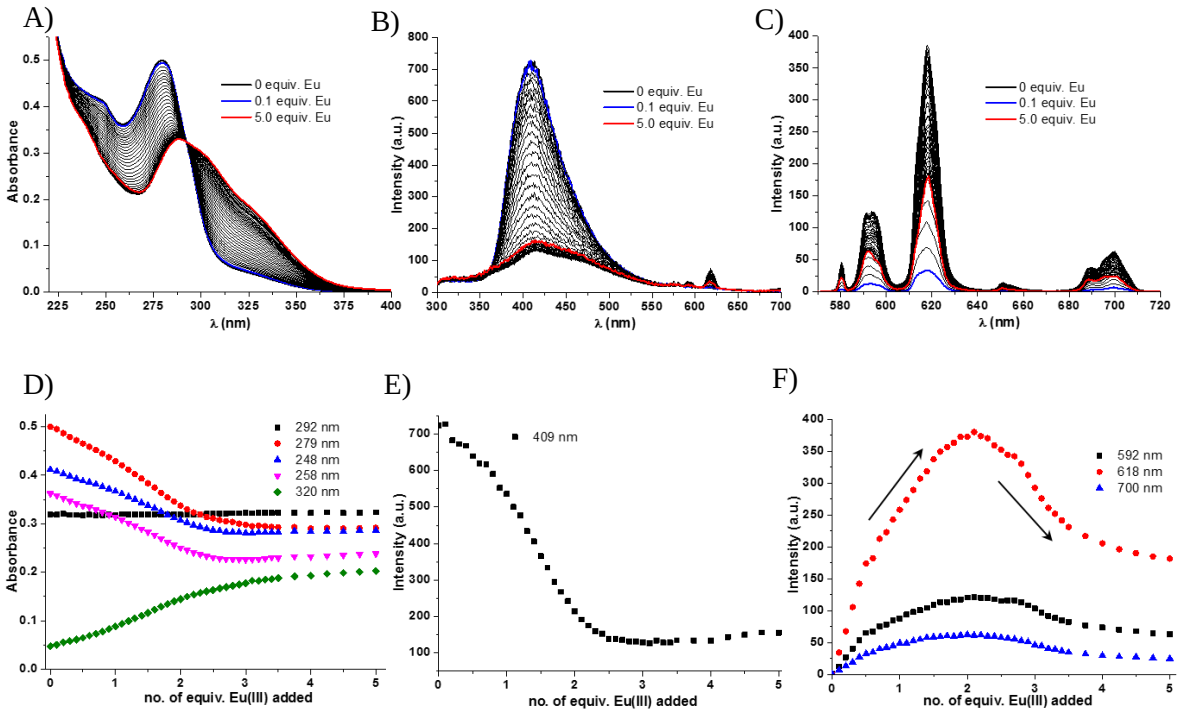

Figure 2.12: A) Changes in the absorption, B) fluorescence and C) phosphorescence spectrum of **89R** (5×10^{-6} M) upon titrating with $Eu(CF_3SO_3)_3$ ($0 \rightarrow 5$ equiv.) in CD_3OD at 22 ^oC. D) Experimental absorption binding isotherms at 248, 258, 280, 292 and 320 nm for the complexation of **89R**, E) fluorescence binding isotherm at 410 nm and F) experimental phosphorescence binding isotherms at 592, 618 and 700 nm. Repeating this experiment three times, same results were obtained.

The results of non-linear regression analysis of the data obtained for this titration showed the same binding model as observed in MeOH with the formation of 1:1, 2:1 and 3:1 (Eu:L) species with slight variation in the values of binding constants from that observed in the case of titration in CH_3OH (see the Appendices A2.29.1 - 2.29.2 for the recalculated spectra, experimental binding isotherm with the fit and speciation distribution diagram of absorption and fluorescence spectrum for the titration in CD_3OD). Furthermore, the fitting data obtained from the phosphorescence titration conducted in CD_3OD afforded the recalculated phosphorescence spectra, binding isotherm and speciation distribution diagram (Figure 2.13), which are in good agreement with the fitted UV-vis and fluorescence titration data. The resulting binding constants found for the formation of complex species as observed by the titration in CD_3OD are shown in Table 2.4.

Comparing the results of the fitting data of **89R** titrations in CD_3OD, from UV-vis absorption, fluorescence and phosphorescence data, it is possible to say that the speciation distribution diagram follows the same trend as for the non-deuterated solvent, where 3:1 (Eu:L) stoichiometric species are predominant in the solution at the end of the titration in

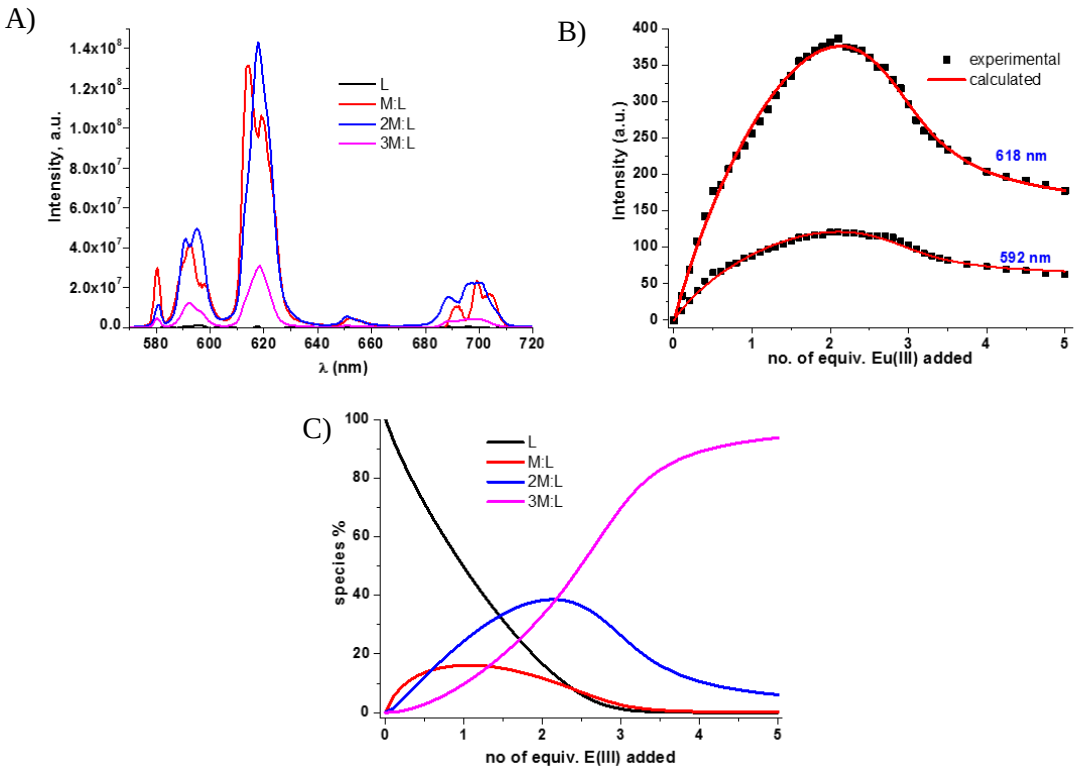

Figure 2.13: A) Recalculated phosphorescence spectra, B) experimental binding isotherms and their corresponding fit, C) speciation distribution diagram obtained from the fit for the phosphorescence titration of **89R** (5×10^{-6} M) with $Eu(CF_3SO_3)_3$ in CD_3OD at 22 °C by means of SPECFIT. (See Appendix A2.29.1 – A2.29.2 for the results of absorbance and fluorescence fitting data).

the presence of higher quantities of Eu(III). The binding constants for the formation of Eu(III) assemblies with L (L = **89R**) were calculated as log$\beta_{1:1}$ = 8.0, log$\beta_{2:1}$ = 14.4 ± 0.1 and log$\beta_{3:1}$ = 20.1 ± 0.1 using the absorbance fitting data. In the case of fluorescence, the binding constants were found to be log$\beta_{1:1}$ = 7.8 ± 0.1, log$\beta_{2:1}$ = 14.6 ± 0.1 and log$\beta_{3:1}$ = 20.1. From the phosphorescence fitting data, binding constants of log$\beta_{1:1}$ = 6.2 ± 0.8, log$\beta_{2:1}$ = 12.9 ± 0.05 and log$\beta_{3:1}$ = 19.1 ± 0.1 were obtained. On comparing these logβ values obtained from the CD_3OD and CH_3OH titration, the values agreed closely (with small difference ± 1) which indicates the similar stability of species present in both the solutions.

As a conclusion to this section, sufficient information has been provided to support the formation of stable self-assemblies of Eu(III) and **89** (R and S) in both CH_3OH and CD_3OD. The results obtained revealed the successive formation of 1:1, 2:1, 3:1 species of **89** (R and S) and Eu(III) in CH_3OH. Their corresponding binding constants were determined and reported.

Table 2.4: Summary of the results obtained through non-linear regression analysis of the data from the UV-vis, fluorescence and phosphorescence titrations of **89R** (c = 5×10^{-6} M) with $Eu(CF_3SO_3)_3$ in CD_3OD and the results reported for **86** (c = 1×10^{-5} M) in CH_3OH for direct comparison.

Ligand	log$\beta_{1:1}$	log$\beta_{2:1}$	log$\beta_{3:1}$	% yield of 1:1 species at 1.0 equiv.	% yield of 2:1 species at 2.0 equiv.	% yield of 3:1 species at 5.0 equiv.
Absorbance						
89R	8.0*	14.4 ± 0.1	20.1 ± 0.1	74 %	54 %	54 %
Fluorescence						
89R	7.8 ± 0.1	14.6 ± 0.1	20.5*	61 %	60 %	58 %
Phosphorescence						
89R	6.2 ± 0.8	12.9 ± 0.1	19.1 ± 0.1	16 %	38 %	67 %
	log$\beta_{1:1}$		**log$\beta_{3:2}$**	**% yield of 1:1 species at 1.0 equiv.**		**% yield of 3:2 species at 5 equiv.**
86	7.2 ± 0.3		23.3 ± 0.4	95 %		28 %

* The value has been proposed manually and fixed in order to achieve better fit of the experimental data in accordance with results of factor analysis.

2.5.6 The Lifetime of Eu(III) centred emission during the titration of ligands 89 (R and S)

During the titration of **89R** and **89S** with Eu(III), the luminescence lifetimes of the species formed in solution were measured at intervals of 0.5 equivalents of metal ions added. It was noted that, upon the addition of 1 equivalent of Eu(III) ions, 1:1 (M:L) species was formed with Eu(III) the luminescence lifetimes of τ_{MeOH} = 0.67 ± 0.0 ms and 0.81 ± 0.0 ms for **89R** and **89S**, respectively. These values correspond very closely to the lifetimes measured for the 1:1 complex synthesised under thermodynamic control and discussed in Sections 2.2 – 2.4. As anticipated, slightly longer lifetimes values were observed in CD_3OD due to the absence of quenching mediated by the OH group of CH_3OH. In addition, the luminescence lifetime was found to be τ_{CD3OD} = 1.66 ± 0.0 ms for 1:1 (M:L) species which is close the to the lifetimes of Eu:L (1:1) complexes (**Eu.89R** and **Eu.89S**) measured in CD_3OD. This gave a strong evidence of the formation of 1:1 (M:L) complex as the first intermediate kinetic species, in which all three tpy moieties of the molecule bound to Eu(III) metal with no bound water molecules to metal centre. Upon further addition of metal ions, the equilibrium shifts towards the formation of species with a 2:1 Eu:L stoichiometry, having a Eu(III) luminescence lifetime of τ_{MeOH} = 0.65 and 0.7 ms for **89R** and **89S**, respectively. This decrease of lifetime may be attributed to the binding of solvent molecules to the Eu(III) metal centre after the dechelation of tpy groups. The same trend continued upon further addition of metal ions to the ligand until the formation of the 3:1 M:L species at the end of the titration. Titrations carried out at a ligand concentration of 5×10^{-6} M did not show the formation of higher ordered species or beginning of polymerisation was not observed. This confirmed the existence of **89** (R and S) molecules as monomers at this concentration and helped in predicting the mechanism of self-assembly process occurring between Eu(III) ions

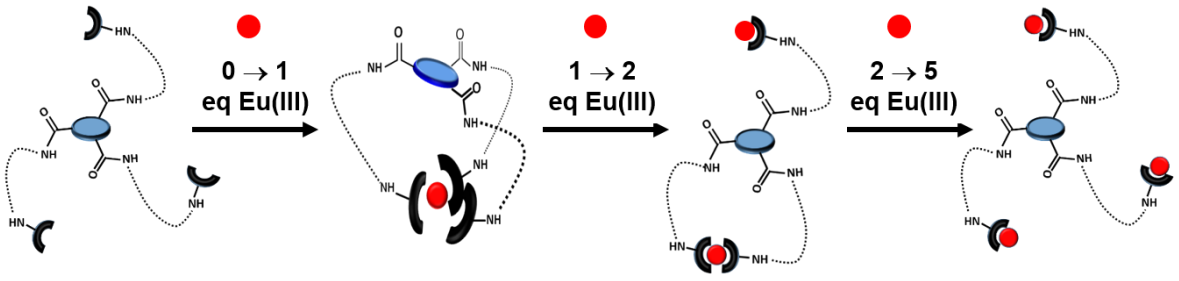

Figure 2.14: Schematic representation of the successive formation of 1:1, 2:1 and 3:1 species in solution upon the addition of 1, 2 and 3 equivalent of Eu(III) ions at c = 5×10^{-6} M.

and ligand (See Appendix Table A2.2 for the lifetimes of Eu(III) emission during the titrations of **89R** and **89S** with Eu(III).

As such we can propose the scheme below representing the successive formation of 1:1, 2:1 and 3:1 (Eu:L) species in solution upon the addition of 1, 2 and 3 equivalents of Eu(III) ions (Figure 2.14).

2.6 Monitoring self-assembly processes of chiral tripodal ligands with Eu(III) by UV-vis absorbance and luminescence spectroscopy at $c_L = 1 \times 10^{-5}$ M

In the interest of understanding the effect of concentration on the formation of higher ordered self-assemblies, similar spectrophotometric titration experiments were carried out for **89R** and **89S** with $Eu(CF_3SO_3)_3$ in MeOH at a higher concentration of 1×10^{-5} M and the changes in the UV-vis absorption, fluorescence and the Eu(III) centred emission were monitored. It has been previously found that at this concentration, interactions between the ligands occur which might make a difference in the self-assembly properties of molecules (see Section 2.5 and Figure 2.6). The experiments discussed below were reproduced several times using fresh stock solution of ligands to ensure the reproducibility of the data and the same results were obtained every time.

2.6.1 UV-vis absorption titration of 89R with $Eu(CF_3SO_3)_3$ in MeOH at $c_L = 1 \times 10^{-5}$ M

The UV-vis absorption titrations were carried out in the same manner as discussed in Section 2.5.1. The concomitant changes in the UV-vis absorption spectra of **89R** ($c_L = 1 \times 10^{-5}$ M, 2.7 mL) upon titrating against the standard solution of $Eu(CF_3SO_3)_3$ ($c = 1 \times 10^{-3}$ M) resulted

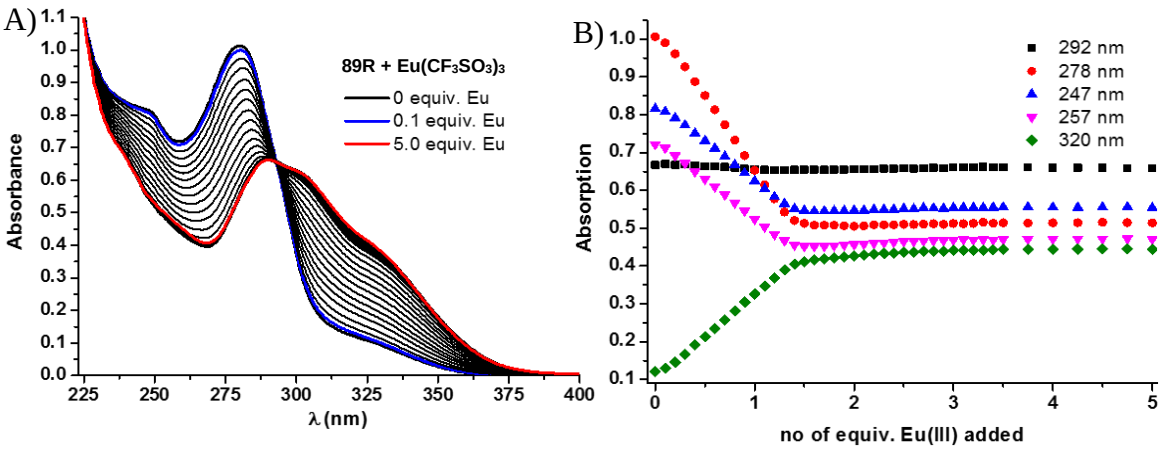

Figure 2.15: A) Changes in the absorption spectra of **89R** (1×10^{-5} M) upon titrating with $Eu(CF_3SO_3)_3$ (0 → 5 equiv.) in MeOH at 22 °C. B) Binding isotherms for the complexation of **89R** recorded at 247, 257, 278, 292 and 326 nm. The titration shown here represents the reproducible trends observed several times (4 - 5 times).

in a hypochromic shift of the band centred at 280 nm with the simultaneous hyperchromic shift of the band centred at 326 nm. An isobestic point was observed at 292 nm (Figure 2.15A). This was similar to the previously performed titration at $c_L = 5\times10^{-6}$ M. However, in this case ($c_L = 1 \times 10^{-5}$ M) these changes occurred upon addition of approx. ~1.5 equivalents of Eu(III) with the following formation of the plateau (Figure 2.15B). Unlike that at $c_L = 5 \times 10^{-6}$ M (Section 2.5.1) these changes occurred until the addition of *ca*. 2.0 equivalents of Eu(III), indicating the clear effect of the ligand concentration on the self-assembly equilibria in the solution. As expected, the changes observed in this titration are in good agreement with UV-vis absorption titrations performed using **86** with Eu(III) under same condition ($c = 1 \times 10^{-5}$ M) previously reported form our laboratory.[281] The photophysical data for the titration of **89S** can be found in the Appendix (A2.30.1 – A2.30.3).

2.6.2 Fluorescence titration of 89R with $Eu(CF_3SO_3)_3$ in MeOH at $c_L = 1 \times 10^{-5}$ M

The fluorescence emission of **89R** ($c_L = 1 \times 10^{-5}$ M) was also monitored upon excitation at 280 nm, with emission observed at λ_{max} = 411 nm. This emission was found to be quenched by 89% upon addition of Eu(III) ions (Figure 2.16A). The quenching of the ligand fluorescence emission at 411 nm was observed until approx. 1.4 equivalents of Eu(III) had been added with the following formation of a plateau (Figure 2.16B). These changes correspond very well to the changes observed for absorption titration above (Section 2.6.1). As expected, changes observed in this titration are in good agreement with fluorescence titrations performed using **86** with Eu(III) ions under same condition previously reported form our laboratory at $c = 1 \times 10^{-5}$ M.[281]

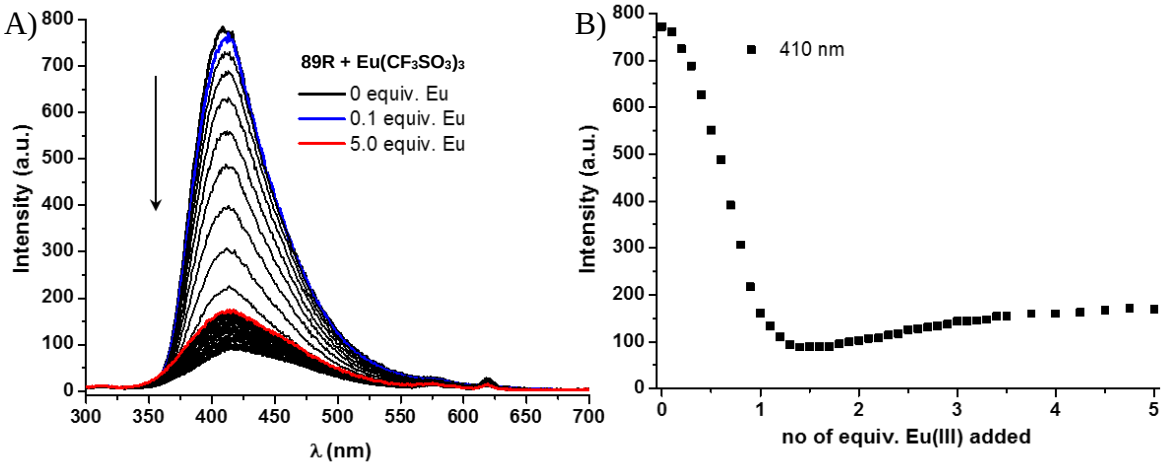

Figure 2.16: A) Fluorescence spectra of **89R** (1×10^{-5} M) upon titrating with $Eu(CF_3SO_3)_3$ (0 → 5 equiv.) in CH_3OH at 22 °C. B) Experimental binding isotherm recorded at 410 nm. The titration shown here represents the reproducible trends observed several times (4 - 5 times), which was in good agreement with UV-vis absorption titrations shown above.

2.6.3 Eu(III) centred luminescence titration of 89R with $Eu(CF_3SO_3)_3$ in MeOH at c_L = 1×10^{-5} M

Upon exciting the same solution ($c_L = 1 \times 10^{-5}$ M) at 280 nm, the evolution in the Eu(III) centred emission was observed following each addition of Eu(III) ions (Figure 2.17A). Monitoring the changes in the bands centred at 595, 618 and 697 nm, showed an increase of the intensities till the addition of approx. 1.2 equivalents of Eu(III) ions followed by the decrease in the intensity and a formation of plateau at *ca*. 2.0 equivalents of metal addition. While in the case of titration at lower concentration of 5×10^{-6} M (Section 2.5.3), maximum emission is found to be at ~2.0 equivalents of Eu(III) ions added and formation plateau at ~3.0 equivalent of metal addition. This difference suggests the formation of different Eu:L assemblies at $c_L = 1 \times 10^{-5}$ M demonstrating the effect of concentration on the self-assembly processes. As expected, changes observed in this titration are in good agreement with phosphorescence titrations performed using **86** with Eu(III) ions under same condition previously reported form our laboratory at $c = 1 \times 10^{-5}$ M.[281]

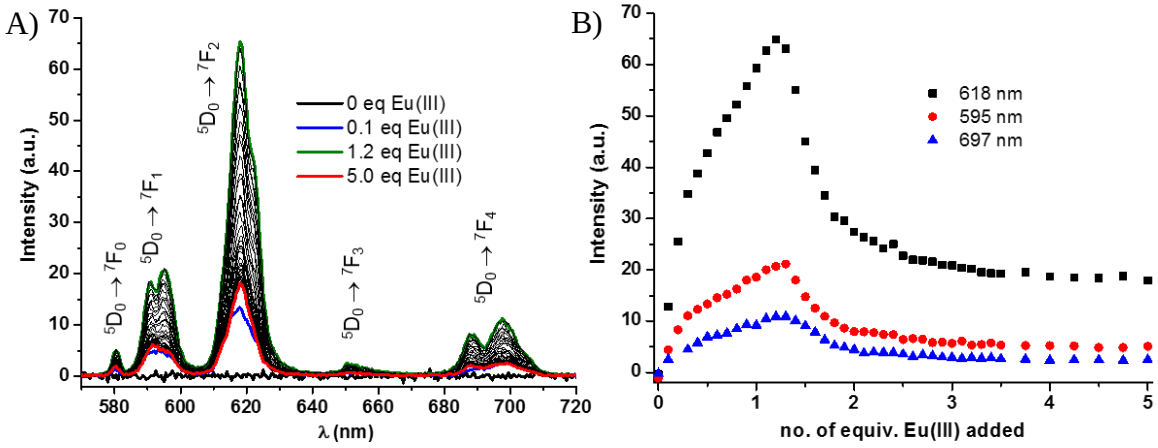

Figure 2.17: A) Phosphorescence spectra from the titration of **89R** (1×10^{-5} M) with $Eu(CF3SO_3)_3$ (0 → 5 equiv.) in MeOH at room temperature upon excitation at 280 nm, B) binding isotherms of the complexation of **89R** measured at 618, 595 and 697 nm. Titration shown here represents the reproducible trends observed several times (4 - 5 times), which was in good agreement with UV-vis absorption anf fluorescence titrations shown above.

2.6.4 Non-linear regression analysis of the changes in the UV-vis absorption, fluorescence and Eu(III) centred emission titration data at $c_L = 1 \times 10^{-5}$ M

The data obtained from the titrations at a higher ligand concentration of $c_L = 1 \times 10^{-5}$ M were analysed using the nonlinear regression analysis program SPECFIT as discussed above. As before, factor analysis of the data suggested the presence of three species in the case of UV-

vis and fluorescence data, and two species for the Eu(III) centred emission titrations. This agrees with previous results obtained within the group for a similar ligand **86**, where the successive formation of 1:1 and 3:2 M:L species was observed in CH_3OH at the same concentration of 1×10^{-5} M.[281] The stability constants from this analysis are listed in Table 2.5.

The results obtained from fitting the UV-vis absorption titrations of both enantiomers **89R** and **89S**, produced a recalculated absorption spectrum (Figure 2.18A) corresponding to the experimental spectrum and experimental binding isotherms exhibiting an excellent fit of the titration data (Figure 2.18B).

The speciation-distribution diagram indicates the presence of two major M:L species in solution (Figure 2.18C). Upon addition of Eu(III) to the solution of ligand **89R** (or **89S**), the formation of 1:1 (Eu:L) stoichiometric species was observed reaching a maximum of 62% at 1.0 equivalent of Eu(III). On continuing the addition of Eu(III) ions, a second species with 3:2 (Eu:L) stoichiometry started to form with the simultaneous consumption of Eu:L, reaching a 91% after upon the addition of 5.0 equivalent of Eu(III). However, in the previous case of the titration at $c_L = 5 \times 10^{-6}$ M the successive formation of 1:1, 2:1 and 3:1 M:L species was observed with 3:1 being the major species at the end of the titration (Section 2.5.4). The stability constants for the obtained species are listed in Table 2.5. Comparison of these values with the stability constant of **86** previously reported form our group,[281] **89R** and **89S** are having similar or slightly higher stability constant values as depicted in Table 2.5 for comparison. See Appendix for Figures A2.32.1 – A2.32.2 with the results of the fit for the titrations of **89S** ($c_L = 1 \times 10^{-5}$ M) with $Eu(CF_3SO_3)_3$ in CH_3OH.

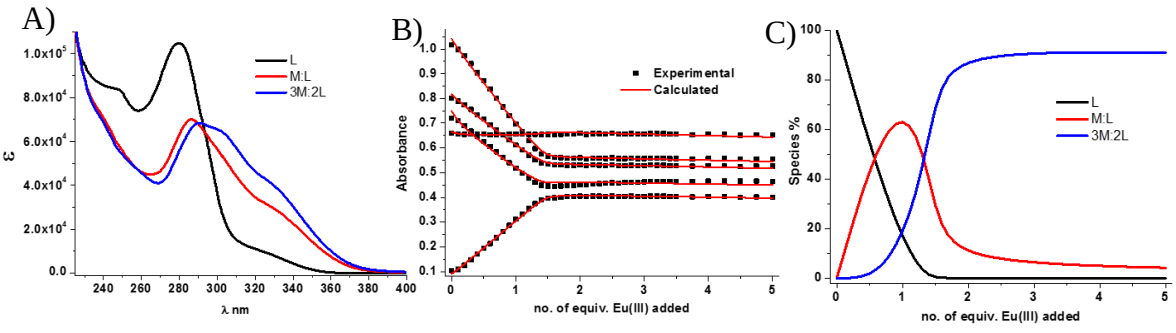

Figure 2.18 A) Recalculated absorption spectra, B) experimental binding isotherms and their corresponding fit and C) speciation distribution diagram obtained from the fitting of UV-vis titration of **89R** (1×10^{-5} M) with $Eu(CF_3SO_3)_3$ in MeOH at 22 °C by means of SPECFIT (see appendix A2.31.1 – A2.31.2 for fluorescence and phosphorescence fit).

Table 2.5: Summary of the results obtained through fitting of the data from the UV-vis, fluorescence and phosphorescence titrations of **89R** and **89S** (c_L = 1×10^{-5} M) with $Eu(CF_3SO_3)_3$ in CH_3OH. And stability constant values of **86** are provided for comparison.

Ligand	$\log\beta_{1:1}$	$\log\beta_{3:2}$	% yield of 1:1 species at 1.0 equiv.	% yield of 3:2 species at 5.0 equiv.
		Absorbance		
89R	8.1 ± 0.4	28.17 ± 0.6	62 %	91 %
89S	6.68 ± 0.11	23.98 ± 0.24	63 %	80 %
86	7.2 ± 0.3	23.3 ± 0.4		
		Fluorescence		
89R	7.9*	26.9 ± 0.29	73 %	85 %
89S	7.9*	27.9 ± 0.39	64 %	84 %
86	6.0 ± 0.1	23.2 ± 0.2		
		Phosphorescence		
89R	7.33 ± 0.09	26.88 ± 0.22	39 %	91 %
86	6.0*	24.9 ± 0.4		

* The value has been proposed manually and fixed in order to achieve better fit of the experimental data in accordance with results of factor analysis.

From the speciation distribution diagram and the binding constants obtained from the fitting data of this titration, adequate information was acquired to support the formation of highly stable self-assembled 1:1 and 3:2 (Eu:L) species in solution. This was further supported by the lifetime measurements of Eu(III) centred emission, where on addition of 1 equivalent of Eu(III) ions, the lifetimes were found to be τ_{MeOH} = 0.9 and 0.79 ms for **89R** and **89S** respectively. These values are in good agreement with the lifetime of Eu in the 1:1 complex synthesised previously (see Appendix Table A2.3 for the lifetime measurements of Eu(III) emission during the titration of **89R** and **89S** with Eu(III) at concentration c = 1×10^{-5} M). By considering the results obtained by fitting UV-vis absorption, fluorescence and phosphorescence titrations data performed at c = 1×10^{-5} M, it can be concluded that **89** (**R** and **S**) show similar self-assembly behaviour as **86** under same concentration.

Therefore, we can propose the schematic representation showing the formation of 1:1 and 3:2 (Eu:L) species in solution upon successive addition of Eu(III) ions (Figure 2.19). Leaving Eu_3L_2 as the predominant species at the end of the titration with higher concentration of Eu(III). In the 3:2 species, two tpy units coordinate to one Eu(III) ion while the third tpy unit acts to bridge between two such assemblies, coordinating to a central Eu(III) ion suggesting the formation higher of ordered M:L species in solution at c_L = 1×10^{-5} M. (Figure F2.19).

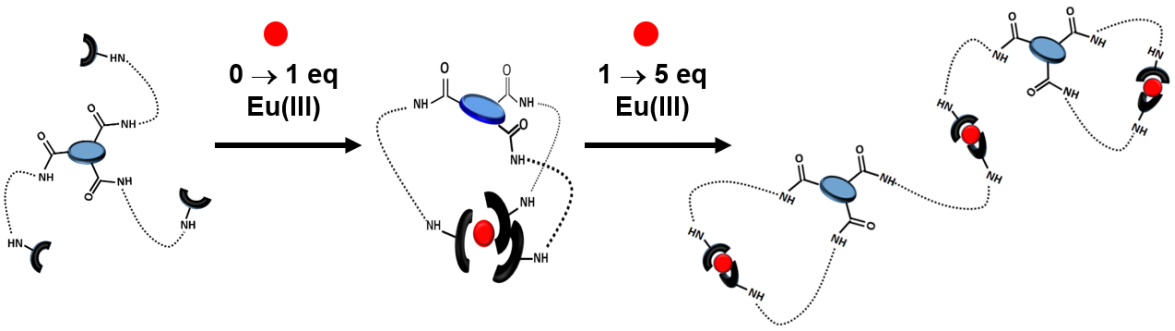

Figure 2.19: Schematic representation of the successive formation of 1:1 and 3:2 species in solution upon the addition of 1-5 equivalent of Eu(III) ions at c = 1×10^{-5} M.

2.7 Conclusion

The work described in this chapter has concentrated on the successful synthesis of an achiral tripodal (glycine based) molecule and 3 sets of enantiomers of chiral tripodal ligands, based on the benzene-1,3,5-tricarboxamide framework. These ligands contained chiral amino acid residues, which were connected to tpy antennae suitable for the sensitisation of Ln(III) excited states, in particular those of Eu(III). Complexation of these ligands was carried out with $Eu(CF_3SO_3)_3$, and mass spectrometry of the synthesised complexes showed the presence of the 1:1 (**Eu:L**) stoichiometry in the solid state. The hydration states (*q* values) of both complexes were determined through luminescence lifetime measurements in CH_3OH and CD_3OD and were found to be 0.3 ± 0.5 and 0.2 ± 0.5 for **89R** and **89S,** respectively. This indicated the presence of zero bound solvent molecules, suggesting that the Eu(III) centre is coordinatively saturated, by all three tpy moieties of the ligand.

Previously from our group, the self-assembly studies of the **86** with Eu(III) ions in MeOH solution were performed at $c_L = 1 \times 10^{-5}$ M. In this case the binding model corresponded to the formation of 1:1 and 3:2 (Eu:L) species, but the successive formation of 1:1, 2:1 and 3:1 species was not observed.[281] Therefore, it was anticipated that the ligand concentration must be the reason for this behaviour, as at higher concentration the formation

of the dimeric species through hydrogen bonding interaction between BTA cores of the neighbouring molecules can occur.[156] Therefore, initially the photophysical properties of **89** (R and S) versus the concentration were investigated and found that indeed the concentration of the ligand has an effect on the photophysical properties of the system. Therefore, in order to investigate the self-assembly properties between **89** (R and S) with Eu(III) in CH_3OH solution, two different concentrations of the ligand were chosen, namely 5×10^{-6} M and 1×10^{-5} M. In the first case (5×10^{-6} M) no interaction between the ligand molecules was observed and therefore we hypothesise that **89** (R and S) exist in the solution as the single molecules.

The UV-vis absorption and luminescence titrations of **89R** and **89S** with $Eu(CF_3SO_3)_3$ in CH_3OH carried out at two different concentrations of ligand, $c_L = 5\times10^{-6}$ and 1×10^{-5} M confirmed the presence of stable luminescent self-assembled species in solution. Experiments conducted in CD_3OD supported the results obtained when CH_3OH was used as a solvent. The titration data of **89R** and **89S** performed at above mentioned concentrations of ligand ($c_L = 5 \times 10^{-6}$ and 1×10^{-5} M), showed the effect of concentration on the Eu(III)-ligand binding equilibrium. The self-assembly studies at lower concentration (5×10^{-6} M) revealed the successive formation of 1:1, 2:1 and 3:1 (Eu:L) species in the solution. Going to higher concentration of the ligand 1×10^{-5} M, the formation of 1:1 and 3:2 (Eu:L) species is observed.

It can be concluded that, by increasing the concentration, the self-assembly process tends towards the formation of higher ordered coordination species in solutions. This may be because at higher ligand concentrations, the molecules interact more frequently and at lower concentrations, the ligands behave as single molecules. The self-assembly behaviour exhibited by **89** (**R** and **S**) at higher concentration (1×10^{-5} M) is analogous to that shown by **86** previously reported from our laboratory.[281] However, the studies performed and reported in this Chapter, discusses the self-assembly behaviour of newly synthesised compounds **89** (R and S) at further lower concentration (5×10^{-6} M), which is not reported.

After studying the Eu(III) binding of tripodal ligands, their gelation and self-assembly was analysed in detail. This will be discussed in the following chapters.

Chapter 3

Self-assembly studies of tripodal molecules in solution: gelation and microsphere formation

3 Introduction

As detailed in the Introduction chapter, supramolecular chemistry has become one of the most widely studied areas of chemistry in the last few decades.[298] The combination of macromolecular and supramolecular chemistry opens up new ways to obtain functional materials, which can be designed for specific applications. Utilising synthetic organic chemistry and polymerization techniques, new molecules can be designed and synthesised with the aim of introducing supramolecular moieties into the polymer architecture.[298-299] Self-assembly of such synthetic systems has seen major developments and applications, particularly in the formation of dynamic and non-equilibrium structures.[75, 80, 300] These supramolecular systems can generally be defined as supramolecular polymers, in which small molecules are held together though reversible, non-covalent and highly directional interactions.[2, 70, 301] A large number of examples of such systems can be found in hydrogen bonded systems, systems employing metal-ligand interactions, ionic interactions and so on, [69, 302-303] many of which were discussed in Chapter 1.

In terms of macromolecular arrangement, assembly of such molecules through non-covalent interactions leads to the formation of one dimensional structures such as fibres, which, upon crosslinking and entanglement, form supramolecular gels. Many various families of low molecular weight gelators (LMWGs) have been reported which self-assemble in different ways.[12-13, 197-198] In all such supramolecular gels, the molecules in the fibrous network are held together through reversible, non-covalent interactions. This reversibility plays a major role in the applications of gels as stimuli responsive materials,[304] biomaterials[305] and also as delivery systems in the controlled release of the entrapped guest molecules. The gels derived from LMWGs have attracted considerable attention because of their many interesting properties and their applications in several areas ranging from food to cosmetics to pharmaceuticals, *etc*.[122, 306] as detailed before within this thesis. By careful selection of substituents and strategic design of the gelators, many gels with tailored properties have been developed by several research groups.[307-315] However, the direct tuning of the properties of the gels, for example stability and morphology, is a topic that needs further investigation.

In understanding the self-assembly on a molecular level, molecules with C_3-symmetry are widely studied.[144, 159-160, 173, 190, 299] Among the C_3-symmetrical tripodal compounds, molecules with a benzene-1,3,5-tricarboxamide (BTA) central core as the skeleton are of much interest, owing to their ease of functionalisation (Chapter 1, Section

1.2.1). The advantage of using a BTA core with an amide functionality is its ability to facilitate the initial self-assembly of the molecules into helices, which are stabilised through threefold hydrogen bonding, as discussed in Chapter 1. This allows for straightforward access to the intermolecular interactions necessary for building large supramolecular architectures, which is the main topic of this PhD thesis.[136, 141, 146]

3.1 Design and self-assembly studies of the tripodal molecules

With an interest in studying the self-assembly of tripodal systems, we designed a system comprising a BTA moiety as the central core, functionalised with triple amide linkages connecting various amino acids and a terpyridine moiety though a propyl chain. These structures are shown below in Figure 3.1. The synthesis of these molecules and their solution state properties were discussed previously in Chapter 2.

The BTA moiety connected to amino acids makes the central core of the molecule rigid, giving a platform for the π – π interaction between the benzene groups. The presence of three amide groups can provide the primary intermolecular interactions through hydrogen bonding.[316] The chiral groups from the amino acid part direct the self-assembly in a helical manner, with the expectation of a different morphology compared to self-assembled

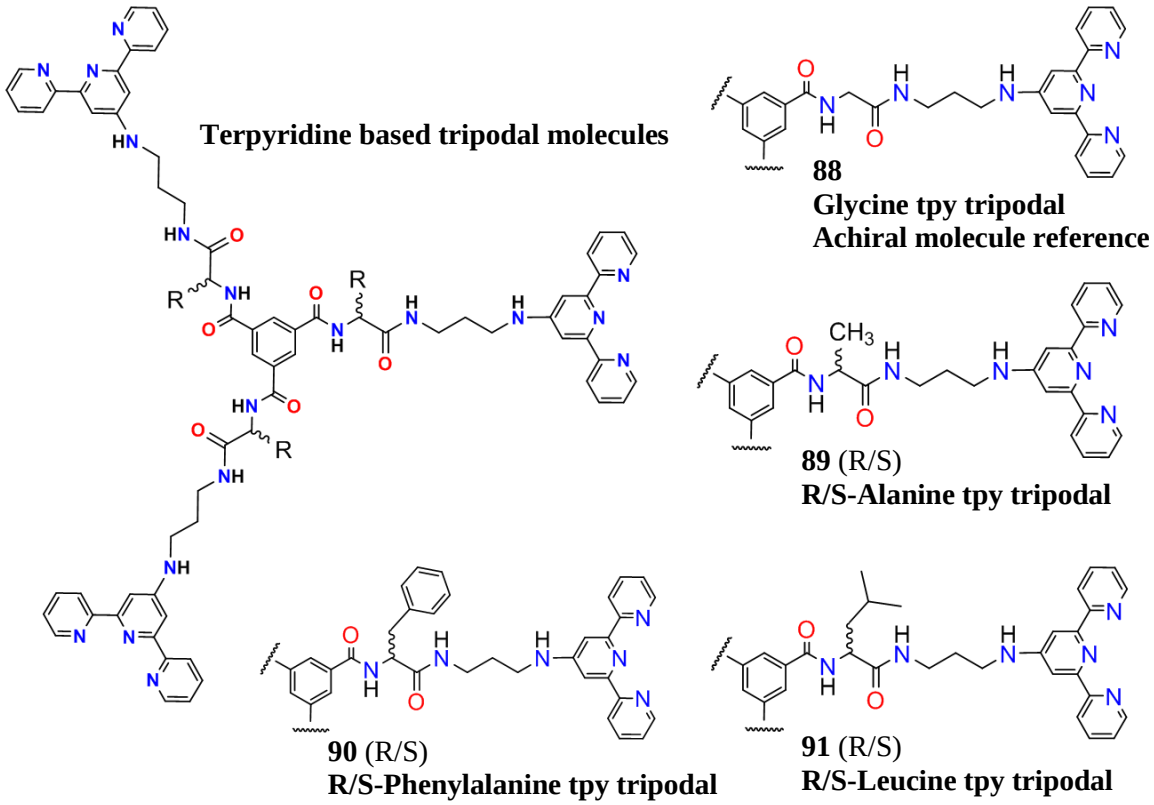

Figure 3.1: Structure of synthesised terpyridine based tripodal molecules with BTA core with various amino acids.

supramolecular structures as well as providing a hydrophobic environment shielding the H- bonding units in the central core of the ligands. Incorporating a further amide group into the side chains helps the molecule to hydrogen bond with H_2O, facilitating better chelation in aqueous solutions, while the terpyridine groups act as binding units for metal ions. Overall, the combination of these different functionalities makes this family of ligands amphiphilic in nature, possessing both partial hydrophobic and hydrophilic properties, aiding in the necessary interplay with the solubility between organic and aqueous media, which is used in the gelation process. This behaviour of the molecules is very supportive towards the development of soft materials like gels and studying their aggregation properties.

Chiral analogues of the BTA molecule incorporating terpyridine functionality have not been reported in the literature to the best of our knowledge. As defined in Chapter 2, we synthesised the ligands **88 - 91** using 4 different amino acids, out of which glycine (referred as **88** throughout) is achiral, making it a reference structure for comparison with the chiral derivatives in investigating the self-assembly processes. Chiral analogues of the tripodal molecules were obtained using enantiomerically pure R/S isomers of alanine (referred to as **89** (R/S) throughout), phenylalanine (referred as **90** (R/S) throughout) and leucine (referred as **91** (R/S) throughout), the structures of which are shown in Figure 3.1. Having synthesised and characterised the various physical properties of **89** (R/S) in Chapter 2, the next objective was to explore their use as LMWGs. Hence, the self-assembly and aggregation properties of **88 - 91** were examined in organic-aqueous solvent media, which will be discussed in this chapter.

3.2 Gelation properties of the tripodal molecules

The gelation properties of **88 - 91** were investigated by dissolving an appropriate amount of the gelator in organic solvent or organic-aqueous solvent mixture by first heating to the boiling point of the respective solvent used and then cooling to room temperature. A preliminary investigation revealed that compounds **88** – **91** were readily soluble in organic solvents with low polarity, such as chlorinated organic solvents, (like $CHCl_3$, CH_2Cl_2) and polar aprotic solvents (like DMSO and DMF). On the other hand they were found to be insoluble or partially soluble in polar solvents (like CH_3OH, C_2H_5OH, $(CH_3)_2CHOH$), and CH_3CN. However, upon addition of water to partially dissolved solutions of **88 - 91** in polar solvents in varying proportions (40 – 80%, v/v), the compounds dissolved completely resulting in the clear solutions. None of these resulted in gel formation. From these preliminary tests, the compounds were found to be amphiphilic in nature due to their

Table 3.1: Gelation of studies of tripodal compounds in organic and organic-aqueous mixtures

Solvent	Compounds			
	Gly trimer 88 (0.5–2% w/v)	**R-ala trimer 89R** (0.5–2% w/v)	**R-Phe trimer 90R** (0.5–2% w/v)	**R-leu trimer 91R** (0.5–2% w/v)
CH_2Cl_2	S	S	S	S
$CHCl_3$	S	S	S	S
CH_3CN/H_2O 40 – 80% v/v	Gel (0.5% w/v) 60% CH_3CN/H_2O	S (≥50% CH_3CN) P (≤50%CH_3CN)	S (≥50% CH_3CN) P (≤50% CH_3CN)	S (≥50% CH_3CN) P (≤50% CH_3CN)
CH_3OH/H_2O 40 – 80% v/v	WG (1% w/v)	S (≥50% CH_3OH) P (≤50% CH_3OH)	S (≥50% CH_3OH) P (≤50% CH_3OH)	S (≥50% CH_3OH) P (≤50% CH_3OH)
C_2H_5OH/H_2O 40 – 80% v/v	WG (1% w/v)	S (≥50% C_2H_5OH) P (≥50% C_2H_5OH)	S (≥50% C_2H_5OH) N (≥50% C_2H_5OH)	S (≥50% C_2H_5OH) N (≥50% C_2H_5OH)
i-PrOH/H_2O 40 – 80% v/v	VS (1% w/v)	S (≥50% i-PrOH) P (≤50% i-PrOH)	S (≥50% i-PrOH) N (≤50% i-PrOH)	S (≥50% i-PrOH) N (≤50% i-PrOH)
DMSO/H_2O 40 – 80% v/v	S	S	S	S
DMF/H_2O 40 – 80% v/v	S	S	S	S

G: gel; S: solution; P: precipitate; WG: weak gel; VS; viscous solution; N: not checked; ≥50 % CH_3CN: above 50 % CH_3CN v/v in CH_3CN-H_2O mixture; ≤50 %CH_3CN: above 50 % CH_3CN v/v in CH_3CN-H_2O mixture.

solubility in organic/H_2O mixtures. This nature of the compounds was expected due to the molecular design, as described in Section 3.1. The detailed gelation tests carried out on the tripodal compounds **88 - 91** are depicted in Table 3.1.

More detailed gelation tests revealed that only the achiral glycine derivative **88** was found to be an efficient gelator; forming a gel in CH_3CN/H_2O (6:4 v/v) at 0.5% w/v and weak gels or viscous solutions in CH_3OH/H_2O and C_2H_5OH/H_2O mixtures. The formation of the gel was confirmed by the so called 'inverted tube' tests as shown in Figure 3.2. The other chiral derivatives (**89** – **91**) did not form a gel in any of the organic/H_2O mixtures investigated and stayed in solution as viscous media over a long period of time (weeks). Therefore, the discussion below will focus only on the gels obtained from **88** in this section, the aggregation studies of other compounds **89 - 91** will be discussed in the further sections. Using a mixture of 6:4 CH_3CN/H_2O and increasing the gelator concentration slowly, the critical gelation concentration (*CGC*) was found to be 0.5% w/v, which is the property of a supergelator, having the ability to form a gel in less than 1% w/v. The gels formed at lower gelator concentration were found to be transparent, while those formed at higher gelator

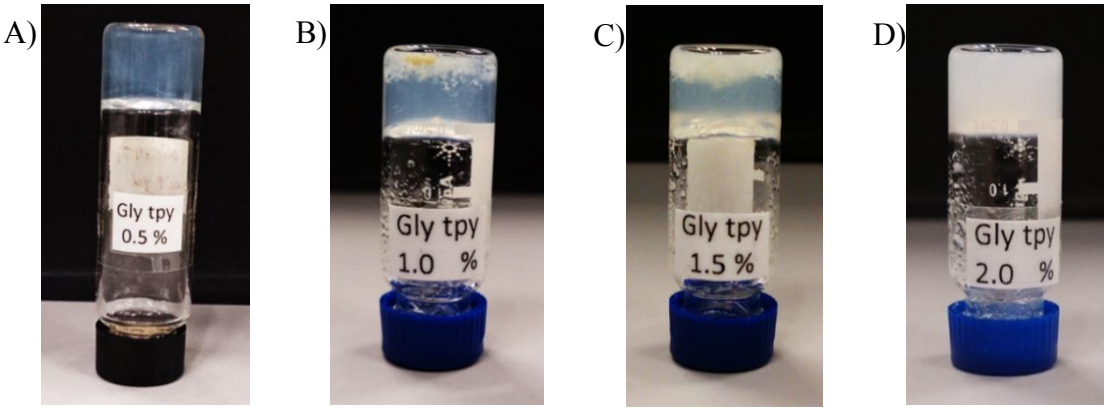

Figure 3.2: Photographs of **88** gels in 6:4 CH_3CN/H_2O mixture at different concentrations. A) 0.5%, B) 1%, C) 1.5% and D) 2% w/v.

concentration, were translucent and turbid (Figure 3.2). Having observed gel formation, next the physical properties of the soft matter were investigated. This will be outlined in next few sections.

3.2.1 Thermogravimetric analysis of gel

Thermogravimetric analysis (TGA) is a technique in which the mass of a substance is monitored as a function of temperature, where upon heating the sample, its weight decreases. The gels formed by **88** (both 0.5 and 1%) in 6:4 CH_3CN/H_2O mixture were subjected to TGA analysis for the determination of the exact concentration of the gelator. The TGA analysis of the gels was carried out by placing the small amount of gel into the heating crucible pan supported by a precision balance and heating the sample from 25 to 800 ^oC under N_2 atmosphere. The results demonstrate that the % weight of the sample decreased steadily until 0.6 and 1.1 % weight for the 0.5% and 1% gels, respectively, corresponding to ~120 - 130

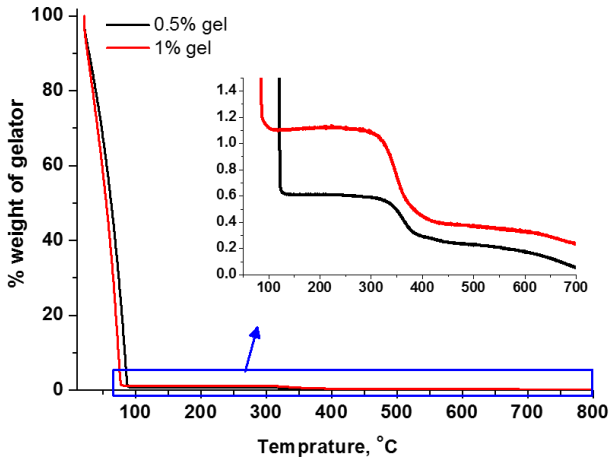

Figure 3.3: TGA of **88** gels (0.5 and 1%) in CH_3CN/H_2O (6:4), Inset: zoomed area on the curve of the same gel.

^{o}C, which is the clear indication for the loss of entrapped solvent molecules (CH_3CN/H_2O) from inside the gel matrix. This point of the TGA graph proves that the gel is comprised of 0.5 and 1 weight % of the gelator and the rest is solvent. Upon continued heating of sample, the remaining gelator was found to be thermally stable until 300 ^{o}C. Further heating resulted in the thermal decomposition of the gelator compound. Hence these results show that **88** is a super gelator, having the ability to gel at concentration less than 1% w/v.

3.2.2 Reversible stimuli responsive properties of 88 gel

Materials that exhibit dramatic changes in their properties in response to environmental stimuli are classified as being stimuli responsive materials.[203] They are further classified depending on the responsive nature to different stimuli, such as thermo, mechano, chemo, photo, *etc*.[317-320] supramolecular chemistry provides a platform for the development of such materials, where the individual components are held together by reversible interactions and the degree of these interactions (binding energy/constants) is influenced by the environment. Supramolecular gels formed through weak inter-molecular interactions can be reformed after the effect of external stimuli is removed. In this section the reversible properties of the gels of **88** which are responsive to external stimuli such as shaking and heating, will be discussed.

Formation of the gel from **88** (c = 1% w/v) made in CH_3CN/H_2O (6:4 v/v) was confirmed after it passed the tube inversion test. The mechanoresponsive properties of the gel were first tested by giving it a strong shake, upon which it lost its gel state and turned into free flowing liquid. Standing at rest for ~1 hour resulted in the reformation of the gel,

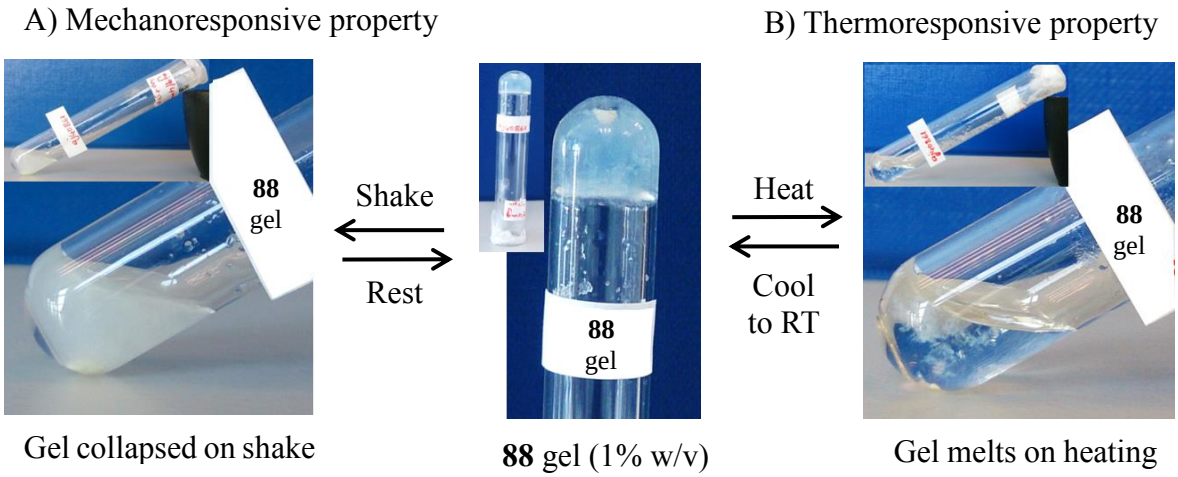

Figure 3.4: A) Mechanoresponsive nature of **88** gel (1%) showing the collapse and reformation of the gel after shaking. B) Thermoresponsive nature of the gel showing melting upon heating to 100 ^{o}C and reforming of the gel upon cooling to RT. Inset: picture showing the inverted tube test for the gels. **88** gel of c = 0.5% also showed the same stimuli-responsive properties.

thereby the gel exhibited thixotropic (shear-thinning) behaviour (Figure 3.4A). Similarly, the thermoresponsive properties of the same gel (1% w/v) were tested by heating the gel. Upon heating the gel of **88** to 100 ^{o}C, it melted, and upon cooling back to room temperature, the gel was found to reform, demonstrating the thermoresponsive properties, (Figure 3.4B).

3.2.3 Thermal stability and enthalpy of 88 gel

The thermal stability of the gel (T_{gel}) was tested by heating the gel of **88** in an inverted tube. The temperature at which the gel melts and loses its gel properties and falls down, is taken as T_{gel}.[321] Thermal stability was investigated for a number of **88** gel samples, where the concentration of **88** was increased from 0.5 to 1.5% w/v. As expected, the T_{gel} values increased with increasing concentration of gelator. The variation in the thermal stability with respect to the concentration was represented by plotting T_{gel} versus concentration (Figure 3.5A). The T_{gel} measurements was repeated three times and the values reported are the average of three measurements for each gel.

Another important parameter that can be derived from this plot is the enthalpy (ΔH) associated with the gel-sol transition process. This parameter can be obtained by plotting lnC (concentration of gelator) versus $1/T_{gel}$ (Figure 3.5B). The molar enthalpy values are then determined by the slope of this linear fit using Schröder-van Laar equation.[122, 321]

$$\mathbf{lnC = - \Delta H/RT_{gel} + K} \qquad \text{Schröder-van Laar equation (3.1)}$$

In equation 3.1, C is the concentration of the gelator (M), ΔH is the molar enthalpy associated with the gel-sol transition, T_{gel} is the gel-sol transition temperature as defined before and K is a constant. Using the Schröder-van Laar equation for the plot of lnC vs $1/T_{gel}$ (Figure

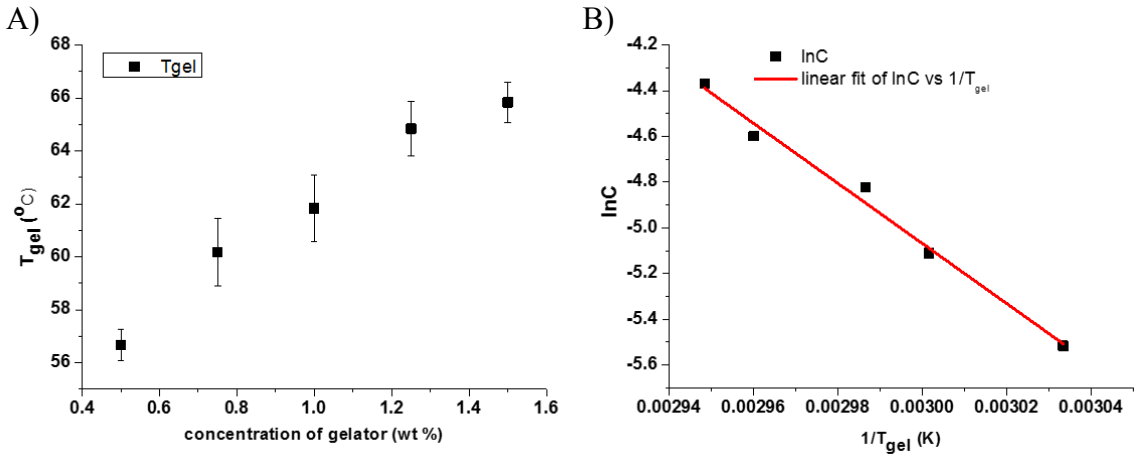

Figure 3.5: A) plot of T_{gel} *vs* concentration for **88** in CH_3CN/H_2O (6:4) gel showing the linear increase of T_{gel} with concentration. Values reported here are the average of three measurements for fresh samples. B) Schröder van Laar plot for the same compound.

3.5B), enthalpy values for the gel-sol transition were determined for **88** from the slope of the linear fit and the value was found to be $\Delta H = 109$ kJ mol^{-1}.

After studying the stimuli-responsive and thermal properties of the **88** gel, in order to investigate the morphology and the orientation of supramolecular fibres formed with in the gels, dried samples were analysed using SEM and TEM, and these results are discussed in the following section.

3.2.4 Morphology studies of 88 gels by electron microscopy

The morphology of the xerogel of **88** was investigated by Scanning Electron Microscopy (SEM) and Transmission Electron Microscopy (TEM). The xerogel samples of the gel of **88** were prepared by placing a thin layer of the wet gel onto a silica wafer which was then dried in air for 12 hrs and then in vacuo for 2 hrs prior to imaging.

3.2.4.1 Scanning electron microscopy (SEM)

The xerogel samples prepared from the **88** gels (1% gel in 6:4 CH_3CN/H_2O mixture) were initially imaged under SEM. The SEM images showed the highly entangled network of fibres with cavities inside the gel matrix, where the solvent molecules were previously entrapped. To investigate whether the concentration of the gelator had any effect on the morphology of the gel, SEM images were recorded for xerogels prepared from **88** wet gels for two different concentrations, 0.5 and 1% w/v.

In the case of 0.5% gel, the size of individual fibres was found to be ~ 30-50 nm in width and their length was found to be more than few micrometres. In some places, the fibres (approx. 5–10 in number) were found to form bundles of 70-100 nm in width, Figure 3.6A. The analysis of the morphological features of the 1% gel showed that,

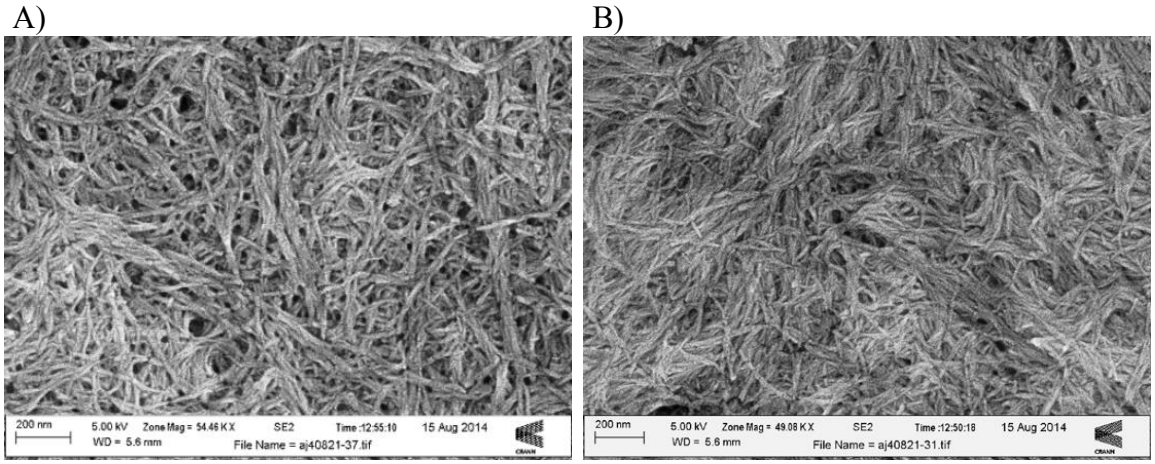

Figure 3.6: SEM images of xerogels of **88** in 6:4 CH_3CN/H_2O. A) 0.5 % gel and B) 1% gels. Scale bar 200 nm.

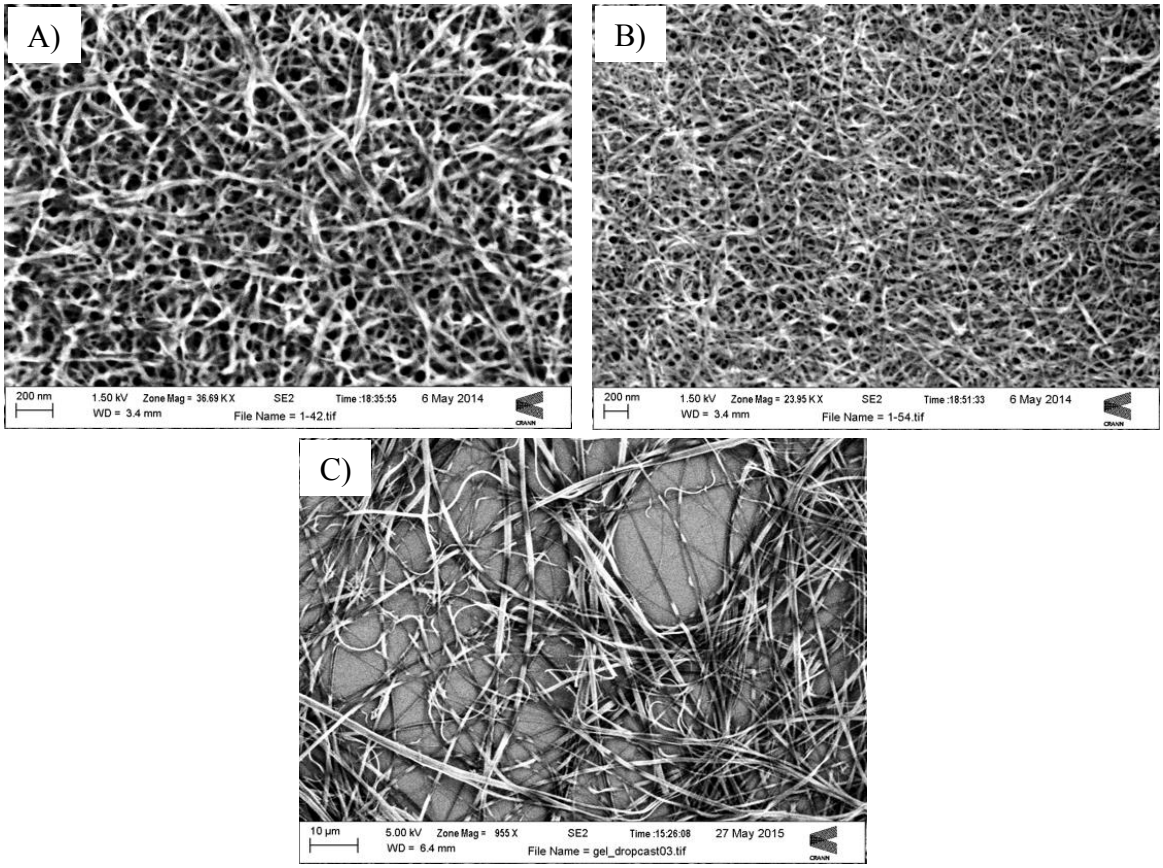

Figure 3.7: SEM images of xerogels of **88** gel (c = 1% w/v) in (A) CH_3OH/H_2O, (B) C_2H_5OH/H_2O and (C) dropcasted viscous solution of **88** in *i*-$PrOH/H_2O$ mixtures (c = 1% w/v).

although there was no significant variation in the fibrous arrangement, a slight decrease in the average width of the fibres was observed. The bundles formed within this gel were made of a higher number of fibres with a larger width of approx. 150-200 nm. The size and the number of cavities also decreased compared to that seen for the 0.5% sample. These minor, but noticable changes in the morphology are a clear indication of the effect of the concentration of the gelator and as a result, the gel with higher concentration (1%) appeared to be stronger by visual observation (Figure 3.6B). Furthermore, the weak gels of **88** (c = 1% w/v) formed in CH_3OH/H_2O and C_2H_5OH/H_2O, that failed the inversion tube test, were also examined using SEM. The morphologies of these weak gels were found to be different to that seen for the CH_3CN/H_2O gel, demonstrating the effect of changing in the solvent media. The morphologies of the gels from CH_3OH/H_2O and C_2H_5OH/H_2O were found to be similar to those shown in Figure 3.7, A and B. This result was not unexpected, as both gels are made of polar protic solvents with similar properties. In comparison to the CH_3CN/H_2O gel (Figure 3.6), the fibres of both of these weak gels were smaller in width (less than 30 nm), with more cavities and less dense in the gel matrix. Also, the formation

of bundles was not observed in this case, which may be the reasons for the formation of weaker gels from CH_3OH/H_2O and C_2H_5OH/H_2O mixtures (Figure 3.7 A and B). The viscous solution formed in *i*-$PrOH/H_2O$ mixture was dropcasted and imaged in SEM showed that **88** formed only elongated fibres, but failed to form the crosslinks of the fibrous network, which is necessary for the entrapment of solvent molecules and the formation of a gel. This explained the failure of gel formation from **88** in *i*-$PrOH/H_2O$ mixture (Figure 3.7C).

3.2.4.2 Transmission Electron Microscopy (TEM)

After analysing the surface morphology of the **88** gel using SEM, the same gels were next analysed using TEM. The xerogels prepared from the **88** gels (in 6:4 CH_3CN/H_2O) of two different concentrations (0.5 and 1% gel) were imaged. The TEM images of both of these xerogels showed a similar entangled network of fibres (Figure 3.8), as observed previously from their SEM images (Figure 3.8). The fibres were confirmed to be *c.a.* 30-50 nm in width, along with some smaller sized fibres and were found to form a cross-linked network that grew in three dimensions. The TEM images of these gels revealed similar features to that observed for the SEM analysis above. In the junction zones of cross-linking, the fibres formed bundles with the size of ~100 – 200 nm. Another common observation was the presence of aggregates (~50-100 nm in size) in some areas of the sample. These aggregates probably originated from partial precipitation of the gelator within the gel.

On comparison with the SEM and TEM images of gels from other BTA molecules, such as **20**,[124] **36**[125] and ligand gel of **86**[281] (previously reported in our group), **88** showed

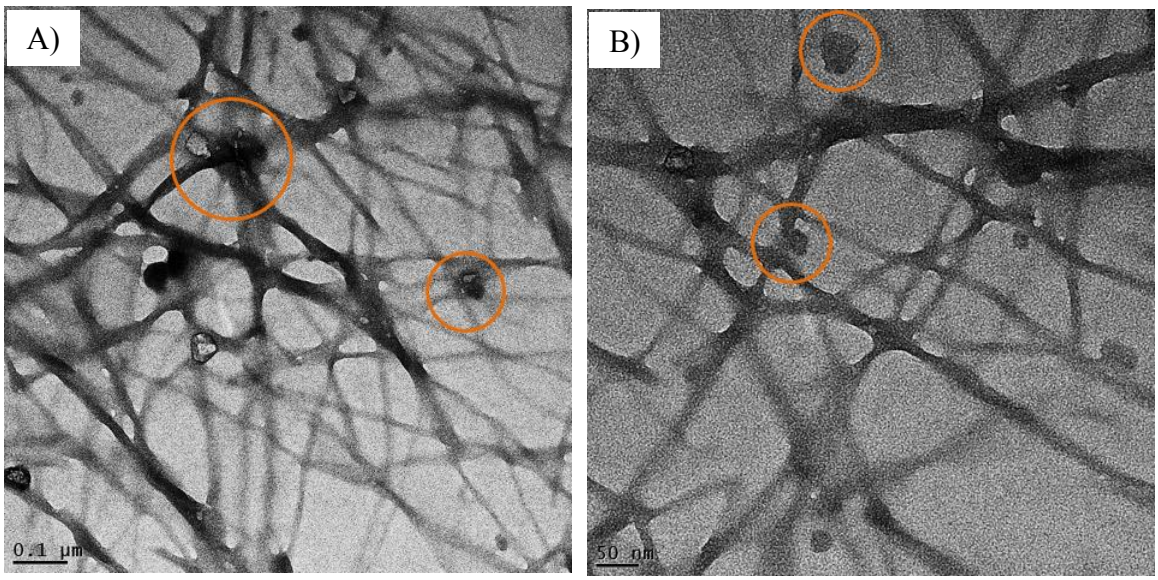

Figure 3.8: TEM images of xerogels obtained from **88** gels in CH_3CN/H_2O: (A) c = 1 wt %, Scale bar 100 nm and (B) 0.5 wt %, Scale bar 50 nm. Circles highlighting the aggregates of gelator.

better morphological features with a more easily distinguishable fibrous network, making them different from other BTA derivatives.

As a conclusion, the gelation tests carried out on the synthesised tripodal molecules showed that only the achiral derivative **88** formed a gel and the chiral analogues **89** – **91** did not show gelation in any of the solvents systems studied. The aggregation properties of the chiral analogues **89 - 91** will be discussed in further sections.

3.2.5 Rheological studies of 88 gel

The mechanical properties for the **88** gels discussed above were investigated by dynamic rheology experiments. Gels are viscoelastic materials, therefore they store and dissipate energy.[15, 255] Three kinds of rheology experiments were performed: ***1***) Frequency sweep (at fixed stain of 0.1%), ***2***) strain sweep (at a fixed frequency of 1.0 Hz) and ***3***) recovery test. From the frequency sweep experiments, dynamic storage modulus G′ ('solid-like' behaviour) and loss modulus G″ ('liquid-like' behaviour) data are obtained. For soft solid-like materials such as gels, the storage modulus (G′) is expected to be greater than loss modulus (G″). From the strain sweep experiments yield strain is obtained. At this (or a higher value) of applied strain, the gel starts to flow. As **88** formed a more transparent gel at 0.5% than at higher concentrations (1%, *etc*., Figure 3.2), dynamic rheology experiments were performed on the 0.5% gel in 6:4 CH_3CN/H_2O, and those will be discussed in this section. All rheology experiments discussed here were performed in collaboration with Prof. Matthias Möbius, School of Physics, Trinity College, Dublin. The viscoelastic properties measured are similar to those commonly observed for cross-linker polymer networks.

3.2.5.1 Frequency and strain sweep experiments on 88 gel

The frequency sweep experiment performed on the **88** gel, shows a dependence of storage (G′) and loss modulus (G″) on the frequency in the linear viscosity region, showing solid like behaviour where G′ > G″, confirming the gel nature of the sample (Figure 3.9A). In addition to this, corresponding strain sweep experiments were also carried out. The storage modulus G′ initially displayed a value of 1040 Pa, which is relatively low for a gel, but is much higher than the value of loss modulus G″ at the same strain amplitude (0.1%). This is the indicative of an elastic rather than viscous material, which is a characteristic behaviour of cross-linked gel formed by weak interactions.[126] At low strain amplitude, the gel behaves like a solid and the G′ remains constant until yield strain is reached (1.4%), the point where G′ starts to decrease and the gel starts to flow. As a result, the crossover point is observed occurring around ~4% strain, corresponding to the change in solid like region (Figure 3.9B).

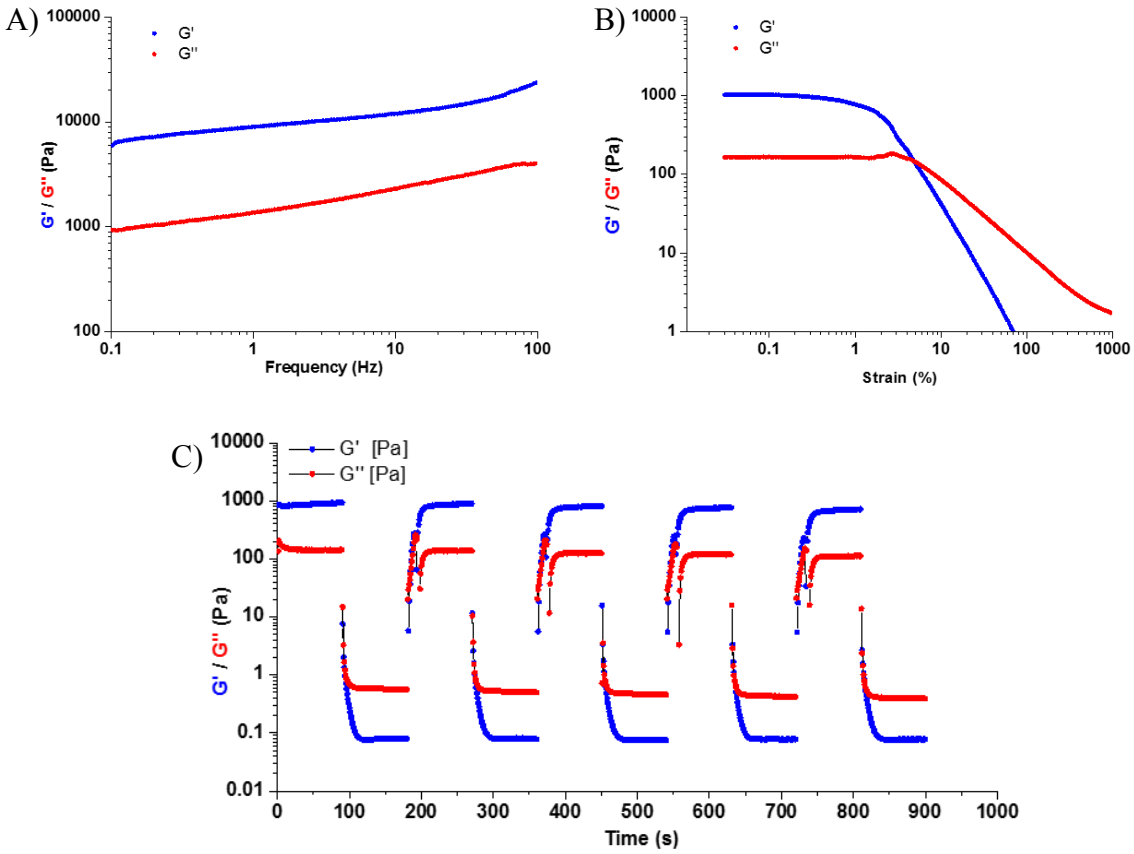

Figure 3.9: Rheology measurements of **88** gels (0.5% in 6:4 CH_3CN/H_2O). A) Frequency sweep experiment, Frequency dependence of G′ and G″ at strain amplitude of 0.1%. B) Strain sweep experiment (at frequency = 1Hz). C) Recovery test by applying alternating strain amplitude of 2500% and 0.1% with 90 seconds intervals (at frequency = 1 Hz).

The self-healing properties of the **88** gel were also investigated by carrying out a recovery test. The measurements were performed by imposing an alternating low strain rate (0.1%, 1 Hz for 90 seconds) and a high strain rate (2500%, 1 Hz for 90 seconds), beyond the liquid transition point.[322] The variation of storage modulus G′ and loss modulus G″ are given in Figure 3.9C Showing that the gel went from liquid-like (G″ > G′) to solid-like (G′ > G″) behaviour rapidly, with a quick recovery time of approx. 30 seconds to the original strength. This instant recovery behaviour was observed over five consecutive cycles of measurements. This illustrates the self-healing nature of the **88** gel. This rapid recovery might be due to the strong intermolecular triple H-bonding between the molecules of **88**. In addition to this, SEM images recorded for the **88** gel sample after the rheological measurements showed the same morphological features seen before (See Appendix Figure 3.2.1), which supports the self-healing nature of the gel.

When compared to the rheological behaviour of the gels from other BTA molecules such as **20**,[124] **36**[125] and **86**[255], **88** showed similar (or higher) G′ values from the frequency sweep experiments. From the recovery test experiments, the **88** gel (0.5%) showed faster recovery to the gel state (approx. 30 s) than the other gels previously reported from our group.[255, 285]

3.3 Microsphere formation from chiral derivatives of terpyridine tripodal molecules 89 – 91 (R and S)

After having studied the gelation properties of the glycine tripodal derivative **88** in various solvent systems, the gelation/aggregation properties of the chiral tripodal molecules were next investigated. The *R* and the *S* isomers of **89**, **90** and **91** (0.5 to 2 % w/v) were dissolved in organic-aqueous solvent mixtures by heating at 100 ^{o}C and cooling to RT, in a similar way to that described in Table 3.1. Having been able to obtain a gel from **88**, it was anticipated that the chiral analogues **89**, **90** and **91** (R/S) would also form gels of a similar nature to that discussed above.[138, 145, 176, 323] However, in all cases, as defined above no gelation was observed, either in similar conditions (CH_3CN/H_2O mixture) as used for **88**, or in aqueous mixtures of CH_3OH, C_2H_5OH, *i*-PrOH DMSO and DMF. Unlike **88**, these chiral derivatives were found to have no gelation capabilities, rather they were found to remain in solution or resulted in the formation of precipitates. However, it was observed that the solvent media for **89 - 91** appeared visually different; becoming viscous in a few cases, such as in CH_3CN/H_2O, CH_3OH/H_2O and C_2H_5OH/H_2O solutions. This suggested the formation of self-assemblies or possible higher order aggregates, which might be one dimensional supramolecular polymers formed though triple hydrogen bonding between the tripodal molecules.[156, 176] These viscous samples were thus imaged using electron microscopy analysis in a similar manner as above, where the solutions of **89 - 91** (R/S) (c = 0.5 - 0.2% w/v) were dropcasted on to the silica wafers, dried and imaged using SEM.

From the SEM analysis, the expected formation of one dimensional supramolecular polymer fibres was not observed. Instead, the formation of remarkable microspheres was observed as demonstrated in Figure 3.10. Among all the solutions of **89**, **90** and **91** (R/S) of various concentrations in different solvent systems as described above, a solution of concentration c = 0.2% (w/v) in CH_3CN/H_2O (6:4 v/v) showed the most highly monodisperse microspheres, as shown Figure 3.10. The formation of microspheres was unexpected, as no evidence of the formation of such a morphology has been reported to date for BTA structures. Furthermore, the BTA molecules substituted with simple alkyl chains

such as **35 - 36**[125] or with the urea side chain derivatives **52 - 53**,[144] discussed in Chapter 1, neither of these showed the formation of such spherical aggregates.

From the SEM analysis shown in Figure 3.10, the dropcast solution of **89S** in CH_3CN/H_2O (6:4, c = 0.2% w/v) showed the formation of highly monodisperse microspheres (Figure 3.10A and B). These microspheres were found to have a very smooth surface and uniform size distribution throughout the sample without showing any kind of aggregation or the formation of bundles. Upon closer observation, these microspheres remained as individual particles without any connections between them, even in regions of higher concentration of sample (Figure 3.10B). Particle size distribution calculated for the SEM images, showed that the size of the **89S** microspheres was in the range of approx. 0.8 - 1.1 μm in diameter with a mean particle size of 0.97 ± 0.08 μm (with polydispersity of 8.45%). Helium ion beam microscope (HIB) image of the same sample also showed the

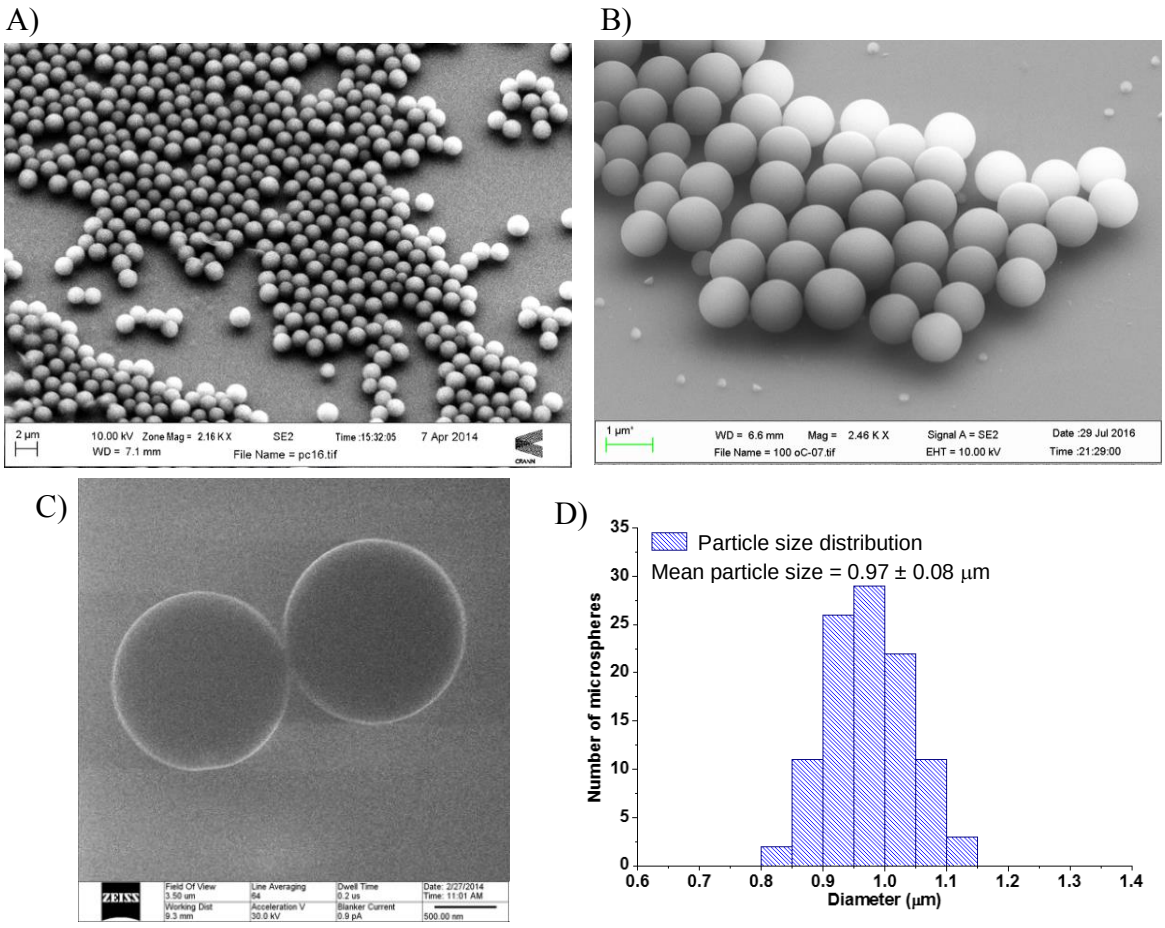

Figure 3.10: SEM images of the microspheres from **89S** formed in CH_3CN/H_2O (6:4, c = 0.2% w/v). A) Uniform distribution of microspheres without any aggregation, B) magnified image of the same sample taken at 50° angle, Scale bar 1 μm, B) Helium ion beam microscope image of the same sample, scale bar 500 nm, D) particle size distribution diagram calculated from SEM images using ImageJ software**.**

formation of monodisperse microspheres which were in good agreement with the observation made form SEM images (Figure 3.10C).

Similarly, when imaging other derivatives such as the S-phenylalanine terpyridine **90S** and the S-leucine terpyridine **91S** tripodal compounds in 6:4 CH_3CN/H_2O, c = 0.2% w/v solutions, the formation of very similar microspheres, with small differences in appearance, was observed under similar conditions. Particle size distribution calculated for the microspheres formed from **90S** had a broader size distribution with the particle size ranging from 0.4 - 1.4 μm in diameter, with a mean particle size of 1.08 ± 0.17 μm (polydispersity = 15%, Figure 3.11, A and C). Microspheres from **91S** however showed a reasonably narrow size distribution, ranging from 0.6 - 0.9 μm in diameter with a mean particle size of 0.78 ± 0.07 μm (polydispersity = 9.6 %, Figure 3.11, B and D). As expected, the formation of microspheres from *R* enantiomers of **89** - **91** were also observed. SEM and HIB images and particle size distribution of **89R**, **90R** and **91R** are provided in Appendix Figure: A3.3.1 - A3.3.3. Furthermore, as previously mentioned, among the different concentrations tested in 6:4 CH_3CN/H_2O solvent mixture, the solutions of c = 0.2% w/v

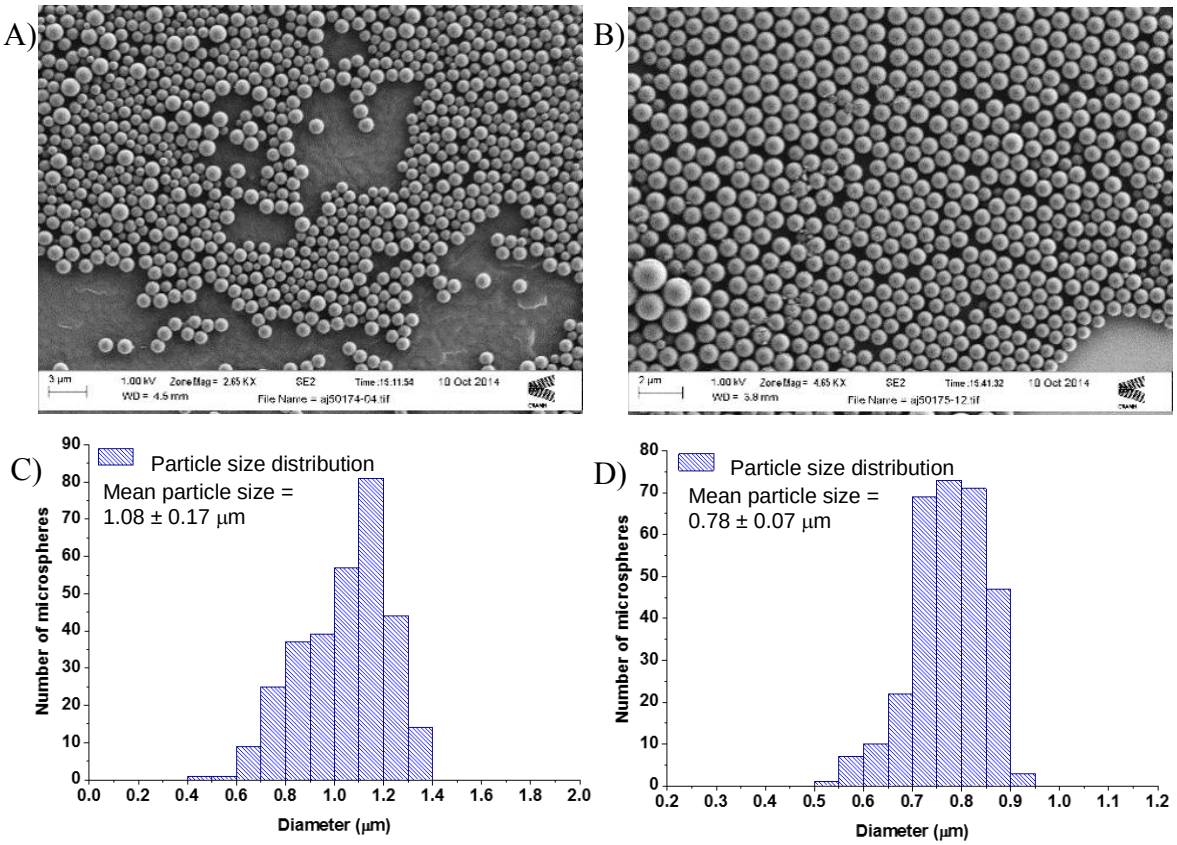

Figure 3.11: SEM images of the microspheres from (A) **90S**, Scale bar 3 μm. (B) **91S**, scale bar 2 μm, in 6:4 CH_3CN/H_2O (c = 0.2% w/v). C) and D) are their corresponding particle size distribution diagrams calculated from SEM images using ImageJ software.

showed better monodispersity of the microspheres in comparison to higher concentrations (*eg.*, c > 0.5%) as observed from SEM. Among these 3 chiral tripodal derivatives, the microspheres from the alanine derivative **91S** had the narrowest size distribution (approx. 1.0 ± 0.2 μm) with the least polydispersity. Hence, microspheres formed from **91S** will be used in most of the experiments discussed in the further sections. A summary of the particles size distribution of **89** – **91** (R and S) determined form SEM images is found in Table 3.2.

The microscopic investigations of the chiral derivatives **89** - **91** (R and S) revealed very different self-assembly behaviours to that of the achiral analogue **88**. From the dramatic changes in the morphology of the self-assembled structures, it can be concluded that, by changing the molecule from non-chiral to chiral, one dimensional linear supramolecular structures can be changed to spherical particles. This unexpected discovery inspired us to further investigate their functional properties. This will be discussed in the following sections.

Table 3.2: Summary of the particle size distribution of **89** – **91** (R and S) determined form SEM images.

Compound	Mean Particle size	Compound	Mean Particle size
89R	1.11 ± 0.08	**89S**	0.97 ± 0.08
90R	0.81 ± 0.11	**90S**	1.08 ± 0.17
91R	1.05 ± 0.64	**91S**	0.78 ± 0.07

3.3.1 Investigation of microsphere formation in different organic solvents/H_2O media using SEM

The effect of solvent on the formation of microspheres was first investigated. Therefore, microspheres from **89** (R and S) were prepared in a series of various organic solvents and aqueous mixtures. In organic solvents alone, appropriate samples for imaging could not prepared because of the volatile nature of some solvents, ($CHCl_3$, CH_2Cl_2, THF, *etc*) and the compounds were insoluble in other organic solvents alone (CH_3OH, C_2H_5OH, CH_3CN, *etc*.), even upon heating to the boiling point of solvents used. Hence this investigation was done in organic solvent/H_2O mixtures (1:1 v/v) wherein the compound **89** (R and S) was soluble (Table 3.3).

SEM images of dropcasted solutions of **89S**, in different solvent systems as depicted in Table 3.3, showed similar formation of microspheres in most of the solvent systems with some variation in the particle size. In a mixture of CH_3OH/H_2O (1:1 v/v), 1 - 1.5 μm sized

Table 3.3: Microspheres made from **89** (R and S) in different solvent systems.

Compound 89 (R and S)	**Solvent system (v/v)**	**Result**
0.2 wt %	CH_3CN/H_2O (1:1)	Uniformly sized microspheres
0.2 wt %	CH_3OH/H_2O (1:1)	Different sized microspheres
0.2 wt %	C_2H_5OH/H_2O (1:1)	Different sized microspheres
0.2 wt %	*i*-PrOH/H_2O (1:1)	Different sized microspheres
0.2 wt %	Acetone /H_2O (1:1)	Random sized microspheres
0.2 wt %	THF/H_2O (1:1)	Fused microspheres
0.2 wt %	1,4-dioxane/H_2O (1:1)	NO microspheres

The use of higher proportion of H_2O in the solvent mixture resulted in the precipitation of compound.

particles were formed along with smaller ones and little disturbance in the smooth surface and shape (Figure 3.12A) was observed. In the case of C_2H_5OH/H_2O (1:1 v/v) and *i*-PrOH/H_2O (1:1 v/v) mixtures, the particles sizes were smaller, by *c.a.* 500 nm (Figure 3.12, B and C). However, in acetone/H_2O (1:1 v/v) mixture, a random size distribution of particles was observed (Figure 3.12D). Microspheres formed from THF/H_2O (1:1 v/v) were found to be unusual, as the particles were fused to each other (Figure 3.12E) unlike that seen for other solvent systems. No particles were observed in 1,4-dioxane/H_2O (1:1 v/v) mixtures, instead a film was observed probably because of complete dissolution of the compound (Figure 3.12F). As expected, the **89R** sample also showed very similar morphologies to **89S** (Appendix Figure A3.3.4).

From these differences observed in different solvent systems, **89** (R and S) showed the formation of monodisperse sized microspheres in CH_3CN/H_2O media. This might probably because, the CH_3CN/H_2O mixture provides an appropriate balance between the hydrophobicity and hydrophilicity for the aggregation of **89** (R and S) to form uniform sized particles. Furthermore, among various ratios of CH_3CN/H_2O mixture tested, monodispersed particles were formed in 6:4 v/v ratio. Additionally, it was also observed that, upon increasing the concentration of **89** (R/S) to more than 0.5% w/v, precipitation was observed. Therefore, to avoid precipitation and to maintain consistency, the concentration of **89** (R/S) of 0.2 – 0.4% w/v and CH_3CN/H_2O mixture with 6:4 v/v ratio (with higher proportion of CH_3CN) was considered to be the most suitable medium to prepare uniform monodispersed microspheres used in all of the experiments discussed in further sections.

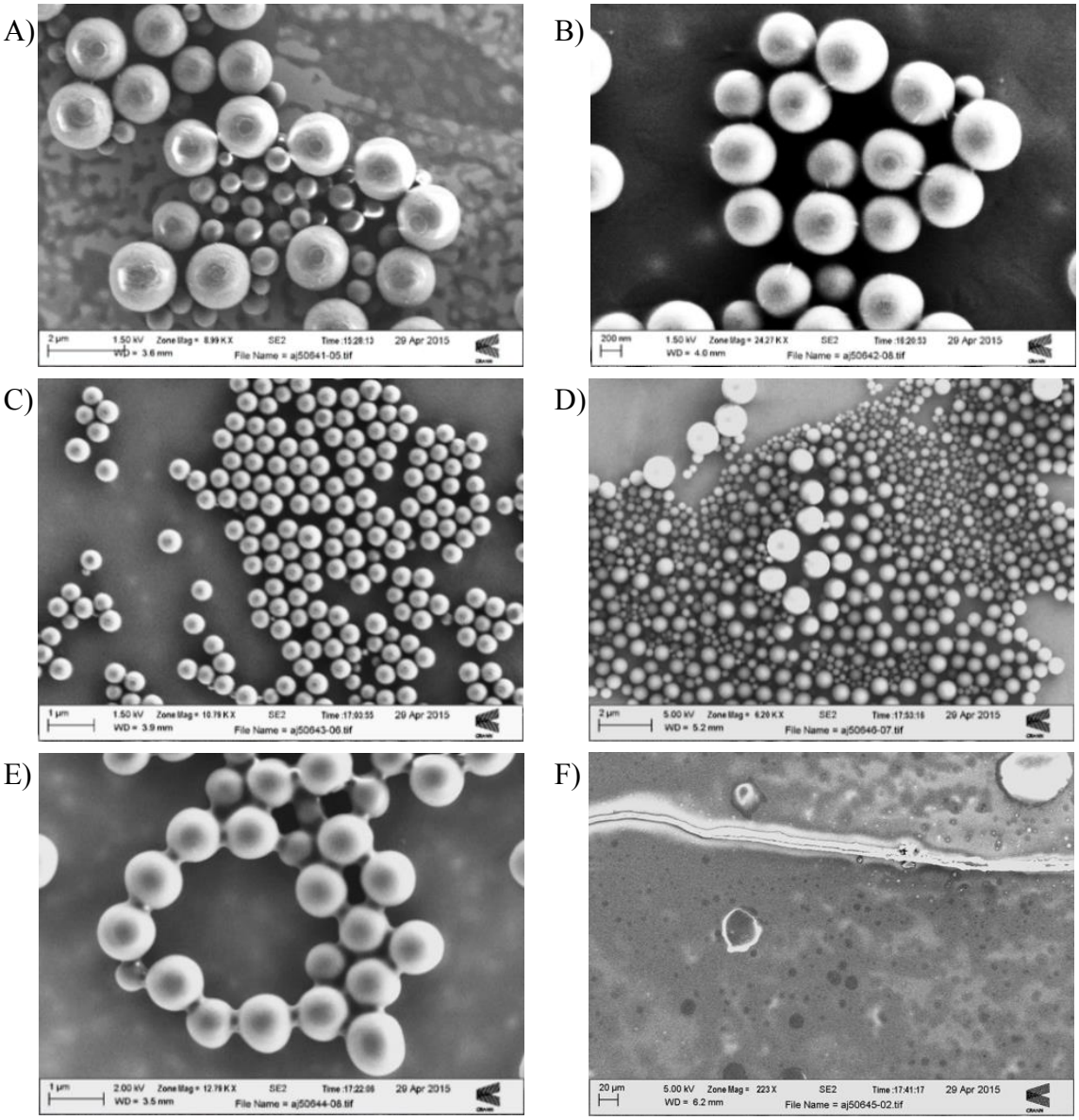

Figure 3.12: SEM images of **89S** microspheres in different organic solvent/aqueous (1:1 v/v) media (c = 0.2% w/v) A) CH_3OH/H_2O, scale bar 2 μm, B) C_2H_5OH/H_2O, scale bar 200 nm, C) *i*-$PrOH/H_2O$, scale bar 1 μm, D) Acetone/H_2O, scale bar 2 μm, E) THF/H_2O, scale bar 1 μm. F) 1,4-dioxane/H_2O, scale bar 20 μm. SEM images of **89R** microspheres formed in the same solvent medium are given in Appendix Figure A3.3.4.

3.4 Dynamic light scattering measurement of microspheres in solution

The size distribution of the microspheres obtained from the chiral tpy tripodal molecules **89S – 91S** was analysed by Dynamic Light Scattering (DLS) technique using a solution of CH_3CN/H_2O (6:4 v/v) mixture at 22 ^oC (Figure 3.13). As discussed above, to maintain consistency and avoid precipitation, CH_3CN/H_2O (6:4 v/v) was used as solvent medium. Homogeneous monodisperse microspheres were observed for all samples. The Hydrodynamic diameter measured for the microspheres of **89S – 91S** in CH_3CN/H_2O (6:4)

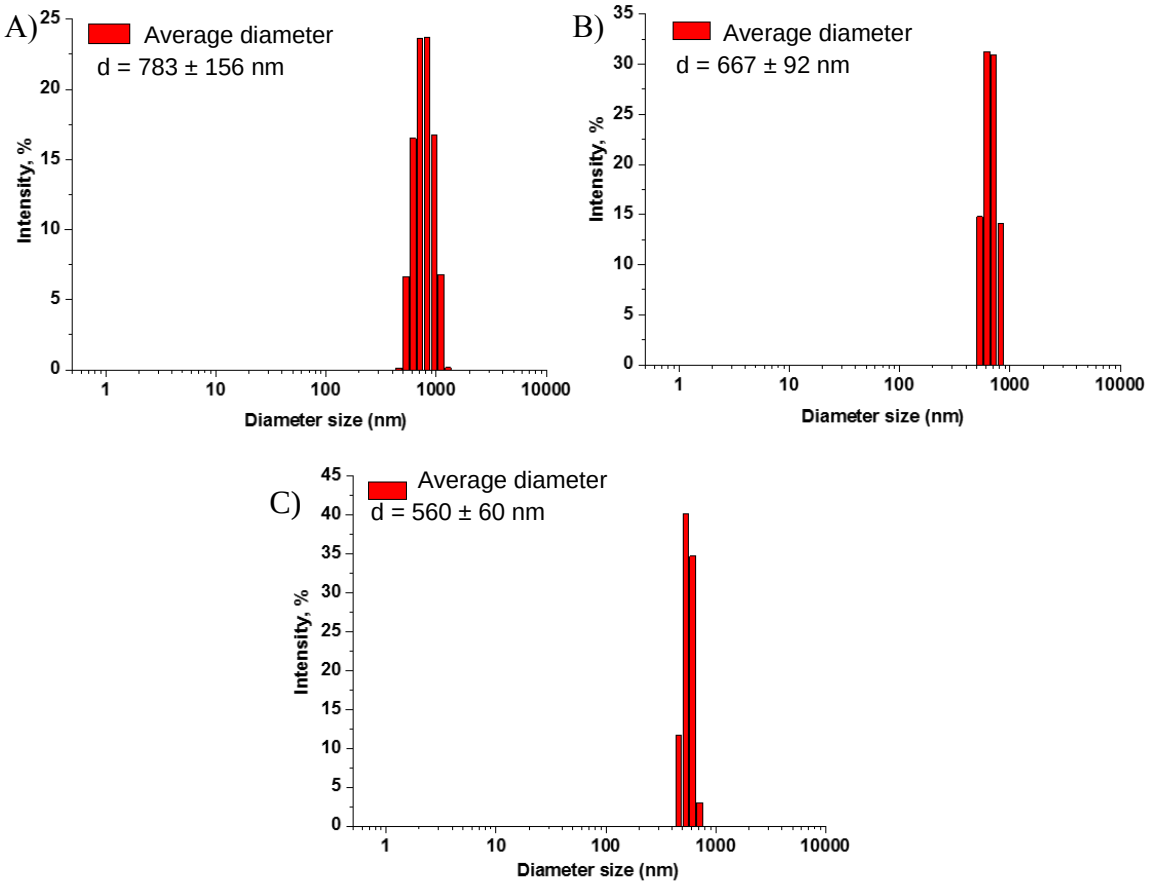

Figure 3.13: Average particle size distribution determined using DLS technique for microspheres prepared in 6:4 CH_3CN/H_2O (c = 1.55 × 10^{-3} M, at 22 °C) from A) **89S**, B) **90S** and C) **911S**.

solution at a concentration 1.55 × 10^{-3} M (0.2% w/v) were found to be in the range of 550 – 800 nm. The individual size distribution measurements performed on the **89S** microspheres showed an average diameter of 783 ± 156 nm. Similarly, microspheres from **90S** and **91S** were found to have diameters of 667 ± 92 nm and 560 ± 60 nm, respectively (Figure 3.13).

From the DLS measurements, all the samples showed a narrow size distribution for the microspheres with the diameter size close to 1000 nm. This value is in good agreement with the particle size distribution obtained by analysis of the SEM images, wherein **89S**, **90S** and **91S** showed a mean particle size distribution of 0.97 ± 0.08, 1.08 ± 0.17 and 0.78 ± 0.07 μm respectively. However, small differences in the value of particle size distribution obtained from DLS and SEM images might be because the measurement was performed on different samples. The preparation of the microsphere samples every time by heating-cooling cycle, result in the dissolution of the compound followed by aggregation. This aggregation occurs in similar manner in each sample resulting in the particles formation in the range of approx. 1 μm each time, with minor difference in their sizes. This difference was observed

between the DLS and SEM measurements. Repeating the same experiment three times, showed similar results.

3.5 Investigation of the aggregation process in the formation of microspheres using fluorescence

The widely used method to determine the aggregation of the surfactants was developed by Thomas *et al.*[324] In this method, pyrene was used as a fluorescent probe to follow the aggregation process of the surfactant, upon increasing its concentration, by monitoring the intensities of band 1 and 3 (I_3/I_1 ratio) of pyrene. Recently, De cola *et al.* demonstrated the evolution of the formation of self-assemblies by monitoring the different emission properties of the aggregates, wherein the time-dependent transformation showed a decrease in the fluorescence emission of the diminishing species and the increase in the emission of growing species.[325] Analogous to this method, using fluorescence spectroscopy, the aggregation process of the **89S** was monitored as a function of its concentration. But in this case the molecules of **89S** itself act as the fluorescent probe. By monitoring the different emission properties of each species (used as a fingerprint), the formation of self-assemblies were monitored. From the initial fluorescence experiments it was found that, upon excitation of **89S** solution ($c \leq 1 \times 10^{-5}$ M in CH_3CN/H_2O 6:4) at λ_{ex} = 280 nm, fluorescence emission from the individual free molecules was observed at λ_{max} = 413 nm. On the other hand, upon excitation of **89S** microspheres solution at λ_{ex} = 405 nm, fluorescence emission from the microspheres was observed at λ_{max} = 489 nm. This difference in the excitation and the fluorescence emission wavelength between free molecules and microspheres was used to monitor the aggregation process and self-assembly formation leading to the formation of microspheres.

In order to follow the formation of self-assemblies, a series of solutions were prepared by increasing the concentration of **89S** from 5×10^{-6} M to 3×10^{-4} M in CH_3CN/H_2O (6:4). Upon excitation of these solutions at λ_{ex} = 280 nm, emission from free molecules (only) is observed at λ_{max} = 413 nm (Figure 3.14A, blue). When exciting the same solution at λ_{ex} = 405 nm, emission from the microspheres (only) was seen at λ_{max} = 489 nm (Figure 3.14A, red). Fluorescence for all the samples was measured in a similar manner and the variation in the emission intensities was analysed from their intensity profiles *vs* concentration range. As expected, although the same solution was excited at two different

wavelengths (λ_{ex} = 280 and 405 nm), the emission from only one species is observed at a time. The coexistence of both the emissions was not observed in any of the cases.

In the case of free molecules, the emission intensity (λ_{max} = 413 nm) increases with concentration and reaches a maximum at the concentration approx. ~1 × 10^{-5} M. When the concentration of the free molecules was increased further beyond 1.25 × 10^{-5} M, emission intensity decreases because the aggregation, resulting in the consumption of the free molecules (showing emission at 413 nm). This effect continues as the concentration was increased. Finally, at higher concentration the emission from the free molecules was completely diminished. Presumably as the free molecules were consumed for the microspheres formation (Figure 3.14 B and C, blue). However, this was contrary in the case

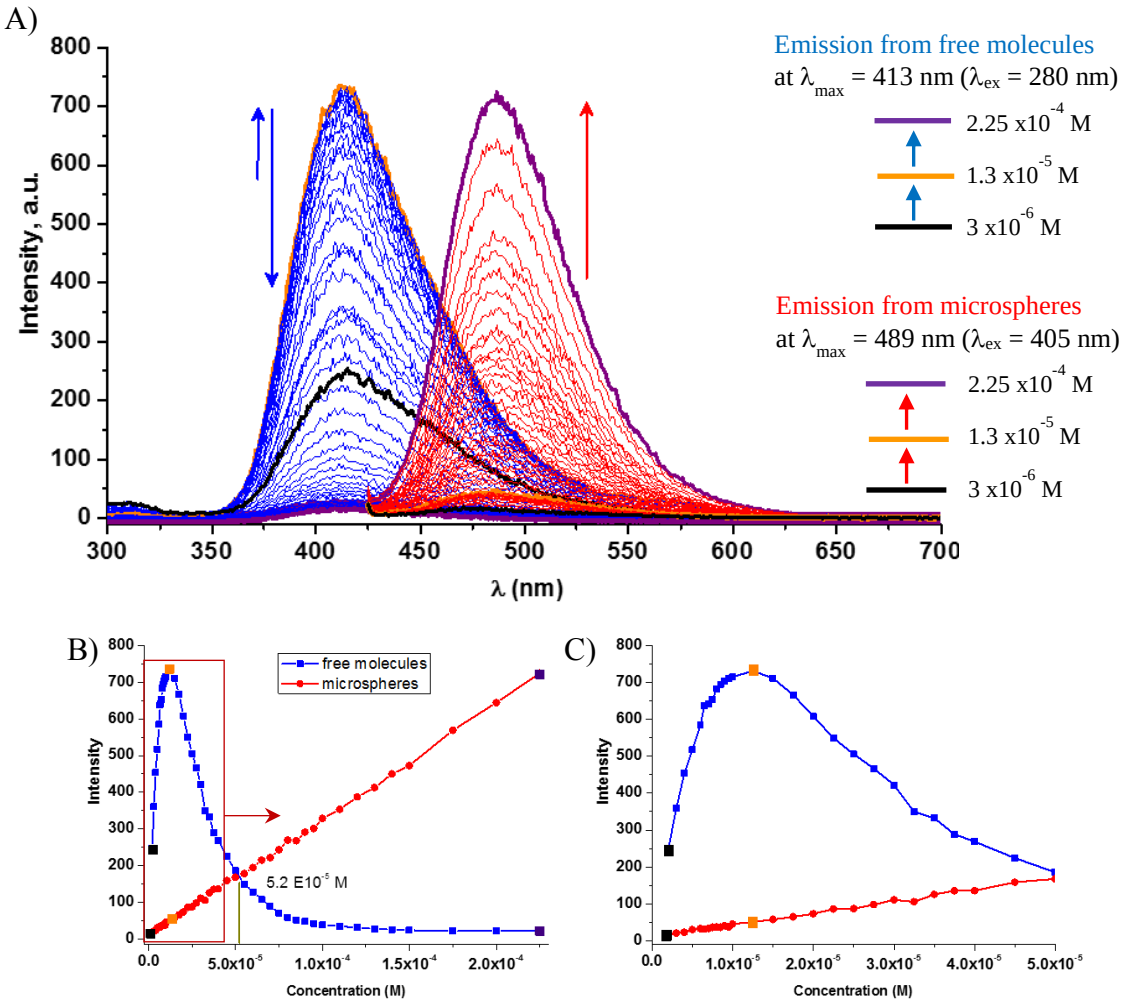

Figure 3.14: A) Fluorescence spectrum of the **89S** at different concentrations showing the emission from free molecules at λ_{max} = 413 nm (blue) and microspheres λ_{max} = 489 nm (red); B) fluorescence binding isotherms showing the variation in the emission intensities upon increasing the concentration; C) expanded fluorescence isotherm showing the absence or very less number of microspheres at lower concentration.

of microspheres. At lower concentration, below c = 1 × 10^{-5} M, the emission from the microspheres (λ_{max} = 489 nm) was not observed as there were none formed at this concentration (Figure 3.14 B and C, red). When increasing the concentration above 1.25 × 10^{-5} M, emission from the microspheres gradually increased because of aggregation. Beyond a concentration of 1.5 × 10^{-5} M, simultaneously, the emission from the free molecules decreased (413 nm band, blue) and the emission from microspheres (489 nm band, red) increased linearly. The decrease of the 413 nm band was indicative of the consumption of free molecules (diminishing species) through the dimerisation and the stacking of the monomers. While the increase of the 489 nm band was due to the formation of microspheres (growing species).

It was observed that the emission intensity of free molecules was intercepting with increasing emission intensity of microspheres at a point of approx. ~ 4.7 × 10^{-5} M concentration. Absorption and fluorescence excitation spectra of the solution of free molecules and the microspheres are provided in appendix A3.5.1. Repeating this experiment 4 times, gave similar results. As mentioned previously in Chapter 1, Section 2.5, dimerisation of the molecules was also confirmed by mass spectrometry analysis, where one of the precursor, **101R** with BTA core showed the peak for its dimerised molecule at 953.3391 for [M_2.Na] recorded at C = 2 × 10^{-5} M. Similar dimerised molecules were also observed from other precursors (Appendix A2.1.3). This dimerisation is an additional evidence supporting the decreasing of fluorescence intensity at higher concentration because of dimerisation later leading to the stacking and aggregation, finally forming microspheres.

3.6 Transfer of microspheres by static force of interactions in SEM

The microspheres sample preparation procedure involves the drying stage, wherein, the microspheres adhered strongly to the surface of the silica wafer. From SEM analysis, the microspheres appeared to be strong and robust. In order to examine whether these particles can be moved on the surface or can be transferred from one place to another, an attempt was made to pick up and transfer these microspheres using a micrometre sized needle. This experiment was performed in collaboration with Prof. John Boland (CRANN, Trinity College, Dublin) and Shaun Mills.

An experiment was conducted inside the SEM microscope with an additional setup, where a movable needle was used to pick up the microspheres (Figure 3.15A). The **89S** microspheres were placed inside the SEM as for the previous experiments and the needle was then placed on top of the sample as demonstrated in Figure 3.15, A and B. The needle

was operated from a unit outside the microscope to control its movements, such as forward, retract, up, down, *etc*. When the needle was placed very close to the sample (Figure 3.15C), the microspheres were instantaneously transferred from the surface of the silica wafer on to the tip of the needle as detailed in Figure 3.15D. This is most likely due to the static force of attraction between the microspheres and needle. In this case, it was observed that only the microspheres close to the tip of the needle were transferred on to the needle, and the others were undisturbed, demonstrating that the microspheres can be transferred and do not adhere

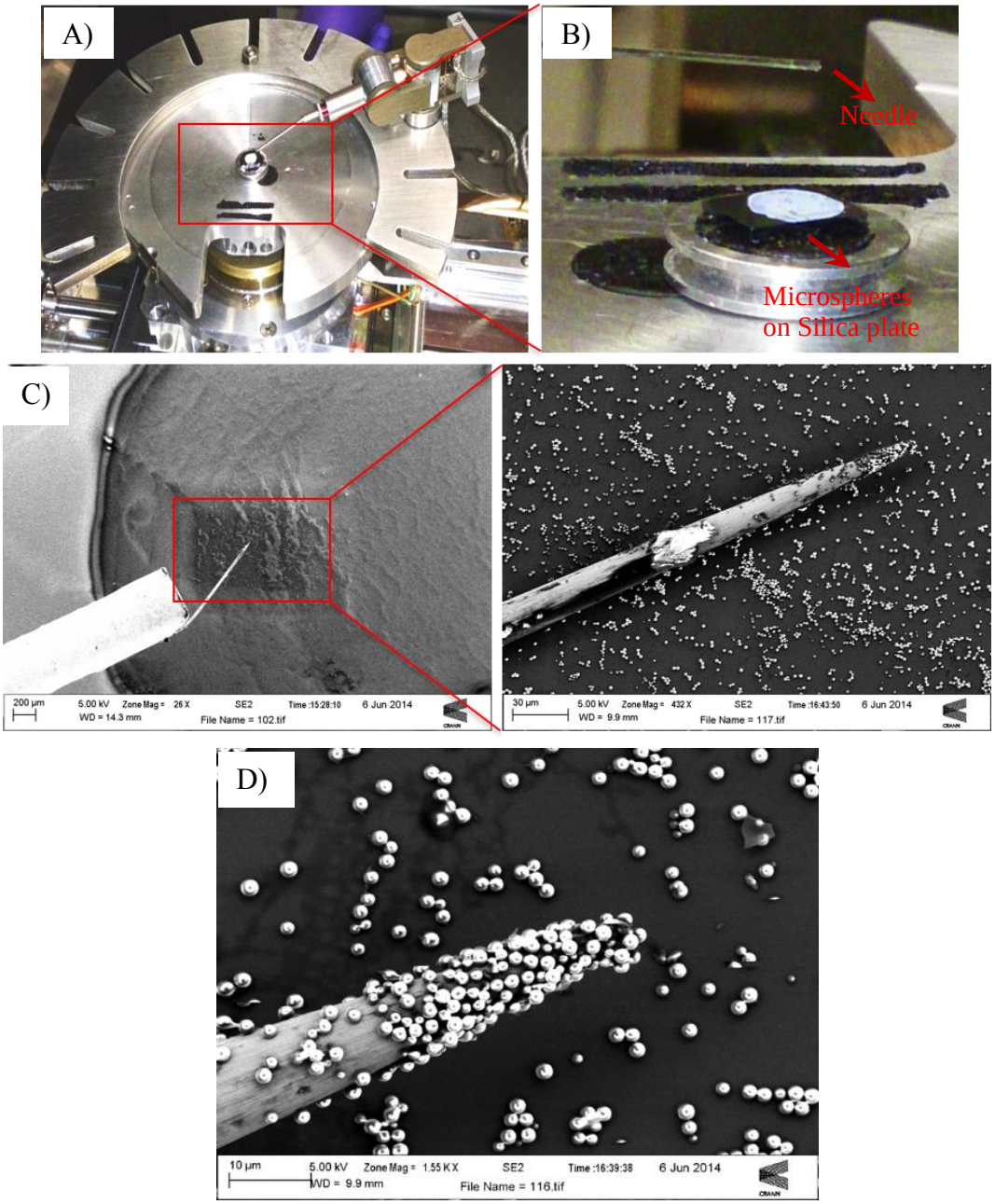

Figure 3.15: Experimental setup in SEM fitted with additional stage holding the movable needle and **89S** microspheres: A) top view; B) side view; C) needle before the contact with microspheres, scale bar 200 µm and 30 µm; D) microspheres on the tip of the needle, scale bar 10 µm.

to the surface (Figure 3.15D). It is important to point out that, from the images, the surface of the microspheres appears to have dots, however, this is only a visual artefact because of charging on the surface due to instrumentation.

3.7 Understanding the mechanism of the formation of microspheres

The mechanism of formation of the microspheres was investigated further upon addition of an external additive that prevents their formation. It was expected that the driving force for microsphere formation was intermolecular triple H-bonding though amide moieties in combination with π – π stacking and hydrophobic effects. In order to prove this, urea was chosen as an external additive, because it is used as a reagent to interact with amide moieties involved in H-bonding, such as in the denaturation of proteins[326-327] and the denaturation of J-aggregates (formed through intermolecular H-bonding between amide moieties)[328-329] *etc*. Additionally, urea has a simple and small molecular structure, with high specificity and affinity towards H-bonding sites, without disturbing any other interactions. It was anticipated that, when **89S** was dissolved in the presence of urea, the urea would interact with the amide moieties of **89S** by competitive intermolecular H-bonding, preventing intermolecular H-bonding between **89S** molecules, consequently preventing the formation of microspheres. Urea was chosen because it as a known competitive H-bonding agent and also used in biological samples as mentioned above.

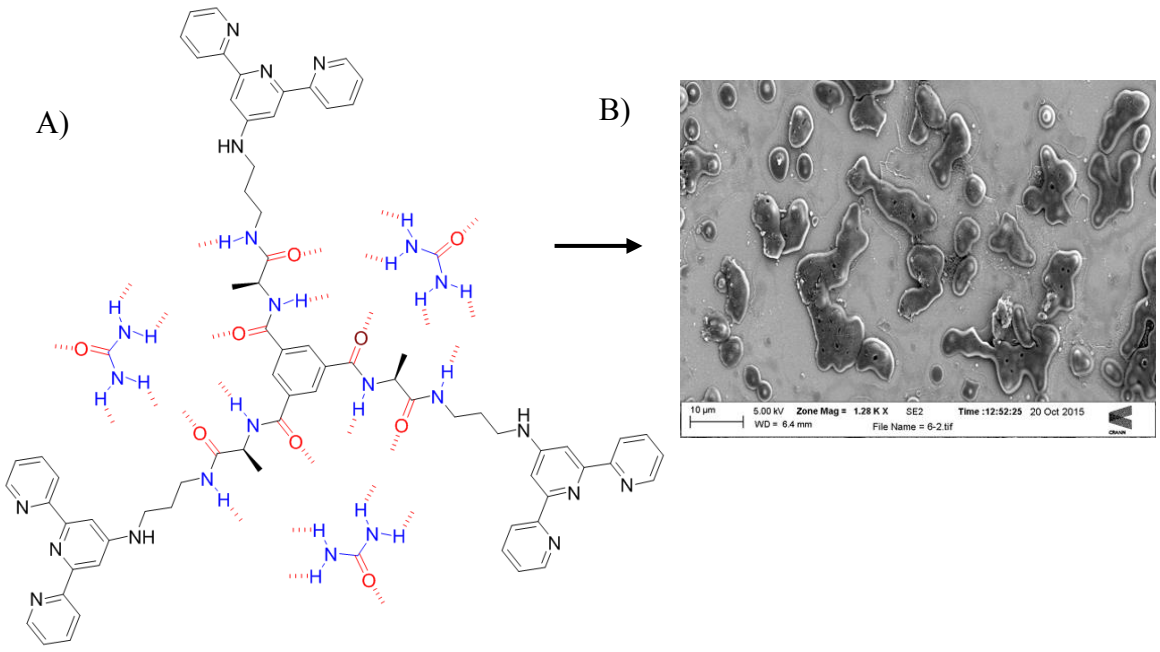

Figure 3.16: A) Representation of possible sites H-bonding interactions between urea and **89S**, resulting in the prevention of microspheres formation and B) SEM of the dropcased solution of urea bound **89S** showing the microspheres being not formed in presence of urea.

When the procedure for forming **89S** microspheres was followed in the presence of excess urea (10 equivalents with respect to **89S**) in CH_3CN/H_2O (6:4), no microspheres were observed (Figure 3.16B). This clearly indicates the inhibiting effect of urea on the formation of microspheres. This gives a strong indication that the intermolecular H-bonding interactions play an important role as the primary support for the microspheres formation. With the added urea, H-bonding to the amide units can occur before intermolecular H-bonding, resulting in the formation of adducts such as that shown in Figure 3.16A. This does not allow the formation of intermolecular H-bonding between **89S** molecules, which is crucial for the formation of microspheres. The other possible H-bonding interactions between **89S** and urea are shown in Appendix Figure A3.7.1.

3.7.1 Determination of "Critical urea concentration" for the prevention of microsphere formation

The 'critical urea concentration' to prevent the formation of microspheres in solution was determined in a similar manner to that described in Section 3.7. However, here the microspheres were prepared in the presence of gradually increasing urea concentration. The mixture of **89S** and urea ($1 \rightarrow 10$ equivalents) was dissolved in CH_3CN/H_2O (6:4) solvent mixture by heating. The effect of the gradual increase of the urea concentration on the formation of microspheres was then observed by dropcasting the solutions onto silica wafers and monitoring the morphology of the resulting samples using SEM.

Initially, 1, 2 and 3 equivalents of urea were used in the mixture of **89S** (c = 2 mg/ml, 1.55×10^{-6} moles) and urea in CH_3CN/H_2O (6:4, 1 ml) solution. This low concentration of urea used in the mixture did not show any effect on microsphere formation nor their morphology (Figure 3.17 A-C). However, when 4 – 5 equivalents of urea were used in the mixture, only deformed microspheres were observed (shown in Figure 3.17, D and E). Upon further increasing the amount of urea to 6 equivalents, the formation of microspheres was not observed at all, a clear indication that the urea prevented the formation of the microspheres as shown in Figure 3.17F.

This study suggested that the triple H-bonding between these ligands was found as the primary support for the formation of microspheres in solution. The 'critical concentration' of urea that prevents the formation of microspheres was found to be 6 - 7 equivalents; possibly as of this number could potentially break the intermolecular H-bonding between 6 amide groups (H-bonding sites) of neighbouring **89S** molecules.

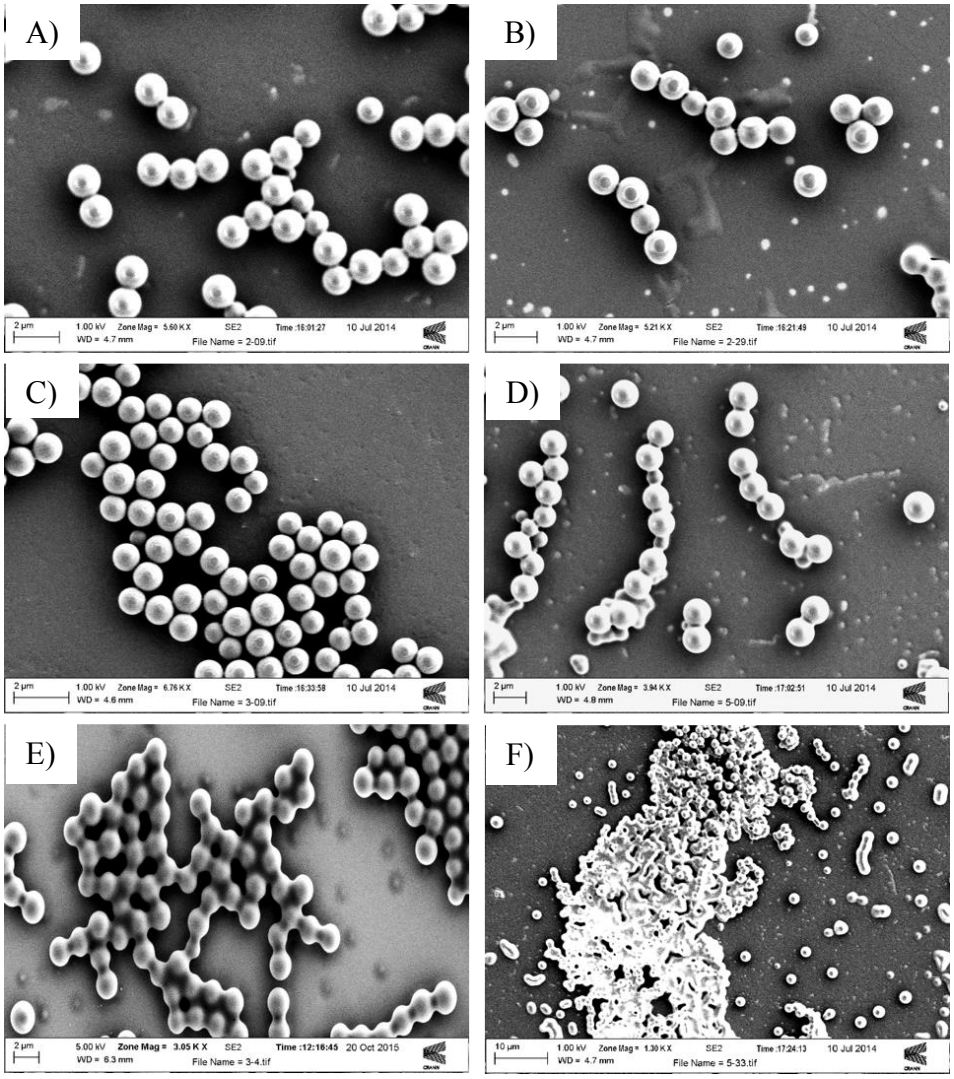

Figure 3.17: SEM images of the **89S** microspheres with increasing concentration of urea added prior to the formation of microspheres: A) 1 mole equiv., (B) 2 mole equiv., (C) 3 mole equiv. of urea showing no effect of urea on the microspheres formation, (D) 4 mole equiv. (E) 5 mole equiv., scale bar 2μm and (F) 6 mole equiv., scale bar 10 μm, showing disturbance of microsphere formation in presence of urea.

Following this study, 6 mole equivalents of urea were then added to the solution of preformed **89S** microspheres to investigate the disassembly of the microspheres over a period of time. This will be discussed in the next section.

3.7.2 Time dependent degradation of microspheres using urea

To a solution of preformed microspheres of **89S** (c = 2 mg/ml, 1.55 × 10^{-6} moles) in CH_3CN/H_2O (6:4, 1 ml), 6 mole equivalents of urea (0.56 mg, 9.3 × 10^{-6} moles) was added and the resulting mixture was stirred at RT. This solution was dropcasted onto silica wafers at 30 min time intervals and imaged using SEM to monitor the degradation process of the microspheres. From the SEM images, it was observed that, the microspheres were intact and

did not show any noticeable effect of the presence of urea for up to 3 hrs (Figure 3.18A). Upon increased exposure to urea in solution, a slow disintegration of the microspheres was observed after 4 hrs, and this continued to increase with time (Figure 3.18B). After 6 hrs, most of the microspheres had disintegrated, as shown in Figure 3.18C.

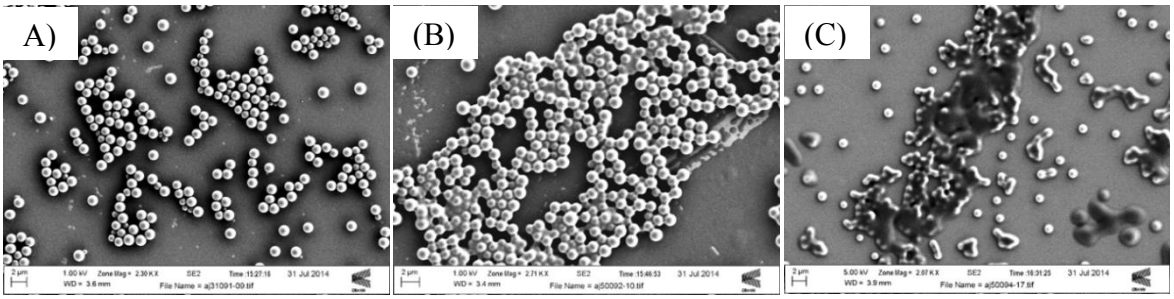

Figure 3.18: SEM images representing time dependent decomposition of the **89S** microspheres after urea addition: (A) 3hrs, (B) 4 hrs, (6) 6 hrs. Scale bar 2μm.

On considering the previous results discussed in this section (3.7 and 3.7.1), it can be concluded that added urea competes with the intermolecular H-bonding within **89S** microspheres and, as a result, a slow degradation of the microspheres occurs. It was also observed that, upon performing this experiment at higher concentrations of urea, the microspheres were found to disassemble more quickly, demonstrating the effect of the urea concentration. When 10, 15 and 18 mole equivalents of urea were added to solutions of **89S** microspheres, the microspheres were fully degraded after 4, 3 and 2.5 hrs respectively, as shown in the SEM images in Appendices Figure A3.7.2.

These experiments were repeated 3 - 4 times, and the same results were obtained on each occasion, demonstrating that 6 – 7 equivalents of urea prevent the formation of microspheres (when taken in the solution before the microspheres were formed) as observed in section 3.7.1. Upon addition of urea to a solution of preformed microspheres, the microspheres were found to disassemble after 5 – 6 hours, as seen in section 3.7.2. As expected, similar studies performed using **89R** also showed similar results. The disintegration of microspheres with urea was also studied using optical microscopy, the results of which will be discussed in Chapter 4. On comparing these results with the urea mediated disassembly process of J-aggregates (formed by H-bonding between amide moieties leading to vesicles formation) by Ghosh *et al.*,[328-329] **89S** microspheres also showed urea mediated disassembly process.

3.8 Interaction of microspheres with lanthanides: formation of microspheres chain and network

Since these microspheres are made from tripodal molecules comprising tpy moieties which are known ligands for metal ions, the interaction of the microspheres with lanthanides and transition metals were studied in solution. The lanthanide metal salts chosen for the investigation were $Ln(CF_3SO_3)_3$ (Ln = Eu(III) or Tb(III)), as they have been studied to form luminescent red and green light emitting particles. The transition metal salts chosen were $FeCl_2$ and $ZnCl_2$. After addition of these metal salts to the solution of preformed microspheres, the resulting particles formed in solution were dropcast (5 μL) on silica wafers and imaged using SEM.

3.8.1 Interactions with Lanthanides

Upon addition of $Ln(CF_3SO_3)_3$ (Ln = Eu(III) or Tb(III), 1 mole equiv.) to the solution of preformed microspheres of **89S** (c = 0.4% in 6:4 CH_3CN/H_2O), the microspheres were found to be connected to each other and arranged in linear chains, as depicted in the schematic representation shown in Figure 3.19A. This effect was most likely due to the coordination occurring between the Ln(III) ions and the tpy units exposed on the surface of the

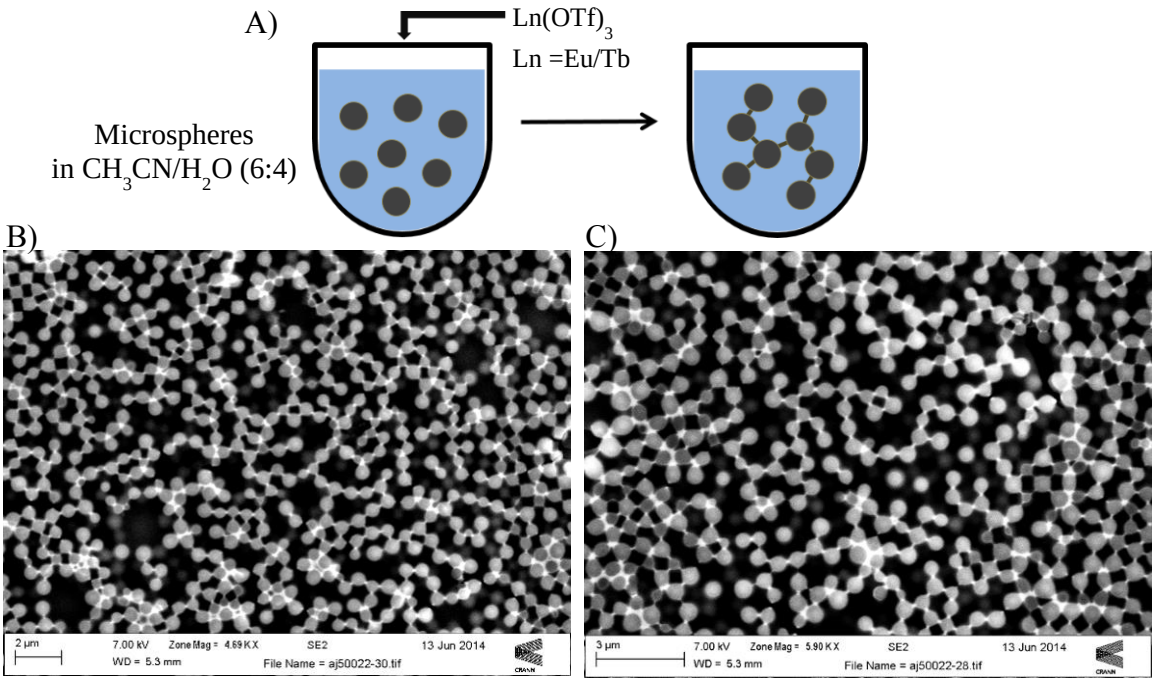

Figure 3.19: A) Schematic representation of the microspheres chain formation on addition of $Ln(CF_3SO_3)_3$ to **89S** microsphere solution. SEM images of the microsphere chains formed on addition of B) $Eu(CF_3SO_3)_3$, scale bar 2 μm and C) $Tb(CF_3SO_3)_3$, scale bar 3μm. These results were reproduced several times (4 – 5) in order to make sure of the reproducibility of the data.

microspheres which connects the microspheres by making the bridges between them resulting in the formation of elongated chains (Figure 3.19 B and C).

Closer examination of the images reveals that addition of Ln(III) ions to the solution of microspheres of low concentration (**89S**, 1 mg/ml), results in the particle forming simple short chains (Figure 3.20A). On the other hand, when a solution of higher concentration was used (**89S**, >2 mg/ml), an extended network of microspheres was observed in which all the particles are interconnected to each other (Figure 3.20B), indicating the effect of the concentration of microspheres on the morphologies formed. In some parts of the sample, ordered arrangement of the microspheres into grid-like structures was observed. (Figure 3.20C).

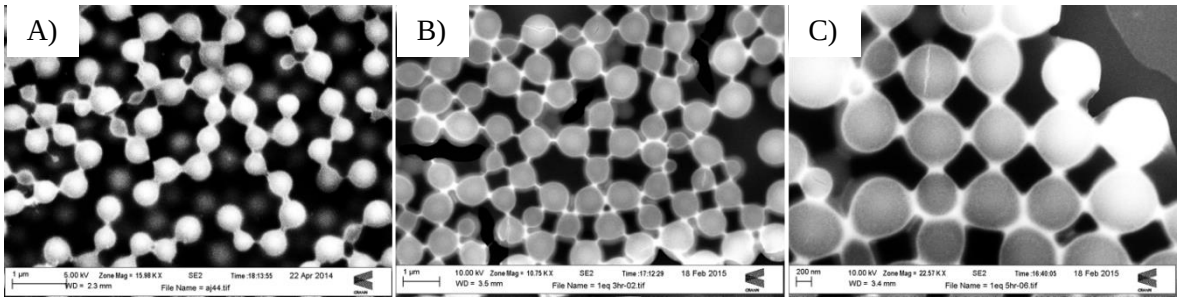

Figure 3.20: A) SEM image of linear chains of **89S** microspheres on addition of $Eu(CF_3SO_3)_3$, scale bar 1μm; B) extended network of microspheres at higher concentration formed through interconnection of microspheres, scale bar 1μm and C) magnified images of the network showing the ordered arrangement of microspheres in a grid manner. See Appendix Figure A3.8.1, A and B for **89S** microspheres chains and networks formed upon interaction with $Tb(CF_3SO_3)_3$.

Moreover, by adding different amounts of $Eu(CF_3SO_3)_3$ (0.5 → 1.0 mole equivalents) to the solutions of preformed microspheres, it was found that a minimum of 0.7 equivalents of $Eu(CF_3SO_3)_3$ was necessary to make the connection between the particles for the formation of chains and networks, as lesser equivalents of $Eu(CF_3SO_3)_3$ did not show any changes and the microspheres remained as individual particles in solution. Similar chains and networks of microspheres were observed upon addition of $Tb(CF_3SO_3)_3$ to **89S** microsphere solution (Figure 3.19C). Furthermore, the use of **89R** microspheres also showed formation of interconnected microspheres upon addition of Eu(III) and Tb(III) ions to a solution of **89R** microspheres. The SEM images of the interconnected **89R** microspheres are provided in Appendix 3.8.1, C and D. Leaving these microsphere chains in solution for up to 6 hours did not show much change in the morphology. Furhermore, addition of NaCl and KCl did not show any effect on the morphology of the microspheres.

All SEM samples of the Ln(III)-based microsphere chains discussed above were covered with a thin film on their surface. Therefore, the SEM imaging of these samples were performed in presence of that film using an electron beam current of higher voltage ~10 kV in SEM instrument, in order to gain the information about the morphology beneath the film and, in all the samples, connections between the particles were observed. This film was formed upon addition of Ln(III) salts (only) to the solution of microspheres and was not observed in absence of Ln(III) salts or when transition metal salts were added to the microsphere solution even after leaving several hours.

3.8.2 Effect of different counter ions on the formation of microsphere chains and networks

In order to examine the effect of different counter ions and the time required to make the bridging between the particles, lanthanide salts with different anions ($CF_3SO_3^-$, Cl^-, NO_3^- and ClO_4^-) were added to the solutions of the **89S** microspheres and incubated for different time intervals, as summarised in Table 3.4.

Analysis of the above solutions using SEM showed that samples imaged 30 minutes after Ln(III) salt addition did not show the formation of chains or networks. However, after longer mixing times, approximately 1 to 2 hrs, the formation of bridges between the microspheres occurred. The microsphere chains were found to be stable in the solutions for longer than 2 hrs. In the case of $Eu(CH_3COO)_3$, $EuCl_3$ and $Eu(NO_3)_3$ the bridges between the microspheres were generally found to be wider and showed similar patterns of linkages

Table 3.4: Addition of different Ln salts (Ln = Eu and Tb) and incubation time.

Ln salt	Incubation time after addition of Ln salts		
	30 min	1 hr	2 hrs and longer
$Eu(CF_3SO_3)_3$	No connection	Chains and networks	Chains and networks
$Eu(CH_3COO)_3$	No connection	Chains and networks	Chains and networks
$EuCl_3$	No connection	Chains	Chains
$Eu(NO_3)_3$	No connection	Chains	Chains
$Eu(ClO_4)_3$	No connection	Networks	Networks
$Tb(CF_3SO_3)_3$	No connection	Chains and networks	Chains and networks
$Tb(CH_3COO)_3$	No connection	Chains and networks	Chains and networks
$TbCl_3$	No connection	Chains	Chains
$Tb(ClO_4)_3$	No connection	Networks	Networks

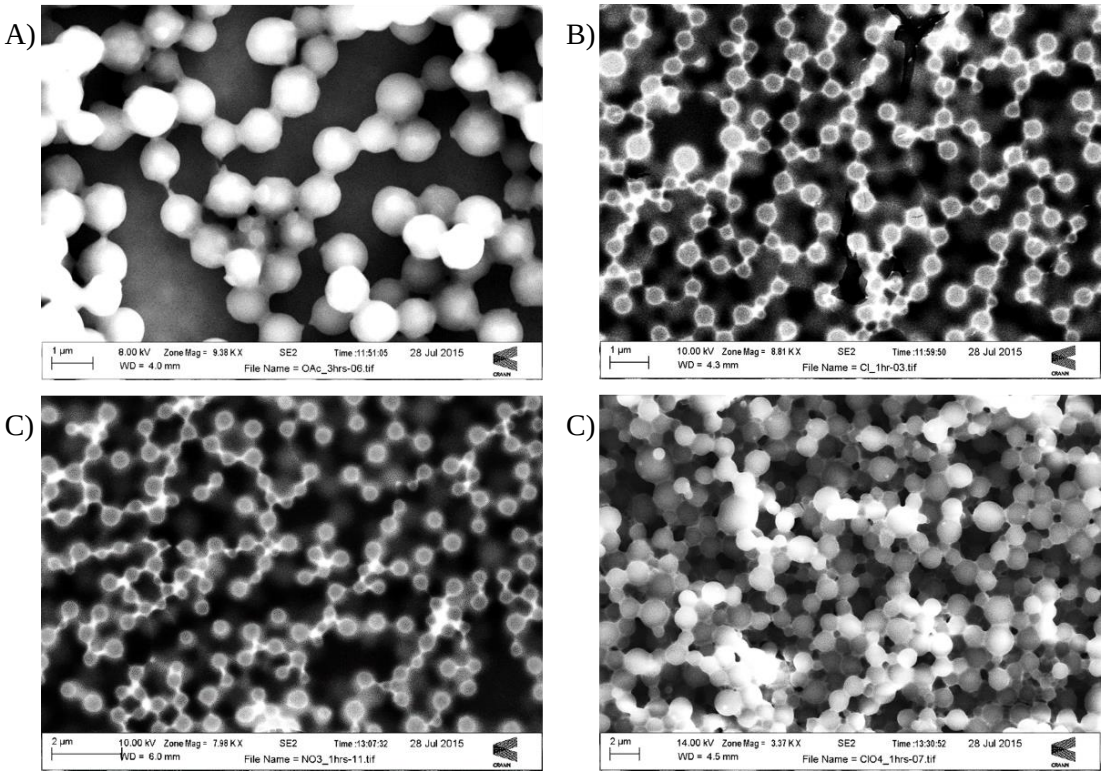

Figure 3.21: SEM images of the **89S** microspheres chains formed on addition of different Eu(III) salts. A) $Eu(CH_3COO)_3$, scale bar 1µm, B) $EuCl_3$, scale bar 1µm, C) $Eu(NO_3)_3$, scale bar 2µm, D) $Eu(ClO_4)_3$, scale bar 2µm.

between the microspheres, indicating that these three Ln(III) salts act similarly in making the connections between particles. In the case of $Eu(ClO_4)_3$ the microspheres were fused together without distinctive connections between them, in contrast to the other Ln salts studied as shown in Figure 3.21. As expected, similar observations were made in the case of the Tb(III) salts. SEM images obtained using Tb(III) salts are provided in the Appendix (Figure A3.8.1 and A3.8.2).

Similarly, the interaction of the microspheres with transition metal ions was studied by adding $FeCl_2$ and $ZnCl_2$ to the solution of the **89S** microspheres, followed by imaging of the resulting samples at different time periods using SEM. The results of that investigation are as summarised in Table 3.5.

SEM analysis of these solutions after addition of Fe(II) to the microspheres of **89S** did not show any changes in the microsphere morphology, although the tpy moiety has high affinity for Fe(II). Formation of chains was not observed and the microspheres were found to remain as individual particles. However in the case of Zn(II), decomposition of the microspheres occurs after the addition of the $ZnCl_2$. This was unexpected, because this result was contradictory to that observation made by J. H. Jung *et al.*, where they showed a change

Table 3.5: Addition of transition metals to the solution containing **89S** microspheres.

Transition metal salt	Incubation time after addition of metal addition		
	1hr	2 hr	3 hrs
$FeCl_2$	No chains, individual particles	No chains	No chains
$ZnCl_2$	No chains, decomposition of microspheres	Decomposition of microspheres	---

in the morphology of linear fibres to aggregated particles (approx.100 nm size) upon addition of Zn(II) to the solution of tripodal molecule **86**.[330] This confirms the different self-assembly nature of the tripodal molecules **89** (R and S) in comparison to the self-assembly properties of other related tripodal systems such as **86** reported in literature. SEM images of the Fe(II) and Zn(II) systems are provided in appendix Figure A3.8.3.

This can be compared this the previously reported work from our group, wherein addition of Eu(III) to the gel of **86**, results in the crosslinking of supramoleculer fibres forming higher ordered assemblies.[281] Analogous to this, microspheres from **89** (R and S) formed the crosslinked structures discussed above. As a summary to the work described in this section, microspheres of **89** (R and S) interact with Ln(III) metal ions to form microsphere chains and networks through coordination interactions. However, the same effect was not observed when transition metal ions were used. Furthermore, the microspheres formed from **89** (R and S) were found to be distinct when compared to the aggregates formed by another structurally similar molecule **86**.[330] More importantly, the morphologies showed here are the first examples of the formation of the chains and networks formed from micropsheres in the presence of Ln(III) ions.

3.8.3 Spectrophotometric studies of lanthanide based microsphere chains

Spectrophotometric investigations were carried out on Eu(III) and Tb(III) microsphere chains of **89S** in CH_3CN/H_2O (6:4) solution. When exciting the Eu(III)-based **89S** microsphere chains in the solution of CH_3CN/H_2O (6:4) with λ_{ex} = 380 nm, the characteristic Eu(III) emission bands were observed with transition peaks centred at 580, 595, 617, 652 and 697 nm and the most intense band at 617 nm, corresponding to $^5D_0 \rightarrow {}^7F_J$ transitions (J = 0 - 4) (Figure 3.22B, Red). This emission was stable even after 1 hr without any decrease in intensity (Figure 3.22B, black, merged with red). This emission occurred due to sensitisation of the Eu(III) excited state by the tpy moieties, thus providing evidence of surface binding, and suggesting the formation of Eu(III) bridges between the microspheres.

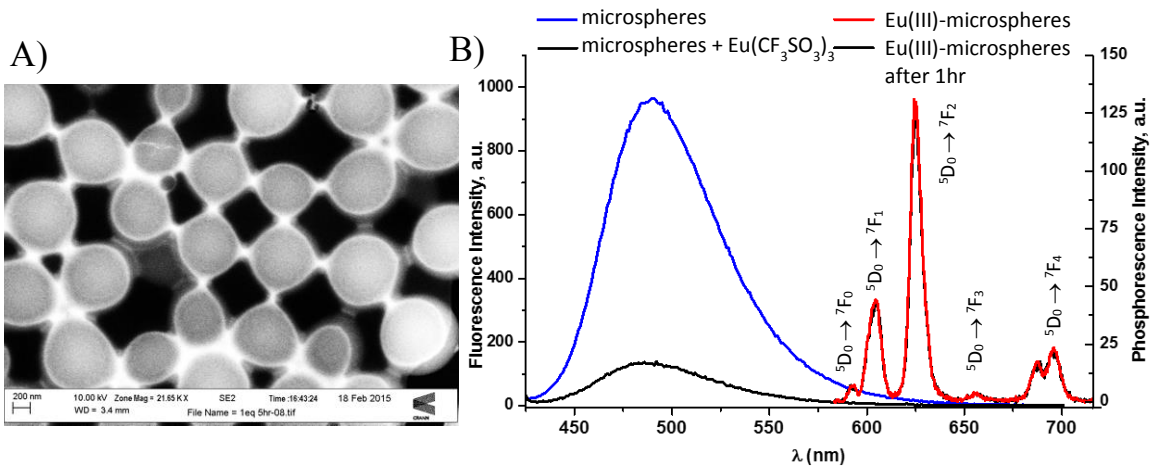

Figure 3.22: A) SEM image (magnified) of Eu(III) based **89S** microsphere chains showing the connections, scale bar 200 nm: B) fluorescence emission from microspheres (λ_{ex} = 405 nm), before (blue) and after (black) the addition of $Eu(CF_3SO_3)_3$ and B) Eu(III) emission from Eu(III)-bound microsphere chains (λ_{ex} = 380 nm, Red)

In addition to this, the fluorescence of the microspheres was significantly quenched after the addition of $Eu(CF_3SO_3)_3$ to the solution of the microspheres (Figure 3.22B, blue and black at λ_{max} = 489 nm). This is the result of energy transfer from the microspheres to the Eu(III) ions. Moreover, sensitisation of Eu(III) from the microspheres was confirmed by exciting the Eu(III) ions alone, in absence of microspheres, resulting in no emission from Eu(III) (excitation spectra (λ_{em} = 617 nm) and Eu(III)-**89S** chain emission spectra taken at different excitation wavelength are shown in Appendix Figure A3.8.4).

Kinetic measurements of the Eu(III) emission was also conducted for the above Eu(III) based microsphere chains with a time interval of 30 minutes. When monitoring the Eu(III)-centred emission over 12 hours, it was found to be stable without showing any decrease in the Eu(III)-centred emission (Figure 3.23). This confirms that a strong

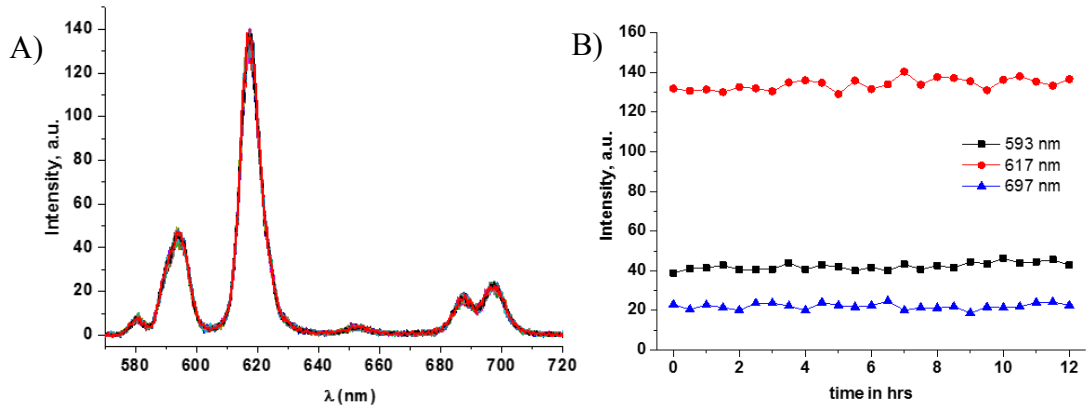

Figure 3.23: Kinetic stability of Eu(III) emission from the Eu(III) based **89S** microsphere chains over a period of 12 hrs at time intervals of 30 minutes: A) Eu(III) emission spectrum over 12 hrs of measurement (λ_{ex} = 380 nm); B) changes in the Eu(III) emission as a function of time.

interaction between the microspheres and Eu(III) ions exists, resulting in stable bridging between the microspheres. In comparison, the Eu(III) emission observed from Eu(III)-**89S** microsphere chains was analogous to that previously reported from our group, wherein the gels formed by **86** in presence of Eu(III) were found to be luminescent due to the coordination of Eu(III) to tpy unites of **86**,[281] supporting the coordination of Eu(III) to tpy moieties on microspheres.

In the case of the Tb(III)-based **89S** microsphere chains, similar observations were made. Excitation of the solution of Tb(III)-**89S** microspheres chains at λ_{ex} = 382 nm resulted in the characteristic Tb(III) emission from $^5D_4 \rightarrow {}^7F_J$ (J = 6 - 3) transitions, giving rise to emission bands at 493, 543, 584 and 621 nm, with the 543 nm transition band being the most intense (Figure 3.24B, green). The fluorescence from the microspheres (λ_{em} = 489 nm, Figure 3.24B, blue) was also shown to be quenched upon addition of $Tb(CF_3SO_3)_3$ (Figure 3.24B, black), confirming the energy transfer from the tpy antenna of the microspheres to Tb(III) resulting in its luminescence, thus exhibiting the antenna effect. Sensitisation of the Tb(III) excited state from the microspheres was confirmed by exciting the Tb(III) ions alone in the absence of microspheres, where very poor Tb(III) emission was observed (see Appendix Figure A3.8.5).

Kinetic measurements of the Tb(III) emission from Tb(III)-based **89S** microsphere chains were conducted over 10 hrs with time intervals of 20 minutes with no decrease in the emission intensities being observed, confirming the stability of the crosslinked microspheres through Tb(III) ions (Figure 3.25).

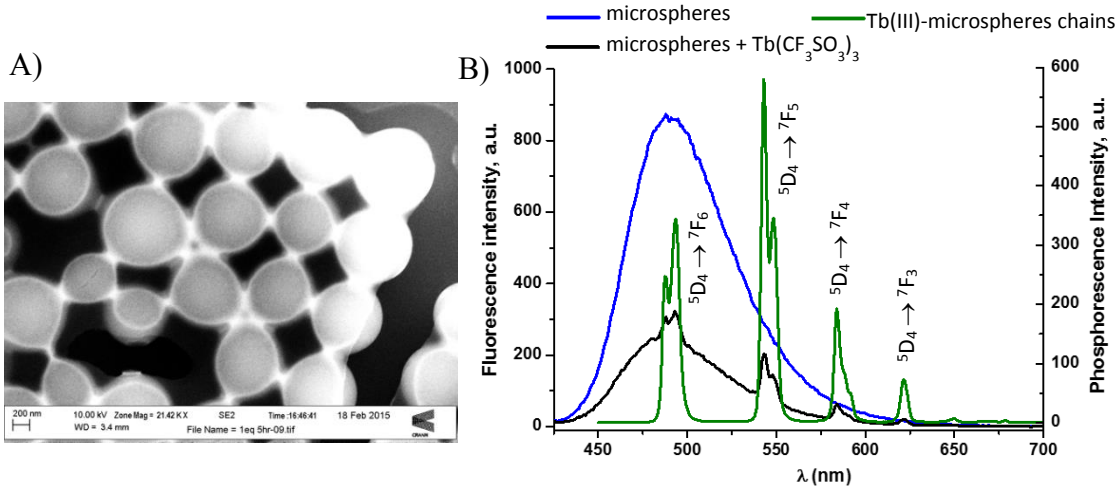

Figure 3.24: A) SEM image (magnified) of Tb (III) based **89S** microsphere chains showing the connections, scale bar 200μm; B) Fluorescence emission from microspheres (λ_{ex} = 405 nm), before (blue) and after (black) addition of Tb $(CF_3SO_3)_3$ and Tb(III)-centred emission from Tb(III)-bound microspheres chain (λ_{ex} = 382 nm) (green).

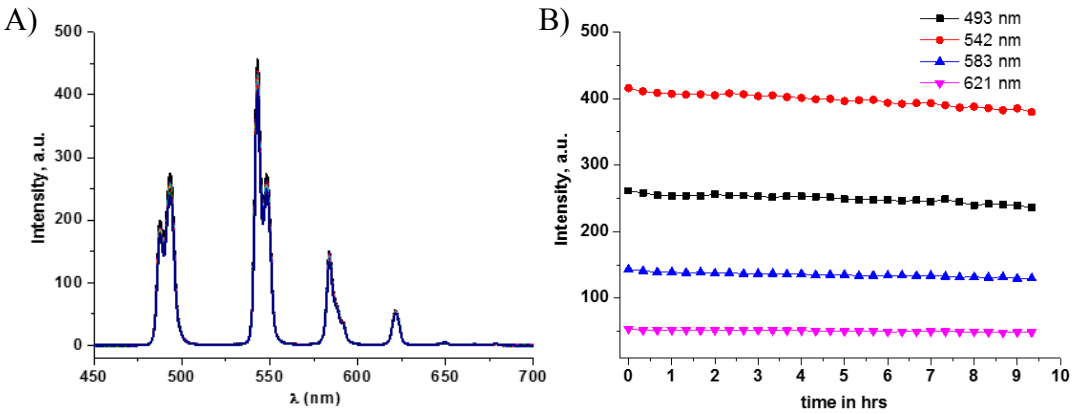

Figure 3.25: Kinetic stability of Tb(III) emission from the Tb(III)-based **89S** microspheres chains over a period of 10 hrs with time interval of 20 minutes: A) overlaid Tb(III) emission spectra over 10 hrs of measurement (λ_{ex} = 382 nm); B) changes in the Tb(III) emission as a function of time.

As a Summary to the results discussed in this section, Ln(III)-based **89S** microspheres sensitised the emission of Ln(III) ions via tpy moieties on the microspheres. This provided strong evidence for the binding of Ln(III) ions onto the tpy moieties on the microspheres, which in turn, suggests the formation of bridges between the microspheres, eventually resulting in their crosslinking.

3.8.4 Energy dispersive X-ray (EDX) analysis of microsphere chains

In order to gain more evidence on the crosslinking of microspheres through the coordination of Ln(III) to tpy moieties on the microsphere surface, the Ln(III)-based microsphere chain samples were analysed using Energy Dispersive X-ray (EDX) spectroscopy to investigate the presence of Ln(III) metals on the surface of the microspheres. In this technique, the combination of SEM and X-ray fluorescence spectrometry (XRF) was utilised to analyse the sample using an electron beam. When a sample is scanned using an electron beam, an electron image is developed from the secondary electrons or the back scattered electrons, and qualitative analysis of the sample is obtained by collecting the X-rays emitted from the electron–specimen interaction. This non-destructive X-ray microanalysis and imaging was performed on the solid sample in 2 modes, *1*) line scan and *2*) mapping modes. Line scan mode was suitable for scanning the Ln(III)-based microsphere chain sample, which prescisely performed the qualitative analysis along the line of interest as depicted in Figure 3.26A. While using mapping mode, the qualitative analysis performed provided information on the elemental distribution on the sample surface. The microsphere chains and networks formed upon addition of Ln(III) salts, were dropcasted on silica wafers (5 μL) and analysed by EDX technique using SEM.

EDX analysis was performed on the Eu(III)-based **89S** microsphere chains in line scan mode by scanning the sample with an electron beam of 20kV (Figure 3.26A). Upon collecting the X-rays emitted from the surface of the sample along the line of interest, the elemental composition of that specific location was obtained which indicated the presence of Eu(III). The X-ray fluorescence spectrum showed a peak for the Eu(III) at 5.84 (Lα) keV and 1.13 (Mα) keV responsible for the X-rays emitted from the L and M shell of the Eu(III) (Figure 3.26C). Similar analysis was performed on the Eu(III)-based coordination polymer core-shell micro-structures,[249] which support the detection of Eu(III) on the surface of **89S** microsphere chains.

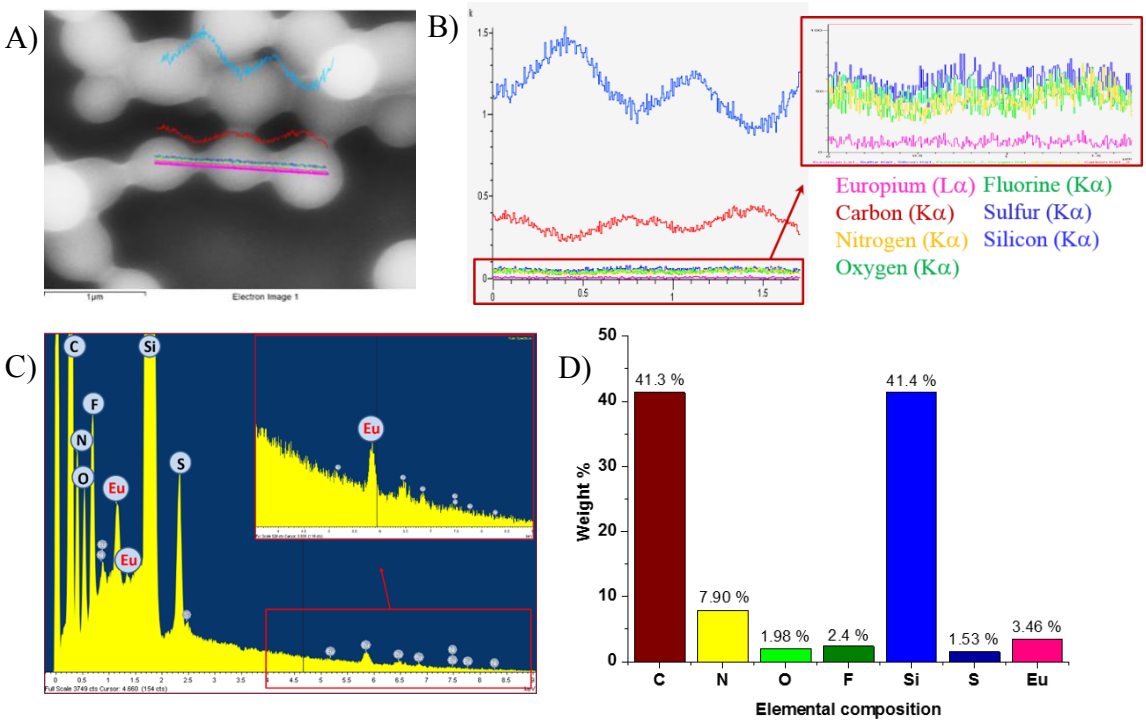

Figure 3.26: A) Eu(III)-based **89S** microsphere chains; B) line scan results showing the composition of microspheres; C) EDX spectrum of the same microspheres and D) weight percentage of each element on the line of interest on the surface of the sample.

Elemental composition indicated 3.46 % of Eu(III) to be present on the sample surface. The detection of Eu(III) on the surface of the sample confirmed the binding of Eu(III) to the tpy moieties on the microsphere surface,[249, 331] and that Eu(III) was most likely responsible for bridging the particles. When repeating this analysis using different modes of scanning, the results obtained were found to be reproducible. Mapping analysis carried out on this sample by scanning the whole sample area is provided in appendix Figure A3.8.6.

Similarly, EDX analysis on the Tb(III) based **89S** microsphere chains was done by scanning the sample with 20kV in mapping mode. An electron image was generated (Figure

3.27A). The X-ray fluorescence spectrum obtained by collecting the X-rays from the surface of sample in the site of interest showed a peak for Tb(III) at 6.27 keV (Lα) and 1.24 keV (Mα), for the X-rays emitting from the L and M shell of Tb(III) respectively. This confirms the presence of Tb(III) bound to tpy units on the surface of the sample. Results of line scanning analysis done on this system gave similar results, and are provided in Appendix, Figure A3.8.7.

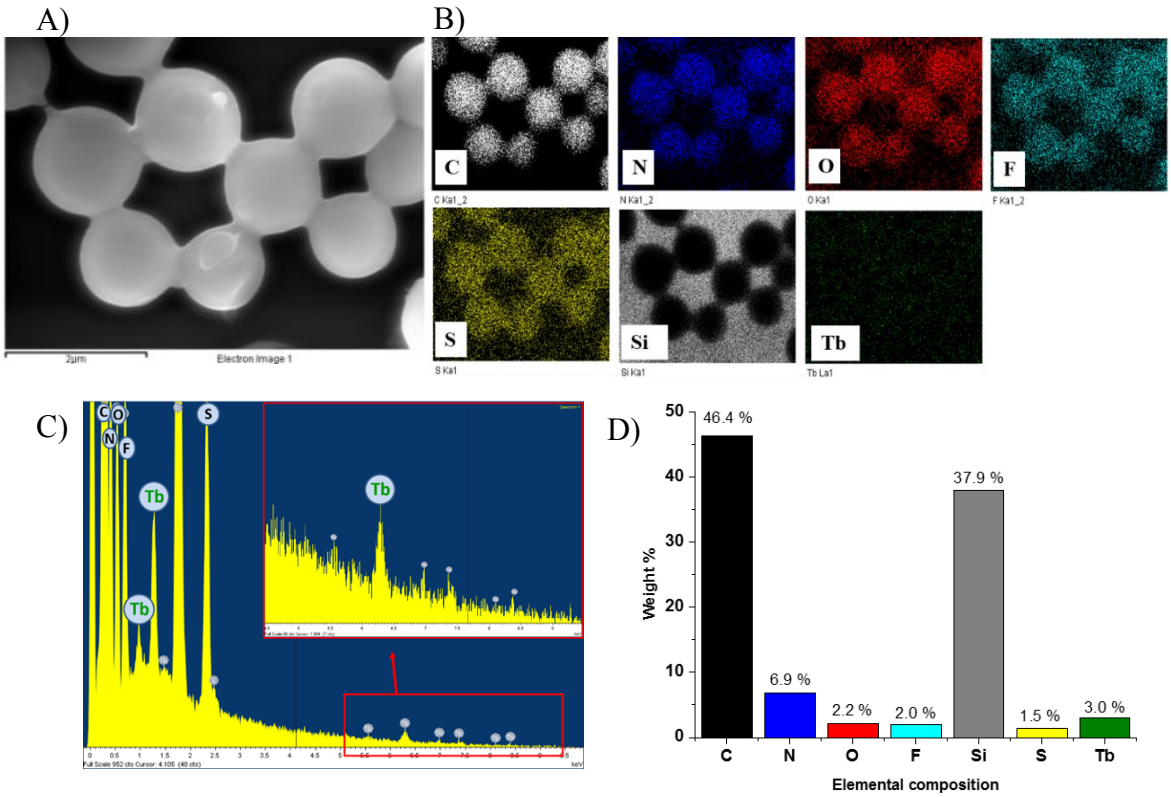

Figure 3.27: A) Tb(III)-based **89S** microsphere chains; B) mapping results showing the composition of the microspheres; C) EDX spectrum of the same microspheres and D) weight percentage of each element on the site of interest on the surface of the sample.

As conclusion to this section, the EDX analysis performed on Ln(III)-based microspheres chain samples showed the presence of Eu(III) and Tb(III) on the surface of microspheres chain confirming its coordination onto tpy moiety of microspheres, which suggests the crosslinking of the microspheres through coordination of Ln(III) ions.

3.9 Focused Ion Beam (FIB) microscopy of microspheres

Having investigated the microspheres using SEM, HIB and EDX techniques, the microspheres appeared to be strong and robust. Hence, in order to investigate the internal structure of the particles, (*i.e.* to see whether the particles are solid or hollow) the

microspheres were analysed using a TEM and Focused Ion Beam (FIB) microscope (in which the microspheres were cut and imaged).

The internal structure of the microspheres was first investigated using TEM analysis in order to reveal whether they are hollow or solid inside. The microspheres of **89S** – **91S** (c = 0.4% w/v) prepared in solution were deposited on carbon coated copper grids and imaged using TEM. TEM images obtained for **89S** microspheres showed the spherical structure of the particles with a size distribution of approx. 0.6 - 1 μm (Figure 3.28A). Since the particles were approximately 1 μm in size, transmission of the electron beam through the sample could not be achieved. TEM images showed only the dark circles of the microspheres indicating the particles are too large for TEM analysis. Hence, any information about the internal structure of the microspheres was not acquired. TEM images taken of the microspheres made from the **90S** and **91S** showed similar results. See Appendix Figure A3.9.1 for TEM images of **90S** and **91S** microspheres. Therefore, an alternative technique such as FIB was used to analyse these microspheres.

Focused ion beam (FIB) is a technique which operates similarly to SEM. However, in the case of FIB, an ion beam is used in place of the electron beam to scan the sample in a raster pattern. Modern FIB instruments comes along with the additional SEM set up so that the system can become a hybrid FIB-SEM instrument for imaging, material removal or deposition in the nanometre to hundreds of micron scale range. FIB uses a finely focussed beam of Gallium ions (Ga^+) instead of the electron beam used in SEM. Depending on the application, FIB uses a different ion beam strength to analyse the sample. At lower beam currents, the ion beam interacts with the sample surface by inelastic interactions resulting in the ionisation and emission of electrons called ion induced secondary electrons (ISEs). These ISEs emitted from the sample surface are collected by the detectors to generate an image. At higher beam currents, the ion beam interacts by elastic scattering. Generally in this case FIB is operated with a beam current of 5 – 30 keV. During this operation, the ion beam collides with the sample surface in the focussed area of interest, where the ion energy is transferred to the target atoms resulting in the displacement of atoms from their initial sites. This displaced primary atom, further displaces a series of atoms generating a volume of atoms of high kinetic energy, finally displacing from the sample surface resulting in the emission of atoms (sputtering). Because of this sputtering action caused by the ion beam, the FIB can be used to locally to remove or mill (controlled damage) the material precisely without affecting the other parts of the sample.[332]

89S microspheres (c = 0.4% w/v) were deposited on silica wafers and were investigated using the SEM-FIB microscope. Analysis of a single microsphere using FIB was conducted and only that microsphere was bombarded with highly focused Ga^+ ions of 30kV strength for 20 minutes to undergo milling (cut/sputtering). During the milling process, because of the continuous bombardment with Ga^+ ions of high beam current, the sample was forced to lose atoms resulting in damage of the focussed area (removal of material). Once the milling process is finished, the sample was imaged in the SEM and it was found to be cut precisely only in the selected area and revealed the microsphere to be a solid particle (Figure 3.28B). Furthermore, the same milling process was used to cut a large number of microspheres with uniform size distribution by selecting a larger area of the same sample. It can be clearly seen that all of the microspheres formed from **89S** were solid particles (Figure 3.28C).

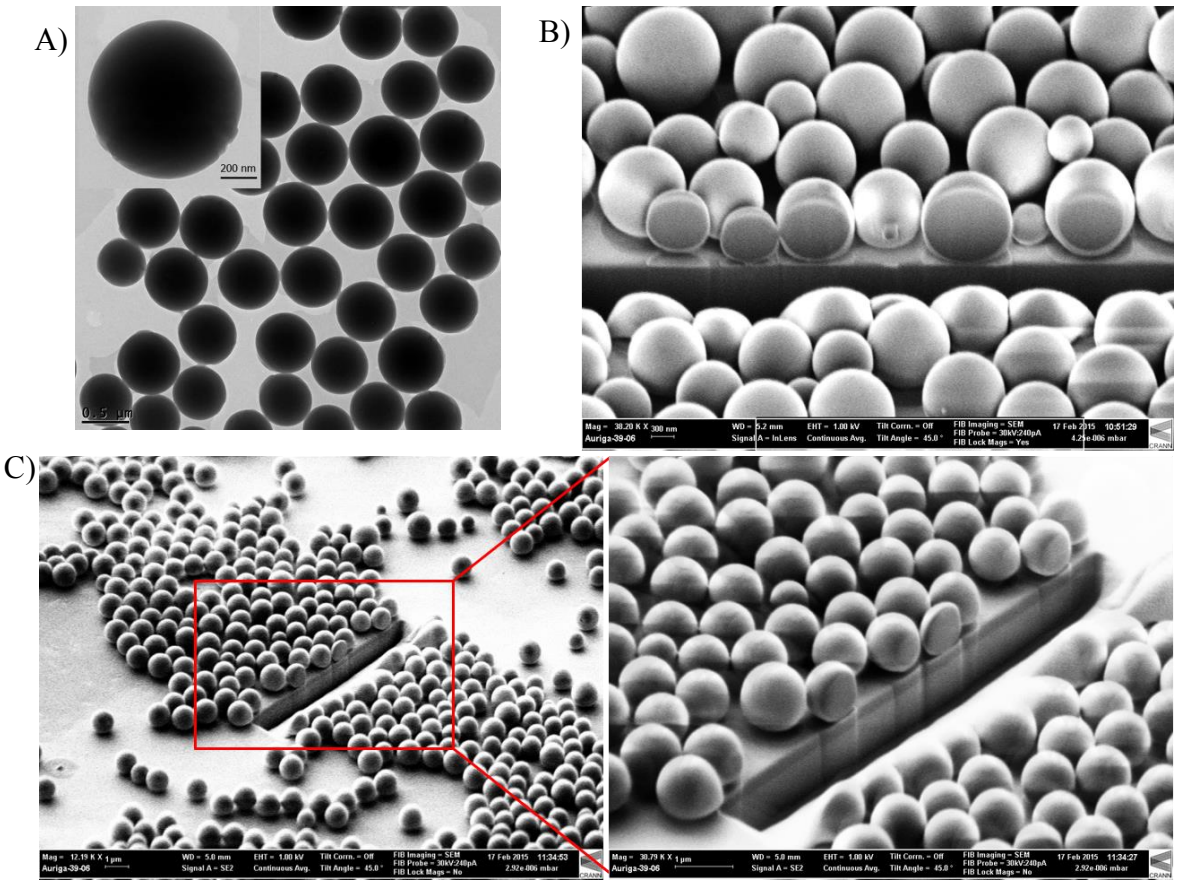

Figure 3.28: A) TEM image of the **89S** microsphere, scale bar 0.5 µm nm (inset: magnified image of same sample, scale bar 200nm; B) SEM image of the single **89S** microsphere cut precisely in FIB in milling process, scale bar 300 nm; C) SEM image of a bunch of **89S** microspheres cut in FIB in a larger area, scale bar 1µm.

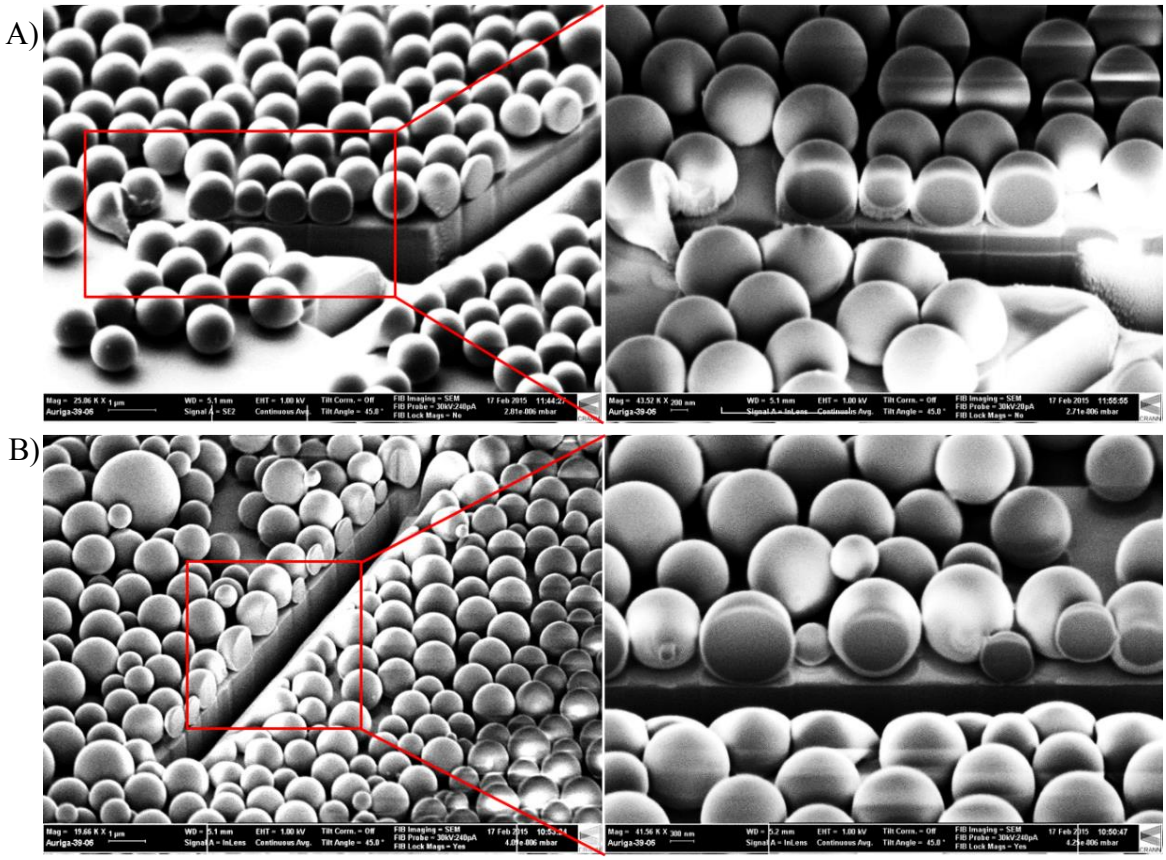

Figure 3.29: SEM images of A) **90S** and B) **91S** microspheres cut in FIB showing the solid nature.

Microspheres made from **90S** (0.4% w/v) and **91S** (0.4% w/v) was also analysed using FIB in a similar manner and imaged using SEM and were also found to be solid particles (Figure 3.29).

3.10 Atomic Force Microscopy (AFM) with Raman spectroscopy analysis of microspheres

Microsphere samples were analysed using an AFM-Raman spectroscopy hybrid technique to obtain information on structural morphology and the Raman scattering behaviour of **89S** microspheres. Using this technique, the surface area of the sample was scanned in order to obtain an AFM image and a Raman image of exactly the same microspheres within a single measurement. In this hybrid technique, the AFM was operated in tapping mode to develop the AFM image of the microspheres from which the structural features and morphology of the microspheres was obtained. During this measurement, the microscope was simultaneously operated in Tip Enhanced Raman Scattering (TERS) mapping mode to record the Raman scattering from the surface of the sample. As a result, a Raman image of the same microspheres sample was obtained. These AFM-Raman measurements in the

microspheres was performed in an AFM workshop conducted by NT-MDT, an AFM manufacturing company.

The solution of microspheres made from **89S** (c = 0.4% w/v) was dropcast on silica wafers and dried to deposit microspheres. Upon scanning microspheres of **89S** using the AFM-Raman microscope, 2D and 3D AFM images of the sample were obtained, from which the microspheres were found to be spherical in shape, consistent with the previous SEM and TEM and HIB analysis. From the AFM measurements, the size of these particles were determined to be in the range of 1.3 – 1.7 μm in diameter (Figure 3.30A). The slightly bigger size of the particles observed here might be because, the microsphere samples was prepared at higher concentration c = 0.4% w/v when compared to previous cases (c = 0.2%). Size distribution measurements of microspheres prepared at different concentration using AMF is discussed in the next section. From the 3D image of this sample, the height profile measurements were done by scanning the sample across the microsphere as shown in Figure 3.30B, inset redline. As a result, the height of the particles was calculated to be 1.7 μm (Figure 3.30B). AFM images of the same sample recorded in Phase contrast, 2D image and Topography mode are provided in appendix A3.10.1.

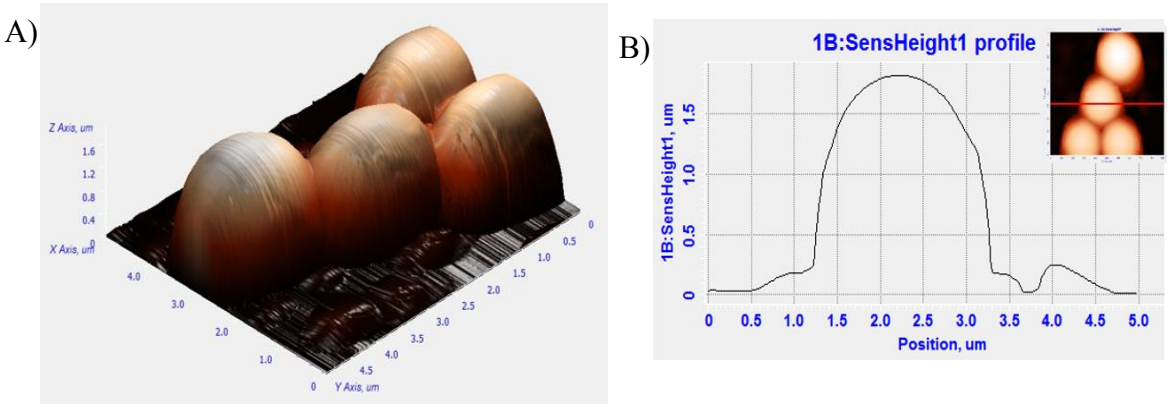

Figure 3.30: A) 3D-AFM Image of **89S** microspheres obtained from AFM-Raman microscope; B) height profile measurement obtained from 3D image by scanning across the microsphere (Inset: 2D image of the same sample, Red line corresponds to of height cross sections).

Raman spectra of the microsphere surface were obtained as, at the time of scanning, the tip of the AFM probe is precisely irradiated with a 514 nm laser. Therefore, the AFM probe acts as the nanoantenna to localise and enhance the excitation laser light near the apex (tip of the probe). Hence, this nanoantenna is effectively serving as the nano-source of light to irradiate a specific spot on the sample with very high spacial resolution. The light enhancement was achieved when the excitation laser light is in resonance with local surface

plasmon resonance at the tip of TERS probe. Therefore, when scanning the sample, an enhanced Raman scattering signal from the apex of the AFM probe is recorded, resulting in the Raman mapping image of the sample surface (Figure 3.31A). As a result, when picking a particular spot on this Raman image, a Raman scattering signal of the molecules (**89S**) may be obtained.

This image was used for mapping of the microspheres as the Raman scattering signal was observed only from the top of the microspheres (Figure 3.31A, red and blue rings). No signal was observed when the area not covered by microspheres was scanned (Figure 3.31A, black ring). The spectrum obtained was the result of inelastic Raman scattering of the **89S** molecule from which the microspheres were made, and the peaks in the spectrum are the result of the stretching of the functional groups in the compound **89S**. The spectrum obtained

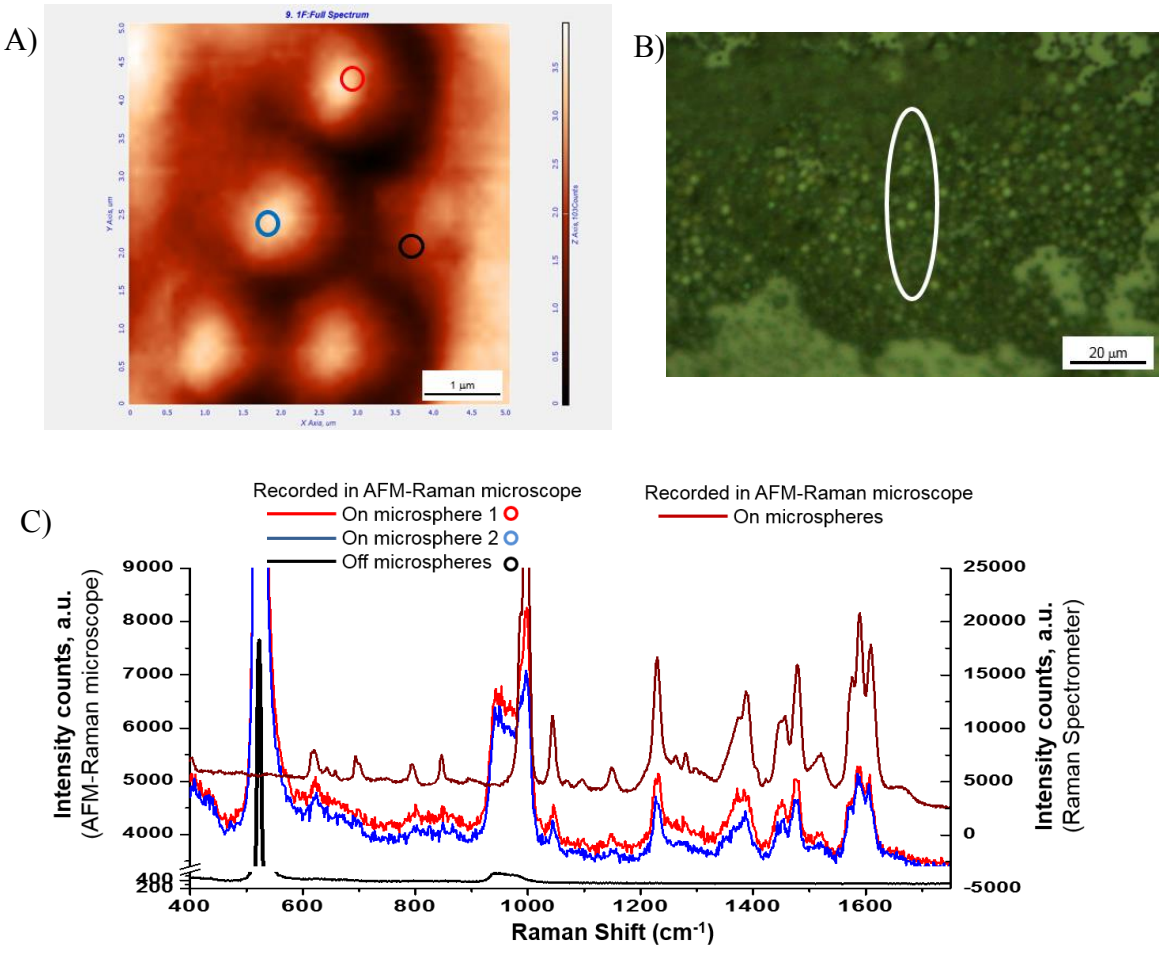

Figure 3.31: A) AFM-Raman image of **89S** microspheres obtained in TERS mode of AFM-Raman microscope, coloured rings indicate the spots on and off the microspheres where Raman spectra were collected; (see (C)); B) Optical microscope image of the same sample from which the Raman spectrum was recorded in spectrometer, white oval area indicate the laser spot; C) Raman spectra of **89S** microspheres taken on (red and blue) and off (black) the microspheres (see image A) in AFM-Raman microscope, and in Raman spectrometer (dark Brown) (image B).

from these three spots are shown in Figure 3.31C. Raman spectra (Figure 3.31C, red and blue) of the microspheres with Raman shifts of 1610, 1590 and 1575 cm^{-1} were attributed to C=O, Ar C=N and Ar ring C=C symmetric vibrational stretching frequencies of **89S**, respectively (Table 3.6). The 1480 cm^{-1} Raman shift was assigned to Ar ring C=C stretching frequency.[333] The two peaks merged together at 1456 and 1446 cm^{-1} are due to C-H asymmetric stretching of aliphatic CH_3 and CH_2 groups along with an additional peak for a CH_3 group at 1386 cm^{-1} (symmetric). An isolated Raman shift at 1230 cm^{-1} was assigned to an aliphatic C-C chain vibrational frequency. A strong peak at 995 cm^{-1} is attributed to Ar ring C=C (tpy) symmetric vibrational stretching frequency, which is usually observed for pyridine derivative.[333]

Table 3.6: Assignment of peaks in Raman spectrum obtained from **89S**.

Raman peaks from microspheres (cm^{-1})	Functional group assigned (vibrational frequencies)	Intensity in Raman spectrum	Intensity in IR spectrum
1610	C=O	strong	strong
1590	Ar C=N	strong	strong
1574	Ar C=C	strong	medium
1480	Ar C=C	strong	medium
1456 and 1446	Aliphatic CH_2 and CH_3 for asymmetric C-H	medium (both)	weak
1386	CH_3 (sym)	medium	weak
1230	Aliphatic C-C chain vibration	medium	medium
996	Ar ring C=C vibration	very strong	weak

These results were cross examined by recording the spectrum of the same sample in a standard Raman spectrometer (Figure 3.31C, dark brown), and were found to match exactly to the spectrum obtained in AFM-Raman microscope (Figure 3.31C, red and blue). Optical microscopy (OM) image of the microsphere sample used to record Raman spectra in the standard spectrometer is shown in Figure 3.31B. The white spot indicates the laser spot, full of microspheres from which the spectrum is obtained, thus confirming that the signals obtained in the AFM-Raman microscope are from the microspheres made of **89S**. The black spot, off the surface of the microsphere did not show any signal as there was no particles found there. Assignment of the Raman shifts of the **89S** microspheres were cross examined further by comparison with the IR spectrum of **89S** compound, and the Raman peaks of **89S** microspheres were consistent with the IR stretching frequency of **89S** molecule

(comparison of IR spectra of the **89S** and the Raman spectra of **89S** microspheres is provided in appendix Figure A3.10.2).

In summary, the results discussed showed the analysis of micropsheres using an hybrid AFM-Raman spectroscopy techinque, in which the AFM and the Raman image of the micropheres was obatained sumulteniously. From the Raman image of the sample the Raman peaks corresponding to compound **89S** (from which the microspheres were made) were observed only from the surface of microspheres. Hence, Raman peaks can be used to map and identify the microspheres. Having analysed the surface spectroscopic properties of microspheres, these particles were analysed for their mechanical properties using AFM techniques, which will be discussed in the next section.

3.11 Mechanical properties of solid microspheres evaluated using AFM

The microspheres were investigated using several microscopic techniques such as SEM, TEM, FIB, AFM-Raman microscopy, and were found to be strong, solid and robust. In order to understand these systems more, the microspheres were investigated by performing mechanical measurements using AFM. As a course of AFM study, 3 types of measurements were performed on solid microspheres prepared from **89S**: *1*) size distribution of solid microspheres; *2*) lateral force displacement studies; and *3*) mechanical strength measurements. The mechanical measurements of the microspheres discussed in this section were perform in collaboration with Prof. John Boland and Mr. Shaun Mills, CRANN, Trinity College, Dublin.

3.11.1 Microspheres size distribution measurements using AFM

89S microsphere samples were prepared at different concentrations (0.1%, 0.25% and 0.5% w/v) by dissolving of **89S** (1, 2.5, 5 mg, respectively) in a CH_3CN/H_2O (6:4) solution and these solutions were then dropcast (10 μL each) onto silica wafer to deposit solid microspheres as described previously. Samples with different concentrations (0.1, 0.25 and 0.5% w/v of microspheres) were used in order to evaluate the size distribution of microspheres using AFM and are the average of measurements on 20 different solid microspheres for each sample.

The size distribution results of the microspheres sample of concentration 0.1% shows that the smallest particle size determined was of diameter of 0.37 μm with the biggest being 0.68 μm in diameter. The average size distribution calculated was 0.52 ± 0.07 μm. Similarly, the 0.25% concentration sample showed the smallest particle size of 0.5 μm and

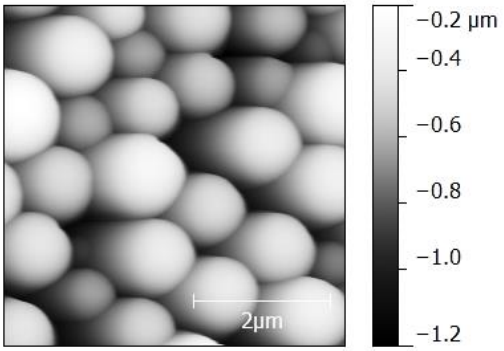

Figure 3.32: AFM image of **89S** solid microspheres prepared at concentration c = 0.25%.

the biggest was 1.02 µm in diameter (Figure 3.32). The average size distribution was found to be 0.75 ± 0.15 µm. whereas the 0.5% sample had the smallest particle size of 0.63 µm with the biggest being 1.16 µm in diameter with an average size distribution of 0.85 ± 0.19 µm. The analysis of the trend of size distribution, reveals that upon increasing the concentration of **89S** from 0.1% to 0.5% w/v, the average size distribution of the microspheres also increased from 0.68 to 1.15 µm. The results are summarized in Table 3.7. Detailed results of the size distribution measurement performed on 20 microspheres of each sample are provided in appendix Table A3.11.1.

Table 3.7: Size distribution measurement of **89S** solid microspheres.
Repeating this measurement two times, the particle size distribution was found to be reproducible with respect to the concentration used.

Microsphere concentration (weight %)	No. of microspheres used in measurement	Minimum size of microsphere (µm)	Maximum size of microsphere (µm)	Average size distribution of microspheres (µm)
0.1 wt. %	20	0.369	0.687	0.52 ± 0.07
0.25 wt. %	20	0.498	1.022	0.75 ± 0.15
0.5 wt. %	20	0.628	1.156	0.85 ± 019

3.11.2 Lateral force displacement studies of microspheres using AFM

It was demonstrated in the section 3.6, that the microspheres were removed from the silica substrate, indicating the particles were not strongly bound to silica surface. Schirmeisen and Qian separately demonstrated the lateral displacement of metallic nanoparticles using an AFM cantilever in the AFM instrument and measured the interfacial friction between particles and the substrate.[334-335] Analogous to this, **89S** microspheres were examined by laterally loading a microsphere using an AFM cantilever as depicted in schematic

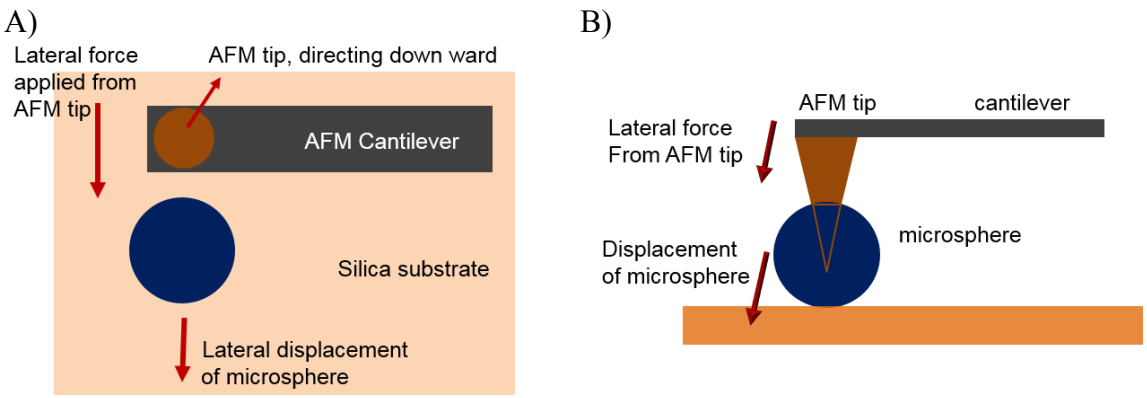

Figure 3.33: Schematic representation of the lateral force displacement of microspheres: A) Top view of the sample within AFM instrument where the microsphere (blue) is placed on the silica substrate next to the AFM tip (brown) and the lateral force applied from sideways of the cantilever. B) side view of the same set up, where the AFM tip is behind the microsphere.

representation Figure 3.33, to examine whether these particles can be displaced or pushed, or rolled. In this experiment, the force required to displace a solid microsphere was determined.

For these experiments, **89S** solid microspheres (c = 0.2% w/v) were deposited on a silica wafer as previously discussed in above. Before applying any force, an indentation was made on the silica substrate next to microsphere to mark its initial position. Keeping this point as a reference, the microspheres were pushed laterally and the distance displaced were measured. In addition to this, an indentation was made on the surface of the microsphere, to see whether the particle will slide or roll on applying lateral force (Figure 3.34A). The result of these measurements are given as a force displacement curves diagram (Figure 3.34E).

When lateral force was applied to the microsphere for the first time (load 1), it was observed that a force of 0.48 μN was required to move the particle. The particle was displaced approx. ~300 nm from its initial position (Figure 3.34B). It was noted that the 0.48 μN force was needed only at the beginning of the displacement. Once the particle had moved, the force required to push the particle further was reduced to ~0.1 μN. This observed phenomenon was similar to the force displacement studies performed on metallic nanoparticles.[334] Initially, more force is necessary for the particle to overcome the force of adhesion to the surface (Figure 3.34E, black) as the microspheres are adhered to surface due to the drying effect during sample preparation. Upon applying a lateral force for the second time (load 2) on the same microsphere, it was found that a lower force of 0.03μN was required to move the microsphere onwards (Figure 3.34E, red) on this occasion the particle was displaced by approx. 500 nm (Figure 3.34C). A similar result was observed when

applying force on the same microsphere for a third (load 3, Figure 3.34D and E, green) and fourth time (load 4, Figure 3.34E, purple). More force (0.48 μN) was needed in order to push the particle only in the beginning (load 1) because, the particles were strongly adhered to the silica surface due to influence of the drying effect. When the particle was moved from its initial position (Figure 3.34A), it overcame the force of adhesion and was no longer strongly

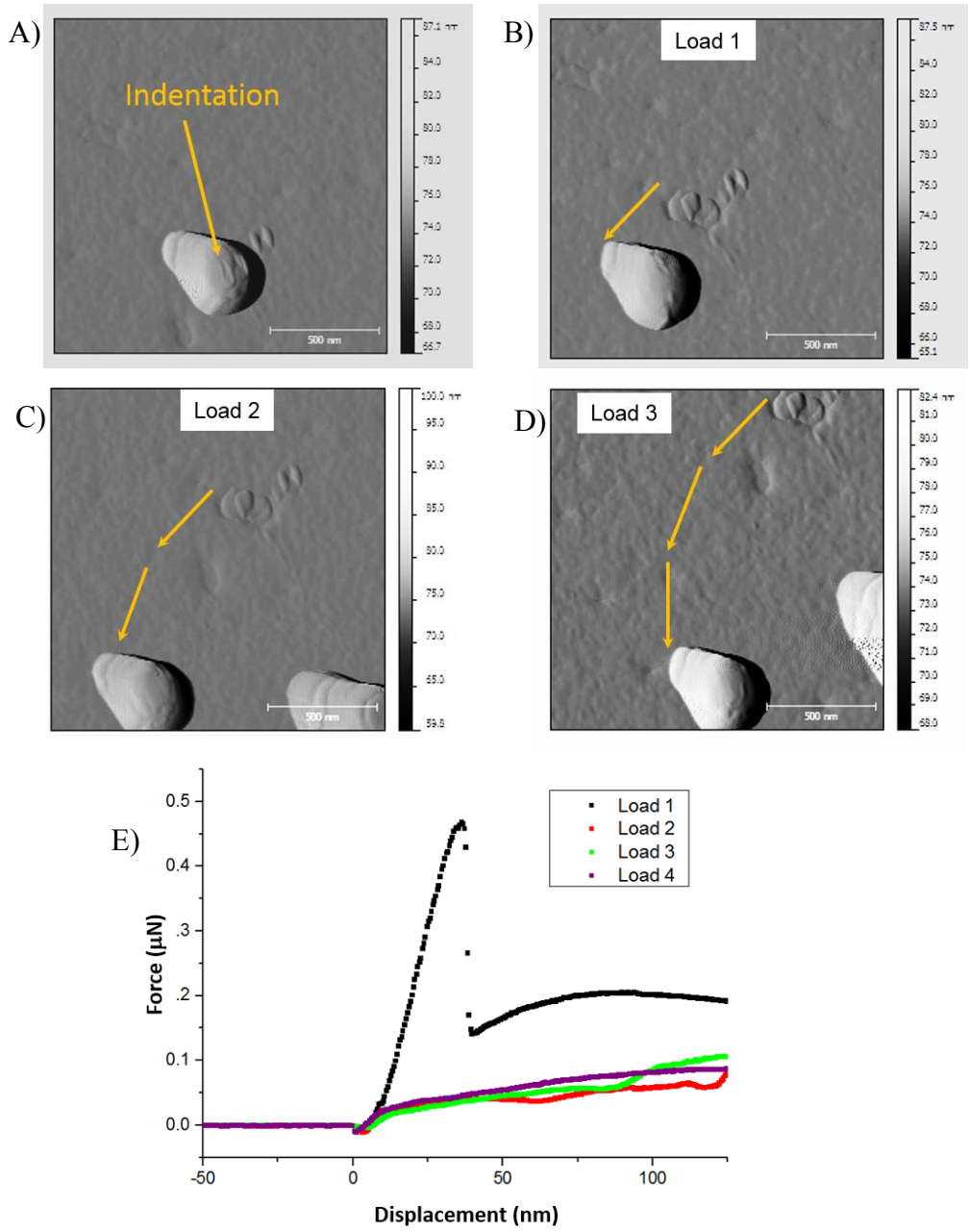

Figure 3.34: AFM images of the **89S** microsphere taken after every lateral force displacement measurement: A) initial position of microsphere before applying any force with the indentation: B) after applying force for the first time (load 1), arrow indicates the direction of the displacement: C) after load 2, D) after load 3, F) force displacement curves after applying lateral force on microspheres. Please note: the non-spherical image of the sphere is due to the convolution of the AFM tip.

adhered to the surface. Similar observations were made by Schirmeisen *et al*.[334] wherein, a higher force was required to laterally displace the nanoparticle for the first time and the force decreased to move for the second time and remained almost similar to move same particle there after multiple times.

It was found that during the course of applying the lateral forces, the indentation made on the microsphere surface (Figure 3.34A) disappeared and a new surface of the particle was seen after applying each load. This confirmed that the microsphere was rolling on the substrate upon application of lateral forces. Similar results were obtained when performing the same experiment on other **89S** microspheres with small changes in the force required to displace the particles for the first time, these results are provided in Appendix Figure A3.11.1. As expected, a similar phenomenon was observed when performing this experiment using the microspheres of **90S** and **91S**. Wherein, the force of 0.41 μN and 0.27 μN was needed to move the microspheres made from **90S** (approx. 700 nm) and **91S** (approx. 500 nm), respectively, for the first time and less force was needed to move the same particle. AFM images and force displacement curves of **90S** and **91S** microspheres are provided in Appendix Figure A3.11.2 and A3.11.3, respectively. In the AFM images, the non-spherical shape observed for the microspheres was only an artefact which arises due to the AFM tip convolution effect. These artefacts are known to occur in AFM imaging.[336]

3.11.3 Mechanical stiffness or strength measurement of microspheres using AFM

Having examined the effect of lateral forces applied to the microspheres, a vertical force was also applied to the microspheres using the AFM tip as shown in the schematic representation Figure 3.35A, B. In this measurement, an attempt was made to examine the stiffness or the mechanical strength of the microspheres of **89S** by applying vertical forces.

Before the start of the experiment, the AFM tip was calibrated on the hard surface of a silicon nitride calibration grid. During the calibration, a vertical force was applied to the calibration grid with the AFM tip. The force curves obtained show that when applying 30 nN of force, the approach curve and retract curves overlap with each other indicating the non-elastic behaviour (hard surface) of the material (Figure 3.35C). Keeping this as the reference, similar measurements were performed on the solid microsphere of **89S** by applying a vertical force of 30 nN to the top of the microsphere. The force curves obtained showed no sharp decrease in the applied force, indicating that the microspheres were hard and solid. In the approach curve (Figure 3.35D black), a little drop in force was observed at 20 nN due to an indentation caused on the surface of the microsphere, indicating the

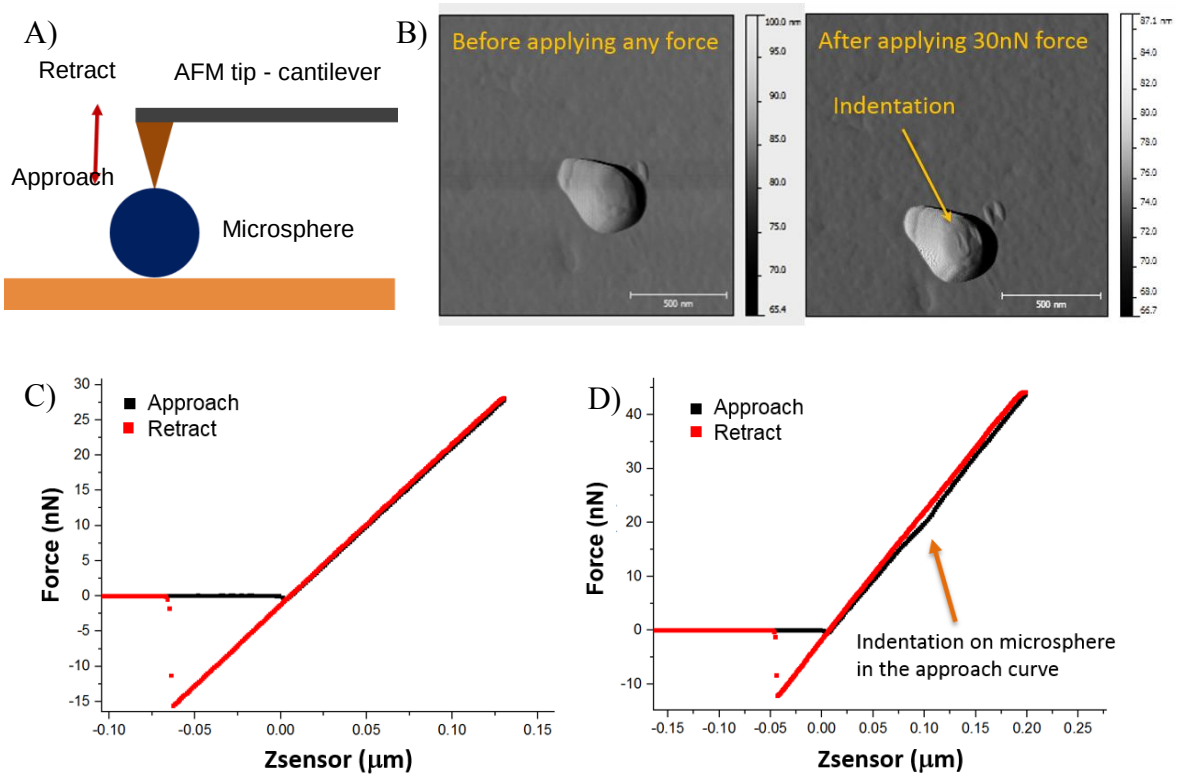

Figure 3.35: A) Schematic representation of the vertical force applied to the microsphere with an AFM tip; B) microsphere before and after applying a vertical force; C) vertical force curves on a non-compliant calibration grid; D) vertical force curves on a microsphere.

hysteresis in the approach and the retract curves. Repeating this measurements on several other microspheres exhibited similar results, showing that all the microspheres have similar spring constants to the calibration grid (Figure 3.36).

From these measurements, within our experimental parameters, it was found that the microspheres had a spring constant comparable to the calibration grid. Therefore, it can be

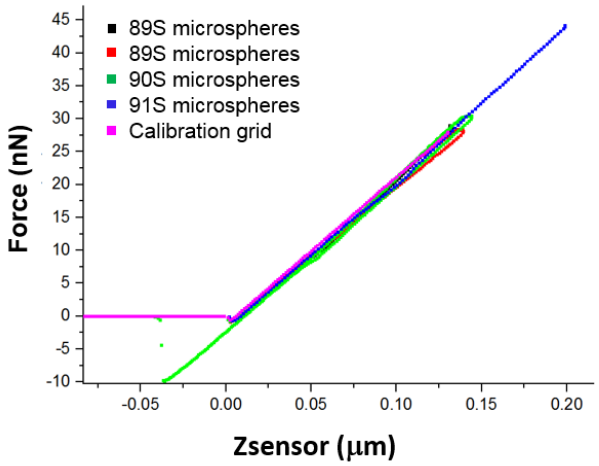

Figure 3.36: Force curves obtained by applying a vertical force on several microspheres of **89S**, **90S** and **91S** and on a calibration grid, indicating all microspheres have a similar spring constant to that of the calibration grid.

concluded that the microspheres are hard, solid and have very similar mechanical stiffness to the non-compliant calibration grid.

3.12 Thermal stability of solid microspheres

As the microspheres were found to be hard and solid with very high mechanical stiffness, next the thermal stability properties of the microspheres were investigated.

Solid microspheres prepared from **89S** (c = 0.2%) were deposited on silica wafers. Several of these samples were heated together at the same time on a hot plate at a heating rate of 2 ^{o}C per minute. Above 100 ^{o}C at 5 ^{o}C intervals, one at a time, the solid microsphere samples were cooled to room temperature and imaged using SEM. The SEM images showed that the solid microspheres kept their spherical shape until 155 ^{o}C. Further heating of the sample resulted in the melting of the microspheres at 160 ^{o}C and thereby losing their spherical structure, as shown in Figure 3.37A. To determine the thermal decomposition of the microspheres further, TGA was performed. In TGA analysis, a small amount of solid microspheres were placed in a heating crucible supported on a balance and heated from 25 to 800 ^{o}C at a rate of 5 ^{o}C in a nitrogen atmosphere.

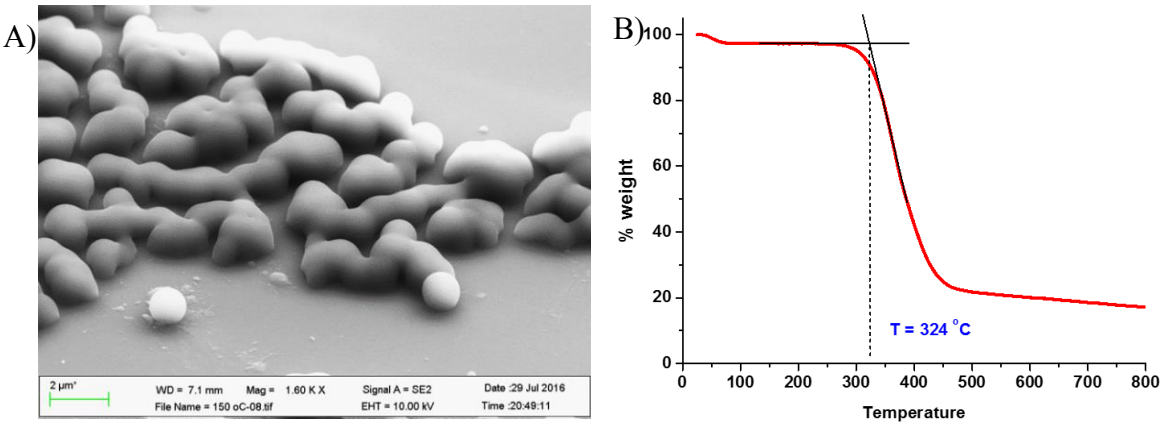

Figure 3.37: Thermal stability of the microspheres. A) SEM image of **89S** solid microspheres melted at 160 ^{o}C; B) TGA curves of the solid microspheres showing the thermal-chemical decomposition at 324 ^{o}C.

The TGA curve showed that the loss of solvent entrapped within microspheres occurred upon heating the microspheres to 50 ^{o}C (3 wt. %) (Figure 3.37B). Further increase of temperature (between 50 – 324 ^{o}C) showed no weight loss. Further heating of the sample resulted in its thermal decomposition. From these two experiments it was found that the microspheres didn't melt until 155 ^{o}C and then melting occurred at 160 ^{o}C where the microspheres lose their spherical structure. On the other hand, the thermal decomposition of microspheres was observed at 324 ^{o}C from TGA analysis corresponding to the thermal

decomposition of the ligand. Similarly, the **90S** and **91S** solid microspheres were shown to melt at 160 ^{o}C and 165 ^{o}C, respectively, and the thermal-chemical decomposition was found to be 317 ^{o}C and 326 ^{o}C for **90S** and **91S** microspheres, respectively. See appendix Figure A3.121 for SEM images **90S** and **91S** melted microspheres and TGA analysis.

3.13 Formation of single layered crosslinked networks of microspheres

It was discussed previously that the microspheres form chains and networks when interacting with Ln(III) ions in the solution medium by forming bridges between the microspheres through co-ordination linkages (Section 3.8). In this case, taking advantage of the poor solubility and amphiphilic nature of the microspheres (or tpy based tripodal compounds from which the microspheres are composed) in aqueous medium, bridging between the solid microspheres was achieved through H-bonding interactions between the molecules without the use of any metal ions. By exploring this kind of behaviour of the microspheres in different conditions, a single layer of 2D network of interconnected microspheres is obtained, which will be discussed in this section.

Microspheres of **89S** (0.3% w/v) were prepared in CH_3CN/H_2O (6:4) mixture and this solution was dropcast and dried on silica wafer to deposit a monolayer of microspheres. After immersion of these solid microspheres in H_2O for 60 minutes they were dried and later analysed using SEM. It was found that the microspheres were connected to each other through the bridges as shown in Figure 3.38. SEM images showing 3 and 4 microspheres bridged together to form triangular and quadrangular structures are shown in the appendix A3.13.1.

Since the microspheres were uniformly distributed over the sample area, an extended network of single layered interconnected solid microspheres was formed. Apart from forming the bridges, these microspheres were stable in H_2O for more than 2 hours without showing any signs of dissolution. It was also observed that the concentration of the microspheres solution affected the chains formed, with lower concentration of **89S** (0.1% w/v) giving rise to simpler chains (Figure 3.39A). Whereas, at higher concentration (0.3% w/v), since all the particles were close to each other, an extended network of interconnected solid microspheres was observed (Figure 3.39B).

In order to understand the formation of bridges, these systems were investigated further by carefully monitoring the progress of bridging by immersing the solid microspheres in H_2O (deionised) for different periods of time. The SEM images of the solid microspheres immersed in H_2O for 20 minutes showed initial stages of the bridging

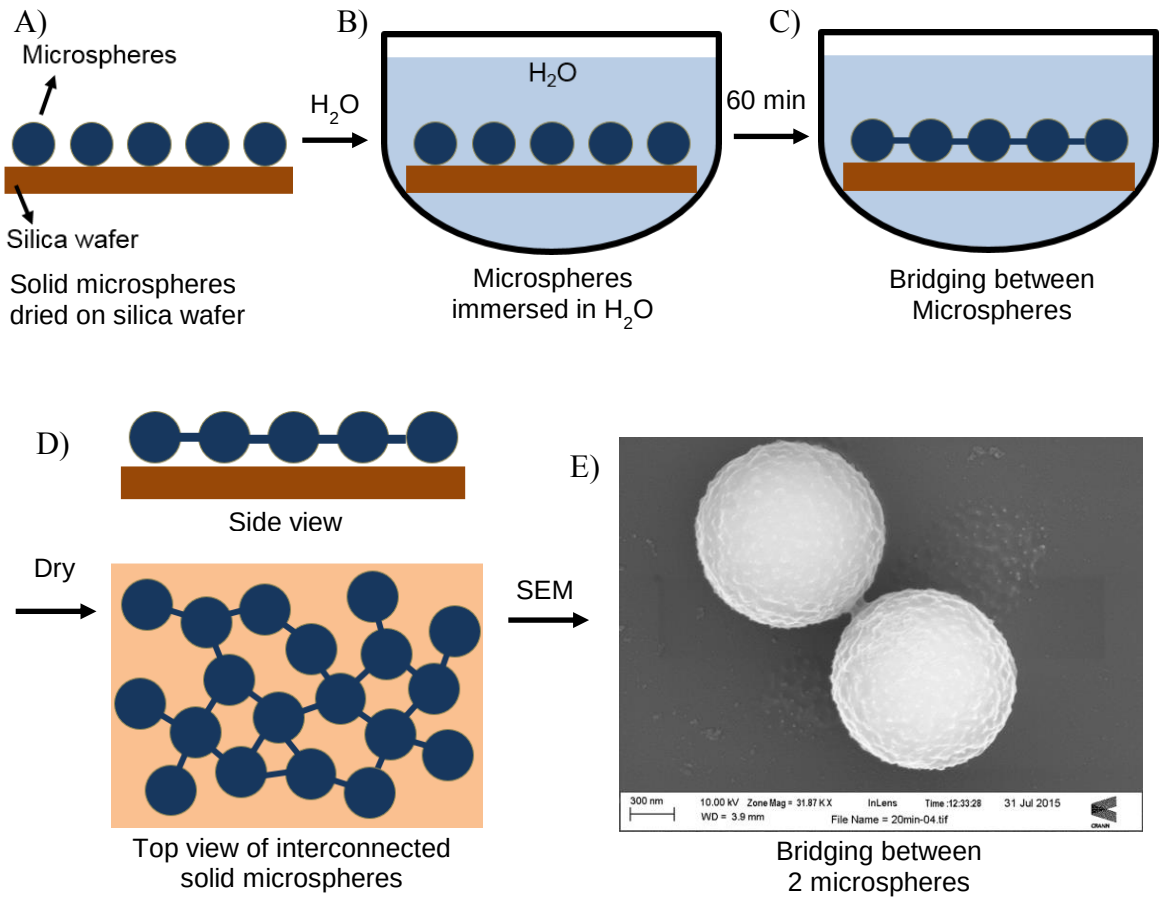

Figure 3.38: Schematic representation of the formation of extended network of interconnected microspheres: A) **89S** microspheres deposited on silica wafer, B) and C) solid microspheres immersed in H_2O for bridging. D) interconnected solid microspheres; E) SEM image of the interconnected solid **89S** microspheres, scale bar 300nm.

process between microspheres (Figure 3.40). After 60 minutes, all the microspheres appeared close to each other were found to be inter-connected. In this case, with the combination of H-bonding and hydrophobic interactions, bridging between the particles was achieved. It is expected that the amphiphilic nature of **89S** (from which microspheres were prepared) might be responsible for this. When the microspheres are immersed in H_2O, due to their amphiphilic nature, the molecules at the interface of microspheres-H_2O are in equilibrium and hence partially dissolve in the aqueous medium, and thus the balance between the hydrophobicity and hydrophilicity plays a significant role. Because of this behaviour, when the microspheres are immersed in H_2O, they interact as a result of their hydrophobic character and make connections between the particles. When the two microspheres are close to each other, the concentration of **89S** molecules is highest at the shortest distance of separation between particles, and hence, the bridges are most likely to form in this region. Above the critical aggregation concentration, these partially dissolved

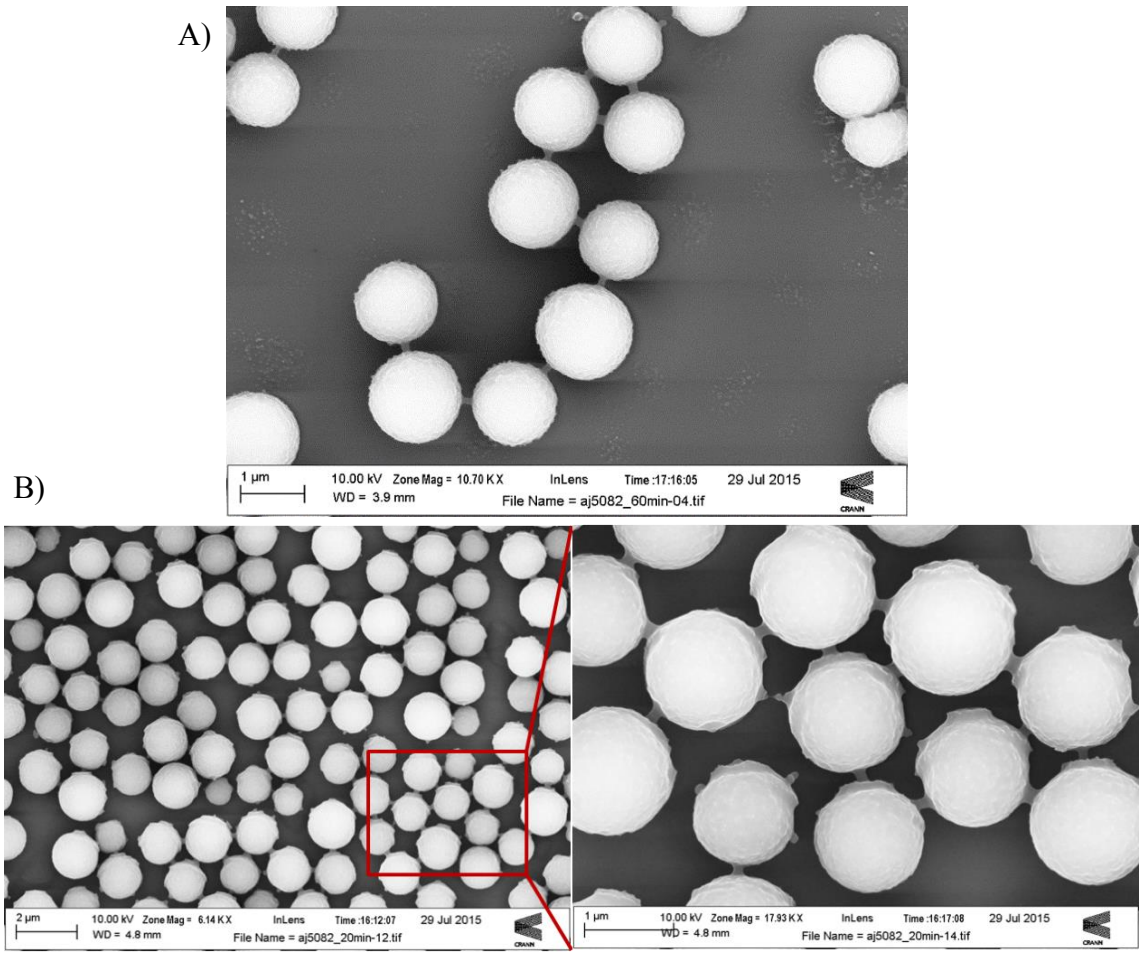

Figure 3.39: A) Chain of 2D monolayer of **89S** microspheres at c = 0.1%; B) extended network of 2D monolayer microspheres network formed by interconnected of microspheres at c = 0.3%.

molecules interact and result in the formation of bridges. This was consistent with all the observation made from SEM images wherein the bridges were observed only between the adjacent particles in close proximity. The microspheres did not show the formation of connections if the distance between them was more substantial. Furthermore, the formation

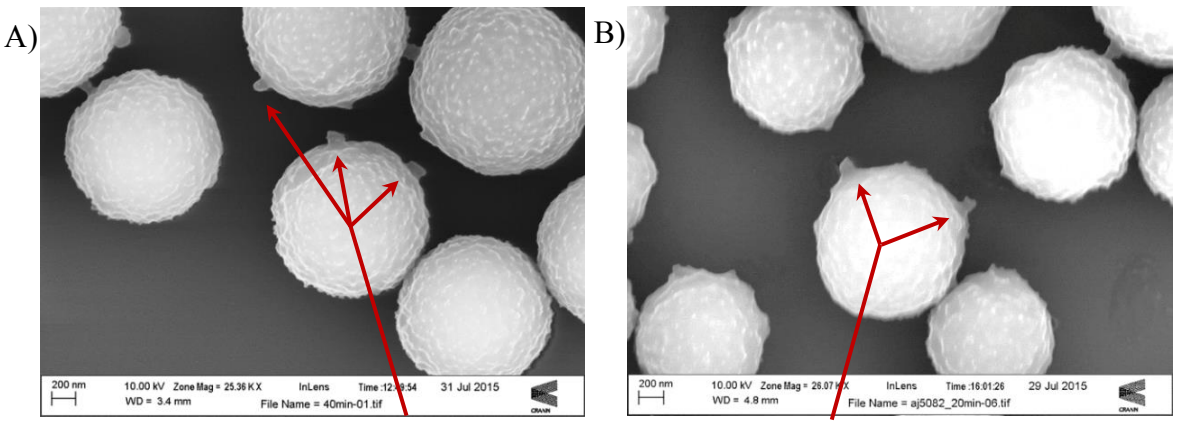

Formation of the bridges between spheres

Figure 3.40: Formation of the bridges between the solid microspheres: A) **89S**, B) **89R**.

of bridging process was observed only in the direction of another microsphere present in its close vicinity of approx. 200 – 300 nm (Figure 3.40). As this effect takes place all over the sample, it results in the formation of extended network of 2D interconnected monolayer of microspheres.

A similar effect was also observed for the microspheres made from **89R**, **90S** and **91S** and their SEM images are provided in appendix A3.13.2. These results were reproduced several times and each time the connections between the microspheres were observed. Stability of the microspheres in H_2O for longer time was analysed using optical microscopy, the results of which are discussed in discussed in Chapter 4.

3.14 Etching of solid microspheres in $Eu(CF_3SO_3)_3$ aqueous solution

In the previous sections, the solid microspheres deposited on silica wafer were found to form a monolayer of interconnected microspheres in aqueous medium through non-covalent interactions. It was also discussed (in section 3.8) that the same microspheres were bridged thorough coordination interactions upon addition of Ln(III) ions in solution media where the microspheres are suspended freely. Therefore, an attempt was made to make a monolayer of microspheres exclusively, where the particles are interconnected using coordination interactions using Ln(III).

With this in mind, **89S** microspheres (0.3 wt. %) were prepared in CH_3CN/H_2O (6:4) mixture and this solution was dropcasted and dried to deposit a monolayer of solid microspheres onto the silica wafer. The dried and solid microspheres were immersed in aqueous solution of $Eu(CF_3SO_3)_3$ ($c = 3 \times 10^{-3}$ M) for 2 hrs and imaged using SEM, the expected formation of bridges between microspheres was not observed. Instead, unexpected formation of micro-edges on the surface of microspheres was observed, making the microsphere surfaces porous (Figure 3.41).

This etching process was monitored over time, after 20 minutes of microsphere immersion in the $Eu(CF_3SO_3)_3$ solutions, the evolution of the etching effect was observed with the formation of tiny pores on the surface of microspheres. The prolonged immersion of microspheres for up to 2 hrs resulted in the conversion of solid microspheres to porous microspheres. SEM images of the etching process upon time is given in Figure 3.42, A - C. When continuing the immersion for longer time, after 4 hrs they were found to be consumed by Eu(III) ions in the solution as shown in Figure 3.42D.

This etching was not observed previously when $Eu(CF_3SO_3)_3$ was added to a solution of **89S** microspheres (section 3.8), probably because the polarity of the solvent CH_3CN/H_2O

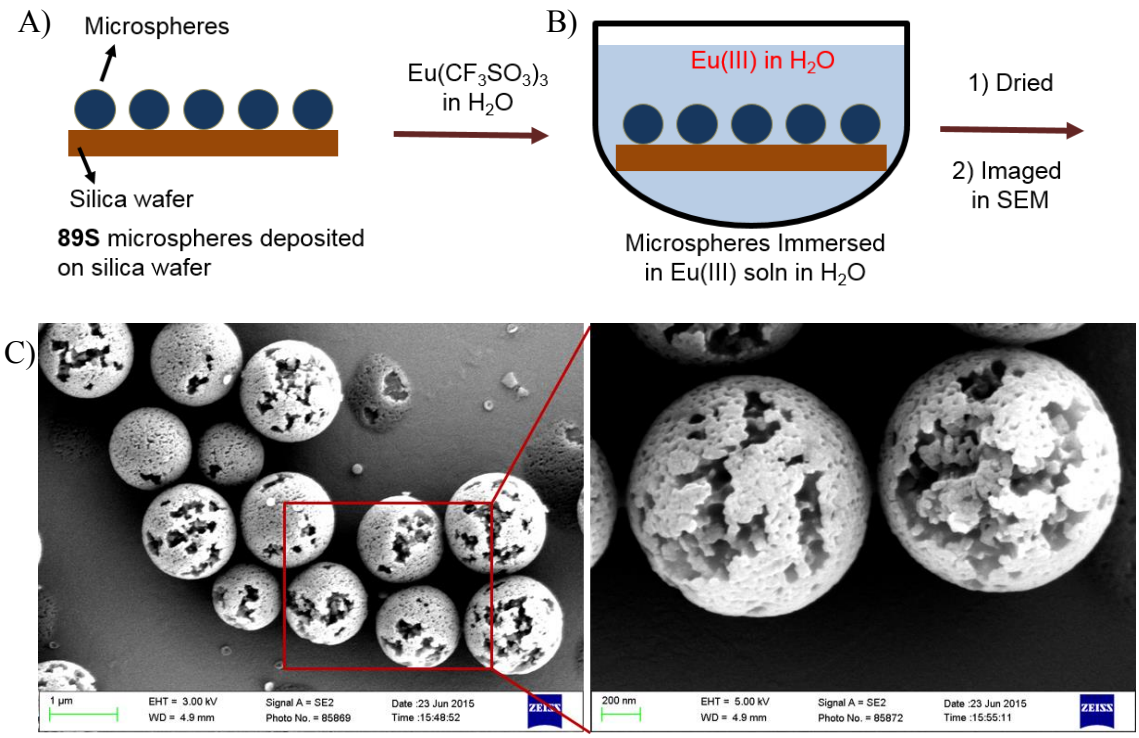

Figure 3.41: Schematic representation of the etching of **89S** microsphere. A) monolayer of **89S** microspheres deposited on silica wafer; B) immersion of monolayer microspheres in aqueous $Eu(CF_3SO_3)_3$ ($c = 3 \times 10^{-3}$M); C) SEM image of microspheres after 2hrs of immersion.

(6:4) mixture provides an appropriate balance between the solvophobicity and solvophilicity, stabilising the microspheres in solution without precipitation or complete dissolution of microspheres, which helps in making the bridges upon addition of Eu(III) ions.

In this case, only an aqueous solution of $Eu(CF_3SO_3)_3$ makes the microspheres lose their stability and Eu(III) ions in the solution interact with the tpy groups on the surface of the microspheres and slowly dissolve the molecules from the surface resulting in the formation of micro edges. When leaving the microspheres in the solution for a longer time, the etching process continued, wherein more molecules were removed from the microspheres resulting from the consumption of microspheres by Eu(III) ion in solution. This etching phenomenon was reproduced several times and each time the micro-etching was observed.

As a conclusion to this section, **89S** microspheres were found to form micro-cavities on their surfaces when exposed to $Eu(CF_3SO_3)_3$ solution. The same effect was not observed in absence of $Eu(CF_3SO_3)_3$ and also when $Eu(CF_3SO_3)_3$ was added to the solution of **89S** microspheres in CH_3CN/H_2O (6:4). Therefore, this etching effect was arising most probably due to the combination of poor solubility microspheres in aqueous media and the consumption of **89S** molecules by Eu(III) ions in solution media, due to the affinity of the

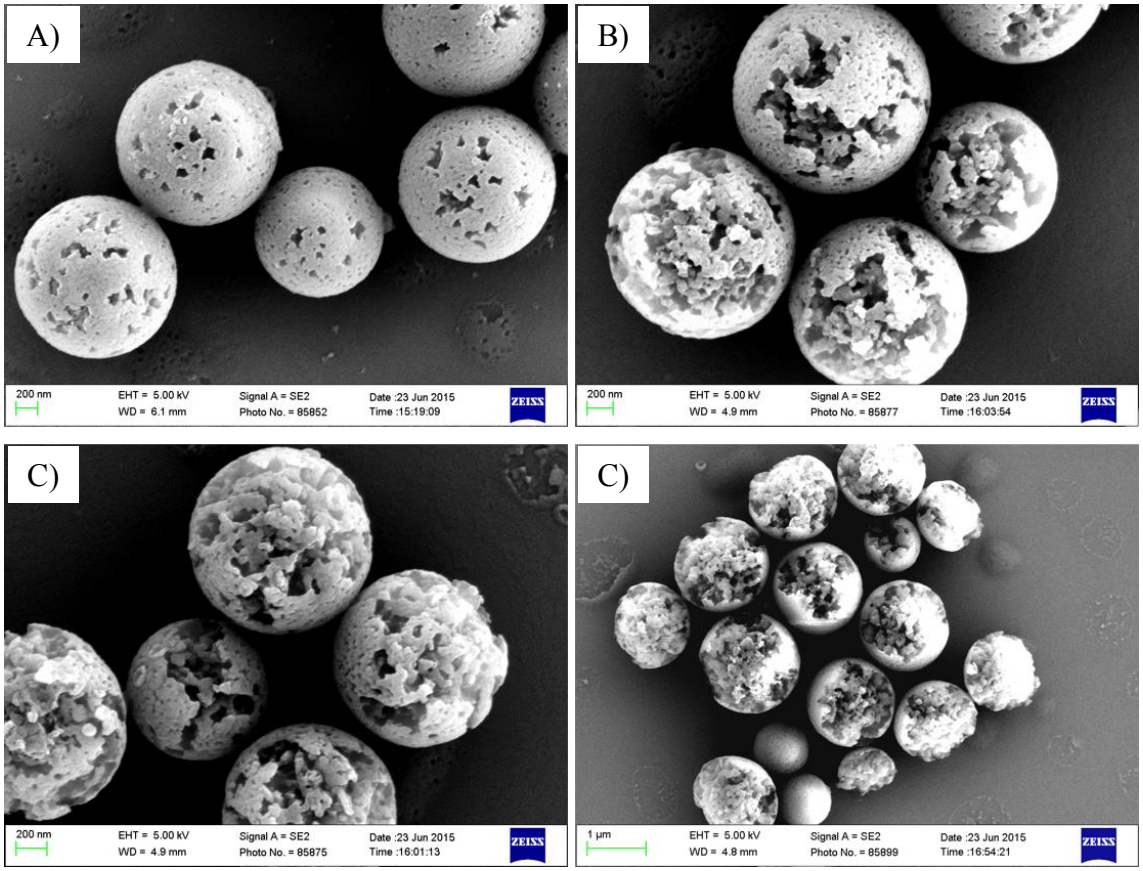

Figure 3.42: Etching process of **89S** solid microspheres at different time intervals: A) 20 min, B) 60 min and C) 2 hrs, D) 4 hrs.

tpy moieties for Eu(III) ions. This resulted in the removal of **89S** molecules from microspheres surface making them porous. Similar etching phenomena were observed during the removal of silica cores from core/shell microparticles.[331]

3.15 Self-sorting of non-chiral and chiral tripodal molecules: embedding the microspheres in gel matrix

The concept of multicomponent supramolecular systems can be used in the development of new functional materials.[177, 233, 337] Such systems are extremely useful because of having the advantage of two components in one system. Materials with multicomponent supramolecular systems that have self-sorting properties are very useful in the development of specially resolved multicomponent gels, crystal growth of organic compounds and many more.[11, 220, 232, 338] However, control over the self-assembly of individual components is still challenging. As mentioned previously, Van Esch *et.al*. showed that compounds **49** – **51** undergoes orthogonal self-assembly in the multicomponent system.[174-175] Analogous to this phenomenon, an attempt was made to build a multicomponent system by controlling the self-assembly of two different individual components having minor differences in their

molecular structures. Utilising this self-sorting behaviour of the synthesised tripodal molecules in a supramolecular gel, the embedding of microspheres in a gel matrix was achieved.

In the family of tripodal molecules synthesised, despite similar molecular structures with only a difference in amino acid linkages, the achiral derivative **88** behaved as gelator which self-assembled to form a fibrous network resulting in the gel formation exhibiting both healable and rapid recovery properties. In contrast, the chiral molecules **89** – **91** (R/S) behaved as non-gelators forming instead microspheres that had the characteristics of a hard material. In order to better understand the significant difference in the self-assembly behaviours, the gelator and the non-gelator molecules were mixed in the same medium with the expectation of intermolecular interactions between gelator and non-gelator to occur. As a result, a multicomponent system was obtained, wherein the individual components resulted in their own self-assembled species. The different combinations of gelator to non gelator mixtures used in the study of self-sorting behaviour of tripodal molecules **88** – **91** are summarised in Table 3.8. These samples were investigated using SEM, which will be discussed in this section.

Table 3.8: The combination of achiral **88** and chiral molecules (**89** – **91**) used to study the self-sorting properties of tripodal molecules. In all the samples, the achiral and chiral compounds were mixed by dissolving the mixture in 60 % CH_3CN/H_2O mixture by heating at 100 °C.

Sample no.	Achiral compound 88	Chiral compounds (% wt. ratio to 88)	CH_3CN/H_20 60:40 (v/v)	Result
1	5 mg (0.5 wt. %)	**89S** 1.5 mg (30 % wt. ratio to 88)	1.2 ml	Formed gel. Gel fibres with broken microspheres
2	3 mg (0.3 wt. %)	**89S** 1 mg (30 % wt. ratio to 88)	1.2 ml	Formed gel. Gel fibres with embedded microspheres
3	3 mg (0.3 wt. %)	**89R** 1 mg (30 % wt. ratio to 88)	1.2 ml	Formed gel. Gel fibres with embedded microspheres
4	3 mg (0.3 wt. %)	**89S** (as preformed microspheres in sol) 1 mg	1.2 ml	Weak gel. Gel fibres with microspheres
5	4 mg (0.4 wt. %)	**90S** 1 mg (25% wt. ratio to 88)	1.0 ml	Weak gel. Gel fibres with embedded microspheres
6	4 mg (0.4 wt. %)	**91S** 1 mg (25 % wt. ratio to 88)	1.0 ml	Weak gel. Gel fibres with embedded microspheres

In the beginning, a mixture of gelator, **88** (5mg) and non-gelator **89S** (1.5 mg, 30 wt. % w.r.to **88**) was dissolved in CH_3CN/H_2O mixture (60:40, 1.2 ml) by heating to 100 ^oC. Upon cooling this mixture to room temperature, a turbid gel (c = 0.5% w/v) was obtained (sample 1, Figure 3.43A). SEM images of this turbid gel showed a highly dense fibrous structure formed from the gelator component **88**, along with broken microspheres, from **89S** (Figure 3.43B). This might be because, during the gelation process, the formation of a fibrous network and microspheres takes place simultaneously. Due to the higher concentration of gelator component **88**, the formation of a dense crosslinking fibrous network might be hindering the diffusion of **89S** molecules thus disturbing their self-assembly/aggregation. For to this reason, the formation of microspheres was disturbed, resulting in the incomplete formation of microspheres.

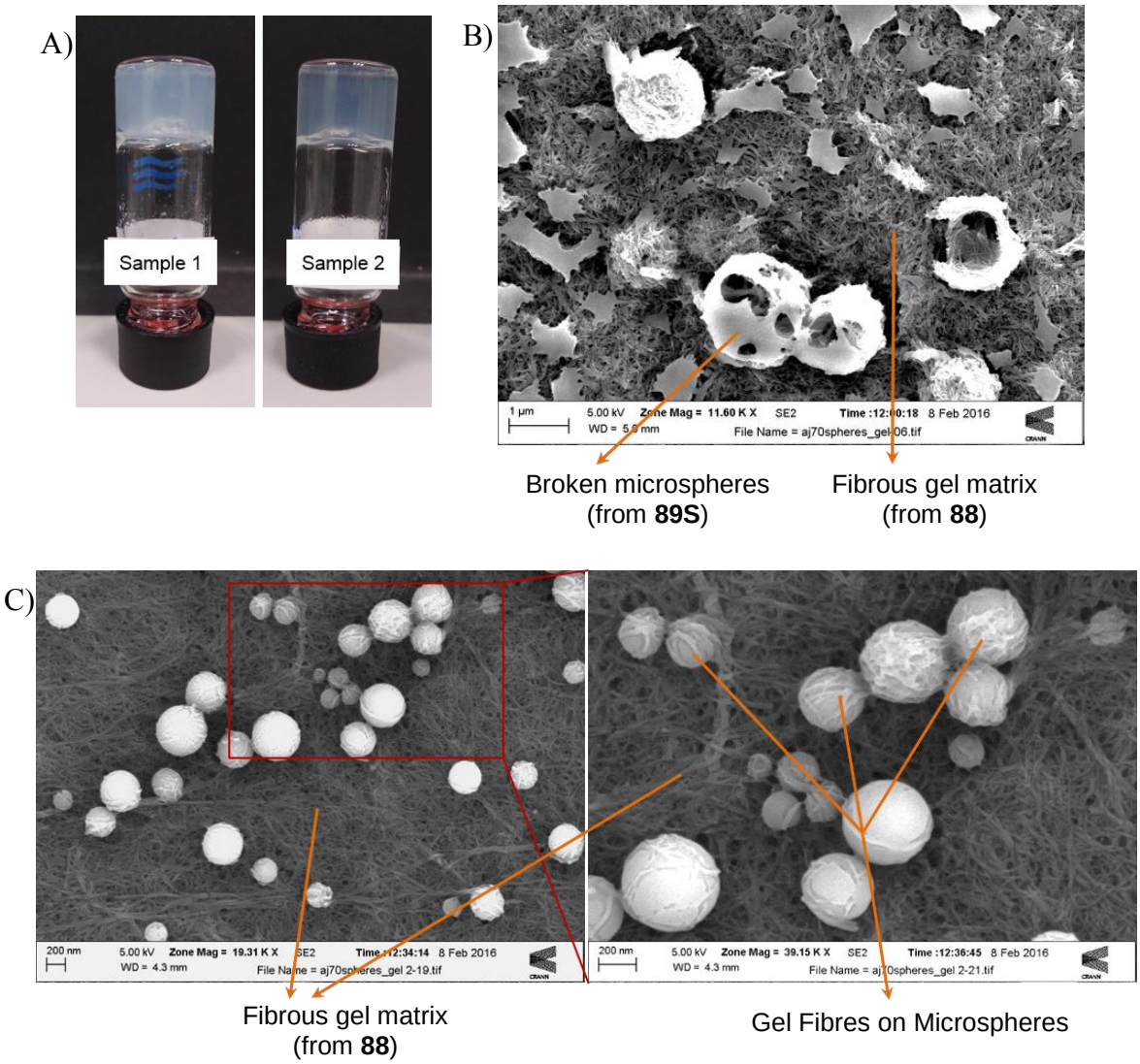

Figure 3.43: A) Pictures of gels obtained by combining of **88** and **89S.** Left: 0.5% and 0.15% respectively (sample 1) and Right: 0.3% and 0.1% respectively (sample 2). B) SEM image of sample 1, scale bar 1µm. C) SEM image of sample 2, scale bar 200 nm.

In order to find a balance the between the formation of the gel and the microspheres to occur at the same time independently, the concentration of the components were altered, but the ratio between the components was kept the same. The decrease of gelator **88** concentration from 5 mg/ml to 3 mg/ml and non-gelator S- **89S**, from 1.5 mg/ml to 1 mg, (33% weight ratio to **88**) resulted in the formation of a translucent gel (c = 0.3% w/v) in CH_3CN/H_2O mixture (6:4) (Sample 2). SEM images of the gel showed fibrous structures from **88** along with formation of microspheres from **89S** (Figure 3.43C). In this sample, the microspheres from **89S** were formed without any disturbance (unlike in sample 1) in the **88** gel matrix and were found to be wrapped around the gel fibres. In this sample, the **88** gel formed at lower concentration (compared to sample 1) had a less dense fibrous network, which most likely facilitated for the diffusion of **89S** molecules and self-assembly to occur, resulting in the formation of **89S** microspheres in the gelation medium. As this process takes place throughout the gel medium, the microspheres are embedded inside the gel matrix.

In this case, although the molecules **88** and **89S** were present in the same medium, due to the independent self-assembling properties of the individual components they did not interact and exhibited self-sorting properties. This resulted in the co-existence of the two independent self-assembled species in the same medium. Similar results were obtained by mixing **88** (3 mg/ml) and **89R** (1 mg, 30 % wt. ratio to achiral component) with the formation of a translucent gel (c = 0.3%) (Sample 3). The phenomenon observed here was similar to observation made by Van Esch, using molecules **49** – **51**, which formed their independent fibrous structures in presence of surfactants.[173-174] SEM images of sample 3 showing similar morphologies to sample 2 are provided in appendix figure A3.15.1A.

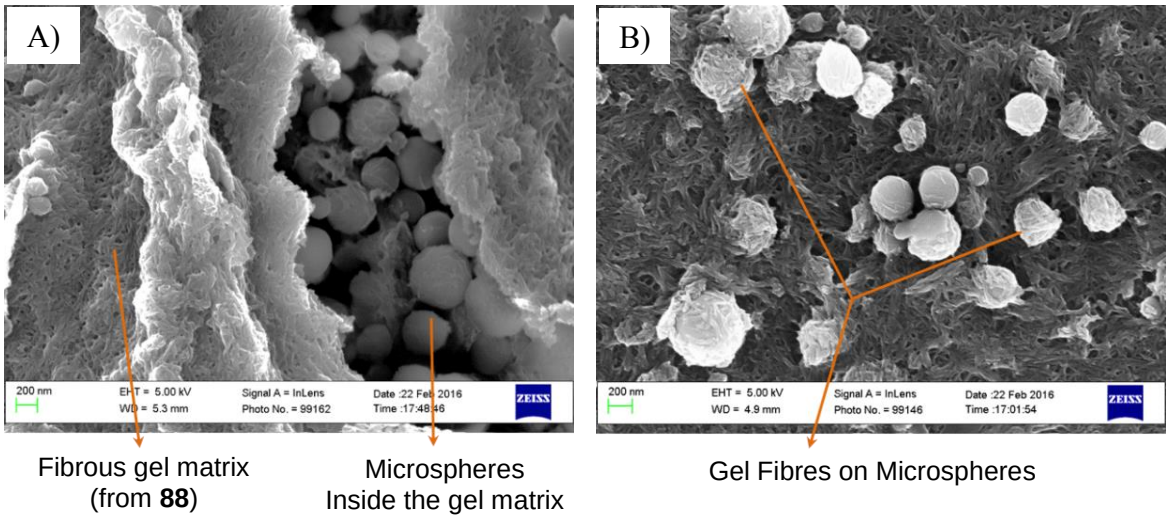

Figure 3.44: SEM images of the A) **88** and **90S** mixted gel (sample 5), scale bar 200 nm. And B) **88** and **89S** mixed gel (sample 6), scale bar 200 nm.

In sample 4, gelator **88** was dissolved in the solution containing preformed microspheres of **89S** in CH_3CN/H_2O (6:4) medium. In this case a weak gel was obtained. The SEM images showed similar morphologies with fibrous structures and the microspheres, as seen in the previous case (Appendix Figure A3.15.1, B). The reason for this weak gel might be the presence of preformed microspheres in the medium and disturbing the crosslinking process, which was necessary for the formation of gel strong.

Furthermore, the combination of **88** (4 mg) with **90S** (1 mg) and **91S** (1 mg) was used in sample 5 and 6 respectively (Table 3.8). Both the combinations yielded gels in CH_3CN/H_2O (6:4) medium. As expected, SEM images of both the samples showed the gel fibres and microspheres as seen in the previous cases (Figure 3.44). In some places the microspheres were found buried beneath the gel fibres confirming their embedding in the gel matrix (sample 5).

In the various combinations outlined in Table 3.8, gels were obtained showing that the microspheres were embedded inside the gel matrix. Moreover, in all the cases discussed in the previous sections, microspheres synthesised alone from **89 - 91** were always in the size 600 – 1000 nm. However, in all the samples discussed here, the microspheres formed were in the size range of 200 - 500 nm. It was noticed that, synthesising these microspheres in presence of gelator **88,** limited the size of particles to 500 nm. The reason for this is that, as a course of gelation process of **88,** although **89S** have enough space for the microsphere formation, the simultaneous formation of the fibrous network restricts the growth of the microspheres beyond 500 nm in size, without affecting the spherical structures. Hence, particles bigger than 500 nm were not seen in any of the above cases. From this observation it can be concluded that this self-sorting gel matrix can be used to control the size of the microspheres.

In all the cases, approx. 0.3 mole equivalents of the chiral component (**89** – **91**) were used in the mixture, which is a 30 % weight ratio to **88**. Increasing the amount of chiral component to 1 mole equivalent (1:1 weight ratio) resulted in weak gels being obtained. However, the SEM images showed both the fibrous network and microspheres. This is probably because, the higher concentration of microspheres hinders the crosslinking of fibrous network responsible for strengthening the gel matrix.

Recently, similar observation was made by Hamachi *et al*., wherein they showed a multicomponent hydrogel consisting of self-sorted supramolecular nanofibers, prepared using a peptide gelator and an amphiphilic phosphate, exhibiting their independent self-assembly behaviour forming their independent fibrous network.[339] In addition to this, there

are other examples of the multicomponent gels exhibiting self-sorting behaviour,[220] orthogonal self-assembly,[174, 340] crystal growth[233] in the gel matrix *etc*., the samples discussed above are the first examples a multicomponent gel consisting of a fibrous network and the microspheres due to the self-sorting properties of a family BTA molecules.

3.16 Conclusions

The work described in this chapter was focussed on the self-assembly properties of the BTA based tripodal molecules functionalised with different amino acids in different solution media. Each amino acid attached to the BTA core was shown to direct the self-assembly in a different way, resulting in the variation of the morphology of the aggregated structures. Gelation tests carried out on the synthesised tripodal molecules showed gel formation only for the achiral molecule **88**, which formed a one dimensional supramolecular structures to form fibres, which further aggregates to grow as fibres in three dimensions leading to gel formation in CH_3CN/H_2O (6:4). The achiral derivative forms a gel in c = 0.5 wt. %, with interesting reversible stimuli responsive properties. SEM and TEM analyses showed the highly fibrous entangled network responsible for the gelation of the medium. Rheology measurements performed on the **88** gel (0.5% in 6:4 CH_3CN/H_2O) showed the storage modulus (G′) value of 1040 Pa in strain sweep experiment displaying the solid like behaviour. However, when the strain value reached 1.4%, the G′ decreased and a crossover point was observed where the gel behaves as liquid. When the recovery test was performed on the same gel, it demonstrated the remarkable self-healing properties, where the gel recovered to the same G′ value as observed at the start with in less than 30 seconds. In comparison, the rapid recovery of **88** gel was faster than the previously reported gels from our group.[255, 285]

In contrast to the above, chiral derivatives, **89** – **91**, formed aggregates in the shape of the microspheres under similar conditions. The particle size analysis from SEM images and DLS measurements revealed the diameter of these microspheres to be in the range of 0.6 – 1.1 μm, depending on the compound used. It was also observed that the particle size distribution varies depending on the different solvent medium and the concentration. From the dramatic changes in the morphology of the self-assembled structure, we can say that, when changing the molecule from achiral to chiral, one dimensional linear supramolecular architectures can be changed to spherical particles. Such behaviour of **89** – **91** was due to the combination: *1*) intermolecular triple H-bonding between molecules; *2*) Nature of the chirality; and *3*) increased hydrophobicity caused by the additional hydrophobic substituents

present at the chiral centres of amino acid part. Out of all three chiral tripodal molecules, **89** (R and S) showed the formation of microspheres with uniform and relatively narrow size distribution between 0.8 – 1.1 μm, with mean particle size of 0.92 ± 0.08 μm. Hence the microspheres prepared form **89S** were used in most of the studies discussed in this chapter. When compared to other BTA molecules such as **35**, **36**,[125] **52**, **53,**[144] **86,**[281] the formation of such morphologies was not observed, which demonstrates the distinctive self-assembly properties of **89** – **91**.

Understanding the mechanism of the formation of microspheres using urea, proved that the microspheres were formed through intermolecular triple H-bonding interactions, which is crucial for the self-assembly of **89** – **91** to occur due to the competitive intermolecular H-bonding. This was confirmed by addition of urea at the beginning of the synthesis of the formation of microspheres in solution.

Adding the Ln(III) metal ions to the microspheres caused the formation of chains, linking the particles thorough co-ordination interactions. The binding of Ln(III) ions to tpy groups was confirmed by the spectrophotometric investigation, where the emission for the respective Ln(III) ions was observed through the energy transfer from tpy groups to Ln(III) metal centres. This bridging was found to be stable over more than 15 hrs in solution. However, this behaviour was not observed for transition metal ions. The microsphere chains and networks formed upon Ln(III) addition was the first example of such morphologies.

The investigation of microspheres using the FIB technique, involved the particles being precisely cut using Ga ions, and revealed the particles to be solid. AFM measurements showed the average size distribution of 0.52 ± 0.07, 0.72 ± 0.15 and 0.856 ± 0.19 μm for **89S** microspheres prepared at the concentrations of 0.1%, 0.25% and 0.5% w/v, respectively, showing a trend in the increase of particle sizes upon increasing the **89S** concentration. From AFM-Raman microscope, when scanning the **89S** microspheres sample in TERS mode, Raman scattering from the sample surface was recorded from which the Raman image of sample was obtained. As a result, the Raman peaks corresponding to **89S** was observed only from the microspheres surface (top).

From the lateral force displacements measurements of **89S** microspheres, the particles were not strongly adhered to the silica substrate. Upon applying lateral force to the microsphere, 0.48 μN force was required to move/roll the particle for first time from its initial position and the force dropped to ~ 0.1 μN to move the same particle later on. This observed phenomenon was similar to the force displacement studies performed on metallic

nanoparticles.[334] Mechanical stiffness measurements performed on same solid microspheres by applying the vertical force on top of the microspheres using the AFM tip, showed that particles to be strong, solid and robust in nature. The force curves obtained showed that the microspheres have the same spring constant comparable to the silicon nitride calibration grid within our experimental parameters, indicating that the microspheres were as strong as the calibration grid. Thermal stability and the thermogravimetric analysis showed that microspheres were stable up to 155 ^{o}C, melting at 160 ^{o}C.

When **89S** solid microspheres were immersed in H_2O, bridging between the microspheres was observed, forming linear 2D chains and networks. The bridging in this case (without use of any metal ions) was most likely occurred through H-bonding, due to the diffusion of molecules from microspheres by H-bond interactions. However, the bridging was seen only when the particles were in close proximity (100 – 200 nm apart). Lateral force displacement experiments on the linked microspheres could not be performed as the particles were interconnected and more force was needed to push by AFM cantilever.

In the next step, with the aim of bridging the particles through coordination interaction, the microspheres were immersed in a solution of $Eu(CF_3SO_3)_3$. From the SEM investigations, the expected formation of the bridges between the particles (through coordination interaction) was not observed, instead, the formation of micro cavities on the surface of the microspheres was seen making the surface porous. This was probably because, during the aging process, Eu(III) ions in the solution were coordinating with the tpy groups on the surface of the microspheres and removing the molecules from the microspheres slowly resulting in the etching of microspheres. Similar phenomenon was observed during the removal of silica cores from the core/shell microparticles.[331]

In the family of tripodal molecules synthesised, the difference in the molecular structures is only in the chiral centres. Mixing of these different compounds (*i.e.* achiral **88** and chiral analogues **89** – **91** (R and S)) the expected interaction between the molecules was not observed, but instead they showed self-sorting behaviour. When mixing the achiral and chiral molecules together, the achiral compound self-assembles to form one dimensional supramolecular polymers with fibrous structures resulting in the formation of gels (as above). While the chiral derivatives at the same time self-assemble to form microspheres in the same medium. This is the strong evidence of self-sorting behaviour of these tripodal molecules. Moreover, the particles formed in this gel medium are no larger than 500 nm in diameter because of the restrictions introduced by gel fibrous matrix. Hence the gel matrix used here can be used to prepare the microspheres with controlled diameter sizes.[337] Similar

self-sorting phenomena were observed between a peptide amphiphile and amphiphilic phosphate.[339]

Based on the observations made above and the information obtained on the self-assembly of BTA molecules, a proposed mechanism for microsphere formation form **89** – **91** is shown in Figure 3.45. The synthesised BTA molecules **89** – **91** had a *1*) central benzene core *2*) amino acid part (with potential H-bonding sites) and *3*) a hydrophobic alkyl chain and terpyridine moiety at the periphery, as shown Figure 3.45A. Preparation of microspheres involved a heat-cool cycle. While cooling the hot solution, dissolved BTA molecules **89** – **91** self-assemble by stacking though triple H-bonding and π – π interactions to form a helical and linear one dimensional supramolecular fibrils, which is a well-known phenomenon exhibited by similar BTA molecules (Figure 3.45, B and C).[281, 316] These structures consisted the hydrophobic tpy groups at the periphery of the fibrils. While cooling process continues, fibrils undergoes further aggregation by axial alignments *via* side chain hydrophobic effect caused between tpy groups to form supramolecular fibres (Figure 3.45D), which is a

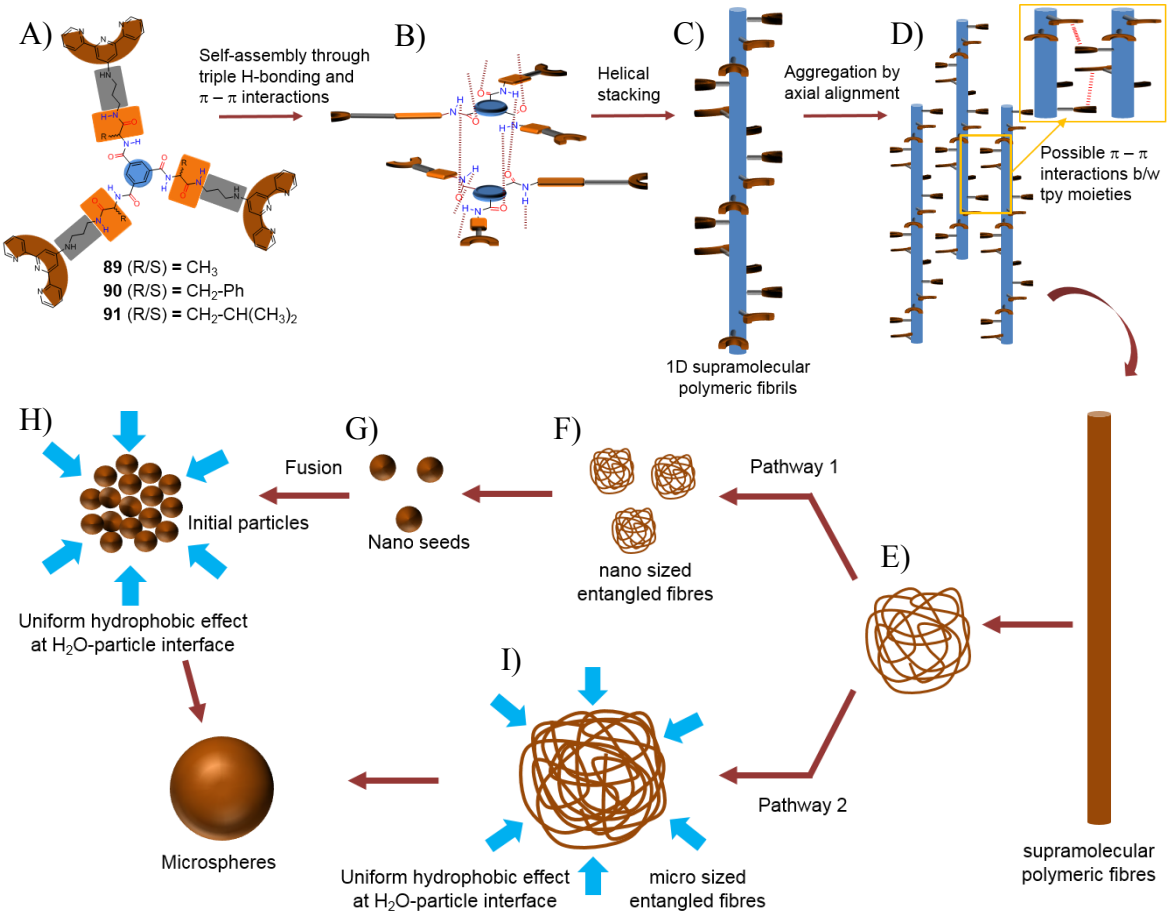

Figure 3.45: Schematic representation of the proposed mechanism for the microspheres formation from BTA molecules.

phenomenon observed in coiled coils.[341] Coiled coil is a structural motif in protein, consisting a heptad repeating unit $(abcdef)_n$, generally have the hydrophobic residues at a and d position, and polar residues at e and g positions. This repeating units folded to form the amphiphilic alpha-helical secondary structure. In aqueous environment, the hydrophobic nature of these structures causes them to undergo aggregation by axial alignment, which is a natural phenomenon seen in such structures. By varying the position of the hydrophobic residues dimers, trimers and tetramers have been reported.[341-343] When the a and d positions were replaced by phenylalanine a five-helix pentamer was reported.[344] Similarly, a heptamer was reported when e and g position was replaced with alanine.[345] Analogous to these aggregation, the supramolecular fibrils formed (Figure 3.45C) behave as coiled coils and may undergo axial alignment as discussed above (Figure 3.45D).

These fibres undergo entanglement due to their hydrophobic nature (Figure 3.45E). From this stage, two pathways might be are possible: *1*) Pathway one: If the entangled aggregates are nano-sized materials, they can form initial nano-seeds, which might undergo fusion, annealing and tight packing processes to finally yield microparticles, which was observed for tröger's base-based ICP particle by Mirkin *et.al*. (Figure 3.45, F-H);[247] or *2*) Pathway 2: If the entangled aggregates are micro-sized materials, they may form higher ordered aggregates by hydrophobic effect. These structures are then forced to undergo tight packing because of uniform hydrophobic effect at the particle-H_2O interface exerted by the H_2O molecules (Figure 3.45I). In either of the pathways proposed, the solid particles are obtained. Further investigation these systems were performed using optical microscopy techniques, which will be discussed in the next chapter.

In summary, the work described thus far, showed the difference in the self-assembly behaviour of the synthesised BTA molecules. The achiral molecule **88** formed the supramolecular gel having the rapid recovery properties, and such materials are highly attractive for applications as stimuli responsive materials. Because of the self-sorting property of **88**, it formed gel in presence of additives. Because of such properties, these systems are very attractive for the applications as multicomponent gel used in the synthesis of nanoparticles with controlled size and crystal growth of organic compounds in the gel matrix. The chiral analogues **89** - **91** (R and S) formed the microspheres. Investigation of these microspheres using various techniques such as, SEM, TEM, HIB, DLS, AFM, confirmed their solid spherical structures with the size of approx. 1 – 1.5 μm in diameter. These microspheres were disassembling when treated with urea, and such behaviour of the

microspheres is very attractive towards their application as delivery agents by encapsulating the cargo and its controlled release. Similarly self-sorting property of the chiral analogues **89** – **91** (R and S) forming microspheres in presence of second component draws the attention to use such systems to embed in other gel mediums for controlling their sizes. These results highly augmented the previous work of the Gunnlaugsson group relating to the self-assembly of BTA molecules. At the same time, this research has taken the work to the next level, with the introduction of new class of BTA molecules showing difference in their self-assembly properties to form different morphologies. Considering these results, the mechanism of the formation of microspheres through triple H-bonding and π - π interactions was proposed as discussed above. Further investigation these systems were performed using optical microscopy techniques, which will be discussed in the next chapter.

Chapter 4

Optical microscopy studies of microspheres

4 Introduction

Optical microscopy continues to be an important tool in the life sciences, allowing researchers to image, and therefore investigate the systems in sub-micrometre levels.[346] However, conventional fluorescence microscopy can have several drawbacks, such as light scattering and unwanted background noise induced by autofluorescence from chromophores.[347] The use of long-lived luminescent probes combined with pulsed excitation, and followed by subsequent delay prior to imaging or spectral acquisition, can eliminate these drawbacks.[348] Hence, time resolved or time-gated luminescence microscopy (TRLM) offers many advantages over conventional fluorescence microscopy.[349] The use of lanthanides as probes for such time-gated microscopy can be advantageous because of their various photophysical properties discussed previously (Section 1.5),[264] *e.g.* long lived emission properties (μs to ms), allowing time resolved detections and imaging.[350]

Microspheres formed from the chiral derivatives **89** – **91** (R and S) were investigated using a number of different microscopy techniques such as SEM, TEM, AFM and FIB as discussed in Chapter 3. In order to gain better understanding of these microspheres, they were next investigated using optical and laser scanning confocal microscopy (LSCM) techniques. The Ln(III)-based microspheres were analysed using an epifluorescence microscope adapted to perform the time-gated imaging and spectroscopic measurements,[350] the results of which are discussed in this chapter. As it was observed previously that the **89** (R and S) formed monodisperse microspheres in CH_3CN/H_2O mixture (6:4), therefore, **89** (R/S) was used in preparing the microspheres samples for optical microscopy investigations. Many of the studies done on microspheres described in this chapter, such as, optical microscopy (OM), LSCM imaging, time gated imaging and spectral acquisition, CPL and helical luminescence light (HLL) measurement were performed in collaboration with Dr Sandra Bright, School of Biochemistry, Trinity College, Dublin and Dr Robert Pal, Department of Chemistry, Durham University, UK.

4.1 Optical microscopy of microspheres

The microspheres used in the proposed experiments were prepared in solution in a similar manner to that described in Chapter 3, where **89** (R/S, 3 mg) was dissolved in a CH_3CN/H_2O mixture (6:4, 1 ml) by heating (100 ^oC) followed by cooling to RT. This resulted in a solution of microspheres with a concentration of 0.3% w/v. 100 μL of this solution of microspheres was transferred into a flow cell (ibidi μ-slides) (Figure 4.1A) and dried in air (12 hours) and

A)

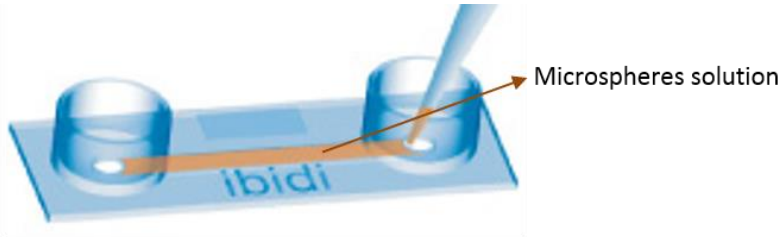

B) 488 nm transmittance image C) 458 nm reflectance image D) B and C merged.

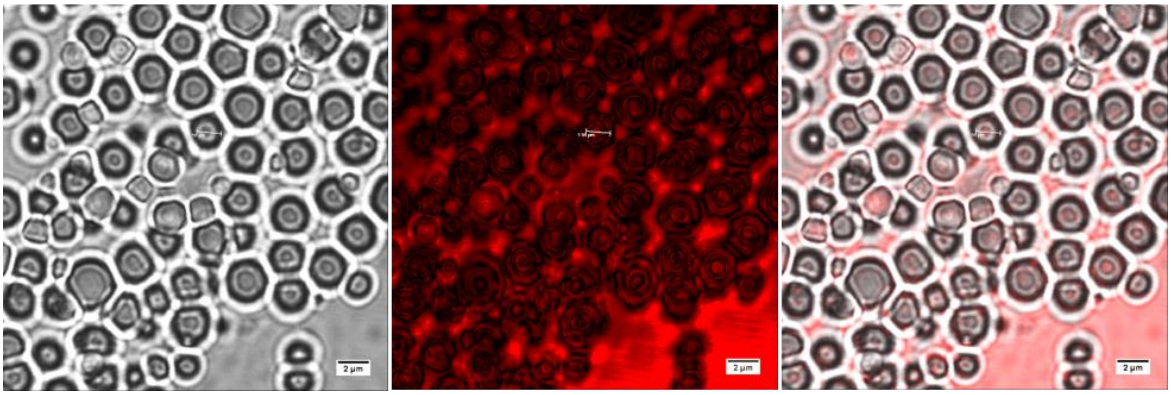

Figure 4.1: A) Schematic representation of transfer of microspheres solution into a flow cell. LSCM images of **89S** microspheres taken in different modes: B) 488 nm transmittance, C) 458 nm reflectance modes and D) A and B images merged.

vacuum (3 hours) to deposit the microspheres in the flow cell. After drying, the samples were imaged using Laser Scanning Confocal Microscope (LSCM) in optical microscopy modes: 488 nm transmission and 458 nm reflectance modes. From the images, microspheres were found to be spherical and distributed uniformly throughout the sample. The microspheres remained as individual particles, without showing aggregation or the connections between them, even in the regions of higher concentration of microspheres, similar to those observed in SEM, HIB and TEM as discussed Chapter 3. The particles were of different sizes varying from 1.5 – 2 μm in diameter (Figure 4.1, B-C). The apparent edges of the particles observed here instead of a spherical shape was only an artefact arising from the transmitted light from the source at the bottom and the close proximity of the particles. This was confirmed when the individual particles (staying apart) showed spherical shapes. As expected, **89R** showed similar images which are provided in Appendix A4.1.1.

4.2 Laser Scanning Confocal Microscopy (LSCM) of microspheres (in fluorescence mode)

The microsphere sample was imaged using LCSM using 405 nm as the excitation wavelength. Since the microspheres were prepared from tripodal molecules **89** (R and S) comprising fluorescent tpy moieties, it was envisaged that the microspheres would be also fluorescent in nature. As previously discussed in Chapter 3, the solutions of microspheres

showed a fluorescence band at λ_{max} = 489 nm on excitation at λ_{ex} = 405 nm. LSCM imaging of the **89** (R and S) microspheres discussed in this section 4.2 was performed in collaboration with Dr Sandra Bright, School of Biochemistry, Trinity College, Dublin.

Microspheres were prepared using **89** (R and S, c = 0.3% w/v) in solution of CH_3CN/H_2O (6:4) mixture by a heating-cooling cycle as described in Section 4.1 above. 10 µL of this solution was dropcast on a quartz slide and dried in air (12 h) and vacuum (3 h) to deposit the microspheres. Upon imaging the **89S** microspheres, the particles with similar spherical structures (as observed from SEM images discussed in Chapter 3) and blue fluorescence emission were observed, as shown in Figure 4.2. The fluorescence spectrum of these microspheres recorded in LSCM showed the emission band centred at 492 nm which was in good agreement with the fluorescence spectrum recorded using steady state fluorescence measurements (Figure 4.2C). This confirmed that the blue emission was

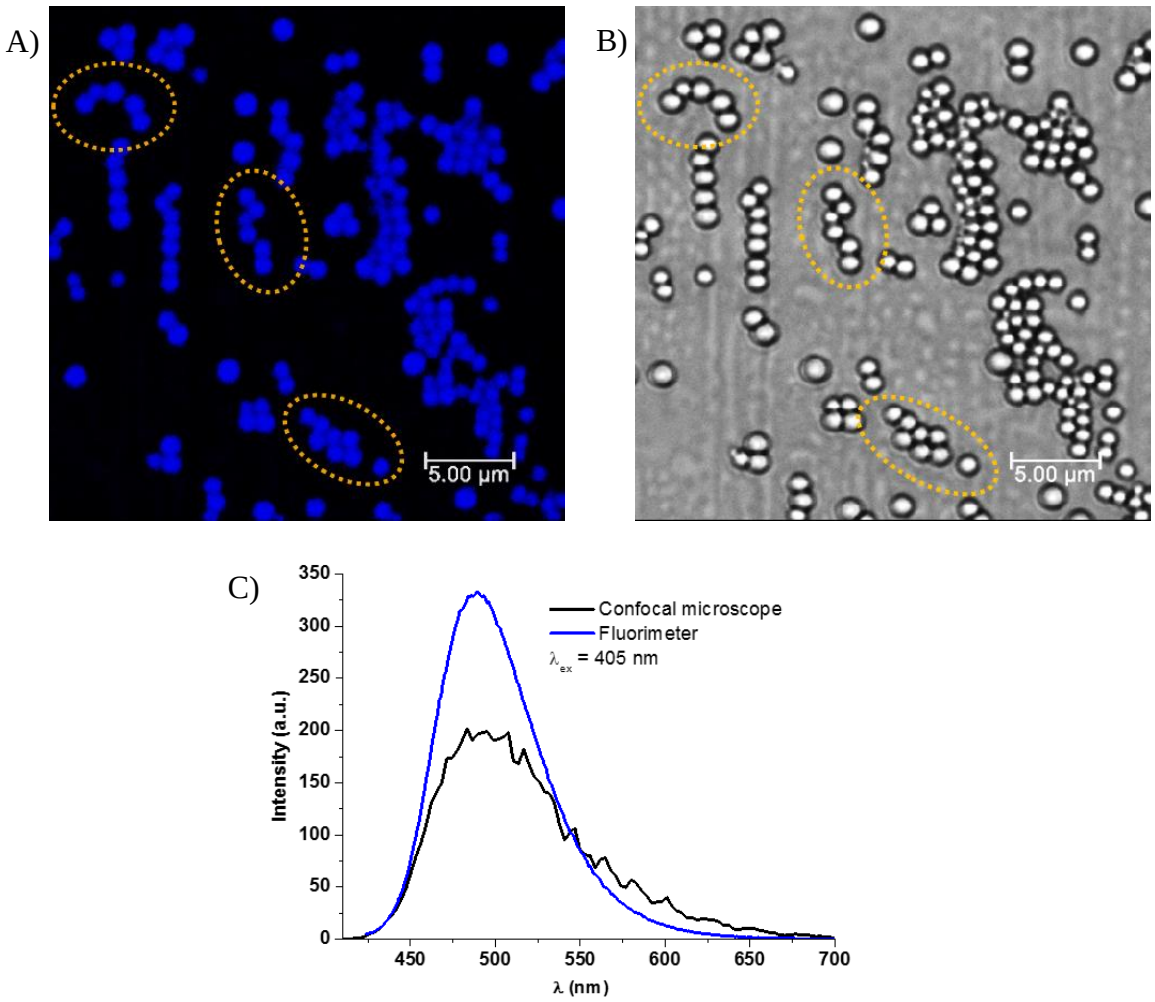

Figure 4.2: A) LSCM image of **89S** microspheres upon excitation at λ_{ex} = 405 nm, B) phase contrast image of the same sample and C) fluorescence spectrum of **89S** microspheres recorded in confocal microscope (black) and fluorimeter (blue).

exhibited from the tpy moieties when they were in an aggregated state forming the microspheres. This was confirmed further when the fluorescence emission recorded in the different areas of the sample showed a similar emission spectrum with no change in emission wavelength (λ_{max} = 492 nm). The LSCM image and the fluorescence spectrum recorded from different areas are provided in Appendix Figure A4.2.1. As expected, **89R** microspheres showed identical results to **89S** microspheres, indicating no difference between the two samples in their fluorescence emission, which showed the blue emission when imaged using LSCM upon excitation at λ_{ex} = 405 nm with fluorescence emission band centred at 492 nm. The LSCM images of the **89R** microspheres and its emission spectrum are provided in Appendix Figure A4.2.2.

4.3 LSCM Imaging of 89S microspheres in solution

After analysing the dried samples of microspheres exhibiting blue fluorescence, the microspheres were next imaged in solution media consisting of 6:4 CH_3CN/H_2O mixture using LSCM. Imaging of the microspheres in solution media preserves the structural morphology of the self-assembled aggregates/microspheres and avoids any possible change from the drying effects which might be possible in the conventional dried microspheres samples. The solution containing **89S** microspheres (c = 0.3%, 20 μL) was placed into a closed quartz petri dish and imaged using LSCM upon excitation at λ_{ex} = 405 nm (20 μL of sample solution was used here, instead of 10 μL as above, to avoid the quick drying of the solvent). LSCM images showed the presence of microspheres floating in the solution media

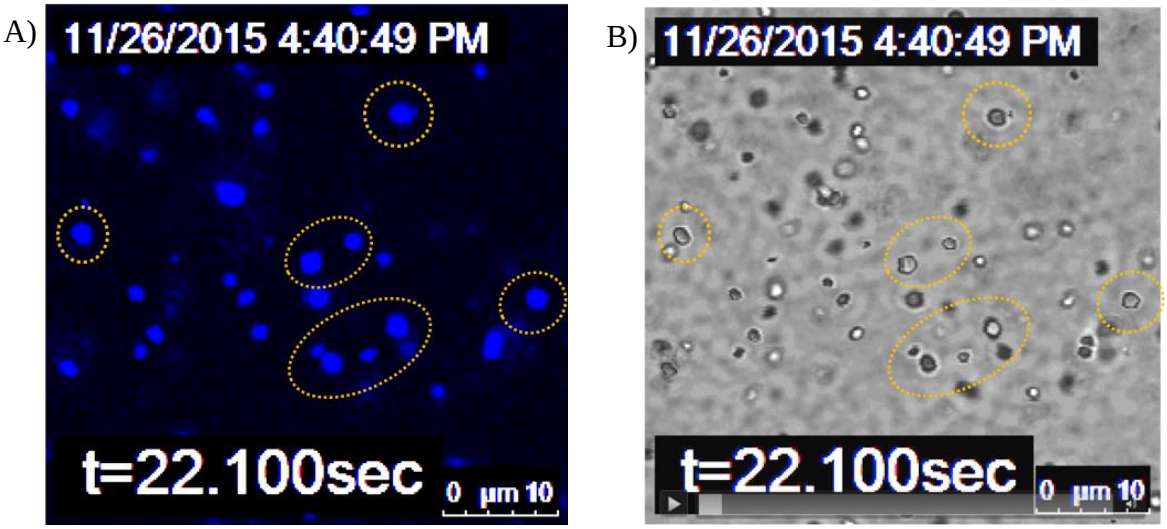

Figure 4.3: A) LSCM image of **89S** microspheres in solution media (6:4 CH_3CN/H_2O, λ_{ex} = 405 nm) and B) phase contrast image of the same sample. Movie recorded for this sample, showed the **89S** microspheres present in the solution appear and disappear at the surface, due to their constant movement.

exhibiting blue luminescence (Figure 4.3A). The particles were in the spherical shape as previously seen for dried samples in LSCM and SEM. From the LSCM image of the microspheres solution, only the particles which appear close to the surface were in focus (circled), and the others suspended beneath the surface were out of focus. This visual evidence again confirmed the microspheres existed in solution and ruled out the possibility of formation of microspheres during the drying process, when dropcast. Upon drying of the solvent, the microspheres suspended in the solution deposited on the quartz slide exhibiting the same spherical shape and blue luminescence as observed before in Figure 4.2, indicating the minor influence of the drying process on the structural morphology of the microspheres. As expected the **89R** microspheres also showed the presence of blue fluorescent microspheres in solution. (Appendix Figure A4.3.1), again, demonstrating that no difference was observed between R and S isomers.

4.3.1 Real-time investigation of the formation of 89S microspheres in solution using LSCM

After imaging the microspheres of **89S** present in the solution, their formation in solution was investigated in real-time using LSCM utilising the same experimental conditions as above. As discussed previously, in all the cases, the microspheres were prepared by a heat-cool cycle. Hence, it was hypothesised that while cooling, the dissolved compounds at higher temperature start to self-assemble and aggregate to form microspheres. Hence, in order to prove this, the **89S** (2 mg) was dissolved in CH_3CN/H_2O mixture (6:4, 1 ml) by heating to 100 ^oC. This hot solution (20 μL) was placed into a closed quartz petri dish and while this solution was cooling to RT, time-lapse observation was performed using LSCM at an excitation wavelength of 405 nm. As previously observed the blue luminescence exhibited by microspheres allowed the real-time imaging of the formation of microspheres. The images of the hot solution taken at different time intervals are shown in Figure 4.4 showing the formation of the microspheres (and the movie is also recorded for the same sample).

Upon imaging the hot solution, with in the time framed (while cooling), $t_0 - t_{31s}$, no aggregates were observed (Figure 4.4A). When the solution started to cool, it became clear that **89S** molecules started to form aggregates that became luminescent and could be observed. These luminescent aggregates (formed while cooling process continued) appeared at t_{31s}, (Figure 4.4B). Further decrease in the temperature resulted in the spontaneous formation of more microspheres at t_{33s}, indicating the beginning of microsphere formation (Figure 4.4C), and after t_{37s}, all the **89S** molecules in the dissolved state aggregated to form

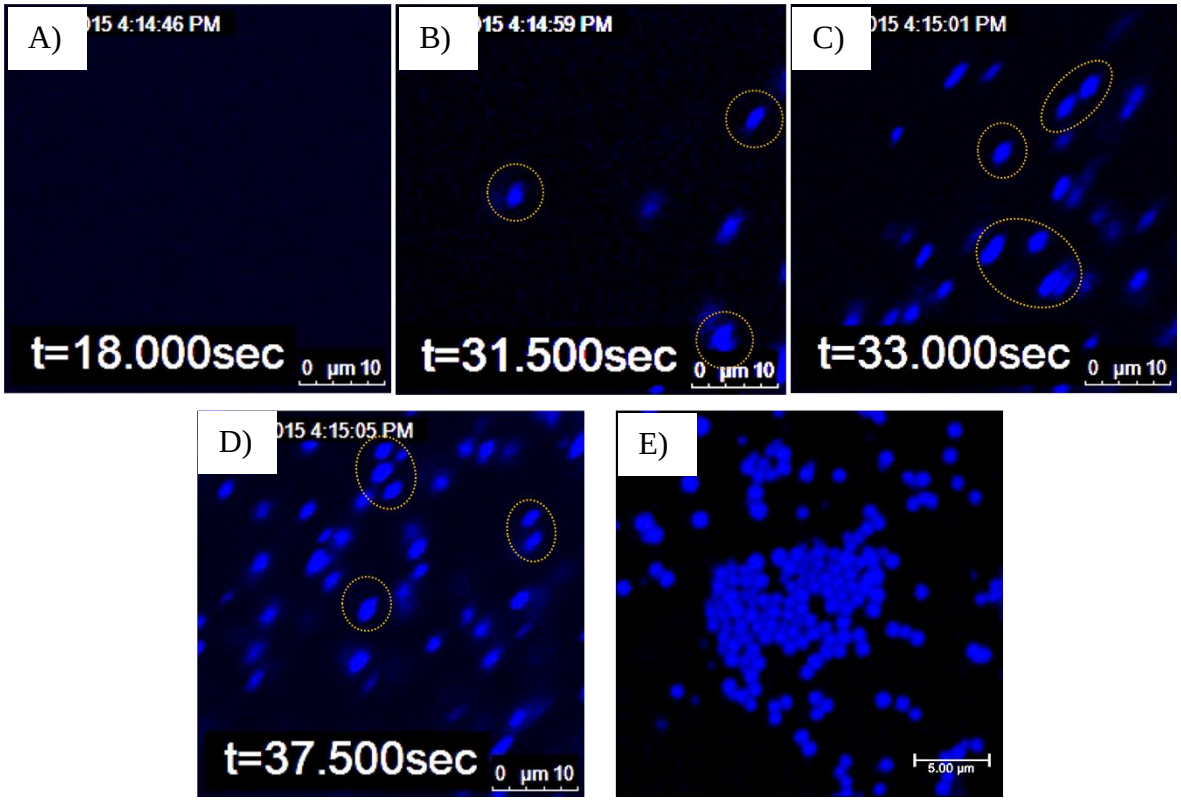

Figure 4.4: Snapshots taken from the movie recorded in LSCM, upon cooling the hot solution of **89S** in CH_3CN/H_2O mixture (6:4) with λ_{ex} = 405 nm. A) - D) LSCM images taken at different time intervals 18, 19.5, 33 and 37 seconds showing the formation of **89S** microspheres, scale bar 10 µm. E) LSCM image of the same sample after drying.

a large number of microspheres as observed in Figure 4.4D. Thus formed **89S** microspheres are stable in solution media and it was also observed that the microspheres are always in constant movement in solution without showing any signs of settling to the bottom. The constant movement of the microspheres is most likely due to the convection currents in the solution. When the dropcast solution was completely dried, the microspheres deposited in the quartz Petri dish, as shown in Figure 4.4E, appeared exactly as they were observed before in Figure 4.2. This matched exactly with the SEM images taken previously for the **89S** microspheres as discussed in Chapter 3. This real-time imaging of microsphere formation using LSCM is strong evidence that the microspheres are spontaneously formed in solution upon cooling the hot solution of **89S**. This again ruled out the possibility of formation of microspheres upon drying the drop-casted solution. The movie recorded for this sample showed the same results. LSCM images showing the formation of **89S** microspheres in more detail for the same sample are provided in Appendix Figure A4.3.2 and A4.3.3. The observations made here strongly support the proposed mechanism for the formation of microspheres discussed in Chapter 3, Section 3.16 (Figure 3.45). Similar observations were

made by De Cola *et al*., wherein, using LSCM they showed the real time transformation of the self-assembled species to form a thermodynamically stable self-assembled product over a longer time scale at room temperature.[325] Additionally, Hamachi *et al*. showed the real-time imaging of the formation of nanofibers by a peptide amphiphile (rapid formation in seconds time scale), when a hot solution of peptide amphiphile was deposited in buffer solution containing seeds.[339]

4.4 Stability of 89S microspheres in H_2O

In Chapter 3, section 3.13, it was discussed that, when the microspheres were immersed in H_2O, they were found to be interconnected to from a 2D network. In order to investigate this behaviour more, the dried microspheres were immersed in H_2O and analysed using LSCM. The advantage of using optical microscopy is that, the same area of the sample can be continuously monitored, which is difficult to achieve using SEM. The stability of the **89S** microspheres in H_2O and their disassembly process (using urea solution) discussed in this and following sections were performed in collaboration with Dr Robert Pal, Durham University.

To carry out this analysis, the microspheres were prepared in CH_3CN/H_2O (6:4, 1ml) solution in a similar manner described in Section 4.1 using **89S** (3 mg). 100 μL of this solution was transferred (dropcast) into a flow cell (ibidi μ-slides) (as shown in Figure 4.1A) and dried in air (12 h) and vacuum (3 h) to deposit microspheres in the channel of the flow cell. Then 100 μL of H_2O was added into the flow cell in order to immerse the dried microspheres in H_2O before analysing using LSCM. Imaging this sample over a period of time showed that after 60 mins the connections between the microspheres appeared, as shown in Figure 4.5. This gave additional evidence for the bridging between the

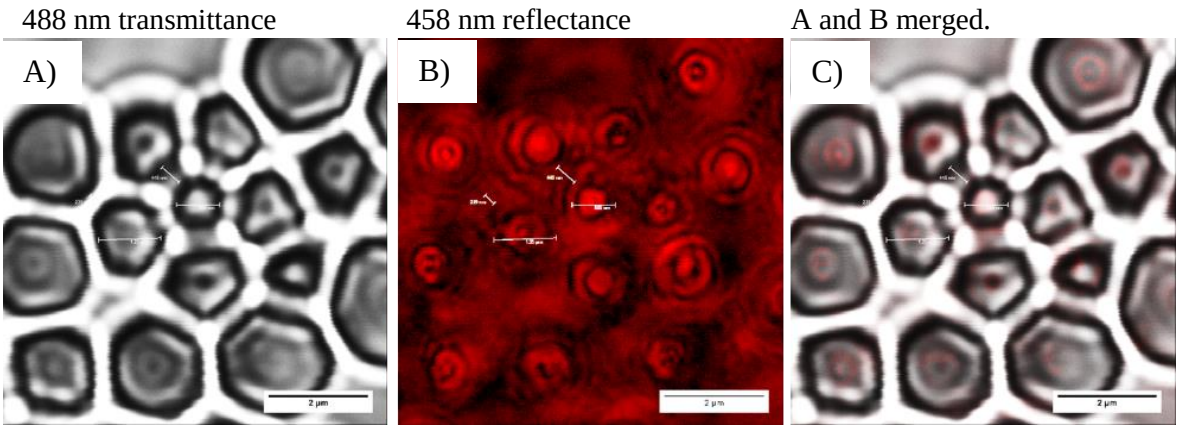

Figure 4.5: 89S microspheres connected to each other after immersion in H_2O for 60 mins. A) 488 nm transmittance, B) 458 nm reflectance modes and C) A and B images merged.

microspheres upon immersion in H_2O as discussed in Chapter 3, Section 3.13. As previously mentioned, the amphiphilic nature of the microspheres might be responsible for the bridging between the microspheres.

In order to investigate the stability of the microspheres in H_2O, in the next step, the microspheres were immersed in H_2O for a longer time and images were taken at different time intervals as shown in Figure 4.6 up to 8 hours. The microspheres were found to be stable up to 0 to 6 hours without showing any signs of dissolution (Figure 4.6, A - D). After 7 hours, some of the microspheres slowly started to merge with each other, indicating some dissolution of the microspheres (Figure 4.6E). After 8 hours, all the microspheres were found to be completely merged and the transformation of spherical shaped microspheres to solution based material occurred in H_2O (Figure 4.6F). LSCM images taken in 488 nm transmission and 458 nm reflectance modes at different time intervals are provided in Appendix Figure A4.4.1.

As a conclusion to this section, the results observed here supported the formation of bridges between microspheres discussed in Chapter 3. And in addition, the microspheres

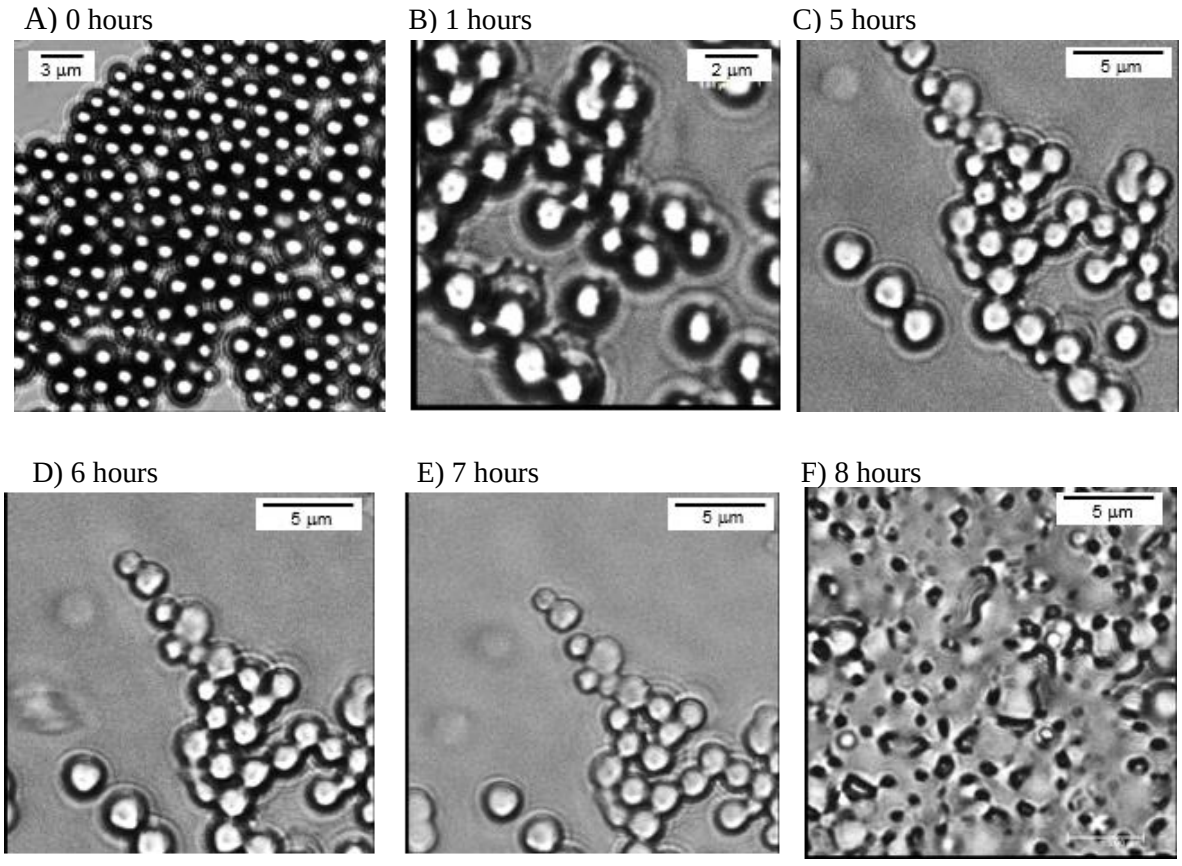

Figure 4.6: LSCM images (488 nm transmission mode) of **89S** microspheres immersed in H_2O taken at different time intervals, scale bar 5 µm.

were found to be stable and intact (preserving its structural morphology) for 6 hours in H_2O before merging with each other after 8 hours.

4.5 Interaction of solid microspheres with Urea in solution

In Chapter 3, section 3.7.2, the time dependent disassembly of **89S** microspheres was studied in the presence of urea using SEM. In order to gain better understanding of this disassembly process, the disassembly of **89S** microspheres were analysed in an urea solution of higher concentration (c_{urea} = 1% and 10% w/v) using LSCM.

4.5.1 Disassembly of microspheres using solution of Urea (C_{urea} = 1% and 10% w/v)

Microspheres prepared from **89S** (c = 0.3% w/v in 6:4 CH_3CN/H_2O) were deposited into a flow cell in a similar manner to that described in section 4.1. To this, 100 μL of urea solution in H_2O of concentration 1% w/v was added and the time dependence of disintegration of **89S** microspheres was monitored using LSCM. The LSCM images taken at different time intervals are shown in Figure 4.7.

It was observed that during the first 60 minutes, the microspheres were stable in the urea solution (c = 1% w/v) showing that their spherical shape was intact, and not showing any signs of disassembly (Figure 4.7, A – C). After 90 minutes, the microspheres were found to slowly begin to fuse with each other, indicating the start of the disassembly process. However, at this stage the microspheres still displayed aggregated spherical-kind structures, as can be seen in Figure 4.7D. After 120 minutes, all the microspheres were fused together and the spherical structure of the microspheres were completely lost (Figure 4.7E). After 150 minutes, the microspheres were completely disintegrated (Figure 4.7F). This indicates that the microspheres are stable in 1% urea solution until 90 minutes. LSCM images taken in 458 nm reflectance mode at different time intervals are provided in Appendix Figure A4.5.1.

Similarly, when urea solution with higher concentration of 10% w/v was used, the rate of **89S** microsphere disassembly was increased. From the LSCM images, the **89S** microspheres were stable in 10% urea solution until 20 minutes. After 30 minutes, the microspheres started to merge with each other (Figure 4.8A). After 40 minutes, the microspheres were completely fused and their spherical shape was lost (Figure 4.8B). Finally after 50 minutes, most of the microspheres had completely disassembled (Figure 4.8C). The same effect was observed after 150 minutes when 1% urea solution was used, as discussed above. From the rate of disassembly of **89S** microspheres in 1% and 10% urea solutions, respectively, it is observed that upon increasing the urea concentration tenfold, the rate of

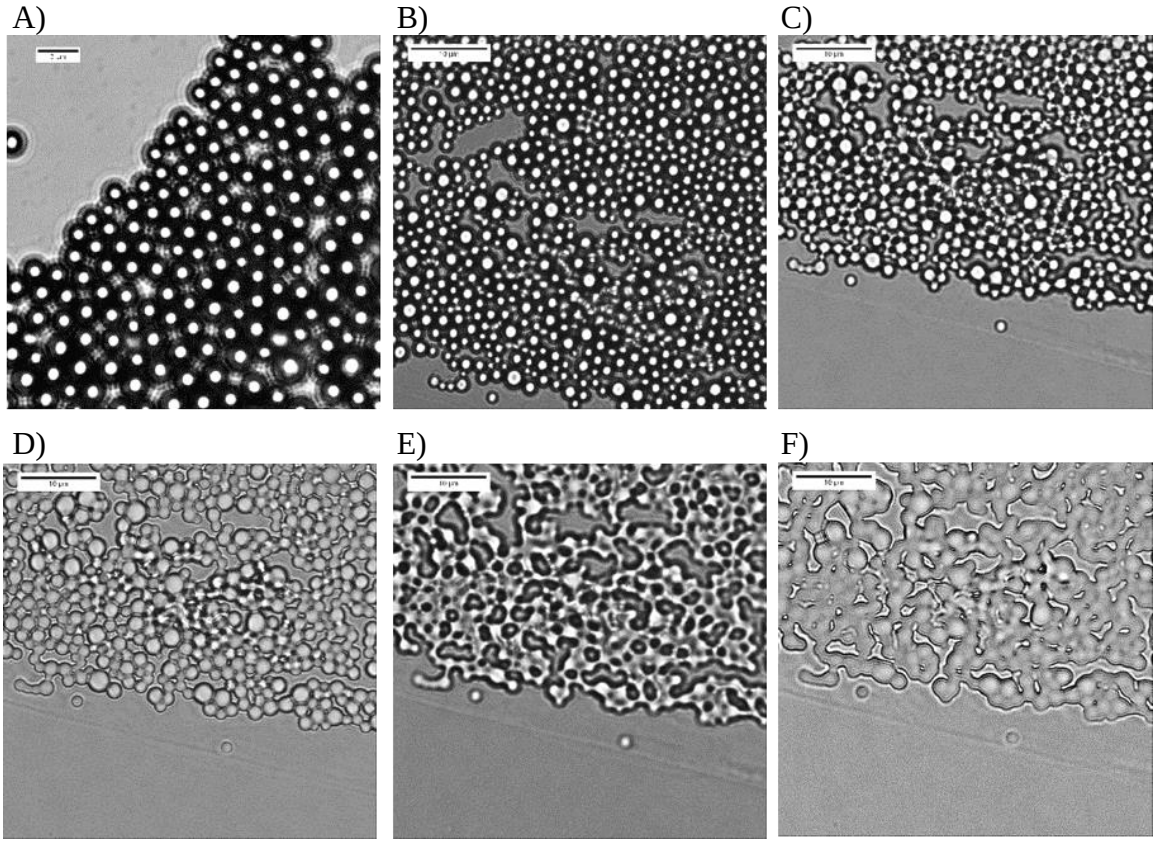

Figure 4.7: LSCM images (488 nm transmission mode) of **89S** microspheres in 1% urea solution showing disassembly process upon time: A) 0 mins, B) 30 mins, C) 60 mins, D) 90 mins, E) 120 minutes, F) 150 mins, scale bar 10 μm.

microsphere disassembly increased threefold. When the **89S** microspheres were treated with the urea solutions, competitive binding to the amide moieties of **89S** molecules on the surface of microspheres occurs (responsible for the self-assembly of the ligands). This resulted in the dissociation of the intermolecular H-bonding, with the consecutive disassembling of the microspheres.

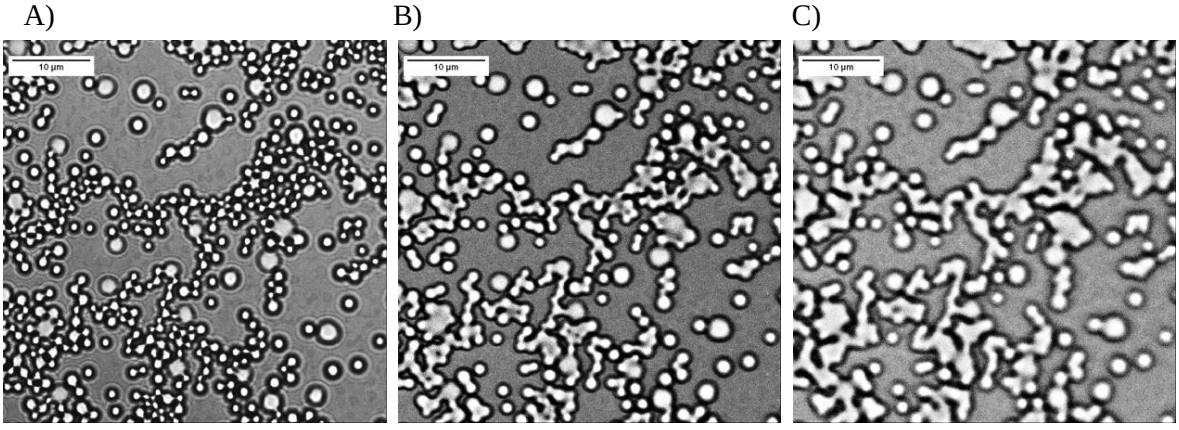

Figure 4.8: LSCM images (488 nm transmission mode) of **89S** microspheres in 10% urea solution showing disassembly process upon time: A) 20 min, B) 40 min and C) 60 min, scale bar 10 μm.

The results obtained in this section gave additional evidence for the disassembly of **89S** microspheres in the presence of urea to that observed previously in Chapter 3, Section 3.7.2. The progress of disassembly process of **89S** microspheres in 1% and 10% urea solutions are summarised in Table 4.1. This direct comparison of the rate of disassembly process in different concentration of urea clearly shows that the disassembly process of **89S** microspheres was three times faster in the 10% than the 1% solution urea solution. More detailed LSCM images showing the disassembly process of **89S** microspheres from 0 to 60 minutes in 10% urea solution are provided in Appendix Figure A4.5.2.

Table 4.1: Summary and comparison of the disassembly process of **89S** microspheres in 1% and 10% urea solutions.

Progress of disassembly process of 89S microspheres in 1% and 10% urea solution				
	time			
	60 min	**90 min**	**120 min**	**150 min**
1% urea solution	microspheres stable	microspheres started to fuse to each other	microspheres were completely fused to each other	microspheres were completely disintegrated
	time			
	20 min	**30 min**	**40 min**	**50 min**
10% urea solution	microspheres stable	microspheres started to fuse to each other	microspheres were completely fused to each other	microspheres were completely disintegrated

4.5.2 Effect of Urease on urea bound disassembled microspheres

In the previous sections it was discussed that, the binding of urea to microspheres resulted in competitive H-bonding that 'denatured' the microspheres and carefully disassembled them as a period of time. To investigate whether this was a reversible process, an attempt was made to remove the urea which was bound to disassembled microspheres, using an enzymatic approach, wherein the urea could be hydrolysed. In order to do that, first **89S** microspheres were treated with 10% urea solution for 60 minutes to disassemble the microspheres in similar manner as discussed in the previous section. The sample was then washed with water to remove excess of unbound urea, and the remaining sample treated with aqueous solution of urease (100 μL, as supplied) and the effect monitored using LSCM over a period of 3 hours. The use of urease catalyses the hydrolysis of urea in to CO_2 and NH_3 and results in the removal of urea bound to disassembled microspheres.[351] The recovery of the microspheres to their initial spherical structure was not observed, confirming the

irreversible nature of the disassembled microspheres using urea. The LSCM images of urease treated microspheres are provided in Appendix A4.5.3.

4.6 Effect of 355 nm UV irradiation on 89S microspheres

After studying the stability of microspheres in different conditions, to investigate their behaviour further, the photostability of the microspheres was analysed upon 355 nm UV irradiation with high laser power. To achieve this, a solution of **89S** microspheres (0.3% w/v, 10 µL) was dropcast on a 9 mm coverslip and dried, as previously described, to deposit **89S** microspheres. Then a predefined (greater than the total field of view) area was selected on the sample and irradiated using a 355 nm laser with 100% laser intensity (80 mW, 25 x 25 µm area, 512x512 pixel, 100 Hz bidirectional scan, 4 υs/pixel dwell time) for 10 minutes continuously. It was observed that only the microspheres exposed to the 355 nm UV irradiation (inside the aforementioned Region Of Interest (ROI) area, highlighted in a yellow

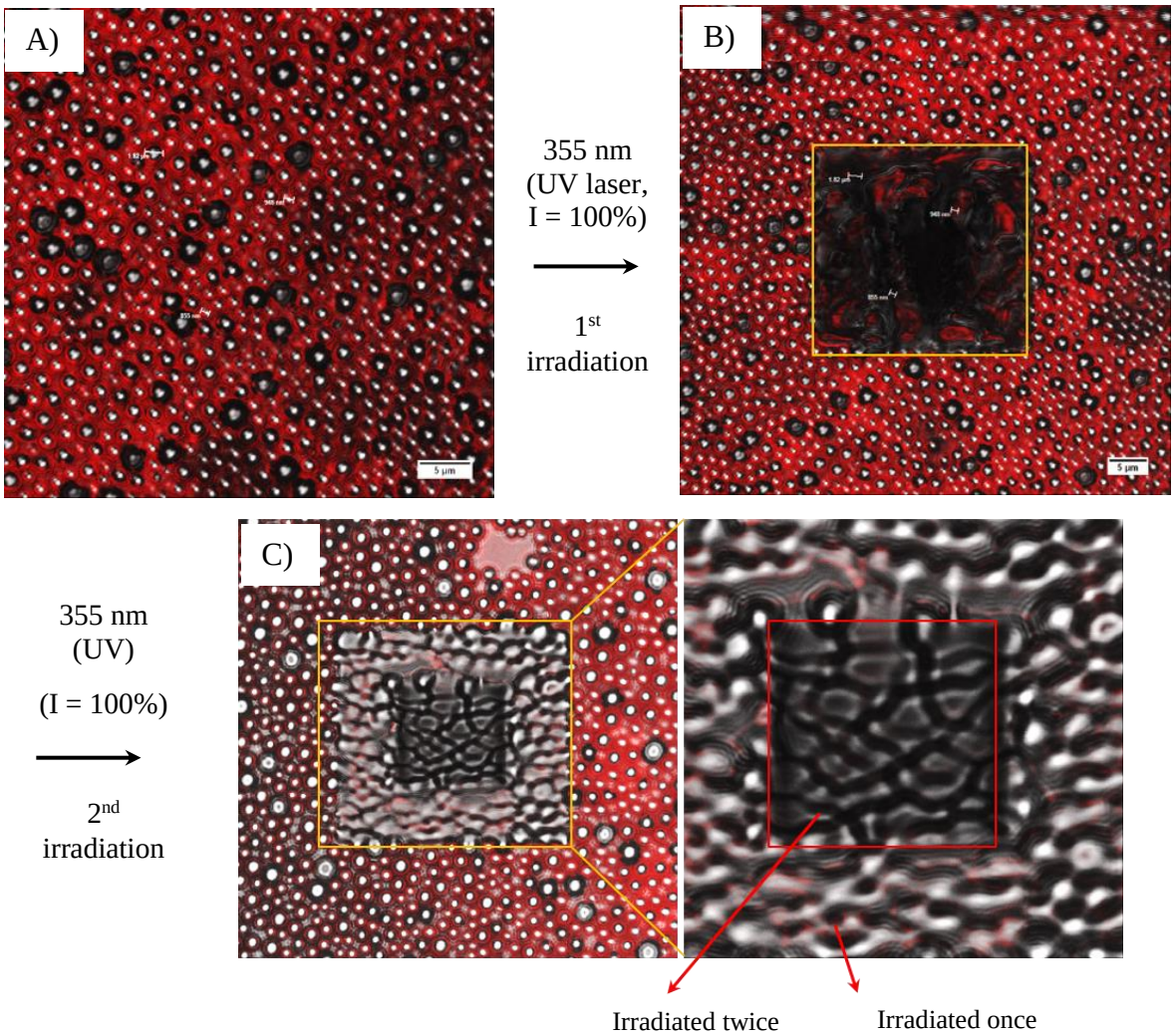

Figure 4.9: LSCM images (488 nm transmittance and 458 nm reflectance mode images merged) A) **89S** microsphere before UV irradiation, Scale bar 5 µm, B) After 355 nm UV irradiation inside a selected area (yellow square) and C) After irradiating a second time.

box, Figure 4.9B) were disassembled and it was clear that they lost their spherical structures. It was verified by infrared thermospot analysis (built in microscope feature) that, even upon irradiating the sample for a longer time, the temperature was not increased, hence the possibility of melting or thermal degradation of the microspheres was ruled out. However, the microspheres in the unexposed part of the sample were undisturbed. Upon second irradiation, a larger area was selected outside the original section and irradiated (also using 355 nm UV laser with 100% laser intensity for 10 minutes); the results are shown in Figure 4.9C: it was observed that, the inner part of the exposed area (red square) showed more damage due to the longer exposure time, while the outer part (yellow square) showed the same effect to that observed after the first irradiation. It was predicted that, irradiating the sample with of the 355 nm UV laser (with 100% intensity), might result in the excitation of the **89S** molecules in the microspheres and may cause the intermolecular H-bonds to break (which was responsible for microsphere formation), thus resulting in the disassembly of microspheres. LSCM images of the same sample in 488 nm transmittance and 458 nm reflectance mode are provided in Appendix Figure A4.6.1. Since the disassembled microsphere sample was in very small quantity, the analysis of the sample by NMR or mass spectrometry were not be possible in order to check the chemical decomposition of the **89S** molecules. Presumably this phenomenon was analogous to the photobleaching or instability of many organic dyes via irreversible photodegradation.[352-353]

From this experiment, the microspheres were found to be disassembled when irradiated with excessive 355 nm UV laser power. However, when using the same laser at the lower, suitable intensity of ~10%, showed no effect on the morphology of the microspheres and also the disintegration of the microspheres was not observed over long periods of continues scanning. Therefore, using this 355 nm UV laser with 10% intensity, the Ln(III)-based luminescent microspheres were imaged, which will be discussed in the further sections.

4.7 Lanthanide based luminescent microspheres

The two most frequently used visible light emitting lanthanides are Eu(III) and Tb(III).[16] In chapter 3, Sections 3.8, it was discussed, that upon addition of Ln(III) (Ln = Eu and Tb) ions to the solution of **89R** and **89S** microspheres, the Ln(III) ions became coordinated to the tpy moieties on the surface of the microspheres, resulting in interconnections between the microspheres; this lead to the formation chains and networks. It was also shown that connections between the microspheres were achieved only after adding more than 0.7 mole

equivalents of Ln(III) salts (with respect to **89R** and **89S**) to the microspheres solution and after 1 hour of exposure. Spectrophotometric analysis also showed the characteristic emission from respective Ln(III) ions bound to the microspheres. Hence, it was envisaged that by adding appropriate amount (controlled addition) of Ln(III) ions to the solution of microspheres, luminescent microparticles can be obtained (Figure 4.10)

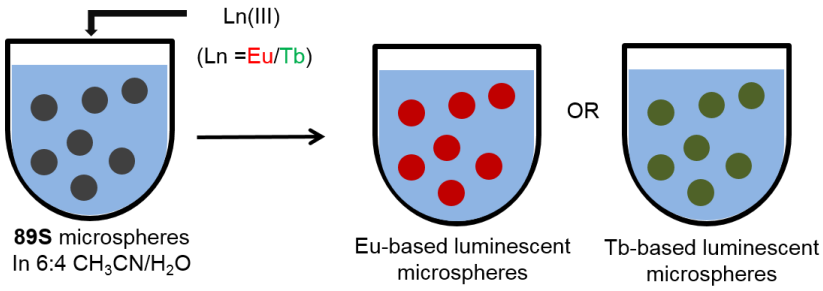

Figure 4.10: Schematic representation of Eu(III) and Tb(III)-based luminescent microspheres.

4.7.1 Determination of minimum amount of Ln(III) ions required for the formation of luminescent microspheres

The appropriate amount of Ln(III) ions (Ln = Eu and Tb) required to obtain luminescent microspheres with maximum emission intensity was determined. In order to do so, both the fluorescence and the Ln(III)-centred emission spectra were recorded and monitored after the addition of the respective Ln(III) ions to the solution of the **89S** microspheres. Monitoring the spectral changes as a function of Ln(III) concentration allowed the determination of maximum emission obtained from the Ln-based microspheres. These experiments were reproduced several times (4 – 5 times) in order to ensure the reproducibility of the data.

4.7.1.1 Determination of Eu(III) concentration for the formation of luminescent microspheres

As above, **89S** microspheres were prepared in solution using **89S** (4 mg) in 6:4 CH_3CN/H_2O (2 ml) to obtain a concentration of microspheres of c = 1.55×10^{-3} M (this is also the concentration of **89S** as molecular components). $Eu(CF_3SO_3)_3$ was then added from a stock solution ($c_{Eu} = 3 \times 10^{-2}$ M, in 6:4 CH_3CN/H_2O) and the changes in the fluorescence emission spectra were monitored upon excitation at 380 nm. The fluorescence emission from the microspheres at 489 nm immediately began to be quenched upon addition of Eu(III) as shown in Figure 4.11; the decrease in the luminescence (by *ca*. 88%) *ca*. after the addition of *ca*. 0.6 equiv. of Eu(III) before gradually quenching completely. This behaviour was the consequence of the sensitisation process occurring through the energy transfer between the

triplet excited state of the microsphere ($S_1 \rightarrow T_1$) acting as an antenna to the $^5D_0$ excited state of the Eu(III), indicating the binding of Eu(III) ions to the tpy moieties. These results were found to be reproducible with minor variation after repeating the experiment 4 times, confirming in all occasions the luminescence quenching upon the addition of *ca.* 0.6 equiv. of Eu(III).

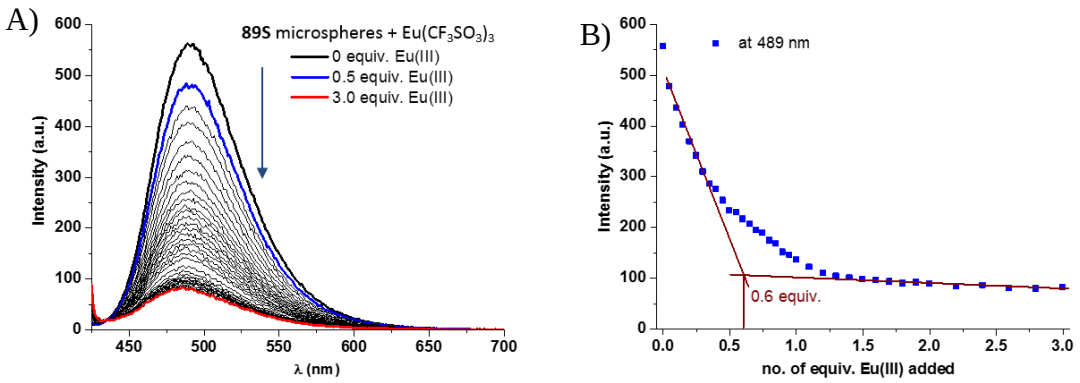

Figure 4.11: A) Fluorescence spectra of **89S** microspheres (1.55×10^{-3} M) upon addition of $Eu(CF_3SO_3)_3$ ($0 \rightarrow 3$ equiv.) in 6:4 CH_3CN/H_2O (λ_{ex} = 380 nm). B) Binding isotherm showing the changes at 489 nm.

The Eu(III) luminescence emission resulting from the sensitisation process was also monitored by recording the phosphorescence spectra upon excitation at 380 nm (Figure 4.12). Over the course of the Eu(III) titration, gradual enhancement in the characteristic Eu(III) luminescence was observed until the addition of 0.55 equivalents, of Eu(III). This indicates the binding of Eu(III) ions onto the microsphere and as such the successful transfer of energy from tpy moieties to Eu(III) metal centre. In particular, $^5D_0 \rightarrow {}^7F_{1\text{-}4}$ transitions were observed, showing the emission bands centred at 580, 618, 653 (very weak) and 697 nm respectively. After 0.55 equivalents, a decrease was observed in the emission intensity. Upon further increasing the concentration of Eu(III), intensity continued to decrease until 1.3 equivalents leading to the observed intensity changes as shown in Figure 4.12B.

In conjunction with these titrations, the Eu(III) centred luminescence lifetimes were measured by fitting the Eu(III) excited state decay profiles of the most intense peak (λ = 618 nm) to monoexponential decays, these being seen in Figure 4.12C. The longest lifetime of 0.49 ms was recorded upon the addition of 0.55 equivalent of Eu(III). Further addition of Eu(III) resulted in decreased lifetimes values, this being in good agreement with the Eu(III) emission profiles observed above. These experiments were found to be reproducible using fresh stock solutions of **89S** microspheres.

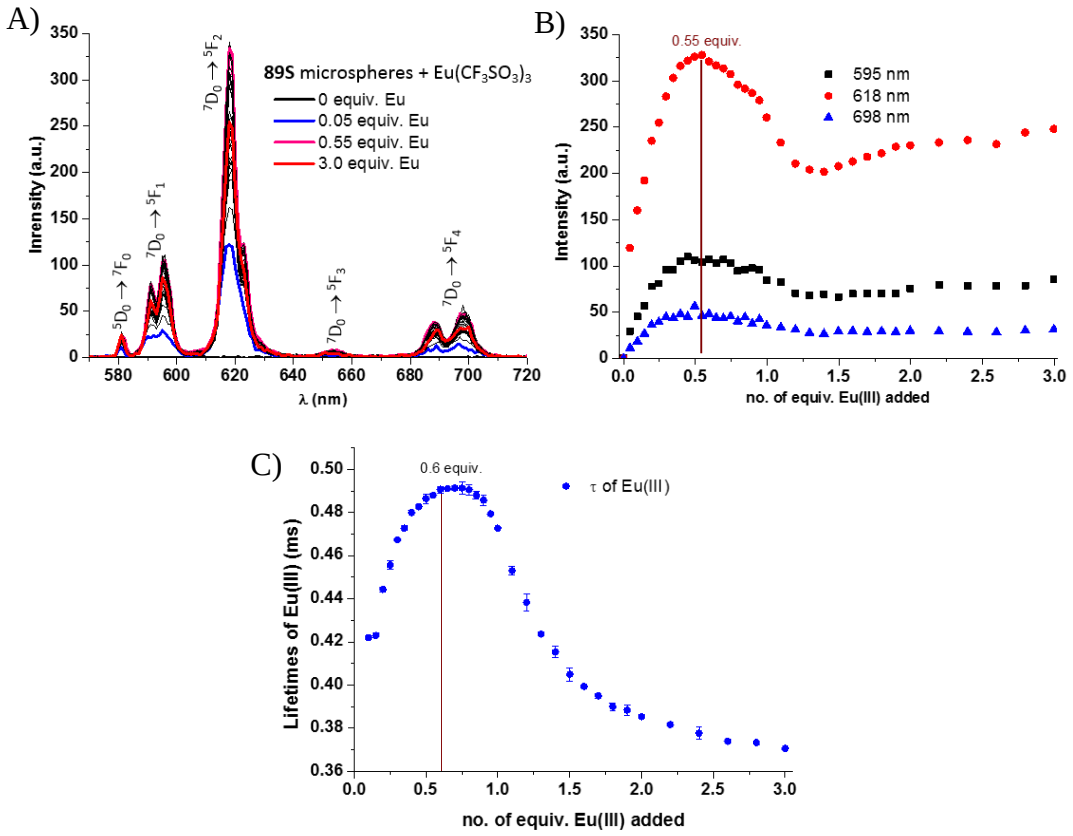

Figure 4.12: A) Phosphorescence spectra recorded upon addition of $Eu(CF_3SO_3)_3$ (0 → 3 equiv.) to the solution of **89S** microspheres (1.55×10^{-3} M) in 6:4 CH_3CN/H_2O. B) Binding isotherms showing the changes in Eu(III) centred emission at 595, 618 and 698 nm. C) Variation in the Eu(III) centred luminescence lifetimes during the course of Eu(III) addition to **89S** microspheres. Lifetime values showed here are the average of three measurements. The excitation spectrum (λ_{em} = 618 nm) recorded for this titration are provided in Appendix A4.7.1. The titration shown here represents the reproducible trends observed several times (4 – 5 times).

In order to see if any effect was observed by counter ion, the same experiments were performed using $Eu(NO_3)_3$, wherein identical results were obtained, the results are provided in Appendix Figure A4.7.2. When $Eu(CF_3SO_3)_3$ and $Eu(NO_3)_3$ salts were used, in both cases, microspheres were most luminescent when 0.55 – 0.6 mole equiv. of Eu(III) ions were added.

4.7.1.2 Determination of Tb(III) concentration for the formation of luminescent microspheres

The spectroscopic changes observed upon addition of $Tb(CF_3SO_3)_3$ to a solution of **89S** microspheres were comparable to those discussed above for Eu(III). The fluorescence intensity of **89S** microspheres centred at 489 nm was quenched upon addition of Tb(III) ions until reaching the plateau upon addition of 1.2 equiv. of Tb(III) (Appendix Figure A4.7.3).

The phosphorescence emission spectra recorded upon excitation at 377 nm showed the characteristic Tb(III) emission bands centred at 494, 543, 584 and 621 nm (the $^5D_4 \rightarrow {}^7F_J$ transitions, where $J = 6 - 3$) as shown in Figure 4.13. Addition of Tb(III) resulted in the gradual enhancement of the Tb(III) centred emission until 1.2 equivalents. Further addition of metal ions (up to 4.0 equivalents) resulted in only minor changes in the emission.

During the course of the Tb(III) titration, the excited state lifetimes were measured by fitting the Tb(III) excited state decay profiles of 543 nm band to monoexponential decays. The longest lifetime of 0.38 ms was recorded when 1.2 equivalents of Tb(III) had been added, with the minor increase in lifetimes upon further Ln(III) addition. This is in good agreement with the Tb(III) emission profiles observed. These experiments were fully reproduced 4 times using fresh stock solutions of **89S** microspheres. As expected, identical

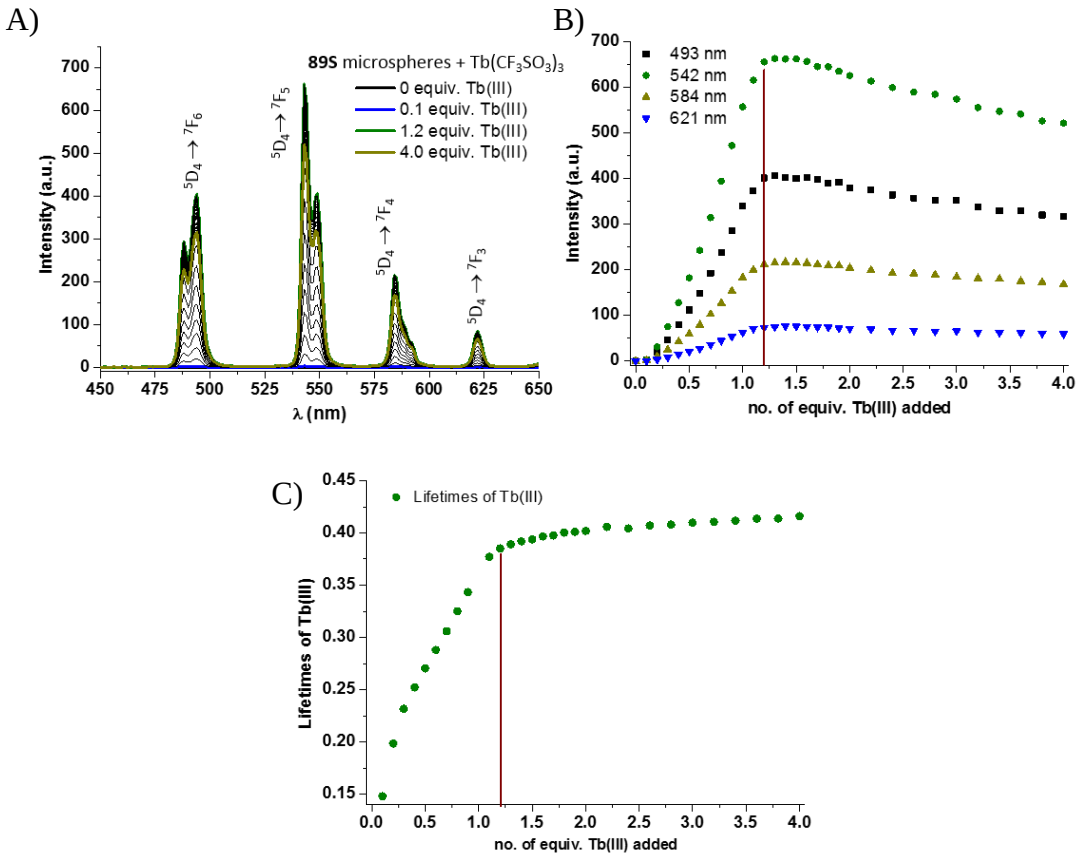

Figure 4.13: A) Phosphorescence spectra recorded upon addition of $Tb(CF_3SO_3)_3$ ($0 \rightarrow 4$ equiv.) to the solution of **89S** microspheres (1.55×10^{-3} M) in 6:4 CH_3CN/H_2O. B) Binding isotherms showing the changes in Tb(III) centred emission at 493, 542, 584 and 621 nm. C) Variation in the Tb(III) centred luminescence lifetimes during the course of Tb(III) addition to **89S** microspheres. Lifetime values showed here are the average of three measurements. The excitation spectrum (λ_{em} = 543 nm) recorded for this titration are provided in Appendix A4.7.3. The titration shown here represents the reproducible trends observed several times.

results were obtained when the same experiments were performed using $Tb(NO_3)_3$, the results of which are provided in Appendix Figure A4.7.4.

From the information obtained from these two experiments, 0.6 and 1.0 equiv. of Eu(III) and Tb(III) ions, respectively, were added to the solutions of **89S** microspheres and the resulting Ln(III)-based luminescent microspheres were investigated using LSCM, the results of which will be discussed in further section.

4.8. Investigation of Lanthanide based luminescent microspheres using LSCM

Having investigated the Ln(III) emission intensity profiles of the microspheres as a function of Ln(III) ion concentration, the next step was to prepare the Ln(III)-based luminescent microspheres. In order to do so, the appropriate amounts of either Eu(III) or Tb(III) ions were added to the solutions of microspheres. The resulting solutions were then dropcast on quartz slides and imaged using LSCM equipped with an excitation source of 355nm (~10% laser intensity was used) and triple channel imaging detector. These channels were; Channel 1: 390 – 500 nm (window for the autofluorescence from the microspheres), Channel 2: 500 – 550 nm (window for Tb(III) emission) and Channel 3: 570 – 720 nm (window for Eu(III) emission). As expected, the LSCM images of these Ln(III)-microspheres showed that they were luminescent giving either green or red emission. Additionally, the spectroscopic and lifetime measurements of these Ln(III)-microspheres were performed using a second microscope (adapted for spectral measurements) with excitation source of λ_{ex} = 365 nm.[350] The two microscopes used for the above mentioned investigations had limited (fixed) excitation sources. Therefore, the excitation sources of λ_{ex} = 355 nm and 365 nm were used for LSCM imaging and spectral measurements, respectively. All the LSCM imaging, spectroscopic and lifetime measurements of Ln(III)-based microspheres using the microscope were performed in collaboration with Dr Robert Pal, Department of Chemistry, Durham University. The results of these studies are discussed below.

4.8.1 Eu(III) and Tb(III) based luminescent 89S microspheres

89S microspheres were prepared in 6:4 CH_3CN/H_2O (1 ml) using **89S** (3 mg, 2.33×10^{-3} moles, c = 0.3% w/v) as described in section 4.1. To this solution $Eu(CF_3SO_3)_3$ (0.84 mg in 17 μL H_2O, 0.6 equivalent) was added (as shown in Figure 4.10) and the resulting solution was stirred for 20 minutes (to minimise the ‘‘aggregation or connections’’ between particles), and 10 μL of this solution was dropcasted on a quartz slide and dried. The resulting Eu(III)-**89S** microspheres were investigated using aforementioned LSCM with an

A) B) C)

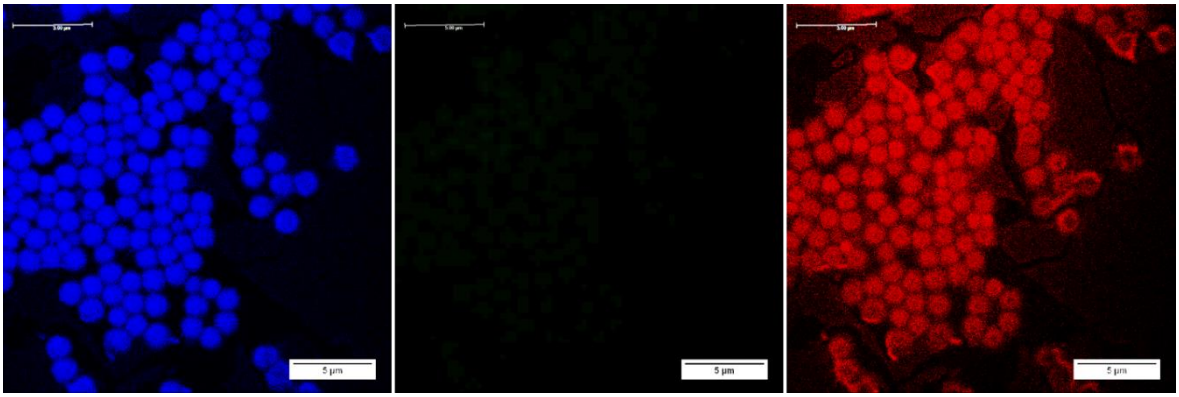

Figure 4.14: LSCM images of Eu(III)-**89S** microspheres in three different channels. A) Channel 1 showing autofluorescence from **89S** microspheres, B) Channel 2 showing no emission (due to lack of Tb(III)) and C) Channel 3 showing red emission form Eu(III) ions. Scale bar 5 μm.

excitation wavelength of 355 nm (laser intensity = 10%). Channel 1 showed the blue luminescent microspheres due to the autofluorescence, and Channel 3 showed the red light emitting microspheres as the result of sensitisation of Eu(III) ions from tpy moieties of microspheres as shown in Figure 4.14, A and C. As expected nothing was observed from Channel 2 as Tb(III) was not present (Figure 4.14B).

Similarly, addition of $Tb(CF_3SO_3)_3$ (1.4 mg in 28 μL H_2O, 1 equivalent) to the solution of **89S** microspheres resulted in the formation of Tb(III)-**89S** microspheres. LSCM images of Tb(III)-microspheres (λ_{ex} = 355nm, laser intensity = 10%) showed the blue autofluorescence of particles in Channel 1 and Channel 2 showed the green emitting microspheres possessing Tb(III) ions. As expected nothing was observed from Channel 3 as Eu(III) was absent (Figure 4.15).

A) B) C)

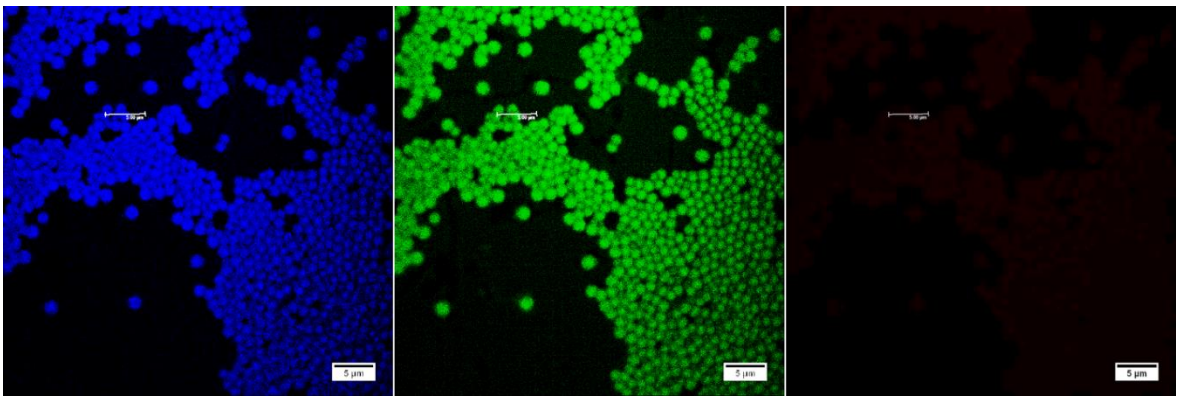

Figure 4.15: LSCM images of Tb(III)-**89S** microspheres in three different channels. A) Channel 1 showing autofluorescence from **89S** microspheres, B) Channel 2 showing green emission form Tb(III) and C) Channel 3 showing no emission (due to lack of Eu(III)). Scale bar 5 μm.

4.8.2 Mixed Eu(III)-Tb(III) based luminescent 89S microspheres

Since the combination of blue, green and red emission gives white light,[354] it was expected that, upon addition of a mixture of Eu(III) and Tb(III) ions to the solution of the **89S** microspheres, might result in the formation of mixed Eu(III)-Tb(III) based luminescent hybrid microspheres with the emission characteristics of both the Ln(III), and exhibit white-light emission. Hence, a mixture of Eu(III) and Tb(III) at 0.3 and 0.5 mole equivalents, respectively, was added to the solution of prepared **89S** microspheres (**89S** = 3 mg, 2.33×10^{-3} moles) in 6:4 CH_3CN/H_2O (1 ml) solution mixture (Figure 4.16). The resulting solution was dropcast (10 μL) onto a quartz slide and analysed using LSCM in the similar manner to that previously discussed (*i.e.* λ_{ex} = 355nm, laser intensity = 10 %). From the LSCM images, Channel 1 showed once again the blue luminescent **89S** microspheres (due to the autofluorescence) and Channel 2 showed the green light emitting microspheres due to the successful sensitisation of the Tb(III) exclusively, and while in Channel 3 the red light, due to the sensitisation of Eu(III) ions, was observed, Figure 4.17, A- C.

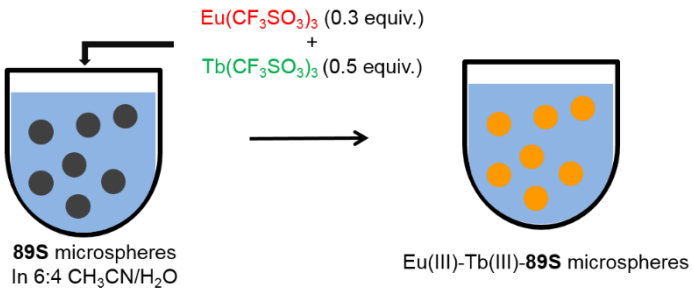

Figure 4.16: Schematic representation of the formation of mixed Eu(III)-Tb(III)-**89S** luminescent microspheres.

As anticipated, when merging channels 2 and 3, an orange-yellow light emitting microspheres were observed due to the contribution of the two primary colour (green and red), Figure 4.17E. While merging all 3 Channels, white-light emitting microparticles were observed, Figure 4.17D, as the result of the contribution from the blue, green and red light emissions. The LSCM images of Ln(III)-**89S** microspheres taken in OM modes and the CIE chromaticity diagram with coordinates 0.63 and 0.35 for Figure 4.17E showing orange particles are provided in Appendix Figures A4.8.1 – A4.8.3. Since a time-gated spectra was recorded for this sample in the microscope, CIE coordinates for Figure 4.17D could not be obtained.

Similarly, Andersen *et al*. reported a white-light emitting metallogel using the terpyridyl-end-capped polymer as ligand and Eu(III)/Tb(III) mixture.[355] Very recently our

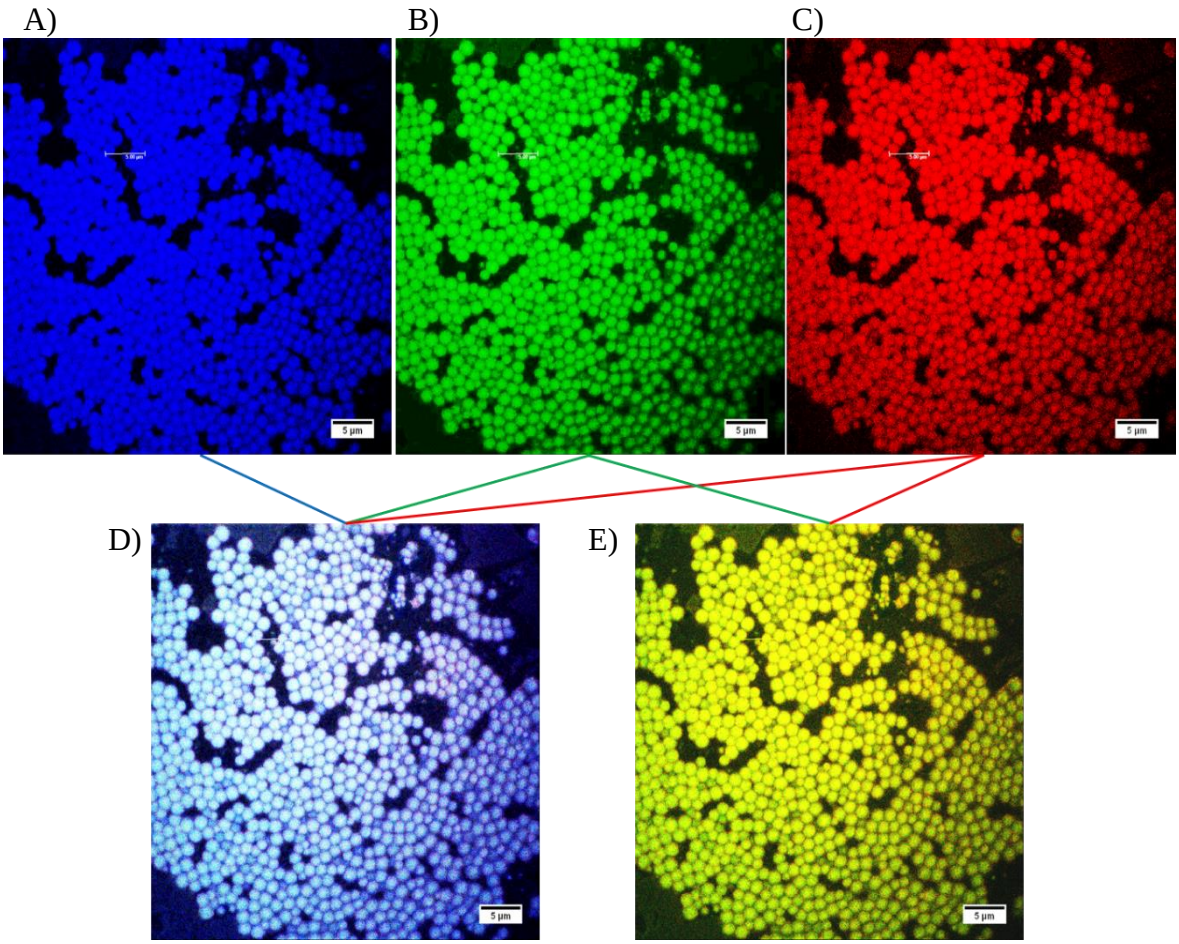

Figure 4.17: LSCM images of mixed Eu(III)-Tb(III)-**89S** microspheres in three different channels. A) Channel 1 showing autofluorescence from **89S** microspheres, B) Channel 2 showing green emission form Tb(III), C) Channel 3 showing red emission from Eu(III), D) Channel 1, 2 and 3 merged: showing white light emitting particles. The particles are little bluish because of strong autofluorescence and E) Channel 2 and 3 merged: showing orange particles. Scale bar 5 μm.

group reported a white-light emitting system based on a discrete heterometallic Ln(III) complex using a ligand possessing terpyridyl moieties.[354]

4.8.3 Time gated imaging and spectral measurements of Ln(III)-89S microspheres

The above Ln(III) based luminescent microspheres were further investigated using a custom built epifluorescence microscope that had been adapted for time gated imaging and spectroscopy. The adaption involves the use of pulsed light source (λ_{ex} = 365 nm), time gated camera, spectrometer and photon counting detector. This setup allowed the time gated imaging, emission spectroscopy and lifetime, measurements to be probed.[350] The camera also allowed variable acquisition time, with high signal to noise ratio (S/N) and high sensitivity.

Time gated full frame imaging of Ln(III)-**89S** microspheres was achieved using a time gated monochromatic camera coupled to the above described microscope. The conditions for imaging involved a 1 ms illumination pulse, followed by a 5 μs delay time and subsequent 50 ms averaging time. The accumulated 50 images were averaged to 1. Time-gated images of the Eu(III)-**89S** microspheres, Tb(III)- **89S** microspheres and the mixed Eu(III)-Tb(III)-**89S** microspheres showed their respective luminescence as represented in Figure 4.18. Since the camera used for accumulating images was monochromatic, and hence, the emission from Eu(III) and Tb(III) appeared as white instead of the red and green, respectively.

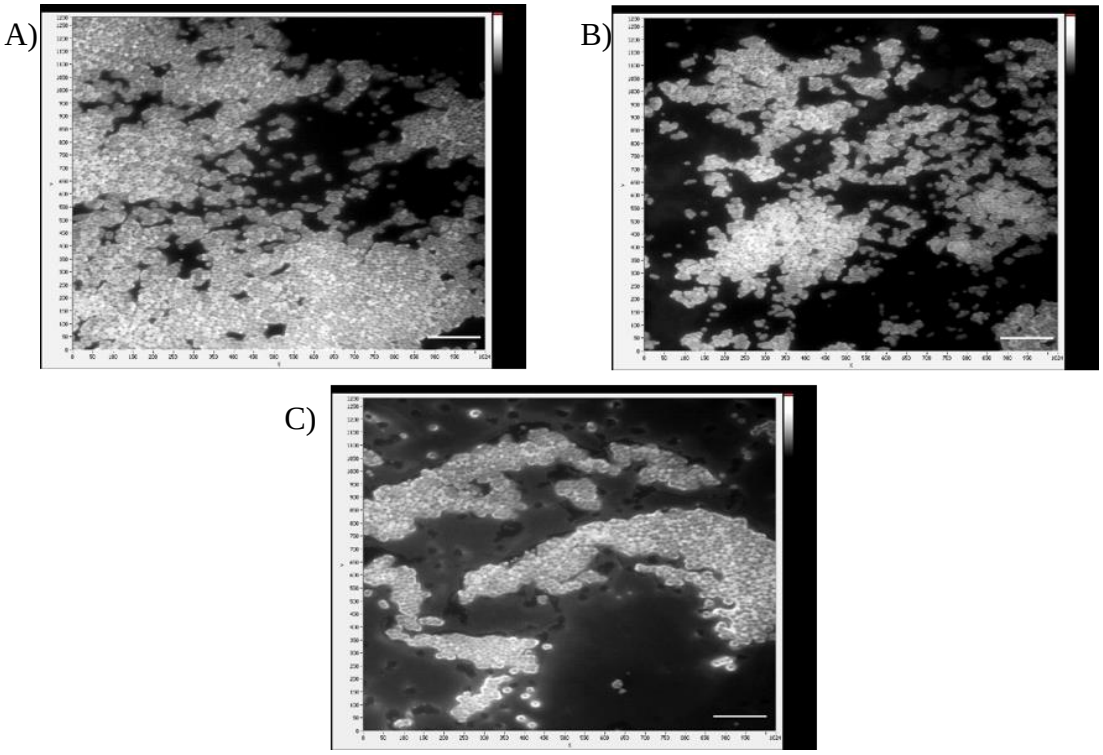

Figure 4.18: Time gated epifluorescence image of A) Eu(III)-**89S** microspheres, B) Tb (III)-**89S** microspheres and C) mixed Eu(III)-Tb(III)-**89S** microspheres ($t_{illumination}$ = 1 ms, t_{delay} = 5ms, $t_{acquire}$ = 50 ms and 50 average acquisition image), scale bar = 10 μm.

Time-gated spectroscopic measurements of the emission of Ln(III)-**89S** microspheres was achieved using the same microscope attached with a time gated CCD spectrograph system ($t_{illumination} = 1\ ms, t_{delay} = 20\ \mu s, t_{acquire} = 1–3\ ms$). Exciting the Ln(III)-**89S** microspheres with λ_{ex} = 365 nm pulse of light resulted in the appearance of the respective characteristics sharp line-like emission bands between 450 – 720 nm. Hence, the Eu(III)-**89S** microspheres showed emission bands centred at 580 (very weak), 594, 617, 651 (very weak) and 698 nm, all of which were the Eu(III)-centred emissions (Figure 4.19, red).[249, 356] Similarly, the Tb(III)-**89S** microspheres showed emission bands centred at 491,

544, 584 and 622 nm, (Figure 4.19, green). The emission spectra of the Eu(III) and Tb(III) based **89S** microspheres recorded in the aforementioned setup microscope were structurally similar to the emission spectrum obtained in solution and discussed in section 4.7 above. The spectra showed predominantly, Eu(III) emission bands, with the Tb(III) emission being much less intense (Figure 4.19, orange-yellow). This indicates that the Tb(III) emission was being quenched by the Eu(III) ions,[354] which might be the reason for predominantly orange luminescence.

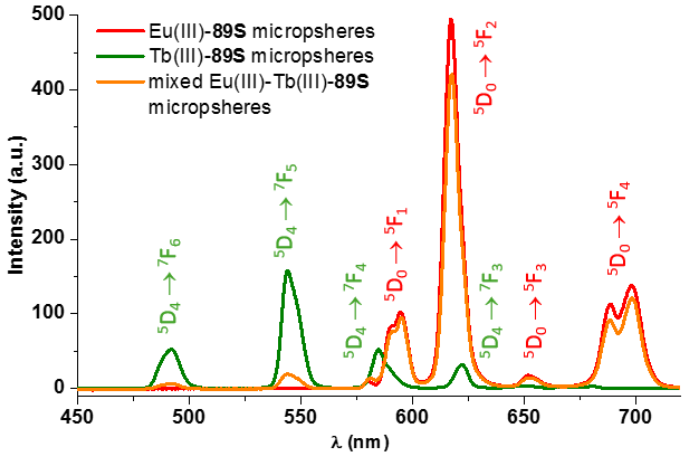

Figure 4.19: Time gated emission spectra of Tb(III)-**89S** microspheres (green), Eu(III)-**89S** microspheres (red) and mixed Eu(III)-Tb(III)-**89S** microspheres (orange), λ_{ex} = 365 nm.

Further investigation of these systems was performed by measuring the Ln(III) luminescence lifetimes of the Ln(III)-**89S** microspheres using the same microscope equipped with a time-correlated photon counting detector. This detector was coupled to an interference filter for Eu(III) and Tb(III) and a digitizer, which can perform 100-1000 accumulation cycles with a variable delay time (of 10 – 100 μs) between illumination and time correlated multiphoton counting (TCMPC). The software allows the decay profile to be fitted to mono exponential decays to obtain the lifetime (τ). Phosphorescence lifetimes of Eu($^5D_0$) and Tb($^5D_4$) were obtained by fitting the decay profiles of the λ_{em} = 620 nm and 546 nm peaks for Eu(III) and Tb(III), respectively to monoexponential decays (wherein the $\lambda_{excitation}$ = 365 nm, $t_{illumination}$ = 100 μs, t_{delay} = 20 μs, $t_{acquire}$ = 50ms, 1000 accumulations). For Eu(III)-**89S** microspheres, the Eu(III) excited state lifetimes were found to be 1.40 ms, and 0.50 ms for Tb(III)-**89S** microspheres. In the case of mixed Eu(III)-Tb(III)-**89S** microspheres, the Eu(III) and Tb(III) lifetimes were found to be 1.09 ms and 0.18 ms, respectively, Figure 4.20. In mixed Eu(III)-Tb(III)-**89S** microspheres, the Eu(III) lifetime was quenched by 33% in

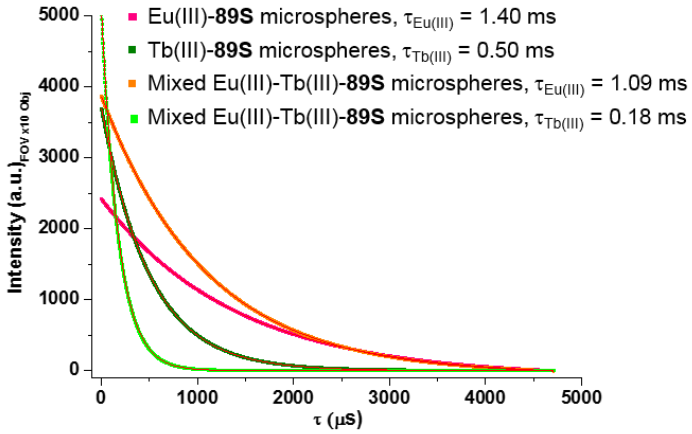

Figure 4.20: Eu(III) and Tb(III) centred luminescence lifetimes in Ln(III)-based microspheres. red: $\tau_{Eu(III)}$ in Eu(III)-**89S** microspheres = 1.4 ms, olive: $\tau_{Tb(III)}$ in Tb(III)-**89S** microspheres = 0.5 ms, orange: $\tau_{Eu(III)}$ in mixed Eu(III)-Tb(III)-**89S** microspheres = 1.09 ms, green: in mixed Eu(III)- Tb(III)-**89S** microspheres = 0.18 ms.

comparison with Eu(III)-**89S** microspheres and the Tb(III) lifetime was quenched by 65% in comparison to that seen for the Tb(III)-**89S** microspheres. This observation indicated that an energy transfer was likely taking place from the Tb($^5D_4$) excited sate to the Eu($^5D_0$).[354] Therefore, it can be concluded that orange-yellow emission from the mixed Eu(III)-Tb(III)-**89S** microspheres is due to the energy transfer form Tb(III) to Eu(III) metal centres. Similar observations were made in multimetallic Ln(III)-based trinuclear[357] and dinuclear Ln(III) complexes,[358] polymers doped with mixed Ln(III) complexes aggregated to form nanoparticles,[356] MOF,s possessing mixed Eu/Tb-adipate framework.[359]

Ln(III)-**89S** microsphere solutions dropcast and dried on a quartz slide showed their luminescence under UV light (λ_{ex} = 365 nm) is shown in Figure 4.21. As expected **89S** microspheres showed only blue fluorescence (Figure 4.21A), while Eu(III)-**89S** microspheres and Tb(III)-**89S** microspheres showed their red and green luminescence,

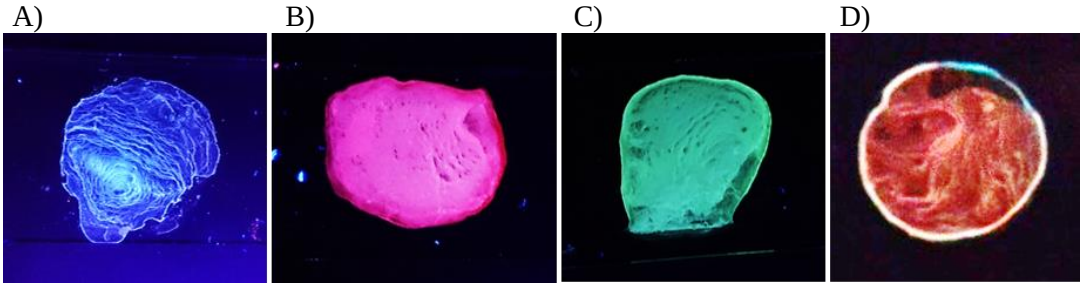

Figure 4.21: Luminescence of A) **89S** microspheres, B) Eu(III)-**89S** microspheres, Tb(III)-**89S** microspheres, mixed Eu(III)-Tb(III)- **89S** microspheres under UV light (λ_{ex} = 365 nm).

respectively (Figure 4.21 B and C), and the mixed Eu(III)-Tb(III)-**89S** microspheres showed orange-yellow luminescence (Figure 4.21D).

4.8.4 Mixture of Eu(III)-89S microspheres and Tb(III)-89S microspheres

In section 4.8.2, the addition of Eu(III) and Tb(III) ions to a solution of **89S** microspheres, yielded the orange light emitted by mixed Eu(III)-Tb(III)-**89S** microspheres. Having observed this, an attempt was made to obtain an image of this system in which both the Eu(III)-**89S** microspheres and the Tb(III)-**89S** microspheres exist independently, exhibiting red and green emission in the same sample, as depicted schematically in Figure 4.22.

In order to do this so, the solutions of Eu(III)-**89S** microspheres and Tb(III)-**89S** microspheres were prepared separately as described in section 4.8.1. Then, equal volumes of each solution (0.5 ml) were mixed, and 10 μL of the resulting solution dropcasted onto a quartz slide and dried. This gave a deposit of Eu(III)-**89S** microspheres and Tb(III)-**89S** microspheres mixture, that was then imaged in LSCM upon excitation at 355 nm (laser intensity 10%). Unfortunately, distinguishable Eu(III)-**89S** microspheres and Tb(III)-**89S** microspheres, showing red and green particles in the same image were not observed. Instead, an orange light emitting particles were observed as had previously been seen in the case of mixed Eu(III)-Tb(III)-**89S** microspheres in Figure 4.23A. (LSCM images of the same sample taken in different channels are provided in Appendix Figure A4.8.4.)

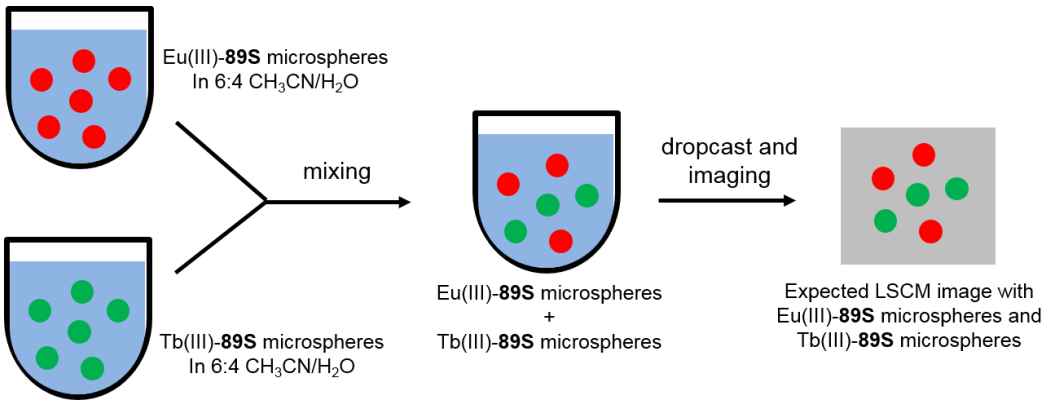

Figure 4.22: Schematic representation of the Eu(III)-**89S** microspheres and Tb(III)-**89S** microspheres in the same image.

Upon closer examination of Figure 4.23A, some particles appeared to be more orange coloured than others, while other particles appeared to be more greenish. This indicated that the Eu(III)-**89S** microspheres emitted predominantly orange light and Tb(III)-**89S** microspheres emitted predominantly green light, suggesting that the two Ln(III)-**89S**

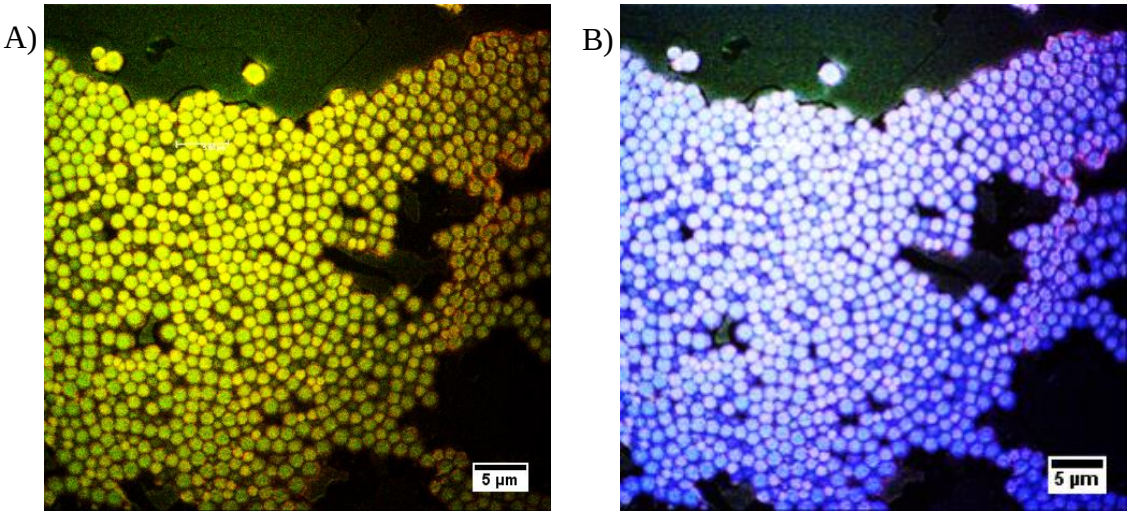

Figure 4.23: LSCM image of mixture of Eu(III)-**89S** microspheres and Tb(III)-**89S** microspheres solution. A) Channel 2 and 3 merged, and B) Channel 1, 2 and 3 merged.

microspheres existed independently in the same system upon mixing. However, this difference in the shading between the particles was not observed in the previously discussed Eu(III)-Tb(III)-**89S** microspheres (Figure 4.17E). Wherein all the particles exhibited unified orange light emission due to the contribution from Eu(III) and Tb(III) both present within the same microsphere.

Time gated luminescence measurements (t_{delay} = 20 µs) performed on this sample, exciting at λ_{ex} = 365 nm (using the above mentioned microscope adapted with time gated spectrograph systems), showed the two main emission bands at 544 nm and 618 nm, occurring from the respective Tb(III)-**89S** microspheres and Eu(III)-**89S** microspheres (Figure 4.24A). Both of these bands were roughly of equal intensities, without showing any

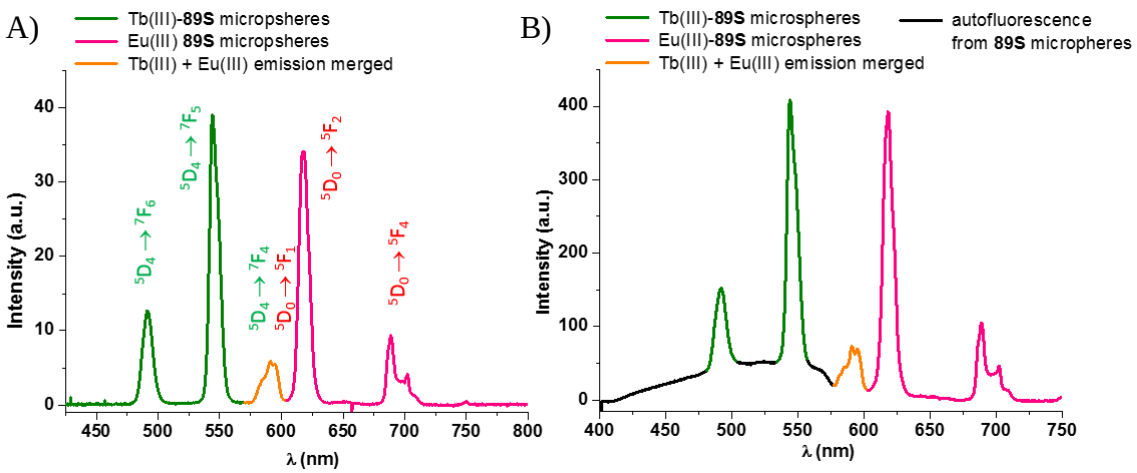

Figure 4.24: Emission spectra of the mixture of Tb(III)-**89S** microspheres and Eu(III)-**89S** microspheres recorded in a custom built microscope. A) Time gated emission spectrum (t_{delay} = 20 µs) and B) steady-state emission spectrum of the same sample.

kind of quenching in the Tb(III) emission as observed previously in the mixed Eu(III)-Tb(III)-**89S** microspheres systems (Figure 4.19). This indicated again that the Tb(III)-**89S** microspheres and Eu(III)-**89S** microspheres exist independently in the sample.

When non-time gated luminescence spectra (t_{delay} = 0 μs) of the same sample were measured, emission from the Tb(III)-**89S** microspheres (Figure 4.24B, green) and the Eu(III)-**89S** microspheres (Figure 4.24B, red) was observed along with the autofluorescence band associated with **89S** microspheres (Figure 4.24B, black, 450 – 650 nm range). This broad autofluorescence band covers the green region (525 – 575 nm) and the orange region (575 – 625 nm) of the visible spectrum. Therefore, the orange luminescence arising from the tailing effect (575 – 625 nm) was merging with the green emission from the Tb(III)-**89S** microspheres making it orange-green particles instead of pure-green. Furthermore, when the green luminescence from the autofluorescence (525 – 575 nm region) merged with the red emission form Eu(III)-**89S** microspheres, an orange emission instead of red was observed.

Having analysed these particles with LSCM, time-gated and steady-state spectroscopic methods, it was found that the autofluorescence was merging with Ln(III) emission resulting in the orange-green and orange emission instead of green and red emission from Tb(III)-**89S** microspheres and Eu(III)-**89S** microspheres, respectively.

With the aim to obtain the green and red light emitting particles within the same system, solid Tb(III)-**89S** microspheres and Eu(III)-**89S** microspheres were mixed and analysed. In order to do that, solutions of both the Eu(III)-**89S** microspheres and the Tb(III)-**89S** microspheres were prepared as described in section 4.8.1. Each of these solutions was then dropcast onto a glass slide (separately) and dried to deposit Eu(III)-**89S** microspheres and Tb(III)-**89S** microspheres. After drying, the particles were scratched of the slide and mechanically mixed to obtain a mixture of the microspheres, which was imaged using LSCM (λ_{ex} = 355 nm. 10% laser intensity, delay time of 5 μs). The LSCM images of this sample showed both the green and red light emitting microspheres coexisting in the same sample, Figure 4.25A.

Non-time gated or steady-state luminescence measurements (λ_{ex} = 365 nm, t_{delay} = 0 μs) of the sample using the microscope with spectrograph systems showed the two main emission bands at 544 nm and 618 nm, occurring from the respective Tb(III)-**89S** microspheres and Eu(III)-**89S** microspheres along with a broad autofluorescence band from the **89S** microspheres (Figure 4.25B). This proves the co-existence of the Tb(III)-**89S**

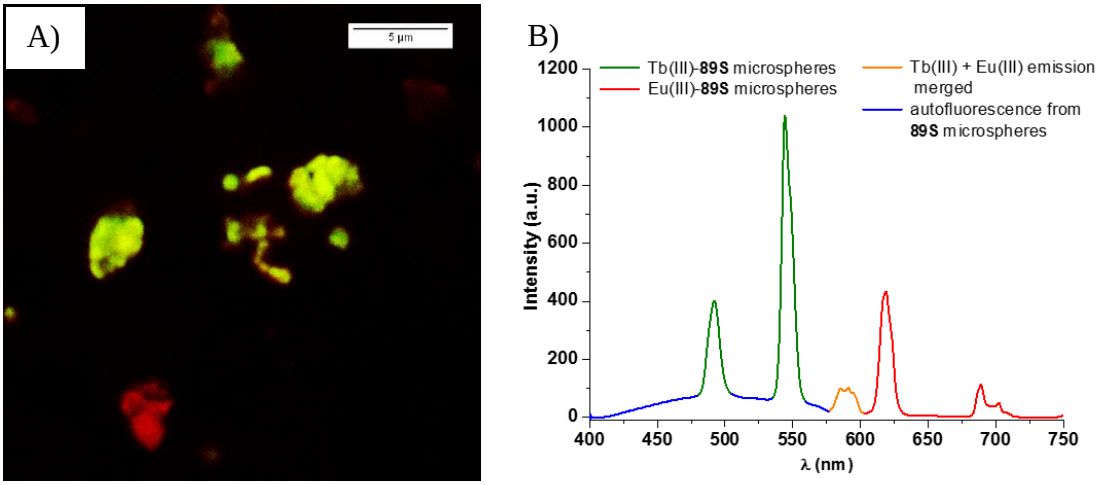

Figure 4.25: A) LSCM image (channel 2 + 3 merged) of mixture of Tb(III)-**89S** microspheres (green) and Eu(III)-**89S** microspheres (red) (λ_{ex} = 355 nm, t_{delay} = 5 µs). B) steady-state emission spectrum (t_{delay} = 0 µs) of the same sample. Images of the same sample in different channels are in Appendix Figure A2.8.5.

microspheres and Eu(III)-**89S** microspheres in the same system exhibiting independent luminescence behaviour.

As a conclusion to this section, LSCM investigations showed that the Ln(III)-**89S** microspheres exhibited blue autofluorescence and the characteristic Ln(III) emissions. The mixed-Eu(III)-Tb(III)-**89S** microspheres showed the white light emission with the combination of the autofluorescence, Eu(III) and Tb(III) emissions. In this systems the quenching of the Tb(III) emission was observed due to the energy transfer from the Tb($^5D_4$) excited state to Eu($^5D_0$). Upon mixing the Ln(III)-microspheres, the coexistence of Tb(III)-**89S** microspheres and Eu(III)-**89S** microspheres were observed in the same system exhibiting the green and red emission respectively.

4.9 Circularly polarised luminescence (CPL) of Ln(III)-microspheres

Circularly polarised luminescence (CPL) is a technique to probe the chiral nature of luminescent molecule.[360] The intensity of the CPL signal, ΔI, is defined as the difference in emission of left- and right-handed circularly polarised light, Equation 4.1.

$$\Delta I = I_L - I_R \qquad \text{Equation 4.1}$$

Where, I_L and I_R = left and right circularly polarised light emission intensity, respectively.

The luminescence dissymmetry factor, g_{lum}, is the parameter used to describe the degree of CPL at a given wavelength or for a given Ln(III) electronic transition, as shown in Equation 4.2.[360] This factor is the ratio between the CPL signal and the total luminescence, T_L, for a given wavelength.

$$g_{lum} = \frac{2 \times (I_L - I_R)}{I_L + I_R} = \frac{2 \times \Delta I}{I_{TL}} \qquad \text{Equation 4.2}$$

CPL is generated from the electronic excited states of the luminescent system reflecting on the chiral structural nature of it. Optical activity of Ln(III) luminescence arises as a result of chiral ligand(s) generating a chiral environment around the metal centre, which perturbs and influences the *f* electrons to assume a chiral configurations.[360-362] Optically active Ln(III) species are ideal for chiral CPL probes, because of their unique photophysical properties.[363-364] Moreover, they often possess significantly higher g_{lum} values than chiral organic molecules, typically seen having magnitudes in the order of 0.1 to 0.5.[360, 365-366] High g_{lum} values of Ln(III) are also possible because of large polarisation anisotropy caused by the highly polarisable Ln(III) core (due to the shielding nature of the *f* electrons). Since chiral lanthanide complexes have been constructed based on the principles of sensitised emission of Ln(III) ions (discussed in Chapter 1, section 1.5), it is possible to obtain Ln(III) complexes exhibiting detectable CPL signals.[360] Therefore, CPL has become a powerful technique to investigate the chiral environment of Ln(III) metal ion.[367]

4.9.1 CPL measurements of Ln(III)-89 (R and S) microspheres

Considering the advantageous properties that optically active Ln(III)-directed self-assemblies can possess, CPL measurements were performed on luminescent Ln(III)-microspheres, in order to evaluate whether chirality had been transferred from microspheres (formed from chiral molecules) to Ln(III) ions through the coordination of organic molecules on the surface of microspheres to Ln(III). All CPL measurements reported herein were carried out in collaboration with Dr Robert Pal in Durham University.

CPL spectra of Tb(III)-**89** (R and S) microspheres dispersed in CH_3CN solution were recorded using a custom built CPL instrument without degassing the sample. The CPL spectra of Tb(III)-**89R** and Tb(III)-**89S** microspheres displayed Tb(III)-centred emission, with each enantiomer showing positive and negative signals of equal magnitude for each band, which is characteristic of *f-f* electronic transitions as shown in Figure 4.26B. For Tb(III)-**89R** microspheres, all major bands corresponds to for $^5D_4 \rightarrow {}^7F_J$ transitions (where, J = 6, 5 and 3) were split such that they crossed the x-axis. Among them, the $^5D_4 \rightarrow {}^7F_6$ transition peak was split into two and the major band was positive. While each peak of the $^5D_4 \rightarrow {}^7F_{5 \text{ and } 3}$ transitions split into three and the major bands were negative. The peak for $^5D_4 \rightarrow {}^7F_4$ transition was positive. The splitting of the peaks into positive and negative bands corresponds to the influence of the geometry of the metal centre on the component vectors

of the transitions.[368] However, standard examples of similar systems have not been parameterised to date, and hence the structural 'fingerprint' of the complex geometry cannot yet be identified.[369] The Tb(III)-**89S** microspheres showed the mirror image of these transitions. The symmetrical distribution of the CPL signals from Tb(III)-**89S** microspheres indicated that the geometry of the Tb(III) was specifically directed from chirality of the self-assembled microspheres, likely corresponding to Λ and Δ configuration of the metal centre influenced by the chiral natures of the ligands.[367] Indeed, the distribution of CPL signals have been used to elucidate the metal stereochemistry in solution for similar Ln(III) self-assemblies.[367, 369]

These measurements confirmed the enantiomeric purity and the chiral nature of the Tb(III)-**89R** and Tb(III)-**89S** microspheres and also the influence of the chiral ligand nature on the *f-f* electronic transitions of Tb(III) ions. Dissymmetry factor values (g_{lum}) were also determined for these Tb(III) based microspheres. g_{lum} values for the most intense transition $^5D_4 \rightarrow {}^7F_5$ (550 nm) were +0.077 and –0.056 for *R* and *S* Tb(III)-**89** microspheres, respectively (Table 4.2). The highest g_{lum} values was observed for $^5D_4 \rightarrow {}^7F_3$ (615 nm)

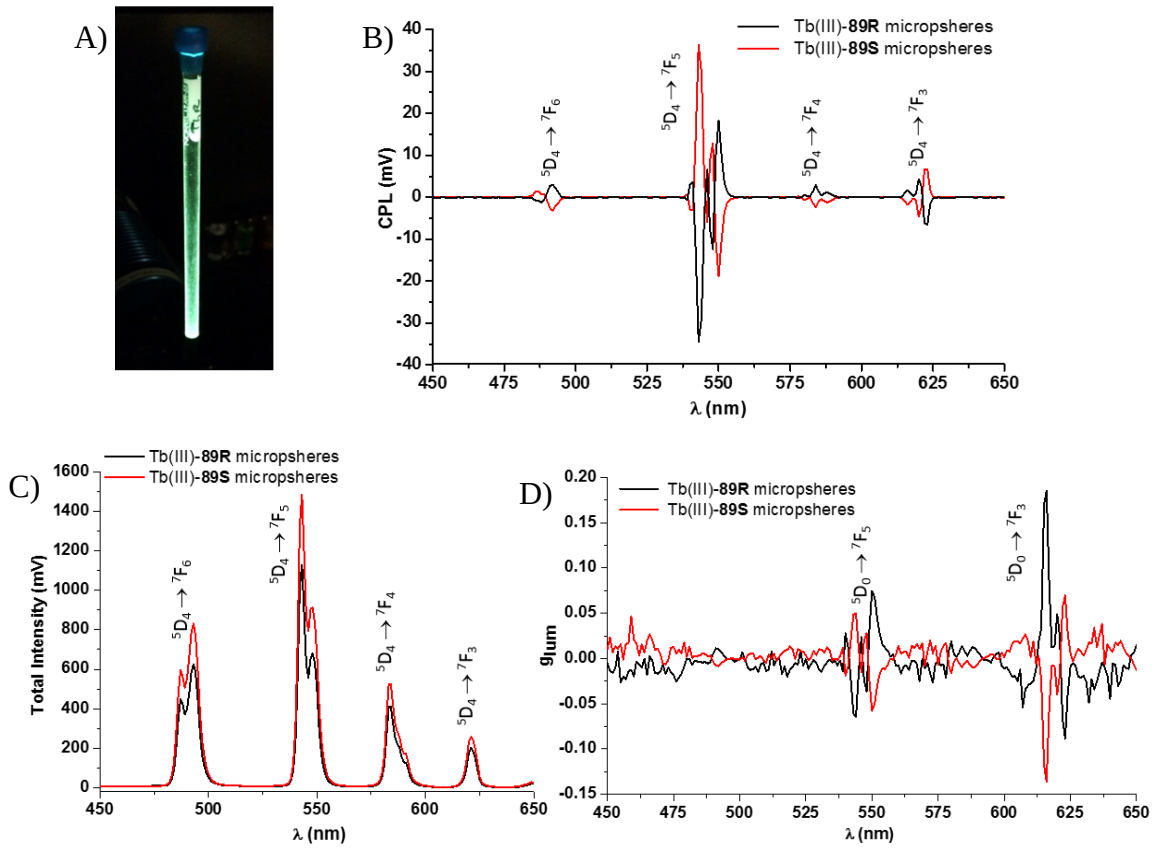

Figure 4.26: A) Luminescence of Tb(III)-**89R** microspheres in CH_3CN under UV light while measuring CPL, B) CPL spectra of Tb(III)-**89** (R and S) microspheres in CH_3CN, C) Total luminescence spectra and D) g_{lum} values of the same sample.

transition with values of +0.184 and -0.134 for *R* and *S* Tb(III)-**89** microspheres, respectively. g_{lum} values for other transitions are detailed in Table 4.2. These values showed that the Tb(III)-**89** (R and S) microspheres possess quite low luminescence dissymmetry factor, g_{lum} values, when compared to previous work by Muller[370] and the Tb(III) complexes reported in our laboratory,[371-372] however, it still suggests the chiral environment around the metal centre. The Eu(III)-**89** (R and S) microspheres also showed their nature of chiral emission confirming again the enantiomeric purity of the microspheres, however, they were poorly emissive. The CPL spectra could not be obtained using standard techniques, since the poor emission was also observed in the magnitude of the CPL signals. Their spectra are provided in Appendix Figure A4.9.1.

As a conclusion to this section, Tb(III)-**89** (R and S) microspheres exhibited the CPL emission confirming the enantiomeric purity of the **89R** and **89S** microspheres. Although the g_{lum} values obtained for this was quite low when compared to Tb(III)-complexes,[361, 372] this is still the first example of Tb(III)-centred CPL emission obtained from the Tb(III)-based microspheres. On the other hand, Eu(III)-**89S** microspheres showed poor CPL emission, but still confirmed their chiral environment around the metal centre. The CPL spectra for both Tb(III)- and Eu(III)-**89** (**R** and **S**) microspheres were obtained using helically luminescence light (HLL) measurement which will be discussed in the further section.

Table 4.2: Luminescence dissymmetry factor, g_{lum}, for $^5D_4 \rightarrow {}^7F_J$ transitions of the Tb(III)-**89** (R and S) microspheres.

$^5D_4 \rightarrow {}^7F_J$ Wavelength (nm)		g_{lum}	
		Tb(III)-**89R** microspheres	Tb(III)-**89S** microspheres
$^5D_4 \rightarrow {}^7F_6$	491.9	+0.010	-0.008
$^5D_4 \rightarrow {}^7F_5$	543.2	-0.062	+0.048
	550.0	+0.074	-0.056
$^5D_4 \rightarrow {}^7F_4$	584.0	+0.013	-0.009
$^5D_4 \rightarrow {}^7F_3$	615.9	+0.184	-0.134
	622.6	-0.087	+0.070

4.9.2 Time gated helically luminescence light (HLL) measurement of Ln(III)-89S (R and S) microspheres

In the next attempt to obtain the CPL signals from both Tb(III)-**89** (R and S) microspheres and Eu(III)-**89** (R and S) microspheres, time-gated helically luminescent light (HLL) measurements were performed on them using a custom built HLL measuring instrument. In

HLL measurement, CPL and elliptically polarised luminescence (EPL) were merged using a novel dual channel time resolved detection system (patented). EPL is analogous to CPL, and represents the difference in emission of left- and right-handed elliptically polarised light. Elliptically polarised light comprises of helical light where the magnetic and electric field vector shift is not equal to 90 degrees (as in standard CPL).

A conventional CPL instrument records only the differential circularly polarised light due to its cumbersome experimental design. That means, it is only capable of distinguishing +90 and -90 degrees helicity in light (left and right handed circularly polarised light). Also due to the photo elastic modulator (PEM's) 50 kHz operating frequency, time resolved measurements are not supported. The new HLL measuring instrument is capable of recording all helical light. That means, this instrument is capable of detecting any degrees of helical polarisation from +90 to -90 degrees, because of the incorporated dual channel detection systems. In this case, previously unrecorded information (in standard CPL) can be deduced identifying both EPL and CPL emitted from the emissive lanthanide entity. Additionally, due to the CCD based detection layout of the instrument, time resolved detection is also facilitated and in all measurements a delay time (t_{delay}) of 5 μs was applied during the measurements.

The relative CPL spectra for Tb(III)-**89** (R and S) microspheres obtained from HLL measurement were similar to the standard CPL spectra discussed above (Figure 4.26). For Tb(III)-**89R** microspheres, all major bands responsible for $^5D_4 \rightarrow {}^7F_{6\text{-}3}$ transitions were split such that they crossed the x-axis, which was in good agreement with conventional CPL seen above. Maximum intensity was observed for $^5D_4 \rightarrow {}^7F_5$ transition peak. However, the major differences observed were in the $^5D_4 \rightarrow {}^7F_6$ and $^5D_4 \rightarrow {}^7F_4$ transition peaks, which were split into three major peaks and the central bands were negative and positive, respectively. As expected Tb(III)-**89S** microspheres showed the mirror image of these transitions, as shown in Figure 4.27B.

Dissymmetry factor values obtained from HLL ($g_{lum(H)}$) were also determined from these measurements. $g_{lum(H)}$ values for all major transitions are detailed in Table 4.3. The $g_{lum(H)}$ values for the most intense transition $^5D_4 \rightarrow {}^7F_5$ (537 nm) was found to be -0.152 and +0.152 for R and S Tb(III)-**89** microspheres, respectively. And the highest $g_{lum(H)}$ values was observed for the $^5D_4 \rightarrow {}^7F_6$ transition (482 nm) with values of -0.2 and +0.2 for R and S Tb(III)-**89** microspheres, respectively.

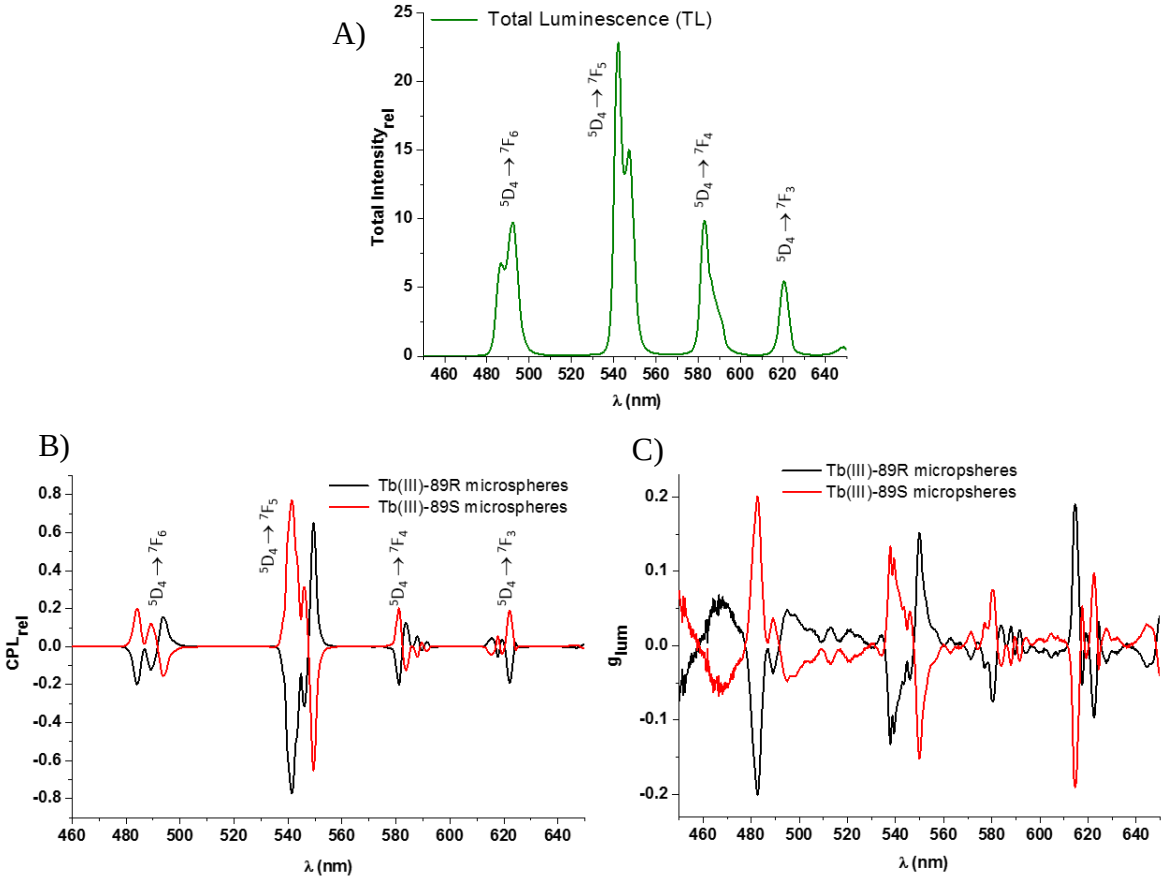

Figure 4.27: A) HLL spectra of Tb(III)-**89** (R and S) microspheres in CH_3CN obtained from HLL measurement, B) Total luminescence spectra and C) $g_{lum(H)}$ values of the same sample, respectively.

Similarly, the relative CPL spectra of Eu(III)-**89** (R and S) microspheres were obtained by measuring its HLL as shown in Figure 4.28B, since the clear CPL spectra could not be achieved from standard CPL measurements. The CPL spectra of Eu(III)-**89R** microspheres and Eu(III)-**89S** microspheres displayed Eu(III) centred emission. Maximum intensity was observed for three major transition peaks, $^5D_0 \rightarrow {}^7F_J$ transitions (where, J = 1, 2 and 4). The relative intensities of the transitions were consistent with the magnetic dipole (MD) character of the $^5D_0 \rightarrow {}^7F_1$ and the selection rules of *f-f* transition.[373] Among them, the $^5D_0 \rightarrow {}^7F_{1 \text{ and } 4}$ transitions were split into several peaks which were negative and $^5D_0 \rightarrow {}^7F_2$ transition was split into three peaks, which was positive. The CPL spectrum showed that the transitions $^5D_0 \rightarrow {}^7F_{1, 2 \text{ and } 4}$ were resolved into 2, 3 and 6 peaks, respectively, which could be consistent with the trigonal symmetry class. This symmetry observed here has been reported for the tpy containing systems as well as other acyclic assemblies.[373] However, the splitting in any of the transitions did not cross the x-axis, unlike that observed for Tb(III)-**89** (R and

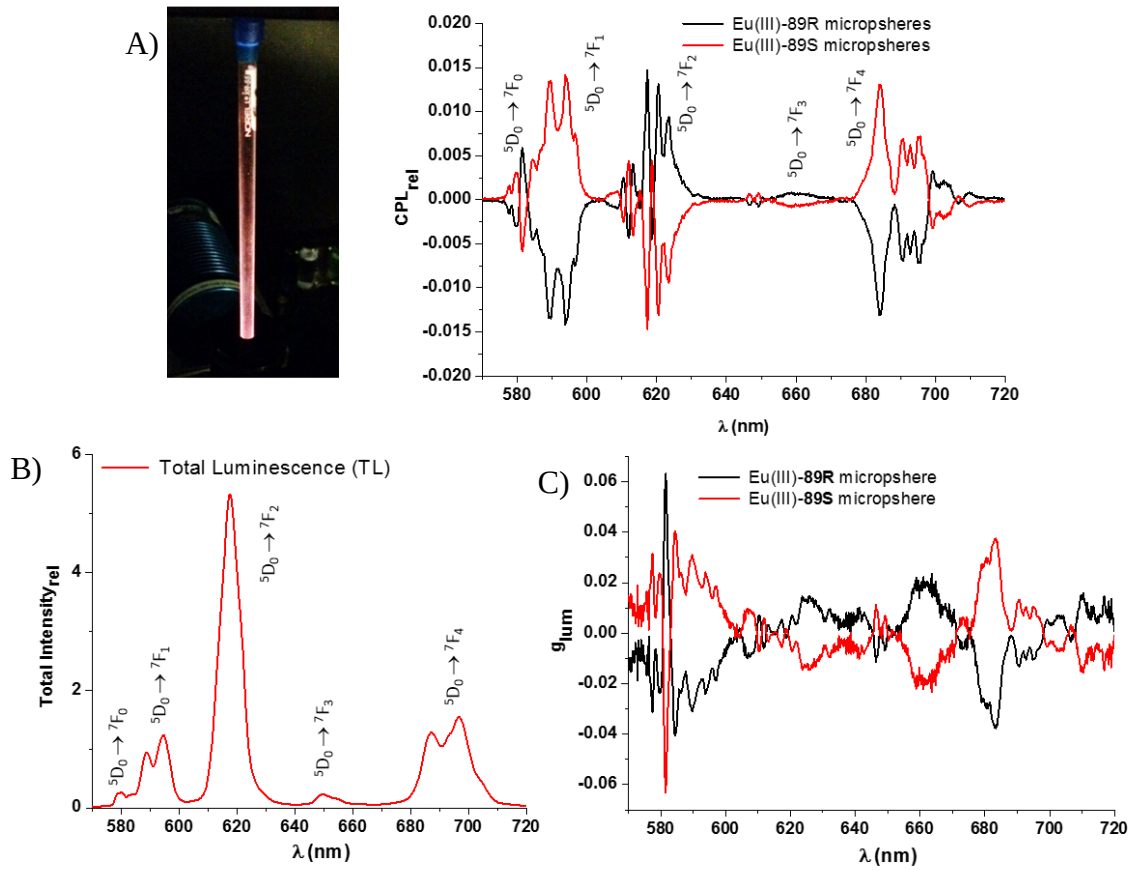

Figure 4.28: A) Luminescence of Eu(III)-**89R** microspheres in CH_3CN under UV light while measuring HLL, B) HLL spectra of the same sample obtained from HLL measurement, C) Total luminescence spectra and D) $g_{lum(H)}$ values of the same sample.

S) microspheres. Again in this case, the differences in the sign of the CPL are unique to the nature of the transitions in the specific metal configuration. Again, however, the standard examples for the structural 'fingerprint' of the similar self-assemblies are not reported as discussed above, and this is the first example for the relative CPL for Eu(III)-based microsphere obtained from HLL. As expected Eu(III)-**89S** microspheres showed the mirror image of these transitions.

Dissymmetry factor values ($g_{lum(H)}$) determined for major transitions are detailed in Table 4.3.The $g_{lum(H)}$ values for the most intense transition $^5D_0 \rightarrow {}^7F_2$ (617 nm) was found to be +0.005 and -0.005 for R and S Eu(III)-**89** microspheres, respectively. The highest $g_{lum(H)}$ values were observed for the $^5D_0 \rightarrow {}^7F_0$ transition (581 nm) with values of +0.063 and -0.063 for R and S Eu(III)-**89** microspheres, respectively.

In summary, both the Tb(III)-**89** (R and S) microspheres and Eu(III)-**89** (R and S) microspheres displayed CPL emission from the HLL measurements, indicating the chiral environment around the Ln(III) ions. This chirality arises from the chiral arrangement of the

Table 4.3: Luminescence dissymmetry factor, $g_{lum(H)}$, of $^5D_4 \rightarrow {}^7F_J$ and $^5D_0 \rightarrow {}^7F_J$ transitions of the Ln(III)-**89** (R and S) microspheres.

Electronic transition	**Wavelength (nm)**	**$g_{lum(H)}$**	
$^5D_4 \rightarrow {}^7F_J$		Tb(III)-**89R** microspheres	Tb(III)-**89S** microspheres
$^5D_4 \rightarrow {}^7F_6$	482.5	-0.201	+0.200
$^5D_4 \rightarrow {}^7F_5$	537.8	-0.152	+0.152
$^5D_4 \rightarrow {}^7F_4$	580.3	-0.075	+0.075
$^5D_4 \rightarrow {}^7F_3$	614.5	+0.190	-0.190
$^5D_0 \rightarrow {}^7F_J$		Eu(III)-**89R** microspheres	Eu(III)-**89S** microspheres
$^5D_0 \rightarrow {}^7F_0$	581.5	+0.063	-0.063
$^5D_0 \rightarrow {}^7F_1$	589.7	-0.031	+0.031
$^5D_0 \rightarrow {}^7F_2$	617.3	+0.005	-0.005
$^5D_0 \rightarrow {}^7F_3$	649.2	-0.007	+0.007
$^5D_0 \rightarrow {}^7F_4$	683.6	-0.038	+0.038

ligands in the microspheres. Therefore, this gave the strong evidence for the formation of helical self-assemblies of the ligands during the formation the microspheres as discussed previously in Chapter 3, Section 3.16.

4.10 Conclusion

The work described in this chapter was focused on the investigation of the microspheres using optical microscopy (OM) and LSCM. Optical microscopy images of the microspheres (prepared at c = 0.3% w/v) taken in different modes (488 nm transmittance and 458 nm reflectance modes) showed the spherical structures and that they were formed with diameter between 1 - 2 μm. This was in good agreement with the observation made form SEM, HIB and TEM investigation discussed in Chapter 3. LSCM images of the **89** (R and S) microspheres showed the blue fluorescence emission arising from the tpy moieties of **89R** and **89S**. The emission spectrum recorded by LSCM showed the emission band at 492 nm, which is in good agreement with the spectrum recorded using the steady-state fluorescence measurements, confirming that the emission is arising from the microspheres.

Similarly, upon imaging the solution of **89S** microspheres using LSCM, the blue fluorescent microspheres were observed. This confirmed the existence of microspheres in solution and ruled out the possibility that the microspheres were only formed during the drying process post-dropcasting. From the real-time investigation, performed using LSCM, the formation of the **89S** microspheres was observed upon cooling a hot solution of **89S**,

which gave the additional evidence of the formation of microspheres in solution. The observation made here is the first experiment which showed the real-time imaging of the formation of the microspheres in solution media using LSCM on a very short time-scale.

On immersing the dried microspheres in H_2O, it was observed (after 60 min), that the microspheres were connected to each other, similar to the observation made from SEM investigation discussed in Chapter 3, Section 3.13. The disassembly process of the **89S** microspheres in the presence of urea was investigated using OM. From the OM images, it was shown that the microspheres had completely disassembled after 150 minutes when treated with 1% urea solution. However, when using 10% urea solution, complete disassembly was more rapid and was observed within 50 minutes. This suggested that, upon increasing the urea concentration by an order of 10 times, the rate of disintegration of **89S** microspheres increased by an order of 3 times. Furthermore, when the **89S** microspheres were irradiated with 355 nm laser with 100% laser intensity in a particular area, the microspheres were disintegrated selectively.

Upon addition of Ln(III) (Ln = Eu or Tb) ions to the solution of **89S** microspheres, the binding of the Ln(III) ions to the tpy moieties on the surface of microspheres occurred, forming Ln(III)-**89S** microspheres. As a result, Eu(III) and Tb(III) ions present on the surface of **89S** microspheres were sensitised, showing their respective characteristic Ln(III) emissions. Stepwise addition of Eu(III) ions to the solution of **89S** microspheres resulted in the formation of Eu(III)-**89S** microspheres, which showed maximum emission when *ca*. 0.6 equivalents of Eu(III) was added. Similarly, addition of Tb(III) to solution of **89S** microspheres formed Tb(III)-**89S** microspheres, which showed the maximum emission when 1.2 equivalents of Tb(III) was added. Using this information, the Eu(III)-**89S** microspheres and Tb(III)-**89S** microspheres were prepared by adding 0.6 and 1.0 equivalents of Eu(III) and Tb(III) ions to the solution of **89S** microspheres, respectively.

Imaging these Ln(III)-**89S** microspheres using LSCM in three different channels (blue green and red channels), the luminescent behaviour of the microspheres was observed. Eu(III)-**89S** microspheres showed the blue autofluorescence from microspheres and red emission from Eu(III). Similarly, Tb(III)-**89S** microspheres showed the blue autofluorescence and green emission from Tb(III). Mixed Eu(III)-Tb(III)-**89S** microspheres showed emission in all three channels, with: blue autofluorescence, green emission from Tb(III) and red emission from Eu(III) respectively. Similarly, when Channels 1, 2 and 3 were merged, white-light-emitting microspheres were observed as expected. This observation was similar to the white light emission was observed in a metallogel formed form terpyridyl-end-

capped polymer as ligand and Eu(III)/Tb(III) mixture,[355] and also from a discrete heterometallic Ln(III) complex using a ligand possessing terpyridyl moieties.[354] However, this is the first example of the white light emitting Ln(III)-containing organic microspheres possessing tpy moieties, *via* the energy transfer process between the Ln(III) present in the same microsphere.

Time-gated spectral measurements of the Ln(III)-**89S** luminescent microspheres showed the emission spectra of the respective Ln(III) ions used. Mixed Eu(III)-Tb(III)-**89S** microspheres showed the predominant Eu(III) emission, due to the energy transfer taking place from the Tb($^5D_4$) excited state to the Eu($^5D_0$) level, which was confirmed by performing the lifetimes measurements of the Ln(III) present in the microspheres. Excited state lifetimes were measured to be 1.40 ms and 0.50 ms for Eu(III)-**89S** microspheres and Tb(III)-**89S** microspheres, respectively. However, in the case of mixed Eu(III)-Tb(III)-**89S** microspheres, the lifetimes of Eu(III) and Tb(III) were found to be 1.09 ms and 0.18 ms, respectively. Similar obsevation of the energy transfer process between the Tb($^5D_4$) excited state to Eu($^5D_0$) level was made in multimetallic Ln(III)-based trinuclear[357] and dinuclear Ln(III) complexes,[358] mixed Ln(III) complexes doped polymers aggregated to form nanoparticles,[356] and MOF,s possessing mixed Eu/Tb-adipate framework.[359]

When mixing the solution of Eu(III)-**89S** microspheres and Tb(III)-**89S** microspheres, LSCM images did not show the expected colours red and green, respectively. Instead, upon close observation by LSCM imaging, separate predominantly orange particles and predominantly green particles were seen, indicating that the Eu(III)-**89S** microspheres and Tb(III)-**89S** microspheres coexisted independently. This was confirmed further by spectral measurements, which showed roughly the equal intensities of two Ln(III) emission. Non-time gated spectral measurements of the same sample showed the Eu(III) and Tb(III) emission bands of approximately equal intensities along with a broad autofluorescence band arising from the organic chromophore of the microspheres. This autofluorescence emission was merging with the Eu(III) and Tb(III) emission and giving rise to the orange and greenish-orange coloured emission.

Since the microspheres were prepared from chiral **89R** and **89S** molecules, standard CPL signals were observed from Tb(III)-**89** (R and S) microspheres. However, the Eu(III)-**89** (R and S) microspheres gave poor quality spectra. g_{lum} values of the Tb(III)-**89** (R and S) microspheres obtained from standard CPL measurements were quite low in comparison to Tb(III)-complexes reported by Muller[21] and our group.[372] However, it is the first example of Tb(III)-centred CPL emission obtained from the Tb(III)-based microspheres. Additionally,

when performing HLL measurements, the relative CPL spectra from both the Tb(III)-**89** (R and S) microspheres and Eu(III)-**89** (R and S) microspheres could be obtained for the Ln(III) centred emissions. This was the first example of the CPL spectra obtained from HLL measurements and also the first example of the CPL spectra from the Ln(III)-based microspheres. Both the conventional CPL spectra and the relative CPL spectra from HLL measurement indicated the chiral environment around the Ln(III) ions, arising from the chiral arrangement of the ligands assembled in the microspheres. This again confirmed the formation of helical self-assemblies of the ligands during the formation the microspheres as discussed previously in Chapter 3, Section 3.16.

In summary, the work described within this chapter described the morphological features, luminescent property, and the disassembly of the **89S** microspheres using OM and LSCM techniques, which supported the results discussed in Chapter 3. The real-time imaging of the formation of microspheres in solution was achieved using LSCM, and this is the first experiment showing the formation of such assemblies. Additionally, the white-light-emission was achieved from mixed Eu(III)-Tb(III)-**89S** microspheres. The standard CPL and the relative CPL of Ln(III)-**89S** microspheres from HLL confirmed the chiral environment of the Ln(III) metals, and thus supported the formation of helical assemblies during the formation the microspheres as discussed in the proposed mechanism in Chapter 3, Section 3.16. However, this was the first example of the HLL measurements from the Ln(III)-based microspheres. These results greatly complement the studies previously reported by Gunnlaugsson relating the studies of BTA molecules utilising new techniques such as real-time imaging in LSCM, CPL and HLL.

The future work will focus on the application of the microspheres as the delivery agents. The disassembly process of microspheres in presence of urea attracts the use of such systems as potential delivery agents and the controlled cargo release. Additionally, the work will also focus on obtaining the more monodispersed sized microspheres by making the appropriate modifications in the molecular structure, and/or using different solvent systems in the microspheres formation. Additionally, the attempts will also be made in the controlling the microspheres sizes by incorporating in gel mediums. The attempts will also be carried out to obtain the hollow microspheres, which can be used to deliver cargos better than solid microspheres. Furthermore, the Ln(III) with Near-infrared (NIR) emission properties can be coordinated to microspheres, and as such systems are very attractive and are ideal for *invo* applications as luminescent imaging agents.

General Conclusion

General conclusion for the work described in this thesis

The work discussed in this thesis described the synthesis of a new series of tripodal molecules based on BTA framework, bearing terpyridine motifs, and their self-assembly behaviour leading to various supramolecular structures.

The Eu(III)-directed self-assembly of a pair of enantiomers **89** (R and S) in solution at two different ligand concentrations were studied using UV-vis absorption, fluorescence and phosphorescence spectroscopy. The titration data analysed using non-linear regression fitting indicated the formation of 1:1. 2:1 and 3:1 (M:L) species at lower concentration ($c_L = 1 \times 10^{-6}$ M) and 1:1. 3:2 (M:L) species at higher concentration ($c_L = 1 \times 10^{-5}$ M). This clearly indicated the effect of concentration on the formation of higher ordered self-assembled coordination species in solutions.

Then, the synthesised BTA molecules were analysed for their self-assembly properties for the formation of gels. The achiral molecule **88** formed gel (0.5% w/v) in CH_3CN/H_2O (6:4). SEM and TEM analysis showed the highly fibrous entangled network responsible for gelation. Rheological measurements showed the remarkable self-healing properties. In contrast to above, the chiral derivatives **89** – **91**, formed microspheres under similar conditions. Such behaviour of chiral derivatives was due to the combination of intermolecular triple H-bonding, increased hydrophobicity, and nature of the chirality. The SEM and the DLS measurements revealed the particles size were in the range of 0.6 – 1.1 μm in diameter. The particle size distribution varied depending on the compound, solvent medium and concentration used. Among the chiral derivatives, **89** (R and S) formed the microspheres with relatively narrow size distribution and a mean particle size of 0.92 ± 0.08 μm. However, the formation of such spherical morphologies was not observed for any of the previously reported BTA derivatives. This demonstrated the distinctive self-assembly properties of the our new chiral BTA molecules **89** - **91**.

Addition of urea to **89** – **91** at the beginning of the synthesis of microsphere prevented the formation of microspheres because of the competitive H-bonding. This confirmed the crucial role of the intermolecular triple H-bonding for the self-assembly of **89** – **91** to occur in the formation of microspheres. Using the FIB technique, the particles were precisely cut, which revealed the microspheres were solid. AFM measurements showed the trend in increase of particle size distribution upon increase in the concentration. Addition of Ln(III) metal ions to microspheres, resulted in the formation of microspheres chains, bridging the

particles through coordination interactions with the tpy moieties exposed on the microspheres surface.

The lateral force displacement measurements of **89S** microspheres revealed that the particles were not strongly adhered to the silica substrate. Applying lateral force multiple times showed that more force (0.48 nN) was required for the first time and much lesser force (0.1 nN) was required to move the same particle. Mechanical stiffness measurements, performed by applying vertical force on top of microspheres using AFM tip, showed that the particles were strong and robust. From the force curves obtained, microspheres were found to have the same spring constant comparable to the silicon nitride calibration grid. Thermal stability and TGA analysis showed that microspheres were stable up to 155 ^{o}C, and melted at 160 ^{o}C.

When solid microspheres were immersed in H_2O, formation of a 2D chains and network was observed through the bridging between the microspheres. This bridging most likely occurred through the H-bonding, due to the diffusion of molecules from microspheres. Similarly, when the solid microspheres were immersed in $Eu(CF_3SO_3)_3$ solution, the formation of micro-cavities were observed on their surface. When the achiral **88** and the chiral **89** – **91** (R and S) compounds were mixed, they displayed the self-sorting behaviour. Where in the achiral **88** formed one dimensional fibres resulting in gel, and the chiral analogues **89** – **91** (R and S) formed microspheres in the gel medium.

From the information obtained on the self-assembly of these BTA molecules, a mechanism was proposed for the microsphere formation (Figure 3.45). Wherein the BTA molecules self-assemble through intermolecular triple H-bonding interactions leading to the formation of one dimensional helical supramolecular fibrils, which further aggregate by axial alignment to form supramolecular fibres. These fibres may undergo entanglement to form either initial nano-seed, or micron-sized material, which further aggregates to form microspheres as shown in Figure 3.45.

Investigation of the microspheres using OM and LSCM showed their spherical structure which was in good agreement with the observation made from SEM, TEM, and HIB discussed earlier. The LSCM images showed the existence of the microspheres in solution and ruled out the possibility of their formation during drying post dropcasting. Additionally, the real-time imaging showed the formation of **89S** microspheres upon cooling a hot solution of **89S** which gave the additional evidence of the formation of microspheres in solution. The disassembly of **89S** microspheres in presence of urea, was monitored using

LSCM showed that upon increasing the urea concentration by an order of 10 times, the rate of disintegration increased by an order of 3 times.

Ln(III) containing microspheres imaged under LSCM with three different channels showed their respective Ln(III) emission due to the sensitisation from tpy moieties. Where in, the Eu(III)-**89S** microspheres and Tb(III)-**89S** microspheres displayed red and green emission, respectively, in addition to the blue autofluorescence. Mixed Eu(III)-Tb(III)-**89S** microspheres showed emission in all three channels, with: blue autofluorescence, green emission from Tb(III) and red emission from Eu(III). When all three channels were merged, white-light-emitting microspheres were observed. CPL signals were observed from Tb(III)-**89** (R and S) microspheres, and the Eu(III)-**89** (R and S) microspheres gave poor quality CPL spectra. However, HLL measurements showed the relative CPL spectra from both the Tb(III)- and Eu(III)-**89** (R and S) microspheres, which gave strong evidence for the formation of helical self-assemblies of the ligands during the formation the microspheres discussed previously.

Future work will focus on gaining control over the synthesis of monodispersed sized microspheres by making the appropriate modifications for the exiting molecular structure and the design of new systems. The attempted to control the microspheres using the gel medium will also be carried out. The supramolecular gel of **88**, having rapid recovery properties, are highly attractive for its application as stimuli responsive materials. Due to the self-sorting properties of gel, **88** will be utilised in multicomponent gel systems for the synthesis of nanoparticles and organic microspheres with controlled size, crystal growth of organic compounds, *etc*. Additionally, the work will focus on the application of these microspheres for catalysis and delivery agents. The disassembly of microspheres in presence of urea attracts the use of such systems as potential delivery agents for controlled cargo release. The Ln(III) with near-infrared (NIR) emission properties can be coordinated to microspheres which are very attractive and are ideal for *in vivo* applications as luminescent imaging agents.

The work discussed in this thesis augmented the previous work of the Gunnlaugsson group, and also this research has taken the work to a new level with the introduction of new class of BTA molecules which showed distinctive self-assembly properties that was not reported previously in the literature.

Chapter 5

Experimental details

Chapter 5: Experimental details

5.1 General: All chemicals were purchased from Sigma-Aldrich Ireland Ltd., Acros Organics, TCI Ltd., and Chematech, and were used without further purification, unless otherwise stated. Dry solvents were prepared in accordance with standard procedures described by Vogel, with distillation prior to each use.[374] Thin-layer chromatography (TLC) was conducted using Merck Kiesegel 60 F_{254} silica plates, and the separation was observed by UV light or developed in an iodine chamber. Chromatographic columns were run on a Teldyne Isco Combiflash Rf200 automatic machine using pre-packed silica columns. Melting Points were determined using an Electrothermal IA900 digital melting point apparatus.

Deuterated solvents for NMR analysis were all obtained from Apollo Scientific. NMR spectra were recorded using either a Bruker DPX-400 Avance spectrometer, operating at 400.13 MHz for ^{1}H NMR and 100.60 MHz for ^{13}C NMR, or a Bruker AV-600 spectrometer, operating at 600.10 MHz for ^{1}H NMR and 150.90 MHz for ^{13}C NMR. All NMR spectra were measured at 293 K. Tetramethylsilane (TMS) was used as an internal standard and chemical shifts were referenced relative to the internal non-deuterated solvent signal, with chemical shifts being expressed in parts per million (ppm or δ). For ^{1}H NMR spectra, the number of protons, splitting pattern, coupling constant where applicable, and proton assignment are also reported (in that order). Multiplicities are abbreviated as follows; singlet (s), doublet (d), triplet (t), quartet (q), quintet (qu), multiplet (m), and broad (br).

Electrospray mass spectra were recorded on Bruker microTOF-Q III spectrometer connected to Dionex UltiMate 3000 LC detector using HPLC grade CH_3CN or CH_3OH as carrier solvents. Accurate molecular weights were determined by a peak-matching method, using Agilent Technologies ESI-1 low concentration tuning mix as the internal lock mass. Maldi-Q-Tof mass spectra were carried out on a MALDI-Q-TOF-Premier (Waters Corporation, Micromass MS technologies, Manchester, UK). High-resolution mass spectrometry was performed using leucine enkephaline (H-Tyr-Gly-Gly-Phe-Leu-OH) as the standard reference (m/z = 556.2771); all accurate masses were reported within ± 5 ppm of the expected mass.

Infrared spectra were recorded on a Perkin Elmer Spectrum One FT-IR spectrometer fitted with a universal ATR sampling accessory. Elemental analysis weas performed on an Exter Analytical C3440 elemental analyser at the Microanalysis Laboratory, School of Chemistry and Chemical Biology, University College Dublin.

5.1.1 Ultraviolet-visible Spectroscopy

The UV-visible absorption spectra were recorded at room temperature using 1.0 cm path length quartz cell in Varian Cary 50 spectrometer. The solvents were of spectrophotometric grade. The wavelength range was set from 200 to 450 nm with a scan rate of 300 nm/min. The blank was a sample of the solvent system in which the titration was carried out *i.e.* CH_3OH. Before the start of the titration baseline correction was used in all spectra. Stock solution of ligand with concentrations either 1×10^{-3} or 2×10^{-3} M for the titration in CH_3OH were prepared in 20% $CHCl_3/CH_3OH$ mixture and then diluted to desired concentration before titration to *ca*. 1×10^{-5} or 5×10^{-6} M. The $Eu(CF_3SO_3)_3$ stock solution was prepared in CH_3OH (1×10^{-3} M) and diluted to 5×10^{-4} M for the titration. The titrations were repeated 3-5 times in order to see the reproducibility of the results.

5.1.2 Fluorescence measurements

The fluorescence measurements were carried out on a Varian Cary Eclipse Fluorimeter equipped with a 1.0 cm path length quartz cell at room temperature. The solvents were all of spectroscopic grade. Fluorescence data were collected between 300 to 800 nm. The concentration of the ligands and the complexes were the same as those used for the UV-vis absorption measurements. The settings of the fluorimeter for the luminescence titrations carried out in Chapter 2 are shown in Table 5.2.1. Please note, the voltage of the PMT detector was adjusted as necessary to prevent signal saturation in different measurements.

Table 5.2.1: Fluorescence settings for the titration described in chapter 2.

Mode: Fluorescence	**Excitation:** 280 nm	**Scans:** 300 – 800 nm
Excitation slit: 20 nm	**Emission slit:** 5 nm	**PMT Voltage:** 600 - 700 V
Averaging time: 0.1 s	**Scan rate:** 600 nm/min	**Data Interval:** 0.5 nm

5.1.3 Eu(III) centred emission measurements

The phosphorescence measurements were carried out on a Varian Cary Eclipse Fluorimeter equipped with a 1.0 cm path length quartz cell at room temperature. The solvents used were all of spectroscopic grade. The luminescence data were collected between 570 nm to 720 nm for Eu(III) emission. The concentration of the ligands, complexes and lanthanide stock solutions were the same as those used for the UV-vis absorption and fluorescence measurements. The settings of the fluorimeter for the luminescence titrations carried out in

Chapter 2 are shown in Table 5.2.2. Please note, the voltage of the PMT detector was adjusted as necessary to prevent signal saturation in different measurements.

Table 5.2.2: Luminescence settings for the titration described in Chapter 2.

Mode: Phosphorescence	**Excitation:** 280 nm	**Scans:** 570 – 720 nm
Excitation slit: 20 nm	**Emission slit:** 2.5 nm	**PMT Voltage:** 600 – 800 V
No. of Flashes: 1	**Gate time:** 5 ms	**Delay time:** 0.2 ms
Averaging time: 0.1 s	**Total decay time:** 0.02 s	**Data Interval:** 0.5 nm

5.1.4 Life time measurements of Eu(III) complexes

The luminescence lifetime measurements of Eu(III) centred life time emission of **Eu.89R** and **Eu.89S** in CH_3OH and CD_3OD were conducted on a Varian Cary Eclipse Fluorimeter. The settings of the fluorimeter for the lifetime measurements carried out in Chapter 2 are shown in Table 5.2.3.

Life time values of Eu(III) ($_5D_0$) excited state were measured in solution in time resolved mode. For each system the lifetime values are averages of three independent measurements, which were made by monitoring the emission decay at 617 nm, which corresponds to maximum of the $^5D_0 \rightarrow {}^7F_2$ transition, enforcing a delay.

Table 5.2.3: Settings of the Varian Cary Eclipse Fluorimeter for measuring Eu(III) centred luminescence decays.

Indirect excitation: 280 nm	**Emission:** 617 nm	**Delay:** 0.01
Excitation slit: 20 nm	**Emission slit:** 20 nm	**Gate:** 0.02 – 0.045 ms
No. of Flashes: 1	**Total decay:** 20 ms	**No. of Cycles:** 50

5.2 Experimental details for Chapter 2

5.2.1 General procedure for the synthesis of compound 101 – 103 (R and S)

Thionyl chloride (11 equiv) was added to a suspension of *R*/*S*-amino acids [**92** - **95** (R/S)] (1 equiv.) in CH_3OH at 0 ^oC. The reaction mixture was allowed to reach room temperature and left stirring for 6 hrs. After the reaction, CH_3OH and $SOCl_2$ were removed under reduced pressure to yield a solid of *R/S*-amino acids methyl ester hydrochloride **96** - **99** (R and S both). Crude compounds **96** - **99** (R/S) were then used for the further reactions without any purification. The compound **96** - **99** (R/S) (1 equiv.) was dissolved in CH_2Cl_2 and triethlyamine was added, in order to neutralise trace amounts of $SOCl_2$ before the addition of 1,3,5-benzene tricarbonyl trichlorie (0.2 equiv.). The latter one was added to CH_2Cl_2

solution of **96 - 99** (R/S) which was cooled down to 0 ^{o}C and was stirred for 12 hrs then at room temperature. Completion of the reaction was monitored by silica TLC using 94% CH_2Cl_2/CH_3OH. Once the reaction was complete, the reaction mixture was diluted with CH_2Cl_2 and washed with 1N HCl, sat. $NaHCO_3$ solution and H_2O. CH_2Cl_2 layer was dried over Na_2SO_4, filtered and evaporated under reduced pressure to yield **100 - 103** (R/S). The crude **100 - 103** (R/S) were purified using neutral silica column chromatography using 94% CH_2Cl_2/CH_3OH as mobile phase to yield the pure compounds **100 - 103** (R and S both).

Tris-glycine-trimethylester-benzene-1,3,5-tricarboxamide (100)

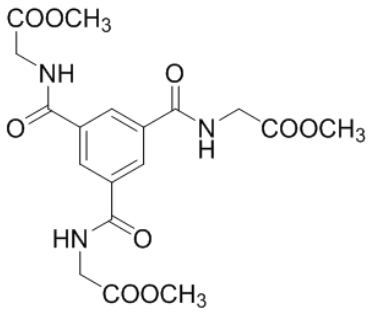

Compound **100** was synthesised as described in the section 5.2.1, using glycine (**92**) (1.8 g, 23.9 mmol, 1 equiv.) in CH_3OH (60 mL) and $SOCl_2$ (18 mL, 246 mmol, 11 equiv.). Resulting glycine methyl ester hydrochloride (**96**) was then dissolved in CH_2Cl_2 (50 mL) and reacted with 1,3,5-benzene tricarbonyl trichloride (0.8 g, 3.0 mmol, 0.2 equiv.) to obtain compound **100** (0.85 g, 67 % yield). $\boldsymbol{R_f}$ = 0.5 in 94% CH_2Cl_2/CH_3OH); **m.p** 260-264 ^{o}C.; **HRMS** (*m/z*) (MS ES$^+$) calculated for $C_{18}H_{21}N_3O_9Na$ *m/z* = 446.1180 [M + Na], found *m/z* = 446.1175; **^{1}H NMR** (400 MHz, $CDCl_3$) δ_H = 8.18 (1H, s, $\underline{C}H_{Ar\text{-}H}$) 7.93 (1H, t, *J* = 5.8 Hz, N$\underline{H}$), 4.15 (2H, d, *J* = 5.8 Hz, C$\underline{H}$)), 3.76 (3H, s, COOC$\underline{H}_3$); **^{13}C NMR** (100 MHz, $CDCl_3$): δ_C = 171.2 ($\underline{C}$OO), 166.68 (CO), 134.62 ($\underline{C}H_{Ar\text{-}C}$), 128.78 ($\underline{C}H_{Ar\text{-}C}$), 52.66 (COO$\underline{C}H_3$), 42.07 ($\underline{C}$H); **IR** υ max (cm^{-1}): 3245.3, 3070.2, 2952.6, 1753.8, 1642.2, 1561.0, 1437.2, 1399.0, 1362.6, 1309.1, 1203.1, 1178.7, 1092.2, 1028.2, 1002.3, 920.8, 891.5, 848.4, 798.6, 690.6.

(*R*,*R*,*R*)-Tris-alanine-trimethylester-benzene-1,3,5-tricarboxamide (101R)

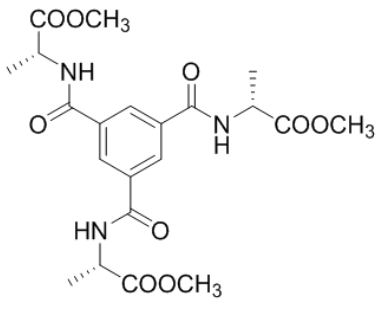

Compound **101R** was synthesised as described in the section 5.2.1, using *R*-alanine (**93R**) (1.0 g, 11.2 mmol, 1 equiv.) in CH_3OH (50 mL) and $SOCl_2$ (9.0 mL, 123 mmol, 11 equiv). Resulting *R*-alanine methyl ester hydrochloride (**97R**) was then dissolved in CH_2Cl_2 (50 mL) and reacted with 1,3,5-benzene tricarbonyl trichloride (594 mg, 2.24 mmol, 0.2 equiv.) to obtain compound **101R** (0.85 g, 85 % yield). $\boldsymbol{R_f}$ = 0.5 in 94% CH_2Cl_2/CH_3OH). **m.p** 290-292 ^{o}C. **HRMS** (*m/z*) (MS ES$^+$) calculated for $C_{21}H_{28}N_3O_9$ *m/z* = 466.1826 [M + H], found *m/z* = 466.1809; **^{1}H NMR** (400 MHz, $CDCl_3$) δ_H = 8.15 (3H, s, C$\underline{H}_{Ar\text{-}H}$) 7.65 (3H, d, *J* = 7.5 Hz, N$\underline{H}$), 4.77 (3H, m, C$\underline{H}$), 3.79 (9H, s, COOC$\underline{H}_3$), 1.58 ppm (9H, d, *J* = 7.3 Hz, CH_3); **^{13}C NMR** (100 MHz, $CDCl_3$): δ_C = 174.09 ($\underline{C}$OO), 166.28 (CO), 135.26 ($\underline{C}H_{Ar\text{-}C}$),

128.99 (<u>C</u>H$_{Ar-C}$), 52.88 (COO<u>C</u>H$_3$), 49.17 (<u>C</u>H), 17.82 ppm (<u>C</u>H$_3$); **IR** υ max (cm^{-1}): 3217, 3071, 2994, 2947, 1746, 1639, 1556, 1452, 1281, 1206, 1161, 1132, 1053, 723, 689.

(*S*,*S*,*S*)-Tris-alanine-trimethylester-benzene-1,3,5-tricarboxamide (101S)

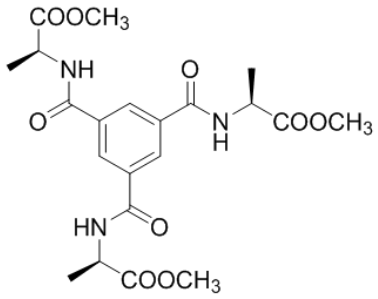

Compound **101S** was synthesised as described above (section in 5.2.1) using *S*-alanine (**93S**) (0.8 g, 8.97 mmol, 1 equiv.) in CH_3OH (50 mL) and $SOCl_2$ (7.0 mL, 90 mmol, 10 equiv.). Resulting *S*-alanine methyl ester hydrochloride (**97R**) was dissolved in CH_2Cl_2 (50 mL) and reacted with 1,3,5-benzene tricarbonyl trichloride (476 mg, 1.79 mmol, 0.2 equiv) to obtain compound **101S** (0.58 gm, 69 % yield). $\boldsymbol{R_f}$ = 0.5 in 94% CH_2Cl_2/CH_3OH). **m.p** 290^{o}C. **HRMS** (*m/z*) (ES MS $^+$) calculated for $C_{21}H_{28}N_3O_9$ *m/z* = 466.1826 [M + H], found *m/z* = 466.1819; **^{1}H NMR** (400 MHz, $CDCl_3$): δ_H = 8.15 (3H, s, C<u>H</u>$_{Ar-H}$), 7.65 (3H, d, *J* = 7.64 Hz, N<u>H</u>), 4.78 (3H, m, C<u>H</u>), 3.80 (9H, s, COOC<u>H</u>$_3$), 1.58 ppm (9H, d, *J* = 7.32 Hz, C<u>H</u>$_3$); **^{13}C NMR** (100 MHz, $CDCl_3$): δ_C = 173.90 (<u>C</u>OO), 166.07 (CO), 135.03 (<u>C</u>H$_{Ar-C}$), 128.79 (<u>C</u>H$_{Ar-C}$), 52.69 (COO<u>C</u>H$_3$), 48.97 (<u>C</u>H), 17.62 ppm (<u>C</u>H$_3$); **IR** υ max (cm^{-1}): 3219, 3071, 2998, 2947, 1747, 1639, 1557, 1318, 1281, 1207, 1161, 1132, 1053, 985, 724, 689.

(*R*,*R*,*R*)-Tris-phenylalanine-trimethylester-benzene-1,3,5-tricarboxamide (102R)

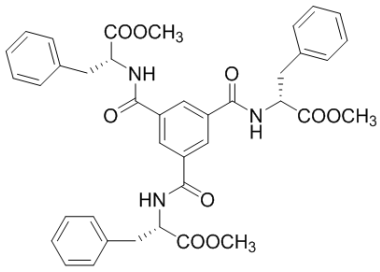

Compound **102R** was synthesised as described above (section 5.2.1) using *R*-phenylalanine (**94R**) (1.0 g, 6.053 mmol, 1 equiv.) in CH_3OH (50 mL) and $SOCl_2$ (4.5 mL, 60 mmol, 10 equiv.). Resulting *R*-phenylalanine methyl ester hydrochloride (**98R**) was dissolved in CH_2Cl_2 (50 mL) and reacted with 1,3,5-benzene tricarbonyl trichloride (482 mg, 1.81 mmol, 0.2 equiv.) to obtain compound **102R** (0.8 gm, 63 % yield). $\boldsymbol{R_f}$ = 0.5 in 95% CH_2Cl_2/CH_3OH). **m.p** 240-246 ^{o}C; **HRMS** (*m/z*) (MALDI $^+$) calculated for $C_{39}H_{40}N_3O9$ *m/z* = 694.2765 [M + H], found *m/z* = 694.2748 [M + H]; **^{1}H NMR** (400 MHz, $CDCl_3$): δ_H = 8.18 (1H, s, C<u>H</u>$_{Ar-H}$), 7.31 – 7.18 (5H, m, Ph$_{Ar}$-H), 7.07 (3H, d, *J* = 7.64 Hz, N<u>H</u>), 5.06 (1H, m, C<u>H</u>), 3.77 (3H, s, COOC<u>H</u>$_3$), 3.30 – 3.17 ppm (2H, m, C<u>H</u>$_2$); **^{13}C NMR** (100 MHz, $CDCl_3$): δ_C = 172.3(<u>C</u>OO), 165.31 (CO), 136.0 (<u>C</u>H$_{Ar-C}$), 134.48 (<u>C</u>H$_{Ar-C}$), 129.34(<u>C</u>H$_{Ar-C}$), 128.85(<u>C</u>H$_{Ar-C}$), 128.71(<u>C</u>H$_{Ar-C}$), 127.39 (<u>C</u>H$_{Ar-C}$), 54.25 (COO<u>C</u>H$_3$), 52.72 (<u>C</u>H), 38.03 (<u>C</u>H$_2$) ppm; **IR** υ max (cm^{-1}): 3227.8, 3179.4, 3056.1, 3029.7, 2995, 2845, 1749.3, 1643.5,

1560.0, 1542.3, 1502.9, 1459.6, 1436.9, 1335.6, 1313.6, 1216.8, 1168.5, 1106.8, 1049.6, 992.43, 728.3, 697.5, 640, 606.

(*S,S,S*)-Tris-phenylalanine-trimethylester-benzene-1,3,5-tricarboxamide (102S)

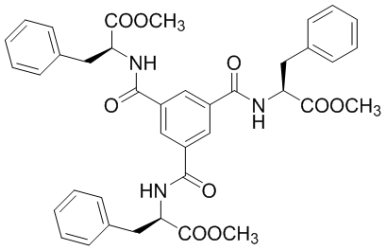

Compound **102S** was synthesised as described above (section 5.2.1) using *S*-phenylalanine (**94S**) (1.0 g, 6.053 mmol, 1 equiv.) in CH_3OH (50 mL) and $SOCl_2$ (4.5 mL, 60 mmol, 10 equiv.). Resulting *S*-phenylalanine methyl ester hydrochloride (**98S**) was dissolved in CH_2Cl_2 (50 mL) and reacted with 1,3,5-benzene tricarbonyl trichloride (482 mg, 1.81 mmol, 0.2 equiv.) to obtain compound **102S** (0.85 gm, 67 % yield). $\boldsymbol{R_f}$ = 0.5 in 95% CH_2Cl_2/CH_3OH). **m.p** 244 – 248 ºC **HRMS** (*m/z*) (ES MS $^+$) calculated for $C_{39}H_{40}N_3O_9$ *m/z* = 694.2765 [M + H], found *m/z* = 694.2750; **^{1}H NMR** (400 MHz, $CDCl_3$): δ_H = 8.16 (1H, s, CHAr-H), 7.32 – 7.18 (5H, m, Ph CHAr-H), 7.06 (1H, d, *J* = 7.8 Hz, N<u>H</u>), 5.06 (1H, m, C<u>H</u>), 3.78 (3H, s, COOC<u>H</u>$_3$), 3.31 – 3.18 (2H, m, C<u>H</u>$_2$). **^{13}C NMR** (100 MHz, $CDCl_3$): δ_C 172.14 (<u>C</u>OO), 165.16 (<u>C</u>OO, 135.90 (<u>C</u>$_{Ar}$), 134.68 (<u>C</u>$_{Ar}$), 129.19 (<u>C</u>$_{Ar}$), 128.70 (<u>C</u>$_{Ar}$), 128.54 (<u>C</u>$_{Ar}$), 127.25 (<u>C</u>$_{Ar}$), 54.09 (O<u>C</u>H$_3$), 52.56 (<u>C</u>H), 37.87 (<u>C</u>H$_2$); **IR** υ max (cm^{-1}): 3227.8, 3065, 3025.3, 2950.3, 2928.5, 2845.0, 1749.3, 1639.3, 1542.5, 1436.9, 1216.8, 1168.4, 1049.6, 764.1, 702.1, 618.4.

(*R,R,R*)-Tris-leucine-trimethylester-benzene-1,3,5-tricarboxamide (103R)

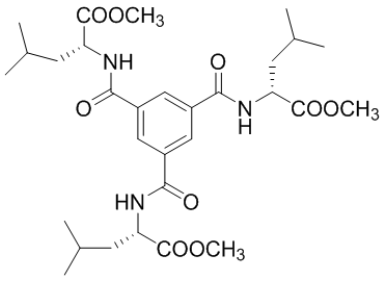

Compound **103R** was synthesised as described above (section 5.2.1) using *R*-leucine (**95R**) (1.0 g, 8.53 mmol, 1 equiv.) in CH_3OH (50 mL) and $SOCl_2$ (6.2 mL, 85 mmol, 10 equiv.). Resulting *R*-leucine methyl ester hydrochloride (**99R**) was dissolved in CH_2Cl_2 (50 mL) and reacted with 1,3,5-benzene tricarbonyl trichloride (452 mg, 1.7 mmol, 0.2 equiv) to obtain compound **103R** (0.62 gm, 62 % yield). $\boldsymbol{R_f}$ = 0.5 in 95% CH_2Cl_2/CH_3OH). **m.p** 210 – 216 ºC; **HRMS** (*m/z*) (MALDI$^+$) calculated for $C_{30}H_{45}N_3ONa$ *m/z* = 614.3048 [M + Na], found *m/z* = 614.3054; **^{1}H NMR** (400 MHz, $CDCl_3$) δ_H = 8.18 (1H, s Ar<u>H</u>), 7.52 (1H, d, *J* = 8.4 Hz, N<u>H</u>), 4.83 (1H, m, C<u>H</u>), 3.77 (3H, s, OC<u>H</u>$_3$), 1.87 – 1.53 (3H, m, C<u>H</u>$_2$ and C<u>H</u>), 0.92 (6H, dd, *J* = 6.2, 2.1 Hz, C<u>H</u>$_3$).**^{13}C NMR** (100 MHz, $CDCl_3$): δc = 174.38 (s, <u>C</u>OO), 165.56 (s, <u>C</u>O), 134.53 (s, <u>C</u>H$_{Ar\text{-}C}$), 128.49 (s, <u>C</u>H$_{Ar\text{-}C}$), 52.58 (s, O<u>C</u>H$_3$), 51.3 (s, <u>C</u>H) 40.90 (s, <u>C</u>H$_2$), 24.9 (s, <u>C</u>H), 23.0 (s, <u>C</u>H$_3$), 21.0 (s, <u>C</u>H$_3$); **IR** υ max (cm^{-1}):.3227, 3179.4, 3065.1, 3029.7, 2955.0, 2845.0, 1749.8, 1643.5, 1560, 1502.3, 1436.9, 1313.6, 1216.8, 1168.4, 1106.8, 992.4, 979.3, 842.8, 750.4, 728.4, 697.6, 609.6.

(*S*,*S*,*S*)-Tris-leucine-trimethylester-benzene-1,3,5-tricarboxamide (103S)

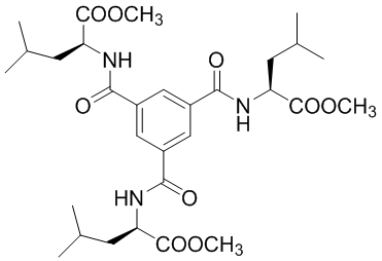

Compound **103S** was synthesised as described above (section 5.2.1) using *S*-leucine (**95S**) (1.0 g, 8.53 mmol, 1 equiv.) in CH_3OH (50 mL) and $SOCl_2$ (6.2 mL, 85 mmol, 10 equiv.). Resulting *S*-phenylalanine methyl ester hydrochloride (**99S**) was dissolved in CH_2Cl_2 (50 mL) and reacted with 1,3,5-benzene tricarbonyl trichloride (452 mg, 1.7 mmol, 0.2 equiv) to obtain compound **103S** (0.68 gm, 68 % yield). $\boldsymbol{R_f}$ = 0.5 in 95% CH_2Cl_2/CH_3OH). **m.p** 218 – 222 ^oC; **HRMS** (*m/z*) (ES MS $^+$) calculated for $C_{30}H_{45}N_3ONa$ *m/z* = 614.3048 [M + Na], found *m/z* = 614.3065; **^{1}H NMR** (400 MHz, $CDCl_3$): δ_H = 8.17 (1H, s Ar<u>H</u>), 7.59 (1H, d, *J* = 8.4 Hz, N<u>H</u>), 4.83 (1H, m, C<u>H</u>), 3.78 (3H, s, OC<u>H</u>$_3$), 1.78 – 1.62 (3H, m, C<u>H</u>$_2$ and C<u>H</u>), 0.92 (6H, dd, *J* = 6.2, 2.0 Hz, C<u>H</u>$_3$).**^{13}C NMR** (100 MHz, $CDCl_3$): δc = 174.51 (s, <u>C</u>OO), 165.69 (s, <u>C</u>O), 134.67 (s, <u>C</u>H$_{Ar-C}$), 128.66 (s, <u>C</u>H$_{Ar-C}$), 52.74 (s, O<u>C</u>H$_3$), 51.45 (s, <u>C</u>H) 41.0 (s, <u>C</u>H$_2$), 25.0 (s, <u>C</u>H), 23.1 (s, <u>C</u>H$_3$), 21.6 (s, <u>C</u>H$_3$); **IR** υ max (cm^{-1}): 3227.8, 3065, 3025.3, 2950.5, 2928.5, 2845.0, 1749.3, 1639.3, 1542.5, 1498.5, 1436.9, 1309.2, 1216.8, 1168.4, 1106.8, 1032.0, 996.8, 917.6, 746.0, 728.4, 702.0, 618.4.

7.2.2 General procedure for the synthesis of compounds 104 – 107 (R and S)

To a suspension of compounds **104 – ch.16 (R** and **S)** (1 equiv.) in CH_3OH, aqueous solution of 1M NaOH (5 equiv.) was added at 0 ^oC and this mixture was stirred at room temperature for 6 hrs. After completion of the reaction, NaOH was neutralized by adding Amberlite IR 120 H^+ resin, until the pH reached 6.5. Resin was filtered and the liquid layer was evaporated under reduced pressure to get compounds **104 – 107** as a white solid. These crude compounds were purified by re-precipitation in CH_3OH/Et_2O mixture to yield white solid powder.

(*R*,*R*,*R*)-Tris-glycine benzene-1,3,5-tricarboxamide (104)

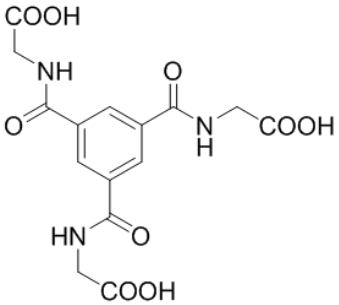

Compound **104** was synthesised according to the procedure described above in section 5.2.2 using the compound **100** (0.75 g, 1.7 mmol, 1 equiv.) in CH_3OH and an aqueous solution of 1N NaOH (8.5 mL, 8.5 mmol, 5 equiv.). Compound **104** was obtained as a white powder (0.55 g, 81 % yield). **m.p** 228.232 ^oC; **HRMS** (*m/z*) (ES MS $^-$) calculated for $C_{15}H_{14}N_3O_9$ *m/z* = 380.0730 [M - H], found *m/z* = 380.0721; **^{1}H NMR** (400 MHz, DMSO-d_6): δ_H = 12.65 (1H, s, COO<u>H</u>), 9.09 (1H, t, *J* = 5.8 Hz, N<u>H</u>), 8.49 (1H, Ar<u>H</u>), 3.97 (2H, d, *J* = 5.7 Hz, C<u>H</u>$_2$); **^{13}C NMR** (100 MHz, DMSO-d_6): δ_C = 171.09 (<u>C</u>OO), 165.63 (<u>C</u>O), 134.50 (<u>C</u>H$_{Ar-C}$), 128.88

($\underline{C}H_{Ar\text{-}C}$), 41.36 ($\underline{C}H_2$); **IR** υ max ($cm^{-1}$): 3395.0, 3346.6, 3078.1, 2981.3, 2933.0, 2633.0, 2552.0, 1740.5, 1722.9, 1639.3, 1590.9, 1551.3, 1524.9, 1414.9, 1318, 1225.6, 1190.4, 1111.2, 930.8, 886.8, 732.8, 671.2, 640, 574.

(*R,R,R*)-Tris-alanine benzene-1,3,5-tricarboxamide (105R)

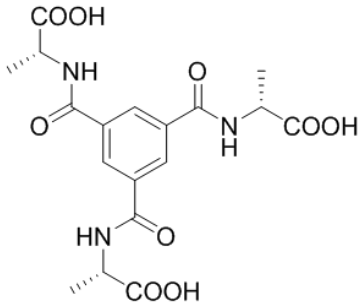

Compound **105R** was synthesised according to the procedure described above in section 5.2.2 using the compound **101R** (0.52 g, 1.11 mmol, 1 equiv.) in CH_3OH and an aqueous solution of 1M NaOH (5.6 mL, 5.58 mmol, 5 equiv.). The compound **105R** was obtained as a white powder (0.4 g, 85 % yield). **m.p**: 210 ºC; **HRMS** (*m/z*) (MS ES^+) calculated for $C_{18}H_{20}N_3O_9$ *m/z* = 422.1200 [M - H], found *m/z* = 422.1222; **^{1}H NMR** (400 MHz, DMSO-d_6): δ_H = 12.57 (2H, br s, COO$\underline{H}$), 8.96 (3H, d, *J* = 7.12 Hz, N$\underline{H}$), 8.47 (3H, s, $C\underline{H}_{Ar\text{-}H}$), 4.46 (3H, m, C$\underline{H}$), 1.42 ppm (9H, d, *J* = 7.32 Hz, $C\underline{H}_3$); **^{13}C NMR** (100 MHz, DMSO-d_6): δ_C = 174.04 ($\underline{C}$OO), 165.52 ($\underline{C}$ONH), 134.50 ($\underline{C}H_{Ar\text{-}H}$), 129.21 ($\underline{C}H_{Ar\text{-}H}$), 48.39 ($\underline{C}$H), 16.9 ppm ($\underline{C}H_3$); **IR** υ max ($cm^{-1}$): 3357, 3344, 3088, 3002, 3925, 2609, 2528, 1722, 1687, 1621, 1590, 1532, 1456, 1286, 1267, 1209, 1170, 1118, 907, 857, 828, 808.

(*S,S,S*) – Tris-alanine benzene-1,3,5 - tricarboxamide (105S)

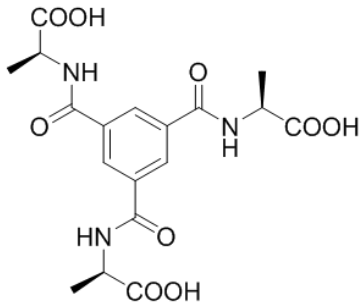

Compound **105S** was synthesised according to the procedure described above in section 5.2.2 using the compound **105S** (0.4 g, 0.85 mmol, 1 equiv) in CH_3OH and an aqueous solution of 1M NaOH (4.25 mL, 4.25 mmol, 5 equiv). The compound **105R** was obtained as a white powder (0.4 g, 85 % yield). **m.p** 220 ºC; **HRMS** (*m/z*) (ES MS^+) calculated for $C_{18}H_{20}N_3O_9$ *m/z* = 422.1200 [M - H], found *m/z* = 422.1209; **^{1}H NMR** (400 MHz, DMSO-d_6): δ_H = 12.63 (3H, br s, COO$\underline{H}$), 8.99 (3H, d, *J* = 6.56 Hz, N$\underline{H}$), 8.47 (3H, s, $C\underline{H}_{Ar\text{-}H}$), 4.45 (3H, m, C$\underline{H}$), 1.42 (9 H, d, *J* = 7.04 Hz, $C\underline{H}_3$); **^{13}C NMR** (100 MHz, DMSO-d_6): δ_C = 174.61 ($\underline{C}$OO), 164.64 ($\underline{C}$ONH), 134.75 ($\underline{C}H_{phe}$), 128.52 ($\underline{C}H_{phe}$), 49.50 ($\underline{C}$H), 18.02 ppm ($\underline{C}H_3$); **IR** υ max (cm^{-1}): 3313, 3071, 2989, 2947, 1716, 1644, 1590, 1528, 1453, 1402, 1349, 1230, 1159, 1127, 1044, 928, 830, 720.

(*R,R,R*)-Tris-phenylalanine benzene-1,3,5-tricarboxamide (106R)

Compound **106R** was synthesised according to the procedure described above in section 5.2.2 using the compound **102R** (1.2 g, 1.73 mmol, 1 equiv.) in CH_3OH and an aqueous

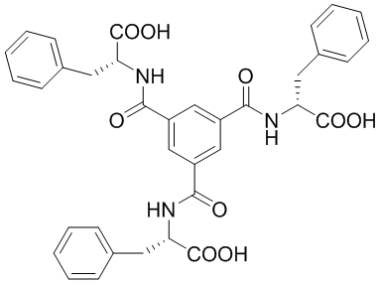

solution of 1N NaOH (14 mL, 10.5 mmol, 6 equiv.). The compound **106R** was obtained as a white powder (0.9 g, 78 % yield). **m.p** 212 – 216 ^{o}C; **HRMS** (*m/z*) (ES MS $^{+}$) calculated for $C_{36}H_{32}N_3O_9$ *m/z* = 650.2144 [M - H], found *m/z* = 650.2112; **^{1}H NMR** (400 MHz, DMSO-d_6): δ_H 12.77 (1H, s, COOH), 8.93 (1H, d, *J* = 8.0 Hz, NH), 8.27 (1H, s, ArH), 7.20 (5H, m, PhH), 4.69 – 4.54 (1H, m, CH), 3.18 – 3.12 (2H, m, CH_2); **^{13}C NMR** (100 MHz, DMSO-d_6): δ_C = 172 (COO), 165 (CO), 136 (CH_{Ar-C}), 134 (CH_{Ar-C}), 129 (CH_{Ar-C}), 129.2 (CH_{Ar-C}), 126.39 (CH_{Ar-C}), 54.0 (CH), 48.6 ppm (CH_2); **IR** υ max (cm^{-1}): 3342.2, 3073.7, 3034.1, 2977.0, 2933.0, 2673.0, 1727.3, 1648.0, 1559.7, 1524.9, 1502.9, 1450.5, 1410, 1265.2, 1221.2, 1186.0, 1102.4, 1040.8, 873.6, 737.2, 702.0, 609, 548.

(*S*,*S*,*S*)-Tris-phenylalanine benzene-1,3,5-tricarboxamide (106S)

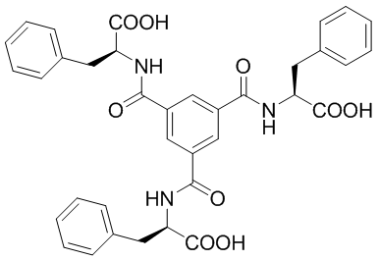

Compound **106S** was synthesised according to the procedure described above in section 5.2.2 using the compound **102S** (1.15 g, 1.65 mmol, 1 equiv.) in CH_3OH and an aqueous solution of 1N NaOH (14 mL, 10.5 mmol, 6 equiv.). The compound **106S** was obtained as a white powder (0.95 g, 87 % yield). **m.p** 208 -212 ^{o}C; **HRMS** (*m/z*) (ES MS $^{+}$) calculated for $C_{36}H_{32}N_3O_9$ *m/z* = 650.2144 [M - H], found *m/z* = 650.2146; **^{1}H NMR** (400 MHz, DMSO-d_6): δ_H = 12.82 (1H s, COOH), 8.98 (1H, d, *J* = 8.1 Hz, NH), 8.31 (1H, s, ArH), 7.31 - 7.16 (5H, m,PhH), 4.66 (1H, m, CH), 3.2 – 2.95 (2H, m, CH_2); **^{13}C NMR** (100 MHz, DMSO-d_6): δ_C = 172 (COO), 165 (CO), 138 (CH_{Ar-C}), 134 (CH_{Ar-C}), 129 (CH_{Ar-C}), 128.2 (CH_{Ar-C}), 126.3 (CH_{Ar-C}), 54.3 (CH), 48.5 ppm (CH_2); **IR** υ max (cm^{-1}): 3232.2, 3060.5, 3029.7, 2955.0, 2853.7, 1749.3, 1649.7, 1538, 1498.5, 1458.9, 1221.2, 1168.4, 1102.4, 1168.4, 1102.4, 1045.2, 913.0, 741.1, 702.0, 614.0, 552.0.

(*R*,*R*,*R*)-Tris-leucine benzene-1,3,5-tricarboxamide (107R)

Compound **107R** was synthesised according to the procedure described above in section 5.2.2 using the compound **103R** (1.0 g, 1.69 mmol, 1 equiv.) in CH_3OH and an aqueous solution of 1N NaOH (11 mL, 10.7 mmol, 6 equiv.). The compound **107R** was obtained as a white powder (0.75 g, 81 % yield). **m.p** 220 – 224 ^{o}C; **HRMS** (*m/z*) (ES MS $^{+}$) calculated for $C_{27}H_{38}N_3O_9$ *m/z* = 548.2613 [M - H], found *m/z* = 548.2605; **^{1}H NMR** (400 MHz, DMSO-d_6) δ_H = 12.64 (1H, s, COOH), 8.93 (1H, d, *J* = 7.9 Hz, NH), 8.46 (1H, s, ArH), 4.57

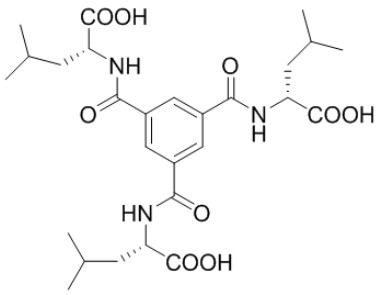

– 4.41 (1H, m, C<u>H</u>),1.81 – 1.62 (2H, m, C<u>H</u>$_2$), 1.70 – 1.55 (1H, m, C<u>H</u>), 0.91 (6H, d, *J* = 12.3, Hz, C<u>H</u>$_3$); **^{13}C NMR** (100 MHz, DMSO-d$_6$): δ_C = 174.0 (<u>C</u>OO), 165.8 (CO), 134.5 (<u>C</u>H$_{Ar-C}$), 129.2 (<u>C</u>H$_{Ar-C}$), 51.0 (CH) 24.49 (<u>C</u>H$_2$), 23.0 (<u>C</u>H), 21.15 ppm (<u>C</u>H$_3$); **IR** υ max (cm^{-1}): 3295.5, 3190.2, 3084.9, 2962.0, 2869.0, 1724.2m 1649.6, 1548.6, 1469.6, 1338.0, 1302.9, 1158.0, 916.6, 749.8, 675.2, 578.6.

(*S*,*S*,*S*)-Tris-leucine benzene-1,3,5-tricarboxamide (107S)

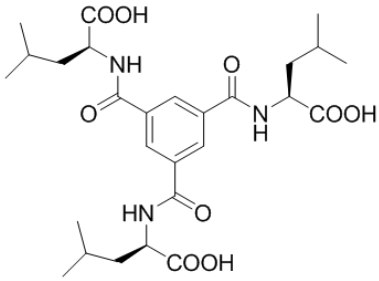

Compound **107S** was synthesised according to the procedure described above in section 5.2.2 using the compound **103S** (1.0 g, 1.69 mmol, 1 equiv.) in CH$_3$OH and an aqueous solution of 1N NaOH (11 mL, 10.7 mmol, 6 equiv.). The compound **107R** was obtained as a white powder (0.68 g, 73 % yield). **m.p** 226 – 230 ^{o}C; **HRMS** (*m/z*) (ES MS $^+$) calculated for $C_{27}H_{39}N_3O_9Na$ *m/z* = 572.2578 [M + Na], found *m/z* = 572.2570; **^{1}H NMR** (400 MHz, DMSO-d$_6$) δ_H = 12.63 (1H, s, COO<u>H</u>), 8.93 (1H, d, *J* = 7.9 Hz, N<u>H</u>), 8.45 (1H, s, Ar<u>H</u>), 4.55 – 4.41 (1H, m, C<u>H</u>), 1.87 – 1.66 (2H, m, C<u>H</u>$_2$), 1.63 - 1.59 (1H, m, C<u>H</u>), 0.92 (6H, d, *J* = 12.4 Hz); **^{13}C NMR** (100 MHz, DMSO-d$_6$): δ_C = 174 (<u>C</u>OO), 165 (CO), 134.45 (<u>C</u>H$_{Ar-C}$), 129.2 (<u>C</u>H$_{Ar-C}$), 51.1 (<u>C</u>H), 24.4 (<u>C</u>H$_2$), 23.0 (<u>C</u>H), 21.15 ppm (<u>C</u>H$_3$); **IR** υ max (cm^{-1}): 3291.1, 3190.2, 3089.2, 2957.6, 2869.8, 1724.2, 1649.6, 1544.3, 1469.6, 1408.2, 1338.0, 1302.9, 1228.2, 1202.0, 1166.8, 1122.9, 859.5, 675.2, 583.0.

The synthesis of *N*-[2,2';6',2'']terpyridin-4'-yl-propane-1,3-diamine (108)[40]

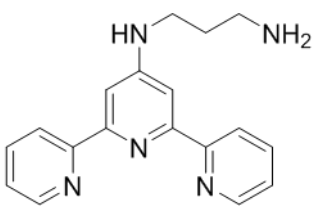

4'-Chloro-[2,2';6',2'']terpyridine (4'-chloroterpyridine) (0.8 g, 2.98 mmol, 1 equiv.) was suspended in 1,3-diamino propane (8.0 ml, 7.04 g, 94 mmol, 30 equiv.). Upon heating a yellow solution was observed. The reaction mixture was then refluxed at 120 °C for 16 hrs. After cooling to room temperature, H_2O (25 mL) was added and a white precipitate was formed, which was filtered and further washed with H_2O. The solid was dissolved in dichloromethane and washed twice with H_2O. The organic layers were then dried over Na_2SO_4, filtered and the solvent removed under reduced pressure to yield a white solid (720 mg, 80 % yield). **m.p** 148 °C; **HRMS** (*m/z*) (ES MS$^+$) calculated for $C_{18}H_{19}N_5$ *m/z* = 306.3734 [M+H], found *m/z* = 306.3728 [M+H]; **^{1}H-NMR** (400 MHz, $CDCl_3$): δ_H = 8.68 (2H, d, *J* = 4.52 Hz, C<u>H</u>$_{tpy}$), 8.62 (2H, d, *J* = 8.04 Hz, C<u>H</u>$_{tpy}$), 7.84 (2H, t, *J* = 8.00 Hz,

C<u>H</u>$_{tpy}$), 7.68 (2H, s, C<u>H</u>$_{tpy}$), 7.31 (2H, t, *J* = 7.56, 5.00 Hz, C<u>H</u>$_{tpy}$), 5.16 (1H, t, *J* = 4.48, 5.04 Hz, N<u>H</u>), 3.47 (2H, m, NHC<u>H</u>$_2$), 2.90 (2H, t, *J* = 6.52 Hz, C<u>H</u>$_2$) 1.82 (2H, m, NH$_2$C<u>H</u>$_2$) 1.23 ppm (2H, bs, N<u>H</u>$_2$); **^{13}C-NMR** (100 MHz, $CDCl_3$): δ_C = 156.87, 155.83, 155.50, 148.85, 136.73, 123.48, 121.34, 104.62, 41.65, 40.42, 32.29 ppm; **IR** υ max (cm^{-1}): 3345, 3240, 3129, 3053, 3011, 2942, 2858, 1605, 1582, 1564, 1523, 1468, 1456, 1447, 1407, 1353, 1333, 1314, 1296, 1256, 1113, 1091, 1069, 1040, 985, 924, 860, 791, 743, 697, 657.

5.2.3 General procedure for the synthesis of compound 88 – 91 (R and S)

Compound **105 – 107** (R/S) was dissolved in DMF/CH_2Cl_2 mixture (1:3 v/v) solvent mixture and cooled down to 0 ^oC in an ice/acetone bath. 1-Ethyl-3-(3-dimethylaminopropyl)carbodiimide (EDCI, 3.9 equiv.) and 1-Hydroxybenzotriazole (HOBT, 3.9 equiv.) were added to this solution and resulting mixture was let to stir for 10 min. Compound **108** was then added and the mixture was allowed to reach room temperature and left stirring for 24 hrs. Once reaction was complete, CH_2Cl_2 was removed under reduced pressure and remaining DMF was poured into ice cold water (approx. 200 mL). The obtained white solid was filtered and dried under vacuum. The dried solid was dissolved in $CHCl_3$ and washed with sat. $NaHCO_3$ solution, H_2O and dried over Na_2SO_4 filtered and the solvent was evaporated under reduced pressure to yield crude compound **88 – 91 (R/S).** This crude compound was purified by column chromatography using neutral alumina as stationary phase and 90% $CHCl_3$/EtOH as mobile phase to yield the pure compound **88 – 91 (R/S)**.

***N*^{1},*N*^{3},*N*^{5}-Tris(*R*,*R*,*R*)-1-(3-(2,6-di(pyridine-2-yl)pyridine-4-ylamino)-glycine benzene-1,3,5-tricarboxamide (88)**

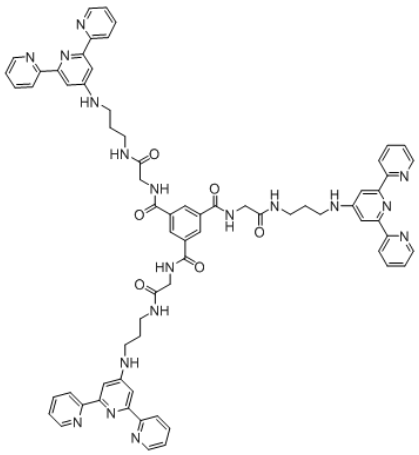

Compound **88** was synthesised according to the procedure described in section 5.2.3 using compound **104** (300 mg, 0.78 mmol, 1 equiv.) in DMF/CH_2Cl_2 (6 mL, 1:3 v/v) with EDCI (592 mg, 3.1 mmol, 3.9 equiv.), HOBT (420 mg, 3.1 mmol, 3.9 equiv.) and compound **108** (960 mg, 3.1 mmol, 3.9 equiv.). Compound **88** was obtained (530 mg, 56 % yield). R_f = 0.5 (90% $CHCl_3$/EtOH). **m.p**: 192 – 196 ^oC; **HRMS** (*m/z*) (MALDI$^+$) calculated for $C_{69}H_{67}N_{18}O_6$ *m/z* = 1243.5491 [M+ H], found *m/z* = 1243.5443; **^{1}H NMR** (600 MHz, DMSO-d_6): δ_H = 8.91 (1H, s, N<u>H</u>), 8.66 (2H, s, C<u>H</u>$_{tpy}$), 8.55 (2H, s, C<u>H</u>$_{tpy}$), 8.53 (1H, s, Ar<u>H</u>), 8.09 (1H, t, *J* = 5.2 Hz, N<u>H</u>), 7.94 (2H, t, *J* = 7.0 Hz, C<u>H</u>$_{tpy}$), 7.67 (2H, s, C<u>H</u>$_{tpy}$), 7.43 (2H, s, C<u>H</u>$_{tpy}$), 6.87 (1H, s, N<u>H</u>), 3.91 (2H, d, *J* = 5.3 Hz, C<u>H</u>$_2$), 3.23 (4H, d, *J*

= 6.0 Hz, C<u>H</u>$_2$), 1.78 (2H, d, *J* = 6.7 Hz, C<u>H</u>$_2$); **^{13}C NMR** (151 MHz, DMSO-d$_6$) δ_C = 168.72, 165.63, 155.97, 155.52, 154.87, 148.95, 137.06, 134.40, 129.05, 123.92, 120.65, 42.79, 40.06, 36.50, 28.50; **IR** υ max (cm^{-1}): 3298.2, 3060.5, 2928.5, 2867, 1652.5, 1608.5, 1586.5, 1564.5, 1529.3, 1467.7, 1252, 1230, 1039, 983, 860, 794.4, 746, 627.

N^1,*N*^{3},*N*^{5}-Tris(*R*,*R*,*R*)-1-(3-(2,6-di(pyridine-2-yl)pyridine-4-ylamino)-alanine benzene-1,3,5-tricarboxamide (89R)

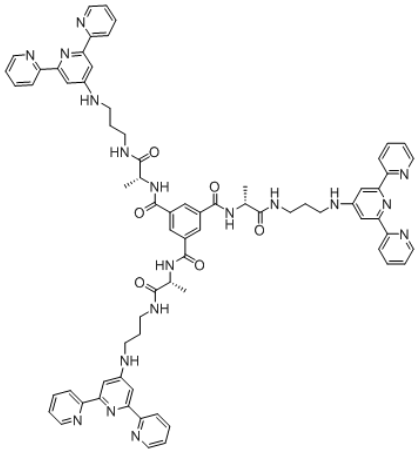

Compound **89R** was synthesised according to the procedure described in section 5.2.3 using compound **105R** (200 mg, 0.472 mmol, 1 equiv.) in DMF/CH_2Cl_2 (4 mL, v/v), and EDCI (296 mg, 1.88 mmol, 3.9 equiv.), HOBT (256 mg, 1.18 mmol, 3.9 equiv.) and compound **108** (576 mg, 1.18 mmol, 3.9 equiv.), compound **89R** was obtained (360 mg, 60 % yield). ***R*$_f$** = 0.5 (90% $CHCl_3$/EtOH). **m.p**: 187 ^{o}C; **HRMS** (*m/z*) (MALDI$^+$) calculated for $C_{72}H_{73}N_{18}O_6$ *m/z* = 1285.5960 [M+ H], found *m/z* = 1285.5948; **^{1}H NMR** (600 MHz, DMSO-*d*$_6$): δ_H = 8.67 (3H, d, *J* = 7.80 Hz, N<u>H</u>), 8.65 (6H, d, *J* = 3.42 Hz, C<u>H</u>$_{tpy}$), 8.52 (6H, d, *J* = 7.38 Hz, C<u>H</u>$_{tpy}$), 8.48 (3H, s, C<u>H</u>$_{phe}$), 8.1 (3H, t, *J* = 5.34 Hz, N<u>H</u>), 7.93 (6H, t, *J* = 7.20 Hz, C<u>H</u>$_{tpy}$), 7.66 (6H, s, C<u>H</u>$_{tpy}$), 7.42 (6H, br s, C<u>H</u>$_{tpy}$), 6.88 (3H, s, N<u>H</u>), 4.50 (3H, m, C<u>H</u>), 3.36 - 3.20 (12H, m, C<u>H</u>$_2$), 1.77 (6H, t, *J* = 6.78 Hz, C<u>H</u>$_2$), 1.36 ppm (9H, d, *J* = 7.1 Hz, C<u>H</u>$_3$); **^{13}C NMR** (150 MHz, DMSO-*d*$_6$): δ_C = 172.28, 165.92, 155.89, 155.01, 148.69, 137.11, 134.92, 129.25, 124.00, 120.68, 105.76, 49.24, 40.03, 36.50, 28.50, 18.20 ppm; **IR** υ max (cm^{-1}): 3300, 3066, 2942, 1649, 1605, 1584, 1565, 1524, 1457, 1447, 1248, 1225, 985, 793, 741, 659, 623; **Elemental analysis:** Calculated for $C_{72}H_{73}N_{18}O_6 \cdot 3H_2O$: C, 64.56; H, 5.87; N, 18.82. Found: C, 64.43; H, 5.39; N, 18.14.

N^1,*N*^{3},*N*^{5}-Tris(*S*,*S*,*S*)-1-(3-(2,6-di(pyridine-2-yl)pyridine-4-ylamino)-alanine benzene-1,3,5-tricarboxamide (89S)

Compound **89S** was synthesised according to the procedure described in section 5.2.3 using compound **105S** (200 mg, 0.472 mmol, 1 equiv.) in DMF/CH_2Cl_2 (4 mL, v/v), and EDCI (296 mg, 1.88 mmol, 3.9 equiv.), HOBT (256 mg, 1.18 mmol, 3.9 equiv.) and compound **108** (576 mg, 1.18 mmol, 3.9 equiv.), compound **89S** was obtained (390 mg, 64 % yield). ***R*$_f$** = 0.5 (90% $CHCl_3$/EtOH). **m.p**: 187 ^{o}C; **HRMS** (*m/z*) (MALDI$^+$) calculated for $C_{72}H_{73}N_{18}O_6$ *m/z* = 1285.5960 [M+ H], found *m/z* = 1285.5946; **^{1}H NMR** (600 MHz, DMSO-*d*$_6$): δ_H =

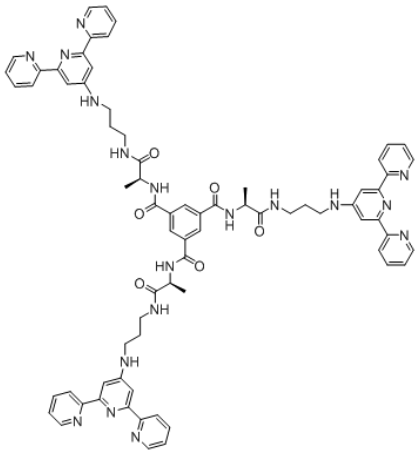

8.69 (3H, d, *J* = 7.76 Hz, NH), 8.65 (6H, d, *J* = 3.61 Hz, CH_{tpy}), 8.54 (6H, d, *J* = 7.40 Hz, CH_{tpy}), 8.48 (3H, s, CH_{phe}), 8.10 (3H, t, *J* = 5.51 Hz, NH), 7.93 (6H, t, *J* = 7.41 Hz, CH_{tpy}), 7.66 (66H, s, CH_{tpy}), 7.42 (6H, t, CH_{tpy}), 6.87 (3H, s, NH), 4.50 (3H, m, CH), 3.32 - 3.23 (12H, m, CH_2), 1.77 (6H, t, *J* = 6.94 Hz, CH_2), 1.35 ppm (9H, d, J = 6.8 Hz, CH_3); **^{13}C NMR** (150 MHz, DMSO-d_6): δ_C = 172.61, 165.65, 156.29, 155.93, 155.28, 149.31, 137.42, 134.67, 129.67, 124.26, 121.01, 101.22, 49.57, 40.03, 36.89, 28.91, 18.59 ppm; **IR** υ max (cm^{-1}): 3300, 3066, 2942, 1649, 1605, 1584, 1565, 1524, 1457, 1447, 1405, 1284, 1225, 1046, 985, 858, 793, 741, 696, 659, 623. **Elemental analysis:** Calculated for $C_{72}H_{73}N_{18}O_6{\cdot}3H_2O{\cdot}3CH_2Cl_2$: C, 56.56; H, 4.69; N, 16.04. Found: C, 56.50; H, 5.31; N, 15.81.

N^1,*N*^{3},*N*^{5}-Tris(*R*,*R*,*R*)-1-(3-(2,6-di(pyridine-2-yl)pyridine-4-ylamino)-phenylalanine benzene-1,3,5-tricarboxamide (90R)

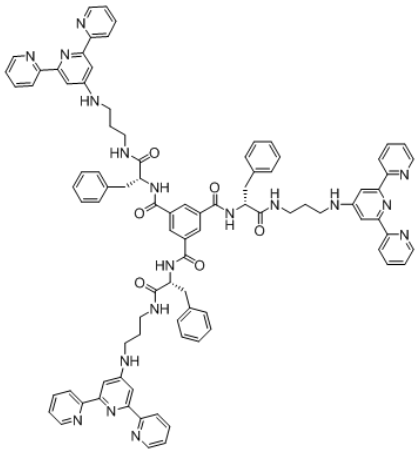

Compound **90R** was synthesised according to the procedure described in section 5.2.3 using compound **106R** (240 mg, 0.368 mmol, 1 equiv.) in DMF/CH_2Cl_2 (5 mL, v/v), and EDCI (230 mg, 1.48 mmol, 3.9 equiv.), HOBT (200 mg, 1.48 mmol, 3.9 equiv.) and compound **108** (440 mg, 1.48 mmol, 3.9 equiv.), compound **90S** was obtained (320 mg, 57 % yield). R_f = ~0.5 (90% $CHCl_3$/EtOH). **m.p**: 190 – 196 ^{o}C; **HRMS** (*m/z*) (MALDI$^+$) calculated for $C_{90}H_{85}N_{18}O_6$ *m/z* = 1513.6899 [M+ H], found *m/z* = 1513.6886; **^{1}H NMR** (600 MHz, DMSO-d_6): δ_H = 8.74 (1H, d, *J* = 8.2 Hz, NH), 8.65 (2H, d, *J* = 3.2 Hz, CH_{tpy}), 8.54 (1H, d, *J* = 7.6 Hz, CH_{tpy}), 8.30 (1H, s, PhArH), 8.28 (1H, s, ArH), 8.21 (1H, t, *J* = 5.4 Hz, PhArH), 7.94 (2H, t, *J* = 7.3 Hz, CH_{tpy}), 7.66 (2H, s, CH_{tpy}), 7.42 (1H, s, NH), 7.28 (2H, d, *J* = 8.1 Hz, CH_{tpy}), 7.21 (2H, t, *J* = 7.7 Hz, PhArH), 7.11 (1H, t, *J* = 6.6 Hz, PhArH), 6.84 (1H, s, NH), 4.73 – 4.69 (1H, m, CH), 3.18 (4H, s, CH_2), 3.10 – 2.97 (2H, m, CH_2), 1.75 – 1.72 (2H, m, CH_2). **^{13}C NMR** (151 MHz, DMSO-d_6): δ_C = 171.02, 165.44, 148.98, 138.05, 137.13, 134.32, 129.15, 128.11, 126.31, 123.99, 120.70, 107.63, 55.08, 40.06, 37.72, 36.58, 28.37. **IR** υ max (cm^{-1}): 3263, 3060.5, 3034.1, 2928.5, 2871.3, 1643.7, 1604, 1586.5, 1568.5, 1529, 1467.7, 1441.3, 1230, 1106.8,

988.3, 856.2, 790, 741, 702, 658, 627, 556. **Elemental analysis:** Calculated for $C_{90}H_{84}N_{18}O_6.3H_2O$: C, 68.95; H, 5.79; N, 16.08. Found: C, 66.78; H, 5.82; N, 13.46.

N^1,*N*^{3},*N*^{5}-Tris(*S*,*S*,*S*)-1-(3-(2,6-di(pyridine-2-yl)pyridine-4-ylamino)-phenylalanine benzene-1,3,5-tricarboxamide (90S)

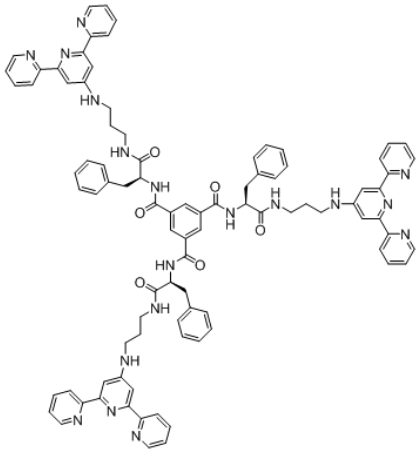

Compound **90S** was synthesised according to the procedure described in section 5.2.3 using compound **106S** (240 mg, 0.368 mmol, 1 equiv.) in DMF/CH_2Cl_2 (5 mL, v/v), and EDCI(230 mg, 1.48 mmol, 3.9 equiv.), HOBT (200 mg, 1.48 mmol, 3.9 equiv.) and compound **108** (440 mg, 1.48 mmol, 3.9 equiv.), compound **90S** was obtained (320 mg, 57 % yield). R_f = ~0.5 (90% $CHCl_3$/EtOH). **m.p**: 196 – 200 ^oC; **HRMS** (*m/z*) (MALDI$^+$) calculated for $C_{90}H_{85}N_{18}O_6$ *m/z* = 1513.6899 [M+ H], found *m/z* = 1513.6842; **^{1}H NMR** (600 MHz, DMSO-d_6): δ_H = δ 8.78 (1H, d, *J* = 7.7 Hz, NH), 8.71 (2H, d, *J* = 10.6 Hz, CH$_{tpy}$), 8.50 (1H, s, CH$_{tpy}$), 8.30 (1H, s, PhArH), 8.24 (1H, s, PhArH), 7.98 (2H, s, CH$_{tpy}$), 7.66 (2H, s, CH$_{tpy}$), 7.49 (2H, s, NH), 7.29 (2H, d, *J* = 7.2 Hz, CH$_{tpy}$), 7.20 (2H, dd, *J* = 14.5, 6.9 Hz, PhArH), 7.11 (1H, t, *J* = 7.3 Hz, PhArH), 4.72 – 4.69 (1H, m, CH), 3.27 – 3.10 (4H, m, CH$_2$), 3.09 – 2.9 (2H, m, CH$_2$), 1.76 (2H, s, CH$_2$).**^{13}C NMR** (150 MHz, DMSO-d_6): δ_C = 170.5, 164.9, 148.5, 137.5, 136.6, 133.8, 128.6, 127.6, 125.8, 123.4, 120.2, 78.7, 54.6, 39.5, 37.2, 36.1, 27.8. **IR** υ max (cm^{-1}): 3258.6, 3065.0, 2928.0, 2871.3, 1648.0, 1608.0, 1582.0, 1564.0, 1524.0, 1463.3, 1441.3, 1406.0, 1265.2, 1230.0, 1039.0, 1001.0, 988.0, 864.0, 790.0, 741.0, 697.0, 622.0. **Elemental analysis:** Calculated for $C_{90}H_{84}N_{18}O_6.3H_2O$: C, 68.95; H, 5.79; N, 16.08. Found: C, 68.26; H, 5.35; N, 15.45.

N^1,*N*^{3},*N*^{5}-Tris(*R*,*R*,*R*)-1-(3-(2,6-di(pyridine-2-yl)pyridine-4-ylamino)-leucine benzene-1,3,5-tricarboxamide (91R)

Compound **91R** was synthesised according to the procedure described in section 5.2.3 using compound **107R** (135 mg, 0.245 mmol, 1 equiv.) in DMF/CH_2Cl_2 (5mL, v/v), EDCI (152 mg, 0.98 mmol, 3.9 equiv.), HOBT (132 mg, 0.98 mmol, 3.9 equiv.) and compound **108** (300 mg, 0.98 mmol, 3.9 equiv.), compound **90S** was obtained (210 mg, 61 % yield). R_f = ~0.5 (90% $CHCl_3$/EtOH); **m.p**: 191 – 195 ^oC; **HRMS** (*m/z*) (MALDI$^+$) calculated for $C_{81}H_{91}N_{18}O_6$ *m/z* = 1411.7369 [M+ H], found *m/z* = 1411.7332; **^{1}H NMR** (600 MHz, DMSO-d_6): δ_H = 8.66 (1H, s, NH), 8.65 (2H, d, *J* = 4.7 Hz, CH$_{tpy}$), 8.55 (2H, d, *J* = 7.9 Hz,

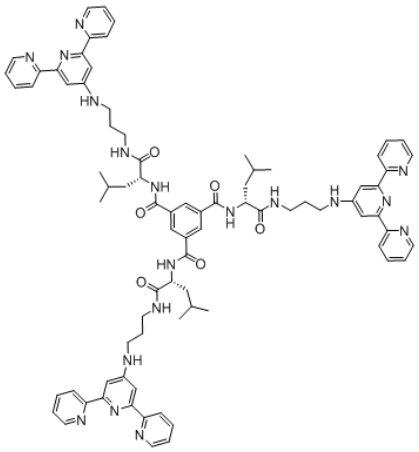

C<u>H</u>$_{tpy}$), 8.44 (1H, s, Ar<u>H</u>), 8.15 (1H, t, *J* = 5.5 Hz, N<u>H</u>), 7.93 (2H, td, *J* = 7.8, 1.5 Hz, C<u>H</u>$_{tpy}$), 7.67 (2H, s, C<u>H</u>$_{tpy}$), 7.41 (2H, dd, *J* = 6.5, 4.9 Hz, C<u>H</u>$_{tpy}$), 6.84 (1H, t, *J* = 5.1 Hz, N<u>H</u>), 4.54 – 4.51 (1H, m, C<u>H</u>), 3.25 – 3.20 (4H, m, C<u>H</u>$_2$), 1.78 – 1.76 (2H, m, C<u>H</u>$_2$), 1.66 (2H, s, C<u>H</u>$_2$), 1.54 – 1.52 (1H, m, C<u>H</u>), 0.87 (6H, dd, *J* = 9.6, 6.4 Hz, C<u>H</u>$_3$); **^{13}C NMR** (150 MHz, DMSO-*d*$_6$): δ_C = δ 172, 165.6, 155.97, 155.52, 154.91, 148.90, 136.98, 134.41, 129.35, 123.81, 120.58, 51.97, 40.78, 40.06, 36.52, 28.40, 24.41, 22.93, 21.54; **IR** υ max (cm^{-1}): 3291.1, 3063.0, 2962.0, 2926.8, 2874.2, 1645.2, 1610.0, 1583.8, 1566.7, 1526.7, 1465.3, 1447.7, 1408.2, 1254.6, 1223.0, 1096.0, 863.9, 793.7, 745.4, 626.0.

N^1,N^3,N^5-Tris(*S*,*S*,*S*)-1-(3-(2,6-di(pyridine-2-yl)pyridine-4-ylamino)-leucine benzene-1,3,5-tricarboxamide (91S)

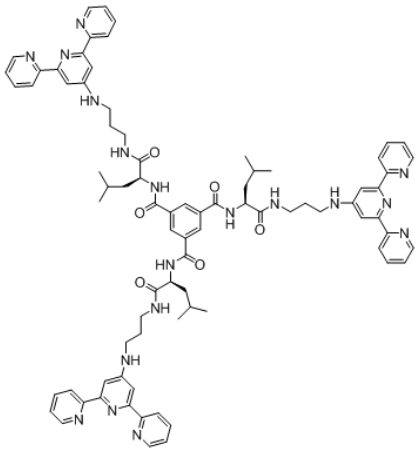

Compound **91S** was synthesised according to the procedure described in section 5.2.3 using compound **107R** (135 mg, 0.245 mmol, 1 equiv.) in DMF/CH_2Cl_2 (5mL, v/v), EDCI (152 mg, 0.98 mmol, 3.9 equiv.), HOBT (132 mg, 0.98 mmol, 3.9 equiv.) and compound **108** (300 mg, 0.98 mmol, 3.9 equiv.), compound **90S** was obtained (240 mg, 69 % yield). R_f = ~0.5 (90% $CHCl_3$/EtOH). **m.p**: 197 – 201 ^{o}C; **HRMS** (*m/z*) (MALDI$^+$) calculated for $C_{81}H_{91}N_{18}O_6$ *m/z* = 1411.7369 [M+ H], found *m/z* = 1411.7341; **^{1}H NMR** (600 MHz, DMSO-*d*$_6$): δ_H = 8.67 (1H, s, N<u>H</u>), 8.65 (2H, d, *J* = 3.7 Hz, C<u>H</u>$_{tpy}$), 8.55 (2H d, *J* = 7.9 Hz, C<u>H</u>$_{tpy}$), 8.45 (1H s, Ar<u>H</u>), 8.16 (1H t, *J* = 5.4 Hz, N<u>H</u>), 7.94 (2H, td, *J* = 7.9, 1.6 Hz, C<u>H</u>$_{tpy}$), 7.67 (2H, s, C<u>H</u>$_{tpy}$), 7.42 (2H, dd, *J* = 6.8, 5.2 Hz, C<u>H</u>$_{tpy}$), 6.85 (1H t, *J* = 5.0 Hz, N<u>H</u>), 4.57 – 4.49 (1H m, C<u>H</u>), 3.27 – 3.18 (4H m, C<u>H</u>$_2$), 1.83 – 1.74 (2H m, C<u>H</u>$_2$), 1.67 – 1.61 (2H m, C<u>H</u>$_2$), 1.55 – 1.52 (1H m, C<u>H</u>), 0.87 (6H dd, *J* = 9.5, 6.5 Hz, C<u>H</u>$_3$); **^{13}C NMR** (150 MHz, DMSO-*d*$_6$): δ_C = 171.16, 170.16, 165.76, 157.61, 149.44, 137.55, 134.31, 129.05, 128.22, 126.34, 124.44, 79.19, 55.18, 40.06, 37.67, 36.51, 28.29; **IR** υ max (cm^{-1}): 3291.1, 3071.7, 2962.0, 2935.6, 2874.2, 1640.8, 1588.2, 1561.8, 1526.7, 1469.6, 1439.0, 1250.2, 1223.9, 1096.6, 986.8, 859.0, 793.0, 741.0, 631.0.

5.2.4 General procedure for the synthesis of Eu(III) complexes (Eu.89R and Eu.89S)

Eu(III) complexes, **Eu.89R and Eu.89S**, were prepared by reacting the relevant ligand (**89R** and/or **89S,** 1 equiv.) with $Eu(CF_3SO_3)_3$ (1 equiv.) in CH_3OH (10 mL), under microwave radiation at 70 ^oC for 1 hr. The reaction mixture was subsequently cooled to room temperature and concentrated to a third of its initial volume and complex was precipitated by ether diffusion. The resulting white solid was collected by decanting the liquid and dried under vacuum, ^1H NMR spectra recorded for the complexes consisted of broader peaks indicating the presence of paramagnetic Eu(III) ions.

Complex Eu.89R

Complex **Eu.89R** was synthesised according to the procedure described in section 5.2.4 by reacting the ligand **89R** (10 mg, 1 equiv.) with $Eu(CF_3SO_3)_3$ (2.33 mg, 1 equiv.). A white solid was obtained (8 mg, 54 % yield). **m.p.** 257 ^oC; **HRMS** (*m/z*) (MALDI$^+$) calculated for $C_{74}H_{72}N_{18}O_{12}F_6S_2$ Eu *m/z* = 1735.4135 [**Eu.89R**.$(CF_3SO_3^-)_2]^+$, found *m/z* = 1735.4149; **^{1}H NMR** (400 MHz, CD_3OD): δ_H = 8.73, 8.70, 8.51, 8.45, 8.39, 8.23, 8.00, 7.93, 7.57, 7.47, 7.41, 1.50ppm; **IR** υ max (cm^{-1}): 3516, 3324, 3276, 3080, 2983, 2948, 2882, 1649, 1623, 1571, 1531, 1470, 1444, 1265, 1160, 1028, 1007, 792, 639.

Complex Eu.89S

Complex **Eu.89S** was synthesised according to the procedure described in section 5.2.4 using the ligand **89S** (10 mg, 1 equiv.) and $Eu(CF_3SO_3)_3$ (2.33 mg, 1 equiv.). A white solid was obtained (9 mg, 61 % yield). **m.p.** 260^oC; **HRMS** (*m/z*) (MALDI$^+$) calculated for $C_{74}H_{72}N_{18}O_{12}F_6S_2Eu$ *m.z* = 1735.4135 [**Eu.89S**.$(CF_3SO_3^-)_2$], found *m/z* = 1735.4211; **^{1}H NMR** (400 MHz, CD_3OD): δ_H = 8.58, 8.46, 8.41, 8.30, 7.96, 7.91, 7.89, 7.43, 7.38, 1.47 ppm. IR υ max (cm^{-1}): 3530, 3320, 3136, 3070, 2939, 2874, 1649, 1614, 1566, 1536, 1470, 1439, 1383, 1278, 1251, 1225, 1160, 1028, 1002, 849, 792, 748, 735, 635, 574. **IR** υ max (cm^{-1}): 3515, 3283, 3091, 3981, 2943, 2875, 1653, 1620, 1528, 1471, 1442, 1279, 1250, 1164, 1030, 1001, 857, 795, 632.

5.3 Experimental Details for Chapter 3

All chemicals were purchased from Sigma-Aldrich Ireland Ltd., Acros Organics, TCI Ltd., and Chematech. All the solvents used were of Spectroscopic or HPLC grade and were used without further purification, unless otherwise stated. Synthesis of all the compounds used in the experiments discussed in Chapter 3, were discussed previously in the section 5.2.

5.3.1 Gelation tests

Gelation tests were carried out by dissolving a known amount (%, weight/volume) of the gelator (compound) in the respective solvent system in a test tube (*d*. 8 mm, *l*. 10 cm) by heating and followed by cooling to room temperature without any disturbance. If the liquid did not flow upon inverting the test tube, it was termed as a gel.

5.3.2 Thermogravimetric analysis

Small amount of gel (~70 – 100 μL by vol.) was placed in TGA crucible and heated in Perkin Elmer Pyrus 1 TGA instrument, equipped with an ultra-microbalance with sensitivity of 0.1 μg. The temperature range is from 25ºC to 800ºC with a heating rate of 5 ºC/min under nitrogen atmosphere. The % weight loss is monitored with respect to temperature change.

5.3.3 Reversible stimuli responsible properties of 88 gels

Thermoreversible properties: Gels were prepared in glass tubes (*d*. 8 mm, *l*. 10 cm), sealed the open end and stabilised for 12 hrs. These gels in the tubes were heated at the rate of ~2 ºC/min until the gel melts and starts to flow as observed by tilting the tube. This hot sol was cooled to room temperature until the gel reforms.

Mechanoreversible properties: For thixotropic property, the gels prepared was given a strong shake until the gel collapsed and becomes liquid. This liquid was kept in rest for ~60 – 90 min until the gels reforms.

5.3.4 Gel-sol transition temperature (T_{gel})

Gels of different concentrations, c = 0.5, 0.75, 1.0, 1.25 and 1.5% w/v, were prepared as described in the section 5.3.1, using **88** in CH_3CN/H_2O (60:40) mixture in glass vials ((*d*. 7 mm, *l*. 4 cm). The gels were stabilized for 12 h prior to T_{gel} measurements. During T_{gel} measurements, these vials were kept upside down in a thermostated silicon oil bath. The temperature of the oil bath was increased in a controlled manner (~ 2 °C/min). The temperature at which the gel fell under gravity was recorded as the T_{gel}.

Enthalpy of gelation: A graph of lnC vs $1/T_{gel}$ (K) was plotted and enthalpy of gelation (ΔH) was calculated for the slope of the graph using schroder van Larr equation.[321]

$$\mathbf{lnC = -\Delta H/RT + K}\text{……} \quad \text{schroder van Larr equation}$$

where, R = gas constant (8.314 $JK^{-1}mol^{-1}$), C = concentration of gelator (M), T = T_{gel},(K) and K = intercept.

So, slope = -ΔH/R (where, value of slope = -13145.2)

Hence, **ΔH = 109 KJmol^{-1}**

5.3.5 Imaging

5.3.5.1 Scanning electron microscopy of gels

Gel samples were prepared by placing a small amount of **88** gels (~10 – 15 μL by vol.) on silicon wafers and making a thin film by smooth smearing. The samples were dried initially in air for 5 - 6 hours followed by drying in high vacuum for 2 - 3 hours. Before recording the images, the samples were gold coated using sputter. These samples were imaged in Carl Zeiss ULTRA Plus, field emission scanning electron microscope (FE-SEM) using beam current of 5 - 10 kV with an SE2 or InLens detector.

5.3.5.2 Transmission electron microscopy of gels

A thin layer of **88** gel was made on a glass slide. Then a carbon coated copper grid was touched over the surface of the gel to make a very thin layer of the gel on the grid. The grid was dried first in the air for 5 – 6 hours followed by drying under high vacuum for a further 3 - 4 hours. These samples were imaged using Titan FEI transmission electron microscope (TEM) using 80kV beam current.

5.3.6 Scanning electron microscopy of microspheres

Microspheres were prepared by dissolving **89** (R/S), **90** (R/S), **91** (R/S) (2 - 5 mg each) in CH_3CN/H_2O (6:4) mixture (1 ml) by heating at 100 ^oC and cooling to room temperature. A solution of microspheres with concentration 0.2 - 0.5% w/v was obtained. These solutions were dropcasted (5 μL each) on silica wafers and dried in air for 5 – 6 hours and finally under high vacuum for 2 – 3 hours to deposit solid microspheres on silica wafers.

These samples were imaged in Carl Zeiss ULTRA plus, scanning electron microscope (SEM) without gold coating. Images were recorded at a beam current of 2 - 10 kV using two secondary electron detectors such as SE2 and InLens detectors. The same set up was used in the imaging of other microspheres samples discussed in Chapter 3.

Images were taken at 45^o and 60^o tilted angle. For 60^o tiled images, a 90^o sample holder was used and the sample stage in the SEM was tilted for 30^o during imaging to get the 60^o view of the sample. And the images were recorded at 10kV beam current. Tilting the sample increases relative local sample surface resulting in the increase of number of secondary electrons emitted directly in the direction of detector making it easier to interpret the surface topography and three-dimensional structures.

5.3.7 Dynamic light scattering measurements

The solutions of microspheres were prepared as described in the procedure above in 5.3.6, using **89S**, **90S**, **91S** (6 mg each) dissolved in CH_3CN/H_2O (6:4) solvent mixture (3 ml) to obtain the solutions of concentration 1.55×10^{-3} M each.

DLS measurements were performed with Malvern Instruments Zetasizer Nano Series at 25 ^oC. Prior to each measurement, the samples were centrifuged for 30 minutes at 3000 rpm to break up any possible aggregates.

5.3.8 Investigation of the aggregation process in the formation of microspheres using fluorescence

Stock solution of **89S** ($c = 3 \times 10^{-4}$ M) was prepared by dissolving 1.9 mg in CH_3Cl/CH_3OH (1:5, 5 ml). Different volumes (in increasing order) of this solution were transferred to different vial and solvent was dried to get the appropriate amounts of compound (in μg) in each vials corresponding to its concentration. These solid compounds were dissolved in CH_3CN/H_2O (6:4) solvent mixture (3 ml) by heating at 100 ^oC and cooling to room temperature. The resulting solutions have the concentration range from 5×10^{-6} to 3×10^{-4} M.

These solutions were used for the Fluorescence measurements of free molecules (ligands) and microspheres. The fluorescence measurements were carried out on a Varian Cary Eclipse Fluorimeter equipped with a 1.0 cm path length quartz cell at room temperature The parameter settings of the fluorimeter for the luminescence measurement carried out in Chapter 3 are shown in Table 5.3.1. Please note, the voltage of the PMT detector was adjusted as necessary to prevent signal saturation in different measurements. The same solution was excited at both 280 nm and 405 nm for the fluorescence emission from free molecules and microspheres.

Table 5.3.1: Parameters for fluorescence emission measurements of free molecules and microspheres in Chapter 3

Mode: Fluorescence	**Excitation:** 280 nm for free molecules 405 nm for microspheres	**Scans:** 300 – 800 nm for free molecules 425 – 800 nm for microspheres
Excitation slit: 20 nm	**Emission slit:** 5 nm	**PMT Voltage:** 720 V for free molecules 775 V for microspheres
Averaging time: 0.1 s	**Scan rate:** 600 nm/min	**Data Interval:** 0.5 nm

5.3.9 Transfer of microspheres by static interactions

Microspheres were deposited on silica wafers as described in the procedure above in 5.3.6, using **89S** (4 mg) dissolved in CH_3CN/H_2O (6:4) solvent mixture (1 ml).

The microsphere sample was placed in the centre of the sample stage and a movable needle was fixed at the edge, so that the tip of the needle is right above the sample, as shown in Figure 3.12A-C. This movable needle is connected to a unit to control its movement (such as forward, retract, up, down, left and right). Using the control unit, the tip of the needle was moved slowly towards the microspheres to pick up some particles and this process was imaged by SEM to see the particles at the tip of needle.

5.3.10 Understanding the mechanism of microspheres formation

5.3.10.1 Critical concentration of urea for the prevention of microspheres

In a series of solutions, **89S** (2 mg) and urea (respective mole equivalents) were dissolved together in CH_3CN/H_2O (6:4) solvent mixture (1 ml) by heating at 100 ^oC and cooling to room temperature (22^oC). Various amounts of urea were added to compounds before the microspheres are formed as depicted below in Table 5.3.2. After cooling, the solutions were dropcasted (5 µL each) on silica wafer and dried in air (5 - 6 hrs) and in high vacuum (2 – 3 hrs). These samples were imaged using SEM without gold coating.

Table 5.3.2: Mole equivalent of urea added to **89S** before the formation of microspheres.

89S (mg/1ml)	Mole equiv. of urea	Amount of urea wt. (moles) [a]
2 mg (1.55×10^{-6} moles)	0	Blank, 0 mg (0 moles)
2 mg (1.55×10^{-6} moles)	1	0.09 mg (1.55×10^{-6} moles)
2 mg (1.55×10^{-6} moles)	2	0.18 mg (3.1×10^{-6} moles)
2 mg (1.55×10^{-6} moles)	3	0.28 mg (4.65×10^{-6} moles)
2 mg (1.55×10^{-6} moles)	4.5	0.42 mg (6.97×10^{-6} moles)
2 mg (1.55×10^{-6} moles)	6	0.56 mg (9.33×10^{-6} moles)
2 mg (1.55×10^{-6} moles)	7.5	0.7 mg (11.6×10^{-6} moles)
2 mg (1.55×10^{-6} moles)	9	0.84 mg (13.9×10^{-6} moles)
2 mg (1.55×10^{-6} moles)	10	0.93 mg (15.6×10^{-6} moles)
2 mg (1.55×10^{-6} moles)	12	1.11 mg (18.6×10^{-6} moles)

[a] A stock solution of urea in water (c = 10 mg/1000 µL) was used in the addition in above samples.

5.3.10.2 Time dependent degradation of microspheres using urea

A solution of microspheres was prepared as described in the procedure above in 5.3.6, using **89S** (2mg, 1.55×10^{-6} moles) dissolved in CH_3CN/H_2O (6:4) solvent mixture (1ml). To the solution of pre-formed microspheres, urea (0.6 mg, 9.33×10^{-6} moles, 6 mole equiv.) was added. For the addition of small amounts of urea, a stock solution of urea was used of c = 10 mg/1ml. After urea addition, these solutions were incubated and dropcasted (5 μL) on silicon wafer for every 30 minutes time interval for 8 hours and dried in air (5 - 6 hrs) and in vacuum (2 - 3 hrs). These samples were imaged in SEM without gold coating.

5.3.11 Interaction of microspheres with lanthanides: formation of microsphere chains and network

5.3.11.1 Interaction with Lanthanides

A solution of microspheres was prepared as described in the procedure above in 5.3.6, using **89S** (4 mg, 3.11×10^{-6} moles) dissolved in CH_3CN/H_2O (6:4) solvent mixture (1 ml). To the solution of pre-formed microspheres, $Eu(CF_3SO_3)_3$ (1.9 mg/47.5 μL, 3.11×10^{-6} moles) was added as solution in H_2O, resulting mixture was warmed at 60 ^oC and cooled to room temperature which resulted in formation the Eu-microsphere chains in solution. For the addition of Eu(III), a stock solution of $Eu(CF_3SO_3)_3$ (c = 20 mg/0.5 ml) in H_2O was used. This solution was dropcasted (5 μL) on silicon wafer for every 60 minutes time interval for 4 hours (0, 1, 2, 3 and 4 hours) and dried in air (5 - 6 hrs) and in vacuum (2 - 3 hrs). These samples were imaged by SEM without Au coating.

In all the samples prepared here, a thin film was formed and covered over the sample surface. Therefore, the SEM imaging of these samples were performed using an electron beam current of higher voltage ~10 kV in SEM instrument.

5.3.11.2 Effect of different counter ions on the formation of microsphere chains and networks

Solutions of microspheres were prepared as described in the procedure above in 5.3.6, using **89S** (4 mg, 3.11×10^{-6} moles) dissolved in CH_3CN/H_2O (6:4) solvent mixture (1 ml). To the solution of pre-formed microspheres, different Ln(III) salts were added, warmed at 60 ^oC and cooled to room temperature to prepare microsphere chains form different Ln(III) ions in solution. The amounts of different Ln salts added to microspheres is depicted below in Table 5.3.3. These solutions were dropcasted (5 μL) on silicon wafer for every 60 minutes time interval for 2 hours (0, 1 and 2 hours) and dried in air (5 - 6 hrs) and in vacuum (2 - 3 hrs). The samples were imaged using SEM without gold coating.

Table 5.3.3: Mole equivalent of different Ln(III) salts added to microspheres.

89S microspheres	Ln (III) salts	Amount of Ln(III) salts wt. (moles) [a]
4 mg (3.11×10^{-6} moles)	$Eu(CF_3SO_3)_3$	1.9 mg (3.11×10^{-6} moles)
4 mg (3.11×10^{-6} moles)	$Eu(CH_3COO)_3.xH_2O$	1.0 mg (3.11×10^{-6} moles)
4 mg (3.11×10^{-6} moles)	$EuCl_3.6H_2O$	1.2 mg (3.11×10^{-6} moles)
4 mg (3.11×10^{-6} moles)	$Eu(NO_3)_3.5H_2O$	1.3 mg (3.11×10^{-6} moles)
4 mg (3.11×10^{-6} moles)	$Eu(ClO_4)_3$ (40 wt. % sol)	0.7 mg (3.11×10^{-6} moles)
4 mg (3.11×10^{-6} moles)	$Tb(CF_3SO_3)_3$	1.9 mg (3.11×10^{-6} moles)
4 mg (3.11×10^{-6} moles)	$Eu(CH_3COO)_3.xH_2O$	1.0 mg (3.11×10^{-6} moles)
4 mg (3.11×10^{-6} moles)	$Tb(Cl)_3.6H_2O$	1.2 mg (3.11×10^{-6} moles)
4 mg (3.11×10^{-6} moles)	$Tb(ClO_4)_3$ (40 wt. % sol)	0.7 mg (3.11×10^{-6} moles)
2 mg (1.55×10^{-6} moles)	$FeCl_2$	0.4 mg (1.55×10^{-6} moles)
2 mg (1.55×10^{-6} moles)	$ZnCl_2$	0.45 mg (1.55×10^{-6} moles)

[a] A stock solution of metal salts in H_2O (c = 10 mg/1000 µL) was used for the addition.

5.3.11.3 Spectrophotometric studies of lanthanide based microsphere chain

Two solutions of microsphere chains with Eu(III) and Tb(III) were prepared as described in the procedure above in 5.3.11.1, using **89S** (6 mg, 4.66×10^{-6} moles) dissolved in CH_3CN/H_2O (6:4) solvent mixture (3 ml) and $Ln(CF_3SO_3)_3$ (where, Ln = Eu(III), 2.8 mg/70 µL, 4.66×10^{-6} moles and Tb(III), 2.8 mg/70 µL, 4.66×10^{-6} moles).

The phosphorescence measurements for the above solution was carried out on a Varian Cary Eclipse Fluorimeter equipped with a 1.0 cm path length quartz cell 22 ^{o}C. The parameter settings of the fluorimeter for the phosphorescence measurement carried out in Chapter 3 are shown in Table 5.3.4. Please note, that the voltage of the PMT detector was adjusted as necessary to prevent signal saturation in different measurements.

Fluorescence measurement was performed using the parameters described in table 5.3.4. The solution was excited at 405 nm to get fluorescence of microspheres at 489 nm before and after the addition of $Eu(CF_3SO_3)_3$. The same solution was used for phosphorescence measurements before and after the addition of $Eu(CF_3SO_3)_3$ using parameters in Table 5.3.4.

Table 5.3.4: Parameters for phosphorescence emission measurements in Chapter 3

Mode: Phosphorescence	**Excitation:** 390 nm for Eu(III) samples 382 nm for Tb(III) samples	**Scans:** 570 – 720 nm for Eu(III) 450 – 650 nm for Tb(III)
Excitation slit: 20 nm	**Emission slit:** 2.5 nm	**PMT Voltage:** high V for Eu(III) 550 V for Tb(III)
No. of Flashes: 1	**Gate time:** 5 ms	**Delay time:** 0.2 ms
Averaging time: 0.1 s	**Total decay time:** 0.02 s	**Data Interval:** 0.5 nm

5.3.11.4 Investigation of lanthanide based microsphere chains by energy dispersive X-ray (EDX) analysis

Two solutions of microsphere chains with Eu(III) and Tb(III) were prepared as described in the procedure above in 5.3.11.1, using **89S** (6 mg, 4.66×10^{-6} moles) and $Ln(CF_3SO_3)_3$. With being Ln = Eu(III) (2.8 mg/70 μL, 4.66×10^{-6} moles) and Tb(III) (2.8 mg/70 μL, 4.66×10^{-6} moles). These solutions of Eu-microsphere chain and Tb-microsphere chains was dropcasted (5 □L) on silicon wafer and dried in air (5 - 6 hrs) and in vacuum (2 - 3 hrs). These samples were used for EDX analysis. During this sample preparation the film formed which covered the sample was removed by exfoliation (peeled off) using an electrical tape.

EDX analysis was carried out in a Carl Zeiss ULTRA plus, scanning electron microscope equipped with EDX detector. The analysis was performed at 10 – 15 kV beam current in mapping, and line scan modes.

5.3.12 Transmission electron microscopy of 89S microspheres

Microspheres were prepared in solution as described in section 5.3.6 using **89S** – **91S** (4 mg) dissolved in CH_3CN/H_2O (6:4) solvent mixture (1ml). These microsphere solutions were dropcasted onto carbon coated copper grids (TEM grids). These grids were dried first in the air for 12 hours followed by drying under high vacuum for a further 3 - 4 hours. These samples were imaged using Titan FEI transmission electron microscope (TEM) using 80kV beam current.

5.3.13 Focused Ion Beam (FIB) microscopy on microspheres

Microspheres were deposited on silica wafers as described in the procedure above in 5.3.6, using **89S** – **91S** (4 mg) dissolved in CH_3CN/H_2O (6:4) solvent mixture (1 ml). These samples was analysed in Carl Zeiss Auriga Focused Ion Beam microscope. An area was

selected over the microspheres and milled with a beam of gallium ions of beam current 30keV. After milling is finished the cut microspheres were imaged using SEM.

5.3.13 AFM-Raman spectroscopy of microspheres.

Microspheres were deposited on silicon wafers as described in the procedure above in 5.3.6, using **89S** (4 mg) dissolved in CH_3CN/H_2O (6:4) solvent mixture (1ml). These samples were analysed in NTEGRA Spectra AFM-Raman microscope. The microscope was operated in AFM tapping mode for recording AFM images. And in Tip enhanced Raman microscopy (TERS) mode using 514 nm laser for Raman imaging.

5.3.14 Mechanical measurements on solid microspheres

All mechanical measurements were performed using an Asylum MFP-3D Atomic Force Microscope using 75-kHz rectangular cantilevers purchased from Budget Sensors. These tips have a nominal spring constant of 3 N/m. These tips were used for both lateral and vertical force measurements.

In order to get quantitative mechanical data from AFM measurements it is necessary to perform a full calibration on the sensitivities (both vertical and lateral) of the AFM tip used and the dimensions of each individual tip used needs also to be measured. The AFM tip was calibrated as in the procedures outlined by Schwarz.[3751]

Before the measurements, the lateral sensitivity of the tip was determined by laterally loading a trench wall of a silicon nitride calibration grid. It is important to calibrate the tip on a non-compliant surface otherwise the sensitivities would be a convolution of the tip and surface sensitivities. The height at which the tip calibrates the grid is user defined. First a tapping mode image across the trench is taken and the feedback loop is then switched off by choosing contact mode. This drives the tip in the manipulation path but the piezo does not adjust the tip height resulting in the tip laterally loading the grid. This is all done using the lithography suite of the Asylum MFP-3D. The signal is recorded on the photodetector and the lateral sensitivity is the slope of the loading curve in V/μm.

The vertical sensitivity is obtained by pushing the AFM tip into the calibration grid. As the AFM tip is pushed into the grid the vertical sensitivity is recorded on the photodetector. It is the slope of the deflection curve in nm/V.

5.3.14.1 Size distribution measurements using AFM

Three solutions of microspheres were prepared as described in the procedure above (section 5.3.6) using **89S** (1, 2.5 and 5 mg) dissolved in CH_3CN/H_2O (6:4) solvent mixture (1 ml).

The resulting 3 samples of microspheres were of various concentration, namely c = 0.1, 0.25 and 0.5% w/v. These 3 samples were used for size distribution measurements using Asylum MFP-3D Atomic Force Microscope (AFM).

5.3.14.2 Lateral force displacement studies of microspheres using AFM

Microspheres were deposited on silicon wafers as described in the procedure above in 5.3.6, using **89S** (2 mg) dissolved in CH_3CN/H_2O microspheres mixture (1ml). These 0.2 wt. % samples were used in lateral force displacement studies in AFM.

To perform lateral manipulation of the microspheres an AFM image of the sphere is obtained. The drive path is defined by the user and the tip height is set to the same height as the calibration grid. The feedback loop is then switched off and the tip pushes the sphere. The lateral signal to move the sphere is recorded on the photodetector.

5.3.14.2 Mechanical stiffness or strength measurement of microspheres using AFM

Sample prepared for the section 5.3.14.2 was used for the mechanical stiffness measurement. For the vertical force curves on a sphere a set point force of 30 nN was selected and the tip pushes into the sphere until that deflection is reached.

5.3.15 Thermal stability of solid microspheres

Microspheres were deposited on silica wafers as described in the procedure above in 5.3.6, using **89S** (2 mg) dissolved in CH_3CN/H_2O (6:4) solvent mixture (1 ml). Several (ca. 20) of these 0.2% w/v samples were prepared and used in the determination of thermal stability.

All of these samples were placed on heating stage and heated at the rate of 2 ^oC/min. Each sample was taken out of the heating stage and cooled at the interval of every 5 ^oC until the temperature is reached 200 ^oC. After cooling these samples were imaged using SEM.

For TGA, the solid microspheres were placed on the TGA crucible and heated at the rate of 5 ^oC/min under N_2 atmosphere. The weight loss upon heating is shown in the graph.

5.3.16 Formation of single layered crosslinked networks of microspheres

Microspheres of **89S** were prepared by dissolving 3 mg of **89S** in CH_3CN/H_2O (6:4) solvent mixture (1 ml) by heating and cooling. 5 μL of this solution was dropcasted on several silica wafers and dried in air (12 hrs) and in vacuum (3 hrs) to deposit a monolayer of microspheres.

All these microspheres deposited on silica wafers were immersed in H_2O. Each sample was taken out from H_2O at different times with time intervals of every 20 min (ie. 20, 40, 60 min,

etc) and dried immediately in vacuum. Dried samples were analysed in SEM without gold coating.

5.3.17 Etching of solid microspheres in $Eu(CF_3SO_3)_3$ aqueous solution

Microspheres were deposited on silicon wafers as described in the procedure above in 5.3.6, using **89S** (3 mg) dissolved in CH_3CN/H_2O (6:4) solvent mixture (1 ml). Several of these 0.3% w/v samples were prepared (approx. 10).

All these microspheres were immersed in $Eu(CF_3SO_3)_3$ solution in H_2O ($c = 3 \times 10^{-3}$ M) and each sample was taken out at the time interval of every 20 min (20, 40, 60 min) and dried immediately in vacuum. Dried samples were analysed by SEM without gold coating.

5.3.18 Self-sorting of non-chiral and chiral tripodal molecules: embedding the microspheres in gel matrix.

The mixture **88** (achiral compound) and **89S - 91S** (chiral compounds) was dissolved together in CH_3CN/H_2O (60:45) solvent mixture by heating at 100 ^oC. Upon cooling to room temperature, gels were obtained. The combinations of **88** with different chiral tpy trimer compounds and the corresponding weight are summarised in section 3.15, Table 3.7.

These gels were prepared by placing a small amount of gel (~10 – 15 μL by vol.) on silica wafers and making a thin film by smooth smearing. The samples were dried initially in air for 5 - 6 hours followed by drying in high vacuum for 2 - 3 hours. These samples were coated with Au using sputter and analysed in SEM.

5.4 Experimental Details for Chapter 4

5.4.1 Optical microscopy of microspheres

89 (R and S, 3 mg) was dissolved in CH_3CN/H_2O (6:4 v/v, 1 ml) by heating at 100 ^oC and cooling to room temperature to obtain a solution of microspheres with concentration 0.3% w/v. 100 μL of this solution of microspheres was transferred to a flow cell (ibidi μ-slides) and dried in air (12 hours) and vacuum (3 hours) to deposit microspheres in the flow cell. The sample was imaged using a Leica SP5 II microscope with 488 nm and 458 nm HeNe or Ar ion laser source

5.4.2 LSCM imaging of microspheres in fluorescence mode

A solution of **89** (R and S) microspheres (c = 0.3% w/v) were prepared as descried in section 5.4.1. 10 μL of this solution was dropcasted on quartz slide and dried in air (12 hours) and vacuum (3 hours) to deposit microspheres. This sample was imaged using Leica SP8 confocal microscope (60X oil immersion lens). The sample was excited by continuous wave

laser at λ_{ex} = 405 nm. The emission spectra of the microspheres were recorded at a resolution of 3.2 nm.

Please note that in all the cases described throughout, the concentration of microspheres mentioned was corresponding to the concentration of the compound **89** (R or S) used in the microspheres preparation.

5.4.3 LSCM Imaging of 89S microspheres in solution

A solution of **89S** microspheres (c = 0.3% w/v) was prepared as descried in section 5.4.1. 20 μL of this solution of microspheres was placed into a closed quartz petri dish and imaged using Leica SP8 confocal microscope (λ_{ex} = 405 nm). Images were taken every 1.5 seconds over a total 6 minutes time window by time-series experiment. The movie was generated by combining these images, showing the **89S** microspheres under continuously movement in solution exhibiting blue luminescence. Brightness and contrast of the movie recorded was modified in order to better distinguish the microspheres.

5.4.3.1 Real-time investigation of the formation of 89S microspheres in solution using LSCM

89S (2 mg) was dissolved in CH_3CN/H_2O (6:4 v/v, 1 ml) by heating at 100 ^oC. 20 μL of this hot solution was immediately placed into a closed quartz petri dish before the microspheres were formed. This solution was monitored while cooling to room temperature over time using Leica SP8 confocal microscope. The samples were excited by continuous wave laser at λ_{ex} = 405 nm. Images were taken every 1.5 seconds over a total 6 minutes time window by time-series experiment. The movie was generated by combining these images, showing the formation of **89S** microsphere with blue fluorescence. Brightness and contrast of the movie recorded was modified in order to better distinguish the microspheres. As the confocal microscope was not equipped with temperature monitoring probe, the temperature of the sample during the time scale of experiment could not be measured.

5.4.4 Stability of 89S microspheres in H_2O

89S microspheres were deposited in a flow cell as described in section 5.4.1. To the dried microspheres, 100 μL of H_2O was added and the sample was monitored using Leica SP5 II microscope with 488 nm and 458 nm HeNe or Ar ion laser source.

5.4.5 Disassembly of microspheres using solution of Urea

89S microspheres were deposited in a flow cell as described in section 5.4.1. To the dried microspheres, 100 μL of Urea solution in H_2O (c = 1% and 10%) was added and the sample

was monitored using Leica SP5 II microscope with 488 nm and 458 nm HeNe or Ar ion laser source.

5.4.6 Effect of 355 nm UV irradiation on 89S microspheres

89S microspheres were deposited on a 9 mm coverslip using the procedure as described in section 5.4.2. Images of the sample was obtained using Leica SP5 II microscope. An area was selected on the sample and irradiated using a Coherent 355nm CW (Nd:YAG) laser with 100 % intensity, operating at 8 mW power. The sample was irradiated 2 times (10 minutes intervals) with smaller and larger selected area in the same place.

5.4.7 Lanthanide based Luminescent microspheres

5.4.7.1 Fluorescence measurements

The fluorescence measurements were carried out on a Varian Cary Eclipse Fluorimeter equipped with a 1.0 cm path length quartz cell at room temperature. Fluorescence data were collected between 300 to 800 nm. The solution **89S** microspheres in CH_3CN/H_2O (6:4 v/v, 2 ml) was used with concentration 1.55×10^{-3} M. A stock solution of Ln(III) ions (Ln = Eu or Tb) prepared in 6:4 CH_3CN/H_2O (3×10^{-2} M) was used. The settings of the fluorimeter for the luminescence titrations carried out in Chapter 4 are shown in Table 5.4.1. Please note, the voltage of the PMT detector was adjusted as necessary to prevent signal saturation in different measurements. Since the microspheres had broad excitation range, the excitation wavelength (λ_{ex}) were varied according to the experiments performed. Concentration of microspheres was corresponded to the concentration of the compound **89** (R or S) used in the microspheres preparation.

Table 5.4.1: Fluorescence settings for the titration described in chapter 4.

Mode: Fluorescence	**Excitation:** 380 - 405 nm	**Scans:** 300 – 800 nm
Excitation slit: 20 nm	**Emission slit:** 5 nm	**PMT Voltage:** 600 - 700 V
Averaging time: 0.1 s	**Scan rate:** 600 nm/min	**Data Interval:** 0.5 nm

5.4.7.2 Ln(III) centred emission measurements

The phosphorescence measurements were carried out on a Varian Cary Eclipse Fluorimeter equipped with a 1.0 cm path length quartz cell at room temperature. The luminescence data were collected between 570 nm to 720 nm for Eu(III) emission and 450 to 650 nm for Tb(III) emission. The concentration of the **89S** microspheres and lanthanide stock solutions were

the same as those used for the fluorescence measurements. The settings of the fluorimeter for luminescence titrations carried out in Chapter 4 are shown in Table 5.4.2. Please note, the voltage of the PMT detector was adjusted as necessary to prevent signal saturation in different measurements. Concentration of microspheres was corresponding to the concentration of the compound **89** (R or S) used in preparing microspheres.

Table 5.4.2: Luminescence settings for the titration described in Chapter 4.

Mode: Phosphorescence	**Excitation:** 380 – 390 nm	**Scans:** 570 – 720 nm 450 – 650 nm
Excitation slit: 20 nm	**Emission slit:** 2.5 nm	**PMT Voltage:** 450 – 800 V
No. of Flashes: 1	**Gate time:** 5 ms	**Delay time:** 0.2 ms
Averaging time: 0.1 s	**Total decay time:** 0.02 s	**Data Interval:** 0.5 nm

5.4.7.3 Life time measurements of Ln(III) centred emission

The luminescence lifetime measurements of Eu(III) and Tb(III) centred life time emission of Eu(III) and Tb(III) based **89S** microspheres in 6:4 CH_3CN/H_2O were conducted on a Varian Cary Eclipse Fluorimeter. The settings of the fluorimeter for the lifetime measurements carried out in Chapter 4 are shown in Table 5.4.3.

Life time values of Eu(III) ($^5D_0$) and Tb(III) ($^5D_4$) excited states were measured in solution in time resolved mode. For each system the lifetime values are averages of three independent measurements, which were made by monitoring the emission decay at 617 nm and 543 nm for Eu(III) and Tb(III), respectively, which corresponds to maximum of the $^5D_0 \rightarrow {}^7F_2$ (for Eu(III)) and $^5D_4 \rightarrow {}^7F_5$ (for Tb(III)) transition, enforcing a delay.

Table 5.4.3: Settings of the Varian Cary Eclipse Fluorimeter for measuring Eu(III) and Tb(III) centred luminescence decays.

Indirect excitation: 380 – 390 nm	**Emission:** 543, 617 nm	**Delay:** 0.01
Excitation slit: 20 nm	**Emission slit:** 20 nm	**Gate:** 0.02 – 0.045 ms
No. of Flashes: 1	**Total decay:** 20 ms	**No. of Cycles:** 50

5.4.7.4 Lanthanide based luminescent microspheres imaging using LSCM

A solution of **89S** microspheres (c = 0.3% w/v, 2.33×10^{-3} moles) were prepared as described in section 5.4.1. To these solutions, $Eu(CF_3SO_3)_3$ (0.84 mg in 17 μL H_2O, 0.6 equivalent) and $Tb(CF_3SO_3)_3$ (1.4 mg in 28 μL H2O, 1 equivalent) were added separately to prepare Eu(III)- **89S** microspheres and Tb(III)-**89S** microspheres, respectively. 10 mL of each

solution was dropcasted on quartz slide and dried in air (12 hrs) and vacuum (3 hrs). These deposited solid Ln(III)-**89S** microspheres were imaged using Leica SP5 II microscope. During the sample preparation of Ln(III)-**89S** microspheres chains, a film was formed which covered the sample was removed by exfoliation (peeled off) using an electrical tape.

The microscope was coupled by an optical fibre to a Coherent 355 nm CW (Nd:YAG) laser, operating at 8mW power. The microscope was equipped with a triple channel imaging detectors, comprising two conventional PMT systems and a HyD hybrid avalanche photodiode detector. Channel 1: 390 – 500 nm, Channel 2: 500 – 550 nm and Channel 3: 570 – 720 nm. Scanning speed was adjusted to 100 Hz in a unidirectional mode, to ensure both sufficient light exposure and enough time to collect the emitted light from the lanthanide based optical probes (1024x1024 frame size, a pixel size of 120 x120 nm and depth of 0.772 μm).

5.4.7.5 Ln(III) centred emission spectrum and luminescence decays measurements using microscope

Time gated full frame imaging of Ln(III)-**89S** microspheres were performed using a custom built microscope (modified Zeiss Axiovert 200M), using a Zeiss APOCHROMAT 63x/1.40 NA objective, combined with a low voltage 365 nm pulsed UV LED collimated excitation source (1.2W). The microscope was equipped at the X1 port with a Peltier cooled 2D-CCD detector (Ocean Optics) used in an inverse 100 Hz time gated sequence. The spectrum was recorded from 400-800 nm with a resolution of 0.24 nm and the final spectrum was acquired using an averaged 10,000 scan duty cycle.

The conditions for time-gated imaging involved a 1 ms illumination pulse, followed by a 5 μs delay time and subsequent 50 ms averaging time. 50 images accumulated were averaged to 1.

Probe lifetimes were measured by time correlated multiphoton counting, on the same microscope platform using a novel cooled PMT detector (Hamamatsu H7155) interchangeable on one of the X1 ports, with the application of pre-selected interference filters as detailed in the main text. Both the control and detection algorithm were written in LabView2011, where probe lifetime was determined by using a single exponential tail-fitting algorithm to the monitored signal intensity decay.

5.4.7.6 Circularly polarised luminescence

Solutions of Ln(III)-**89** (R and S) microspheres (c = 0.3% w/v, 2.33×10^{-3} moles) were prepared as described in section 5.4.7.4. The solvent was removed under reduced pressure

at 35 ^{o}C to obtain the solid Ln(III)-**89** (R and S) microspheres which were-suspended in CH_3CN by sonication and used to measure CPL.

CPL spectra were recorded on a custom built spectrometer in Durham university, consisting of a laser driven light source (Energetiq EQ-99 LDLS, spectral range 170 to 2100 nm) coupled to an Acton SP2150 monochromator (600 g/nm, 300 nm Blaze), allowing excitation wavelengths to be selected with a 6 nm FWHM band-pass. The collection of the emitted light was facilitated (90° angle set up, 1 cm path length quartz cuvette) by a Lock-in amplifier (Hinds Instruments Signaloc 2100) and Photoelastic Modulator (Hinds Series II/FS2AA). The differentiated light was focused onto an Acton SP2150 monochromator (1200 g/nm, 500 nm Blaze) equipped with a high sensitivity cooled Photo Multiplier Tube (Hamamatsu H10723-20 PhotoSensor red corrected). The detection of the CPL signal was achieved using the field modulation lock-in technique. The electronic signal from the PMT was fed into the lock-in amplifier (Hinds Instruments Signaloc 2100). The reference signal for the lock-in detection was provided by the PEM control unit. The monochromators, PEM control unit and lock-in amplifier were interfaced with a desktop PC and controlled by Labview code.

5.4.7.7 Time gated helically luminescence (HL) light measurement

In HLL measurement, CPL and elliptically polarised luminescence (EPL) were merged and a delay time (t_{delay}) of 5 μs was applied during the measurements using a new dual channel instrumental design (GB Patent Appl., GB1507296.0, 2015, R. Pal, L.O. Pålsson and A. Beeby).

References

References:

1. Steed, J. W.; Turner, D. R.; Wallace, K., *Core Concepts in Supramolecular Chemistry and Nanochemistry*. Wiley: 2007; p 1-2.
2. Lehn, J.-M., *Science* **2002,** *295* (5564), 2400.
3. Lehn, J.-M., *Angew. Chem. Int. Ed. Engl.* **1990,** *29* (11), 1304-1319.
4. Feng, J.; Zhang, H., *Chem. Soc. Rev.* **2013,** *42* (1), 387-410.
5. Plush, S. E.; Gunnlaugsson, T., *Dalton Trans.* **2008,** (29), 3801-3804.
6. de Silva, A. P.; Moody, T. S.; Wright, G. D., *Analyst* **2009,** *134* (12), 2385-2393.
7. de Bettencourt-Dias, A.; Barber, P. S.; Bauer, S., *J. Am. Chem. Soc.* **2012,** *134* (16), 6987-6994.
8. Bhowmik, S.; Banerjee, S.; Maitra, U., *Chem. Commun.* **2010,** *46* (45), 8642-8644.
9. Laishram, R.; Bhowmik, S.; Maitra, U., *J. Mater. Chem. C* **2015,** *3* (23), 5885-5889.
10. Tam, A. Y.-Y.; Yam, V. W.-W., *Chem. Soc. Rev.* **2013,** *42* (4), 1540-1567.
11. Buerkle, L. E.; Rowan, S. J., *Chem. Soc. Rev.* **2012,** *41* (18), 6089-6102.
12. Sangeetha, N. M.; Maitra, U., *Chem. Soc. Rev.* **2005,** *34* (10), 821-836.
13. Terech, P.; Weiss, R. G., *Chem. Rev.* **1997,** *97* (8), 3133-3160.
14. George, M.; Weiss, R. G., *Acc. Chem. Res.* **2006,** *39* (8), 489-497.
15. Hooper, A. E.; Kennedy, S. R.; Jones, C. D.; Steed, J. W., *Chem. Commun.* **2016,** *52* (1), 198-201.
16. Binnemans, K., *Chem. Rev.* **2009,** *109* (9), 4283-4374.
17. Bünzli, J.-C. G.; Comby, S.; Chauvin, A.-S.; Vandevyver, C. D. B., *J. Rare Earths* **2007,** *25* (3), 257-274.
18. Surender, Esther M.; Comby, S.; Cavanagh, B. L.; Brennan, O.; Lee, T. C.; Gunnlaugsson, T., *Chem* **2016,** *1* (3), 438-455.
19. Bünzli, J.-C. G., *Chem. Lett.* **2008,** *38* (2), 104-109.
20. Bünzli, J.-C. G., *Chem. Rev.* **2010,** *110* (5), 2729-2755.
21. Elmes, R. B. P.; Orange, K. N.; Cloonan, S. M.; Williams, D. C.; Gunnlaugsson, T., *J. Am. Chem. Soc.* **2011,** *133* (40), 15862-15865.
22. McMahon, B.; Mauer, P.; McCoy, C. P.; Lee, T. C.; Gunnlaugsson, T., *J. Am. Chem. Soc.* **2009,** *131* (48), 17542-17543.
23. Parker, D., *Coord. Chem. Rev.* **2000,** *205* (1), 109-130.
24. McMahon, B. K.; Pal, R.; Parker, D., *Chem. Commun.* **2013,** *49* (47), 5363-5365.
25. Parker, D.; Dickins, R. S.; Puschmann, H.; Crossland, C.; Howard, J. A. K., *Chem. Rev.* **2002,** *102* (6), 1977-2010.
26. Kitchen, J. A.; Gunnlaugsson, T., Supramolecular Chemistry: from Sensors and Imaging Agents to Functional Mononuclear and Polynuclear Self-Assembly Lanthanide Complexes. In *The Rare Earth Elements: Fundamentals and Applications*, Atwood, D. A., Ed. John Wiley & Sons, Ltd: 2013; pp 481-494.
27. Lehn, J.-M., *Science* **1985,** *227* (4689), 849.
28. Pedersen, C. J., *J. Am. Chem. Soc.* **1967,** *89* (10), 2495-2496.
29. Cram, D. J., *Angew. Chem. Int. Ed. Engl.* **1988,** *27* (8), 1009-1020.
30. Barry, D. E.; Caffrey, D. F.; Gunnlaugsson, T., *Chem. Soc. Rev.* **2016,** *45* (11), 3244-3274.
31. Piguet, C.; Borkovec, M.; Hamacek, J.; Zeckert, K., *Coord. Chem. Rev.* **2005,** *249* (5–6), 705-726.
32. Bünzli, J.-C. G.; Petoud, S.; Piguet, C.; Renaud, F., *J. Alloys Compd.* **1997,** *249* (1), 14-24.
33. Chauvin, A.-S.; Comby, S.; Baud, M.; De Piano, C.; Duhot, C.; Bünzli, J.-C. G., *Inorg. Chem.* **2009,** *48* (22), 10687-10696.

34. Comby, S.; Stomeo, F.; McCoy, C. P.; Gunnlaugsson, T., *Helv. Chim. Acta* **2009,** *92* (11), 2461-2473.
35. Constable, E. C., *Nature* **1990,** *346* (6282), 314-315.
36. Constable, E. C.; Ward, M. D.; Tocher, D. A., *J. Chem. Soc., Dalton Trans.* **1991,** (7), 1675-1683.
37. Leigh, D. A.; Wong, J. K. Y.; Dehez, F.; Zerbetto, F., *Nature* **2003,** *424* (6945), 174-179.
38. Erbas-Cakmak, S.; Leigh, D. A.; McTernan, C. T.; Nussbaumer, A. L., *Chem. Rev.* **2015,** *115* (18), 10081-10206.
39. Dietrich-Buchecker, C. O.; Sauvage, J. P., *Chem. Rev.* **1987,** *87* (4), 795-810.
40. Chichak, K. S.; Cantrill, S. J.; Pease, A. R.; Chiu, S.-H.; Cave, G. W. V.; Atwood, J. L.; Stoddart, J. F., *Science* **2004,** *304* (5675), 1308.
41. Amabilino, D. B.; Stoddart, J. F., *Chem. Rev.* **1995,** *95* (8), 2725-2828.
42. Tranchemontagne, D. J.; Mendoza-Cortes, J. L.; O'Keeffe, M.; Yaghi, O. M., *Chem. Soc. Rev.* **2009,** *38* (5), 1257-1283.
43. Murray, L. J.; Dinca, M.; Long, J. R., *Chem. Soc. Rev.* **2009,** *38* (5), 1294-1314.
44. Allendorf, M. D.; Bauer, C. A.; Bhakta, R. K.; Houk, R. J. T., *Chem. Soc. Rev.* **2009,** *38* (5), 1330-1352.
45. Rowsell, J. L. C.; Millward, A. R.; Park, K. S.; Yaghi, O. M., *J. Am. Chem. Soc.* **2004,** *126* (18), 5666-5667.
46. The 2016 Nobel Prize in Chemistry - Press Release. *Nobelprize.org*. Nobel Media AB 2014: 2016.
47. Dietrich-Buchecker, C. O.; Sauvage, J. P.; Kintzinger, J. P., *Tetrahedron Lett.* **1983,** *24* (46), 5095-5098.
48. Dietrick-Buchecker, C. O.; Marnot, P. A.; Sauvage, J. P., *Tetrahedron Lett.* **1982,** *23* (50), 5291-5294.
49. Dietrich-Buchecker, C. O.; Sauvage, J.-P., *Angew. Chem. Int. Ed. Engl.* **1989,** *28* (2), 189-192.
50. Nierengarten, J. F.; Dietrich-Buchecker, C. O.; Sauvage, J. P., *J. Am. Chem. Soc.* **1994,** *116* (1), 375-376.
51. Anelli, P. L.; Spencer, N.; Stoddart, J. F., *J. Am. Chem. Soc.* **1991,** *113* (13), 5131-5133.
52. Ashton, P. R.; Goodnow, T. T.; Kaifer, A. E.; Reddington, M. V.; Slawin, A. M. Z.; Spencer, N.; Stoddart, J. F.; Vicent, C.; Williams, D. J., *Angew. Chem. Int. Ed. Engl.* **1989,** *28* (10), 1396-1399.
53. Livoreil, A.; Dietrich-Buchecker, C. O.; Sauvage, J.-P., *J. Am. Chem. Soc.* **1994,** *116* (20), 9399-9400.
54. Bissell, R. A.; Cordova, E.; Kaifer, A. E.; Stoddart, J. F., *Nature* **1994,** *369* (6476), 133-137.
55. Koumura, N.; Zijlstra, R. W. J.; van Delden, R. A.; Harada, N.; Feringa, B. L., *Nature* **1999,** *401* (6749), 152-155.
56. Eelkema, R.; Pollard, M. M.; Vicario, J.; Katsonis, N.; Ramon, B. S.; Bastiaansen, C. W. M.; Broer, D. J.; Feringa, B. L., *Nature* **2006,** *440* (7081), 163-163.
57. Fletcher, S. P.; Dumur, F.; Pollard, M. M.; Feringa, B. L., *Science* **2005,** *310* (5745), 80.
58. Ruangsupapichat, N.; Pollard, M. M.; Harutyunyan, S. R.; Feringa, B. L., *Nat. Chem.* **2011,** *3* (1), 53-60.
59. Kudernac, T.; Ruangsupapichat, N.; Parschau, M.; Macia, B.; Katsonis, N.; Harutyunyan, S. R.; Ernst, K.-H.; Feringa, B. L., *Nature* **2011,** *479* (7372), 208-211.
60. Wilson, M. R.; Solà, J.; Carlone, A.; Goldup, S. M.; Lebrasseur, N.; Leigh, D. A., *Nature* **2016,** *534* (7606), 235-240.
61. Kay, E. R.; Leigh, D. A., *Angew. Chem. Int. Ed.* **2015,** *54* (35), 10080-10088.

62. De Bo, G.; Kuschel, S.; Leigh, D. A.; Lewandowski, B.; Papmeyer, M.; Ward, J. W., *J. Am. Chem. Soc.* **2014,** *136* (15), 5811-5814.
63. Byrne, J. P.; Blasco, S.; Aletti, A. B.; Hessman, G.; Gunnlaugsson, T., *Angew. Chem. Int. Ed.* **2016,** *55* (31), 8938-8943.
64. Lincheneau, C.; Jean-Denis, B.; Gunnlaugsson, T., *Chem. Commun.* **2014,** *50* (22), 2857-2860.
65. De Greef, T. F. A.; Smulders, M. M. J.; Wolffs, M.; Schenning, A. P. H. J.; Sijbesma, R. P.; Meijer, E. W., *Chem. Rev.* **2009,** *109* (11), 5687-5754.
66. Fouquey, C.; Lehn, J.-M.; Levelut, A.-M., *Adv. Mater.* **1990,** *2* (5), 254-257.
67. Stupp, S. I.; LeBonheur, V.; Walker, K.; Li, L. S.; Huggins, K. E.; Keser, M.; Amstutz, A., *Science* **1997,** *276* (5311), 384.
68. Stupp, S. I.; Son, S.; Lin, H. C.; Li, L. S., *Science* **1993,** *259* (5091), 59.
69. Sijbesma, R. P.; Beijer, F. H.; Brunsveld, L.; Folmer, B. J. B.; Hirschberg, J. H. K. K.; Lange, R. F. M.; Lowe, J. K. L.; Meijer, E. W., *Science* **1997,** *278* (5343), 1601.
70. Aida, T.; Meijer, E. W.; Stupp, S. I., *Science* **2012,** *335* (6070), 813.
71. Hartgerink, J. D.; Beniash, E.; Stupp, S. I., *Science* **2001,** *294* (5547), 1684.
72. Hartgerink, J. D.; Beniash, E.; Stupp, S. I., *Proc. Nat. Acad. Sci.* **2002,** *99* (8), 5133-5138.
73. Mata, A.; Geng, Y.; Henrikson, K. J.; Aparicio, C.; Stock, S. R.; Satcher, R. L.; Stupp, S. I., *Biomaterials* **2010,** *31* (23), 6004-6012.
74. Rajangam, K.; Behanna, H. A.; Hui, M. J.; Han, X.; Hulvat, J. F.; Lomasney, J. W.; Stupp, S. I., *Nano Lett.* **2006,** *6* (9), 2086-2090.
75. Capito, R. M.; Azevedo, H. S.; Velichko, Y. S.; Mata, A.; Stupp, S. I., *Science* **2008,** *319* (5871), 1812.
76. Rożkiewicz, D. I.; Myers, B. D.; Stupp, S. I., *Angew. Chem. Int. Ed.* **2011,** *50* (28), 6324-6327.
77. Abbel, R.; Grenier, C.; Pouderoijen, M. J.; Stouwdam, J. W.; Leclère, P. E. L. G.; Sijbesma, R. P.; Meijer, E. W.; Schenning, A. P. H. J., *J. Am. Chem. Soc.* **2009,** *131* (2), 833-843.
78. Schmid, S. A.; Abbel, R.; Schenning, A. P. H.; Meijer, E. W.; Sijbesma, R. P.; Herz, L. M., *J. Am. Chem. Soc.* **2009,** *131* (48), 17696-17704.
79. Schenning, A. P. H. J.; Jonkheijm, P.; Peeters, E.; Meijer, E. W., *J. Am. Chem. Soc.* **2001,** *123* (3), 409-416.
80. Korevaar, P. A.; George, S. J.; Markvoort, A. J.; Smulders, M. M. J.; Hilbers, P. A. J.; Schenning, A. P. H. J.; De Greef, T. F. A.; Meijer, E. W., *Nature* **2012,** *481* (7382), 492-496.
81. Korevaar, P. A.; de Greef, T. F. A.; Meijer, E. W., *Chem. Mater.* **2014,** *26* (1), 576-586.
82. Jonkheijm, P.; van der Schoot, P.; Schenning, A. P. H. J.; Meijer, E. W., *Science* **2006,** *313* (5783), 80.
83. Qiu, H.; Hudson, Z. M.; Winnik, M. A.; Manners, I., *Science* **2015,** *347* (6228), 1329.
84. Qiu, H.; Du, V. A.; Winnik, M. A.; Manners, I., *J. Am. Chem. Soc.* **2013,** *135* (47), 17739-17742.
85. O'Reilly, R. K.; Hawker, C. J.; Wooley, K. L., *Chem. Soc. Rev.* **2006,** *35* (11), 1068-1083.
86. Boott, C. E.; Laine, R. F.; Mahou, P.; Finnegan, J. R.; Leitao, E. M.; Webb, S. E. D.; Kaminski, C. F.; Manners, I., *Chem. Eur. J.* **2015,** *21* (51), 18539-18542.
87. Rupar, P. A.; Chabanne, L.; Winnik, M. A.; Manners, I., *Science* **2012,** *337* (6094), 559.
88. Qiu, H.; Russo, G.; Rupar, P. A.; Chabanne, L.; Winnik, M. A.; Manners, I., *Angew. Chem. Int. Ed.* **2012,** *51* (47), 11882-11885.
89. Nazemi, A.; Boott, C. E.; Lunn, D. J.; Gwyther, J.; Hayward, D. W.; Richardson, R. M.; Winnik, M. A.; Manners, I., *J. Am. Chem. Soc.* **2016,** *138* (13), 4484-4493.
90. Schmelz, J.; Schedl, A. E.; Steinlein, C.; Manners, I.; Schmalz, H., *J. Am. Chem. Soc.* **2012,** *134* (34), 14217-14225.

91. Sun, L.; Pitto-Barry, A.; Kirby, N.; Schiller, T. L.; Sanchez, A. M.; Dyson, M. A.; Sloan, J.; Wilson, N. R.; O'Reilly, R. K.; Dove, A. P., *Nat. Commun.* **2014,** *5*, 5746.
92. Gilroy, J. B.; Gädt, T.; Whittell, G. R.; Chabanne, L.; Mitchels, J. M.; Richardson, R. M.; Winnik, M. A.; Manners, I., *Nat. Chem.* **2010,** *2* (7), 566-570.
93. Wang, X.; Guerin, G.; Wang, H.; Wang, Y.; Manners, I.; Winnik, M. A., *Science* **2007,** *317* (5838), 644.
94. Ogi, S.; Stepanenko, V.; Sugiyasu, K.; Takeuchi, M.; Würthner, F., *J. Am. Chem. Soc.* **2015,** *137* (9), 3300-3307.
95. Bu, L.; Dawson, T. J.; Hayward, R. C., *ACS Nano* **2015,** *9* (2), 1878-1885.
96. Zhang, W.; Jin, W.; Fukushima, T.; Saeki, A.; Seki, S.; Aida, T., *Science* **2011,** *334* (6054), 340.
97. Zhang, J.; Coulston, R. J.; Jones, S. T.; Geng, J.; Scherman, O. A.; Abell, C., *Science* **2012,** *335* (6069), 690.
98. Appel, E. A.; Biedermann, F.; Rauwald, U.; Jones, S. T.; Zayed, J. M.; Scherman, O. A., *J. Am. Chem. Soc.* **2010,** *132* (40), 14251-14260.
99. Lan, Y.; Wu, Y.; Karas, A.; Scherman, O. A., *Angew. Chem. Int. Ed.* **2014,** *53* (8), 2166-2169.
100. Rauwald, U.; Scherman, O. A., *Angew. Chem. Int. Ed.* **2008,** *47* (21), 3950-3953.
101. Song, Q.; Li, F.; Wang, Z.; Zhang, X., *Chem. Sci.* **2015,** *6* (6), 3342-3346.
102. Moon, K.; Grindstaff, J.; Sobransingh, D.; Kaifer, A. E., *Angew. Chem. Int. Ed.* **2004,** *43* (41), 5496-5499.
103. Ni, X.-L.; Chen, S.; Yang, Y.; Tao, Z., *J. Am. Chem. Soc.* **2016,** *138* (19), 6177-6183.
104. Xu, W.; Ledin, P. A.; Iatridi, Z.; Tsitsilianis, C.; Tsukruk, V. V., *Angew. Chem. Int. Ed.* **2016,** *55* (16), 4908-4913.
105. Yu, Z.; Zhang, J.; Coulston, R. J.; Parker, R. M.; Biedermann, F.; Liu, X.; Scherman, O. A.; Abell, C., *Chem. Sci.* **2015,** *6* (8), 4929-4933.
106. Stephenson, G.; Parker, R. M.; Lan, Y.; Yu, Z.; Scherman, O. A.; Abell, C., *Chem. Commun.* **2014,** *50* (53), 7048-7051.
107. Yu, Z.; Zheng, Y.; Parker, R. M.; Lan, Y.; Wu, Y.; Coulston, R. J.; Zhang, J.; Scherman, O. A.; Abell, C., *ACS Appl. Mater. Interfaces* **2016,** *8* (13), 8811-8820.
108. Yao, X.; Li, T.; Wang, J.; Ma, X.; Tian, H., *Adv. Opt. Mater.* **2016,** *4* (9), 1322-1349.
109. Yu, Z.; Lan, Y.; Parker, R. M.; Zhang, W.; Deng, X.; Scherman, O. A.; Abell, C., *Polymer Chemistry* **2016,** *7* (38), 5996-6002.
110. Biedermann, F.; Elmalem, E.; Ghosh, I.; Nau, W. M.; Scherman, O. A., *Angew. Chem. Int. Ed.* **2012,** *51* (31), 7739-7743.
111. Tian, F.; Jiao, D.; Biedermann, F.; Scherman, O. A., *Nat. Commun.* **2012,** *3*, 1207.
112. Ryan, S. T. J.; del Barrio, J.; Suardíaz, R.; Ryan, D. F.; Rosta, E.; Scherman, O. A., *Angew. Chem. Int. Ed.* **2016,** *55* (52), 16096–16100.
113. Appel, E. A.; Forster, R. A.; Rowland, M. J.; Scherman, O. A., *Biomaterials* **2014,** *35* (37), 9897-9903.
114. Yang, H.; Yuan, B.; Zhang, X.; Scherman, O. A., *Acc. Chem. Res.* **2014,** *47* (7), 2106-2115.
115. Janeček, E.-R.; McKee, J. R.; Tan, C. S. Y.; Nykänen, A.; Kettunen, M.; Laine, J.; Ikkala, O.; Scherman, O. A., *Angew. Chem. Int. Ed.* **2015,** *54* (18), 5383-5388.
116. Appel, E. A.; del Barrio, J.; Loh, X. J.; Scherman, O. A., *Chem. Soc. Rev.* **2012,** *41* (18), 6195-6214.
117. Zheng, Y.; Yu, Z.; Parker, R. M.; Wu, Y.; Abell, C.; Scherman, O. A., *Nat. Commun.* **2014,** *5*, 5772.
118. Huang, Z.; Yang, L.; Liu, Y.; Wang, Z.; Scherman, O. A.; Zhang, X., *Angew. Chem. Int. Ed.* **2014,** *53* (21), 5351-5355.
119. Jones, S. T.; Zayed, J. M.; Scherman, O. A., *Nanoscale* **2013,** *5* (12), 5299-5302.

120. Groombridge, A. S.; Palma, A.; Parker, R. M.; Abell, C.; Scherman, O. A., *Chem. Sci.* **2017,** *8* (2), 1350-1355.
121. Gulik-Krzywicki, T.; Fouquey, C.; Lehn, J., *Proc. Nat. Acad. Sci.* **1993,** *90* (1), 163-167.
122. Weiss, R. G.; Terech, P., *Molecular Gels: Materials with Self-Assembled Fibrillar Networks*. Springer Netherlands: 2006.
123. Cantekin, S.; de Greef, T. F. A.; Palmans, A. R. A., *Chem. Soc. Rev.* **2012,** *41* (18), 6125-6137.
124. Howe, R. C. T.; Smalley, A. P.; Guttenplan, A. P. M.; Doggett, M. W. R.; Eddleston, M. D.; Tan, J. C.; Lloyd, G. O., *Chem. Commun.* **2013,** *49* (39), 4268-4270.
125. Paikar, A.; Pramanik, A.; Haldar, D., *RSC Adv.* **2015,** *5* (40), 31845-31851.
126. Bernet, A.; Albuquerque, R. Q.; Behr, M.; Hoffmann, S. T.; Schmidt, H.-W., *Soft Matter* **2012,** *8* (1), 66-69.
127. Nagarajan, V.; Pedireddi, V. R., *Cryst. Growth Des.* **2014,** *14* (4), 1895-1901.
128. Zhong, J.-L.; Jia, X.-J.; Liu, H.-J.; Luo, X.-Z.; Hong, S.-G.; Zhang, N.; Huang, J.-B., *Soft Matter* **2016,** *12* (1), 191-199.
129. Bhattacharya, S.; Sengupta, S.; Bala, S.; Goswami, A.; Ganguly, S.; Mondal, R., *Cryst. Growth Des.* **2014,** *14* (5), 2366-2374.
130. Jana, P.; Paikar, A.; Bera, S.; Maity, S. K.; Haldar, D., *Org. Lett.* **2014,** *16* (1), 38-41.
131. R. A. Palmans, A.; A. J. M. Vekemans, J.; W. Meijer, E.; R. A. Palmans, A.; Kooijman, H.; L. Spek, A., *Chem. Commun.* **1997,** (22), 2247-2248.
132. Desmarchelier, A.; Alvarenga, B. G.; Caumes, X.; Dubreucq, L.; Troufflard, C.; Tessier, M.; Vanthuyne, N.; Ide, J.; Maistriaux, T.; Beljonne, D.; Brocorens, P.; Lazzaroni, R.; Raynal, M.; Bouteiller, L., *Soft Matter* **2016,** *12* (37), 7824-7838.
133. Stals, P. J. M.; Smulders, M. M. J.; Martín-Rapún, R.; Palmans, A. R. A.; Meijer, E. W., *Chem. Eur. J.* **2009,** *15* (9), 2071-2080.
134. Invernizzi, C.; Dalvit, C.; Stoeckli-Evans, H.; Neier, R., *Eur. J. Org. Chem.* **2015,** *2015* (23), 5115-5127.
135. Besenius, P.; Heynens, J. L. M.; Straathof, R.; Nieuwenhuizen, M. M. L.; Bomans, P. H. H.; Terreno, E.; Aime, S.; Strijkers, G. J.; Nicolay, K.; Meijer, E. W., *Contrast Media & Molecular Imaging* **2012,** *7* (3), 356-361.
136. Besenius, P.; Portale, G.; Bomans, P. H. H.; Janssen, H. M.; Palmans, A. R. A.; Meijer, E. W., *Proc. Nat. Acad. Sci.* **2010,** *107* (42), 17888-17893.
137. Pandurangan, K.; Kitchen, J. A.; Blasco, S.; Boyle, E. M.; Fitzpatrick, B.; Feeney, M.; Kruger, P. E.; Gunnlaugsson, T., *Angew. Chem.* **2015,** *127* (15), 4649-4653.
138. Bose, P. P.; Drew, M. G. B.; Das, A. K.; Banerjee, A., *Chem. Commun.* **2006,** (30), 3196-3198.
139. Rajput, L.; Biradha, K., *J. Mol. Struct.* **2008,** *876* (1–3), 339-343.
140. L., B.; A.P.H.J., S.; M.A.C., B.; H.M., J.; J.A.J.M., V.; E.W., M., *Chem. Lett.* **2000,** *29* (3), 292-293.
141. Cantekin, S.; Balkenende, D. W. R.; Smulders, M. M. J.; Palmans, A. R. A.; Meijer, E. W., *Nat. Chem.* **2011,** *3* (1), 42-46.
142. Smulders, M. M. J.; Buffeteau, T.; Cavagnat, D.; Wolffs, M.; Schenning, A. P. H. J.; Meijer, E. W., *Chirality* **2008,** *20* (9), 1016-1022.
143. Smulders, M. M. J.; Schenning, A. P. H. J.; Meijer, E. W., *J. Am. Chem. Soc.* **2008,** *130* (2), 606-611.
144. de Loos, M.; van Esch, J. H.; Kellogg, R. M.; Feringa, B. L., *Tetrahedron* **2007,** *63* (31), 7285-7301.
145. Veld, M. A. J.; Haveman, D.; Palmans, A. R. A.; Meijer*, E. W., *Soft Matter* **2011,** *7* (2), 524-531.

146. Filot, I. A. W.; Palmans, A. R. A.; Hilbers, P. A. J.; van Santen, R. A.; Pidko, E. A.; de Greef, T. F. A., *J. Phys. Chem. B* **2010,** *114* (43), 13667-13674.
147. Ishioka, Y.; Minakuchi, N.; Mizuhata, M.; Maruyama, T., *Soft Matter* **2014,** *10* (7), 965-971.
148. Stals, P. J. M.; Everts, J. C.; de Bruijn, R.; Filot, I. A. W.; Smulders, M. M. J.; Martín-Rapún, R.; Pidko, E. A.; de Greef, T. F. A.; Palmans, A. R. A.; Meijer, E. W., *Chem. Eur. J.* **2010,** *16* (3), 810-821.
149. Brunsveld, L.; Zhang, H.; Glasbeek, M.; Vekemans, J. A. J. M.; Meijer, E. W., *J. Am. Chem. Soc.* **2000,** *122* (26), 6175-6182.
150. van den Hout, K. P.; Martín-Rapún, R.; Vekemans, J. A. J. M.; Meijer, E. W., *Chem. Eur. J.* **2007,** *13* (29), 8111-8123.
151. Matsuura, K.; Murasato, K.; Kimizuka, N., *J. Am. Chem. Soc.* **2005,** *127* (29), 10148-10149.
152. van Herrikhuyzen, J.; Jonkheijm, P.; Schenning, A. P. H. J.; Meijer, E. W., *Org. Biomol. Chem.* **2006,** *4* (8), 1539-1545.
153. Dankers, P. Y. W.; Hermans, T. M.; Baughman, T. W.; Kamikawa, Y.; Kieltyka, R. E.; Bastings, M. M. C.; Janssen, H. M.; Sommerdijk, N. A. J. M.; Larsen, A.; van Luyn, M. J. A.; Bosman, A. W.; Popa, E. R.; Fytas, G.; Meijer, E. W., *Adv. Mater.* **2012,** *24* (20), 2703-2709.
154. Chebotareva, N.; Bomans, P. H. H.; Frederik, P. M.; Sommerdijk, N. A. J. M.; Sijbesma, R. P., *Chem. Commun.* **2005,** (39), 4967-4969.
155. Lee, S.; Lee, J.-S.; Lee, C. H.; Jung, Y.-S.; Kim, J.-M., *Langmuir* **2011,** *27* (5), 1560-1564.
156. Leenders, C. M. A.; Albertazzi, L.; Mes, T.; Koenigs, M. M. E.; Palmans, A. R. A.; Meijer, E. W., *Chem. Commun.* **2013,** *49* (19), 1963-1965.
157. Stuart, M. C. A.; van de Pas, J. C.; Engberts, J. B. F. N., *J. Phys. Org. Chem.* **2005,** *18* (9), 929-934.
158. Leenders, C. M. A.; Baker, M. B.; Pijpers, I. A. B.; Lafleur, R. P. M.; Albertazzi, L.; Palmans, A. R. A.; Meijer, E. W., *Soft Matter* **2016,** *12* (11), 2887-2893.
159. Besenius, P.; Goedegebure, Y.; Driesse, M.; Koay, M.; Bomans, P. H. H.; Palmans, A. R. A.; Dankers, P. Y. W.; Meijer, E. W., *Soft Matter* **2011,** *7* (18), 7980-7983.
160. Shen, Z.; Wang, T.; Liu, M., *Angew. Chem. Int. Ed.* **2014,** *53* (49), 13424-13428.
161. Huang, X.; Li, C.; Jiang, S.; Wang, X.; Zhang, B.; Liu, M., *J. Am. Chem. Soc.* **2004,** *126* (5), 1322-1323.
162. Yuan, J.; Liu, M., *J. Am. Chem. Soc.* **2003,** *125* (17), 5051-5056.
163. Gillissen, M. A. J.; Koenigs, M. M. E.; Spiering, J. J. H.; Vekemans, J. A. J. M.; Palmans, A. R. A.; Voets, I. K.; Meijer, E. W., *J. Am. Chem. Soc.* **2014,** *136* (1), 336-343.
164. van Houtem, M. H. C. J.; Benaskar, F.; Fitie, C. F. C.; Martin-Rapun, R.; Vekemans, J. A. J. M.; Meijer, E. W., *Org. Biomol. Chem.* **2012,** *10* (30), 5898-5908.
165. Narayan, B.; Kulkarni, C.; George, S. J., *J. Mater. Chem. C* **2013,** *1* (4), 626-629.
166. Roosma, J.; Mes, T.; Leclère, P.; Palmans, A. R. A.; Meijer, E. W., *J. Am. Chem. Soc.* **2008,** *130* (4), 1120-1121.
167. Kreger, K.; Wolfer, P.; Audorff, H.; Kador, L.; Stingelin-Stutzmann, N.; Smith, P.; Schmidt, H.-W., *J. Am. Chem. Soc.* **2010,** *132* (2), 509-516.
168. Fitié, C. F. C.; Roelofs, W. S. C.; Kemerink, M.; Sijbesma, R. P., *J. Am. Chem. Soc.* **2010,** *132* (20), 6892-6893.
169. van Bommel, K. J. C.; van der Pol, C.; Muizebelt, I.; Friggeri, A.; Heeres, A.; Meetsma, A.; Feringa, B. L.; van Esch, J., *Angew. Chem. Int. Ed.* **2004,** *43* (13), 1663-1667.
170. van Gorp, J. J.; Vekemans, J. A. J. M.; Meijer, E. W., *J. Am. Chem. Soc.* **2002,** *124* (49), 14759-14769.
171. Hanabusa, K.; Kawakami, A.; Kimura, M.; Shirai, H., *Chem. Lett.* **1997,** (3), 191-192.

172. Fan, E.; Yang, J.; Geib, S. J.; Stoner, T. C.; Hopkins, M. D.; Hamilton, A. D., *J. Chem. Soc., Chem. Commun.* **1995,** (12), 1251-1252.
173. Heeres, A.; van der Pol, C.; Stuart, M.; Friggeri, A.; Feringa, B. L.; van Esch, J., *J. Am. Chem. Soc.* **2003,** *125* (47), 14252-14253.
174. Brizard, A.; Stuart, M.; van Bommel, K.; Friggeri, A.; de Jong, M.; van Esch, J., *Angew. Chem. Int. Ed.* **2008,** *47* (11), 2063-2066.
175. Brizard, A. M.; Stuart, M. C. A.; van Esch, J. H., *Faraday Discuss.* **2009,** *143* (0), 345-357.
176. Boekhoven, J.; van Rijn, P.; Brizard, A. M.; Stuart, M. C. A.; van Esch, J. H., *Chem. Commun.* **2010,** *46* (20), 3490-3492.
177. Kumar, D. K.; Steed, J. W., *Chem. Soc. Rev.* **2014,** *43* (7), 2080-2088.
178. Moffat, J. R.; Smith, D. K., *Chem. Commun.* **2009,** (3), 316-318.
179. van Herrikhuyzen, J.; Syamakumari, A.; Schenning, A. P. H. J.; Meijer, E. W., *J. Am. Chem. Soc.* **2004,** *126* (32), 10021-10027.
180. Sugiyasu, K.; Kawano, S.-i.; Fujita, N.; Shinkai, S., *Chem. Mater.* **2008,** *20* (9), 2863-2865.
181. Ogata, D.; Shikata, T.; Hanabusa, K., *J. Phys. Chem. B* **2004,** *108* (40), 15503-15510.
182. Shikata, T.; Ogata, D.; Hanabusa, K., *Journal of the Society of Rheology, Japan* **2003,** *31* (4), 229-236.
183. Kenji, H.; Chiemi, K.; Mutsumi, K.; Hirofusa, S.; Akikazu, K., *Chem. Lett.* **1997,** *26* (5), 429-430.
184. P. Lightfoot, M.; S. Mair, F.; G. Pritchard, R.; E. Warren, J., *Chem. Commun.* **1999,** (19), 1945-1946.
185. Hirst, A. R.; Coates, I. A.; Boucheteau, T. R.; Miravet, J. F.; Escuder, B.; Castelletto, V.; Hamley, I. W.; Smith, D. K., *J. Am. Chem. Soc.* **2008,** *130* (28), 9113-9121.
186. Hunt, J. N.; Feldman, K. E.; Lynd, N. A.; Deek, J.; Campos, L. M.; Spruell, J. M.; Hernandez, B. M.; Kramer, E. J.; Hawker, C. J., *Adv. Mater.* **2011,** *23* (20), 2327-2331.
187. Suzuki, M.; Nakajima, Y.; Yumoto, M.; Kimura, M.; Shirai, H.; Hanabusa, K., *Langmuir* **2003,** *19* (21), 8622-8624.
188. Boekhoven, J.; Brizard, A. M.; Kowlgi, K. N. K.; Koper, G. J. M.; Eelkema, R.; van Esch, J. H., *Angew. Chem. Int. Ed.* **2010,** *49* (28), 4825-4828.
189. Hirst, A. R.; Roy, S.; Arora, M.; Das, A. K.; Hodson, N.; Murray, P.; Marshall, S.; Javid, N.; Sefcik, J.; Boekhoven, J.; van Esch, J. H.; Santabarbara, S.; Hunt, N. T.; Ulijn, R. V., *Nat. Chem.* **2010,** *2* (12), 1089-1094.
190. Boekhoven, J.; Poolman, J. M.; Maity, C.; Li, F.; van der Mee, L.; Minkenberg, C. B.; Mendes, E.; van EschJan, H.; Eelkema, R., *Nat. Chem.* **2013,** *5* (5), 433-437.
191. Poolman, J. M.; Boekhoven, J.; Besselink, A.; Olive, A. G. L.; van Esch, J. H.; Eelkema, R., *Nat. Protocols* **2014,** *9* (4), 977-988.
192. Ahmed, E. M., *Journal of Advanced Research* **2015,** *6* (2), 105-121.
193. Jagur-Grodzinski, J., *Polym. Adv. Technol.* **2010,** *21* (1), 27-47.
194. Liu, L. S.; Kost, J.; Yan, F.; Spiro, R. C., *Polymers* **2012,** *4* (2), 997.
195. Buwalda, S. J.; Boere, K. W. M.; Dijkstra, P. J.; Feijen, J.; Vermonden, T.; Hennink, W. E., *J. Controlled Release* **2014,** *190*, 254-273.
196. Weiss, R. G., *J. Am. Chem. Soc.* **2014,** *136* (21), 7519-7530.
197. de Loos, M.; Feringa, B. L.; van Esch, J. H., *Eur. J. Org. Chem.* **2005,** *2005* (17), 3615-3631.
198. Estroff, L. A.; Hamilton, A. D., *Chem. Rev.* **2004,** *104* (3), 1201-1218.
199. Du, X.; Zhou, J.; Shi, J.; Xu, B., *Chem. Rev.* **2015,** *115* (24), 13165-13307.
200. Prasanna de Silva, A., *Chem. Asian J.* **2011,** *6* (3), 750-766.
201. Xie, Z.; Zhang, A.; Ye, L.; Wang, X.; Feng, Z.-g., *J. Mater. Chem.* **2009,** *19* (34), 6100-6102.
202. Draper, E. R.; Adams, D. J., *Chem. Commun.* **2016,** *52* (53), 8196-8206.

203. Jones, C. D.; Steed, J. W., *Chem. Soc. Rev.* **2016,** *45* (23), 6546-6596.
204. Lin, Y. C.; Kachar, B.; Weiss, R. G., *J. Am. Chem. Soc.* **1989,** *111* (15), 5542-5551.
205. Murata, K.; Aoki, M.; Suzuki, T.; Harada, T.; Kawabata, H.; Komori, T.; Ohseto, F.; Ueda, K.; Shinkai, S., *J. Am. Chem. Soc.* **1994,** *116* (15), 6664-6676.
206. Jang, W.-D.; Jiang, D.-L.; Aida, T., *J. Am. Chem. Soc.* **2000,** *122* (13), 3232-3233.
207. George, S. J.; Ajayaghosh, A.; Jonkheijm, P.; Schenning, A. P. H. J.; Meijer, E. W., *Angew. Chem. Int. Ed.* **2004,** *43* (26), 3422-3425.
208. Murata, K.; Aoki, M.; Nishi, T.; Ikeda, A.; Shinkai, S., *J. Chem. Soc., Chem. Commun.* **1991,** (24), 1715-1718.
209. Sohna Sohna, J.-E.; Fages, F., *Chem. Commun.* **1997,** (3), 327-328.
210. Lovitt, J. I.; Hawes, C. S.; Lynes, A. D.; Haffner, B.; Mobius, M. E.; Gunnlaugsson, T., *Inorg. Chem. Frontiers* **2017**.
211. Hirst, A. R.; Smith, D. K., *Chem. Eur. J.* **2005,** *11* (19), 5496-5508.
212. Hirst, A. R.; Smith, D. K.; Feiters, M. C.; Geurts, H. P. M., *Langmuir* **2004,** *20* (17), 7070-7077.
213. Hirst, A. R.; Smith, D. K.; Harrington, J. P., *Chem. Eur. J.* **2005,** *11* (22), 6552-6559.
214. Hirst, A. R.; Miravet, J. F.; Escuder, B.; Noirez, L.; Castelletto, V.; Hamley, I. W.; Smith, D. K., *Chem. Eur. J.* **2009,** *15* (2), 372-379.
215. Basit, H.; Pal, A.; Sen, S.; Bhattacharya, S., *Chem. Eur. J.* **2008,** *14* (21), 6534-6545.
216. Rao, K. V.; Jayaramulu, K.; Maji, T. K.; George, S. J., *Angew. Chem. Int. Ed.* **2010,** *49* (25), 4218-4222.
217. Morris, K. L.; Chen, L.; Raeburn, J.; Sellick, O. R.; Cotanda, P.; Paul, A.; Griffiths, P. C.; King, S. M.; O'Reilly, R. K.; Serpell, L. C.; Adams, D. J., *Nat. Commun.* **2013,** *4*, 1480.
218. Colquhoun, C.; Draper, E. R.; Eden, E. G. B.; Cattoz, B. N.; Morris, K. L.; Chen, L.; McDonald, T. O.; Terry, A. E.; Griffiths, P. C.; Serpell, L. C.; Adams, D. J., *Nanoscale* **2014,** *6* (22), 13719-13725.
219. Raeburn, J.; Alston, B.; Kroeger, J.; McDonald, T. O.; Howse, J. R.; Cameron, P. J.; Adams, D. J., *Materials Horizons* **2014,** *1* (2), 241-246.
220. Draper, E. R.; Eden, E. G. B.; McDonald, T. O.; Adams, D. J., *Nat. Chem.* **2015,** *7* (10), 848-852.
221. Pocker, Y.; Green, E., *J. Am. Chem. Soc.* **1973,** *95* (1), 113-119.
222. Adams, D. J.; Butler, M. F.; Frith, W. J.; Kirkland, M.; Mullen, L.; Sanderson, P., *Soft Matter* **2009,** *5* (9), 1856-1862.
223. Piepenbrock, M.-O. M.; Clarke, N.; Foster, J. A.; Steed, J. W., *Chem. Commun.* **2011,** *47* (7), 2095-2097.
224. Lloyd, G. O.; Piepenbrock, M.-O. M.; Foster, J. A.; Clarke, N.; Steed, J. W., *Soft Matter* **2012,** *8* (1), 204-216.
225. Piepenbrock, M.-O. M.; Clarke, N.; Steed, J. W., *Langmuir* **2009,** *25* (15), 8451-8456.
226. Piepenbrock, M.-O. M.; Clarke, N.; Steed, J. W., *Soft Matter* **2010,** *6* (15), 3541-3547.
227. Byrne, P.; Lloyd, G. O.; Applegarth, L.; Anderson, K. M.; Clarke, N.; Steed, J. W., *New J. Chem.* **2010,** *34* (10), 2261-2274.
228. Meazza, L.; Foster, J. A.; Fucke, K.; Metrangolo, P.; Resnati, G.; Steed, J. W., *Nat. Chem.* **2013,** *5* (1), 42-47.
229. Priimagi, A.; Cavallo, G.; Metrangolo, P.; Resnati, G., *Acc. Chem. Res.* **2013,** *46* (11), 2686-2695.
230. Petrova, R. I.; Patel, R.; Swift, J. A., *Cryst. Growth Des.* **2006,** *6* (12), 2709-2715.
231. Lloyd, G. O.; Steed, J. W., *Nat. Chem.* **2009,** *1* (6), 437-442.
232. Foster, J. A.; PiepenbrockMarc-Oliver, M.; Lloyd, G. O.; Clarke, N.; HowardJudith, A. K.; Steed, J. W., *Nat. Chem.* **2010,** *2* (12), 1037-1043.

233. Foster, J. A.; Damodaran, K. K.; Maurin, A.; Day, G. M.; Thompson, H. P. G.; Cameron, G. J.; Bernal, J. C.; Steed, J. W., *Chem. Sci.* **2017,** *8* (1), 78-84.
234. Kaufmann, L.; Kennedy, S. R.; Jones, C. D.; Steed, J. W., *Chem. Commun.* **2016,** *52* (66), 10113-10116.
235. Cao, Y. C.; Jin, R.; Mirkin, C. A., *Science* **2002,** *297* (5586), 1536.
236. Bell, A. T., *Science* **2003,** *299* (5613), 1688.
237. Wang, J.; Gudiksen, M. S.; Duan, X.; Cui, Y.; Lieber, C. M., *Science* **2001,** *293* (5534), 1455.
238. Yoshizawa, M.; Klosterman, J. K.; Fujita, M., *Angew. Chem. Int. Ed.* **2009,** *48* (19), 3418-3438.
239. Avram, L.; Cohen, Y.; Rebek Jr, J., *Chem. Commun.* **2011,** *47* (19), 5368-5375.
240. Einaga, Y.; Sato, O.; Iyoda, T.; Fujishima, A.; Hashimoto, K., *J. Am. Chem. Soc.* **1999,** *121* (15), 3745-3750.
241. Cassell, A. M.; Asplund, C. L.; Tour, J. M., *Angew. Chem. Int. Ed.* **1999,** *38* (16), 2403-2405.
242. Tominaga, M.; Masu, H.; Azumaya, I., *J. Org. Chem.* **2009,** *74* (22), 8754-8760.
243. Tominaga, M.; Ohara, K.; Yamaguchi, K.; Azumaya, I., *J. Org. Chem.* **2014,** *79* (14), 6738-6742.
244. Lv, K.; Zhang, L.; Liu, M., *Langmuir* **2014,** *30* (31), 9295-9302.
245. Jin, Q.; Zhang, L.; Liu, M., *Chem. Eur. J.* **2013,** *19* (28), 9234-9241.
246. Park, S.; Lim, J.-H.; Chung, S.-W.; Mirkin, C. A., *Science* **2004,** *303* (5656), 348.
247. Jeon, Y.-M.; Armatas, G. S.; Kim, D.; Kanatzidis, M. G.; Mirkin, C. A., *Small* **2009,** *5* (1), 46-50.
248. Oh, M.; Mirkin, C. A., *Nature* **2005,** *438* (7068), 651-654.
249. Cho, W.; Lee, H. J.; Choi, S.; Kim, Y.; Oh, M., *Sci. Rep.* **2014,** *4*, 6518.
250. Mu; Shi; Chang, J. C.; Lee, S.-T., *Nano Lett.* **2008,** *8* (1), 104-109.
251. Bünzli, J.-C. G., *Acc. Chem. Res.* **2006,** *39* (1), 53-61.
252. Bradberry, S. J.; Savyasachi, A. J.; Martinez-Calvo, M.; Gunnlaugsson, T., *Coord. Chem. Rev.* **2014,** *273–274*, 226-241.
253. Katkova, M. A.; Bochkarev, M. N., *Dalton Trans.* **2010,** *39* (29), 6599-6612.
254. Chen, B.; Feng, J., *J. Phys. Chem. C* **2015,** *119* (14), 7865-7872.
255. Martínez-Calvo, M.; Kotova, O.; Möbius, M. E.; Bell, A. P.; McCabe, T.; Boland, J. J.; Gunnlaugsson, T., *J. Am. Chem. Soc.* **2015,** *137* (5), 1983-1992.
256. Leonard, J. P.; dos Santos, C. M. G.; Plush, S. E.; McCabe, T.; Gunnlaugsson, T., *Chem. Commun.* **2007,** (2), 129-131.
257. McCoy, C. P.; Stomeo, F.; Plush, S. E.; Gunnlaugsson, T., *Chem. Mater.* **2006,** *18* (18), 4336-4343.
258. Dickins, R. S.; Howard, J. A. K.; Lehmann, C. W.; Moloney, J.; Parker, D.; Peacock, R. D., *Angew. Chem. Int. Ed. Engl.* **1997,** *36* (5), 521-523.
259. Aime, S.; Barge, A.; Botta, M.; Parker, D.; De Sousa, A. S., *J. Am. Chem. Soc.* **1997,** *119* (20), 4767-4768.
260. Bunzli, J.-C. G.; Piguet, C., *Chem. Soc. Rev.* **2005,** *34* (12), 1048-1077.
261. Gunnlaugsson, T.; Stomeo, F., *Org. Biomol. Chem.* **2007,** *5* (13), 1999-2009.
262. Faulkner, S.; Pope, S. J. A.; Burton-Pye, B. P., *Appl. Spectrosc. Rev.* **2005,** *40* (1), 1-31.
263. Bünzli, J.-C. G., *J. Coord. Chem.* **2014,** *67* (23-24), 3706-3733.
264. Eliseeva, S. V.; Bunzli, J.-C. G., *Chem. Soc. Rev.* **2010,** *39* (1), 189-227.
265. Bünzli, J.-C. G.; Eliseeva, S. V., *In Lanthanide Luminescence: Photophysical, Analytical and Biological Aspects; Hänninen, P.; Härmä, H.* Springer Berlin Heidelberg: 2011; Vol. 7.
266. Huang, C. H., *Rare Earth Coordination Chemistry: Fundamentals and Applications*. Wiley: 2011.

267. Stomeo, F.; Leonard, J.; Nolan, C. a.; Gunnlaugsson, T., Photochemistry and Photophysics of Coordination Compounds: Lanthanides. In *Photochemistry and Photophysics of Coordination Compounds: II*, Balzani, V.; Campagna, S., Eds. Springer Berlin Heidelberg: 2007.
268. Bunzli, J.-C. G.; Eliseeva, S. V., *Chemical Science* **2013,** *4* (5), 1939-1949.
269. Bünzli, J.-C. G.; de Bettencourt-Dias, A., *In Luminescence of Lanthanide Ions in Coordination Compounds and Nanomaterials*. Wiley: 2014.
270. Hanaoka, K.; Kikuchi, K.; Kobayashi, S.; Nagano, T., *J. Am. Chem. Soc.* **2007,** *129* (44), 13502-13509.
271. dos Santos, C. M. G.; Harte, A. J.; Quinn, S. J.; Gunnlaugsson, T., *Coord. Chem. Rev.* **2008,** *252* (23–24), 2512-2527.
272. Heffern, M. C.; Matosziuk, L. M.; Meade, T. J., *Chem. Rev.* **2014,** *114* (8), 4496-4539.
273. Bünzli, J. C. G., Rare Earth Luminescent Centers in Organic and Biochemical Compounds. In *Spectroscopic Properties of Rare Earths in Optical Materials*, Hull, R.; Parisi, J.; Osgood, R. M., Jr.; Warlimont, H.; Liu, G.; Jacquier, B., Eds. Springer Berlin Heidelberg: 2005; Vol. 83, pp 462-499.
274. Horrocks, W. D.; Sudnick, D. R., *Acc. Chem. Res.* **1981,** *14* (12), 384-392.
275. Horrocks, W. D.; Sudnick, D. R., *J. Am. Chem. Soc.* **1979,** *101* (2), 334-340.
276. Bünzli, J.-C. G., *Coord. Chem. Rev.* **2015,** *293–294*, 19-47.
277. Beeby, A.; M. Clarkson, I.; S. Dickins, R.; Faulkner, S.; Parker, D.; Royle, L.; S. de Sousa, A.; A. Gareth Williams, J.; Woods, M., *J. Chem. Soc., Perkin. Trans. 2* **1999,** (3), 493-504.
278. Supkowski, R. M.; Horrocks Jr, W. D., *Inorg. Chim. Acta* **2002,** *340*, 44-48.
279. Aime, S.; Botta, M.; Parker, D.; Williams, J. A. G., *J. Chem. Soc., Dalton Trans.* **1996,** (1), 17-23.
280. Bünzli, J.-C. G.; Piguet, C., *Chem. Rev.* **2002,** *102* (6), 1897-1928.
281. Kotova, O.; Daly, R.; dos Santos, C. M. G.; Boese, M.; Kruger, P. E.; Boland, J. J.; Gunnlaugsson, T., *Angew. Chem. Int. Ed.* **2012,** *51* (29), 7208-7212.
282. Daly, R.; Kotova, O.; Boese, M.; Gunnlaugsson, T.; Boland, J. J., *ACS Nano* **2013,** *7* (6), 4838-4845.
283. McKee, J. R.; Appel, E. A.; Seitsonen, J.; Kontturi, E.; Scherman, O. A.; Ikkala, O., *Adv. Funct. Mater.* **2014,** *24* (18), 2706-2713.
284. Fiore, G. L.; Rowan, S. J.; Weder, C., *Chem. Soc. Rev.* **2013,** *42* (17), 7278-7288.
285. McCarney, E. P.; Byrne, J. P.; Twamley, B.; Martinez-Calvo, M.; Ryan, G.; Mobius, M. E.; Gunnlaugsson, T., *Chem. Commun.* **2015,** *51* (74), 14123-14126.
286. Caffrey, D. F.; Gunnlaugsson, T., *Dalton Trans.* **2014,** *43* (48), 17964-17970.
287. Galanti, A.; Kotova, O.; Blasco, S.; Johnson, C. J.; Peacock, R. D.; Mills, S.; Boland, J. J.; Albrecht, M.; Gunnlaugsson, T., *Chem. Eur. J.* **2016,** *22* (28), 9709-9723.
288. Bradberry, S. J.; Byrne, J. P.; McCoy, C. P.; Gunnlaugsson, T., *Chem. Commun.* **2015,** *51* (92), 16565-16568.
289. Tobin, G.; Comby, S.; Zhu, N.; Clerac, R.; Gunnlaugsson, T.; Schmitt, W., *Chem. Commun.* **2015,** *51* (68), 13313-13316.
290. Comby, S.; Surender, E. M.; Kotova, O.; Truman, L. K.; Molloy, J. K.; Gunnlaugsson, T., *Inorg. Chem.* **2014,** *53* (4), 1867-1879.
291. Gunnlaugsson, T.; Leonard, J. P., *Chem. Commun.* **2005,** (25), 3114-3131.
292. Sénéchal-David, K.; Leonard, J. P.; Plush, S. E.; Gunnlaugsson, T., *Org. Lett.* **2006,** *8* (13), 2727-2730.
293. Wild, A.; Winter, A.; Schlutter, F.; Schubert, U. S., *Chem. Soc. Rev.* **2011,** *40* (3), 1459-1511.
294. Schmatloch, S.; van den Berg, A. M. J.; Alexeev, A. S.; Hofmeier, H.; Schubert, U. S., *Macromolecules* **2003,** *36* (26), 9943-9949.

295. Gampp, H.; Maeder, M.; Meyer, C. J.; Zuberbühler, A. D., *Talanta* **1985,** *32* (2), 95-101.
296. Gampp, H.; Maeder, M.; Meyer, C. J.; Zuberbühler, A. D., *Talanta* **1986,** *33* (12), 943-951.
297. Haas, Y.; Stein, G., *J. Phys. Chem.* **1972,** *76* (8), 1093-1104.
298. Lehn, J.-M., *Polym. Int.* **2002,** *51* (10), 825-839.
299. Brunsveld, L.; Folmer, B. J. B.; Meijer, E. W.; Sijbesma, R. P., *Chem. Rev.* **2001,** *101* (12), 4071-4098.
300. Carnall, J. M. A.; Waudby, C. A.; Belenguer, A. M.; Stuart, M. C. A.; Peyralans, J. J. P.; Otto, S., *Science* **2010,** *327* (5972), 1502.
301. Leininger, S.; Olenyuk, B.; Stang, P. J., *Chem. Rev.* **2000,** *100* (3), 853-908.
302. Schmuck, C.; Wienand, W., *Angew. Chem. Int. Ed.* **2001,** *40* (23), 4363-4369.
303. Guan, Y.; Yu, S.-H.; Antonietti, M.; Böttcher, C.; Faul, C. F. J., *Chem. Eur. J.* **2005,** *11* (4), 1305-1311.
304. Liu, Q.; Wang, Y.; Li, W.; Wu, L., *Langmuir* **2007,** *23* (15), 8217-8223.
305. Stupp, S. I., *Nano Lett.* **2010,** *10* (12), 4783-4786.
306. van Esch, J. H.; Feringa, B. L., *Angew. Chem. Int. Ed.* **2000,** *39* (13), 2263-2266.
307. Gronwald, O.; Sakurai, K.; Luboradzki, R.; Kimura, T.; Shinkai, S., *Carbohydr. Res.* **2001,** *331* (3), 307-318.
308. Gronwald, O.; Shinkai, S., *J. Chem. Soc., Perkin. Trans. 2* **2001,** (10), 1933-1937.
309. Yoza, K.; Amanokura, N.; Ono, Y.; Akao, T.; Shinmori, H.; Takeuchi, M.; Shinkai, S.; Reinhoudt, D. N., *Chem. Eur. J.* **1999,** *5* (9), 2722-2729.
310. Masayoshi, A.; Kazunori, S.; Norifumi, F.; Seiji, S., *Chem. Lett.* **2004,** *33* (2), 120-121.
311. Suzuki, M.; Yumoto, M.; Kimura, M.; Shirai, H.; Hanabusa, K., *Tetrahedron Lett.* **2004,** *45* (14), 2947-2950.
312. Suzuki, M.; Yumoto, M.; Kimura, M.; Shirai, H.; Hanabusa, K., *Chem. Eur. J.* **2003,** *9* (1), 348-354.
313. Kazuhiko, I.; Yoshiyuki, O.; Yasumasa, K.; Kenji, H.; Seiji, S., *Chem. Lett.* **1999,** *28* (5), 429-430.
314. Menger, F. M.; Caran, K. L., *J. Am. Chem. Soc.* **2000,** *122* (47), 11679-11691.
315. Menger, F. M.; Yamasaki, Y.; Catlin, K. K.; Nishimi, T., *Angew. Chem. Int. Ed. Engl.* **1995,** *34* (5), 585-586.
316. Lynes, A. D.; Hawes, C. S.; Ward, E. N.; Haffner, B.; Mobius, M. E.; Byrne, K.; Schmitt, W.; Pal, R.; Gunnlaugsson, T., *CrystEngComm* **2017,** *19* (10), 1427-1438.
317. Beck, J. B.; Rowan, S. J., *J. Am. Chem. Soc.* **2003,** *125* (46), 13922-13923.
318. Russell, T. P., *Science* **2002,** *297* (5583), 964.
319. Nath, N.; Chilkoti, A., *Adv. Mater.* **2002,** *14* (17), 1243-1247.
320. Finch, C. A., *Polym. Int.* **2001,** *50* (9), 1054-1054.
321. Banerjee, S.; Vidya, V. M.; Savyasachi, A. J.; Maitra, U., *J. Mater. Chem.* **2011,** *21* (38), 14693-14705.
322. Wang, Q.; Mynar, J. L.; Yoshida, M.; Lee, E.; Lee, M.; Okuro, K.; Kinbara, K.; Aida, T., *Nature* **2010,** *463* (7279), 339-343.
323. Srinivasulu, G.; Sridhar, B.; Ravi Kumar, K.; Sreedhar, B.; Ramesh, V.; Srinivas, R.; Kunwar, A. C., *J. Mol. Struct.* **2011,** *1006* (1–3), 180-184.
324. Kalyanasundaram, K.; Thomas, J. K., *J. Am. Chem. Soc.* **1977,** *99* (7), 2039-2044.
325. Aliprandi, A.; Mauro, M.; De Cola, L., *Nat. Chem.* **2016,** *8* (1), 10-15.
326. Canchi, D. R.; Paschek, D.; García, A. E., *J. Am. Chem. Soc.* **2010,** *132* (7), 2338-2344.
327. O'Brien, E. P.; Dima, R. I.; Brooks, B.; Thirumalai, D., *J. Am. Chem. Soc.* **2007,** *129* (23), 7346-7353.
328. Rajdev, P.; Molla, M. R.; Ghosh, S., *Langmuir* **2014,** *30* (8), 1969-1976.

329. Das, A.; Ghosh, S., *Chem. Commun.* **2016,** *52* (42), 6860-6872.
330. Jung, S. H.; Kwon, K.-Y.; Jung, J. H., *Chem. Commun.* **2015,** *51* (5), 952-955.
331. Park, J.-U.; Lee, H. J.; Cho, W.; Jo, C.; Oh, M., *Adv. Mater.* **2011,** *23* (28), 3161-3164.
332. Volkert, C. A.; Minor, A. M., *MRS Bull.* **2007,** *32* (5), 389-399.
333. Socrates, G., *Infrared and Raman Characteristic Group Frequencies: Tables and Charts*. Wiley: 2004.
334. Dietzel, D.; Mönninghoff, T.; Jansen, L.; Fuchs, H.; Ritter, C.; Schwarz, U. D.; Schirmeisen, A., *J. Appl. Phys.* **2007,** *102* (8), 084306.
335. Xu, K.; Kalantari, A.; Qian, X., *IEEE Transactions on Nanotechnology* **2012,** *11* (4), 666-675.
336. Josep, C.-F.; Eugenio, C.; Alicia, F.-A.; Elena, P.-C., *Nanotechnology* **2014,** *25* (39), 395703.
337. Bhowmik, S.; Gorai, T.; Maitra, U., *J. Mater. Chem. C* **2014,** *2* (9), 1597-1600.
338. Draper, E. R.; Adams, D. J., *Nat. Chem.* **2016,** *8* (8), 737-738.
339. Onogi, S.; Shigemitsu, H.; Yoshii, T.; Tanida, T.; Ikeda, M.; Kubota, R.; Hamachi, I., *Nat. Chem.* **2016,** *8* (8), 743-752.
340. Boekhoven, J.; Brizard, A. M.; Stuart, M. C. A.; Florusse, L.; Raffy, G.; Del Guerzo, A.; van Esch, J. H., *Chem. Sci.* **2016,** *7* (9), 6021-6031.
341. Grigoryan, G.; Keating, A. E., *Current Opinion in Structural Biology* **2008,** *18* (4), 477-483.
342. Woolfson, D. N., The Design of Coiled-Coil Structures and Assemblies. In *Adv. Protein Chem.*, Academic Press: 2005; Vol. Volume 70, pp 79-112.
343. Liu, J.; Zheng, Q.; Deng, Y.; Li, Q.; Kallenbach, N. R.; Lu, M., *Biochemistry* **2007,** *46* (51), 14951-14959.
344. Liu, J.; Zheng, Q.; Deng, Y.; Kallenbach, N. R.; Lu, M., *J. Mol. Biol.* **2006,** *361* (1), 168-179.
345. Liu, J.; Zheng, Q.; Deng, Y.; Cheng, C.-S.; Kallenbach, N. R.; Lu, M., *Proc. Nat. Acad. Sci.* **2006,** *103* (42), 15457-15462.
346. Murphy, D. B.; Davidson, M. W., *Fundamentals of Light Microscopy and Electronic Imaging*. Wiley: 2012.
347. Valeur, B.; Berberan-Santos, M. N., *Molecular Fluorescence: Principles and Applications*. Wiley: 2013.
348. Marriott, G.; Clegg, R. M.; Arndt-Jovin, D. J.; Jovin, T. M., *Biophys. J.* **1991,** *60* (6), 1374-1387.
349. Beeby, A.; Botchway, S. W.; Clarkson, I. M.; Faulkner, S.; Parker, A. W.; Parker, D.; Williams, J. A. G., *J. Photochem. Photobiol. B; Biology* **2000,** *57* (2–3), 83-89.
350. Robert, P.; Andrew, B., *Methods and Applications in Fluorescence* **2014,** *2* (3), 037001.
351. Surender, E. M.; Bradberry, S. J.; Bright, S. A.; McCoy, C. P.; Williams, D. C.; Gunnlaugsson, T., *J. Am. Chem. Soc.* **2017,** *139* (1), 381-388.
352. Butler, S. J.; Delbianco, M.; Lamarque, L.; McMahon, B. K.; Neil, E. R.; Pal, R.; Parker, D.; Walton, J. W.; Zwier, J. M., *Dalton Trans.* **2015,** *44* (11), 4791-4803.
353. Butler, S. J.; Lamarque, L.; Pal, R.; Parker, D., *Chem. Sci.* **2014,** *5* (5), 1750-1756.
354. Kotova, O.; Comby, S.; Lincheneau, C.; Gunnlaugsson, T., *Chem. Sci.* **2017,** *8* (5), 3419-3426.
355. Chen, P.; Li, Q.; Grindy, S.; Holten-Andersen, N., *J. Am. Chem. Soc.* **2015,** *137* (36), 11590-11593.
356. Li, Q.; Li, T.; Wu, J., *J. Phys. Chem. B* **2001,** *105* (49), 12293-12296.
357. Faulkner, S.; Pope, S. J. A., *J. Am. Chem. Soc.* **2003,** *125* (35), 10526-10527.
358. Romanova, K. A.; Freidzon, A. Y.; Bagaturyants, A. A.; Galyametdinov, Y. G., *J. Phys. Chem. A* **2014,** *118* (47), 11244-11252.
359. de Lill, D. T.; de Bettencourt-Dias, A.; Cahill, C. L., *Inorg. Chem.* **2007,** *46* (10), 3960-3965.
360. Carr, R.; Evans, N. H.; Parker, D., *Chem. Soc. Rev.* **2012,** *41* (23), 7673-7686.
361. Nguyen, B. T.; Ingram, A. J.; Muller, G., *Chirality* **2016,** *28* (4), 325-331.

362. Riehl, J. P.; Richardson, F. S., *Chem. Rev.* **1986,** *86* (1), 1-16.
363. Crassous, J., *Chem. Soc. Rev.* **2009,** *38* (3), 830-845.
364. Jennings, L.; Waters, R. S.; Pal, R.; Parker, D., *ChemMedChem* **2017,** *12* (3), 271-277.
365. Han, J.; You, J.; Li, X.; Duan, P.; Liu, M., *Adv. Mater.* **2017,** *29*, 1606503.
366. Lunkley, J. L.; Shirotani, D.; Yamanari, K.; Kaizaki, S.; Muller, G., *Inorg. Chem.* **2011,** *50* (24), 12724-12732.
367. Muller, G.; Riehl, J. P., *Journal of Fluorescence* **2005,** *15* (4), 553-558.
368. Zinna, F.; Di Bari, L., *Chirality* **2015,** *27* (1), 1-13.
369. Kotova, O.; Kitchen, J. A.; Lincheneau, C.; Peacock, R. D.; Gunnlaugsson, T., *Chem. Eur. J.* **2013,** *19* (48), 16181-16186.
370. Muller, G., *Dalton Trans.* **2009,** (44), 9692-9707.
371. Barry, D. E., *Lanthanide-directed self-assembly formation from novel dipicolinic acid derivatives. Ph.D. Thesis, University of Dublin, Trinity College, Dublin* **2014**.
372. Byrne, J. P.; Martínez-Calvo, M.; Peacock, R. D.; Gunnlaugsson, T., *Chem. Eur. J.* **2016,** *22* (2), 486-490.
373. Binnemans, K., *Coord. Chem. Rev.* **2015,** *295*, 1-45.
374. Vogel, A. I.; Furniss, B. S., *Vogel's Textbook of Practical Organic Chemistry*. Longman Scientific & Technical: 1989.
375. Schwarz, U. D.; Köster, P.; Wiesendanger, R., *Rev. Sci. Instrum.* **1996,** *67* (7), 2560-2567.

Appendix

Appendix 2

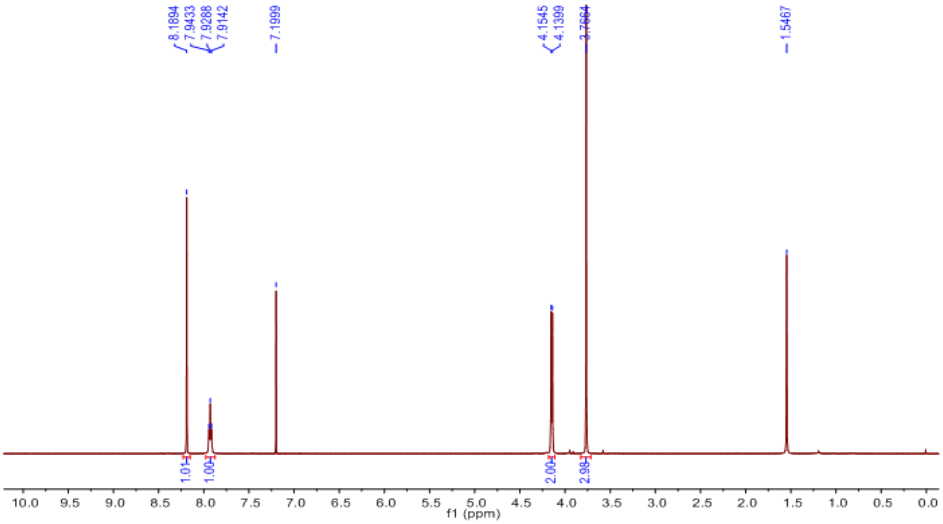

Figure A2.1.1: ^{1}H NMR (400 MHz, $CDCl_3$) spectrum of compound **100.**

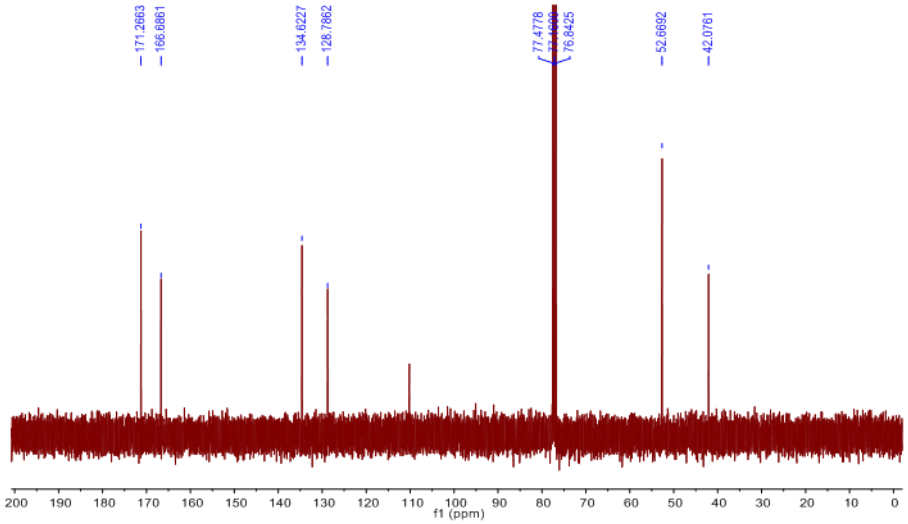

Figure A2.1.2: ^{13}C NMR (400 MHz, $CDCl_3$) spectrum of compound **100.**

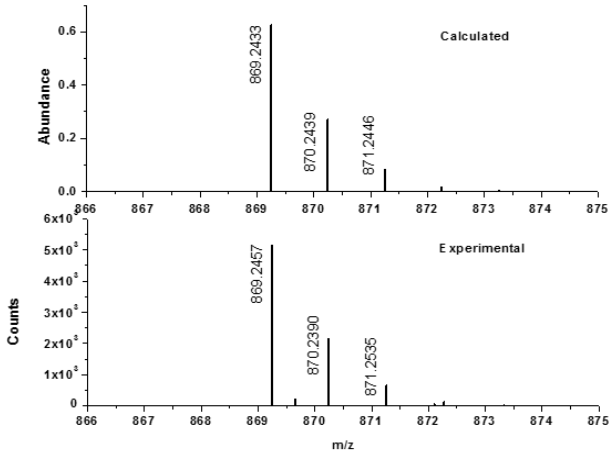

Figure A2.1.3: Calculate and experimental isotopic distribution patterns (MS ESI^{+}) for dimerised **100**.

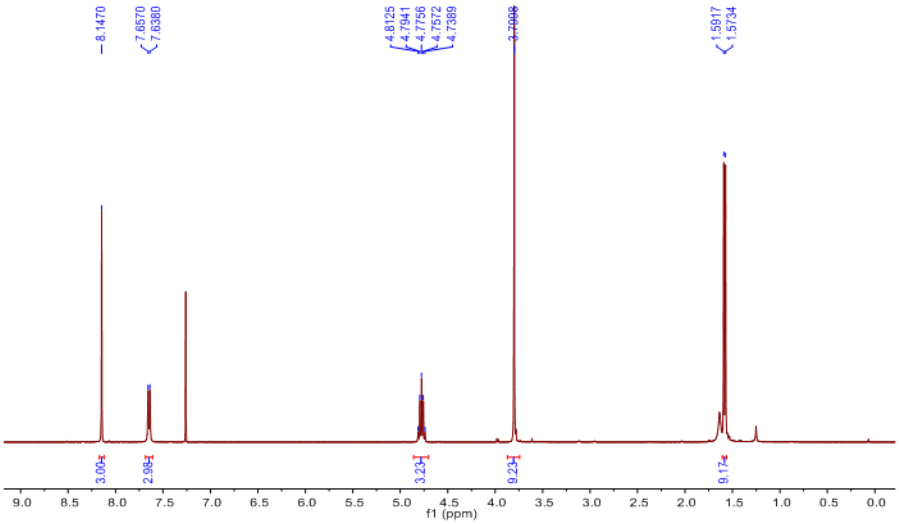

Figure A2.2.1: ^{1}H NMR (400 MHz, $CDCl_3$) spectrum of compound **101R.**

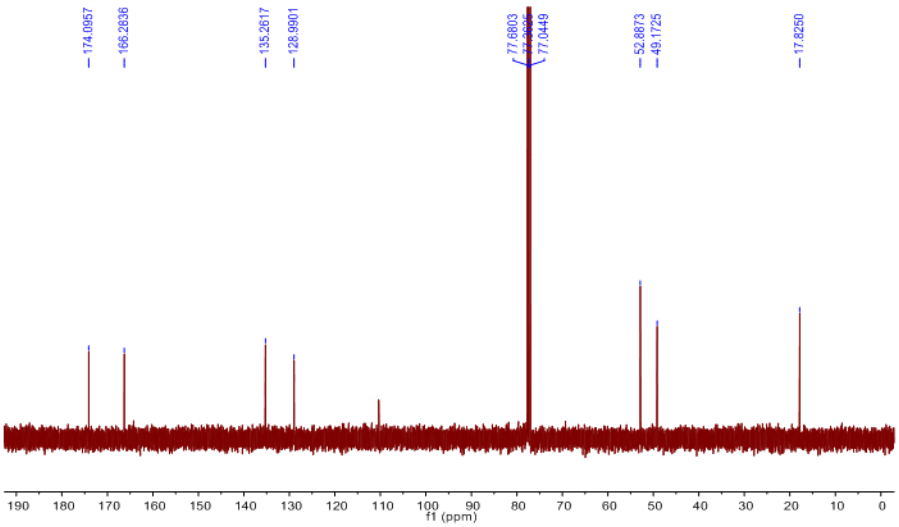

Figure A2.2.2: ^{13}C NMR (400 MHz, $CDCl_3$) spectrum of compound **101R**.

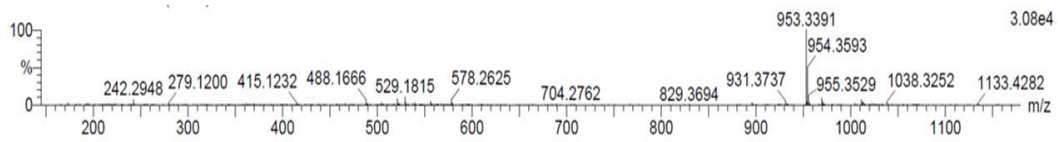

Minimum:				-1.5		
Maximum:		200.0	10.0	100.0		
Mass	Calc. Mass	mDa	PPM	DBE	Score	Formula
953.3391	953.3392	-0.1	-0.1	18.5	1	C42 H54 N6 O18 Na

Figure A2.1.3: Mass Spectrum MALDI **101R**, showing the dimerised molecule peak at 953.3391 [M_2.Na].

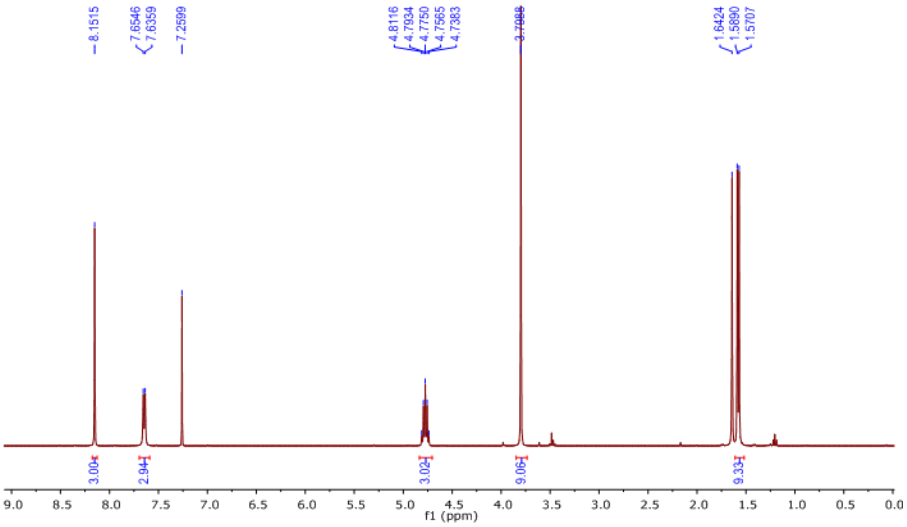

Figure A2.3.1: ^{1}H NMR (400 MHz, $CDCl_3$) spectrum of compound **101S.**

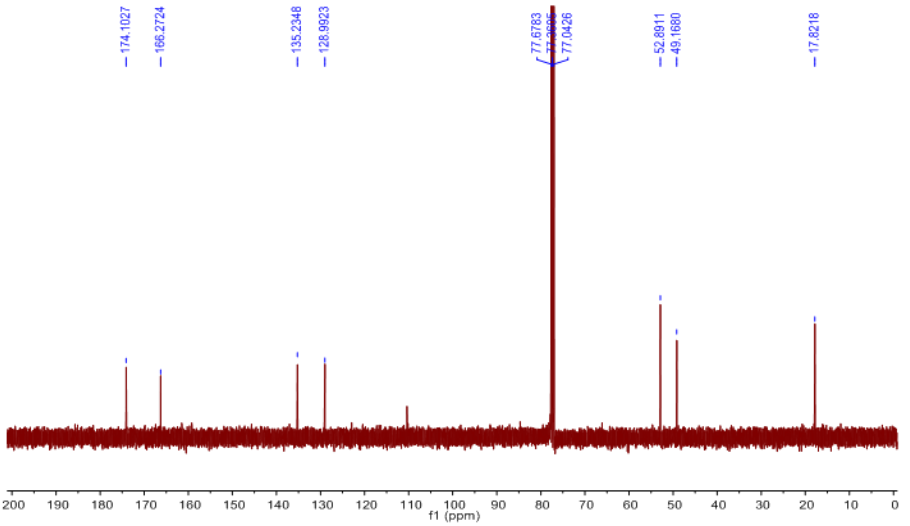

Figure A2.3.2: ^{13}C NMR (400 MHz, $CDCl_3$) spectrum of compound **101S.**

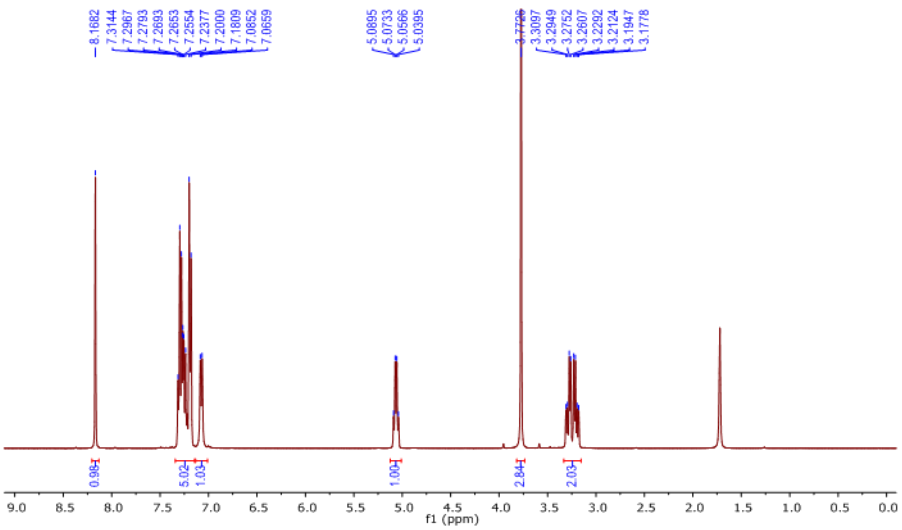

Figure A2.4.1: ^{1}H NMR (400 MHz, $CDCl_3$) spectrum of compound **102R.**

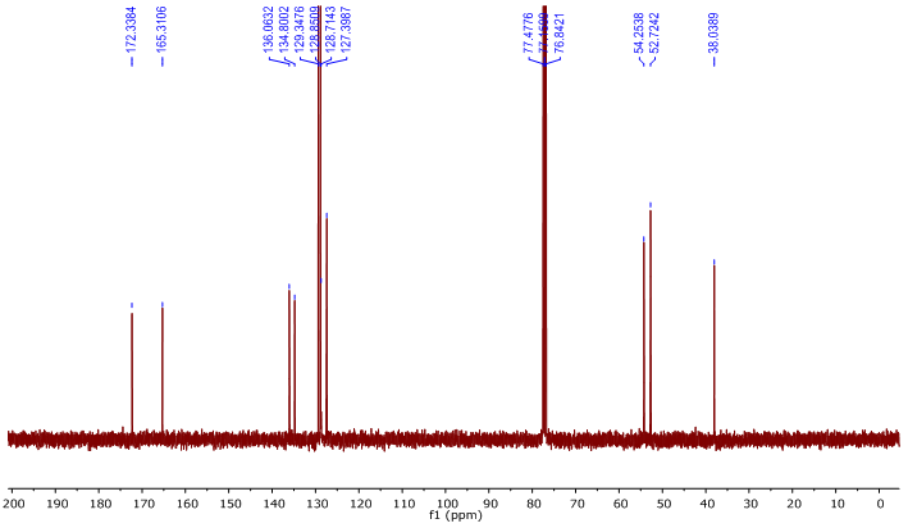

Figure A2.4.2: ^{13}C NMR (400 MHz, $CDCl_3$) spectrum of compound **102R.**

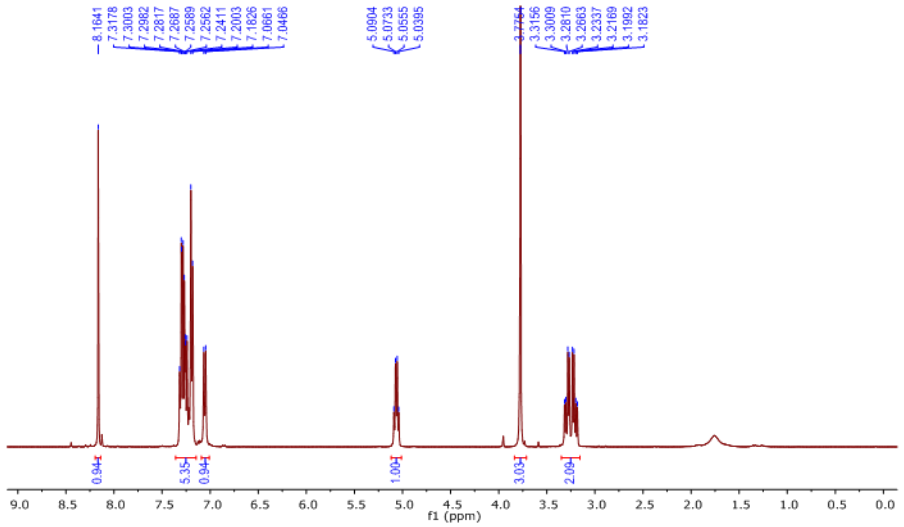

Figure A2.5.1: ^{1}H NMR (400 MHz, $CDCl_3$) spectrum of compound **102S.**

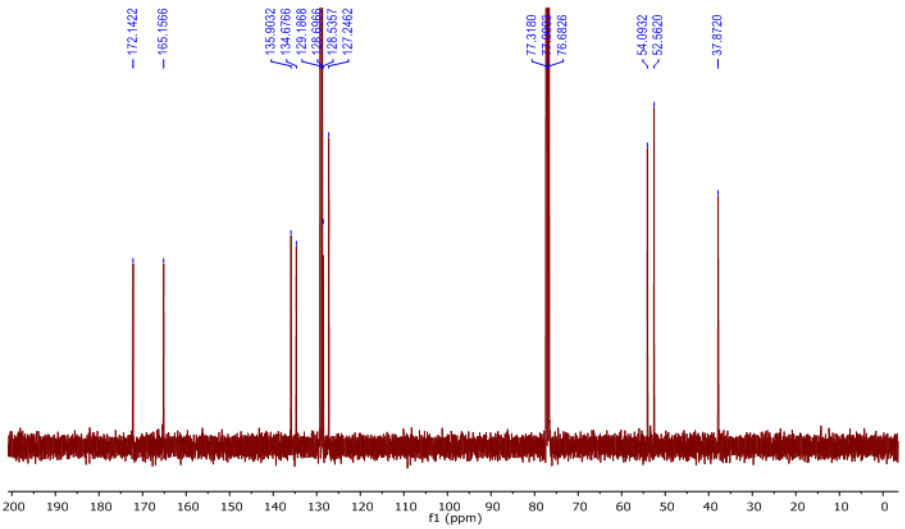

Figure A2.5.2: ^{13}C NMR (400 MHz, $CDCl_3$) spectrum of compound **102S.**

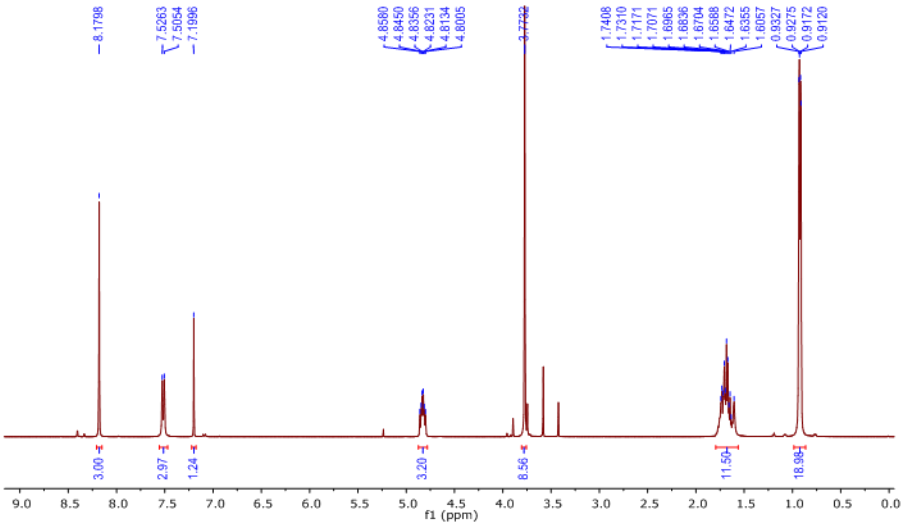

Figure A2.6.1: ^{1}H NMR (400 MHz, $CDCl_3$) spectrum of compound **103R.**

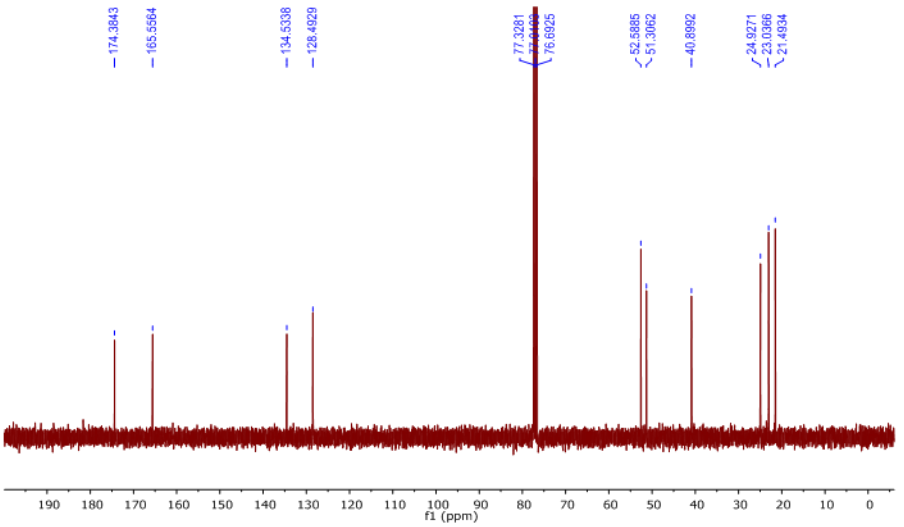

Figure A2.6.2: ^{13}C NMR (400 MHz, $CDCl_3$) spectrum of compound **103R.**

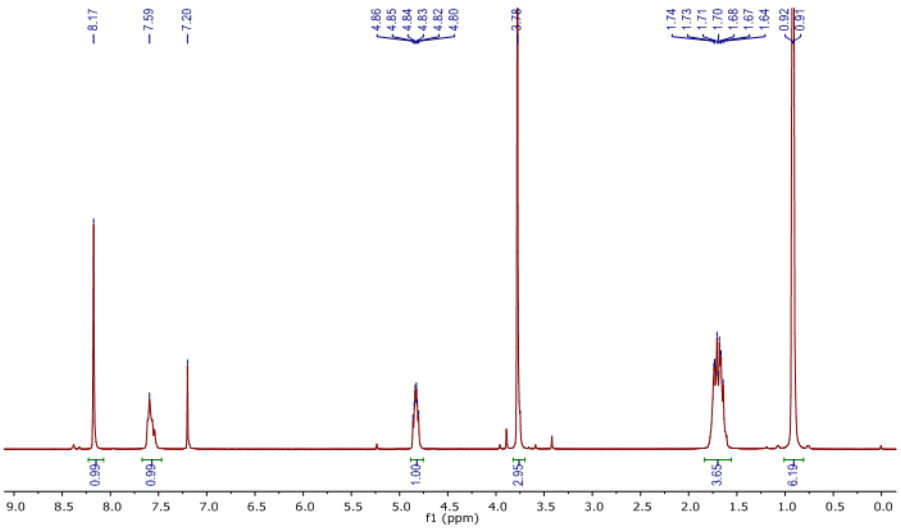

Figure A2.7.1: ^{1}H NMR (400 MHz, $CDCl_3$) spectrum of compound **103S.**

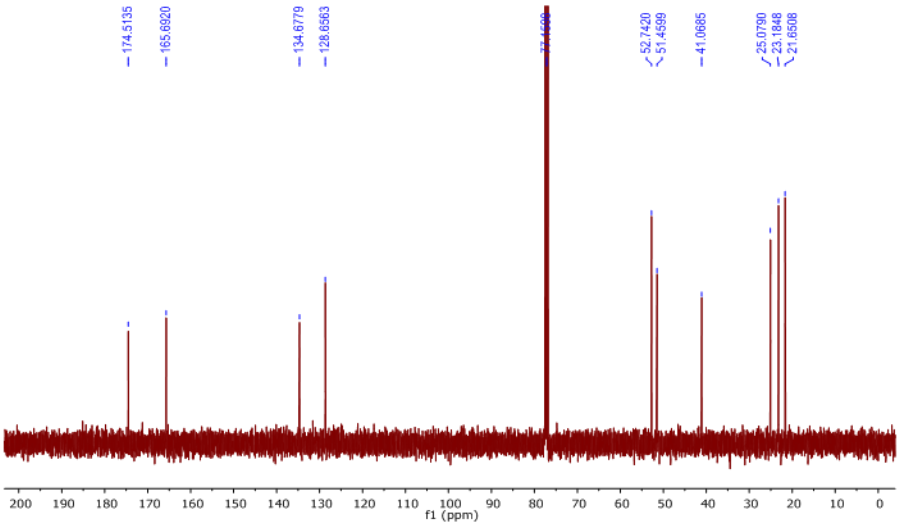

Figure A2.7.2: ^{13}C NMR (400 MHz, $CDCl_3$) spectrum of compound **103S.**

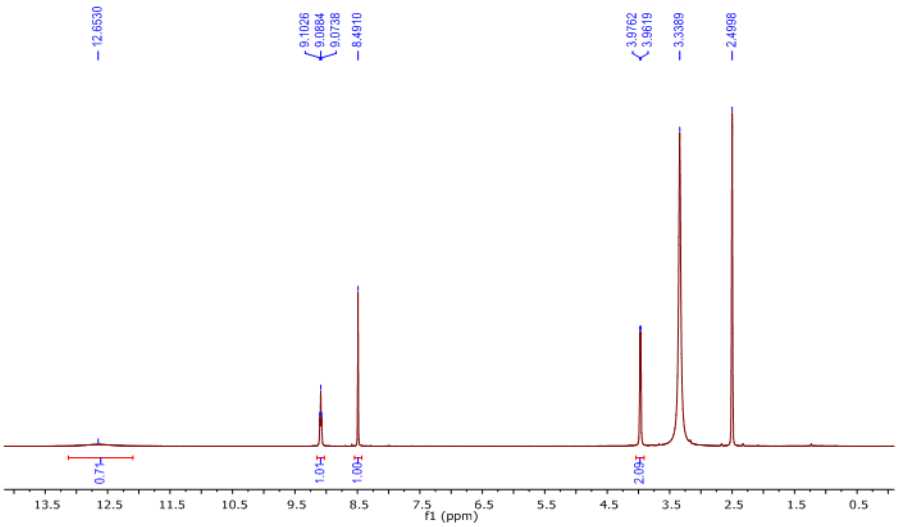

Figure A2.8.1: ^{1}H NMR (400 MHz, DMSO-d_6) spectrum of compound **104.**

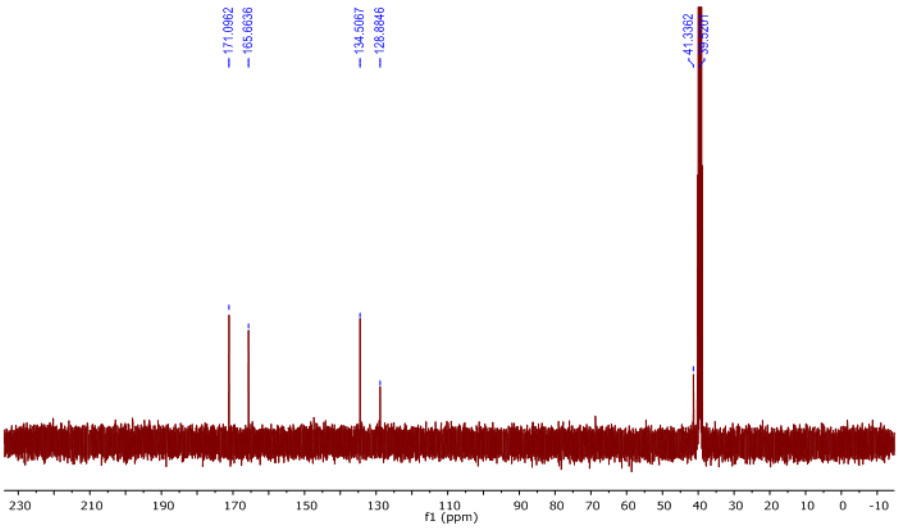

Figure A2.8.2: ^{13}C NMR (400 MHz, DMSO-d_6) spectrum of compound **104.**

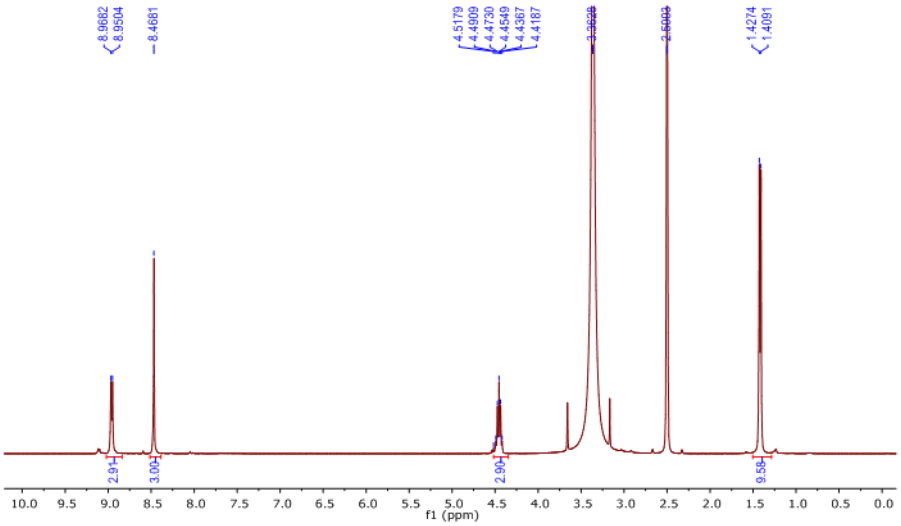

Figure A2.9.1: ^{1}H NMR (400 MHz, DMSO-d_6) spectrum of compound **105R.**

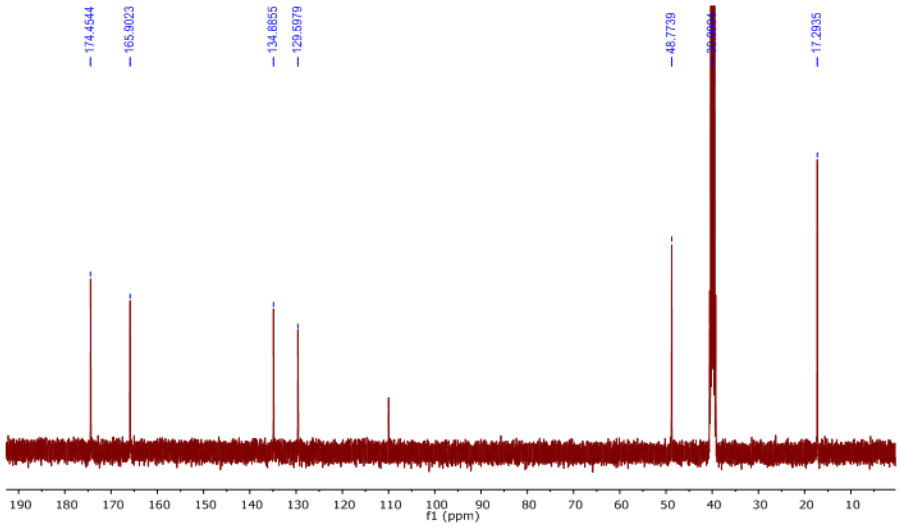

Figure A2.9.2: ^{13}C NMR (400 MHz, DMSO-d_6) spectrum of compound **105R.**

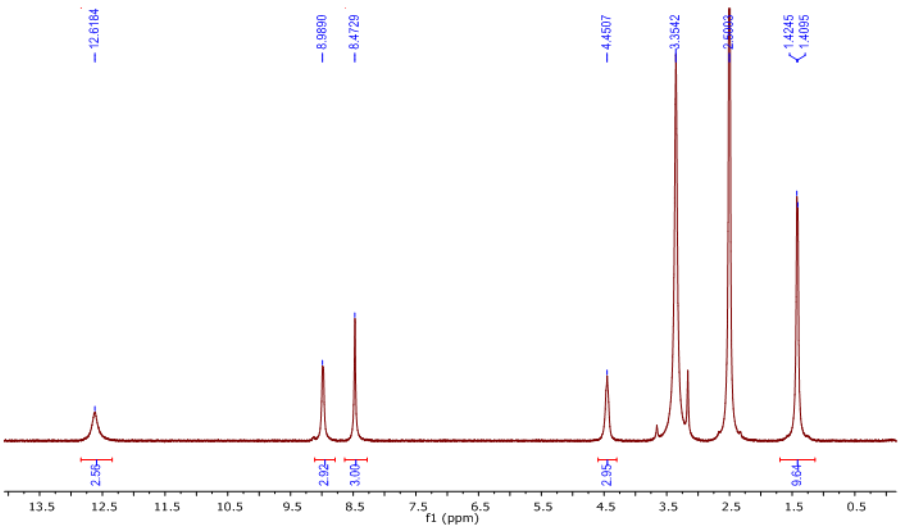

Figure A2.10.1: ^{1}H NMR (400 MHz, DMSO-d_6) spectrum of compound **105S.**

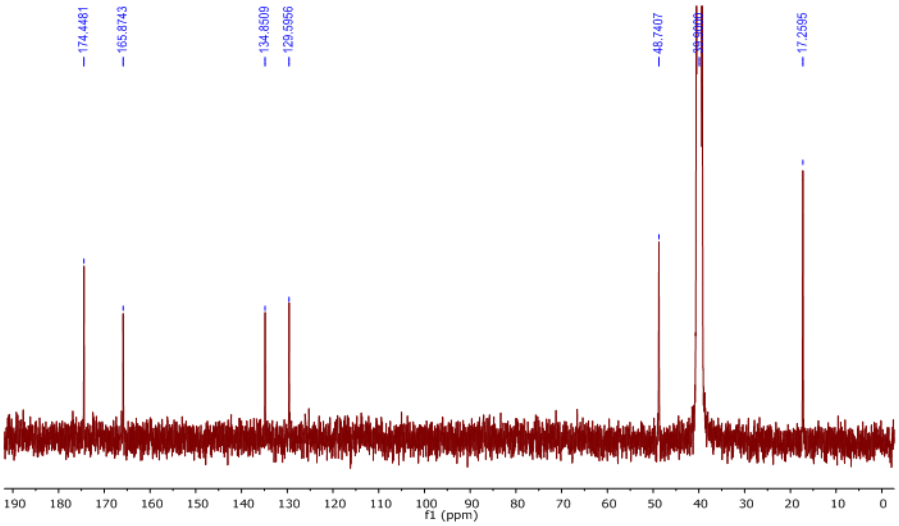

Figure A2.10.2: ^{13}C NMR (400 MHz, DMSO-d_6) spectrum of compound **105S.**

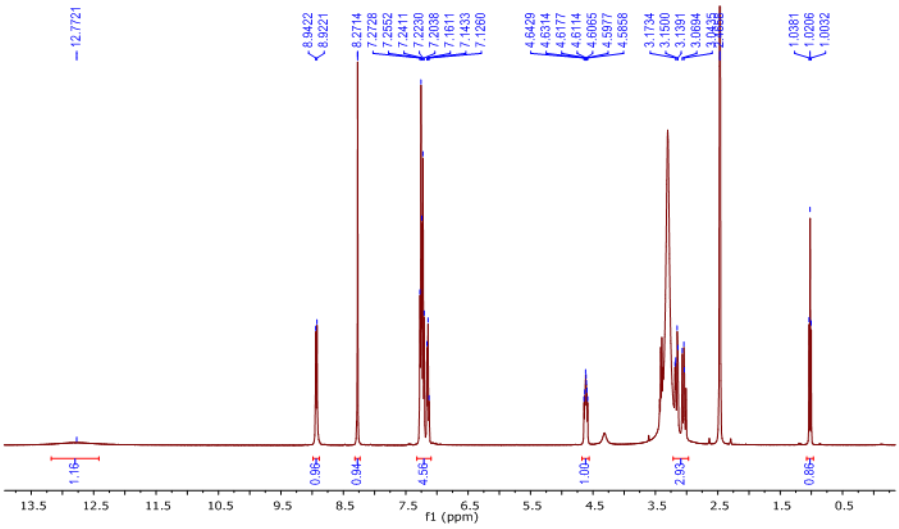

Figure A2.11.1: ^{1}H NMR (400 MHz, DMSO-d_6) spectrum of compound **106R.**

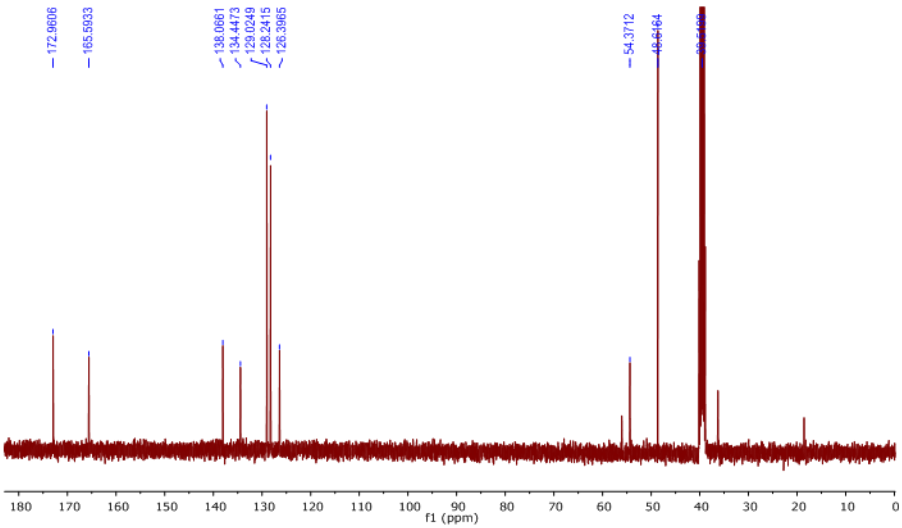

Figure A2.11.2: ^{13}C NMR (400 MHz, DMSO-d_6) spectrum of compound **106R.**

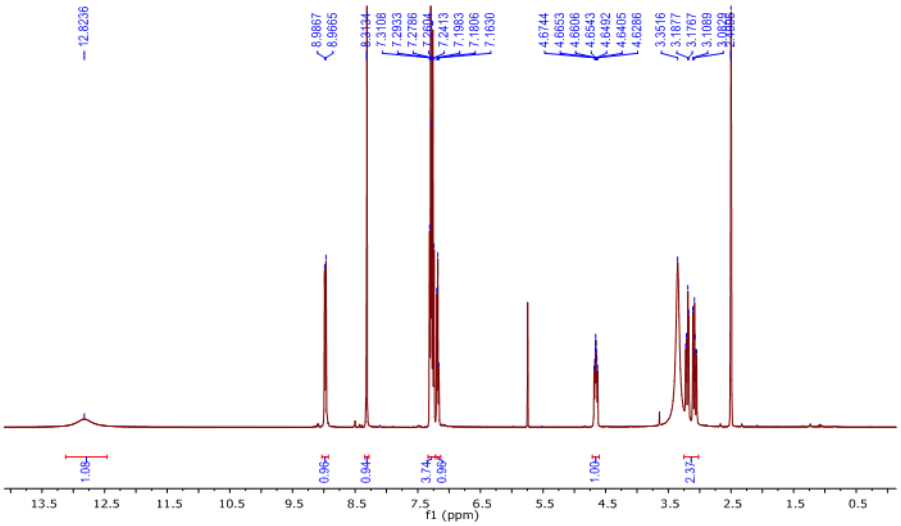

Figure A2.12.1: ^{1}H NMR (400 MHz, DMSO-d_6) spectrum of compound **106S.**

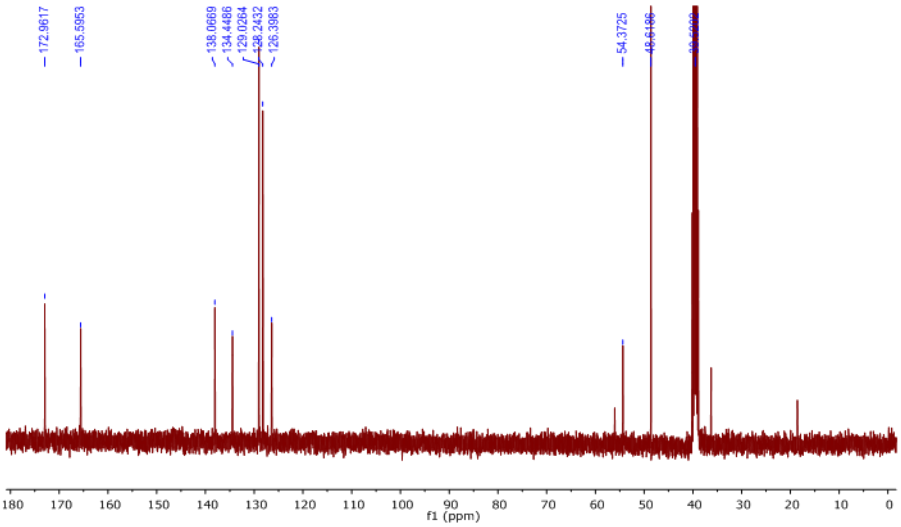

Figure A2.12.2: ^{13}C NMR (400 MHz, DMSO-d_6) spectrum of compound **106S.**

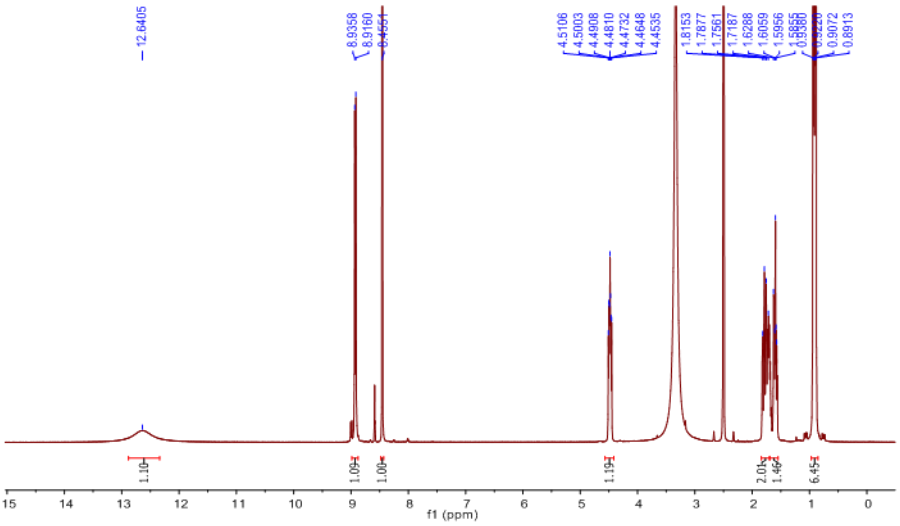

Figure A2.13.1: ^{1}H NMR (400 MHz, DMSO-d_6) spectrum of compound **107R.**

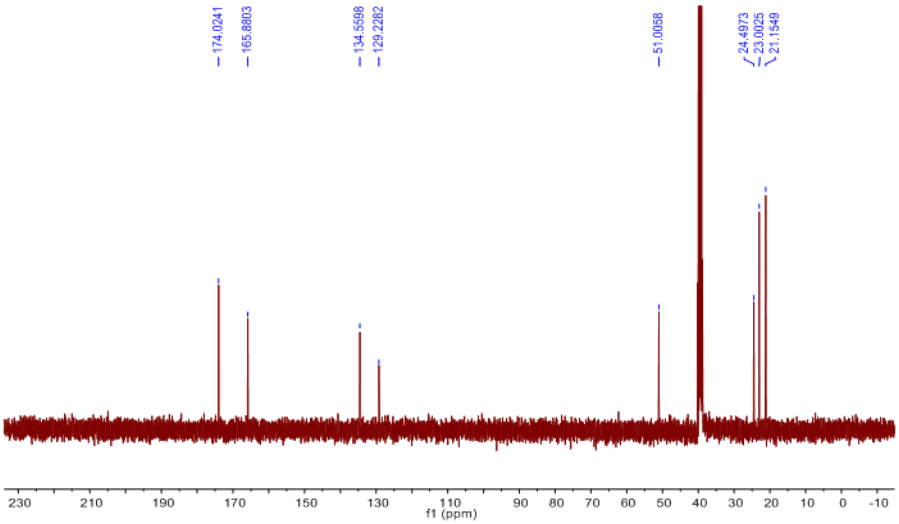

Figure A2.13.2: ^{13}C NMR (400 MHz, DMSO-d_6) spectrum of compound **107R.**

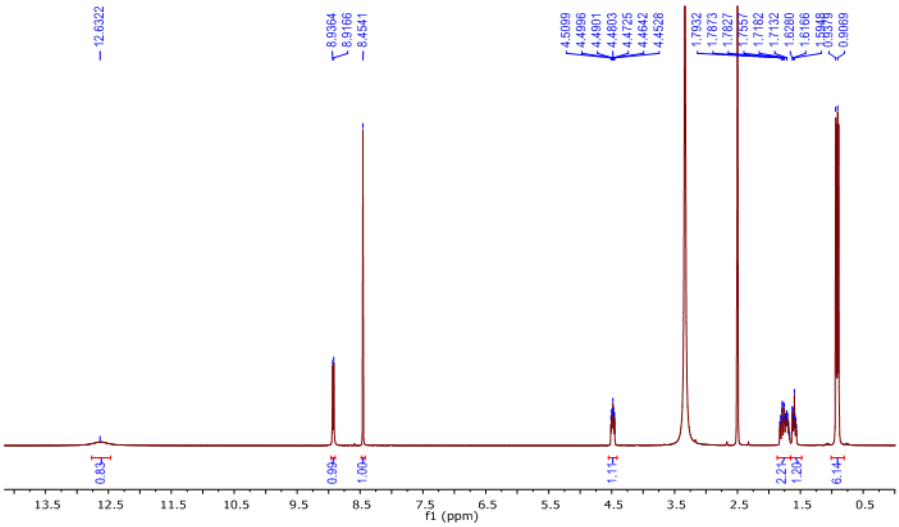

Figure A2.14.1: ^{1}H NMR (400 MHz, DMSO-d_6) spectrum of compound **107S.**

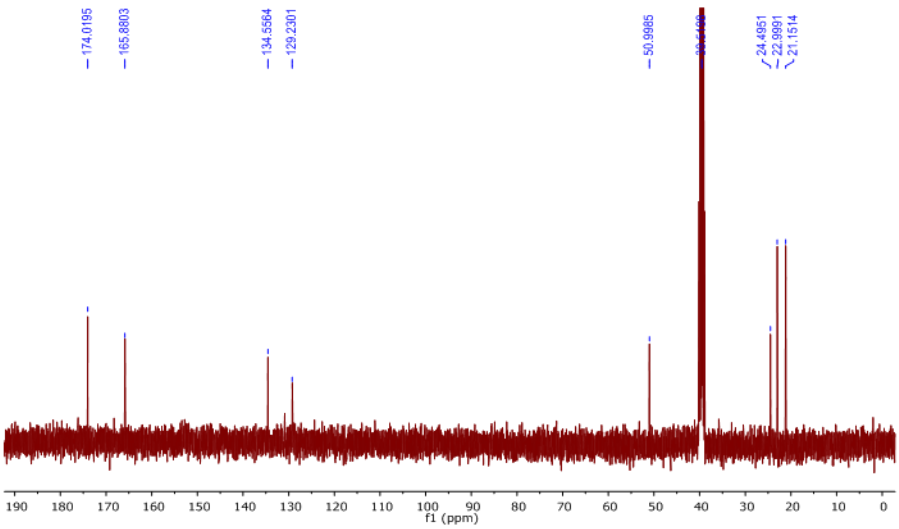

Figure A2.14.2: ^{13}C NMR (400 MHz, DMSO-d_6) spectrum of compound **107S.**

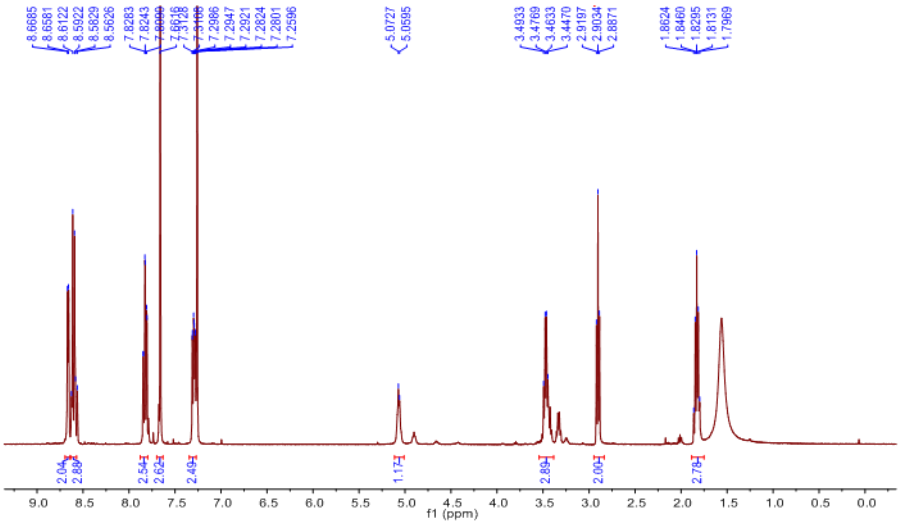

Figure A2.15.1: ^{1}H NMR (400 MHz, DMSO-d_6) spectrum of compound **108.**

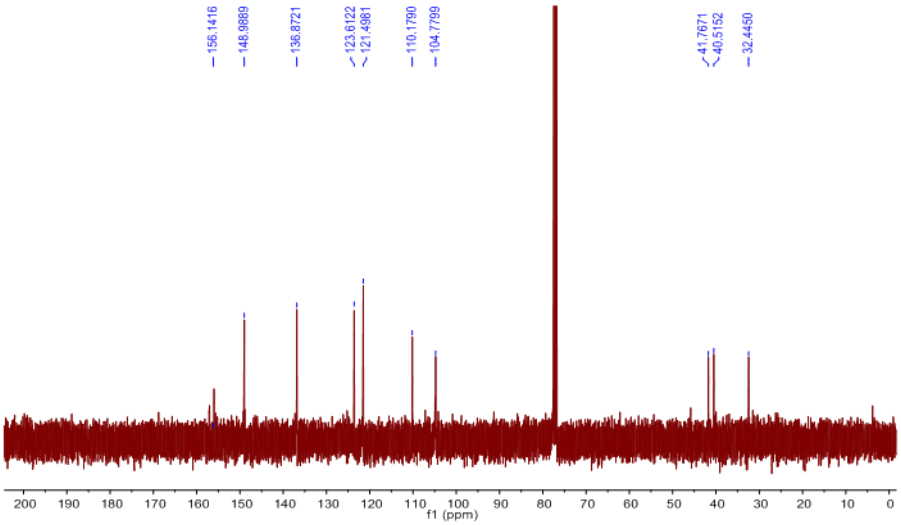

Figure A2.15.2: ^{13}C NMR (400 MHz, DMSO-d_6) spectrum of compound **108.**

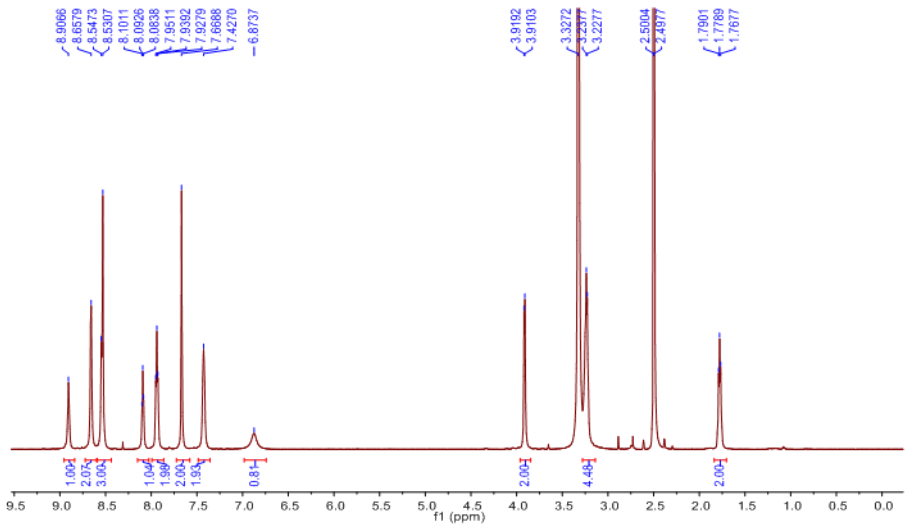

Figure A2.16.1: ^{1}H NMR (400 MHz, DMSO-d_6) spectrum of compound **88.**

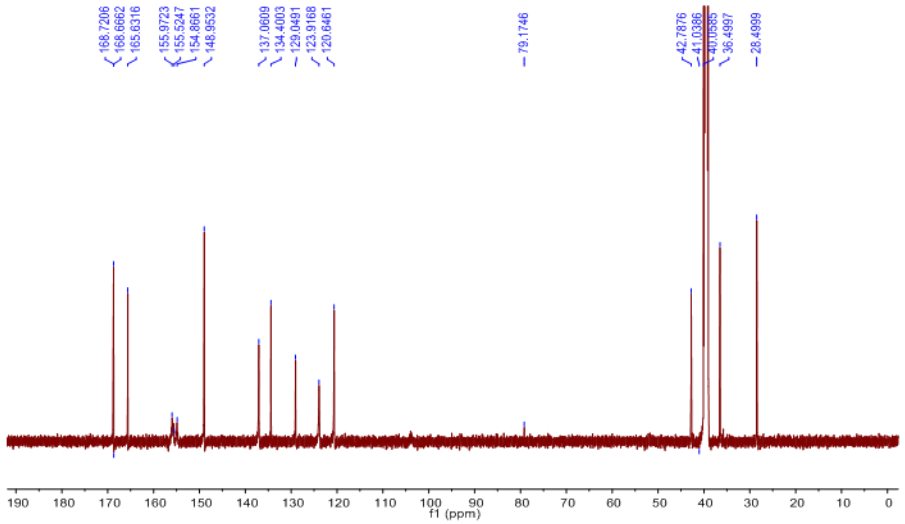

Figure A2.16.2: ^{13}C NMR (400 MHz, DMSO-d_6) spectrum of compound **88.**

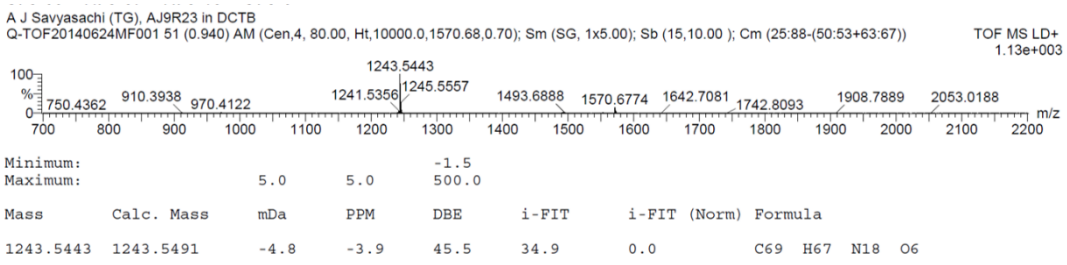

Figure A2.16.3: Mass Spectrum MALDI **88.**

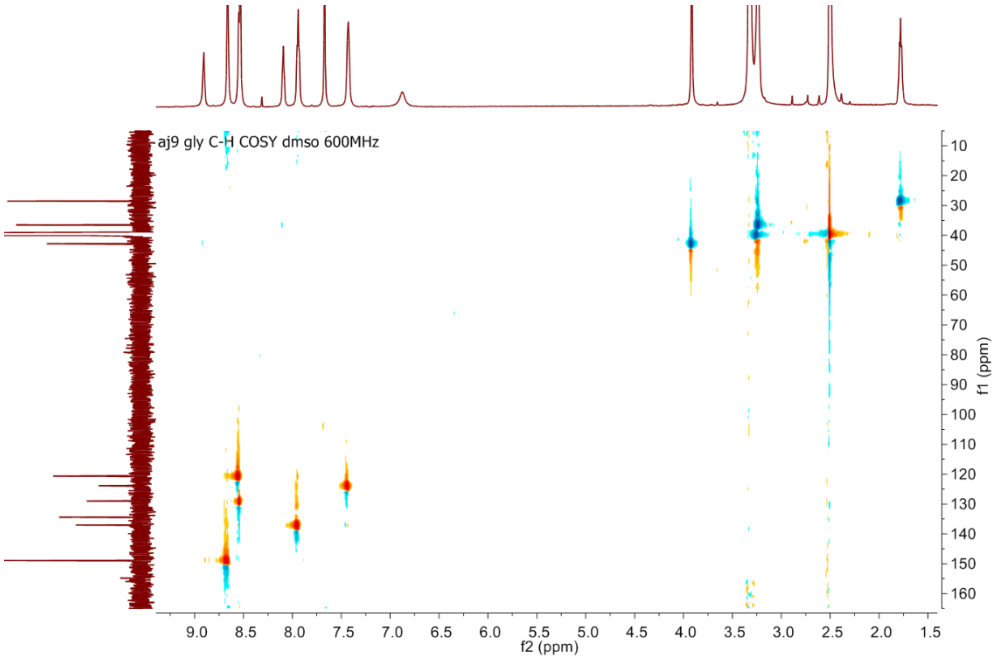

Figure A2.16.5: C-H COSY NMR (600 MHz, DMSO-d_6) spectrum of compound **88.**

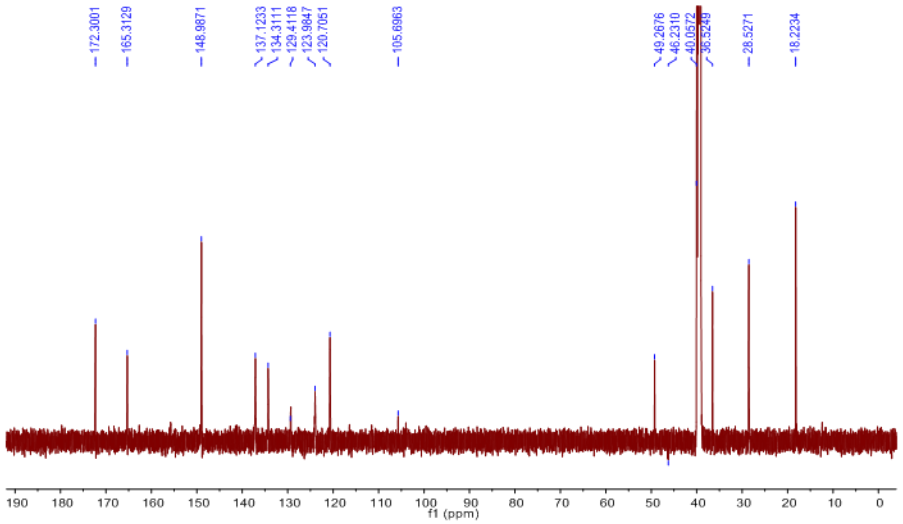

Figure A2.17.1: ^{13}C NMR (400 MHz, DMSO-d_6) spectrum of compound **89R.**

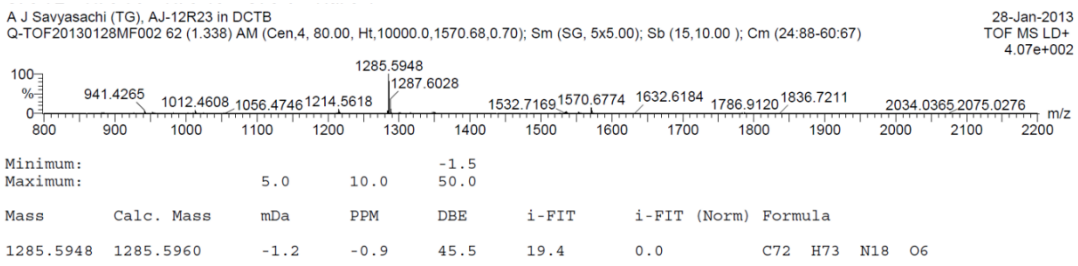

Figure A2.17.2: Mass Spectrum MALDI of **89R.**

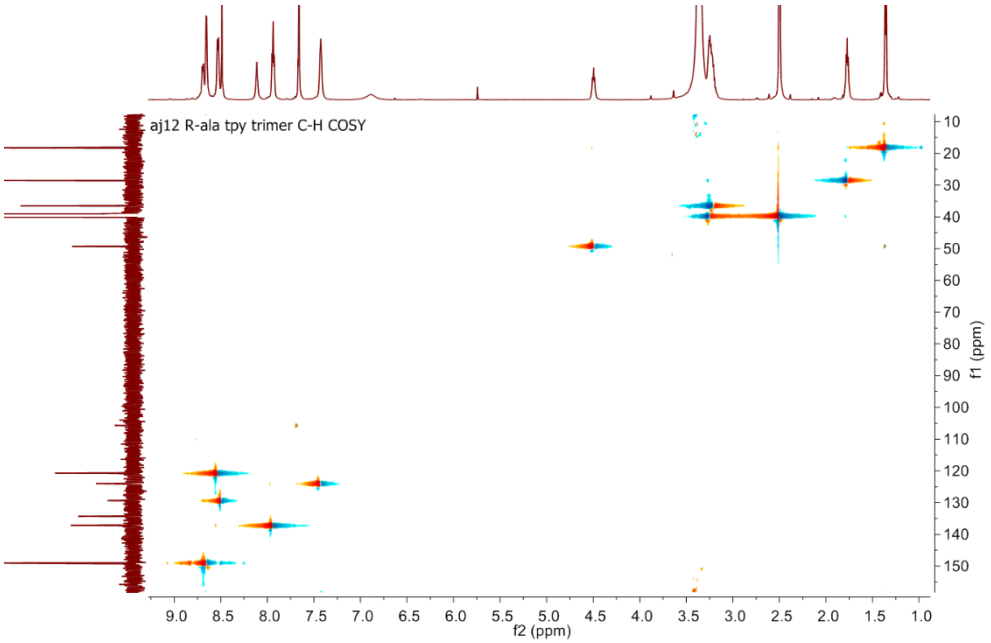

Figure A2.17.3: C-H COSY NMR (600 MHz, DMSO-d_6) spectrum of compound **89R.**

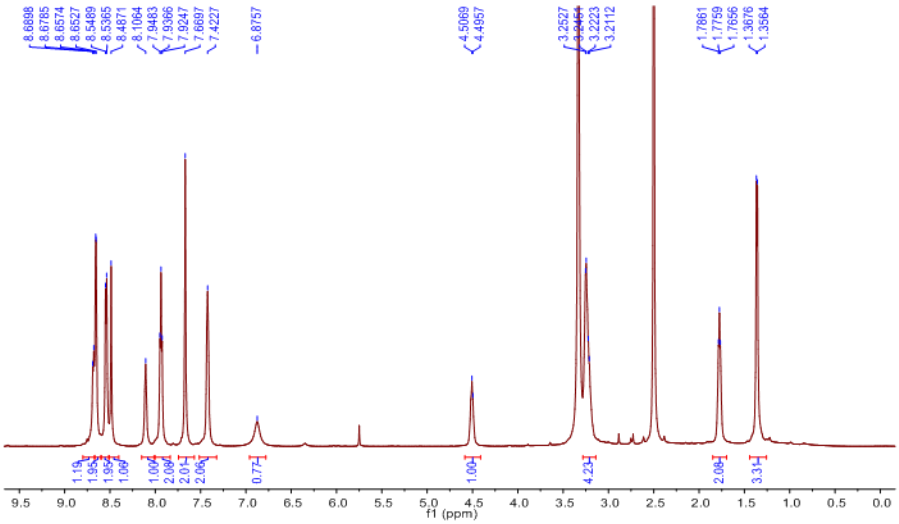

Figure A2.18.1: ^{1}H NMR (400 MHz, DMSO-d_6) spectrum of compound **89S.**

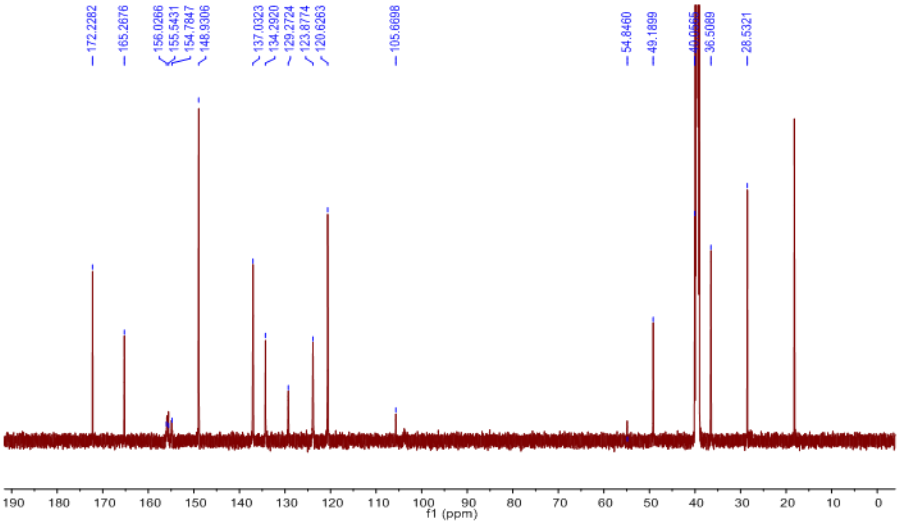

Figure A2.18.2: ^{13}C NMR (400 MHz, DMSO-d_6) spectrum of compound **89S.**

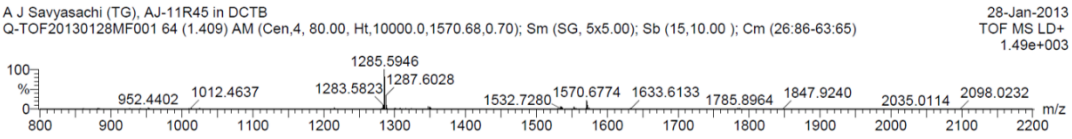

Minimum:				-1.5			
Maximum:		5.0	10.0	50.0			
Mass	Calc. Mass	mDa	PPM	DBE	i-FIT	i-FIT (Norm)	Formula
1285.5946	1285.5960	-1.4	-1.1	45.5	33.0	0.0	C72 H73 N18 O6

Figure A2.18.3: Mass Spectrum MALDI **89S**

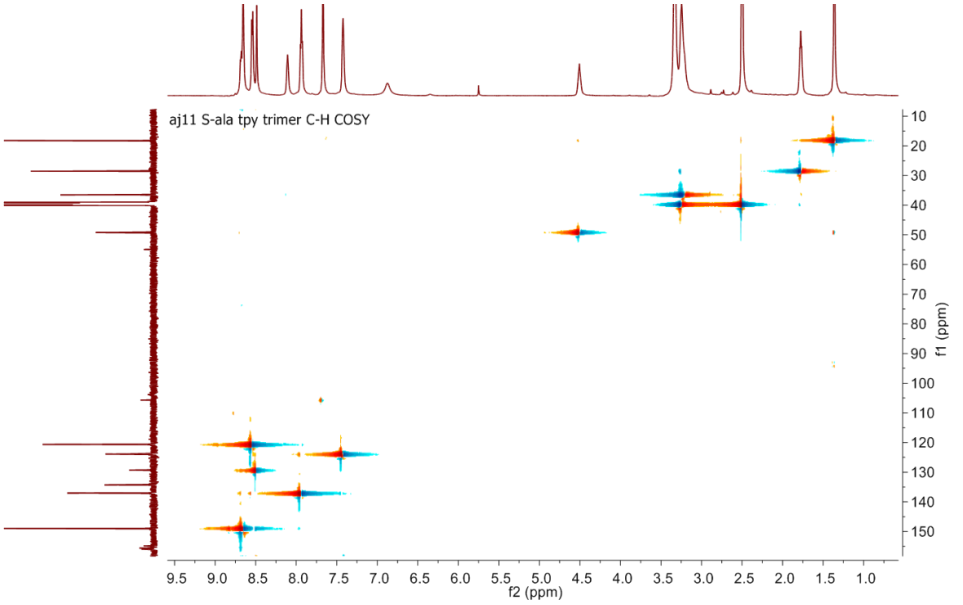

Figure A2.18.5: C-H COSY NMR (600 MHz, DMSO-d_6) spectrum of compound **89S.**

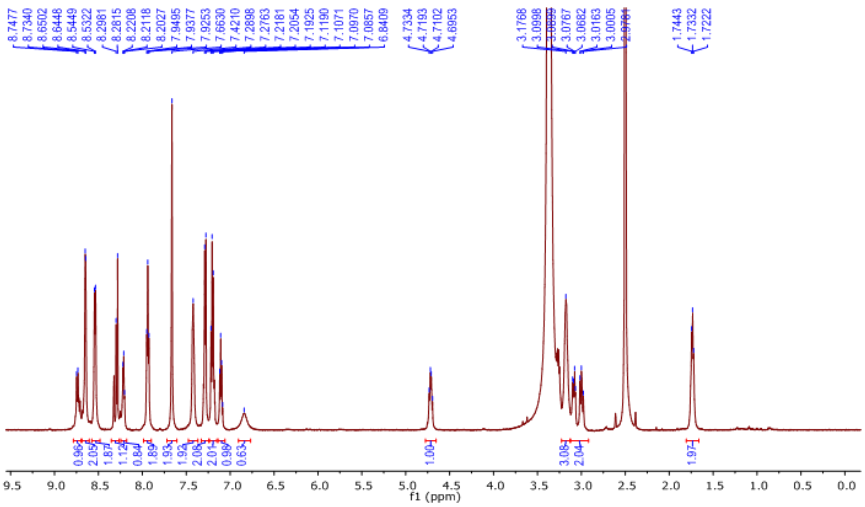

Figure A2.19.1: ^{1}H NMR (400 MHz, DMSO-d_6) spectrum of compound **90R.**

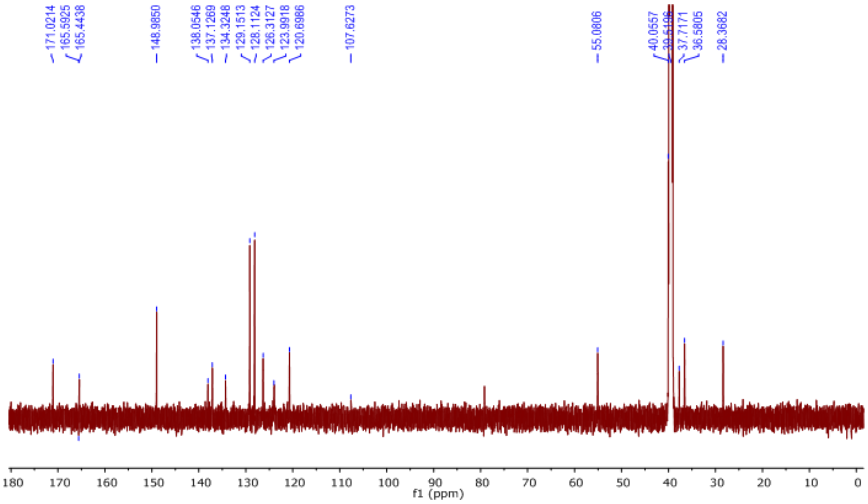

Figure A2.19.2: ^{13}C NMR (400 MHz, DMSO-d_6) spectrum of compound **90R.**

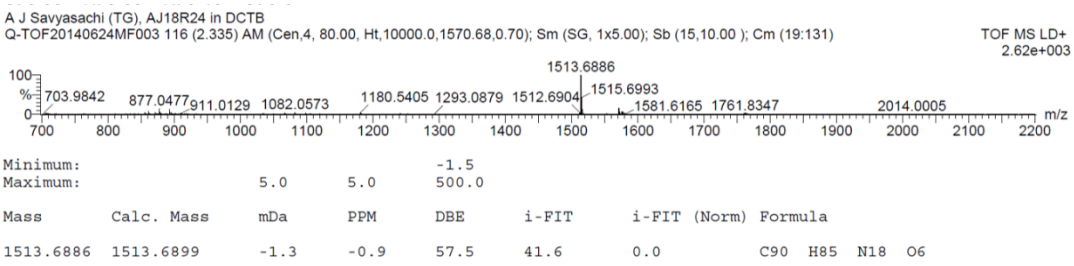

Figure A2.19.3: Mass Spectrum MALDI of **90R.**

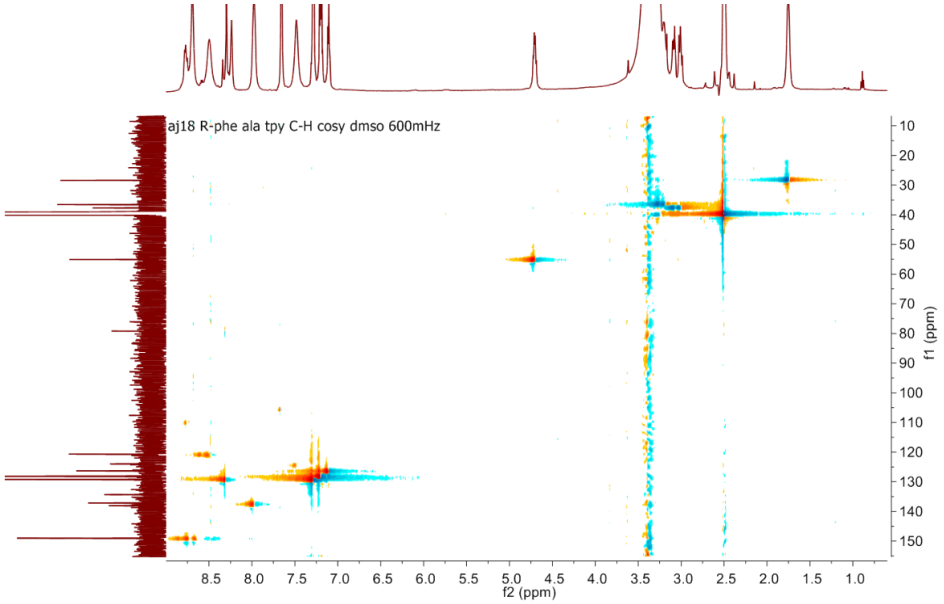

Figure A2.19.5: C-H COSY NMR (600 MHz, DMSO-d_6) spectrum of compound **90R.**

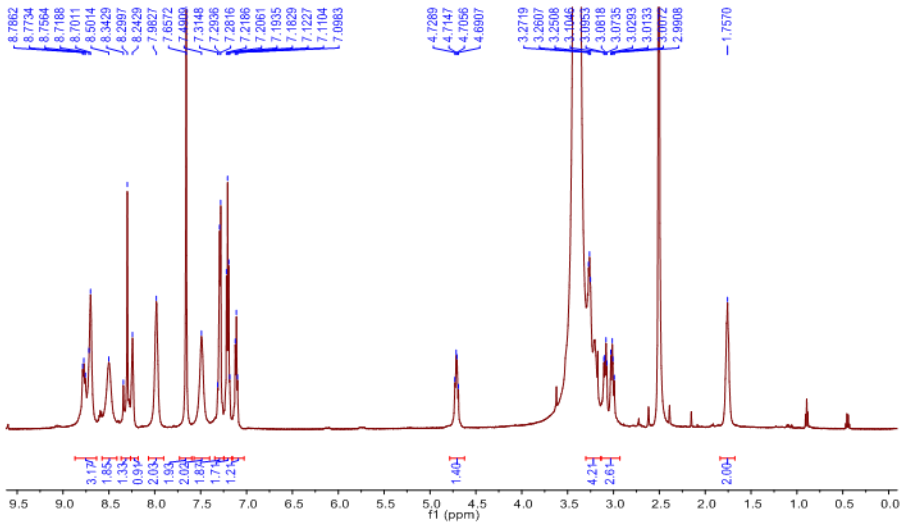

Figure A2.20.1: ^{1}H NMR (400 MHz, DMSO-d_6) spectrum of compound **90S.**

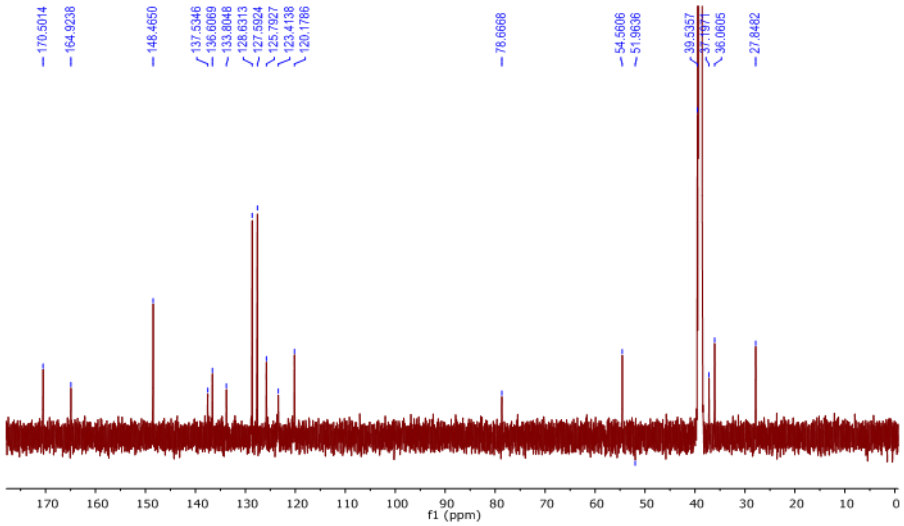

Figure A2.20.2: ^{13}C NMR (400 MHz, DMSO-d_6) spectrum of compound **90S.**

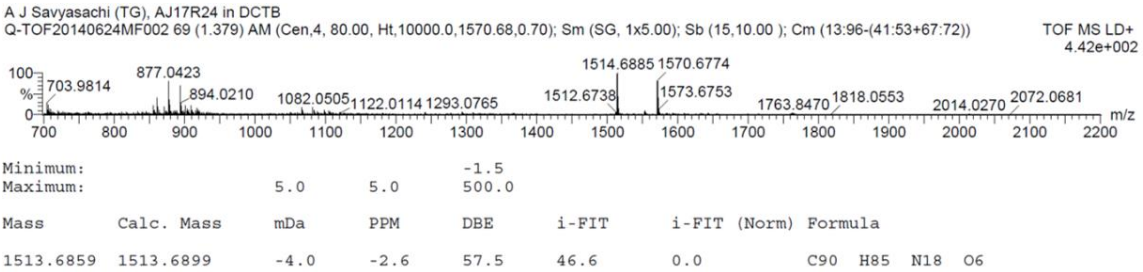

Minimum:				-1.5			
Maximum:		5.0	5.0	500.0			
Mass	Calc. Mass	mDa	PPM	DBE	i-FIT	i-FIT (Norm)	Formula
1513.6859	1513.6899	-4.0	-2.6	57.5	46.6	0.0	C90 H85 N18 O6

Figure A2.20.3: Mass Spectrum MALDI of **90S.**

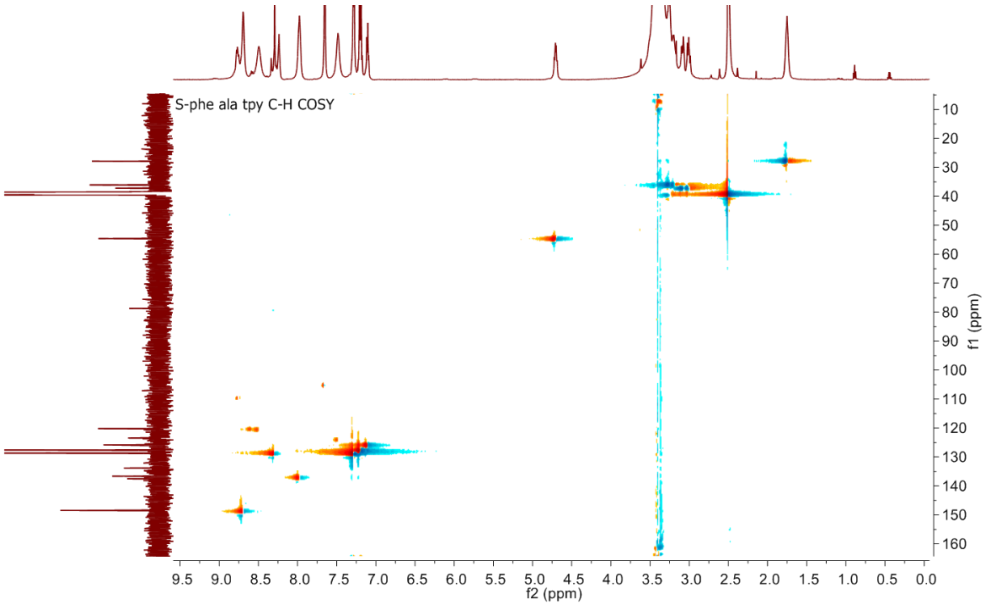

Figure A2.20.5: C-H COSY NMR (600 MHz, DMSO-d_6) spectrum of compound **90S.**

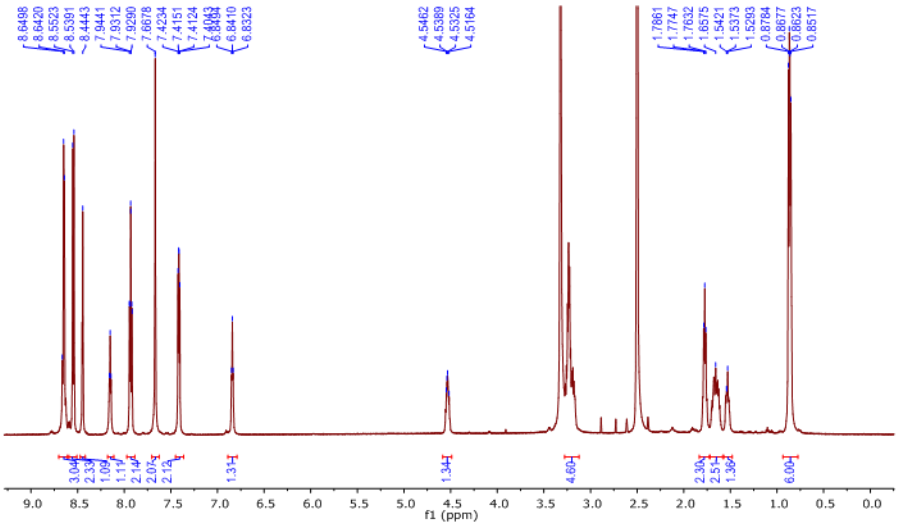

Figure A2.21.1: ^{1}H NMR (400 MHz, DMSO-d_6) spectrum of compound **91R.**

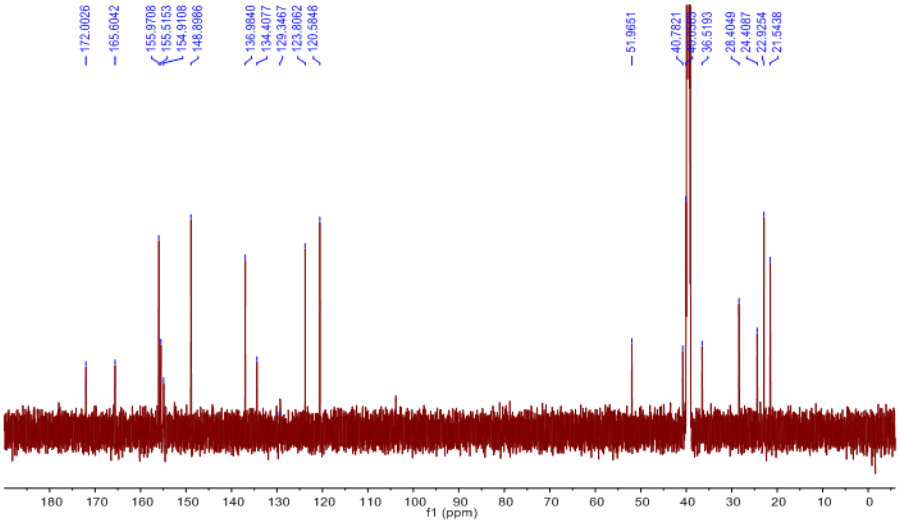

Figure A2.21.2: ^{13}C NMR (400 MHz, DMSO-d_6) spectrum of compound **91R.**

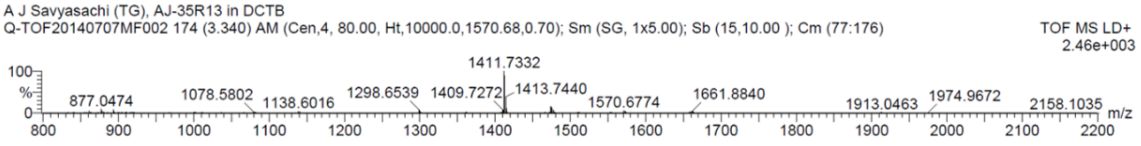

Minimum:				-1.5			
Maximum:		5.0	20.0	500.0			
Mass	Calc. Mass	mDa	PPM	DBE	i-FIT	i-FIT (Norm)	Formula
1411.7332	1411.7369	-3.7	-2.6	45.5	53.9	0.0	C81 H91 N18 O6

Figure A2.21.3: Mass Spectrum MALDI of **91R.**

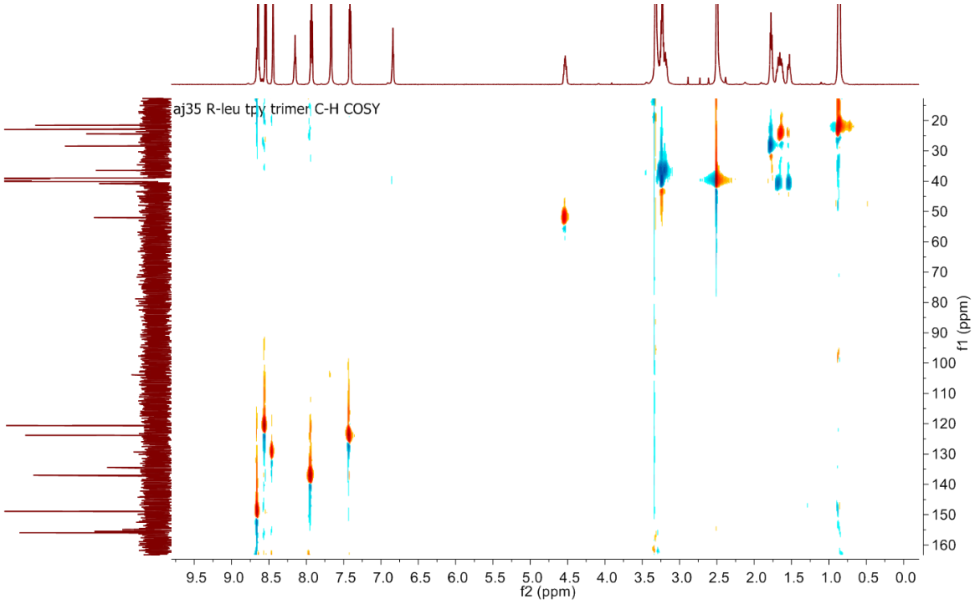

Figure A2.21.5: C-H COSY NMR (600 MHz, DMSO-d_6) spectrum of compound **91R.**

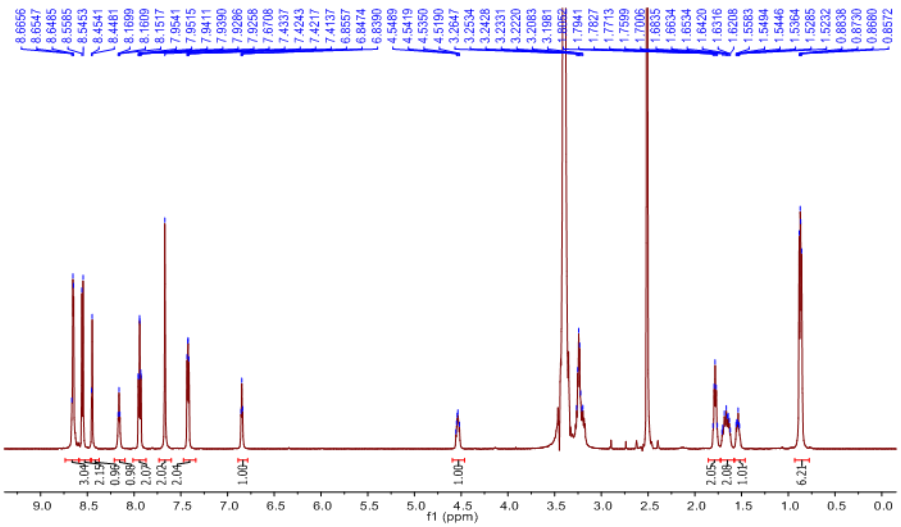

Figure A2.22.1: ^{1}H NMR (400 MHz, DMSO-d_6) spectrum of compound **91S.**

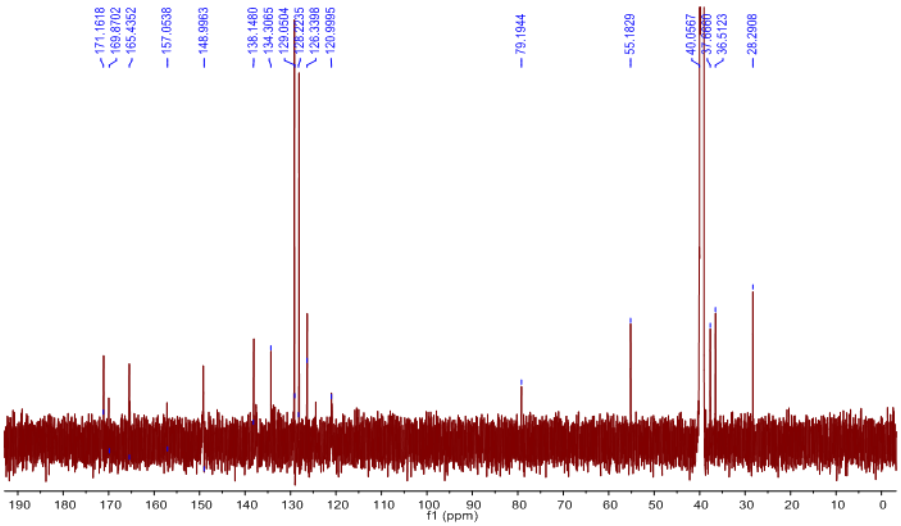

Figure A2.22.2: ^{13}C NMR (400 MHz, DMSO-d_6) spectrum of compound **91S.**

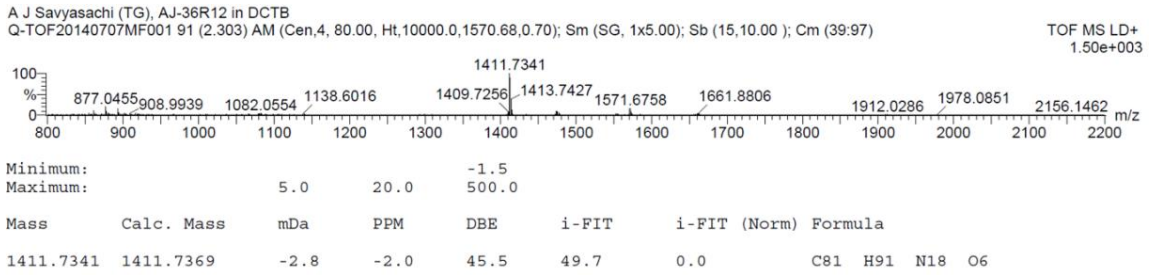

Figure A2.22.3: Mass Spectrum MALDI **91S.**

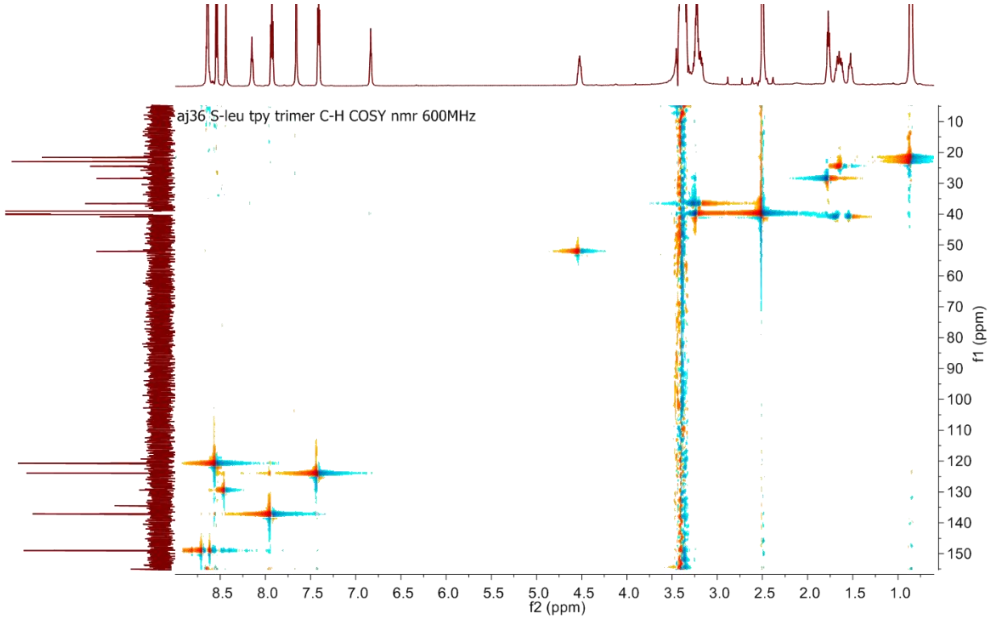

Figure A2.22.5: C-H COSY NMR (600 MHz, DMSO-d_6) spectrum of compound **91S.**

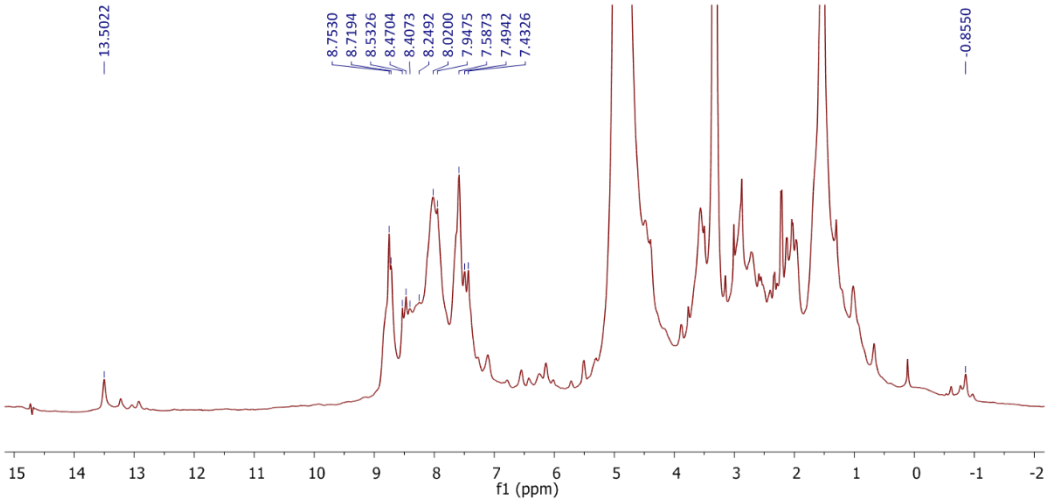

Figure A2.23.1: ^{1}H NMR (400 MHz, 5% D_2O/CD_3OD) spectrum of compound **Eu.89R.**

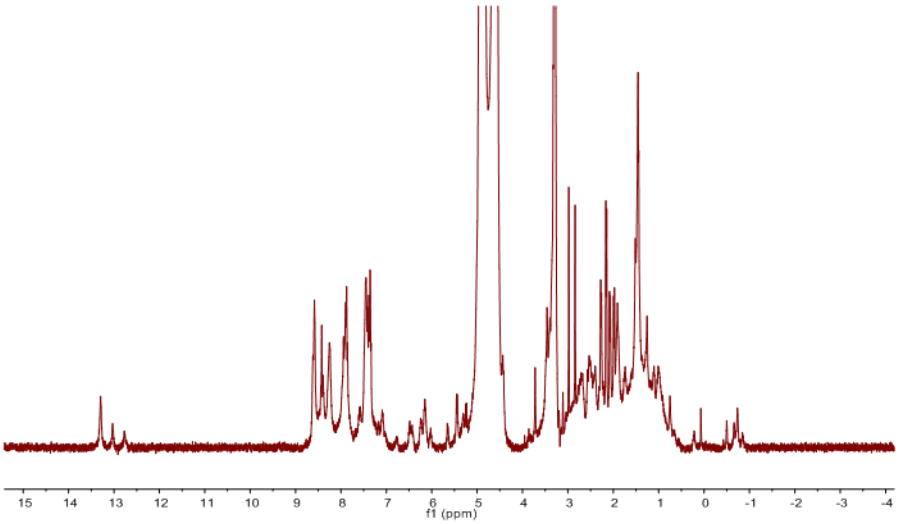

Figure A2.23.2: ^{1}H NMR (400 MHz, 5% D_2O/CD_3OD) spectrum of compound **Eu.89S.**

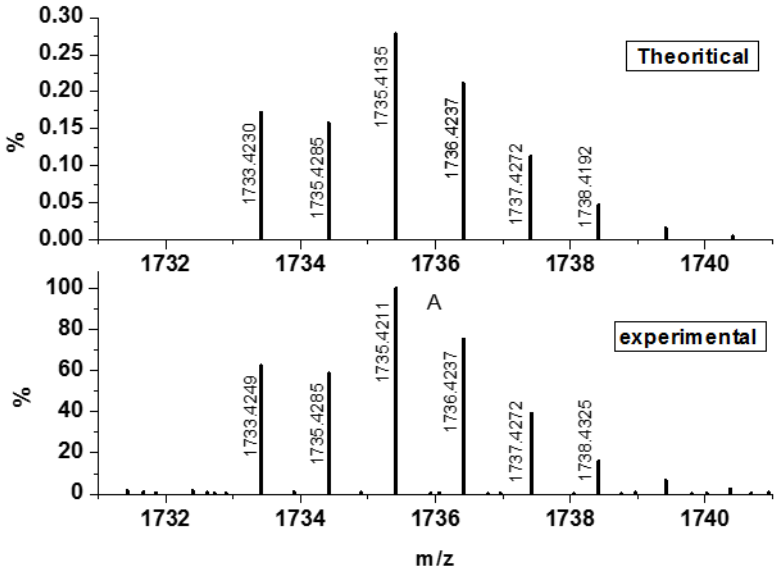

Figure A2.23.2: Mass spectrum of compound **Eu.89S.**

Table A2.1: Summary of all q values obtained for **Eu.89R** and **Eu.89S** in CH_3OH and CD_3OD.

Complex	$\tau_{CH3OH,\ ms}$	$\tau_{CD3OD,\ ms}$	q (± 0.5)
Eu:89R	0.76 ± 0.01	1.27 ± 0.02	0.3
Eu:89S	0.9 ± 0.02	1.43 ± 0.02	0.2

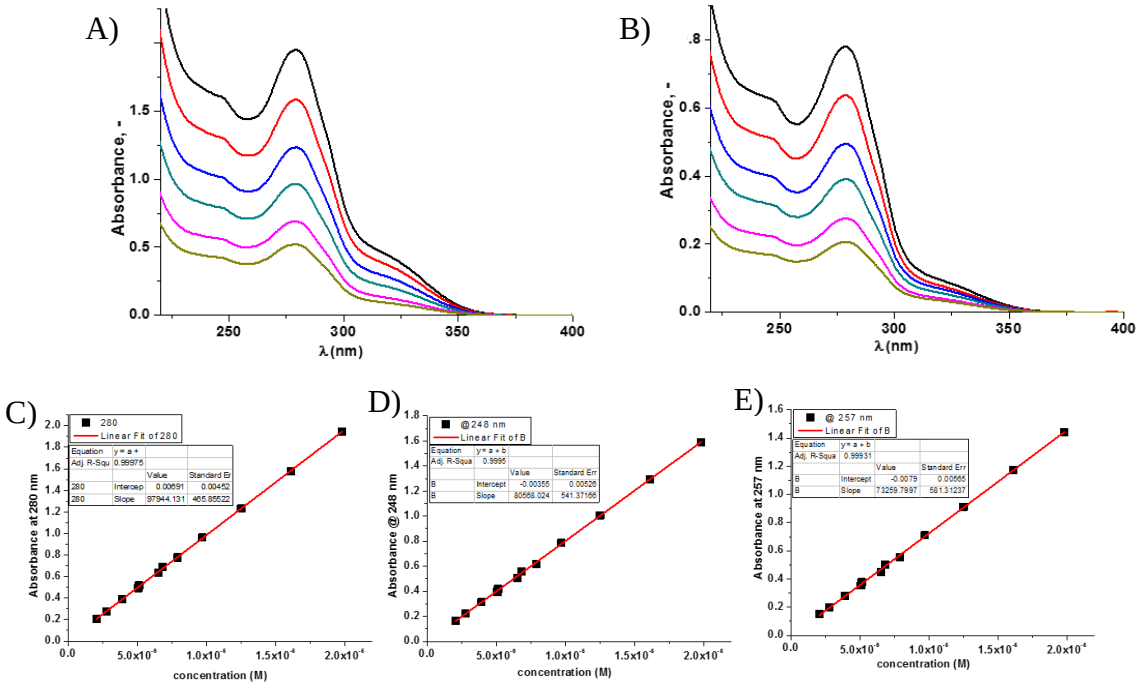

Figure A2.24.1: A) and B) Absorption spectrum of **89R** of two solutions in CH_3OH (c = 1.98 × 10^{-5} M and 0.79 × 10^{-5} M) on decreasing the concentration. C), D) and E) Absorption binding isotherms of the solution A and B merged and its corresponding fits.

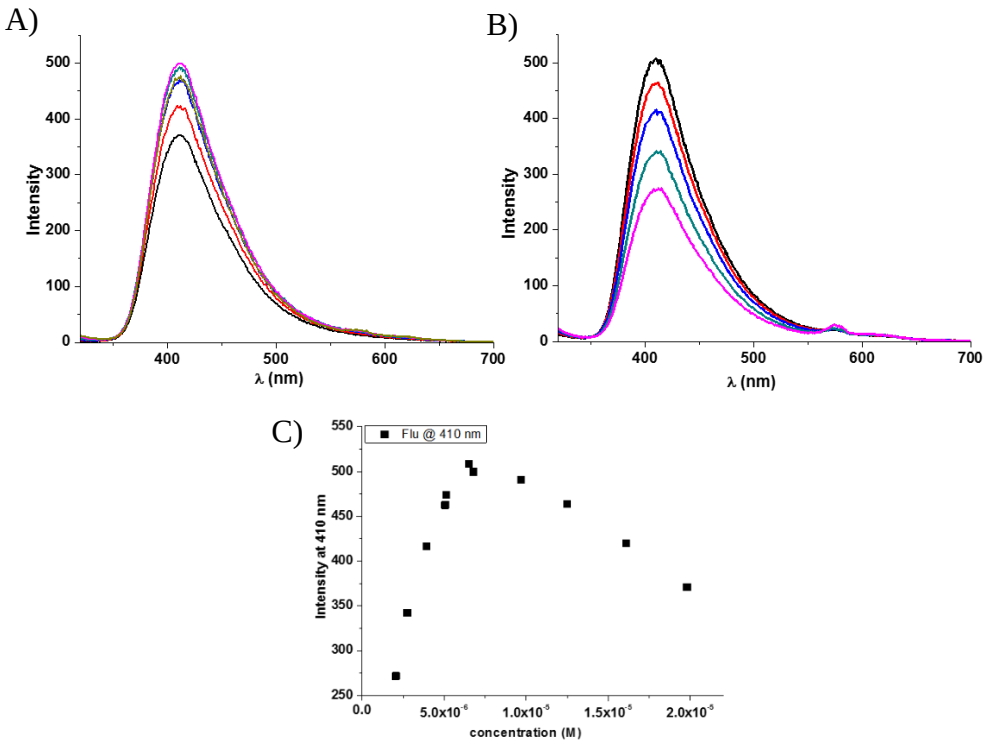

Figure A2.24.2: A) and B) Fluorescence spectrum of **89R** of two solutions in CH_3OH (c = 1.98 × 10^{-5} M and 0.79 × 10^{-5} M) on decreasing the concentration. C), Fluorescence intensity at 410 nm of the solution A and B merged.

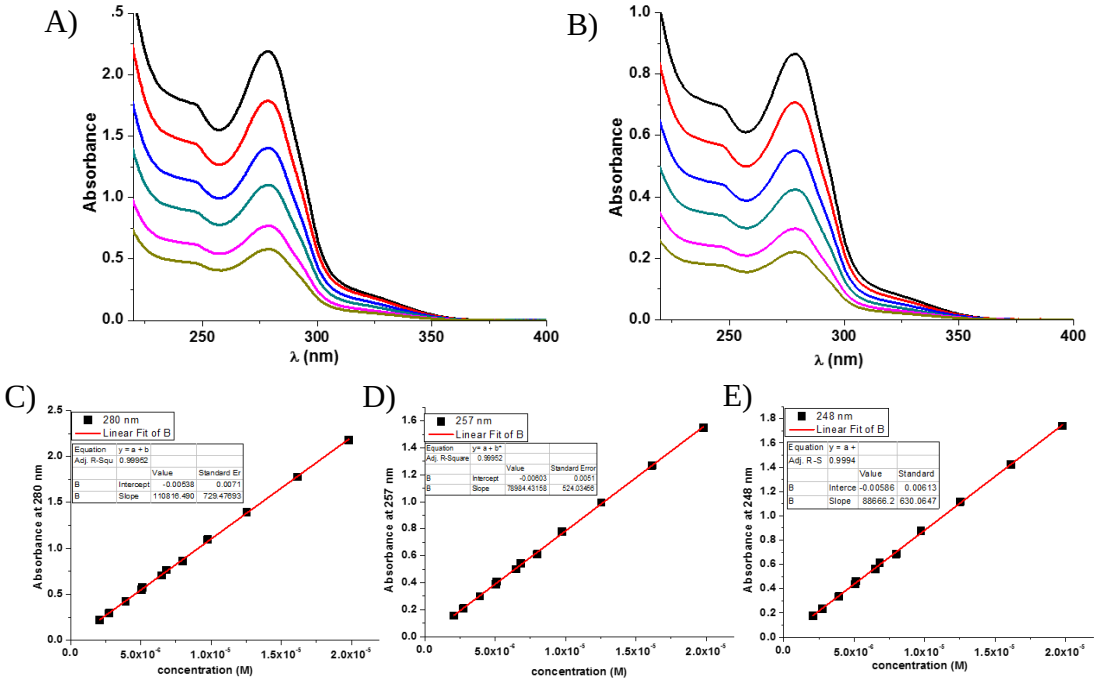

Figure A2.25.1: A) and B) Absorption spectrum of **89S** of two solutions in CH_3OH (c = 1.98 × 10^{-5} M and 0.79 × 10^{-5} M) on decreasing the concentration. C), D) and E) Absorption binding isotherms of the solution A and B merged and its corresponding fits.

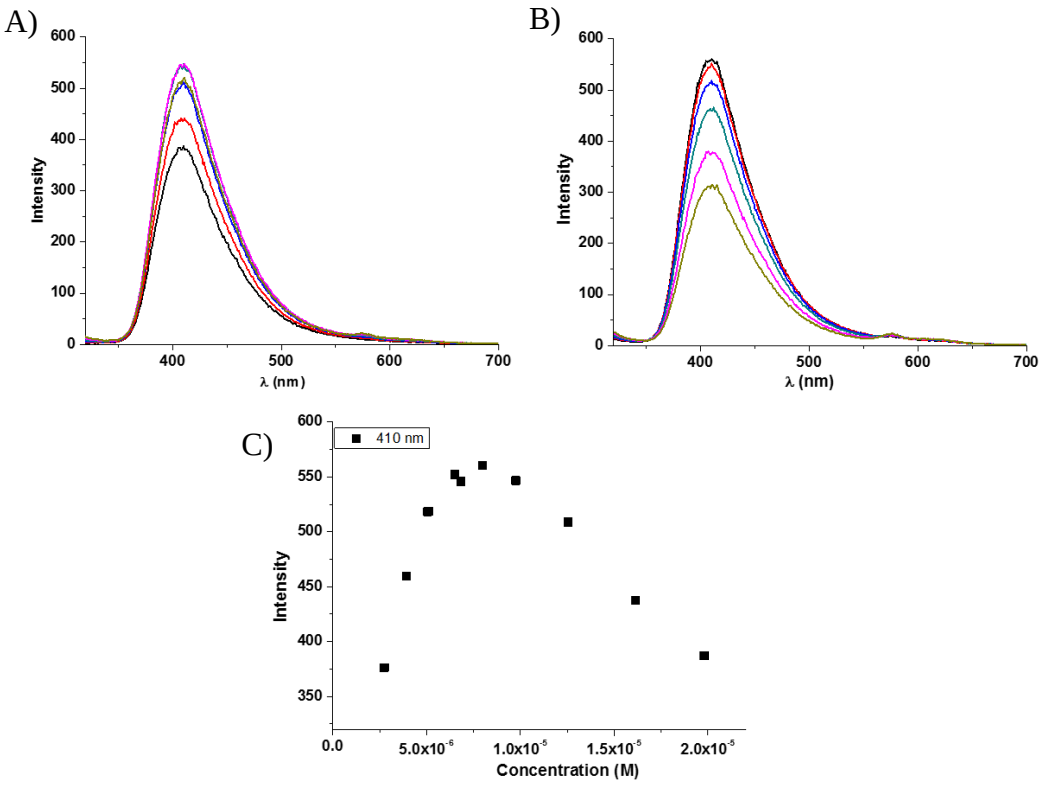

Figure A2.25.2: A) and B) Fluorescence spectrum of **89S** of two solutions in CH_3OH (c = 1.98 × 10^{-5} M and 0.79 × 10^{-5} M) on decreasing the concentration. C), Fluorescence intensity at 410 nm of the solution A and B merged.

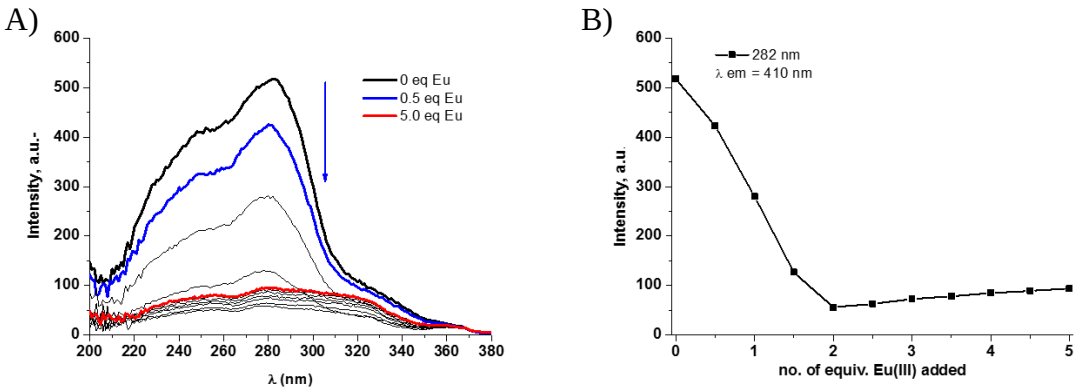

Figure A2.25.2: A) Fluorescence excitation spectrum of **89R** (5×10^{-6} M) upon titrating with $Eu(CF_3SO_3)_3$ (0 → 5 equiv.) in CH_3OH and B) corresponding binding isotherms at the intervals of 0.5 equivalents of Eu(III) ion addition.

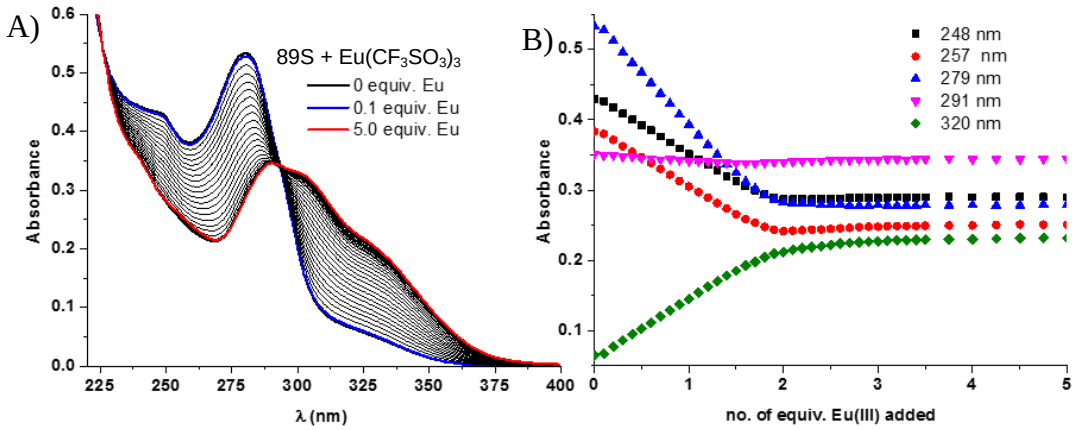

Figure A2.26.1: A) Changes in the absorption spectra of **89S** (c_L = 5 × 10^{-6} M) upon titrating with $Eu(CF_3SO_3)_3$ (0 → 5 equiv.) in CH_3OH. The titration shown here represents the reproducible trends observed several times (3 - 4 times) using fresh stock solutions of ligands and metal salts.

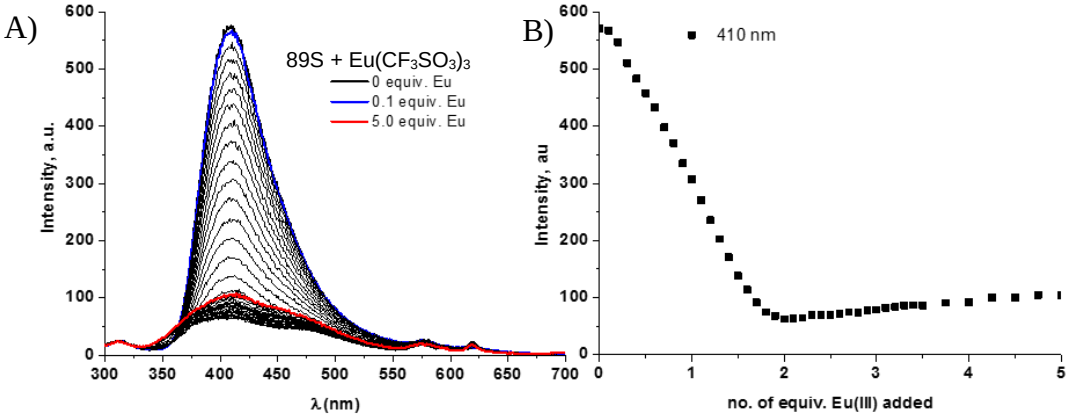

Figure A2.26.2: A) Fluorescence spectra from the titration of **89S** (c_L = 5 × 10^{-6} M) with $Eu(CF_3SO_3)_3$ (0 → 5 equiv.) in CH_3OH. The titration shown here represents the reproducible trends observed several times (3 - 4 times) using fresh stock solutions of ligands and metal salts.

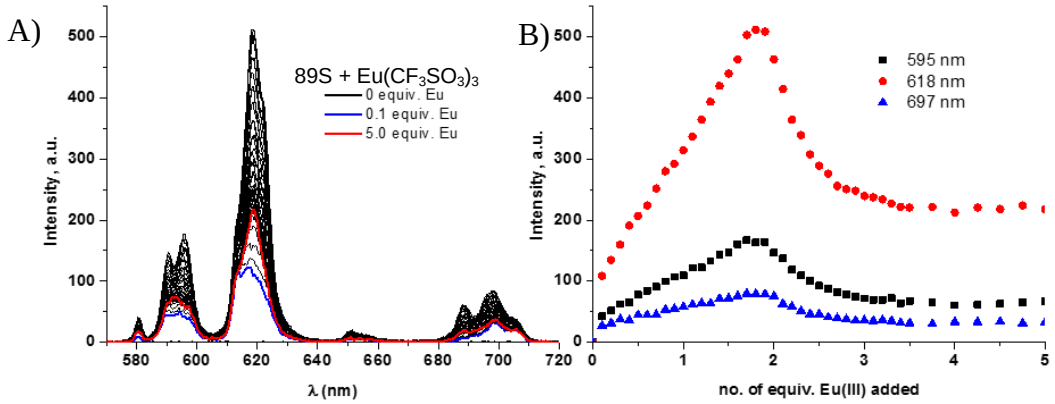

Figure A2.26.3: A) Phosphorescence spectra from the titration of **89S** (c_L = 5 × 10^{-6} M) with $Eu(CF_3SO_3)_3$ (0 → 5 equiv.) in CH_3OH. The titration shown here represents the reproducible trends observed several times (3 - 4 times) using fresh stock solutions of ligands and metal salts.

Table A2.2: Summary of lifetime values of Eu(III) during the titration of **89R** and **89S** in CH_3OH and in CD_3OD at concentration c= 5×10^{-6} M.

Ligands	Equivalent of Eu added								
	0.5	**1.0**	**1.5**	**2.0**	**2.5**	**3.0**	**3.5**	**4.0**	**4.5**
	Life times of Eu (ms)								
89R in CH_3OH 5×10^{-6} M	0.69	0.67	0.66	0.65	0.57	0.5	0.47	0.45	0.44
89S in CH_3OH 5×10^{-6} M	0.9	0.81	0.77	0.70	0.66	0.62	0.6	0.58	0.57
89R in CD_3OD 5×10^{-6} M	2.01	1.66	1.54	1.45	1.45	1.66	1.74	1.81	1.86
q values	0.8	0.8	0.7	0.7	1.0	1.4	1.6	1.7	1.8

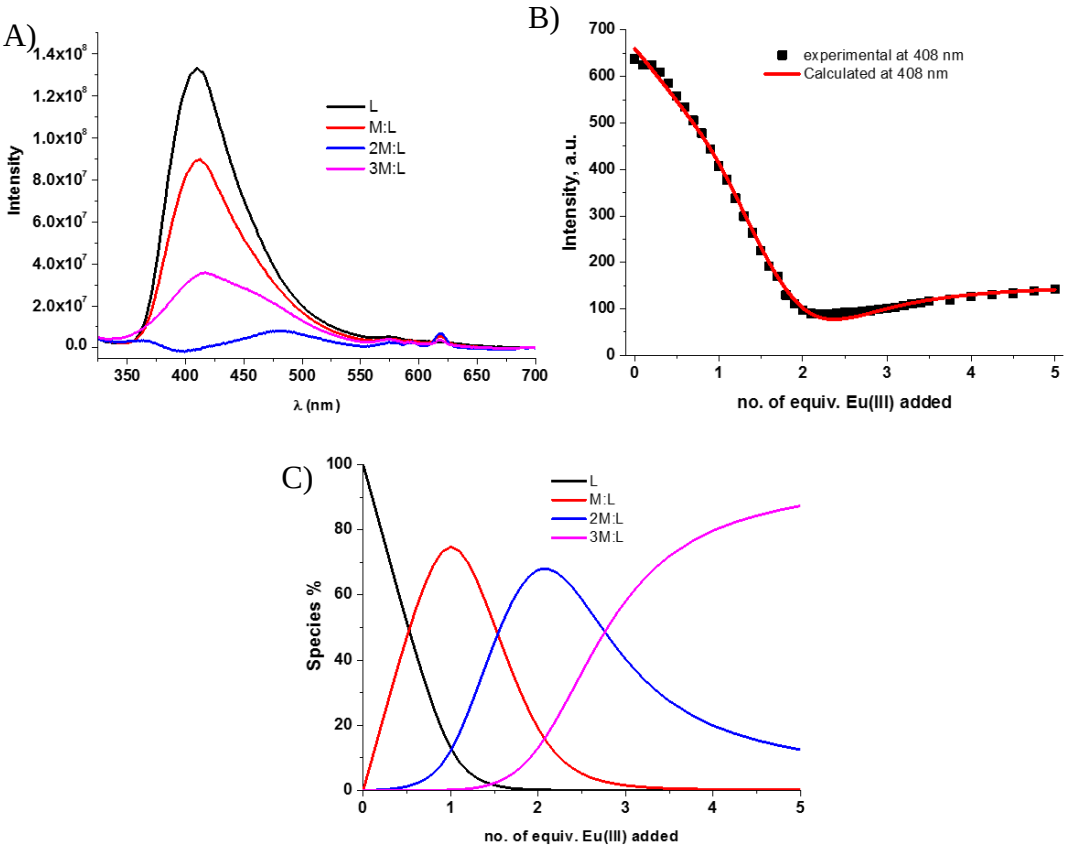

Figure A2.27.1: Recalculated fluorescence spectra, B) Experimental binding isotherm and their corresponding fit and C) speciation distribution diagram obtained from the fit for the fluorescence titration of **89R** (5×10^{-6} M) with $Eu(CF_3SO_3)_3$ in CH_3OH at 22 °C by means of SPECFIT.

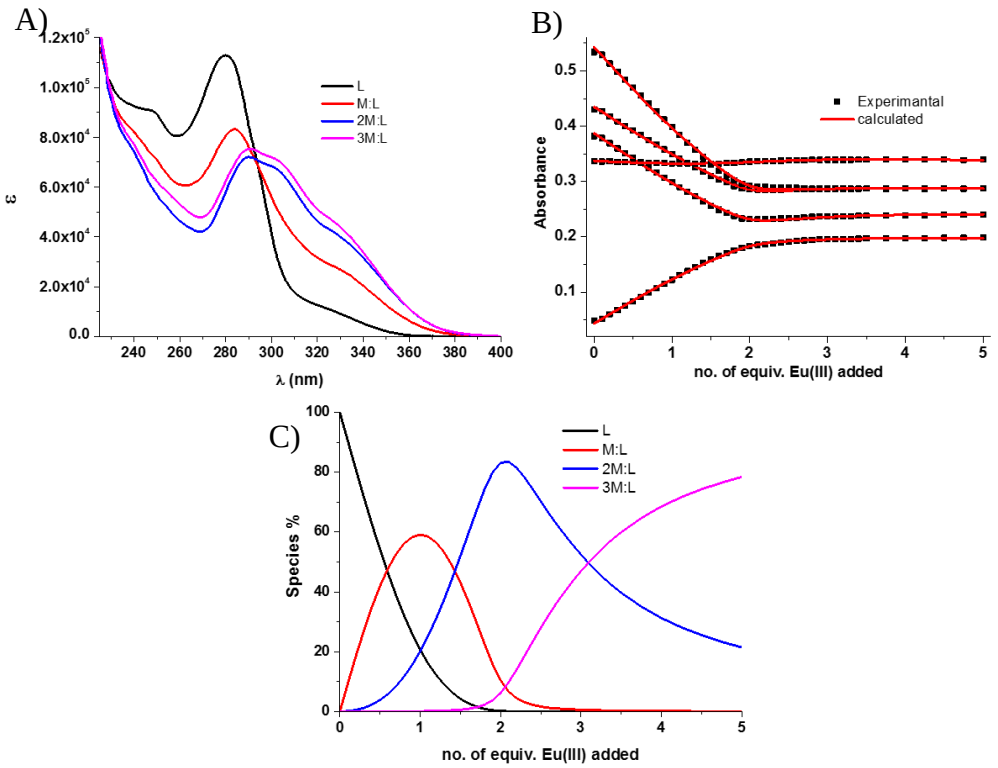

Figure A2.28.1: A) Recalculated absorbance spectra, B) Experimental binding isotherm and their corresponding fit, C) speciation distribution diagram obtained from the fit for the absorption titration of **89S** (5×10^{-6} M) with $Eu(CF_3SO_3)_3$ in CH_3OH at 22 °C by means of SPECFIT.

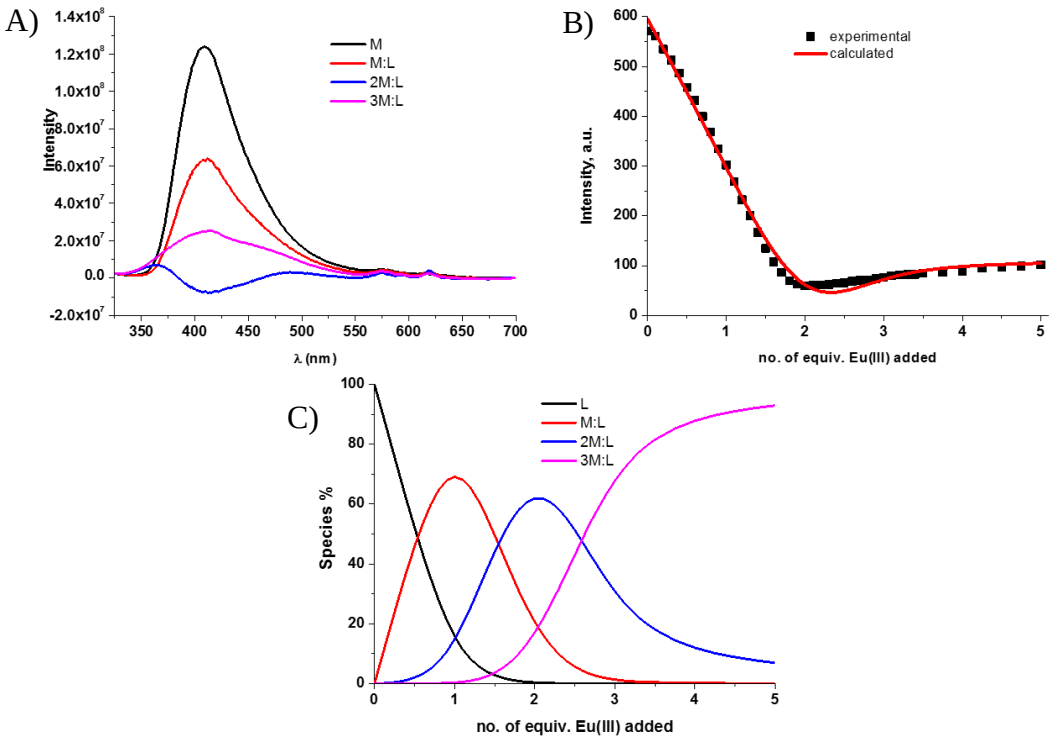

Figure A2.28.2: A) Recalculated fluorescence spectra, B) Experimental binding isotherms and their corresponding fit, C) speciation distribution diagram obtained from the fit for the Fluorescence titration of **89S** (5×10^{-6} M) with $Eu(CF_3SO_3)_3$ in CH_3OH at room temperature by means of SPECFIT.

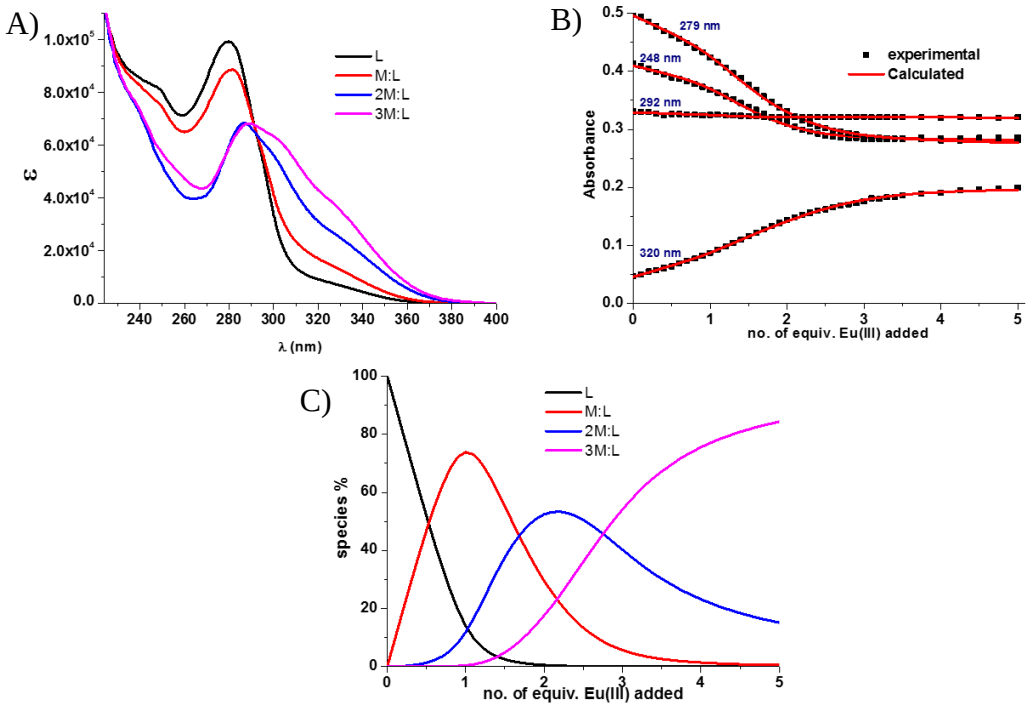

Figure A2.29.1: A) Recalculated absorption spectra, B) experimental binding isotherms and their corresponding fit, C) speciation distribution diagram obtained from the fit for the UV-vis titration of **89R** (5×10^{-6} M) with $Eu(CF_3SO_3)_3$ in CD_3OD at 22 °C by means of SPECFIT.

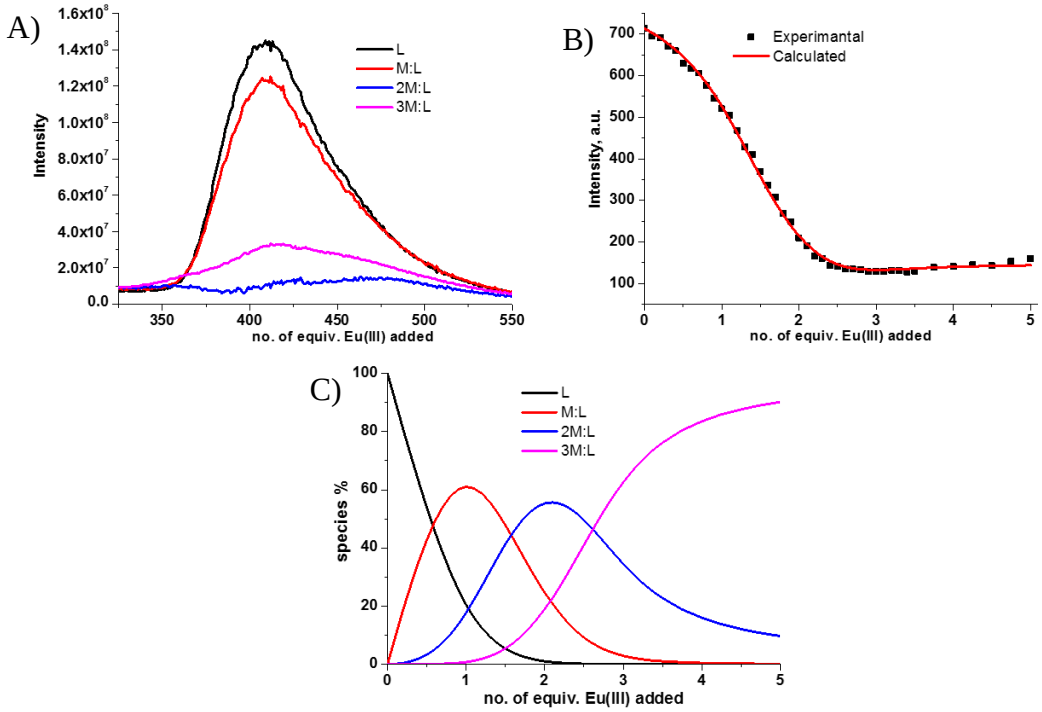

Figure A2.29.2: A) Recalculated fluorescence spectra, B) Experimental binding isotherms and their corresponding fit, C) speciation distribution diagram obtained from the fit for fluorescence titration of **89R** (5×10^{-6} M) with $Eu(CF_3SO_3)_3$ in CD_3OD at room temperature by means of

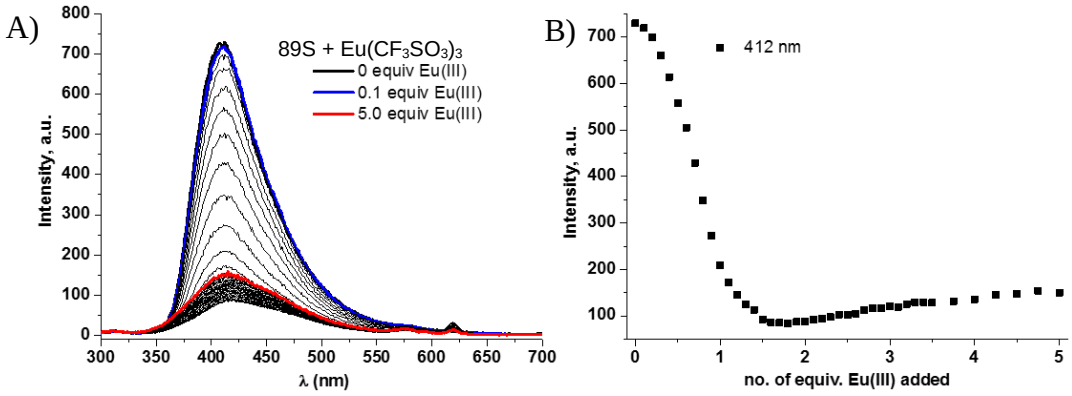

Figure A2.30.2: A) Fluorescence spectra from the titration of **89S** (c_L = 1 × 10^{-5} M) with $Eu(CF_3SO_3)_3$ (0 → 5 equiv.) in CH_3OH. The titration shown here represents the reproducible trends observed several times (3 - 4 times) using fresh stock solutions of ligands and metal salts.

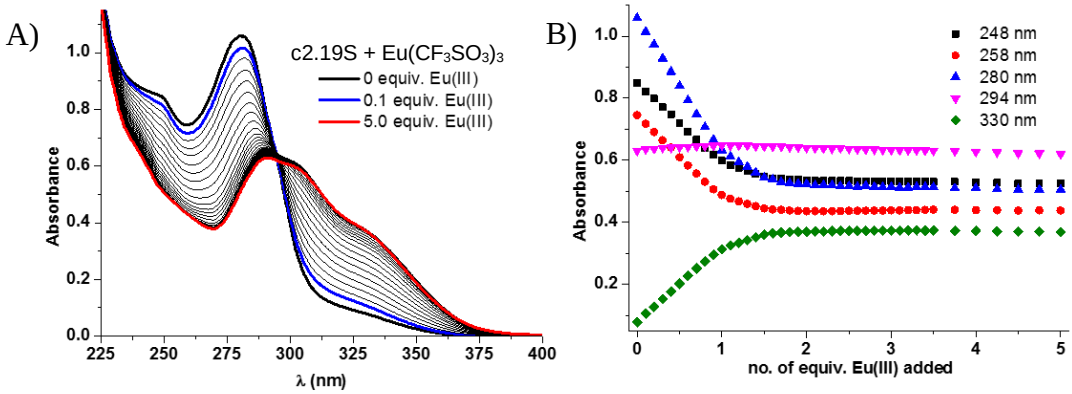

Figure A2.30.1: A) Changes in the absorption spectra of **89S** at concentration of c_L = 1 × 10^{-5} M upon titrating with $Eu(CF_3SO_3)_3$ (0 → 5 equiv.) in CH_3OH. The titration shown here represents the reproducible trends observed several times (3 - 4 times) using fresh stock solutions of ligands and metal salts.

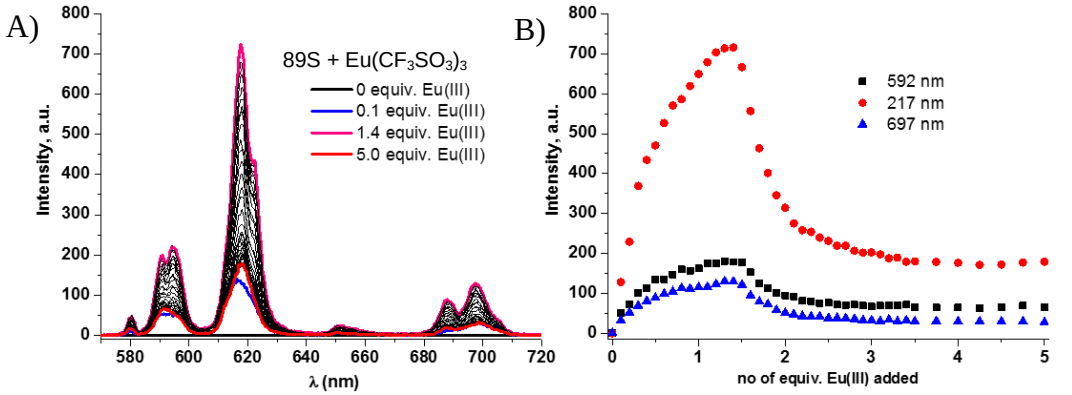

Figure A2.30.3: A) Phosphorescence spectra from the titration of **89S** (c_L = 1 × 10^{-5} M) with $Eu(CF_3SO_3)_3$ (0 → 5 equiv.) in CH_3OH. The titration shown here represents the reproducible trends observed several times (3 - 4 times) using fresh stock solutions of ligands and metal salts.

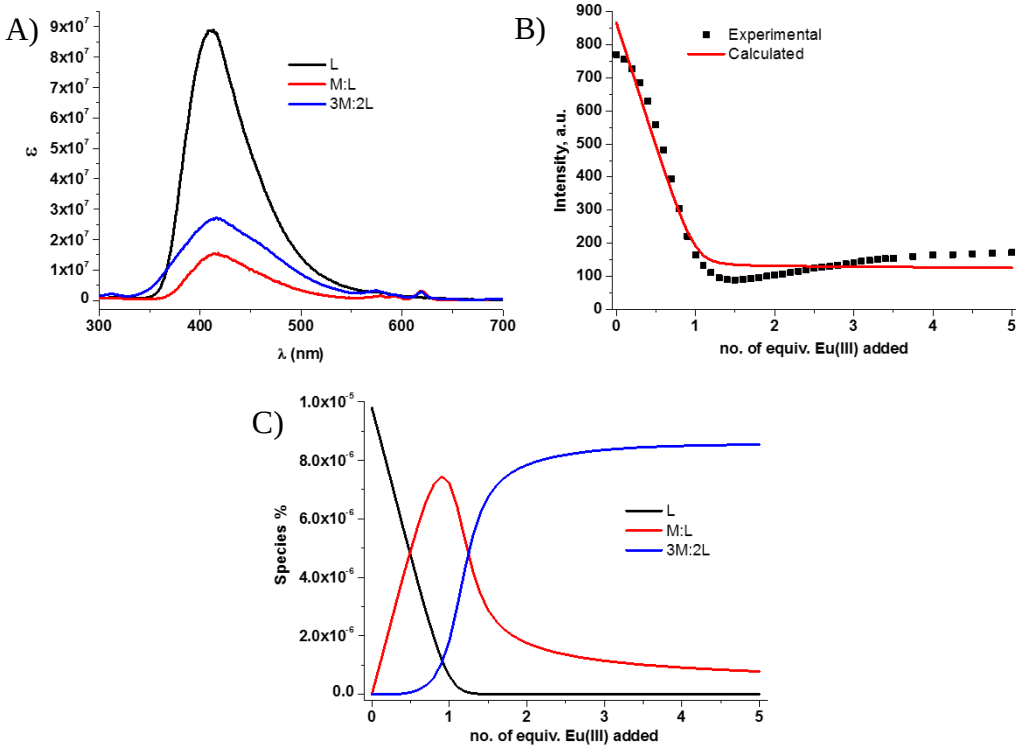

Figure A2.31.1: Recalculated fluorescence spectra, B) experimental binding isotherm and their corresponding fit, C) speciation distribution diagram obtained from the fit for the fluorescence titration of **89R** (1×10^{-5} M) with $Eu(CF_3SO_3)_3$ in CH_3OH at 22 ºC by means of SPECFIT.

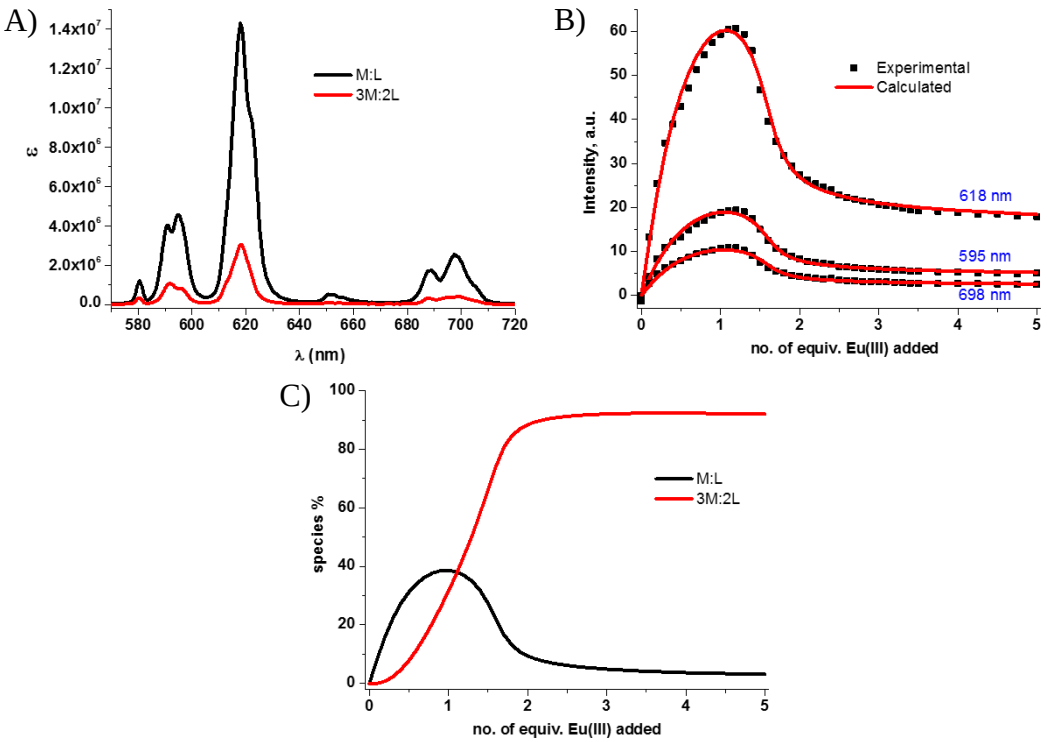

Figure A2.31.2: Recalculated phosphorescence spectra, B) experimental binding isotherm and their corresponding fit, C) speciation distribution diagram obtained from the fit for the fluorescence titration of **89R** (1×10^{-5} M) with $Eu(CF_3SO_3)_3$ in CH_3OH at 22 ºC by means of

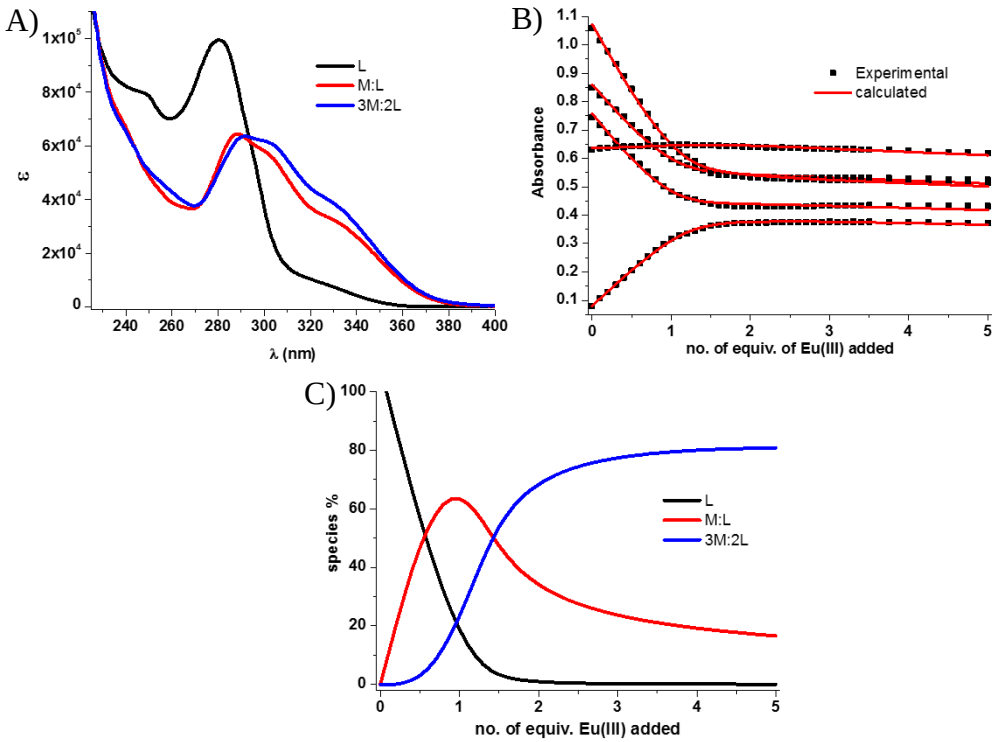

Figure A2.32.1: A) Recalculated absorbance spectra, B) experimental binding isotherms and their corresponding fit, C) speciation distribution diagram obtained from the fit for the absorption titration of **89S** (1×10^{-5} M) with $Eu(CF_3SO_3)_3$ in CH_3OH at 22 ºC by means of SPECFIT.

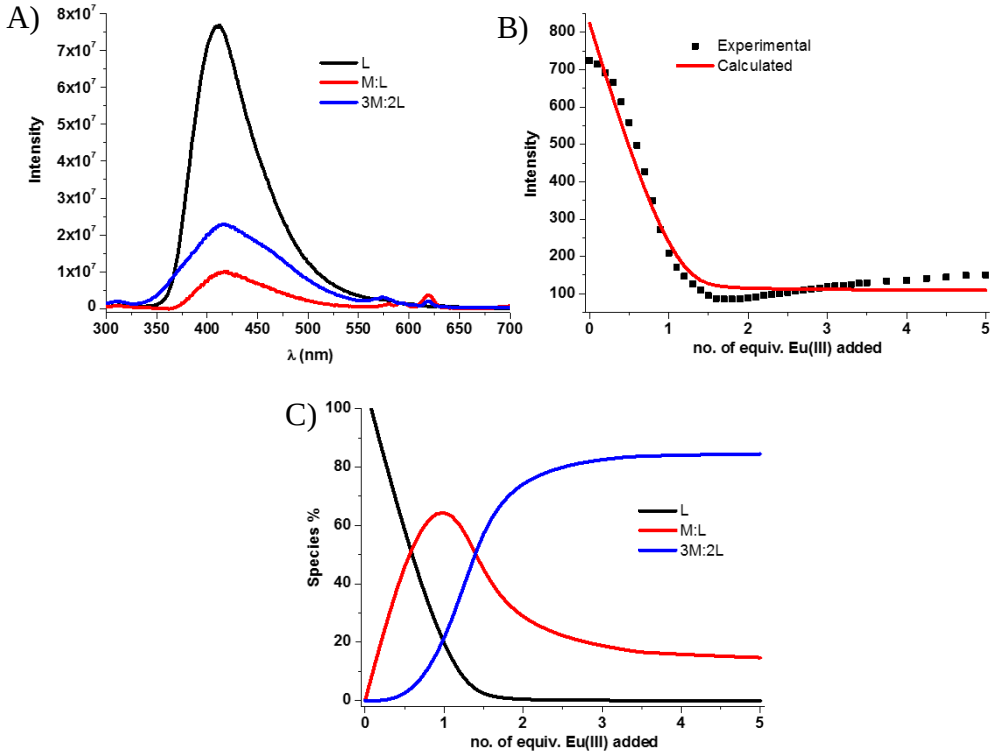

Figure A2.32.2: A) Recalculated fluorescence spectra, B) experimental binding isotherms and their corresponding fit, C) speciation distribution diagram obtained from the fit for the Fluorescence titration of **89S** (1×10^{-5} M) with $Eu(CF_3SO_3)_3$ in CH_3OH at 22 ºC by means of

Table A2.3: Summary of lifetime values of Eu(III) during the titration of **89R** and **89S** in CH_3OH at concentration c= 1×10^{-5} M.

Ligands	**Equivalent of Eu added**								
	0.5	**1.0**	**1.5**	**2.0**	**2.5**	**3.0**	**3.5**	**4.0**	**4.5**
	Life times of Eu(III) (ms)								
89R $\mathbf{1\times10^{-5}}$ **M**	0.95	0.9	0.79	0.73	0.66	0.6	0.57	0.55	0.54
89S $\mathbf{1\times10^{-5}}$ **M**	0.79	0.76	0.65	0.59	0.56	0.54	0.52	0.50	0.49

Appendix 3

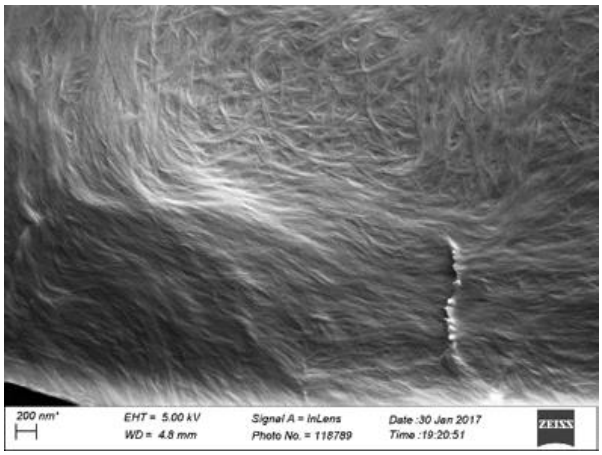

Figure A3.2.1: A) SEM image of **88** gel after the rheology measurements.

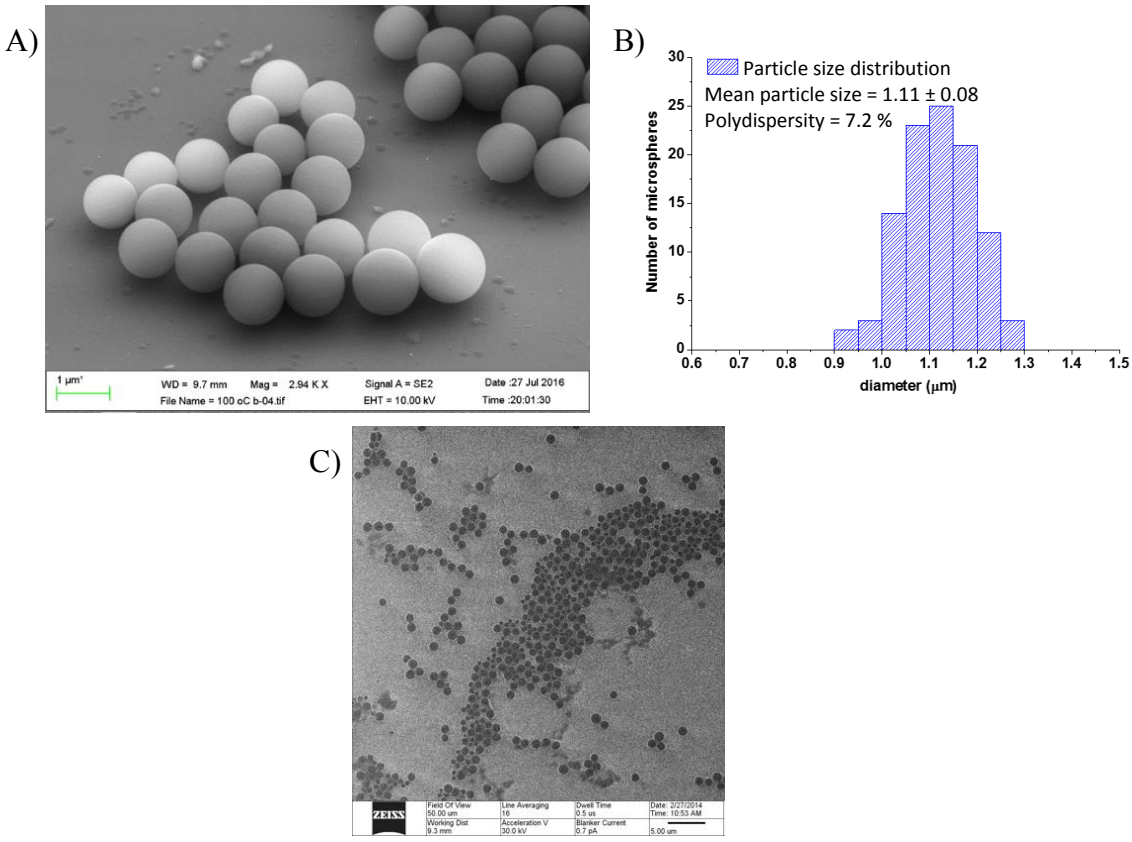

Figure A3.3.1: A) SEM image of **89R** microspheres (c = 0.2% w/v, in 55:45 CH_3CN/H_2O) and B) its corresponding particle size distribution diagram calculated from SEM images using imageJ software. C) HIB image of the same sample.

A) B)

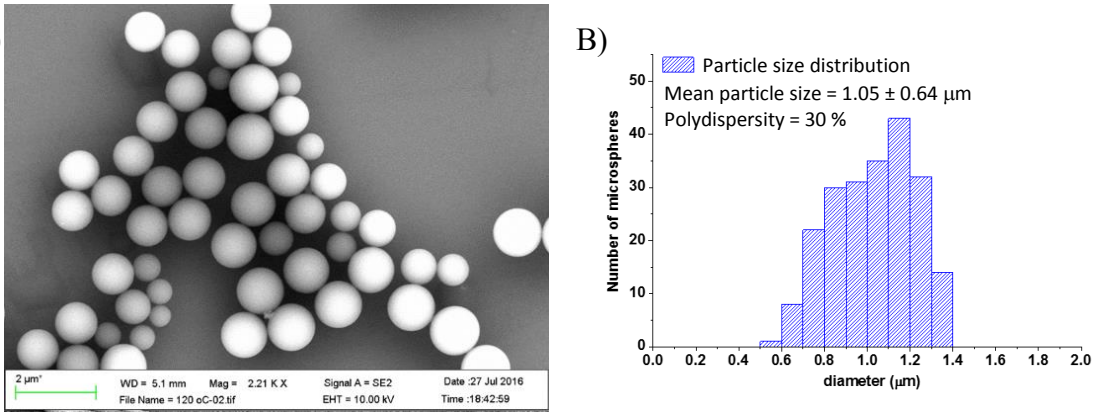

Figure A3.3.2: A) SEM image of **90R** microspheres (c = 0.2% w/v, in 55:45 CH_3CN/H_2O) and B) its corresponding particle size distribution diagram calculated from SEM images using imageJ software.

A) B)

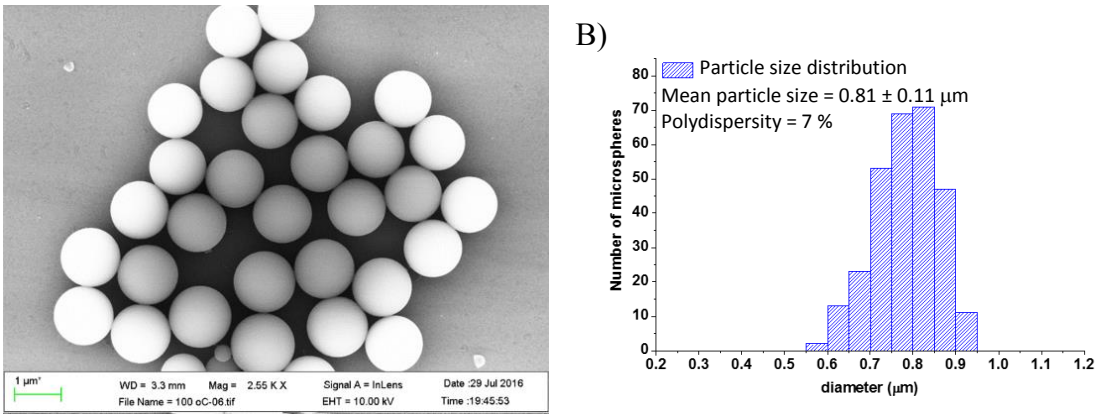

Figure A3.3.3: A) SEM image of **91R** microspheres (c = 0.2% w/v, in 55:45 CH_3CN/H_2O) and B) its corresponding particle size distribution diagram calculated from SEM images using imageJ software.

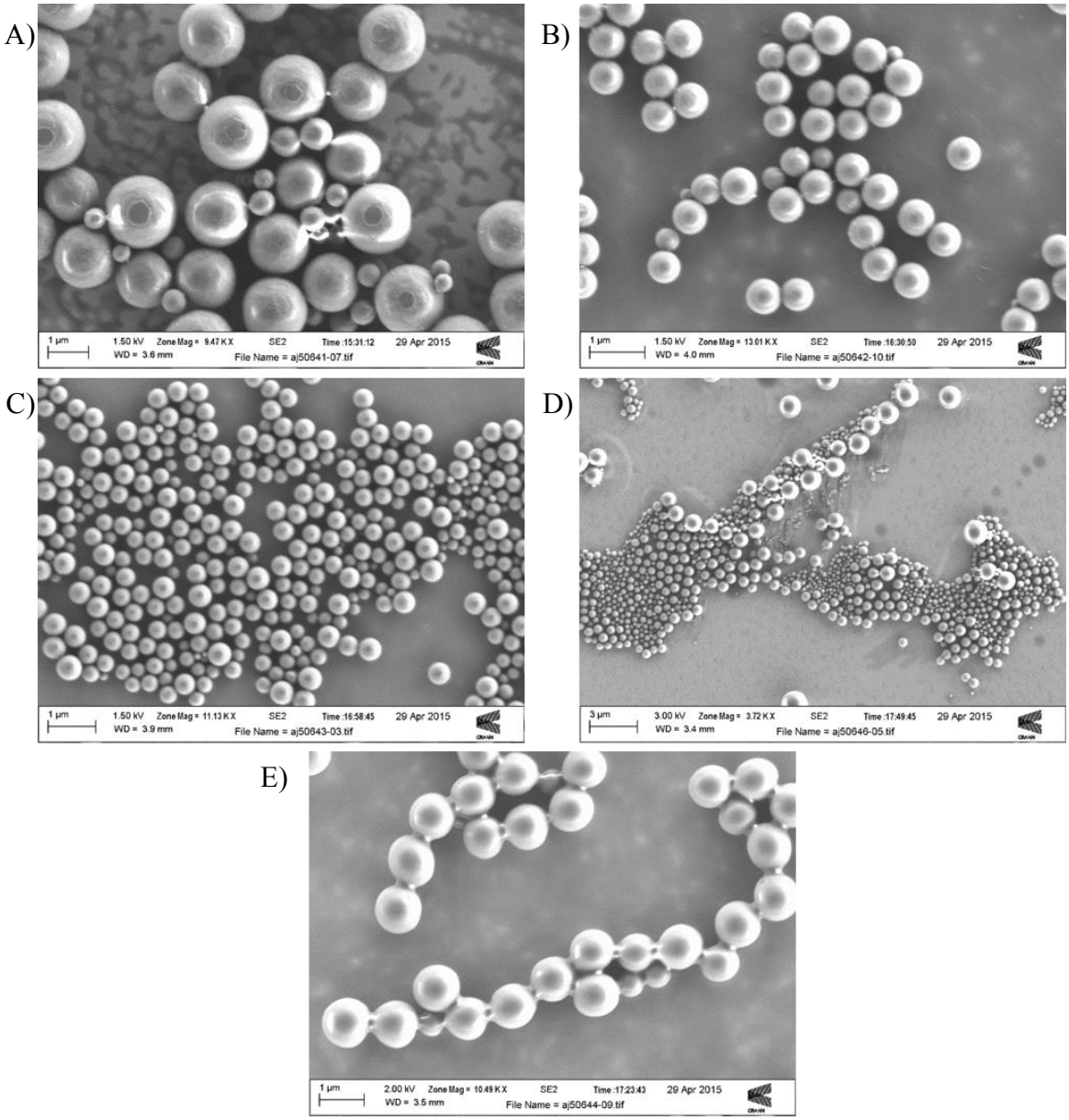

Figure A3.3.4: SEM images of **89R** microspheres in different organic solvent/aqueous media (1:1 v/v and c = 0.2% w/v). (A) CH_3OH/H_2O, Scale bar 2 µm, (B) C_2H_5OH/H_2O, Scale bar 200 nm, (C) *i*-$PrOH/H_2O$, Scale bar 1 µm, (D) Acetone/H_2O, Scale bar 2 µm, (E) THF/H_2O, Scale bar 1 µm.

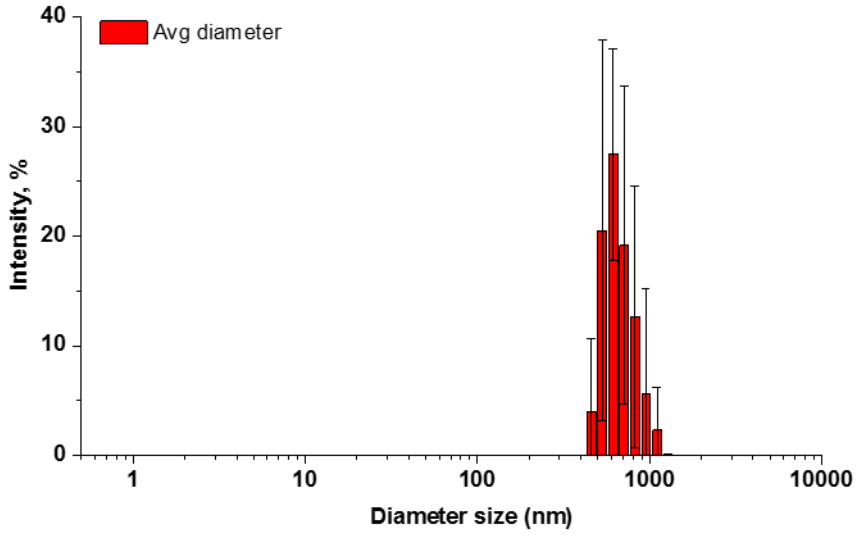

Figure A3.4.1: Average size distribution of microspheres measured using DLS technique in CH_3CN/H_2O (55:45) (c = 1.55 × 10^{-3} M, at 22 ºC). Average size of particles from **89S**, **91S** and **91S** combined together was 670 ± 106 nm in diameter.

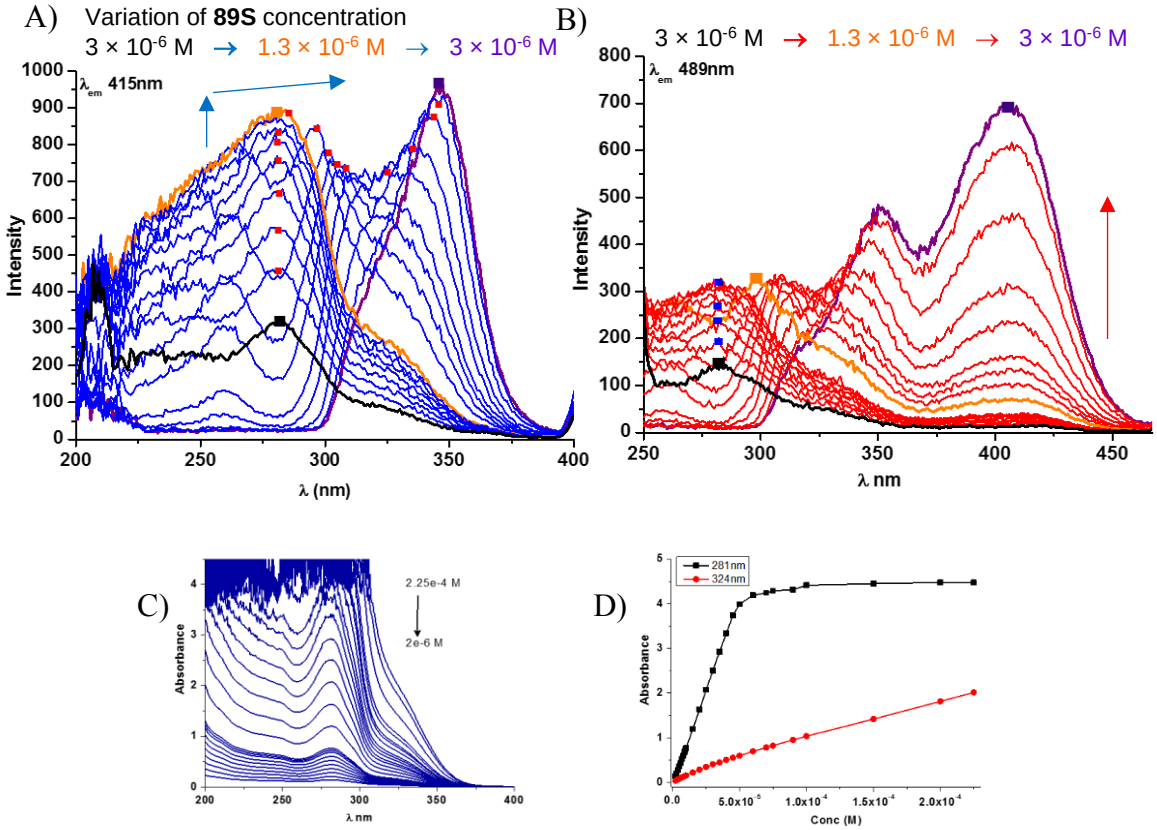

Figure A3.5.1: A) Fluorescence excitation spectrum of **89S** free molecules when monitoring the emission at λ_{em} = 415 nm; B) Fluorescence excitation spectrum of microspheres on emission at λ_{em} = 489 nm.

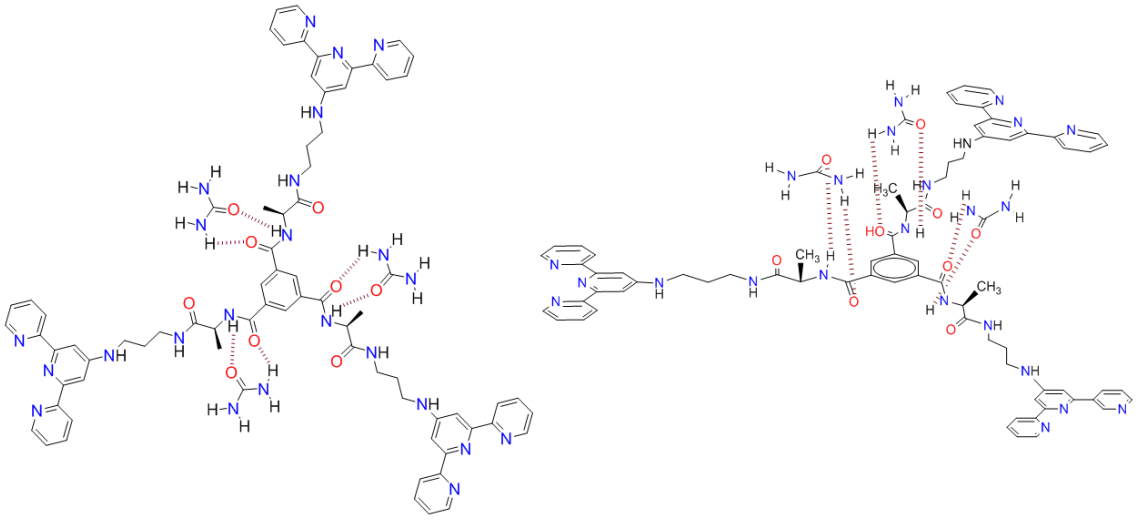

Figure A3.7.1: A) 2D and 2) 3D view of the possible H-bonding interactions between urea and **89S**.

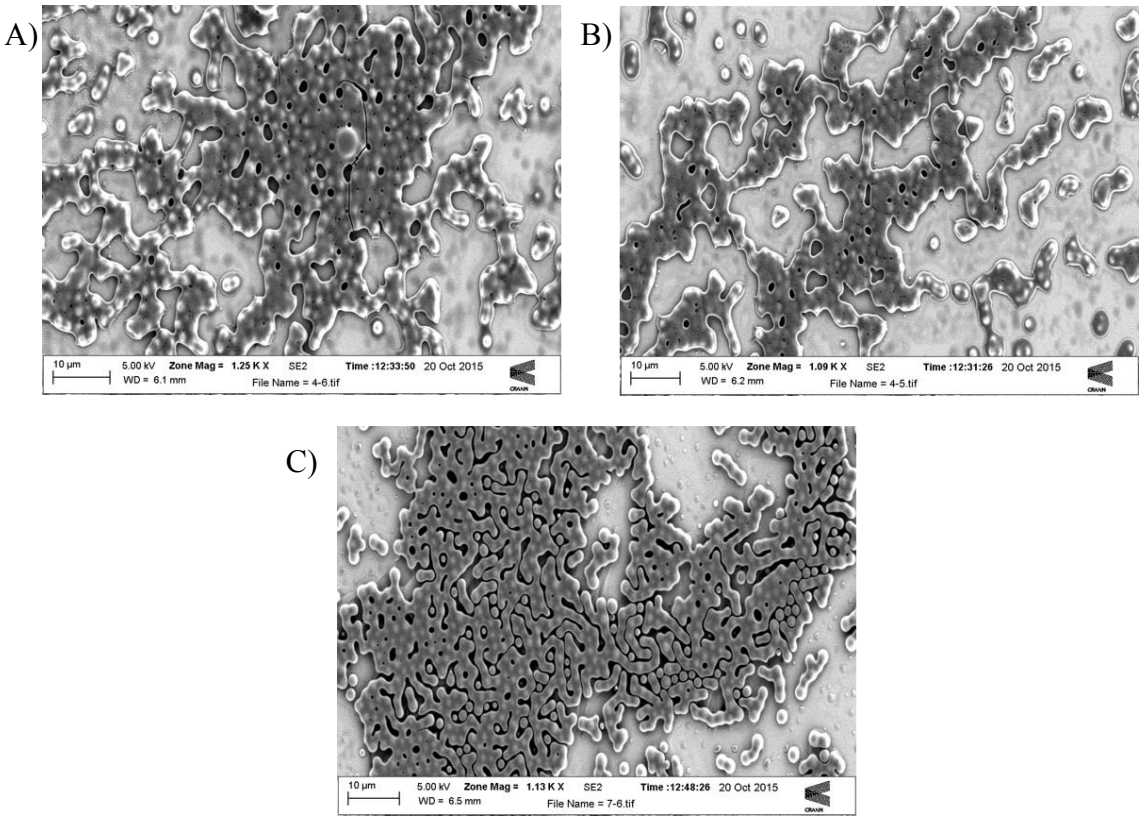

Figure A3.7.2: SEM images of **89S** microspheres decomposed faster when using higher concentration of urea; A) 10 equiv. of urea decomposed microspheres after 4hrs, B) 15 equiv. of urea decomposed microspheres after 3hrs and C) 18 equiv. of urea decomposed microspheres after 2.5 hrs. Scale bar 10 µm.

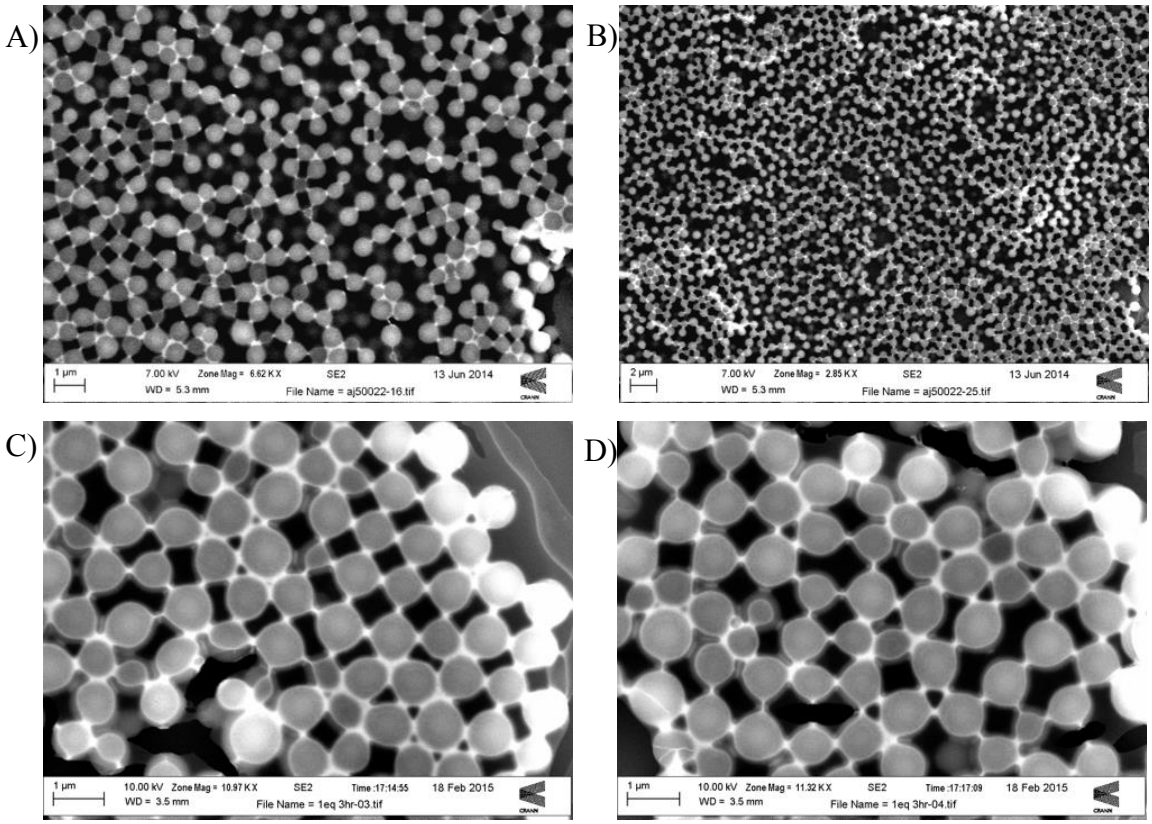

Figure A3.8.1: A) Simple chains of **89S** microspheres, scale bar 1μm; B) Extended network of microspheres formed when using higher concentration of microspheres (c > 0.2%) with of Tb(III), scale bar 2μm. C) and D) interconnected **89R** microspheres by addition of Eu(III) and Tb(III) ions respectively.

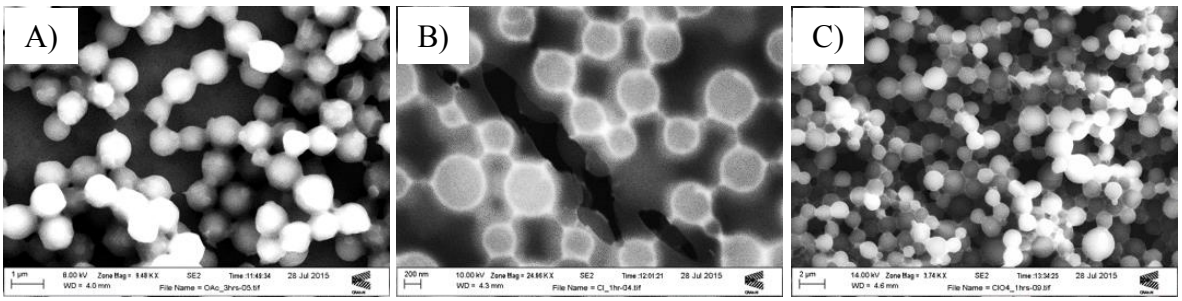

Figure A3.8.2: SEM images of the **89S** microspheres chains formed upon interactions with different Tb(III) salts: A) $Tb(CH_3COO)_3$, scale bar 1μm; B) $TbCl_3$, scale bar 200 nm, C) $Eu(ClO_4)_3$, scale bar 2μm.

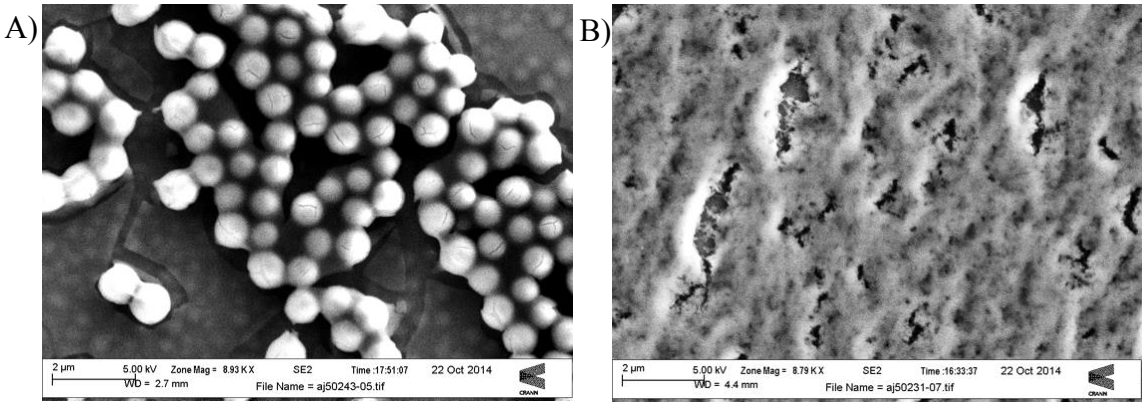

Figure A3.8.3: SEM images of **89S** microspheres after interactions with (A) Fe(II)- solution incubated for 2hrs, scale bar 2µm; B) Zn(II)-microspheres solution incubated 1hr, scale bar, 2µm.

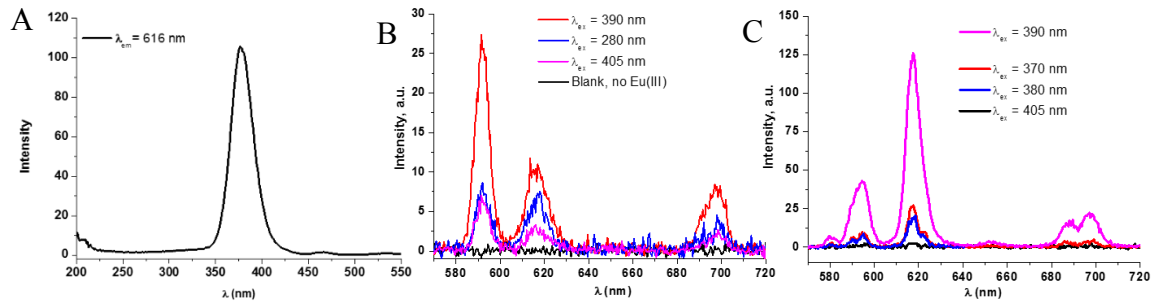

Figure A3.8.4: Excitation spectrum of Eu(III) based microsphere chains of **89S**, λ_{em} = 618 nm; B) Emission spectrum of Eu(III) alone in absence of microspheres, with different excitation wavelength showing no Eu(III) emission at 618 nm ($C_{Eu(III)} = 1.55 \times 10^{-3}$ M in H_2O); C) Emission spectrum of Eu(III) based microspheres chains at different excitation wavelengths, showing the maximum intensity when λ_{ex} = 380 nm.

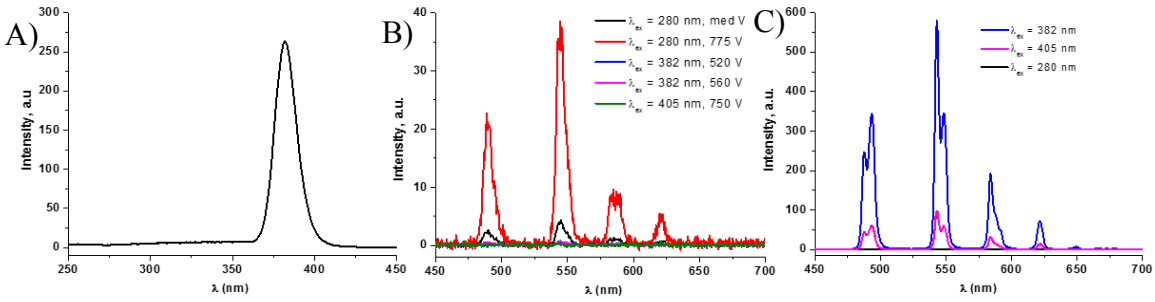

Figure A3.8.5: Excitation spectrum of Tb(III) based microsphere chains of **89S**, λ_{em} = 543 nm; B) Emission spectrum of Tb(III) alone in absence of microspheres showing very weak Tb(III) emission at 544 nm; C) Emission spectrum of Tb(III) based microspheres chains at different excitation wavelength, showing the high luminescence intensity (λ_{ex} = 382 nm).

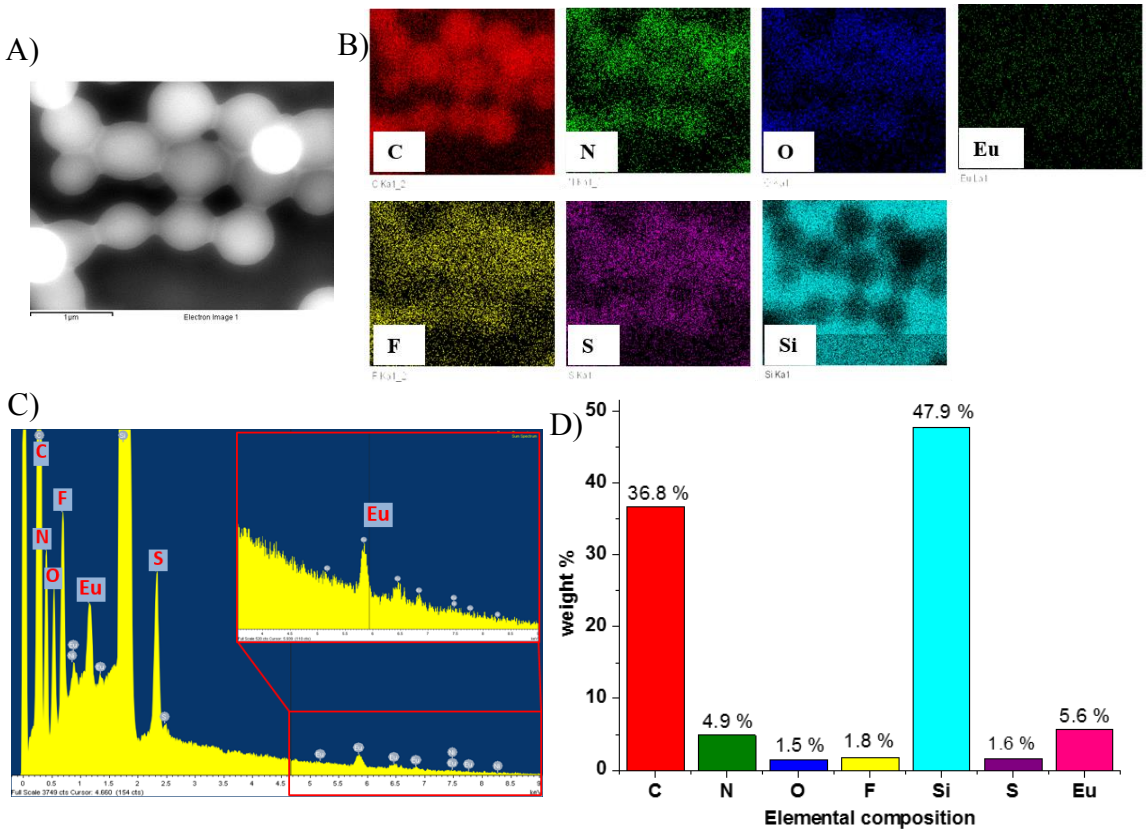

Figure A3.8.6: EDX analysis of the solid Eu(III) based **89S** microsphere chains in mapping mode: A) STEM image of the site of interest, scale bar 1 μm; B) mapping results showing the composition of microspheres, C) EDX spectrum of the same microspheres and D) weight percentage of each element on the site of interest on the surface of sample.

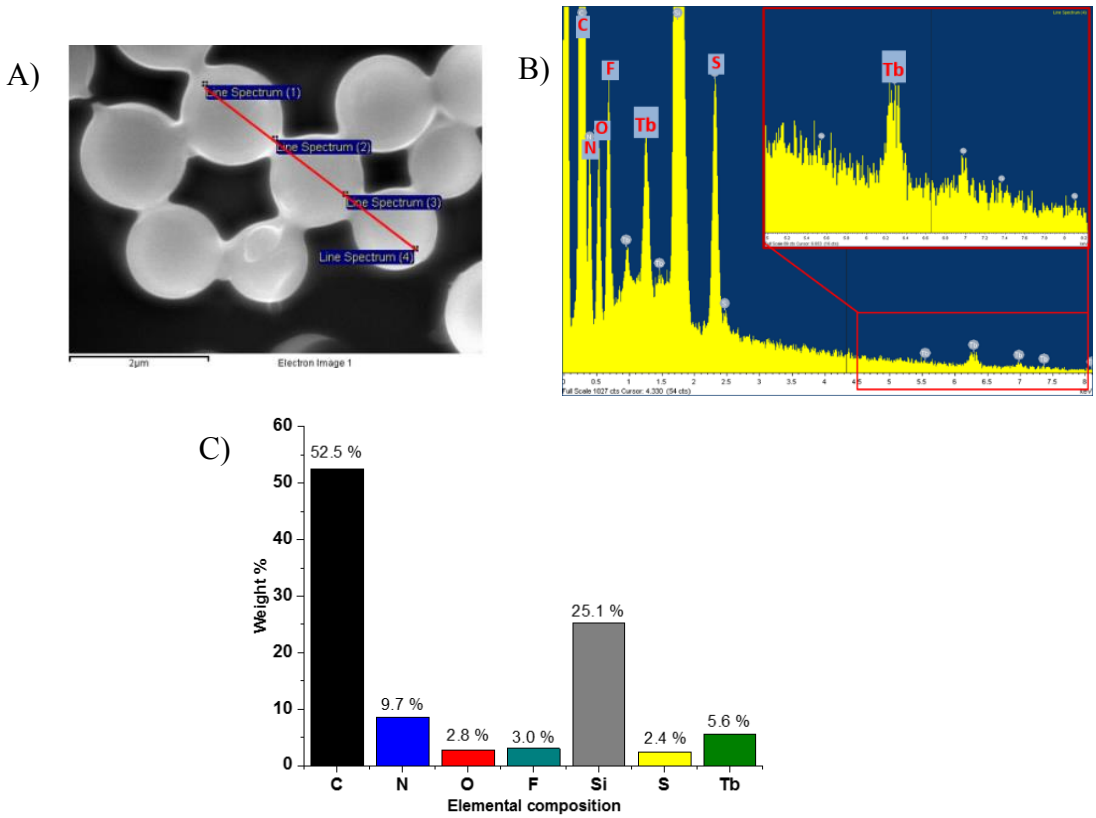

Figure A3.8.7: EDX analysis of the solid Tb(III) based **89S** microspheres chain in line scan mode. A) STEM image of site of interest, scale bar 1 mm. B) EDX spectrum of the same microspheres and C) weight percentage of each element on the site of interest on the surface of sample.

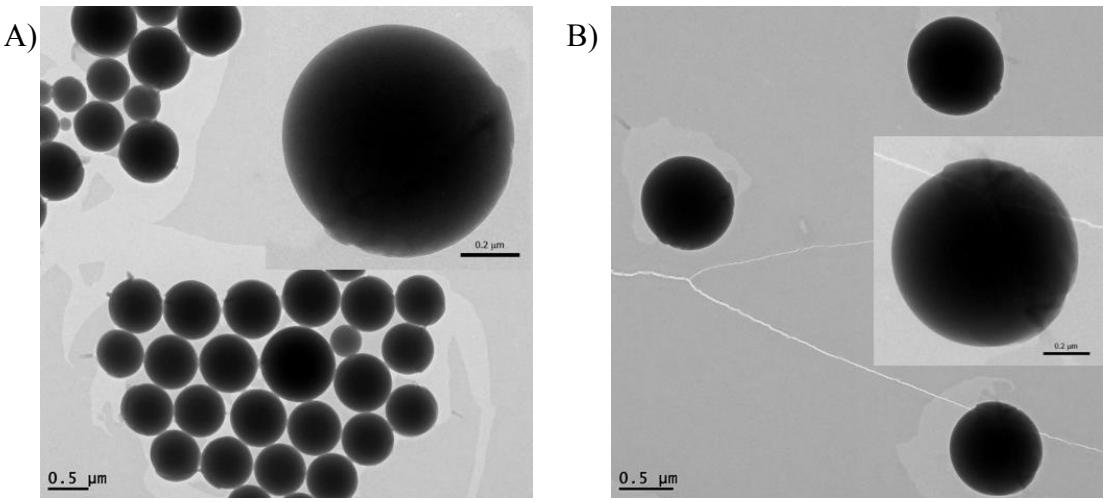

Figure A3.9.1: TEM images of microspheres made of A) **90S** and B) **91S**.

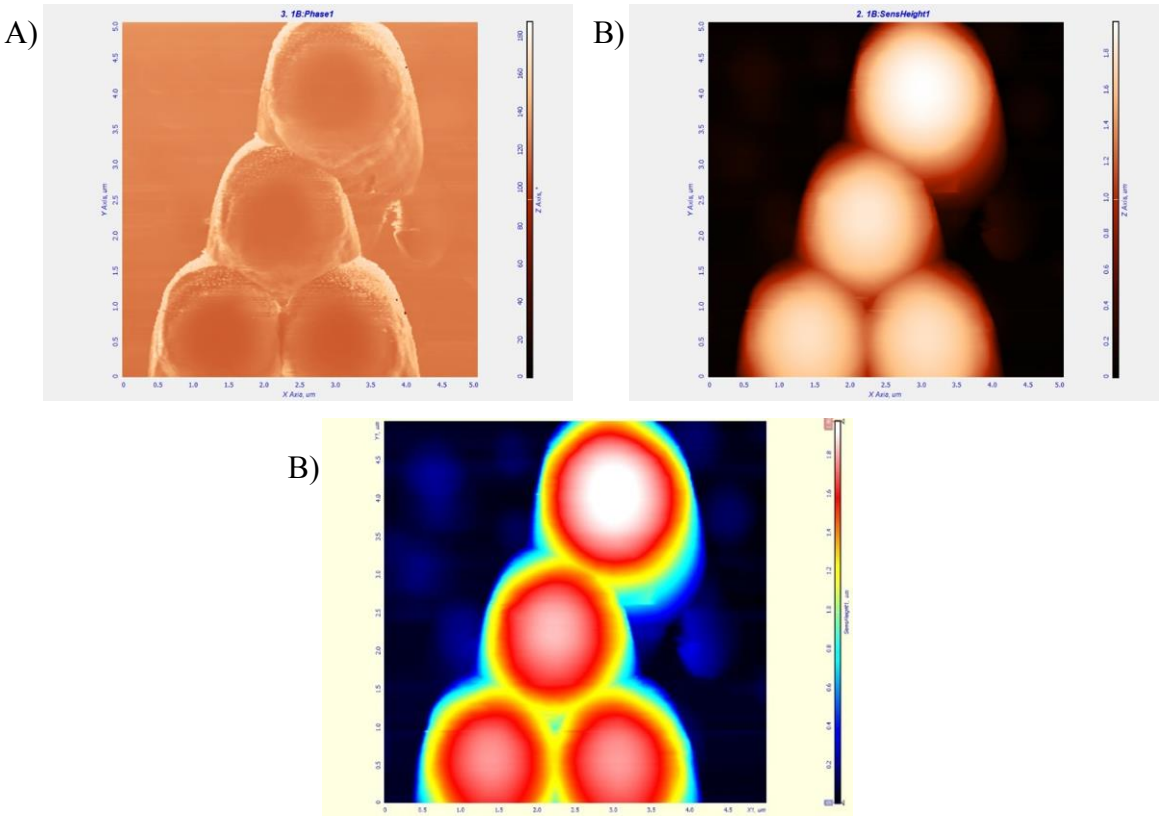

Figure A3.10.1: AFM microscopy of **89S** microspheres: A) Phase contrast image; B) 2D image; C) topography image of the 3D measurements of indicating the height in different colours (blue: 0 – 0.6mm, cyan: 0.6 – 1 mm, yellow: 1 – 1.4 mm, red: 1.4 – 1.7 mm, white: 1.7 – 1.8 mm).

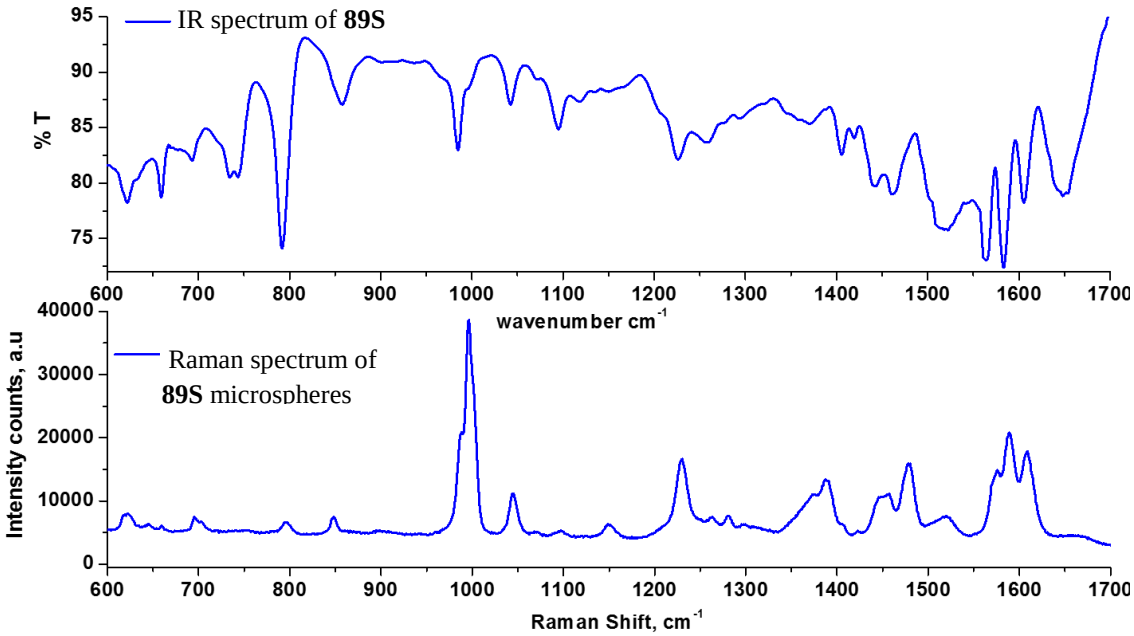

Figure A3.10.2: Comparison of IR of the compound **89S** (top) Raman spectrum of **89S** microspheres (Bottom).

Table A3.11.1: Individual size measurement of **89S** microspheres sample of 3 different concentrations.

Microspheres no.	Size of individual microsphere in diameter (μm) Concentration of microspheres		
	0.1 weight %	0.25 weight %	0.5 weight %
1	0.369	0.942	0.644
2	0.516	0.904	0.762
3	0.503	0.693	0.654
4	0.651	0.616	0.831
5	0.567	0.706	0.632
6	0.56	0.812	0.838
7	0.506	0.912	1.156
8	0.544	0.676	1.14
9	0.399	0.751	0.888
10	0.447	0.833	1.105
11	0.44	1.022	0.734
12	0.475	0.88	1.103
13	0.622	0.87	0.781
14	0.503	0.977	0.628
15	0.505	0.542	1.1092
16	0.687	0.601	0.706
17	0.54	0.587	0.646
18	0.596	0.615	0.732
19	0.488	0.616	0.934
20	0.502	0.498	1.109

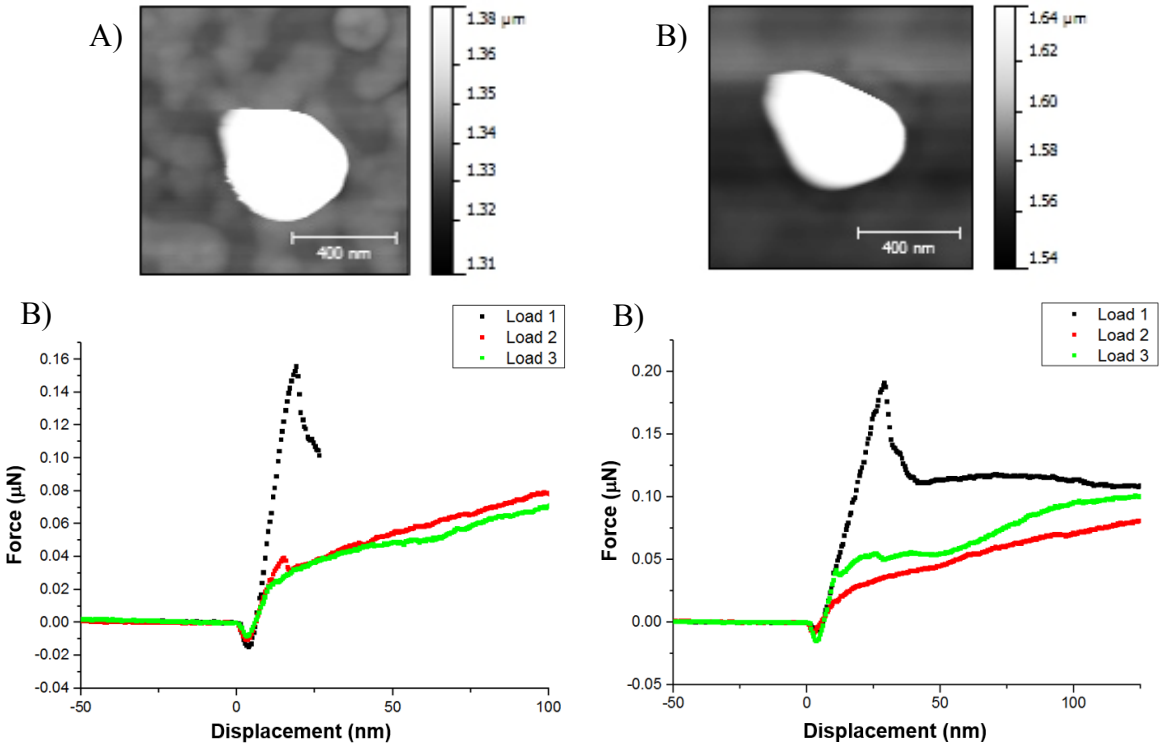

Figure A3.11.1: Results of force displacement measurement performed on different **89S** microspheres: A) and B) AFM images of the microspheres, respectively; C) and D) Force displacement curves obtained from respective microspheres, showing that 0.16 µN and 0.19 µN force required to move the particles for the first time of approx. 500nm size.

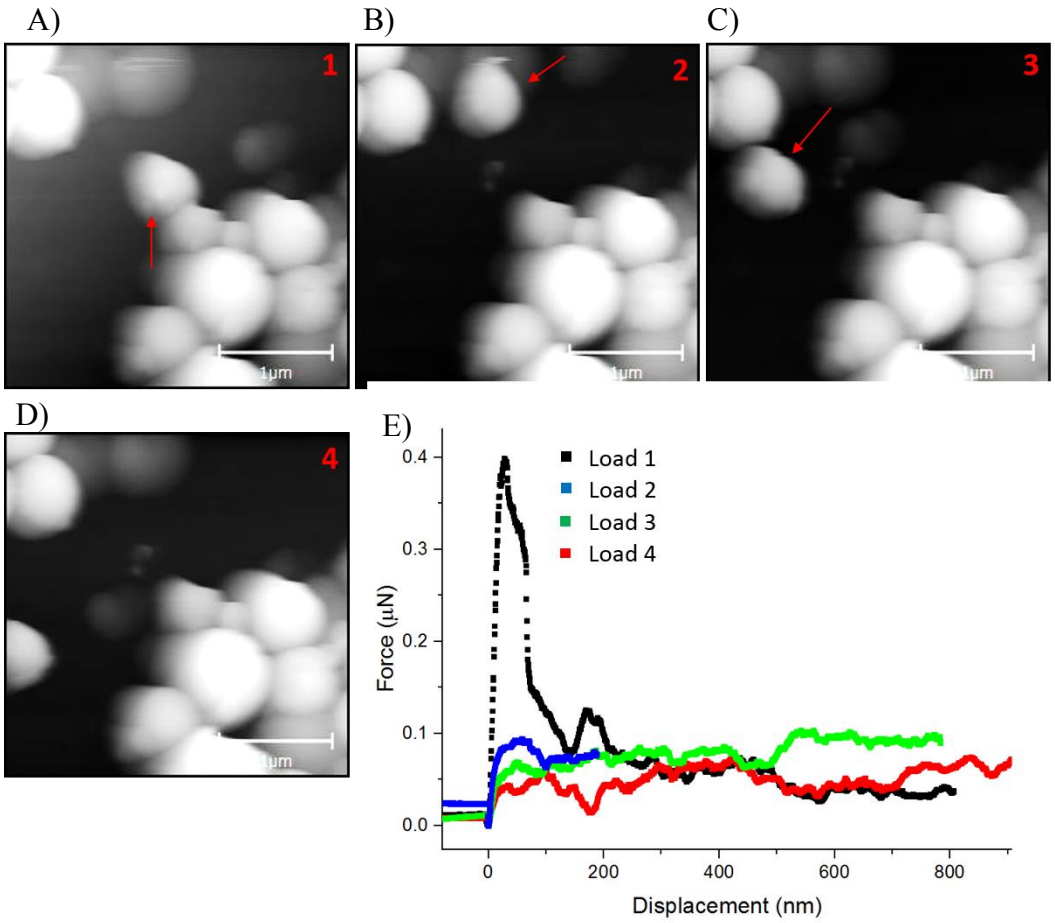

Figure A3.11.2: Force displacement measurements performed on **90S** microspheres. A) – D) AFM images showing the particles moved on applying lateral loads. E) Force displacement curves showing that 0.41 µN force required to move the particles for the first time of approx. 700nm size.

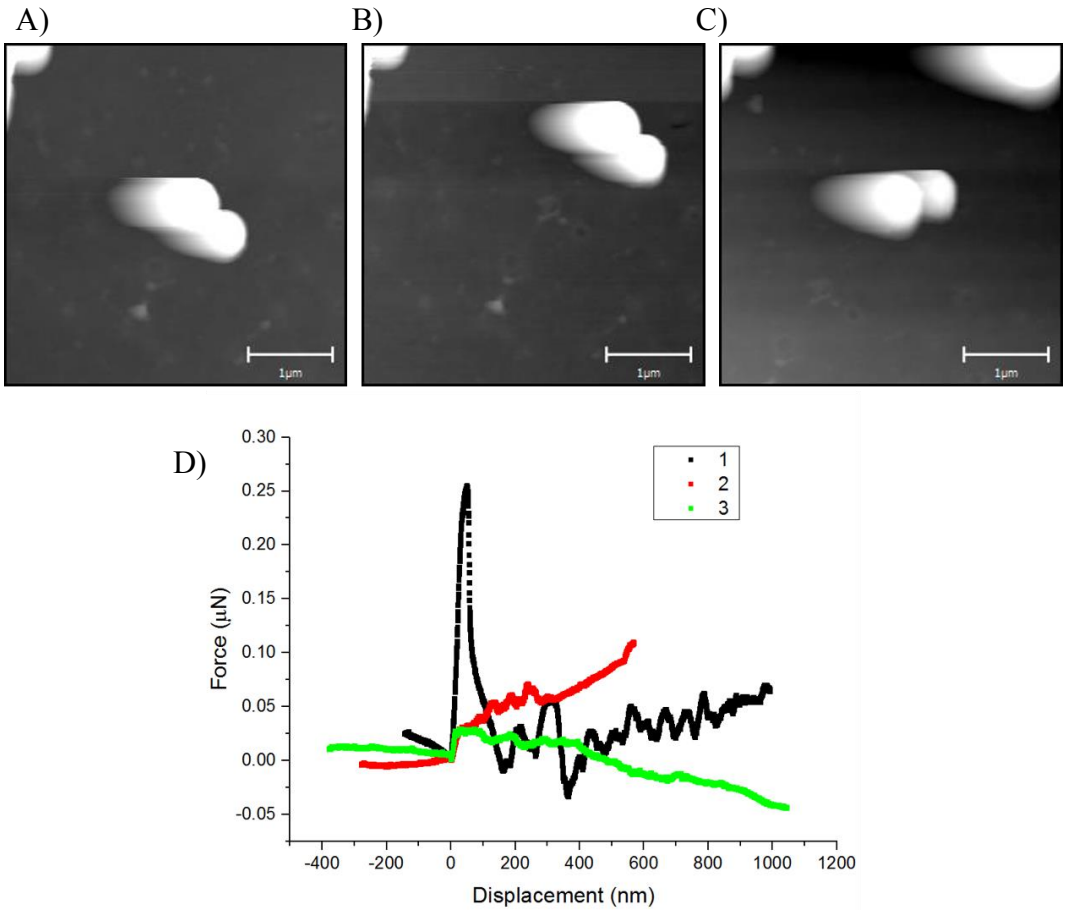

Figure A3.11.3: Force displacement measurements performed on **91S** microspheres. A) – C) AFM images showing the particles moved on applying lateral loads. D) Force displacement curves showing that 0.27 µN force required to move the particles for the first time of approx. 500nm size.

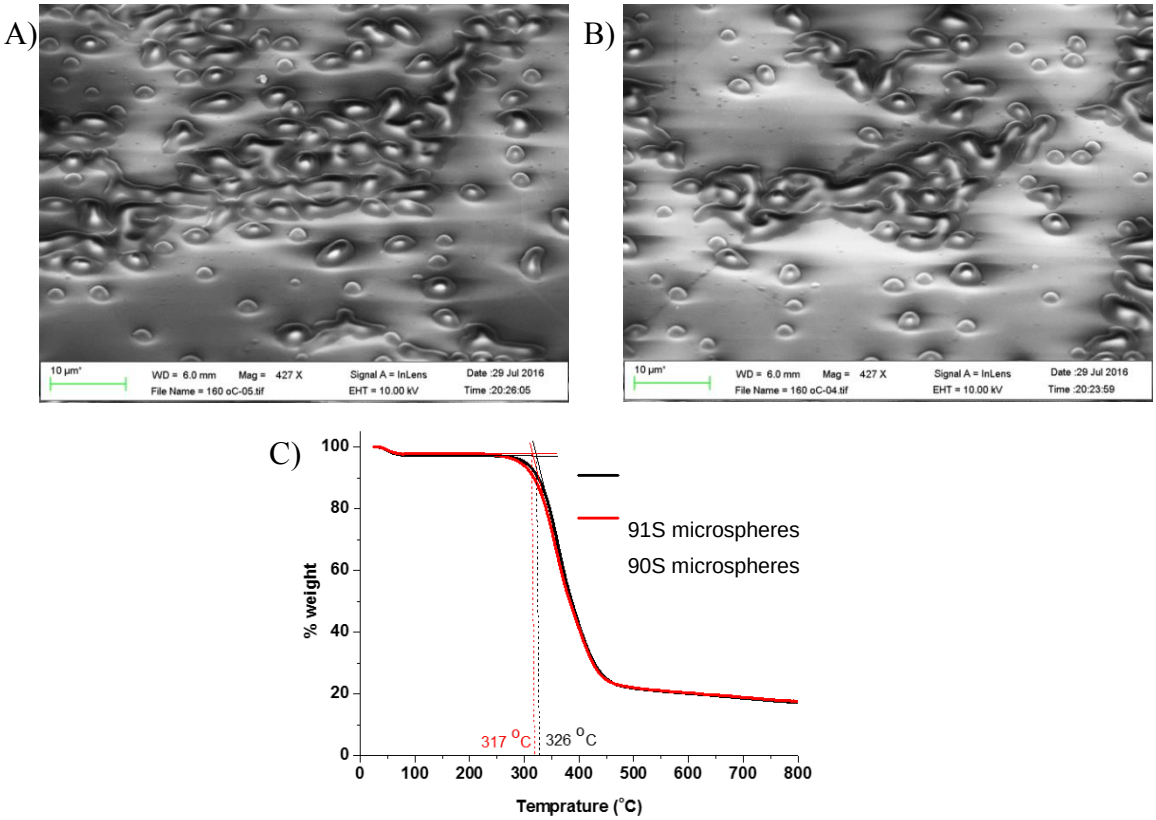

Figure A3.12.1: Thermal stability of the microspheres: SEM image of A) **90S** solid microspheres melted at 160 ºC; B) **91S** solid microspheres melted at 165 ºC; C) TGA curves of the **90S** (red) and **91S** (black) solid microspheres showing the thermal-chemical decomposition at 317 ºC and 326 ºC.

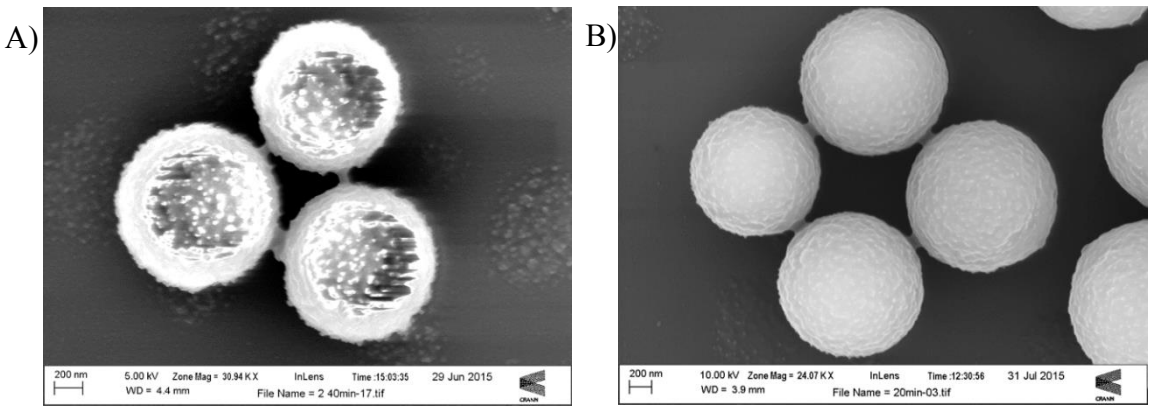

Figure A3.13.1: Bridging between the **89S** microspheres: A) three microspheres interconnected in the shape of triangle; B) four microspheres interconnected in the shape of square.

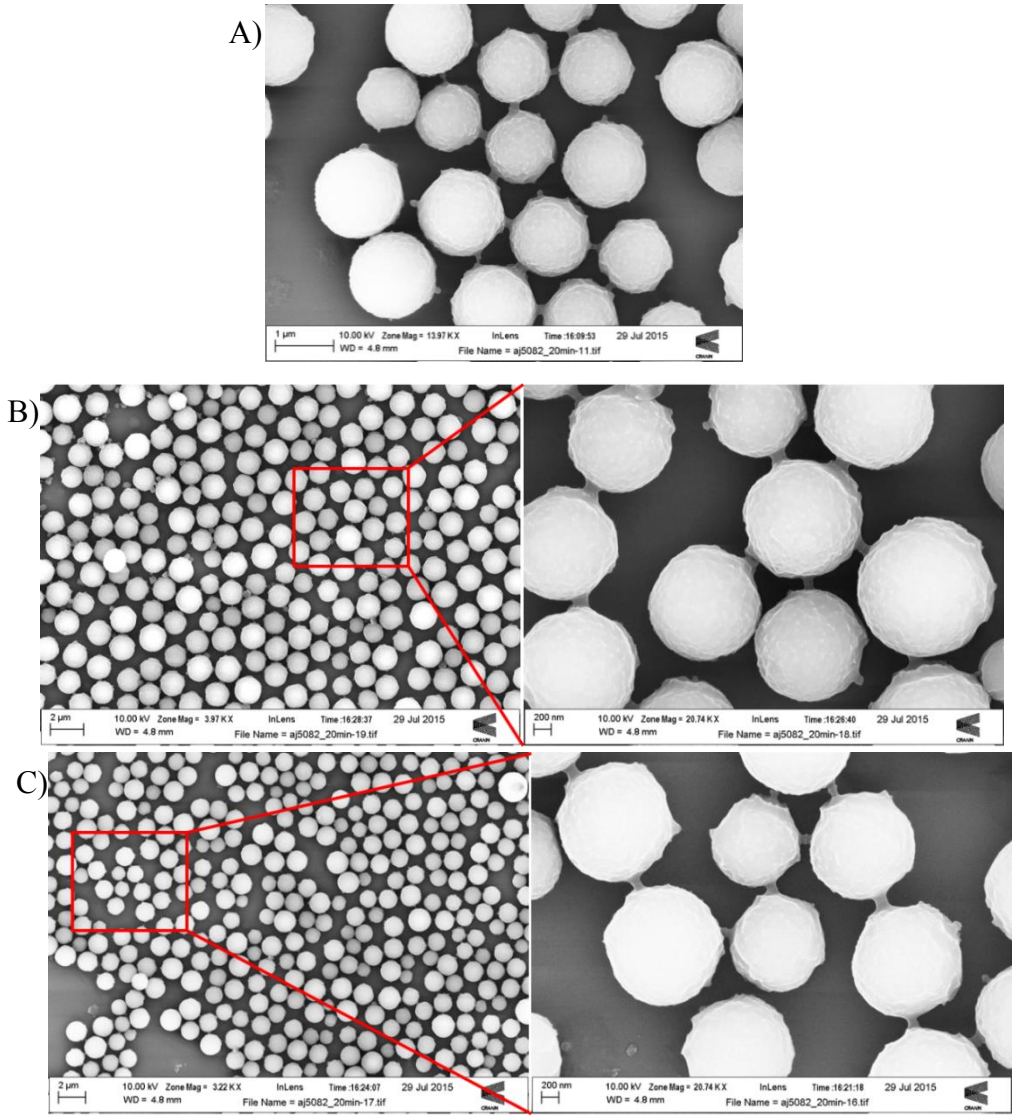

Figure A3.13.2: Bridging between the A) **89R,** B) **90S**) and C) **91S** microspheres.

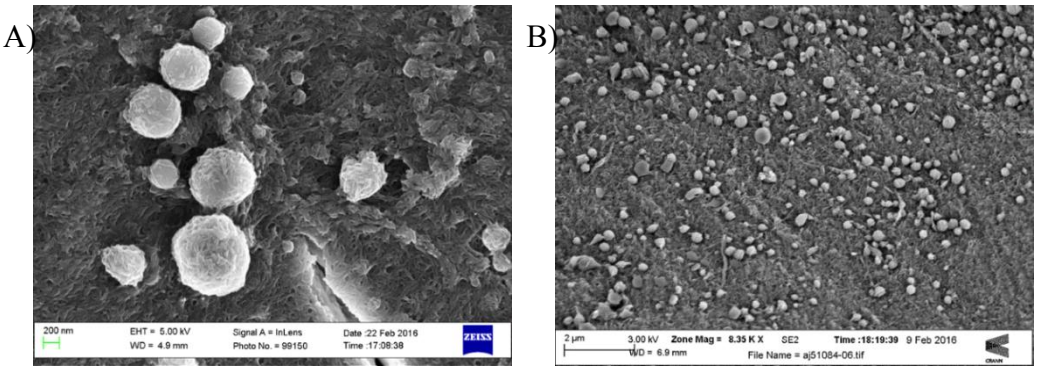

Figure A3.15.1: SEM of: A) **88** and **89R** mixed gel (Sample 3) and B) **88** and **89S** microspheres mixed gel (Sample 4) (see table 3.7 for sample number)

Appendix 4

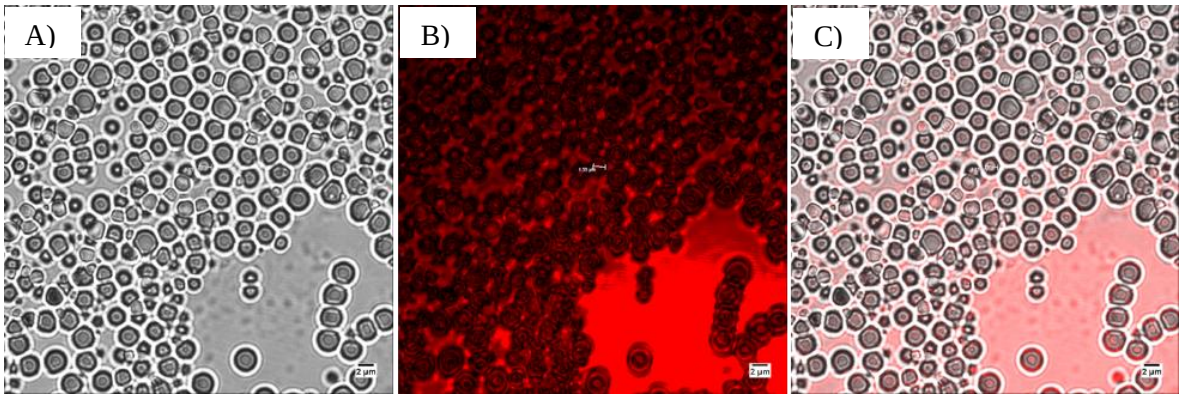

Figure A4.1.1: LSCM images of **89R** microspheres in A) 488 nm transmittance, B) 458 nm reflectance modes and C) A and B images merged.

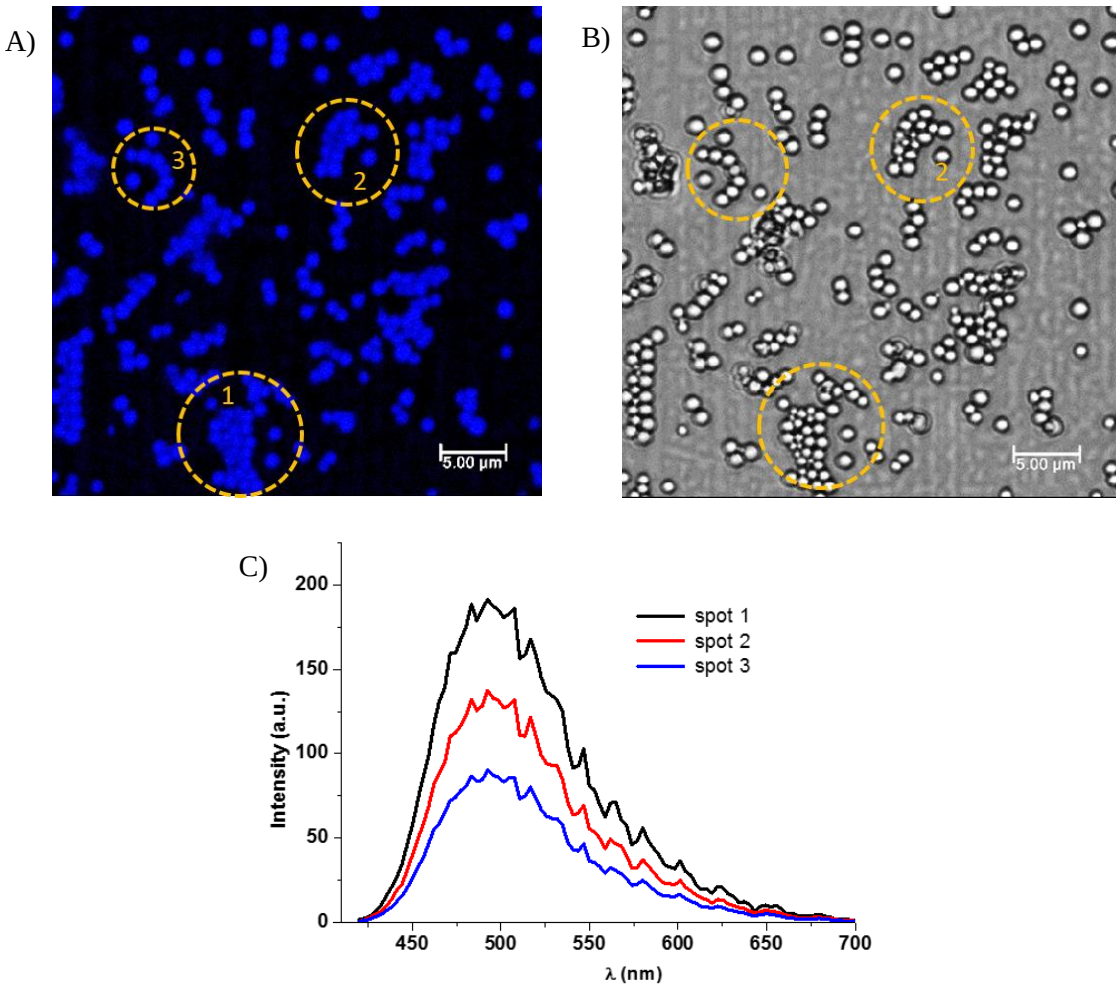

Figure A4.2.1: A) LSCM images of **89S** microspheres upon excitation at λ_{nm} = 405 nm, B) phase contrast image of the same sample and C) fluorescence spectrum of **89S** microspheres in different spots of the sample showing no change in emission maximum wavelength (λ_{max}).

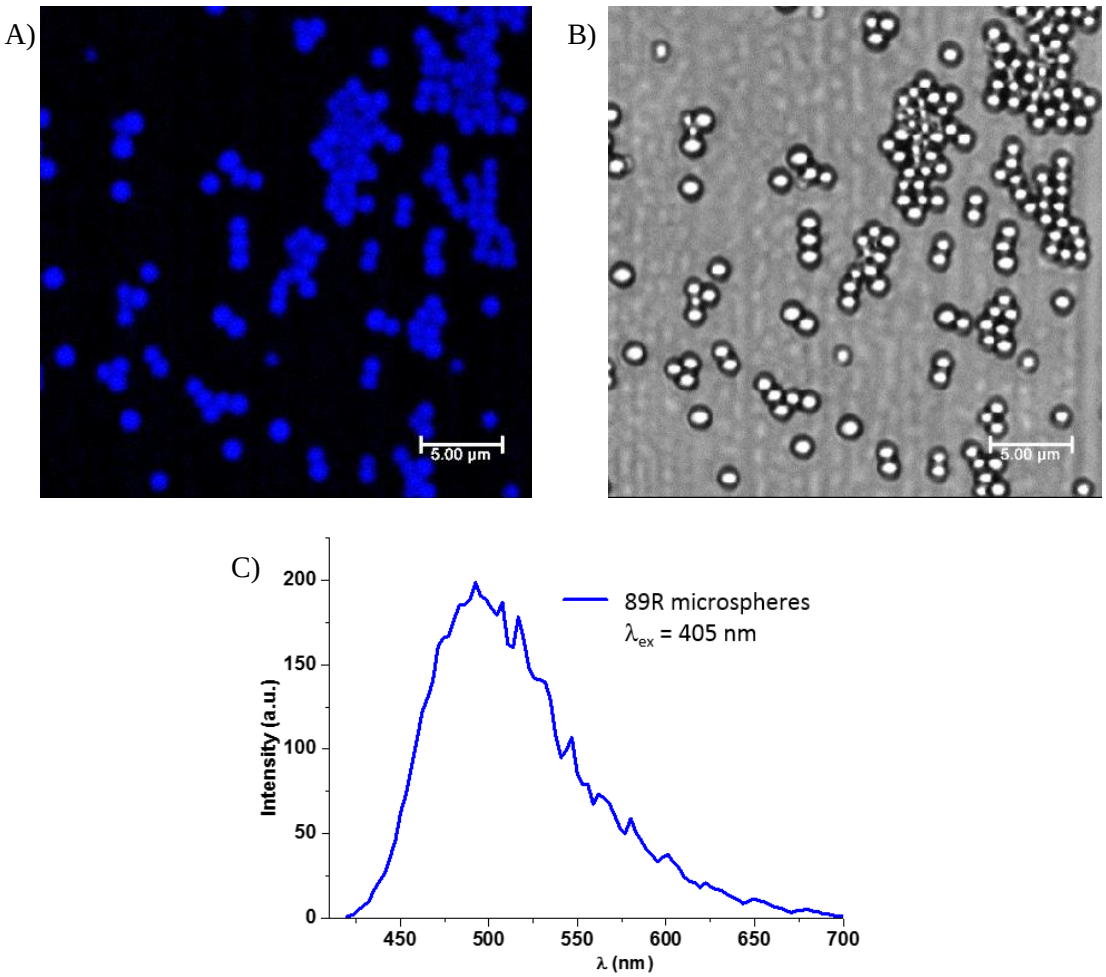

Figure A4.2.2: A) and B) LSCM images of **89R** microspheres upon excitation at λ_{nm} = 405 nm, and its phase contrast image and C) Fluorescence spectrum of **89R** microspheres.

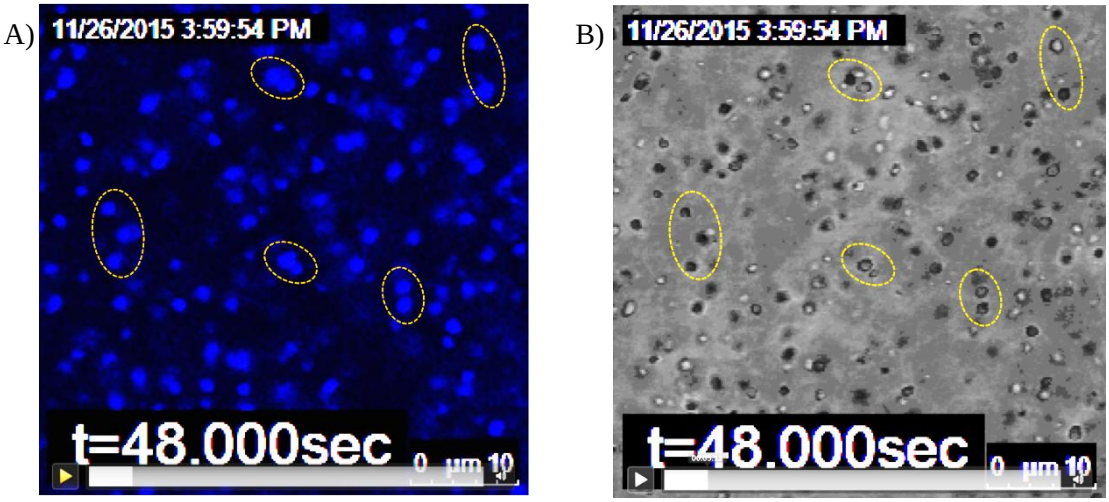

Figure 4.3.1: A) LSCM image of **89R** microspheres in solution media (λ_{ex} = 405 nm) and B) phase contrast image of the same sample

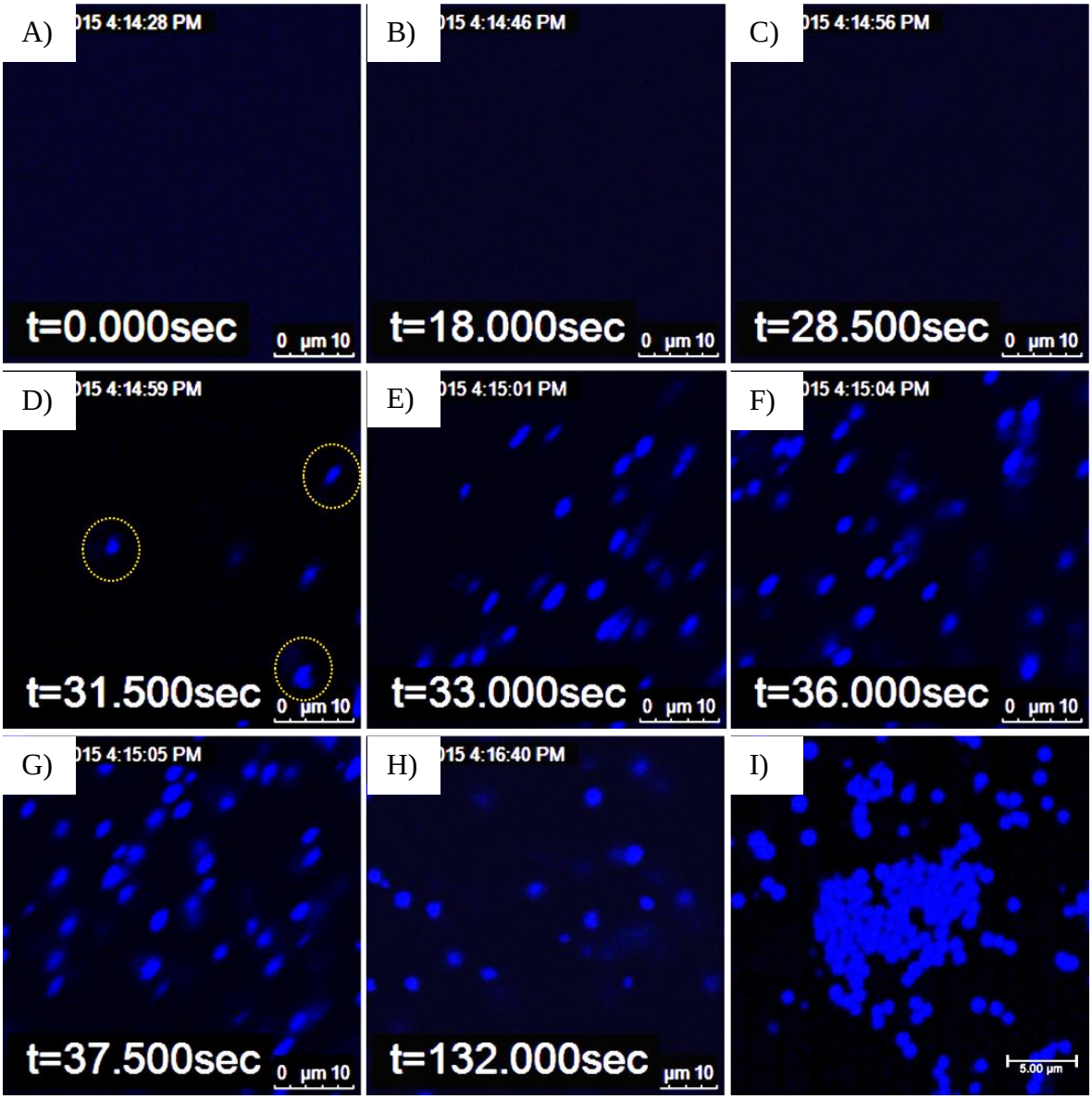

Figure A4.3.2: LSCM images showing the formation of **89S** microspheres in CH_3CN/H_2O (6:4) λ_{ex} = 405 nm. A) – H) Snapshots taken from the movie recorded upon cooling the hot solution of **89S** in CH_3CN/H_2O at different time intervals, scale bar 10 µm. I) LSCM image of **89S** microspheres after drying the same solution, scale bar 5 µm.

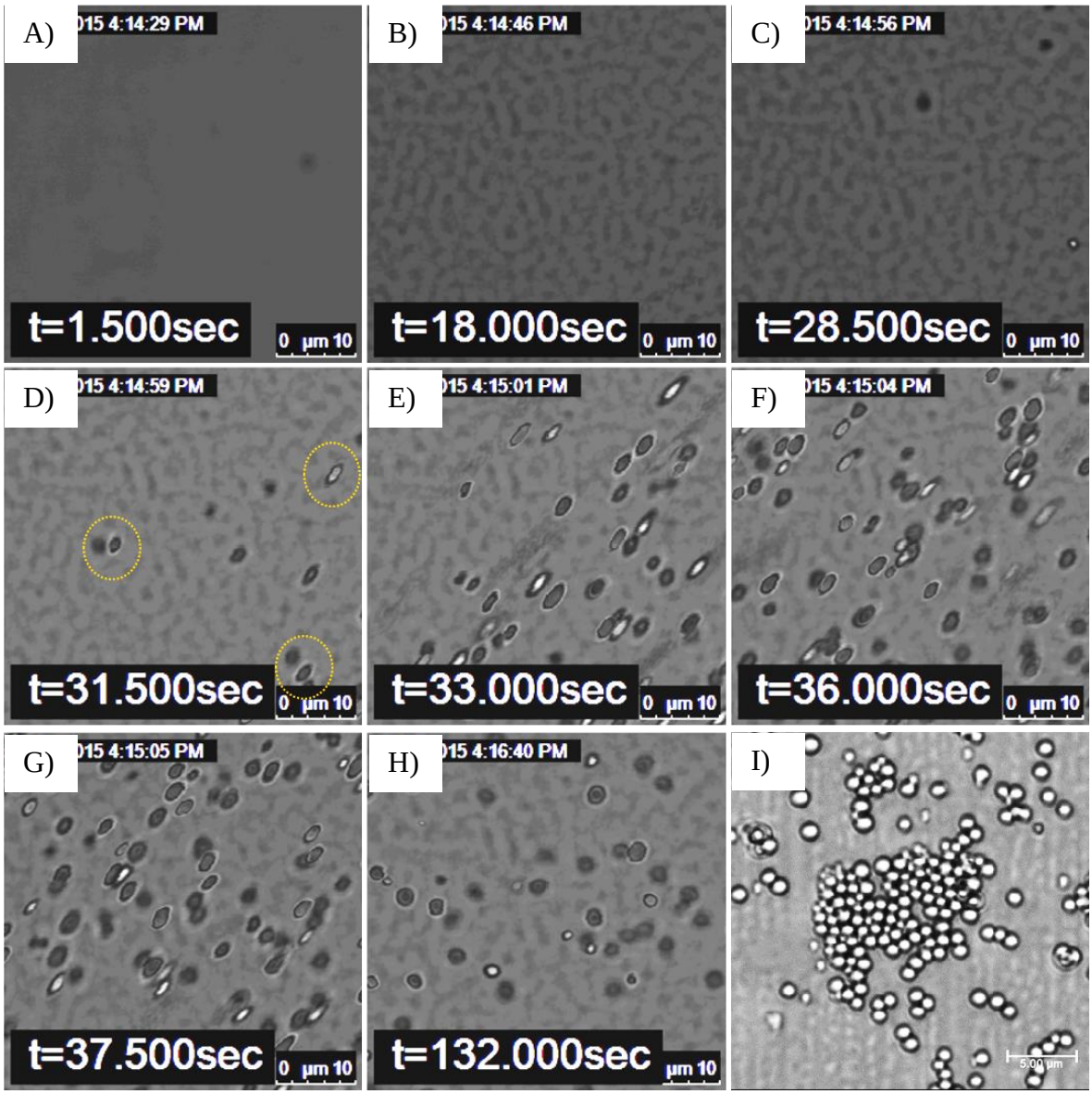

Figure A4.3.3: LSCM phase contrast images showing the formation of **89S** microspheres in CH_3CN/H_2O (6:4) λ_{ex} = 405 nm. A) – H) Snapshots taken from the movie recorded upon cooling the hot solution of **89S** in CH_3CN/H_2O at different time intervals, scale bar 10 µm. I) LSCM image of **89S** microspheres after drying the same solution, scale bar 5 µm.

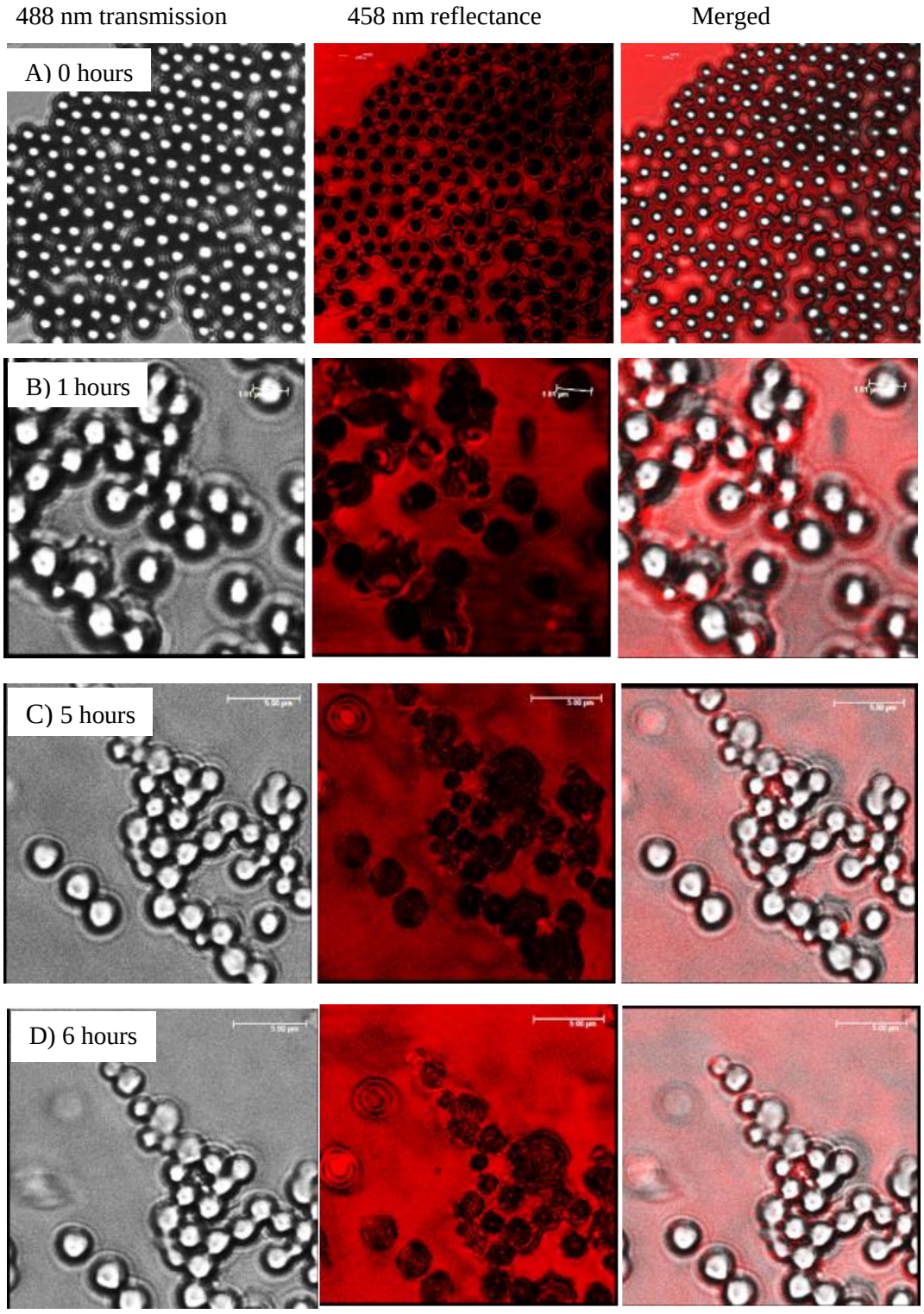

Figure A4.4.1: LSCM images of **89S** microspheres in H_2O. A) – D) Images taken at different time intervals in 488 nm transmission and 458 nm reflectance modes. scale bar 5 μm. continued in next page.

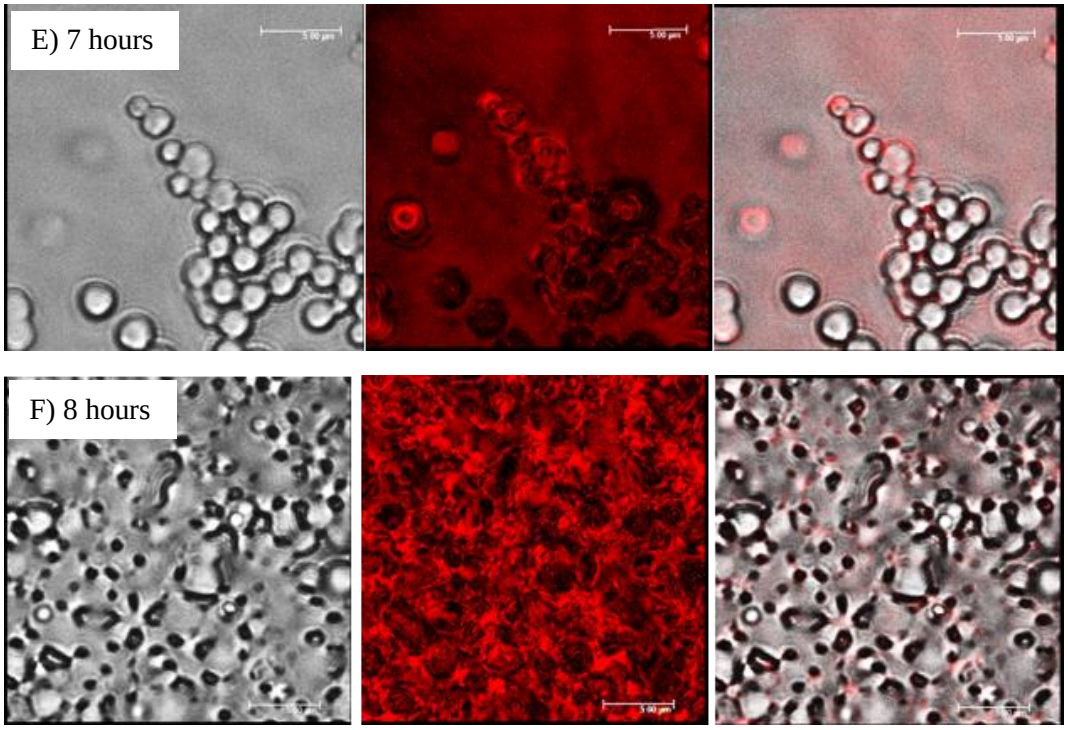

Figure A4.4.1: LSCM images of **89S** microspheres in H_2O at different time intervals. A) – F) Images taken at 0, 1, 5, 6, 7 and 8 hours of time intervals, respectively in 488 nm transmission and 458 nm reflectance modes. scale bar 5 μm.

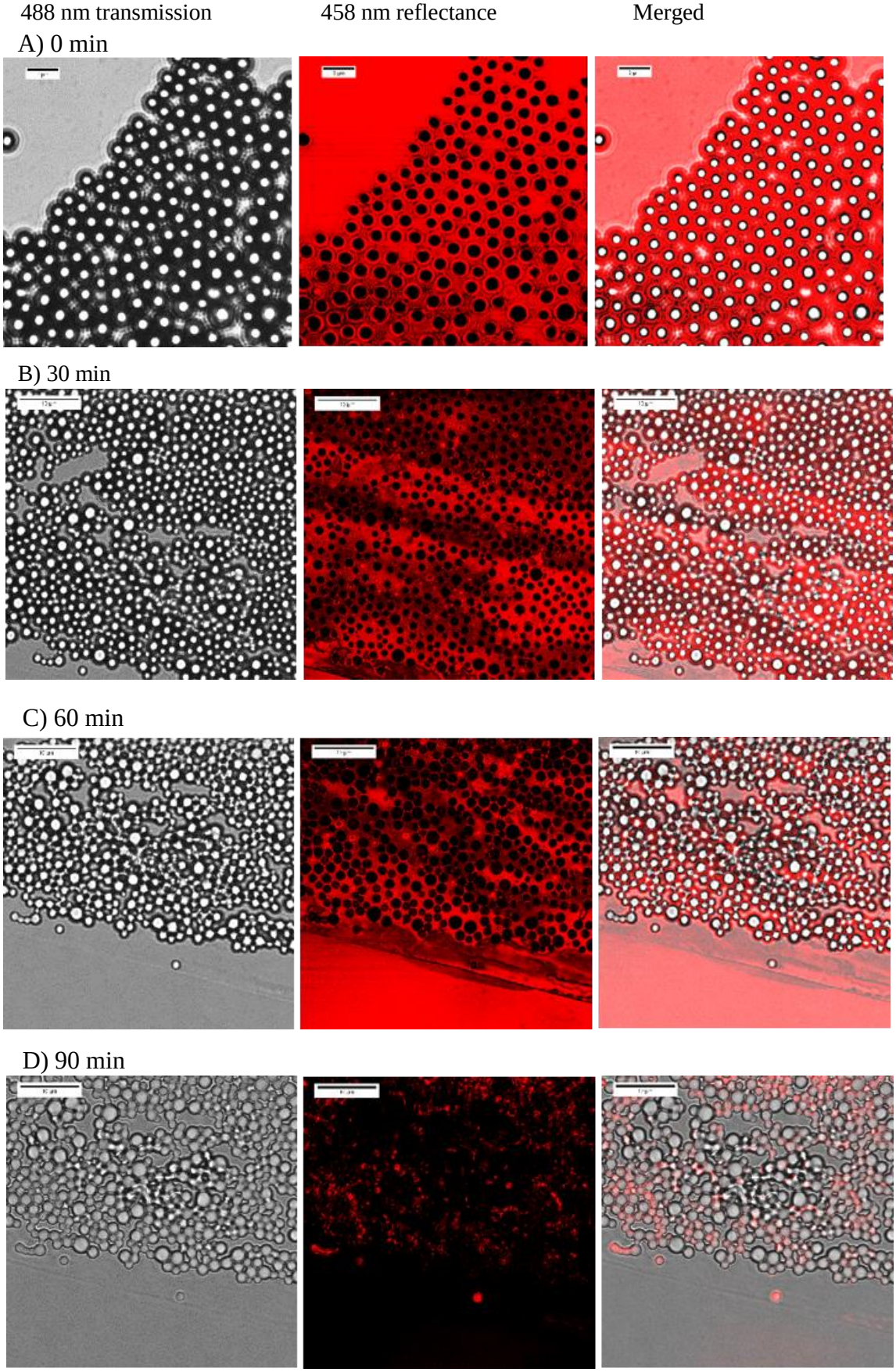

Figure A4.5.1: LSCM images of **89S** microspheres in 1% urea solution showing the disassembly process at different time intervals. Continued in next page.

E) 120 min

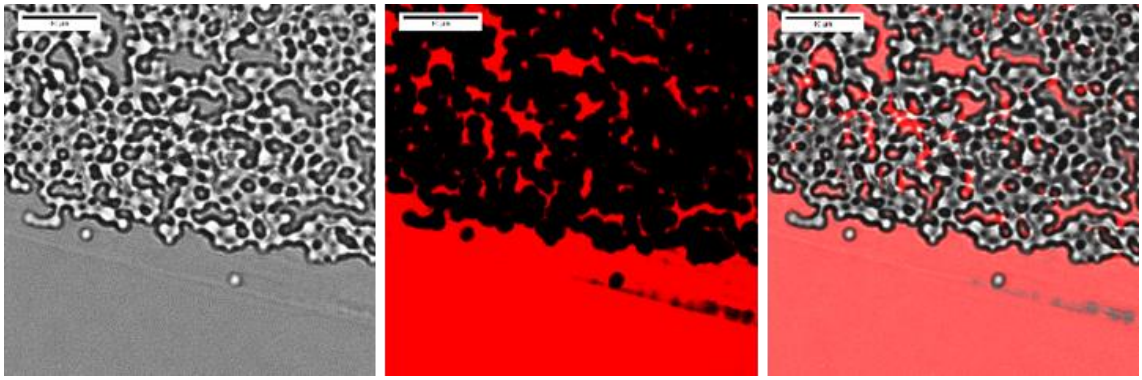

F) 150 min

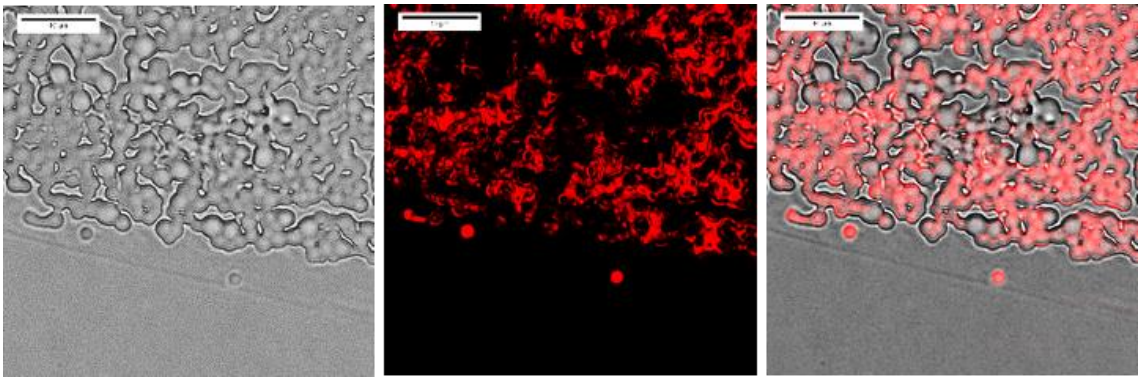

Figure A4.5.1: LSCM images of **89S** microspheres in 1% urea solution showing the disassembly process at different time intervals. A) – F) Images taken at 0, 30, 60, 90, 120 and 150 minutes in 488 nm transmission and 458 nm reflectance modes. scale bar 10 μm.

488 nm transmission 458 nm reflectance Merged

A) 0 min

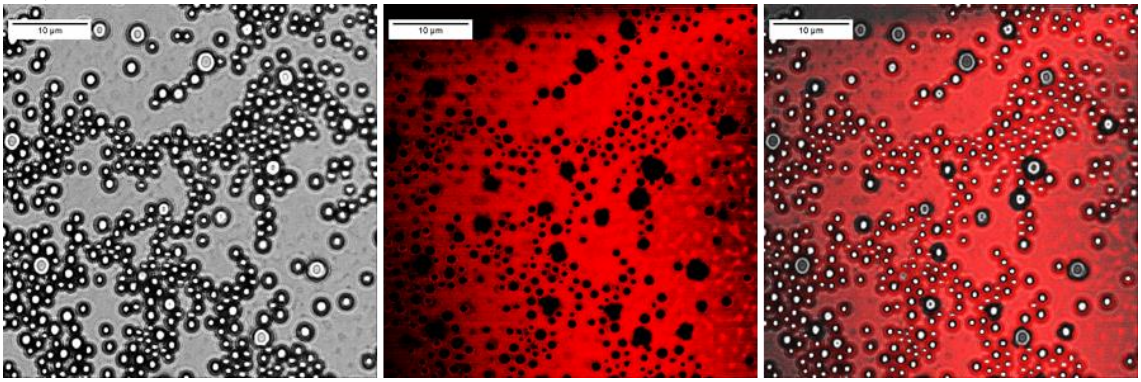

B) 20 min

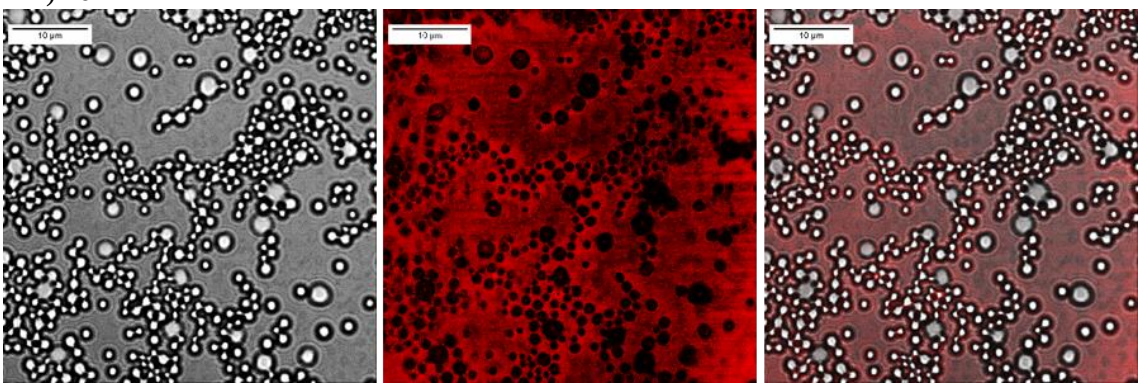

C) 30 min

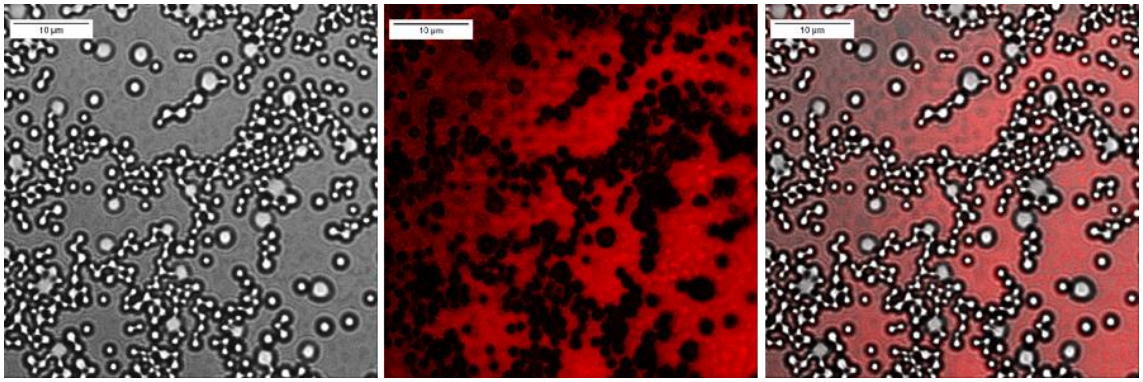

Figure A4.5.2: LSCM images of **89S** microspheres in 10% urea solution showing the disassembly process at different time intervals. Continued in next page.

D) 40 min

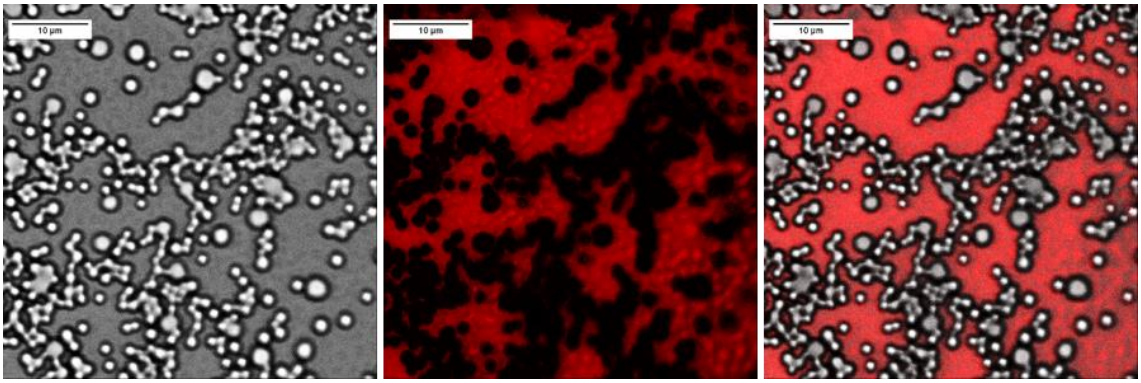

E) 50 min

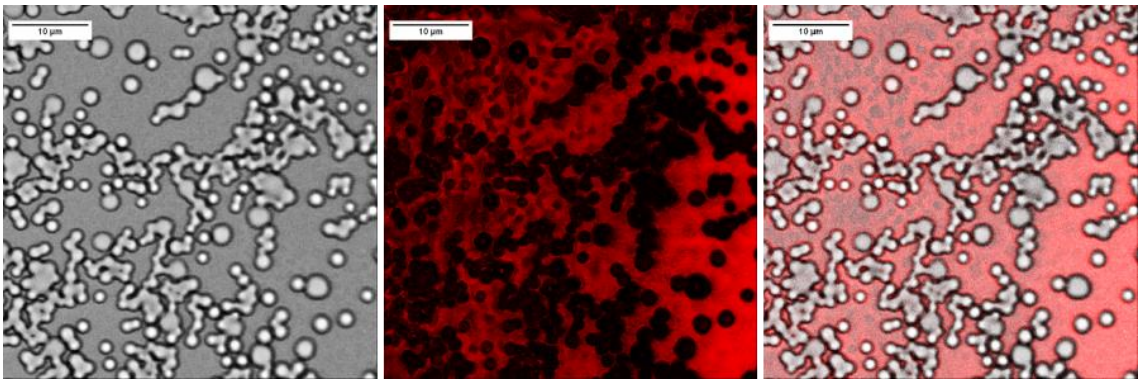

F) 60 min

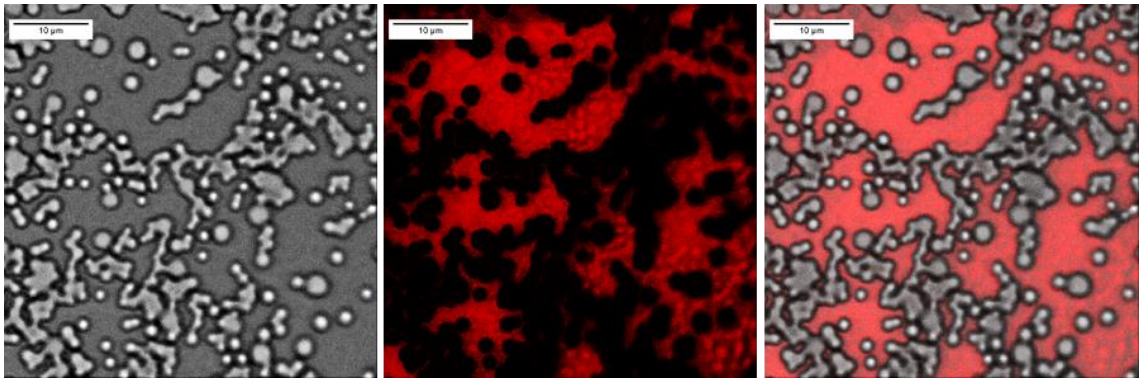

Figure A4.5.2: LSCM images of **89S** microspheres in 10% urea solution showing the disassembly process at different time intervals. A) – F) Images taken at 0, 20, 30, 40, 50 and 60 minutes in 488 nm transmission and 458 nm reflectance modes. scale bar 10 μm.

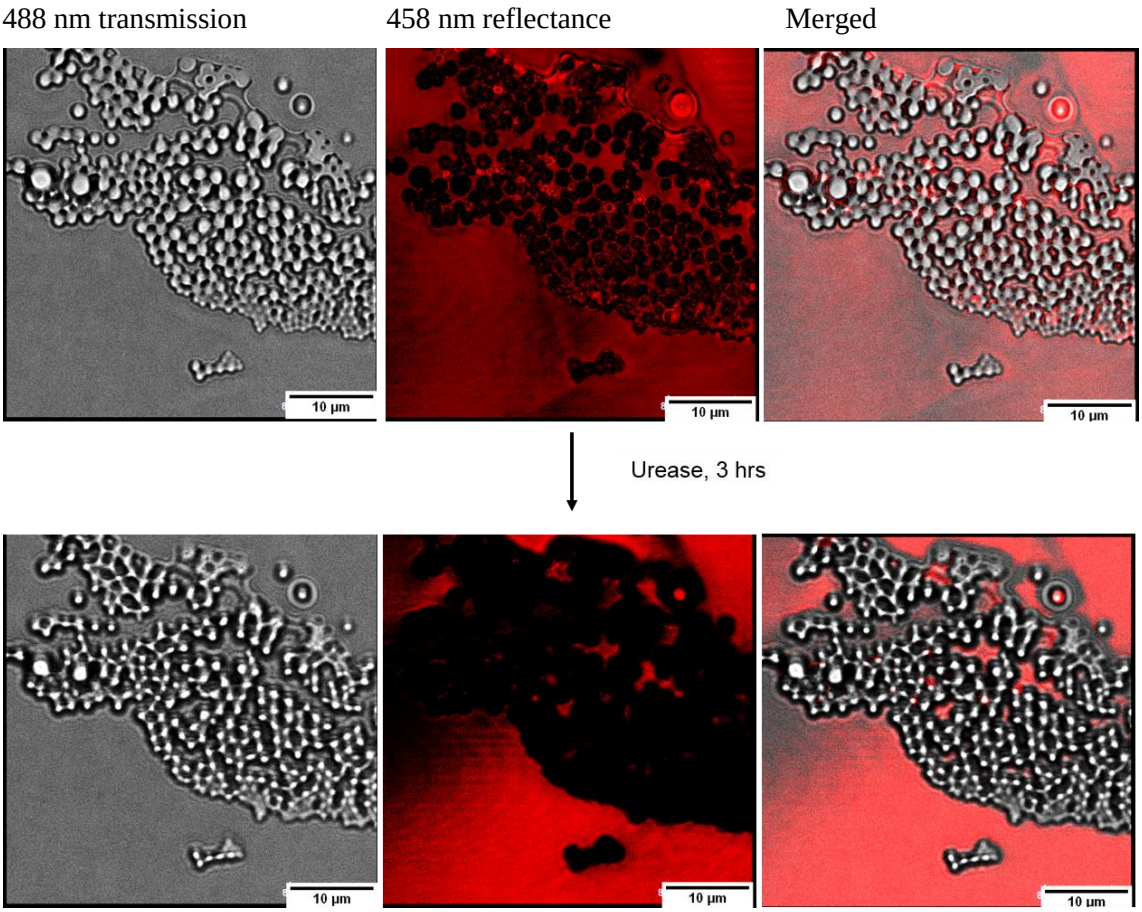

Figure A4.5.3: LSCM images of disassembled **89S** microspheres. Before and after 3 hours of urease addition.

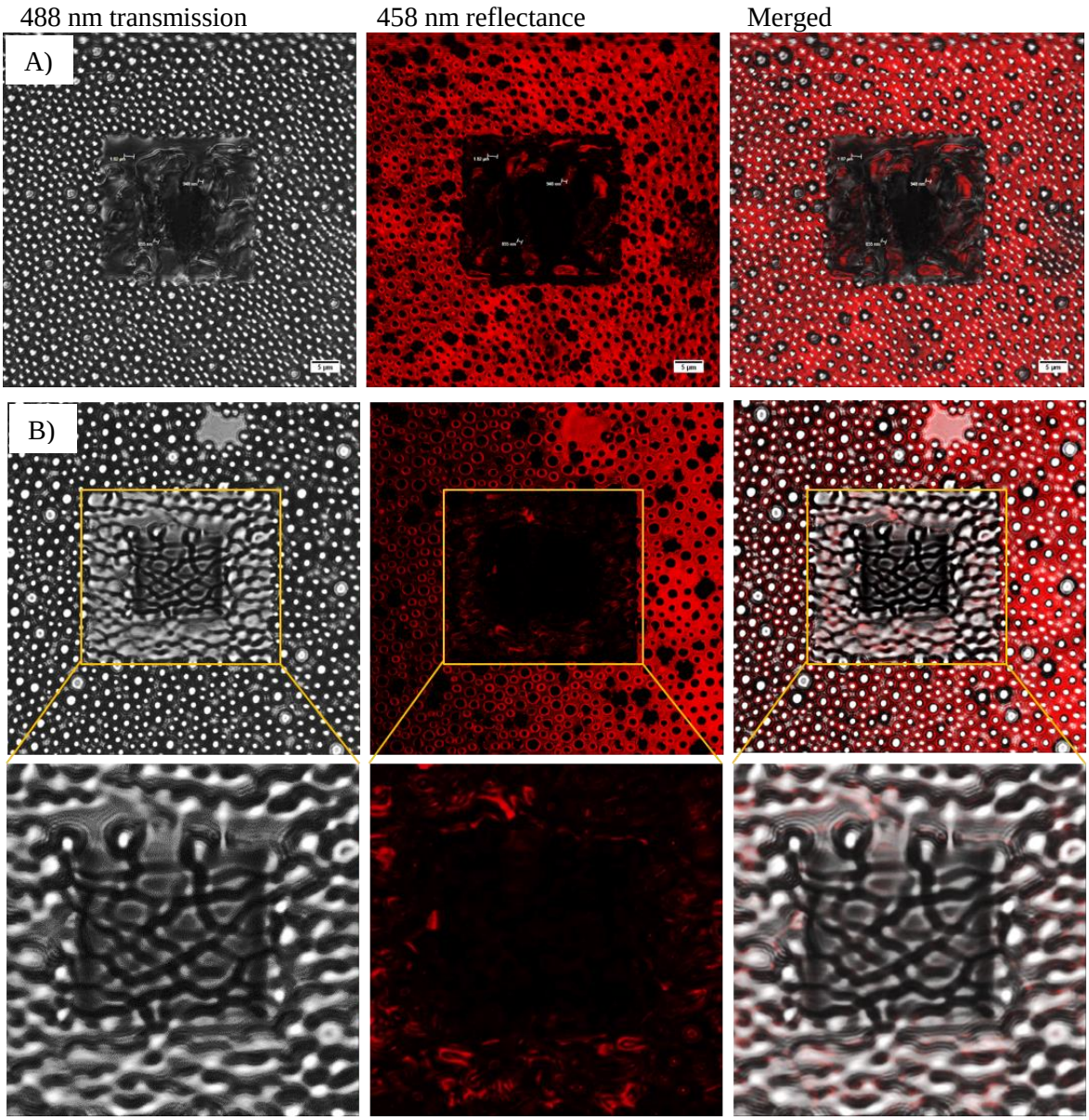

Figure A4.6.1: LSCM images of **89S** microspheres upon 355 nm UV irradiation: A) After 355 nm UV irradiation, scale bar 5 μm, B) After irradiating second time.

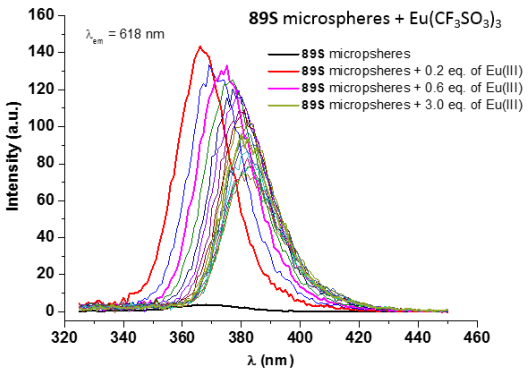

Figure A4.7.1: Excitation spectrum of the titration performed upon addition of $Eu(CF_3SO_3)_3$ 0 → 3 equiv.) to the solution of **89S** microspheres (1.55×10^{-3} M) in 6:4 CH_3CN/H_2O, λ_{em} = 618 nm.

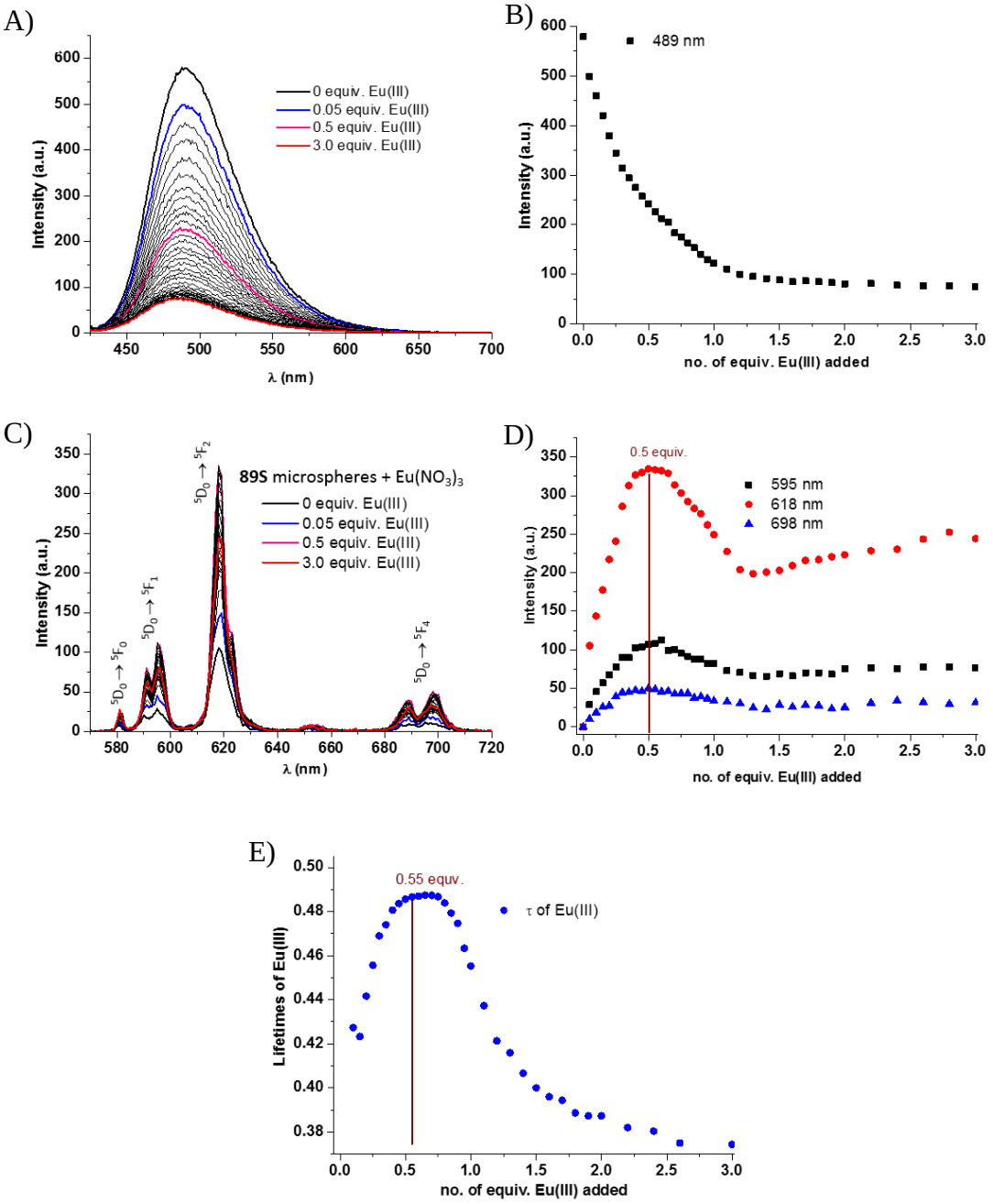

Figure A4.7.2: A) – B) Fluorescence spectra of **89S** microspheres (1.55×10^{-3} M) upon addition of $Eu(NO_3)_3$ (0 → 3 equiv.) in 6:4 CH_3CN/H_2O (λ_{ex} = 380 nm) and its binding isotherms showing the changes at 489 nm. C) – D) Phosphorescence spectra recorded from the same solution and its binding isotherms showing the changes in Eu(III) centred emission at 595, 618 and 698 nm (λ_{ex} = 380 nm) and E) variation in the Eu(III) centred luminescence lifetime during the course of $Eu(NO_3)_3$ addition to **89S** microspheres. These experiments were repeated 3 times and same results were obtained.

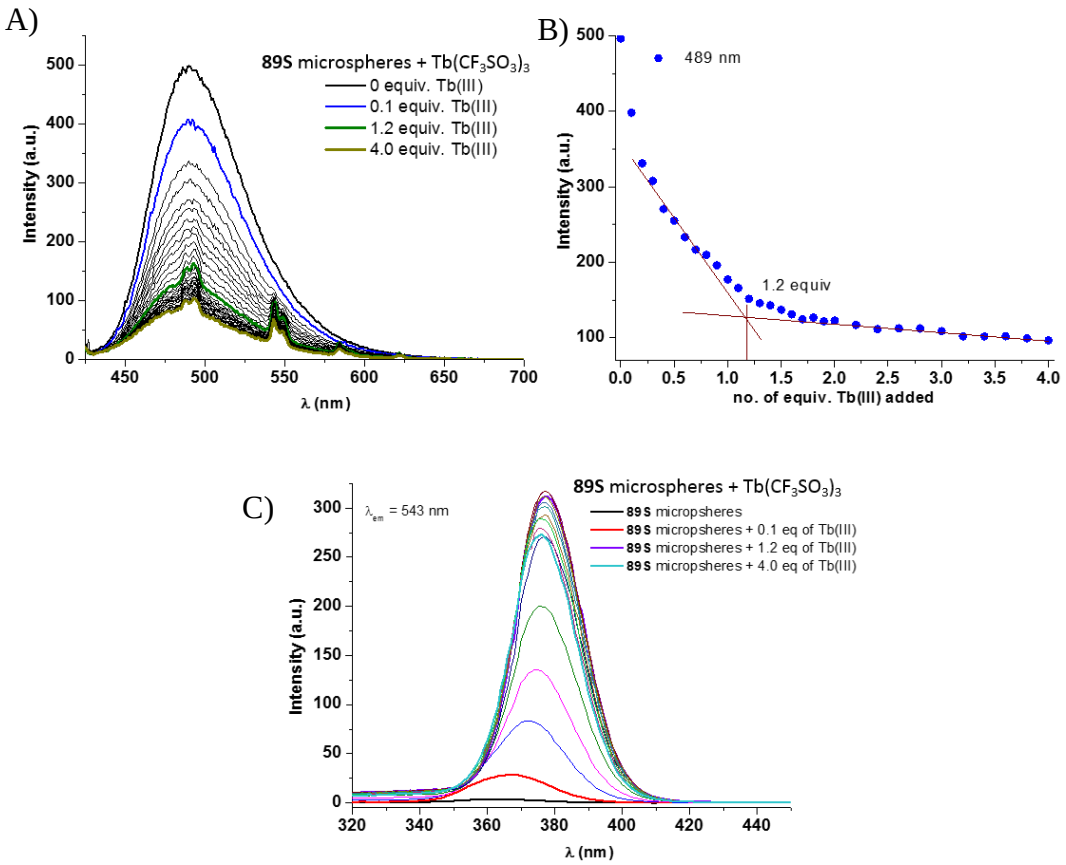

Figure A4.7.3: A) Fluorescence spectra of **89S** microspheres (1.55×10^{-3} M) upon addition of $Tb(CF_3SO_3)_3$ ($0 \rightarrow 3$ equiv.) in 6:4 CH_3CN/H_2O (λ_{ex} = 377 nm), B) binding isotherms showing the changes at 489 nm and C) Excitation spectrum of the titration performed upon addition of $Tb(CF_3SO_3)_3$ $0 \rightarrow 3$ equiv.) to the solution of **89S** microspheres (1.55×10^{-3} M) in 6:4 CH_3CN/H_2O, λ_{em} = 543 nm.

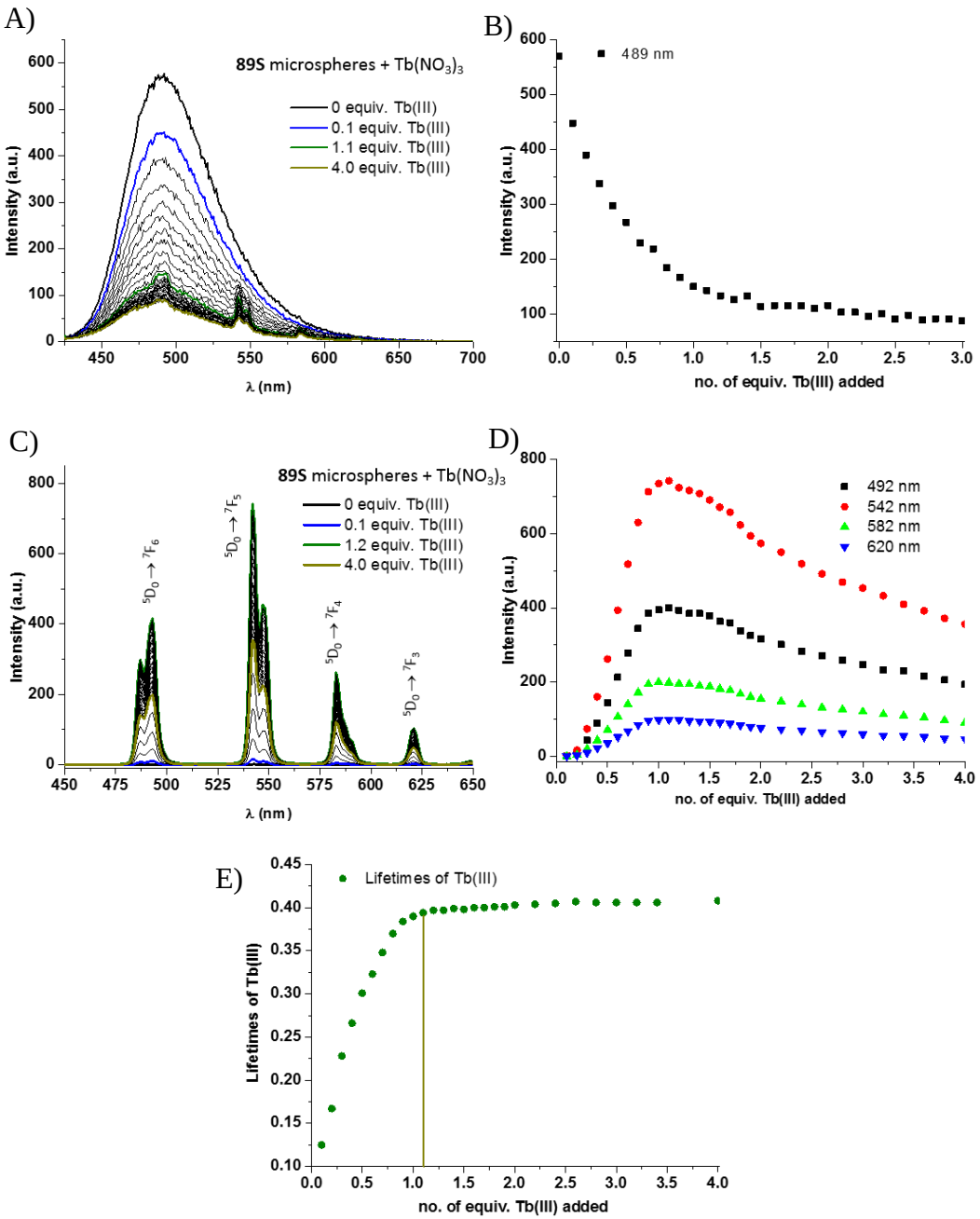

Figure A4.7.4: A) – B) Fluorescence spectra of **89S** microspheres (1.55×10^{-3} M) upon addition of $Tb(NO_3)_3$ ($0 \rightarrow 3$ equiv.) in 6:4 CH_3CN/H_2O (λ_{ex} = 377 nm) and its binding isotherms showing the changes at 489 nm. C) – D) Phosphorescence spectra (λ_{ex} = 377 nm) recorded from the same solution and its binding isotherms showing the changes in Tb(III) centred emission at 492, 542, 582 and 620 nm and E) variation in the Tb(III) centred luminescence lifetime during the course of $Tb(NO_3)_3$ addition to **89S** microspheres. These experiments were repeated 3 times and same results were obtained.

A) Channel 1: 400 – 450 nm

B) Channel 2: 500 – 550 nm

C) Channel 3: 570 – 720 nm

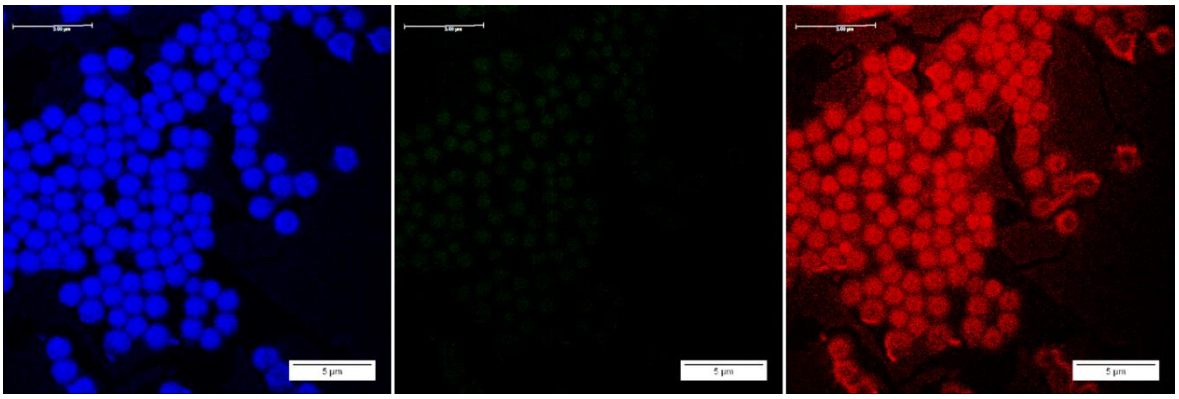

D) OM image

E) OM and Channel 1 merged

F) OM and Channel 3 merged

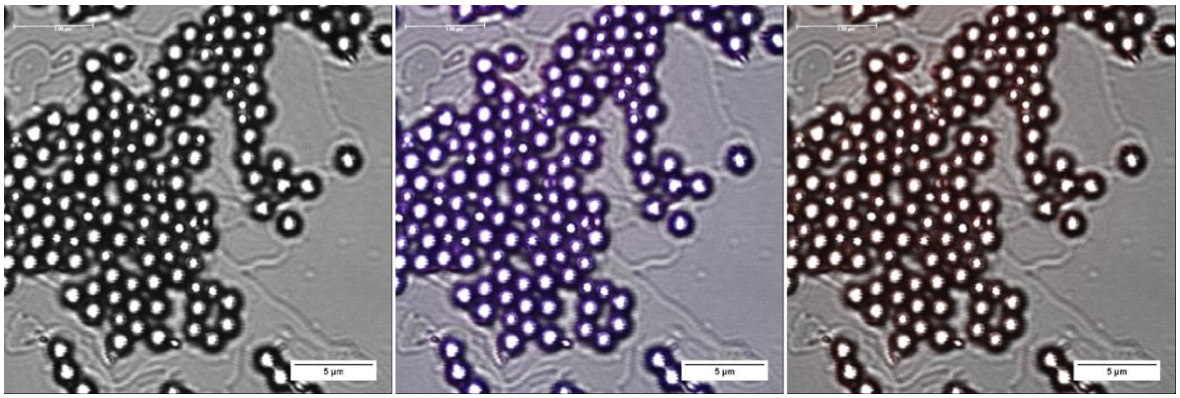

Figure A4.8.1: LSCM images of Eu(III)-**89S** microspheres. A) – C) Eu(III)-**89S** microspheres in three different Channels, D) Optical microscopy (OM) image (488 nm transmittance), E) OM and Channel 1 merged and F) OM and Channel 3 merged.

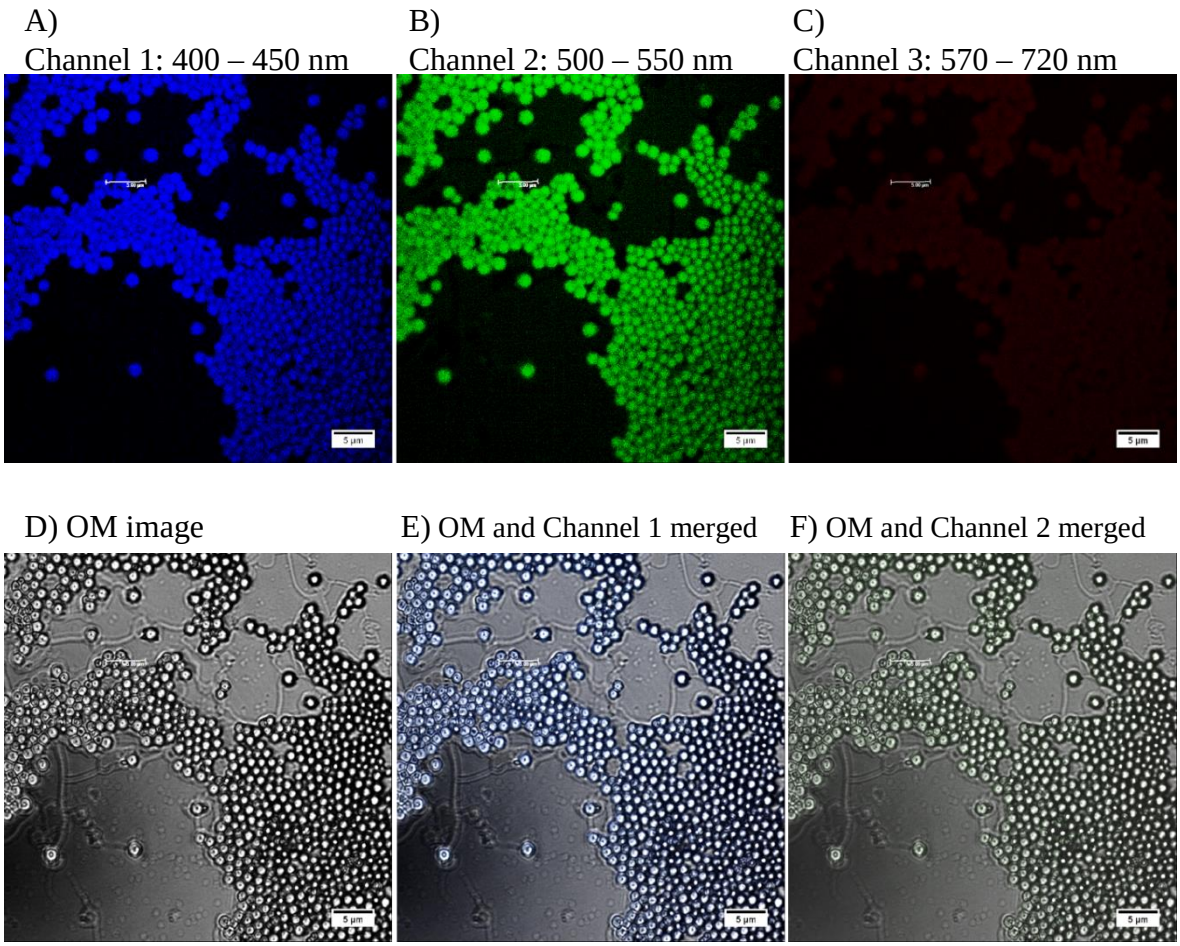

Figure A4.8.2: LSCM images of Tb(III)-**89S** microspheres. A) – C) Tb(III)-**89S** microspheres in three different Channels, D) Optical microscopy (OM) image (488 nm transmittance), E) OM + Channel 1 merged and F) OM + Channel 2 merged.

A) Channel 1: 390 – 500 nm B) Channel 2: 500 – 550 nm C) Channel 3: 570 – 720 nm

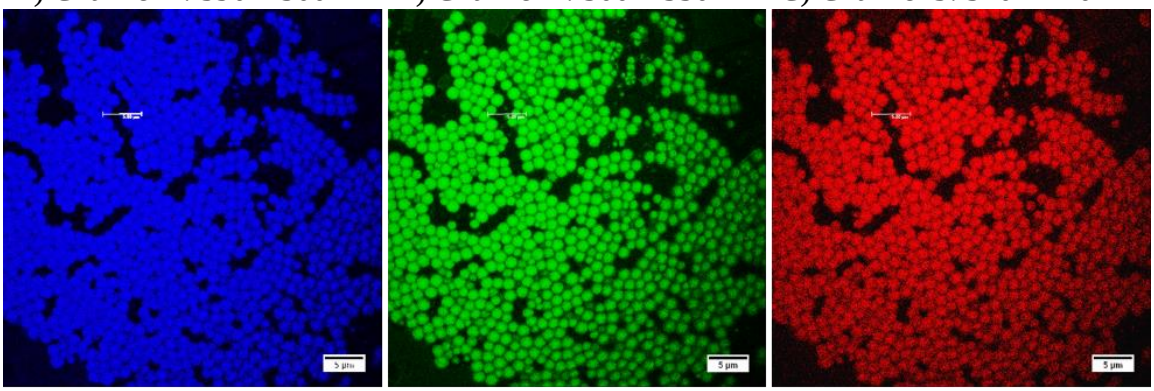

D) Channel 1, 2 and 3 merged E) Channel 2 and 3 merged

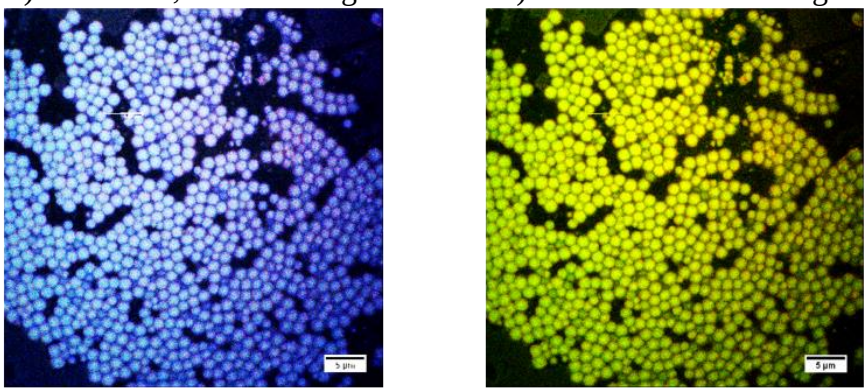

F) OM image G) OM image and Channel 1 merged

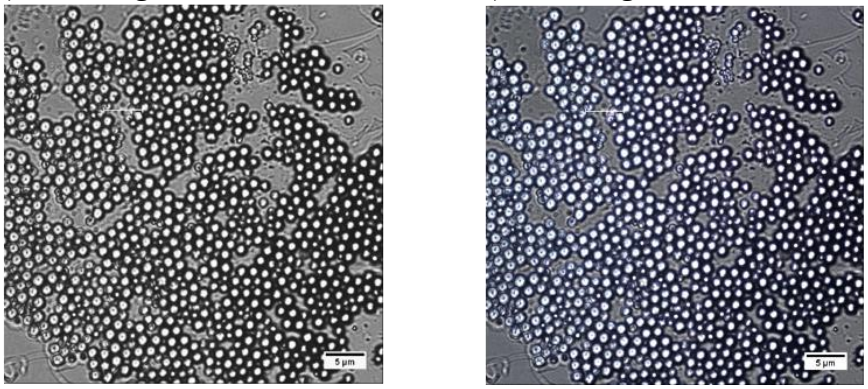

F)

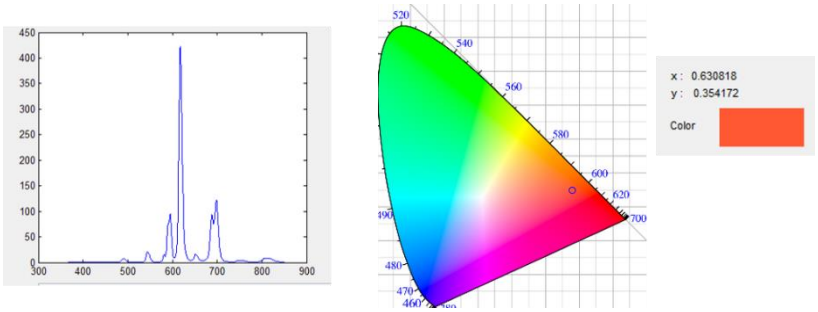

Figure A4.8.3: LSCM images of mixed Eu(III)-Tb(III)-**89S** microspheres. A) – C) Eu(III)-Tb(III)-**89S** microspheres in three different Channels. D) Channel 1, 2 and 3 merged. E) Channel 2 and 3 merged. F) Optical microscopy (OM) image (488 nm transmittance) and G) OM and Channel 1 merged, H) CIE chromaticity diagram of the image E showing orange particle having the coordinates 0.63 and 0.35.

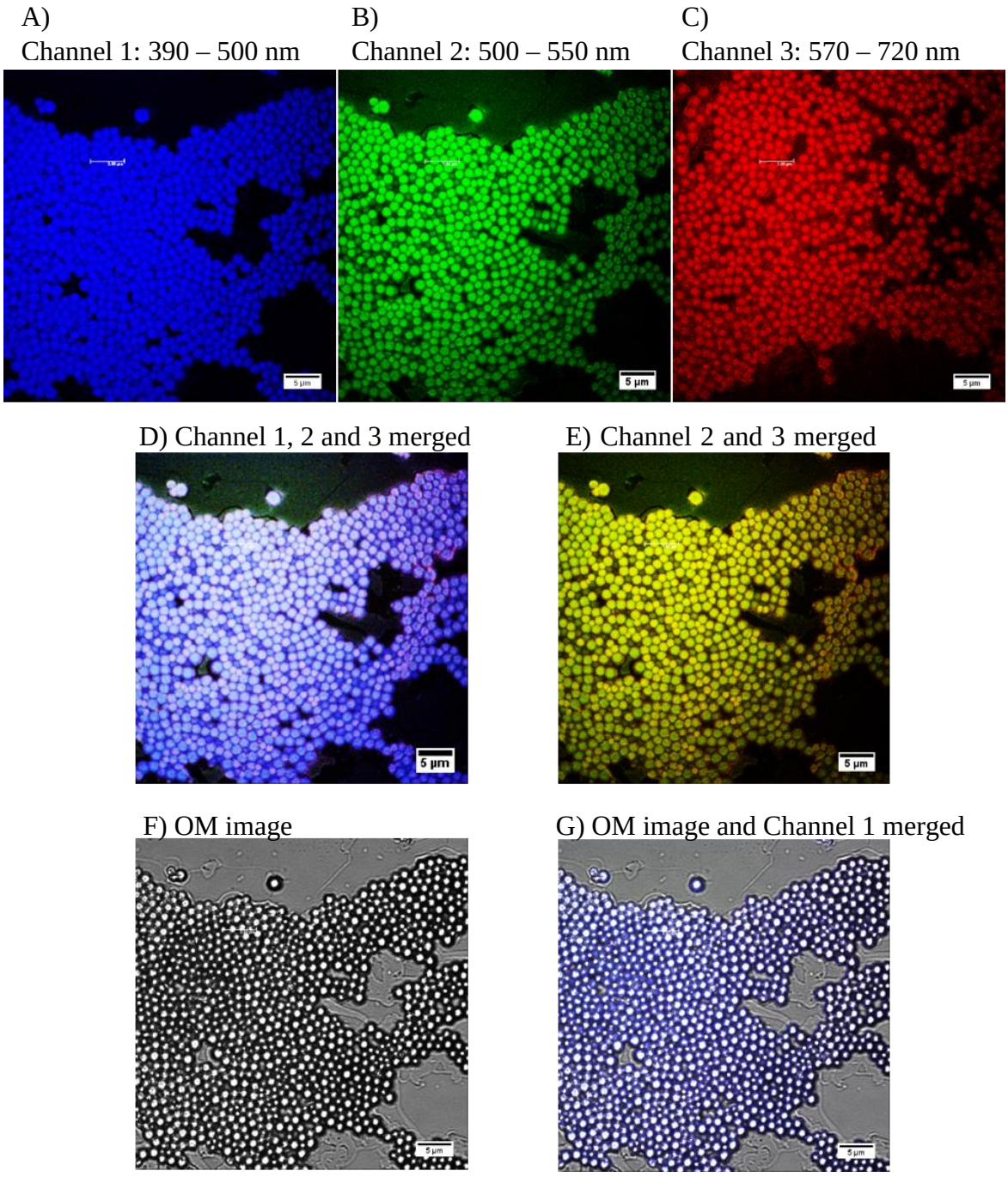

Figure A4.8.4: LSCM images of mixture of Eu(III)-**89S** microspheres and Tb(III)-**89S** microspheres solution. A) – C) images in three different Channels. D) Channel 1, 2 and 3 merged. E) Channel 2 and 3 merged. F) Optical microscopy (OM) image (488 nm transmittance) and G) OM and Channel 1 merged.

A)
Channel 2: 450 – 600 nm

B)
Channel 3: 570 – 700 nm

C)
Channel 2 + 3 merged

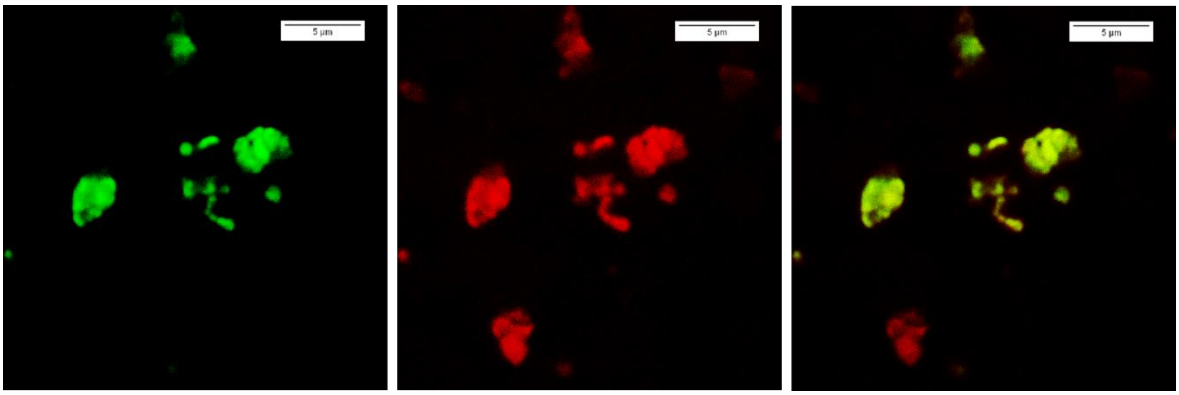

Figure A4.8.5: LSCM images of mixture of Eu(III)-**89S** microspheres and Tb(III)-**89S** microspheres A) and B) images in two different Channels. C) A and B merged

A)

B)

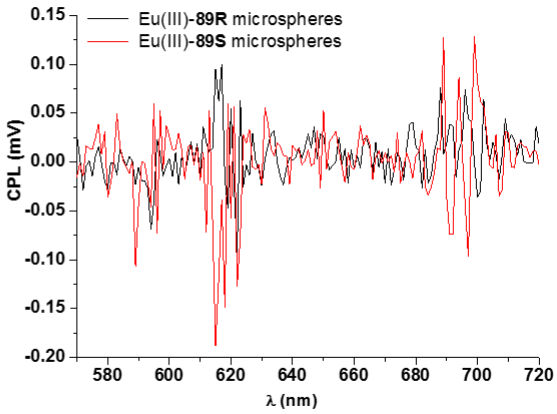

C)

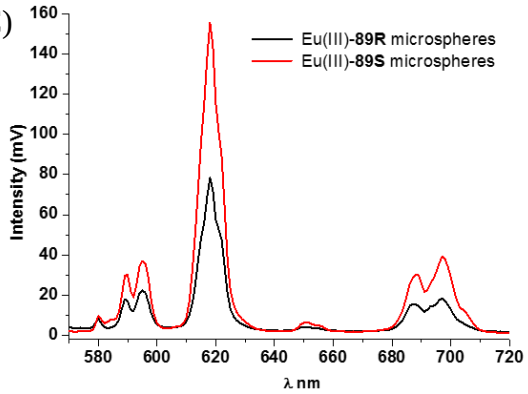

Figure A4.9.1: A) Picture of Eu(III)-**89R** microspheres showing luminescence while measuring CPL in CH_3CN, B) CPL spectra of Eu(III)-**89** (R and S) microspheres in CH_3CN and C) total luminescence spectra.